Evaluation and Optimization of Porous and Hierarchically Porous Materials for Applications in Energy Storage and Conversion

A DISSERTATION
SUBMITTED TO THE FACULTY OF THE GRADUATE SCHOOL
OF THE UNIVERSITY OF MINNESOTA
BY

Nicholas Daniel Petkovich

IN PARTIAL FULFILLMENT OF THE REQUIREMENTS
FOR THE DEGREE OF
DOCTOR OF PHILOSOPHY

Andreas Stein, Advisor

September 2014

Acknowledgements

First, I'd like to thank Prof. Andreas Stein for his insight, guidance, and invaluable help in my journey to become a scientist. He has helped hone my skills as a scientific communicator, and gave me the freedom to explore a diversity of research areas under the aegis of material chemisty. And I need to thank him for the Herculean task of editing the rough drafts of this document.

Several other professors have been generous with their time and support during this process. Their contributions to my learning are massive and they greatly enriched my understanding of areas outside my zone of experise. So, thank you Prof. Jane Davidson, Prof. William Smyrl, Prof. Chris Macosko, and Prof. Lee Penn. It has to be said to Prof. Penn that I owe you for all the X-ray used over my career; thank you for letting me take ~1000 scans on using your PXRD. And I must have used the equivalent of thousands of balloons of He keeping an inert atmosphere in Prof. Smyrl's glove box. The use of your dryroom and glove box was essential for over half my research and I thank you for letting me use them both.

I also would like to thank Prof. Kent Mann and Prof. Wayne Galdfelter for agreeing to be on my committee and helping me at this final stage.

I've had the honor of working alongside an excellent cadre of Stein group scientists during my graduate career. I've been here for a while… so my list is a bit more extensive than most. So, in no particular order, thank you Stephen Rudisill, Ben Wilson, Dr. Melissa Fierke, Jinbo Hu, Camille Malonzo, Siyao He, Dr. David Josephson, Nam Tran, Yuan Fang, Dr. Fan Li, Dr. Nick Denny, Dr. Won Cheol Yoo, Dr. Anh Vu, Dr. Matt Dubay and Dr. Yuqiang Qian. Thank you all so much for your insights, your ability to make me laugh, your commiseration, and helping me grow as a persion.

I've had the good fortune to work with several excellent undergraduate researchers: Daniel Boman, Anwesha Mukherjee, Wenhao Liu, Sammy Shaker, and Clement Chan. They are all continuing onto graduate programs (or intend to continue), and I wish them the best.

Throughout my time at the University of Minnesota, I've been a part of several collaborations and need to thank the other students/postdocs. Luke Venstrom, now an assistant professor at Valparaiso University, deserves special mention. We made a fine team, Luke, and if your teaching of this chemist is any indication, you're going to be a fine teacher. I think that the Autosorb IQ_2 would now be a burning pile of rubble, if not for the help of Myung Seo (alongside Stephen Rudisill and Ben Wilson). Dr. Francis Guillaume helped me with a great many things in the Smyrl lab. And for the graphene oxide composite work (though it is not in this thesis) I have

to thank Yong Tae Park, Taewon Suh, Jerry Yeh, and Dr. Greg Moriarty. Greg's insights and kindness really helped at the end. From Adama Materials, Dr. Frank Thibodeau and Mr. Steve Speak also gave support and offered a wealth of knowledge from industry that will serve me well.

I cannot imagine where I would be without my close friends. I am blessed to have a group of people who have stuck by me for so long… even though I would disappear for weeks under piles of test tubes and papers (figuratively, of course…). To Cliff, Lisa, Whitney, Martin, Jess, Chris, Michael, Laura, Phil, Manley, Stacy, Joe, Renate, and Stacey, you are all amazing and I cannot thank you enough.

And most of all, I'd like to thank my immediate family. They've seen me at my highest and my lowest ebb, and supported me every step of the way. Words fail when I try to describe the gratitude I have for you all. And that's something coming from a person that just wrote a 400+ page document.

Special Acknowledgement for Chapter Three

This chapter contains an analysis of the impedance spectra of various TiO_2-based anodes for lithium-ion batteries. While I carried out the impedance testing, Benjamin Wilson fit the spectra to a model and provided invaluable assistance with the analysis of the fit data. Professor Philippe Bühlmann also provided general guidance for the impedance testing, and assisted by supplying a fitting program to be used with Wolfram Mathematica.

Special Acknowledgement for Chapter Four

This chapter contains an analysis of the impedance spectra of porous tanatalum-doped TiO_2 anodes. Similar to the situation in Chapter 3, Benjamin Wilson fit the collected spectra to a model using a program Professor Philippe Bühlmann wrote for use with Wolfram Mathematica.

Special Acknowledgement for Chapter Seven

This chapter contains an investigation into the H_2 production from 3DOM $Ce_{1-x}Zr_xO_2$. I am extremely grateful for the assistance provided by Luke Venstrom and the University of Minnesota Solar Energy Laboratory. Luke Venstrom (now Professor Luke Venstrom) designed the reactor set-up used for the chemical redox cycling. He also calibrated the mass flow controllers, gas sampling equipment, and determined the sources of error in the reactor. Most cycling experiments were also run by Luke Venstrom. Luke Venstrom also converted the measurements from the gas spectroscopy equipment to gas flow rates, and extracted key fuel production parameters from the data. Both Luke Venstrom and I closely collaborated on analyzing the relationship of various structural features to the H_2 production achieved in various materials. Stephen Rudisill also needs to be thanked for measuring hundreds of pore spacings, pore window diameters, and wall thicknesses from SEM images of the 3DOM materials.

Special Acknowledgement for Chapter Eight

This chapter also contains investigations into H_2/CO production from various materials. Again, this was done in close collaboration with individuals from the University of Minnesota Solar Energy Laboratory. Luke Venstrom designed, calibrated, and ran the reactor for the redox cycling of the praseodymium oxide-based materials. Daniel Boman ran the reactor and analyzed the gas spectrometer data for the chemical redox cycling of the perovskite oxide compound. He also determined the required flow rates of H_2/H_2O need to mirror the reduction of that particular material in inert gas at 1500 °C. Stacey Saba assisted with the integration of the fuel production curves. Luke Venstrom designed the infrared furnace set-up described in the chapter that was used to cycle 3DOM $Ce_{0.8}Mn_{0.2}O_2$. Tingting Quan ran the experiments using that set-up and helped analyze the gas production data.

Abstract

Materials with nm- and μm-scale pores are important in the design of efficient, safe, and versatile energy conversion and storage systems. In the research detailed in this thesis, the synthesis and testing of porous materials for lithium-ion battery anodes and for thermochemical fuel production are explored.

The preparation, modification, and performance of various carbon and transition metal oxide composite materials for lithium-ion battery electrodes are discussed in the first part of this work. Of particular interest are TiO_2/carbon composites that possess a three-dimensionally ordered macroporous (3DOM) structure, and, in some instances, additional mesoporosity. By changing the chelating agent used to stabilize the precursor for TiO_2, crystallites of TiO_2 can either be localized on the surface of the 3DOM structure or buried within the carbon matrix. This positioning has important ramifications for the electrochemical properties of the materials. In addition, the content of carbon in the composite materials can be altered. For carbon-rich composites, improved Li^+ insertion/extraction capacities are attained by changing the voltage window used for cycling. Carbon can also be removed altogether, allowing for the formation 3DOM TiO_2 with good electrochemical properties Conversion of the 3DOM TiO_2 to sodium titanate is demonstrated via the ambient pressure treatment of the 3DOM material in sodium hydroxide. Subsequent ion-exchange with H^+ results in the formation of hydrogen titanate materials with extremely high surface areas. A remnant of the 3DOM structure remains in these materials.

Cerium oxide, praseodymium oxide and perovskite oxide-based catalysts for the thermochemical conversion of solar energy and abundant feedstocks (H_2O and CO_2) into useable fuels (H_2 and CO) are investigated in the second part of this work. All of these materials possess a 3DOM structure and have moderate surface areas intended to improve reaction kinetics. Mixed oxides containing cerium are investigated with the aim of improving the amount of fuel produced, lowering the operational temperature and increasing thermal stability. Initial forays into the praseodymium oxide and perovskite oxide systems are also described, including evaluation of overall fuel production and fuel production kinetics. Special attention is paid to how structural changes during the high-temperature thermochemical reactions affect fuel productivity and kinetics. (351 words)

Table of Contents

List of Tables

List of Figures

Abbreviations and Symbols

°2θ	Degrees two-theta
1D	One-dimensional
2D	Two-dimensional
3DOM	Three-dimensionally ordered macroporous
3DOM/m	Three-dimensionally ordered macroporous with mesoporous walls
Å	Angstrom, unit of distance equal to 1×10^{-10} m
A	Ampere, SI unit of electrical current
a_e	Equilibrium area of a surfactant headgroup on the surface of a micelle
AAO	Anodized aluminum oxide
AC	Alternating current
acac	2,4-pentanedione
ACS	American Chemical Society
AMPD	2,2′-azobis-(2-methylpropionamidine) dihydrochloride
ATR	Attenuated total reflectance
BET	Brunauer-Emmett-Teller
BJH	Barrett-Joyner-Halenda
Brij 56	$C_{16}H_{33}(OCH_2CH_2)_{10}OH$
BTME	1,2-bis(trimethoxysilyl)ethane
BTPN	1,5-bis(3-(triethoxysilyl)propoxy)naphthane
C	Current needed to charge/discharge a battery in one hour (theoretically)
°C	Degrees Celsius (centigrade temperature scale)
CA	Cooperative assembly
CCD	Charge-coupled device

Ce'_{Ce}	Cerium(III) on a Ce site in CeO_{2-x}
Ce^{x}_{Ce}	Cerium(IV) on a Ce site in CeO_{2-x}
CMC	Sodium carboxymethyl cellulose
CSP	Concentrated solar power
CTAB	Cetyltrimethylammonium bromide
CV	Cyclic voltammetry
D	Disordered carbon Raman band
DC	Direct current
DI	Deionized water
e'	Electron defect
E^{θ}	Cell voltage at standard conditions
E_g	Electrolyte stability window
EIS	Electrochemical impedance spectroscopy
EISA	Evaporation-induced self-assembly
eV	Electron volt
F	Farad
$\mathcal{F}$	Faraday's constant
F127	$HO(CH_2CH_2O)_{101}(CH_2CHCH_3O)_{56}(CH_2CH_2O)_{101}H$
FA	Furfuryl alcohol
fcc	Face-centered cubic
FTIR	Fourier-transform infrared spectroscopy
$\Delta G^{\theta}_{H_2O}$	Standard Gibbs free energy of water decomposition
$\Delta G^{\theta}_{OX,H_2O}$	Standard Gibbs free energy of a water splitting step
$\Delta G^{\theta}_{react}$	Standard Gibbs free energy of reaction
ΔG^{θ}_{TR}	Standard Gibbs free energy of the thermal reduction step

g	Gram, SI unit of mass
g	Packing parameter
G	Graphitic carbon Raman band
GO	Graphite oxide
$\Delta H^{\theta}_{f,H_2,OX}$	Standard enthalpy of formation for H_2 at the conditions of the oxidation step
$\Delta H^{\theta}_{f,H_2O,OX}$	Standard enthalpy of formation for H_2O at the conditions of the oxidation step
$\Delta H^{\theta}_{H_2O}$	Standard enthalpy of water decomposition
$\Delta H^{\theta}_{react}$	Standard enthalpy of reaction
ΔH^{θ}_{TR}	Standard enthalpy of the thermal reduction step
h	Hour
HF	Hydrofluoric acid
HIPE	High internal phase emulsion
HOMO	Highest occupied molecular orbital
Hz	Hertz, SI unit of frequency
I	Current
I	Cubic surfactant phases comprised of spherical micelles
I_A	Intensity of anatase reflection in a powder X-ray diffractogram
I_D	Intensity of disordered carbon Raman peak
I_G	Intensity of graphitic carbon Raman peak
I_R	Intensity of rutile reflection in a powder X-ray diffractogram
IH	Inhomogeneous
IR	Infrared
IUPAC	International Union of Pure and Applied Chemistry
J	Joule, SI unit of energy
k	Kilo ($\times 10^3$)

K	Kelvin (Kelvin temperature scale)
KPS	Potassium persulfate
L_a	Graphite domain size
l_o	Surfactant tail chain length
LCT	Liquid crystal templating
LIB	Lithium-ion battery
Ln'_{Ce}	Lanthanoid(III) on a Ce site in CeO_2
LUMO	Lowest unoccupied molecular orbital
M	Molarity (molar concentration in moles·L^{-1})
m	Meter
MMA	Methyl methacrylate
m (prefix)	Milli ($\times 10^{-3}$)
min	Minute
MIPO	Micromolding in inverted polymer opals
mol	Number of moles
mol%	Mole percent of a component
MSS	Methanolic salt solution
n (prefix)	Nano ($\times 10^{-9}$)
n	Number of electrons transferred
NAC	No added carbon
$Nb^{\cdot}_{Ti}$	Niobium(V) on a Ti site in a TiO_2 lattice
O_h	Octahedral node
O^{x}_{O}	Doubly charged oxygen on a O site
P123	$HO(CH_2CH_2O)_{20}(CH_2CHCH_3O)_{70}(CH_2CH_2O)_{20}H$
$p(O_2)$	Partial pressure of oxygen
P/P_o	Relative pressure

Pa	Pascal, SI unit of pressure
PDDA	Poly(diallyldimethylammonium)
PEO	Poly(ethylene oxide)
PF	Phenol-formaldehyde
PFA	Poly(furfuryl alcohol)
PM	Pechini method
PMMA	Poly(methyl methacrylate)
PPO	poly(propylene oxide)
PS	Polystyrene
PU	Polyurethane
PXRD	Powder X-ray diffraction
q	Charge
Q	Heat
Q_{totsl}	Total gas flow rate
QSDFT	Quenched solid density functional theory
r_A	Radius of the A-site cation
r_B	Radius of the B-site cation
r_O	Radius of the oxide ion
RBF	Round bottom flask
RH	Relative humidity
RPM	Revolutions per minute
RT	Room temperature
$S^{\theta}_{H_2,OX}$	Standard entropy of hydrogen at the conditions of the oxidation step
$S^{\theta}_{H_2O,OX}$	Standard entropy of water at the conditions of the oxidation step
$S^{\theta}_{O_2,TR}$	Standard entropy of oxygen at the conditions of the thermal reduction step

$\Delta S^{\theta}_{H_2O}$	Standard entropy of water decomposition
$\Delta S^{\theta}_{react}$	Standard entropy of reaction
ΔS^{θ}_{TR}	Standard entropy of the thermal reduction step
S	Siemens, SI unit of electric conductance
S.A.	Surface area
SAED	Selected area electron diffraction
SAXS	Small-angle X-ray diffraction
SBR	Styrene–butadiene rubber
SEI	Solid-electrolyte interphase
T	Temperature
t	Time
t	Tolerance factor
T1	Sample thermocouple
T2	Control thermocouple
T_d	Tetrahedral node
T_{ox}	Oxidation temperature
$Ta^{\cdot}_{Ti}$	Tantalum(V) on a Ti site in a TiO_2 lattice
TEM	Transmission electron microscopy
TEOS	Tetraethyl orthosilicate
TFA	Trifluoroacetic acid
TGA	thermogravimetric analysis
THF	tetrahydrofuran
TNT	2,4,6-trinitrotoluene
ΔU	Change in potential energy
UV	Ultraviolet

V	Volt, SI unit of electrical potential
V_1	Bicontinuous cubic surfactant phases
V_{OC}	Open circuit voltage
$V_{\ddot{O}}$	Doubly-ionized oxygen vacancy
W	Watt, SI unit of power
W_A	Weight fraction of anatase
W_R	Weight fraction of rutile
W_{out}	Work done on the surroundings
wt%	Weight percent of a component
XPS	X-ray photoelectron spectroscopy
y_{H2O}	Mole fraction H_2O
σ	Warburg coefficient
η	Efficiency
Φ_A	Anode work function
Φ_C	Cathode work function
μ (prefix)	micro ($\times 10^{-6}$)
μ_A	Anode chemical potential
μ_C	Cathode chemical potential
Λ_G	Gravimetric energy density
Λ_V	Volumetric energy density
v_o	Volume of hydrophobic tail
Ω	Ohm, SI unit of electrical resistance

Chapter One

Introduction to Energy Storage in Lithium-Ion Batteries and Energy Conversion via Solar Thermochemical Fuel Production

1.1 Overall Motivation

While he was not the first scientist to consider the effect of atmospheric gases on the temperature of the Earth, Svante Arrhenius was one of the first to offer an analysis of how the absorption of infrared (IR) radiation by varying atmospheric CO_2 concentrations could change global temperatures and humidities.[1] Arrhenius also considered that variations in CO_2 may have contributed to beginning and end of the last glacial period. A friend of Arrhenius, Prof. Arvid Högbom, had investigated what contributed to the release of CO_2 into the atmosphere and what processes removed CO_2 from the atmosphere. Högbom and Arrhenius both concluded in 1896, based on Högbom's analysis of the global CO_2 cycle, it was possible (and even likely) that fluctuations in atmospheric CO_2 content contributed to glaciation and deglaciation.[1] Later research showed that they were not strictly correct; however, changes to global patterns in solar irradiance at the end of the last ice also triggered an increase in the concentration of atmospheric CO_2.[2] This increase in CO_2 emissions is thought to have contributed to the temperature rise that ended the ice age, just as Arrhenius and Högbom had proposed. Unfortunately, Arrhenius and Högbom were incorrect about another critical factor in the interplay between CO_2 and average temperatures. Both researchers knew that the combustion of coal contributed to atmospheric CO_2, but they believed anthropogenic sources of CO_2 did little to alter surface temperature.[1] If fossil fuel use had continued at that level, they may have been correct. How could they foresee that the fossil fuels would play a key part in widespread electrification of cities, allow for revolutionary advances in human transportation, enable the production of key chemicals, and assist in agricultural revolutions that helped dramatically increase the human population? One thing is certain: Arrhenius would have been easily able to realize that an atmospheric CO_2 concentration of 400 ppm—a level reached which was reached in 2013—could have an impact on global temperatures.

Climate science has progressed greatly since Arrhenius published "On the Influence of Carbonic Acid in the Air on the Temperature of the Ground," and much of it is focused on the impact that anthropogenic greenhouse gas emissions have on the global climate. Sophisticated models and scenarios predict that rising sea and surface temperatures will continue through the 21st century, and continued fossil fuel combustion will be a key driver of this change.[3-5] The Fifth Assessment Report of the Intergovernmental Panel on Climate Change determined that there is a greater than 95% likelihood that human activities are responsible for rising surface temperatures.[6] Unfortunately, emissions of CO_2 and other IR absorbing greenhouse gases have increased from the 1970 to 2010, and this trend is unlikely to reverse for at least several decades.[7] Researchers

have gathered information from the latest climate models and emissions scenarios, and plotted how far mean monthly temperatures will deviate from the historical mean of a given month for the years 1961 to 1990.[8] They modeled these divergences for the most important terrestrial and freshwater ecosystems as identified for the World Wildlife Foundation (the Global 200). If the models and scenarios prove to be accurate, temperature deviations of more than two standard deviations (σ) from the historical baseline occur for most of these key ecosystems by 2070 (Figure 1.2).[8] The overall rise in temperatures will likely have a major impact on every aspect of life on Earth. Since temperature rises will impact many of Earth's most diverse and threatened ecosystems, a rapid decline in the number of species on the planet, a "state shift," may occur within this century.[9] Loss of biodiversity could have serious consequences for the discovery of novel plant-based pharmaceuticals,[10] and for the stability of agricultural systems. Food scarcity is likely to increase for the poorest and most vulnerable populations on the planet due to climate change-related agricultural disruptions.[11] Certain infectious diseases of both humans and other organisms will become endemic over much larger areas of the planet.[12] Even if the climatic changes are not as dire as predicted, easily extractable sources of petroleum will dwindle.[13] This could cause economic shocks for many industries that are dependent on petroleum, leading to substantial changes in how fossil fuels are refined.[14] It is not surprising that economists have argued that ignoring the massive risk of global climate change and depletion of certain fossil fuel resources would be extremely foolhardy.[15-17] Indeed, organizations from the United States Government Accountability Office[18] to the World Bank[19] have begun to draft climate change adaptation strategies.

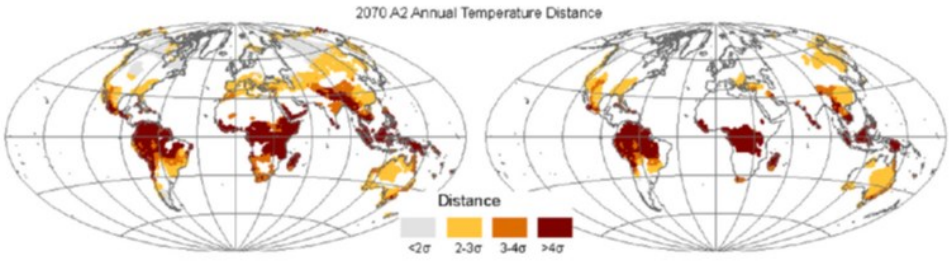

Figure 1.1 Maps showing how far the projected mean monthly temperature for a given region diverges from the historical monthly mean temperatures for the period between 1961 and 1990. Tropical ecosystems are the hardest hit by temperature increases, experiencing projected mean monthly temperatures >4σ higher than the historical mean. The regions analyzed at left include key terrestrial ecosystems, while the regions analyzed at right include key freshwater ecosystems. Image adapted from [8] © 2011 National Academy of Sciences, USA.

Faced with such dire predictions, it is easy to become apathetic and simply ignore the problem, deeming it too massive, too complex, too intractable to solve. However, there is still time to mitigate the impact of climatic changes and to reduce our reliance on fossil fuels.[7] Advancements in science and technology will play an essential role in our response to global climate change. It is unlikely that a single technology or cluster of technologies will be all that is required to adequately curb climate change or transition to a civilization that no longer requires fossil fuel. Instead, it is far more probable that a variety of discoveries and developments will be needed.[20] Considerable research activity (spanning multiple disciplines) is currently focused on key several areas. First, there is a massive push to improve existing systems for generation of renewable (solar, wind, tidal, biomass, etc.) electricity or heat.[21] Second, several major projects are underway for the development of exotic methods for sustainable electricity generation, such as controlled fusion power or space-based solar power.[20,22] Third, it is well-established that many existing technologies and processes can be made more efficient, potentially reducing energy use in the United States, for instance, by 30% below the "business-as-usual" scenario.[23] While some of these improvements can be made using existing technologies, e.g., adoption of solid-state lighting, ongoing research is required in multiple areas, such as the recovery of waste heat.[24] Fourth, various methods to sequester CO_2 are under active investigation.[25,26] Finally, energy storage technologies are under increasing research scrutiny. This is being done in part to address problems with the intermittency of various renewable energy sources, and to aid the development of less CO_2 intensive means for transportation (like electric vehicles).[27,28] Even though the use of fossil fuels is by no means going to stop in the coming decades, advances made in the five areas described above will offset fossil fuel use and provide a path to a civilization less reliant on fossil fuels.

This thesis describes research studies that explore novel materials with deliberately engineered structures intended to improve methods of energy storage or conversion. Two specific means of energy storage/conversion are considered: lithium-ion batteries and the solar thermochemical production of fuels (H_2 and syngas). Both of these energy storage methods have the potential to substantially reduce emissions from fossil fuels. For instance, advanced lithium-ion batteries could be used to store megawatts of renewable electricity. Thermochemically-synthesized hydrogen gas could find use in fuel cells for vehicles that only produce water as a by-product. Before moving to an outline of the research described in this thesis, it is important to give a background of the two energy storage methods that lie at the heart of this work.

1.2 Lithium-Ion Battery Fundamentals

Rechargeable or secondary batteries represent a large family of electrochemical storage devices that are capable of reversibly storing and discharging electricity via reduction-oxidation reactions. In general, secondary batteries are more expensive, store less energy per unit mass/volume, and are worse at retaining their state of charge than non-rechargeable batteries.[29] However, the ability of secondary batteries to be repeatedly charged and discharged offsets any initial expense. Some of these batteries can also be charged and discharged very quickly, providing high power per unit mass/volume.[30] While many different types of secondary battery have been commercialized, the remainder of this introduction focuses on lithium-ion batteries. Aside from the importance of this type of secondary battery for the research described in this thesis, lithium-ion batteries are also widely used in portable consumer electronics, power tools, uninterruptable power supplies, and electric vehicles. The increasing dominance of lithium-ion batteries in the secondary battery market lies in the fact that lithium-ion batteries are better than most other types of secondary batteries in key performance metrics.[30] Of particular note is that lithium-ion batteries can store a large amount of energy per unit mass/volume, can be charged and discharged over 1000 times without experiencing a significant degradation in performance, and can sit unused for months without losing much stored charge.[30,31] That being stated, improvements are still needed for these batteries, especially with regards to their safety and further increasing their ability to store large amounts of charge.[32,33] This section serves as a basic introduction to lithium ion batteries and their operation. Furthermore, a discussion of some of the challenges facing lithium-ion batteries and means to resolve these challenges is presented.

1.2.1 The Lithium-Ion Cell

When discussing lithium-ion batteries, it is helpful to first describe the basic element present in these batteries, a lithium-ion cell. A lithium-ion cell consists of various components that are shown in Figure 1.2. As is the case for any electrochemical cell, two electrodes, the anode and the cathode, are present in the cell. These electrodes are generally composites made from active material particles, conductive carbon particles, and a polymeric binder that holds the composite together. When discharging the cell, an oxidation half-reaction occurs at the anode, releasing electrons and lithium ions. In the cathode, a reduction half-reaction occurs that consumes electrons and lithium ions. Thus, electrons and lithium ions flow from anode to the cathode during discharge. During charging, an external power source is used to supply the energy needed to operate the cell in reverse, causing electrons and lithium ions to flow from the cathode (now

the site of the oxidation half-reaction) to the anode (now the site of the reduction half-reaction). To ensure that electrons flow in the exterior circuit and do not simply cross from the anode to the cathode, the transport of electrons and ions needs to be decoupled. If this does not occur, a large current will develop in the cell itself, and heat will be generated instead of useful work. A porous, electrically-insulating polymeric separator is commonly used to separate the anode from the cathode. A liquid electrolyte is also present in the cell that typically is comprised of a lithium salt (like $LiPF_6$ and $LiBF_4$) that is dissolved in an organic carbonate solvent.[32] While lithium ion conduction is reduced in the organic electrolyte when compared to an aqueous electrolyte, organic electrolytes allow for greater operating voltages, higher energies per unit mass/volume, and a much wider range of suitable electrode materials.[34]

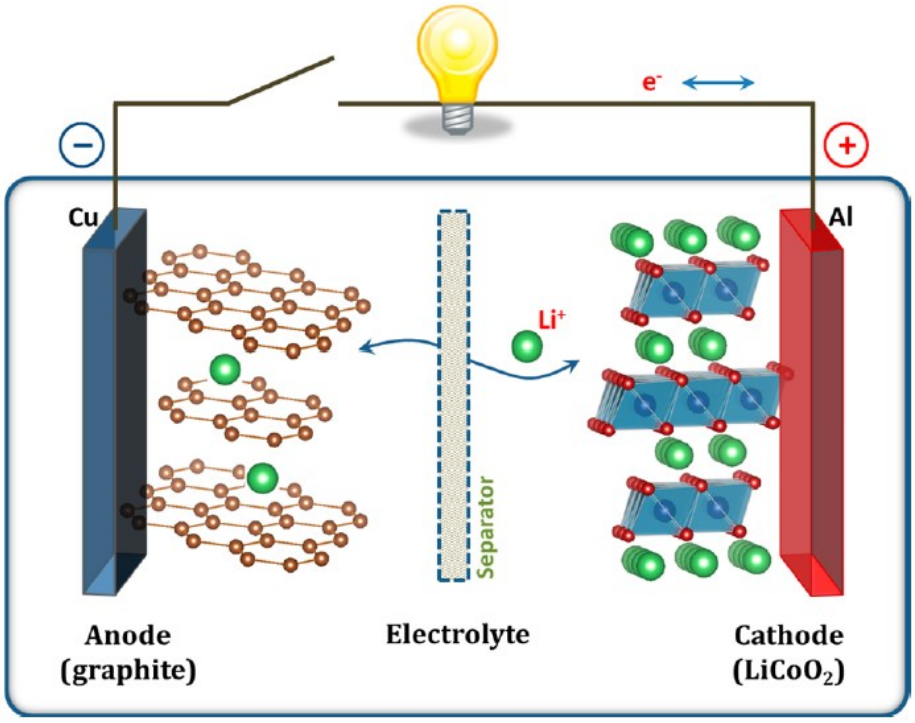

Figure 1.2 Diagram of a lithium-ion cell. The graphite anodes and $LiCoO_2$ cathodes are commonly used in cells that power consumer electronics. Copper and aluminum are used as current collectors due to their electrochemical stability at the anode and cathode, respectively. Image reproduced from [33] © 2013 American Chemical Society.

1.2.2 Basic Thermodynamics and Kinetics of Lithium-Ion Cells

Maier makes a useful analogy to another form of energy storage that is instructive in understanding how the lithium-ion cell operates from a thermodynamic perspective.[35] Figure 1.3 shows a schematic of this analogy, which compares pumped hydroelectric storage to a lithium-ion cell. For pumped hydroelectric storage (Figure 1.3 a), gravitational potential energy can be stored by pumping water from a lower elevation to higher one, and the amount of energy stored can be expressed using the simple relation $\Delta U = m \cdot g \cdot h$. In this equation ΔU is the change in potential energy, m is the mass of water pumped uphill, g is the acceleration due to Earth's gravity (at the surface), and h is the height the water is pumped. When this energy is needed, it can be utilized letting the water flow downhill and power turbines at a hydroelectric dam. A lithium-ion battery contains two electrodes with different chemical potentials. During charging, one can envision transferring neutral Li atoms (lithium ions and electrons) from the electrode with a lower chemical potential (α) to one with a higher chemical potential (β) (see Figure 1.3 b).[35] Work is required for this process, which (in an ideal case) needs to be equivalent to the change in the Gibbs free energy given by equation 1.1.

$$\Delta G^{\theta}_{react} = -n\mathcal{F}E^{\theta} \qquad (1.1)$$

In equation 1.1, n is the number of electrons transferred, $\mathcal{F}$ is Faraday's constant, and E^{θ} is the voltage of the cell at standard conditions. When discharging, lithium is returned to the electrode with a lower chemical potential. Equation 1.1 then gives the theoretical maximum useful work that can be extracted from the cell. Overall, the efficiency of the process can be given by equation 1.2.

$$\eta = \frac{\Delta G^{\theta}_{react}}{\Delta H^{\theta}_{react}} = 1 + \frac{T \cdot \Delta S^{\theta}_{react}}{|\Delta H^{\theta}_{react}|} \qquad (1.2)$$

Since this process does not involve heat transfer, efficiencies can approach 100 %.[29,35] However, in real cells irreversibilities do arise from heat losses that occur since the cell cannot be operated in a purely reversible manner (current has to flow during charge/discharge).[36]

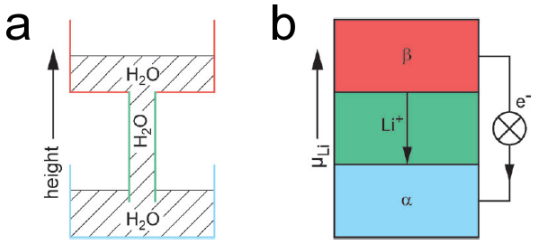

Figure 1.3 Diagram of (a) pumped hydroelectric storage and (b) a lithium-ion battery. With pumped hydroelectric storage, water is transferred from a lower elevation to a higher elevation for storage. This water is returned to a lower elevation when it is needed to drive turbines for the production of electricity. In a lithium-ion battery, during charging, neutral Li is brought from an electrode (α) into an electrode (β) that has a higher μ_{Li}. When discharging, Li is returned to electrode α, and e^- is sent through an external circuit doing useful work. Image adapted from [35] © 2013 John Wiley & Sons.

Several key considerations in the design of lithium-ion cells can be understood by further taking into consideration the thermodynamics and how it relates to several other key parameters. Goodenough and Kim helpfully sketched the energy diagram for a general electrochemical cell (Figure 1.4).[34] In the diagram, Φ_A and Φ_C, are the work functions for anode and cathode, while μ_A and μ_C are electrochemical potentials of the electrodes. The green box represents the electrochemical stability window for the electrolyte with E_g being the energy difference between the highest occupied molecular orbital (HOMO) and the lowest unoccupied molecular orbital (LUMO) of the electrolyte. Provided that the electrochemical potential of the anode remains below that of the HOMO of the electrolyte and the potential of the cathode is above that of the LUMO of the electrolyte, the battery can be stably charged and discharged with a given open circuit voltage, $V_{OC} = \mu_a - \mu_c$ (which is equal to E^θ above).[34,37] For anodes and cathodes that lie outside the E_g window, it is still possible to repeatedly charge and discharge the combined cell. However, a layer of decomposed electrolyte, called the solid electrolyte interphase (SEI), has to be formed.[34] This layer allows for ionic transport from the electrolyte to the electrode, but prevents electronic transport that can further degrade the electrolyte.[38] As can be observed in Figure 1.4, the SEI provides an additional range to the window of stability, but it is kinetic in origin. Later in this thesis, half-cells are analyzed that contain an active electrode (a cathode) and a lithium counter electrode (an anode). Their operation is only possible because a stable SEI can form on the counter electrode, since the Li/Li^+ redox couple lies outside E_g.[34] It should also be noted that one can use the open circuit voltage and the theoretical amount of charge that can be stored per unit mass to determine the theoretical specific energy for a cell (Λ_G, or the gravimetric

energy density). The same can be done using the theoretical maximum amount of charge that can be stored per unit volume (Λ_V) to get the volumetric energy density. Using these quantities, the specific energy is equal to $\Lambda_G \cdot V_{OC}$ and the volumetric energy density is equal to $\Lambda_v \cdot V_{OC}$. For situations where the current does not conform to this thermodynamic limit, the equations (1.3 and 1.4) listed below can be used.

$$q = \int_0^{\Delta t} I dt \qquad (1.3)$$

$$\text{Specific Energy} = \int_0^{\Delta t} IV(t)\, dt/m \qquad (1.4)$$

In these equations, q is the total charge transferred, I is the current, V(t) is the voltage as a function of time, and m is the mass of the electrode. An analogous equation to 1.4 can be written for the volumetric energy density.

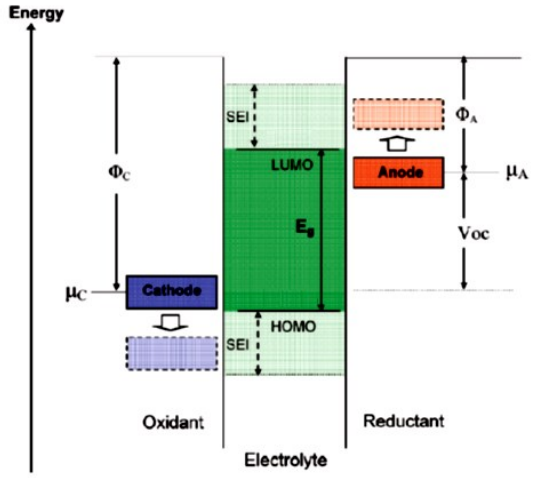

Figure 1.4 Energy diagram for an arbitrary battery. Work functions and chemical potentials are given for the anode (Φ_A, μ_A) and cathode (Φ_C, μ_C). E_g is the window of voltages in which the electrolyte is stable. While the chemical potentials of the anodes and cathodes should lie in E_g for strict thermodynamic stability, a window of kinetic stability can exist outside E_g. Image adapted from [34] © 2010 American Chemical Society.

In addition to the SEI, several other kinetic considerations are of particular importance for lithium-ion cells. These kinetic effects are commonly grouped into three interrelated "polarizations" that alter the performance of the cell when compared to its theoretical maximum.[36,39] Polarizations, in this sense, are deviations from V_{OC} that stem from the various kinetic effects. All of the polarizations cause part of the useful work of the cell to be released as waste heat, thus lowering the overall efficiency of the conversion from chemical potential energy

to electricity.[40] One polarization is termed the Ohmic or *iR* polarization. This polarization arises from a combination of the many internal resistances present in the cell, which includes contributions from electrical, ionic, interfacial resistances. Ohmic polarization also scales with the current of the cell, following Ohm's law.[39,40] Another polarization is the activation polarization, and, as can be inferred from the name, it arises from the charge-transfer reactions occurring at the electric double layer surrounding the electrodes.[36] Full treatments of the activation polarization can be found in standard electrochemistry texts.[41] Finally, a polarization, the concentration polarization, arises from diffusion limitations of electronic and ionic species in various components of the cell. Mass transport limitations can arise from the transport of Li^+ in the electrolyte to the electrode surface, and also from solid state diffusion within the electrodes.[39,40] Addressing mass transport limitations in certain electrode systems is a major component of this thesis.

1.2.3 Lithium-Ion Electrode Materials and Mechanisms

With a basic thermodynamic and kinetic framework of lithium-ion cells in place, the general types of lithium-ion electrode material can be described. There are different ways of grouping these lithium-ion electrode materials, and unified approach is adopted in this section. It is easiest to first categorize electrode materials by their structural similarities (Figure 1.5 a).[42] Once that is done, it is important to consider the underlying storage mechanisms that occur in these groupings (Figure 1.5 b). However, it should be stated that these delineations are a bit blurrier than is shown, and the reason for this is discussed below. The first part of this subsection focuses solely on intercalation compounds, since most storage mechanisms can occur in these materials and the research discussed in this thesis is concerned only with intercalation compounds. A second, shorter part considers the two other groupings.

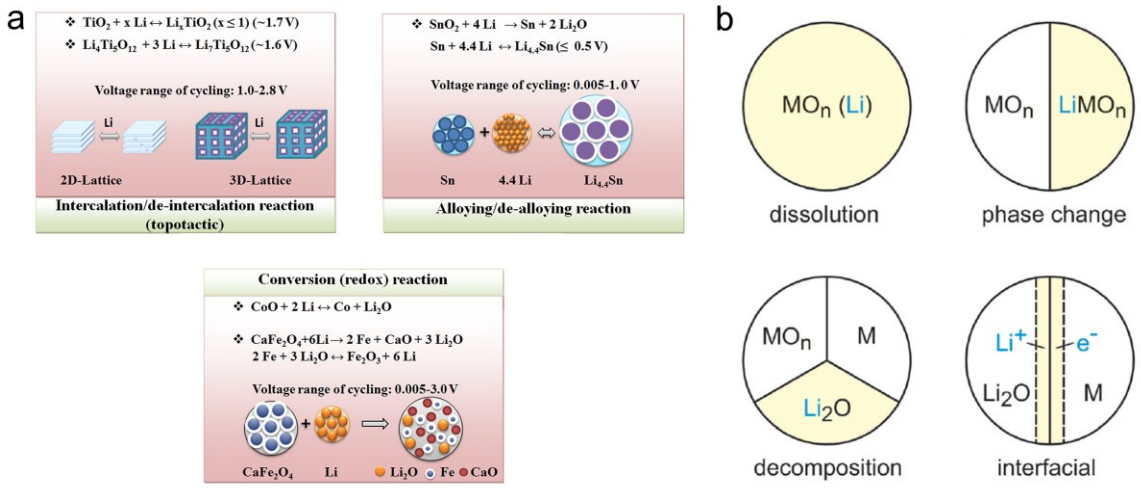

Figure 1.5 The (a) three major types of electrode material from a structural prospective, and (b) the four major mechanisms for Li^+ charge storage. Image (a) adapted from [42] © 2013 American Chemical Society and image (b) adapted from [35] © 2013 John Wiley & Sons.

Starting with the first category in Figure 1.5 a, intercalation compounds are crystalline materials that contain crystallographic sites for lithium insertion and extraction. Two-dimensional (2D) hosts possess layered structures, and Li^+ is intercalated/de-intercalated from interlayer spaces present in these structures. Graphite and $LiCoO_2$–the most popular lithium ion battery anode and cathode materials, respectively–are examples of 2D hosts.[33] Three-dimensional (3D) hosts lack a layered structure, and so Li^+ is inserted and extracted from vacant sites in the host. Many of these structures contain one-dimensional empty channels (including various spinel structures) that allow for Li^+ transport.[34] Insertion and extraction of Li^+ from intercalation compounds takes place via the first three mechanisms shown in Figure 1.5 b.[35,43] First, a dissolution mechanism can take place, in which the parent crystal structure is preserved during Li^+ insertion/extraction. Changes in the population of point defects in the structure do occur, and a solid solution is formed with the added Li ions.[35] During this dissolution process, the voltage of the cell continuously changes. Second, a phase change mechanism can occur that typically involves the formation of a Li-poor and Li-rich phase. This generally occurs with an interface developing in individual crystals, but the phase change can also occur such that crystals with different extents of lithiation co-exist in a particular electrode.[43] While the compositions of Li-poor and Li-rich phases do not change, the relative amounts of each phase do change.[35] Additionally, the chemical potential of lithium also remains constant during this process, and the voltage of the cell remains invariant. Finally, an interfacial charge storage mechanism can arise in

certain materials. Often this mechanism termed intercalation pseudocapacitance, since it involves Li^+ insertion/extraction redox reactions at the electrode-electrolyte interface.[44] Intercalation pseudocapacitance is associated with a cell voltage that changes during operation because of the adsorptive processes that govern the mechanism.[45] Since it occurs at an interface, the kinetic limitations of solid-state diffusion of Li^+ is removed, allowing for rapid charge/discharge kinetics.[46] For a given intercalation compound, multiple charge storage mechanisms can contribute to the overall capacity of a cell. Depending on the extent of lithiation, many compounds transition from dissolution mechanisms to phase change mechanisms.[35] Increasing the interfacial surface area can also cause a shift to Li^+ insertion/extraction dominated interfacial charge. Some authors have called this "extrinsic pseudocapacitance" because it requires that a material is structured at the nanoscale, which is often achieved only through deliberate materials engineering.[46]

Intercalation compounds were the first compounds to be commercialized for lithium-ion battery electrodes; however, two other important classes of compounds exist. Lithium alloys represent a large class of intermetallic compounds that are formed by the insertion and extraction of Li^+ into metals and metalloids. Unlike the insertion compounds, which generally involve the insertion/extraction of up to one lithium per formula unit (or in rare cases two), multiple lithium units can be inserted/extracted from the alloys.[47] As a result, lithium alloys are capable of having extremely high capacities. Uniformly, these types of electrodes insert and extract Li^+ at very low voltages when compared Li/Li^+ and only find use as anode materials.[42] Both dissolution and phase change mechanisms can occur in the alloy materials. Displacement of a particular component of an alloy (such as Cu_6Sn_5 and SnO) can also occur, resulting in a flat voltage profile.[48] Due to the formation of multiple intermetallic phases, multiple phase change events occur. These processes are also accompanied by considerable volume changes that can pulverize electrode particles unless materials are specifically engineered to avoid that problem.[47] Conversion compounds undergo even more dramatic changes than lithium alloys. These compounds (MX_n, where M is a transition metal and X is anionic species) decompose into nanoscale metal particles inside a lithium salt matrix (Li_nX) upon insertion. The parent material is then regenerated during lithium extraction.[49] In many cases, this decomposition is irreversible due to the lack of adequate interfacial area between the metal particles and the lithium oxide (or Li_nX) matrix. It is only possible to reverse the decomposition, if the metal particles have nanoscale dimensions.[49] Most conversion electrodes, including transition metal oxides, are used as anodes, undergoing conversion below 1 V vs. Li/Li^+. However, certain fluoride compounds can be used

as cathodes.[50] Unlike alloys, conversion electrodes are not used in commercially-available lithium-ion batteries.

1.2.4 Improving Lithium-Ion Batteries

As lithium-ion batteries are considered for use as stationary power storage units for the electrical grid and for electric vehicles with long ranges, several key improvements to these batteries must be made.[28,32] First, the safety of lithium-ion batteries needs to be improved, especially since large batteries with a multitude of cells are required for advanced applications. Second, the specific energy and volumetric energy density of these batteries need to be dramatically increased. Finally, the amount of energy that can be extracted or stored in a given period of time, i.e., the specific power/volumetric power density, should be increased. The last two challenges are interrelated and strategies have been devised that simultaneously tackle each difficulty. This subsection addresses each of the three challenges in turn, with a special focus on safer anodes and engineering materials with nanoscale dimensions.

Though perfect conversion of the chemical potential to electricity would not generate heat, various kinetic limitations lead to the generation of waste heat, especially when high currents are used. Since lithium-ion batteries often contain a flammable solvent in the electrolyte and flammable components in their casings, heating and thermal runaway is extremely dangerous situation. While a major means of improving the safety of any battery is by engineering electronic control systems that regulate the connected cells,[29] these systems will not be discussed. Another means to improve safety is to change the material characteristics of the various components of the lithium ion cells. Significant research efforts have been directed at reducing the flammability or extending the voltage window over which an electrolyte is stable with respect to degradation.[32] Additives can also be placed in an electrolyte that increase the thermal stability of a solvent, or can improve the stability of the SEI that forms on electrodes. Alternate electrolyte systems have also been explored, including ionic liquid, polymeric, and inorganic electrolytes that are far less flammable than carbonates.[34] Improving the electrolyte is especially important for cathodes, since these electrodes can operate outside the electrochemical stability window for many organic electrolytes. In most cases, a stable SEI cannot be formed on cathode materials, which means changes to the electrolyte are the only means of preventing unsafe operating conditions.[34] Some success has been achieved at preventing dangerous side reactions by coating cathodes with inorganic compounds.[28,31] This has also helped the safety of cathodes designed to operate at elevated temperatures. Most anodes, in contrast, can form a fairly stable SEI. Unfortunately,

lithium plating can still occur on the SEI layer in anode materials, and this can lead to dangerous short circuits. One remedy has been to consider alternate oxide materials that operate at higher voltages vs. Li/Li^+, thus staying in the stability window of the electrolyte.[42] Titanium dioxide has a capacity comparable to graphite anodes, and is an attractive candidate anode that is explored in this thesis. An extended discussion of TiO_2 anodes can be found in the introduction of Chapter 3.

Energy density concerns for lithium-ion batteries are at the forefront of discussions about how to make electric cars more attractive, and have been held up as a key metric for battery research by the United States Department of Energy.[28] One strategy for improving energy densities is through the discovery of new electrode materials for the lithium-ion cells that comprise lithium-ion batteries. This strategy is most important for cathode materials,[51] since lithium alloy anodes exist with extremely high specific energies and volumetric energy densities.[47] Since new cathodes are not a focus of this thesis, only a few comments should be made. First, part of the discovery process is focused on finding cathodes with suitable redox couples that allow for Φ_C/μ_C to be as high as possible, but within the stability window of the electrolyte.[34] Second, some promising cathode materials have a μ_C slightly outside the range of typical electrolytes, so this search is also liked to discovery of better electrolytes and additives.[31] Third, tailoring the covalency and ionicity of M–O or M–X bonds in the cathode can adjust μ_C or stability for certain compounds. For instance, increased covalency in oxide cathodes can shift the energy of O-2p bands, avoiding a situation in which the cathode material begins to evolve oxygen at sufficiently high voltages vs. Li/Li^+.[34] Part of this search has also focused on compounds that contain polyanions, and have open channels for Li^+ transport. Certain polyanions have substantially increased electronegativity when compared to monoanions, thus increasing the ionic character of the M–X bonds.[51] This alters the energy of the lowest unoccupied metal 3d band, resulting in a lower μ_C and higher V_{oc} (Figure 1.6). Finally, improvements for materials that have solid solution-based insertion/extraction mechanisms can be achieved by incorporation of high degrees of structural disorder.[35]

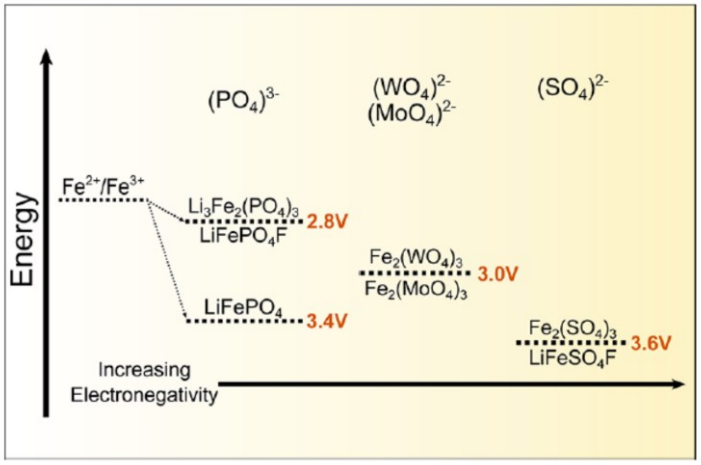

Figure 1.6 Diagram showing how polyanions with increasing electronegativity change the position of μ_C and can increase the open-circuit voltage of a lithium-ion cell. Image adapted from [51] © 2013 American Chemical Society.

In addition to the discovery of new materials, better utilization of a given cathode can be attained by deliberately designing nanoporous or nanocrystalline materials.[28] Anodes can also be improved via structural changes. Electrodes with nanoscale dimensions can have different values for μ_c or μ_a, which can increase the V_{OC} of a lithium-ion cell.[52] These materials also have shorter length scales for diffusion, removing certain kinetic limitations in poorly-conducting materials. In this manner, more energy can be stored and extracted from a cell under practical charge/discharge conditions.[52] Mechanisms for the insertion and extraction of Li^+ can change, allowing for greater charge storage.[43,52] Nanoscale intercalation and lithium alloy anodes can accommodate the strain of insertion/extraction better than their coarser counterparts, which allows for a greater utilization of the theoretical energy density.[47] Unfortunately, improving materials via nanostructuring is often a double-edged sword. While the specific energy is often increased, nanoscale electrodes, especially those that contain pores, have lower densities that can negatively impact the volumetric energy density.[53]

Improvements to the power density of both anode and cathode materials are also a crucial goal for lithium-ion battery research. The general approaches to improving the power density of electrode materials are much the same as for the energy density. Some researchers have searched for novel electrode compositions, and others have sought to engineer existing electrodes so that they deliver more energy high charge/discharge rates. In terms of the latter avenue for improving electrodes, nanostructuring is an extremely attractive route for improving power densities.[53] Nanosized and nanoporous materials have high specific surface areas. When compared to

electrodes with coarser structural features, electrodes with increased electrolyte-accessible surface areas have more available sites for reactions with Li^+ ions, and experience lower current densities at fast charge/discharge rates.[29,52] This can alleviate problems due to activation and concentration polarizations. A high surface can also mean that interfacial charge storage contribute more to overall capacity. Since interfacial charge storage does not require solid-state diffusion, this mechanism allows lithium-ion cells to achieve high power densities.[46] Diffusion lengths are short in these materials, which means that the diffusion time constant for Li^+ is reduced. Since Li^+ can quickly diffuse through an electrode with nanoscale grains, the kinetic limitations of solid-state diffusion disappear and high power densities can be realized.[53] Finally, nanocomposite materials, i.e., materials with two or more phases mixed at <100 nm length scales, can also improve the power density of electrodes.[28] Electrodes with poor electronic conductivity can be coated with a secondary carbon phase that is electronically conductive and does not impede Li^+ transport (Figure 1.7).[54] This arrangement of material can improve power densities, and is further discussed in Chapter 3.

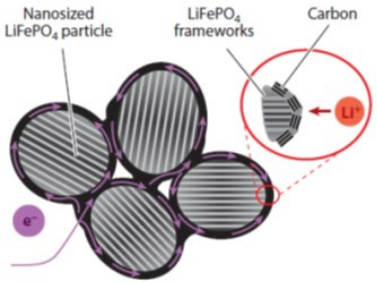

Figure 1.7 An example of a nanocomposite electrode morphology. A thin carbon layer allows for transport of electrons into and out of $LiFePO_4$ particles. Lithium ions can freely move through the carbon, as well. Image from [54] © 2008 John Wiley & Sons.

1.3 Renewable Chemical Fuel Production

Lithium-ion secondary batteries play a crucial role as energy storage devices for a wide range of applications; however, it is unlikely that these batteries will become the dominant means for energy storage. Chemical fuels will complement lithium-ion batteries and other secondary battery systems. There several reasons why many researchers are studying methods to sustainably produce chemical fuels. First, the specific energies and volumetric energy densities attainable in secondary batteries still lag the densities of energy-rich compounds like hydrocarbons, alcohols, and hydrogen (Figure 1.8).[55] These fuels can be directly used in internal combustion engines, or be used in another type of device for the conversion of chemical potential energy to electricity,

the fuel cell. Fuel cells are open systems that require a steady stream of a chemical fuel (H_2 gas, CH_4, alcohols, etc.) and an oxidant (typically O_2) to operate.[56] While more research is needed for fuel cells to be widely adopted, these devices can provide higher specific energies than what is attainable in secondary batteries and, in some cases, higher specific power.[36,57] Second, there is an existing infrastructure for the transport and storage of liquid hydrocarbons, gaseous hydrocarbons, and alcohols. A similar infrastructure has yet to be developed for electric vehicle charging stations and the implementation of such an infrastructure is still being researched.[58] Finally, chemical fuels are cheaper to produce than assembled batteries.[36] Currently, chemical fuels are inexpensive since they are almost exclusively derived from fossil fuel sources. Even hydrogen gas is almost exclusively derived from hydrocarbon feedstocks.[59] However, as fossil fuel resources increase in price and changes to the global climate accelerate, the carbon-neutral production of chemical fuels from sustainable feedstocks will become more attractive.

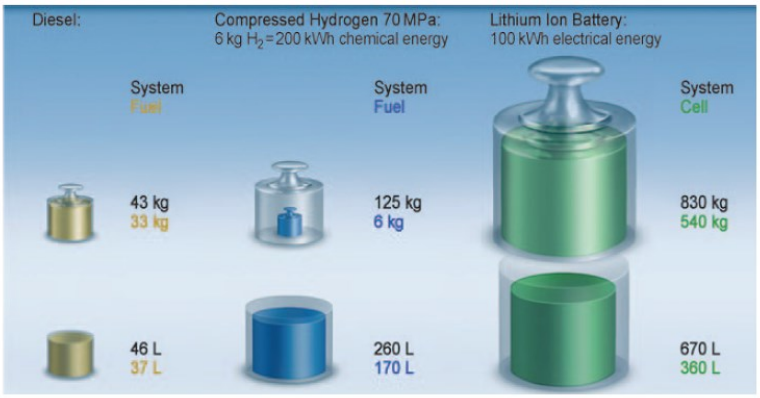

Figure 1.8 Comparison of the masses (top) and volumes (bottom) needed to achieve a 500 km range for a vehicle using diesel fuel (left), compressed hydrogen gas (middle), and a state of the art lithium-ion battery system (right). Image reproduced from [55] © 2009 John Wiley & Sons.

Solar energy has the potential to revolutionize the production of chemical fuels, providing an abundant, renewable energy input for sustainable fuel production. There are multiple means to produce fuels using solar energy, and the most important are ways to convert abundant, small molecule reactants (H_2O and CO_2) into useful fuels (Figure 1.9). Photovoltaic devices can be used to power electrolysis systems, including systems that use advanced fuel cell technologies. High efficiencies are possible with these systems (20–30% solar-to-fuel efficiency).[60] While hydrogen gas production is commonly studied, syngas (a mixture of H_2 and CO) can also be produced using solid oxide electrolysis systems.[61] Syngas can subsequently be converted into liquid hydrocarbons

via the Fischer-Tropsch process over iron or cobalt-based catalysts.[62] Other research teams have studied the use of integrated photoelectrolysis systems that use p-type/n-type semiconductor junctions to produce both H_2 and syngas.[63,64] Realized efficiencies are low, and fuel production is fairly slow in these systems.[63] Aside from inorganic systems, biological systems can also be used for fuel production via the photosynthesis pathways already present in many organisms. Fermentation can aid fuel production, and genetic engineering can be used for the creation of organisms that can produce high yields of specific fuels.[65,66] Unfortunately, the low efficiency of photosynthesis and steep water/nutrient requirements have somewhat hampered the development of these biochemical pathways.[60]

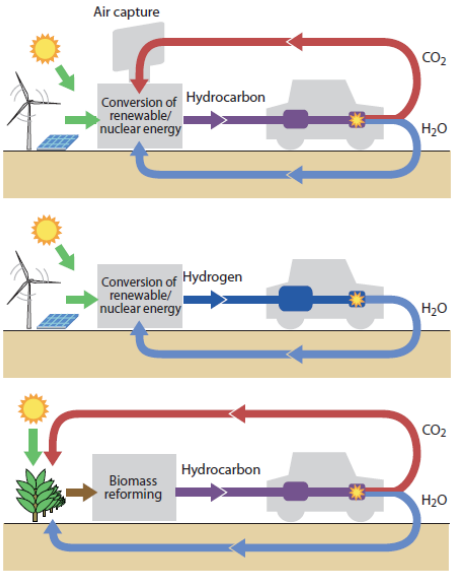

Figure 1.9 Diagrams of three possible pathways to sustainably produce chemical fuels. The top shows the capture and conversion of small molecule reactants (H_2O and CO_2) into hydrocarbon fuels. These fuels can then be combusted or used in a fuel cell. In the middle, only H_2O is captured and turned into H_2 fuel. A scheme for the conversion of biomass (via fermentation, gasification, etc.) into useful fuels is shown at the bottom. Image adapted from [61] © 2011 Elsevier.

1.3.1 Introduction to Concentrated Solar Power for Fuel Production

While the aforementioned techniques harness only part of the solar spectrum, it is possible to use the full solar spectrum by concentrating sunlight (via mirrors) onto a reactor. Extremely high temperatures can be attained at the focal point of the incoming solar radiation.[67,68] In this fashion, it is possible to drive the endothermic reactions that produce H_2 or syngas. While the gasification

of biomass and the decomposition of fossil fuels like coal and oil can be accomplished with concentrated solar radiation,[69,70] this section focuses only on the production of H_2 or syngas from small molecule reactants (i.e., H_2O and CO_2). Though this thermochemical method of producing renewable fuels has yet to be commercialized (as is discussed below), the use of concentrated sunlight is a viable means for the production of electricity.[71] This technology, termed concentrated solar power (CSP), uses the concentrated solar radiation to heat fluids that ultimately drive steam turbines. Both the United States and Spain have operational, megawatt-scale CSP facilities.[72] As a consequence, significant knowledge has been gained regarding the design of the CSP facilities that has, in turn, aided the study of thermochemical fuel production.[73] Specific reactor designs for fuel production have to account for the type of CSP facility to be used, and the efficiency of the solar collection by the CSP facility is an important factor in the overall efficiency of the fuel production process.[74]

Since the only energy input for the solar thermochemical fuel production is from reflector-concentrated sunlight, it is important to present the major CSP technologies (including those that can be adapted for fuel production). Furthermore, it is important to note what CSP technologies can satisfy the steep energetic requirements for the fuel-producing reactions. The basic types of CSP facilities are shown in Figure 1.10; however, the design specifics vary from facility to facility.[68,71] Parabolic trough systems are comprised of sun-tracking mirrors that are curved in the shape of a parabola, and have a fluid-containing pipe (absorber) at their focal points. They are most commonly used for electricity generation, but cannot achieve sufficient temperatures in the absorber tubes for thermochemical fuel production.[71] Linear Fresnel reflectors systems consist of a series of flat, sun-tracking mirrors that concentrate solar radiation along a linear absorber tube. Like the parabolic toughs, insufficient solar concentration is achieved using linear Fresnel reflectors for fuel-producing reactions.[72] However, the other two CSP technologies, the heliostat field (aka the "power tower") and the parabolic dish, are capable of concentrating sunlight to over 1000 times the typical solar irradiance (~1000 W/m^2).[71] Temperatures exceeding 1500 °C can be attained. Heliostat fields accomplish this through the use of an extensive field of mirrors (heliostats) that are capable of tracking the sun along two axes. These mirrors then focus sunlight on a massive receiver tower that contains a reactor or a secondary parabolic mirror that further collects sunlight and focuses it on a reactor on the ground.[67] In contrast, the parabolic dish consists of either a single parabolic shaped mirror or a set of linked mirrors that are capable two-axis tracking of the sun. All of the collected sunlight is focused onto a single point close to the mirror system, and a receiver/reactor is placed at this point.[68] Both the aforementioned systems

have been employed for "on-sun" experiments by the German Aerospace Center (heliostat fields),[75] Sandia National Labs (parabolic dish),[76] and the Weizmann Institute of Science (heliostat fields).[77] To further understand why only heliostat fields and parabolic dishes can be used, the fuel production reactions and their thermodynamics have to be discussed.

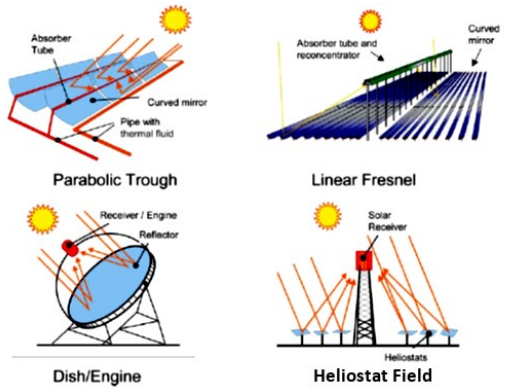

Figure 1.10 Diagrams of the four major CSP technologies. Only the dish/engine and heliostat field systems are suitable for fuel production. Image adapted from [68] © 2012 Royal Society of Chemistry.

1.3.2 One-Step Thermolysis of H_2O

The idea that heat could be harnessed to split water or carbon dioxide has been developed through a series of fits and starts since the 1960s.[78] An initial period of active research stretching from the 1960s to the 1980s laid down much of the ground work for the thermochemical production of hydrogen from water, including fundamental thermodynamic analyses. Even at that point, researchers knew that the splitting of water is extremely unfavorable at ambient conditions (see Figure 1.11).[79] Equation 1.5 at 25 °C and $1 \cdot 10^5$ Pa has the following values for $\Delta H^{\theta}_{H_2O}$, $\Delta S^{\theta}_{H_2O}$, and $\Delta G^{\theta}_{H_2O}$.[80]

$$H_2O(g) \rightleftarrows H_2(g) + 1/2\, O_2(g) \quad (1.5)$$

$$\Delta H^{\theta}_{H_2O} = 286\ \text{kJ/mol}$$

$$\Delta S^{\theta}_{H_2O} = 164\ \text{J/mol} \cdot \text{K}$$

$$\Delta G^{\theta}_{H_2O} = 237\ \text{kJ/mol}$$

Water is assumed to be initially in the liquid phase for the thermodynamic quantities listed in above. While the thermolysis reaction only becomes spontaneous at extremely high temperatures (ca. 4000 °C), Fletcher and others considered the feasibility of direct, one-step water splitting.[79] It was determined that even with only limited conversion to H_2, system efficiencies could be high (~50 %) for reaction temperatures between 2000 °C and 2500 °C. However, an efficient process

can only be realized if some method for separating the product O_2 and H_2 is devised. Several methods have been proposed, including membranes for effusion-based gas separation,[79,81] rapid quenching with a cold gas stream,[82] and separation via the use of solid oxide ionic conductors.[83] Unfortunately, no method has thus far been able effectively separate the gases at ultra-high temperatures and prevent their recombination back into H_2O.[60] Furthermore, later reanalysis of the blackbody re-radiation of light in CSP reactors revealed that efficiency losses are much worse at ≥2000 °C than previously believed.[84] Thus, research into the one-step thermolysis of water has been largely abandoned.

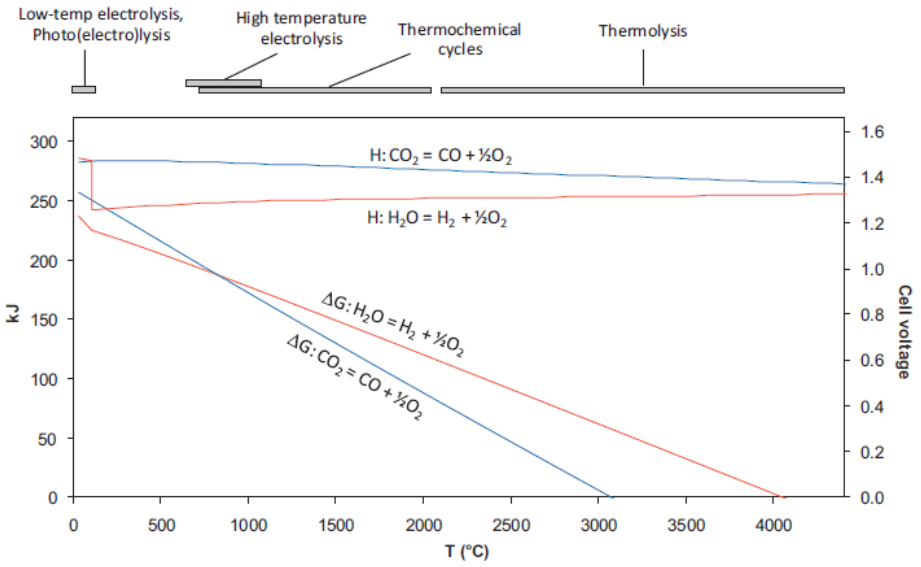

Figure 1.11 Plot showing the change in enthalpy and Gibbs free energy vs. temperature for the splitting of H_2O (red) and CO_2 (blue). Required cell voltages are also shown for electrolysis systems. Image adapted from [61] © 2011 John Wiley & Sons.

1.3.3 Breaking Thermolysis into Multiple Steps

Another direction of the early research into thermochemical fuel production was the discovery and analysis of multiple-step thermochemical cycles that sum to the water thermolysis reaction.[85] By dividing the thermolysis of H_2O into a cycle of reactions, one is essentially increasing the entropy of the overall process at the expense of the maximum attainable efficiency (i.e., a fully reversible Carnot cycle based on the thermolysis reaction).[80] However, as long as the net reaction is the thermolysis of water, the required temperatures for the individual steps are significantly lower than those needed for one-step thermolysis. Abraham and Schreiner,[86] worked out a basic thermodynamic framework for these thermochemical cycles, and analyzed several hypothetical

and experimentally-tested cycles. The key requirement for these processes, assuming complete reversibility for all steps, lies in the required entropy changes. Due to the reversibility of this thermodynamic process, the sum of all the positive entropy processes (associated with heat input steps) and all negative entropy processes (associated with heat rejection steps) needs to equal zero.[86] Therefore, the absolute minimum for the positive entropy change (ΔS_H) of the whole process is given by equation (1.6).

$$\Delta S_H = \frac{Q}{T_{High}} \geq -\Delta G^{\theta}_{H_2O} \Big/ (T_{High} - T_{Low}) \quad (1.6)$$

In this equation: Q is the total heat inputted into the system for a cycle, T_{High} is the maximum temperature reached in a reaction step, T_{Low} is the minimum temperature reached in a reaction step, and $\Delta G_r^{\theta}(H_2O)$ is given above. As a consequence of the entropic requirement, at least three reaction steps are needed to keep T_{High} below 725 °C, provided that T_{Low} is set at 25 °C.[86] Much of the thermochemical fuel production research in the 1960s and 1970s did not consider renewable solar heat, but was focused on the use of heat from fission reactions.[78] Since controlled fission reactions are only capable of heating compounds to ~1000 °C, cycles with three or more steps were extensively studied. Many candidate cycles were developed in this period, including a cluster of related cycles that all include the endothermic decomposition of sulfuric acid.[85] One promising set of reactions, the sulfur-iodide process, is presented as example in reactions (1.7–1.9).

$$H_2SO_4(aq) \rightleftarrows H_2O(g) + SO_2(g) + 1/2\, O_2(g) \quad (1.7)$$

$$2H_2O(l) + xI_2(l) + SO_2(g) \rightleftarrows H_2SO_4(aq) + 2HI_x(aq) \quad (1.8)$$

$$HI_x(g) \rightleftarrows xI_2(g) + H_2(g) \quad (1.9)$$

There are two things to note. Reaction (1.7) occurs in three separate steps that net the written reaction, and HI_x is written since polyiodides (I_3^-) and pure (I_2) can be present in steps 1.8 and 1.9 of the cycle.[67] Research into multistep cycles continues, albeit at a reduced pace when compared to 1970s and 1980s.[87,88] New cycles have been devised that involve high-temperature reactions of metal oxides with liquid alkali hydroxides or less caustic alkali carbonates.[89,90] Overall, the development of multi-step fuel production cycles has been hampered by problems caused by the corrosive nature of many of the materials needed for the reactions (like H_2SO_4 and NaOH), and the energy costs associated with the mixing/separation of reactants and products.[78,88]

1.3.4 Two-Step Solar Thermochemical Fuel Production: General Remarks

In a sense, the comprise solution for solar thermochemical fuel production lies in the development of two-step cycles. These cycles are all based on the endothermic reduction of a metal oxide species alongside the exothermic oxidation of the reduced material by H_2O and/or CO_2.[67] The second step produces a fuel (H_2 or syngas) and regenerates the metal oxide. Reactions 1.10–1.12 are a general representation of the reactions needed for a two-step metal oxide thermochemical cycle.

Endothermic thermal reduction (TR) step:

$$\mathrm{MO}_x \rightleftarrows \mathrm{MO}_{x-\delta} + \delta/2\,\mathrm{O}_2 \qquad (1.10)$$

Exothermic fuel production (OX) steps:

$$\mathrm{MO}_{x-\delta} + \delta\mathrm{H}_2\mathrm{O} \rightleftarrows \mathrm{MO}_x + \delta\mathrm{H}_2 \qquad (1.11)$$

$$\mathrm{MO}_{x-\delta} + \delta\mathrm{CO}_2 \rightleftarrows \mathrm{MO}_x + \delta\mathrm{CO} \qquad (1.12)$$

Here MO_x is an unreduced metal oxide, $MO_{x-\delta}$ is a reduced form of the metal oxide and the abbreviations "TR" and "OX" are used as subscripts for thermodynamic quantities related to the reactions. By splitting the thermolysis of H_2O/CO_2 into two steps, distinct advantages can be realized compared to either one-step or multiple-step cycles. When compared to direct, one-step thermolysis, two-step cycles can reduce the highest temperature needed (in this case for the reduction step) to roughly 1300 °C–1700 °C. Thermal degradation of ceramic materials is lessened at these temperatures, and re-radiation losses are kept to an acceptable level.[84] Two-step cycles can also allow for simpler gas separation, since O_2 and the fuel are produced in different steps. With regards to multi-step cycles (three or more steps), the two step cycles have an inherent advantage from an efficiency standpoint.[86] For many multiple-step cycles, only H_2O can be split to produce H_2.[67,87] There is no analogous limitation for two-step cycles, and CO can be readily produced.[68] Since the thermodynamics of CO_2 thermolysis are similar to those for H_2O thermolysis (see Figure 1.11), only minor differences are typically found when splitting H_2O vs. CO_2 in two-step cycles.[73] Unfortunately, the two-step cycles themselves present many challenges from both materials design/discovery and thermal engineering standpoints.

1.3.4.1 Thermodynamics of Two-Step Cycling

When considering the candidate oxides for two-step thermochemical fuel production, both the overall, material-independent thermodynamics of the two-step cycle and the thermodynamics of specific materials for two-step thermodynamic fuel production need to be considered. Independent of any specific metal oxides, the cycle can be treated as a heat engine connected to a

hypothetical, perfectly efficient fuel cell.[73] Therefore, the output work is simply the Gibbs energy for the thermolysis reaction. Utilizing the general formula for the maximum efficiency ($\eta_{\max}$) for a heat engine (equation 1.13), $\eta_{\max}$ for an arbitrary two-step, water-splitting cycle can be given by equation 1.14.

$$\eta_{\max} = \frac{W_{out}}{Q_{in}} \qquad (1.13)$$

$$\eta_{\max} = \frac{\Delta G^{\theta}_{H_2O}}{\Delta H^{\theta}_{TR}} \qquad (1.14)$$

The quantity ΔH^{θ}_{TR} is the positive enthalpy change of the endothermic reduction step, which is the only heat input. Again, this analysis assumes that all reactions are reversible. With this Carnot-like heat engine, the maximum efficiency can also be given by equation 1.15.

$$\eta_{\max} = \frac{[1-\frac{298}{T_{Thermolysis}}]}{[1-\frac{T_{Low}}{T_{Thermolysis}}]}[1-\frac{T_{Low}}{T_{High}}] \qquad (1.15)$$

For equation 1.15 above, $T_{Thermolysis}$ is the temperature required for the spontaneous thermolysis (of water or CO_2), T_{High} is the temperature used for the thermal reduction step, and T_{Low} is the temperature used for the oxidation step. Miller *et al.* considered the two equations for the maximum efficiency listed above and analyzed the interplay between the relevant variables.[91] Based upon the assumption that $\eta_{max} \geq 0.7$ for the thermochemical process (which is twice what Siegel, Miller, and others believe is needed for a real process), only a limited range of enthalpies (ΔH^{θ}_{TR}< 327 kJ/mol for water-splitting) for the thermal reduction step satisfy this requirement.[91] Additionally, this limitation restricts T_{High} to between ~725 °C to ~1725 °C and establishes a requisite T_{Low} for a given T_{High}. This type of analysis allows one to easily constrain the materials selection process, and avoid unwise choices of materials. Unfortunately, this analysis points to a potential problem. When considering the entropy via equation 1.6, the entropy change of the reduction step should be fairly high. Since the majority of this change in entropy is due to oxygen production (129 kJ/K·mol) and metal oxide only contributes little to the entropy, a fairly severe constraint is established.[91] However, the situation is not as dire as this analysis may suggest. Adjustments to the pressure of the reactor, improvements in heat recovery, and increased fuel production from a material for a given two-step cycle all can favorably change the thermodynamic requirements.[73]

Specific metal oxides can be analyzed using existing thermochemical data and a framework developed by Meredig and Wolverton.[92] They started with the assumption that ΔG^{θ}_{TR} and $\Delta G^{\theta}_{OX,H_2O}$/ $\Delta G^{\theta}_{OX,CO_2}$ have to be less than or equal to zero (i.e., spontaneous). Relating this back to

the formation enthalpies and entropies of the various components, the following equations can be derived (shown here for water-splitting).[92]

$$\Delta G^{\theta}_{TR} = \Delta H^{\theta}_{TR} - T_{High}(\Delta S^{\theta}_{TR} + \frac{1}{2} S^{\theta}_{O_2,TR}) \leq 0 \quad (1.16)$$

$$\Delta G^{\theta}_{OX,H_2O} = -\Delta H^{\theta}_{TR} + \Delta H^{\theta}_{f,H_2,OX} - \Delta H^{\theta}_{f,H_2O,OX} - T_{Low}(-\Delta S^{\theta}_{TR} + S^{\theta}_{H_2,OX} - S^{\theta}_{H_2O,OX}) \leq 0 \quad (1.17)$$

In 1.16 and 1.17, $S^{\theta}_{O_2,TR}$ is the entropy of oxygen at the temperature of the thermal reduction step, $S^{\theta}_{H_2,OX}$ is the entropy of hydrogen at the temperature of the oxidation step, and $S^{\theta}_{H_2O,OX}$ is the entropy of water at the temperature of the oxidation step. Formation enthalpies of hydrogen and water at the temperature of the oxidation step are given by $\Delta H^{\theta}_{f,H_2,OX}$ and $\Delta H^{\theta}_{f,H_2O,OX}$. Merdig and Wolverton noted that these equations do not need to be strictly satisfied for a two-step cycle, since non-equilibrium conditions can be used to drive either reaction (and these conditions are experienced in real reactor systems).[92] Also, O_2 and H_2/CO are produced even when ΔG^{θ}_{TR}/ $\Delta G^{\theta}_{OX,H_2O}$ are slightly positive. Still, this analysis provides a means to screen for potentially useful oxide materials that can be used in two-step cycling. Once reliable thermodynamic data is obtained for a given oxide (experimentally or through a computational method) it is possible to determine suitability from a thermodynamic standpoint. This is shown in Figure 1.12 for several dozen binary oxides, assuming a T_{High} of 1727 °C and a T_{Low} of 727 °C. One item to note is that no binary oxide exists that satisfies the requirements imposed by equations 1.16 and 1.17.[92] Instead, the cycles tend to favor one step, typically the oxidation step. While the binary oxides analyzed by Merdig and Wolverton did not meet the criteria of equations 1.16 and 1.17, Miller *et al.* used the same analysis (T_{High} = 1500 °C) and found that several well-studied materials (with well-known thermodynamics) met the criteria.[91] Part of the reason that Miller *et al.* was able to satisfy these equations is that they adjusted the theoretical T_{Low} and theoretical $p(O_2)$ for the reduction.[91] Both of these can easily be changed in an actual reactor system, and allow for more efficient operation. A final point from these analyses is that an effort should be made to find materials with a high ΔS^{θ}_{TR}, especially for materials cycled for a small T_{High}–T_{Low}.[80] By increasing ΔS^{θ}_{TR} one can potentially access the green region in Figure 1.14 where both reaction steps are favorable; however, there is a distinct chance that such an oxide does not exist.

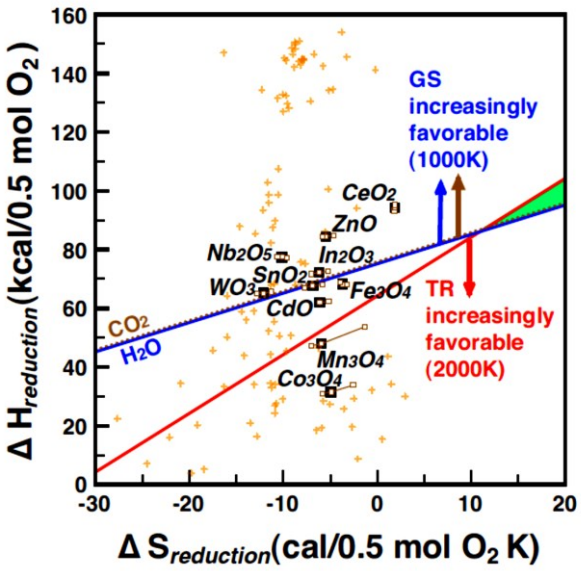

Figure 1.12 Values for ΔH^{θ}_{TR} (called $\Delta H_{reduction}$) and ΔS^{θ}_{TR} (called $\Delta S_{reduction}$) for 105 oxide materials. T_{High} is set at 1727 °C and T_{Low} is set at 727 °C. Previously studied cycles have been labeled. Cycles that lie above the blue/brown line contain a spontaneous gas-splitting reaction step and those below the red line contain a spontaneous reduction reaction. Image reproduced from [92] © 2009 American Physical Society.

1.3.4.2 Kinetics Factors in Two-Step Cycling

While Miller *et al.* and Meredig and Wolverton's analyses are extremely helpful, these analyses only consider the thermodynamics of the cycle and neglect some fairly critical points.[91,92] For instance, the kinetics of the reduction and reoxidation steps are not considered. From an efficiency standpoint (see equation 1.15) it is best to run these cycles so that T_{Low} is as low as possible (i.e. ΔG^{θ}_{OX} is fairly close to zero). However, this has the potential to adversely affect reaction kinetics, creating a situation where fuel production is too sluggish to be of any use. As a result of this challenge, multiple research studies have focused on how to improve the kinetics of the oxidation step. The main strategies have included the synthesis of metal oxides with high surface areas,[93-96] and the use of catalysts.[97] This also explains why many heavily investigated cycles have favorable values for ΔG^{θ}_{OX} at the expense of ΔG^{θ}_{TR}, a point uncovered by Wolverton and Meredig.[92] The thermal reduction step is typically run at such high temperatures that the reaction kinetics are far more rapid than those of the oxidation step. Furthermore, adjustments to the partial pressure of oxygen, $p(O_2)$, in the reduction step (including via vacuum pumping) can improve the extent of reduction for many oxide species.[91] While increasing T_{High} improves the reduction extent for many materials, improves kinetics, and can improve the efficiency, it can cause deleterious changes to the metal oxide. Many candidate metal oxides

sinter extensively in the range of 1000 °C to 1700 °C, leading to a loss of surface area.[94] When this occurs, the kinetics for the fuel production step are degraded, and can even degrade to a point that fuel production essentially stops.[98] Unfavorable solid-state reactions[75] or phase transitions can also occur during this step.[99] Sublimation of a metal oxide is encountered due to the high temperatures need for T_{High}. This phase change is extremely detrimental for metal oxides that are supposed to remain solid during cycling, and presents difficult challenges when complete vaporization is expected (e.g. Zn metal).[91] Later in this section, many of these points are brought up again in the outline of the research work.

1.3.4.3 Reactor Design Concerns in Two-Step Cycling

Before returning to a discussion of candidate materials that generally fit the thermodynamic requirements listed above, a note needs to be made concerning the reactor system. While a comprehensive discussion of reactor design is far beyond the scope of this thesis, a few salient points are useful for the continued discussion. First, no real process exists where the steps are completely reversible. Energetic losses, especially from the transfer of thermal energy out of the reactor system, are widespread. Therefore, sophisticated reactor designs are needed to minimize these losses.[73] Since both the metal oxide and the reactant/product gases are heated to extremely high temperatures, recuperation of some or most of the thermal energy transferred into the system is essential.[100] Unfortunately, solid-phase heat recuperation at >1000 °C is extremely difficult from an engineering standpoint, especially when considering that the recuperator is likely to experience significant creep and thermal shocks.[76] Second, as alluded to with respect to the recuperator, massive thermal gradients are generated in most proposed reactors.[80] These gradients can arise from the fact that incoming solar radiation is spatially non-uniform in a given reactor,[94] Also, these gradients arise because the metal oxides have a finite heat capacity and have to be cycled rapidly between T_{High} and T_{Low}. Deformation or outright fracture of ceramic components can occur under these extreme conditions (Figure 1.13).[98] Since certain reactors rotate the active metal oxide from an "on-sun" hot zone (for reduction) to a cooler zone (for oxidation), the rotating parts in these reactors are especially prone to damage.[76,101] Third, this discussion has so far centered on what is called "temperature-swing" cycling, for obvious reasons. Recently, it has been proposed that isothermal cycling is possible for certain materials.[102,103] Isothermal cycling does have a distinct advantage that thermal gradients generated in the reactor are far less severe than in temperature swing cycling, and a mechanism for switching between high and low temperatures is not needed.[103] However, the thermodynamic feasibility of this process is in

question, especially considering the energy requirements needed to heat CO_2 and H_2O at a suitable isothermal reaction temperature (ca. 1400 °C).[84] Large amounts of gas are potentially needed to sweep out reactants and products, which also require separation. Finally, flowing inert gas or vacuum pumping can be used to establish a low $p(O_2)$ for the reduction step.[88] Vacuum pumping is generally thought to be more energy efficient;[84] however, vacuum pumping is not used in this thesis.

Figure 1.13 A ceramic component containing iron oxide particles in yttrium-stabilized zirconium oxide that has fractured from thermal stresses experienced during cycling. Thirty-two cycles were performed with T_{Low} = 1100 °C and T_{High} = 1400 °C. Image reproduced from [98] © 2008 Elsevier.

1.3.5 Candidate Materials for Two-Step Solar Thermochemical Fuel Production

Many different metals oxides have been analyzed for suitability in two-step solar thermochemical cycling from both a theoretical and experimental standpoint.[91] However, it is believed that only a few kinds of oxide materials have the potential to deliver the ~20 % solar-to-fuel efficiency needed to make this technology competitive.[100,104,105] As a result, research has primarily focused on three main groupings of materials: ferrites, zinc oxide, and cerium oxide-based materials. While these materials all operate on the same principles outlined above (endothermic reduction and exothermic reoxidation/fuel production), there are massive differences between these groupings with respect to their thermodynamics, kinetics, and phase transformations.[68] The next three paragraphs will touch on the particularities for two-step thermochemical cycling of ferrites, zinc oxide, and cerium oxide-based materials. A final short paragraph at the end will describe two promising new classes of compounds that were recently investigated.

1.3.5.1 Iron Oxide and Mixed Metal Ferrites

The first metal oxide considered for thermochemical cycling was Fe_3O_4,[106] and research into mixed metal spinel ferrites $(M_xFe_{1-x})_3O_4$ continues to this day. For the basic undoped iron oxide cycle, the relevant equations for reduction (1.18) and water-splitting (1.19) are given. However, the mixed metal ferrites can be reduced to varying degrees of non-stoichiometry via a more complicated mechanism.[91]

$$Fe_3O_4(s) \rightleftarrows 3FeO(l) + 1/2\ O_2(g) \qquad (1.18)$$

$$3FeO(l) + H_2O(g) \rightleftarrows Fe_3O_4(s) + H_2(g) \qquad (1.19)$$

Fe_3O_4 was initially studied, and is capable of producing good fuel yields for the first few cycles.[67] It is also capable of producing syngas at various ratios.[107] However, fuel production drops substantially as cycling is continued, since the wüstite FeO product melts during thermal reduction. Once FeO melts, substantial liquid phase sintering occurs that reduces the surface area of the active material and closes any open pores.[67] Since the diffusion of ions in Fe_3O_4 is fairly slow, any sintering that increases diffusion lengths can effectively deactivate the material.[91,108] To stabilize the structure of the ferrites, two main strategies have been employed. The first is the addition of transition metal cations to the Fe_3O_4 structure.[104,109-114] This can reduce the temperature needed for thermal reduction and prevent the wüstite phase from melting. Optimal doping levels are essential, since it possible to alter the redox thermodynamics so the oxidation step is highly unfavorable at intermediate temperatures or create materials that sublime during reduction.[91,104,111] Significant boosts in fuel productivity are possible with the correct dopants.[111] The other means of improving stability is to combine either Fe_3O_4 or $(M_xFe_{1-x})_3O_4$ with ZrO_2 or yttrium-stabilized ZrO_2. Both composites and coated supports have been synthesized.[115-119] With respect to the composites, studies have indicated that the active species for water-splitting are Fe ions dissolved in ZrO_2 and Fe ions in small $(M_xFe_{1-x})O$ particles.[118,119] Unfortunately, poor utilization of the Fe ions occurs if the $(M_xFe_{1-x})O$ particles are larger than several μm, due to problems with ionic transport. A high weight percent of the support is required to prevent formation of large particles of active material.[118] Despite the challenges that exist, researchers have developed rotating reactor systems using supported ferrites[120,121] and reactor containing a fluidized bed of unsupported nickel ferrite particles.[122] Batch reactors have also been constructed using ZrO_2-supported ferrites, and these reactors have been tested using a heliostat field CSP system.[75]

1.3.5.2 Zinc Oxide

Unlike the ferrites, when zinc oxide (ZnO) is used for two-step thermochemical fuel production, it is fully reduced to metallic Zn and vaporizes. This phase change makes the zinc oxide cycle quite different from an engineering standpoint than the ferrite-based two-step cycles. The relevant reactions for the ZnO cycle are shown in 1.20 (reduction) and 1.21 (water-splitting).

$$\mathrm{ZnO(s)} \rightleftarrows \mathrm{Zn(g)} + 1/2\,\mathrm{O_2(g)} \qquad (1.20)$$

$$\mathrm{Zn(s)} + \mathrm{H_2O(g)} \rightleftarrows \mathrm{ZnO(s)} + \mathrm{H_2(g)} \qquad (1.21)$$

Once ZnO is reduced, the Zn needs to be separated from oxygen, or the reaction temperature needs to be rapidly lowered.[123] Metallic Zn vapor can react rapidly with oxygen formed during the reduction step, recombining into ZnO without any fuel production. In addition to this difficulty, μm-scale particles of Zn reoxide slowly due to the build-up of ZnO on the surface of these particles.[124] Reaction rates are initially high and are mediated by adsorption at the Zn-gas interface.[125] Once a ZnO layer is formed, the reaction rates decrease and change to a diffusion-controlled mechanism. Transport of Zn ions through the ZnO layer is slow, which causes the poor kinetics.[126,127] As a consequence, attempts have been made to quench and then condense Zn as an aerosol containing nm-scale particles.[128,129] Good fuel production yields (>80 % for H_2/CO) are possible through this technique, and the fuel can be produced from the rapidly from the aerosol, requiring only seconds to reoxidize in a H_2O or CO_2.[126] However, problems still exist surrounding the recovery of ZnO after oxidation is complete. In addition to fundamental studies, an experimental reactor system containing ZnO has been created.[130] This reactor contains a rotating drum that is lined with ZnO tiles. ZnO particles are fed into the reactor, reduced by solar radiation, and then the Zn is swept out to a cool zone for oxidation via an Ar gas stream. While many engineering challenges still exist for the ZnO/Zn system, a recent economic analysis determined that this cycle may be cost competitive in the latter half of the 21st century.[105]

1.3.5.3 Cerium Oxide and Cerium-Containing Mixed Oxides

Cerium dioxide is a relatively new material to be explored for two-step thermochemical fuel production, but has quickly become one of most popular candidate materials for thermochemical cycling. The rise of interest in cerium dioxide is a result of several advantages that material has when compared to other materials studied for production of solar fuels. For typical cycling conditions, CeO_2 is reduced to non-stiochiometric phase that contains Ce^{3+} and Ce^{4+} along with oxygen vacancies.[131] Oxidation restores the CeO_2 and refills the oxygen vacancies in the

structure. Reactions 1.22 and 1.23 are the reduction and oxidation (water splitting) reactions for the two-step cycle.

$$CeO_2(s) \rightleftarrows CeO_{2-\delta}(s) + \delta/2\, O_2(g) \quad (1.22)$$

$$CeO_{2-\delta}(s) + \delta H_2O(g) \rightleftarrows CeO_2(s) + \delta H_2(g) \quad (1.23)$$

$$2Ce_{Ce}^{x} + O_O^x \rightleftarrows V_O^{\cdot\cdot} + 2Ce_{Ce}' + 1/2\, O_2 \quad (1.24)$$

$$H_2O + V_O^{\cdot\cdot} + 2Ce_{Ce}' \rightleftarrows H_2 + 2Ce_{Ce}^{x} + O_O^x \quad (1.25)$$

In reaction 1.24 and 1.25, the reduction and water-splitting reactions in Kröger-Vink notation are shown. For these reactions, $V_O^{\cdot\cdot}$ is a doubly-ionized oxygen vacancy, Ce_{Ce}' is a Ce(III) ion on a Ce site, O_O^x is an oxygen ion on an O site, and Ce_{Ce}^x is a Ce(IV) ion on a Ce site. Reduction temperatures are typically kept between 1200 °C to 1700 °C; corresponding to a δ between ~0.01 and 0.1.[91,95,131] During this whole process, the cerium oxide remains a solid with a cubic fluorite crystal structure. Capping the reduction temperature below 1700 °C also avoids the problematic material losses causes by the high temperature sublimation of cerium oxide.[99] Despite the fact that cerium oxide can only be reduced to a limited degree of oxygen non-stoichiometry, efficiencies of over 20% have been predicted for this cycle, assuming reasonable heat recuperation.[100] Aside from high predicted efficiencies, the fact that cerium oxide remains a solid is a distinct advantage from the standpoint of reactor construction. It is also beneficial that cerium oxide does not need to be combined or supported on an inactive material, like what is required for the ferrites. Still, realized efficiencies are low for cerium oxide. Reactor systems have been engineered and tested,[94,132] but the best reported efficiency is only ~3 %.[95] These reactors are cavity-type reactors that lack heat solid recuperation, so reactor improvements are needed. However, the materials used in the reactors also suffer from kinetic limitations and problematic sintering.[94] Improvements are needed in both increasing the reduction extent (to allow for a lower value of T_{High}) and in enhancing the kinetics of the slower oxidation step.[96,133] Further discussions about cerium oxide-based materials are found in the first sections of both Chapter 7 and Chapter 8.

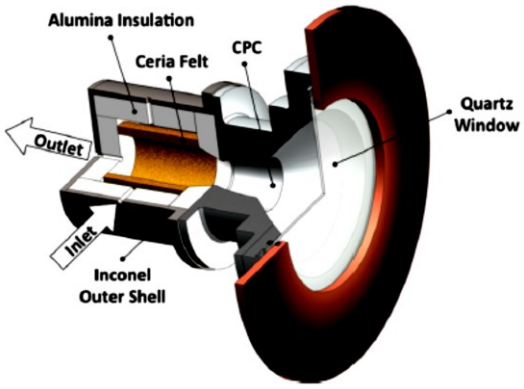

Figure 1.14 Diagram of a cavity-type reactor designed by researchers in Switzerland and the United States. Monolithic pieces of cerium oxide are placed in the cavity and are surrounded by thermal insulation. Incident light is further concentrated by a compound parabolic concentrator (CPC) in the reactor. Image reproduced from [94] © 2012 Royal Society of Chemistry.

1.3.5.4 Hercynites and Perovskites

In the last few years, researchers have published reports on two additional classes of oxides, hercynites and perovskites, which can be used for solar thermochemical fuel production. The two-step hercynite cycle was discovered as a result of atomic layer deposition of a ferrite, $CoFe_2O_4$, on an Al_2O_3 support.[134] During thermal reduction, cobalt ferrite and Al_2O_3 experience a solid-state reaction, forming an iron and cobalt aluminates (reaction 1.26). After oxidation in H_2O or CO_2, the ferrite phase is regenerated and fuel is produced (reaction 1.27, shown for H_2O).

$$CoFe_2O_4(s) + 3Al_2O_3(s) \rightleftarrows CoAl_2O_4(s) + 2FeAl_2O_4(s) + 1/2\ O_2(g) \quad (1.26)$$

$$CoAl_2O_4(s) + 2FeAl_2O_4(s) + H_2O(g) \rightleftarrows CoFe_2O_4(s) + 3Al_2O_3(s) + H_2(g) \quad (1.27)$$

When temperature-swing cycling was used, rapid production of oxygen was observed after reduction at 1460 °C.[135] Similar to cerium oxide, production of CO was found to be slower than O_2 production and is likely controlled by reactions at the surface of the aluminates.[135] Isothermal cycling at 1350 °C was also shown to be possible with these materials, and high levels of H_2 production were reported.[136] However, large quantities of inert gas were needed to sweep reactants out of the reactor. While only $CoFe_2O_4$ has been explored, other ferrite materials may be able to be used for this type of cycling. In contrast to the hercynite cycle, the newly studied pervoskite oxides undergo similar reactions to CeO_2.[137] These materials can be reduced to a certain degree of oxygen non-stoichiometry and then reoxidized.[138-140] Initial reports for some of the materials are quite promising, for instance $Sr_{0.6}La_{0.4}Mn_{0.6}Al_{0.4}O_{3-\delta}$ produces more H_2 than cerium oxide cycled in similar conditions.[139] Another advantage is that a multitude of perovskite

oxide compositions exist that undergo redox reactions suitable for thermochemical fuel production.[141] Furthermore, key thermodynamic properties are known for some of these materials.[137] An extended discussion of the perovskite oxides is given in Chapter 8.

1.4 Outline of the Remainder of the Thesis

While the research in this thesis is focused on materials for the two energy storage and conversion applications discussed in Sections 1.2 and 1.3, certain structural aspects of the synthesized materials are important in the discussions later chapters. Distinct commonalities exist in the methods in which porosity is generated for the materials described. Pores are generated in these materials via the use of sacrificial templates that are removed during processing. An overview of various templating methods is provided in Chapter 2. This chapter both aids later discussion and provides further context for why the use of porous materials is crucial in these energy storage applications.

Chapters 3, 4, 5, and 6 are all part of an investigation into the use of porous TiO_2 and porous composites of TiO_2/C as anode materials for lithium-ion cells. For all of the syntheses described, porosity is generated in the anodes through the use of sacrificial templates. These templates contain ordered lattices of polymer spheres that are few hundred nm in diameter, and the spaces between the spheres are filled with liquid precursors. Removal of the template and conversion of the precursor to a solid generates the porous materials. All the resulting materials contain small crystallites of TiO_2, high electrode-electrolyte surface areas, and short diffusion lengths, allowing for various capacity and power advantages described earlier. Chapter 3 examines the impact that two different chelating agents have on the resulting structure of TiO_2/C materials and the performance of these materials as anodes in lithium-ion cells. An additional focus is placed on how changing pyrolysis temperatures impacts both structures and electrochemical properties. The carbon phase is also eliminated from one of the types of composite, and this porous TiO_2 anode is also electrochemically tested. Chapter 4 describes an exploration of how various cationic dopants change the structure of the porous materials and the capacity of these materials for reversible Li^+ insertion/extraction. Precursor compositions are modified from those described in Chapter 3. Chapter 5 is again focused on undoped TiO_2/C; however, less-toxic precursors are used. Structural changes that result from the use of these precursors are discussed, alongside their electrochemical properties. In addition, theses carbon-rich composites are cycled, so that Li^+ intercalation/deintercalation into the carbon phase occurs. Higher capacities are obtained for the composites than for a porous carbon reference anode. Chapter 6 describes the conversion (via the use of an alkali hydroxide solution) of porous TiO_2 to sodium titanate, hydrogen titanate and

TiO_2. Specific surface areas are increased considerably via this process, and possible mechanism for the conversion is explored.

Chapters 7 and 8 discuss materials for solar thermochemical cycling. Again, porous materials are synthesized via a template comprised of ordered polymeric spheres. This specific pore structure allows for better oxidation kinetics via moderate surface areas, an interconnected pore network, and short diffusion lengths. Chapter 7 investigates the chemical redox cycling of porous cerium zirconium oxide. Zirconium is used as a dopant to improve both the thermal stability of the porous material relative to cerium oxide and its extent of reduction. Cerium zirconium oxide does increase fuel yields, provided the content of Zr is kept below ~30 mol%. Additionally, the effect of phase demixing via the use of specific precursors is explored. Chapter 8 describes a series of explorations focused on the use of various dopants for porous cerium oxide. New porous materials for two-step cycling are also described both from a structural perspective and from their ability to produce fuel. Finally, a brief summary and outlook is given in Chapter 9.

References

(1) Arrhenius, S. On the Influence of Carbonic Acid in the Air Upon the Temperature on the Ground. *Phil. Mag.* **1896**, *41*, 237-279.

(2) Clark, P. U.; Shakun, J. D.; Baker, P. A.; Bartlein, P. J.; Brewer, S.; Brook, E.; Carlson, A. E.; Cheng, H.; Kaufman, D. S.; Liu, Z.; Marchitto, T. M.; Mix, A. C.; Morrill, C.; Otto-Bliesner, B. L.; Pahnke, K.; Russell, J. M.; Whitlock, C.; Adkins, J. F.; Blois, J. L.; Clark, J.; Colman, S. M.; Curry, W. B.; Flower, B. P.; He, F.; Johnson, T. C.; Lynch-Stieglitz, J.; Markgraf, V.; McManus, J.; Mitrovica, J. X.; Moreno, P. I.; Williams, J. W. Global Climate Evolution During the Last Deglaciation. *Proc. Natl. Acad. Sci. USA* **2012**, *109*, E1134-E1142.

(3) Moss, R. H.; Edmonds, J. A.; Hibbard, K. A.; Manning, M. R.; Rose, S. K.; van Vuuren, D. P.; Carter, T. R.; Emori, S.; Kainuma, M.; Kram, T.; Meehl, G. A.; Mitchell, J. F. B.; Nakicenovic, N.; Riahi, K.; Smith, S. J.; Stouffer, R. J.; Thomson, A. M.; Weyant, J. P.; Wilbanks, T. J. The Next Generation of Scenarios for Climate Change Research and Assessment. *Nature* **2010**, *463*, 747-756.

(4) Rosa, E. A.; Dietz, T. Human Drivers of National Greenhouse-Gas Emissions. *Nat. Clim. Change* **2012**, *2*, 581-586.

(5) Knutti, R.; Sedláček, J. Robustness and Uncertainties in the New CMIP5 Climate Model Projections. *Nat. Clim. Change* **2013**, *3*, 369-373.

(6) IPCC Summary for Policymakers. In *Climate Change 2013: The Physical Science Basis. Contribution of Working Group I to the Fifth Assessment Report of the Intergovernmental Panel on Climate Change*; Stocker, T. F., Qin, D., Plattner, G.-K., Tignor, M. M. B., Allen, S. K., Boschung, J., Nauels, A., Xia, Y., Bex, V., Midgley, P. M., Eds.; Cambridge University Press: Cambridge, UK, 2013.

(7) IPCC Summary for Policymakers. In *Climate Change, 2014: Mitigation of Climate Change. Contribution of Working Group III to the Fifth Assessment Report of the Intergovernmental Panel on Climate Change*; Edenhofer, O., Pichs-Madruga, R., Sokona, Y., Farahani, E., Kadner, S., Seyboth, K., Adler, A., Baum, I., Brunner, S., Eickenmeier, P., Kriemann, B., Savolainen, J., Schlömer, S., von Stechow, C., Zwickel, T., Minx, J. C., Eds.; Cambridge University Press: Cambridge, UK, 2014.

(8) Beaumont, L. J.; Pitman, A.; Perkins, S.; Zimmermann, N. E.; Yoccoz, N. G.; Thuiller, W. Impacts of Climate Change on the World's Most Exceptional Ecoregions. *Proc. Natl. Acad. Sci. USA* **2011**, *108*, 2306-2311.

(9) Barnosky, A. D.; Hadly, E. A.; Bascompte, J.; Berlow, E. L.; Brown, J. H.; Fortelius, M.; Getz, W. M.; Harte, J.; Hastings, A.; Marquet, P. A.; Martinez, N. D.; Mooers, A.; Roopnarine, P.; Vermeji, G.; Williams, J. W.; Gillespie, R.; Kitzes, J.; Marshall, C.; Matzke, N.; Mindell, D. P.; Revilla, E.; Smith, A. B. Approaching a State Shift in Earth's Biosphere. *Nature* **2012**, *486*, 52-58.

(10) Ibrahim, M. A.; Na, M.; Oh, J.; Schinazi, R. F.; McBrayer, T. R.; Whitaker, T.; Doerksen, R. J.; Newman, D. J.; Zachos, L. G.; Hamann, M. T. Significance of Endangered and Threatened Plant Natural Products in the Control of Human Disease. *Proc. Natl. Acad. Sci. USA* **2013**, *110*, 16832-16837.

(11) Wheeler, T.; von Braun, J. Climate Change Impacts on Global Food Security. *Science* **2013**, *341*, 508-513.

(12) Altizer, S.; Ostfeld, R. S.; Johnson, P. T. J.; Kutz, S.; Harvell, C. D. Climate Change and Infectious Diseases: From Evidence to a Predictive Framework. *Science* **2013**, *341*, 514-519.

(13) Brandt, A. R.; Millard-Ball, A.; Ganser, M.; Gorelick, S. M. Peak Oil Demand: The Role of Fuel Efficiency and Alternative Fuels in a Global Oil Production Decline. *Environ. Sci. Technol.* **2013**, *47*, 8031-8041.

(14) Kerschner, C.; Prell, C.; Feng, K.; Hubacek, K. Economic Vulnerability to Peak Oil. *Global Environ. Change* **2013**, *23*, 1424-1433.

(15) Stern, N. The Economics of Climate Change. *Am. Econ. Rev.* **2008**, *97*, 1-37.

(16) Weitzman, M. L. On Modeling and Interpreting the Economics of Catastrophic Climate Change. *Rev. Econ. Stat.* **2009**, *91*, 1-19.

(17) Nordhaus, W. *The Climate Casino: Risk, Uncertainty, and Economics for a Warming World*; Yale University Press: New Haven, CT, 2013.

(18) GAO *Climate Change Adaptation: Strategic Federal Planning Could Help Government Officials Make More Informed Decisions*, GAO-10-113, U.S. Government Accountability Office, Washington D.C., 2009.

(19) World Bank *Economics of Adaptation to Climate Change- Synthesis Report*, World Bank, Washington D.C., 2010.

(20) Hoffert, M. I.; Caldeira, K.; Benford, G.; Criswell, D. R.; Green, C.; Herzog, H.; Jain, A. K.; Kheshgi, H. S.; Lackner, K. S.; Lewis, J. S.; Lightfoot, H. D.; Manheimer, W.; Mankins, J. C.; Mauel, M. E.; Perkins, L. J.; Schlesinger, M. E.; Volk, T.; Wigley, T. M. L. Advanced Technology Paths to Global Climate Stability: Energy for a Greenhouse Planet. *Science* **2002**, *298*, 981-987.

(21) Edenhofer, O.; Seyboth, K.; Creutzig, F.; Schlömer, S. On the Sustainability of Renewable Energy Sources. *Annu. Rev. Environ. Resour.* **2013**, *38*, 169-200.

(22) Butler, D. ITER Keeps Eye on Prize. *Nature* **2013**, *502*, 282-283.

(23) National Academy of Sciences, National Academy of Engineering, and National Research Council *Real Prospects for Energy Efficiency in the United States*; The National Academies Press: Washington D.C., 2010.

(24) Chen, H.; Goswami, Y.; Stefanakos, E. K. A Review of Thermodynamic Cycles and Working Fluids for the Conversion of Low-Grade Heat. *Renewable Sustainable Energy Rev.* **2010**, *14*, 3059-3067.

(25) D'Alessandro, D. M.; Smit, B.; Long, J. R. Carbon Dioxide Capture: Prospects for New Materials. *Angew. Chem. Int. Ed.* **2010**, *49*, 6058-6082.

(26) Boot-Handford, M. E.; Abanades, J. C.; Anthony, E. J.; Blunt, M. J.; Brandani, S.; MacDowell, N.; Fernández, J. R.; Ferrari, M.-C.; Gross, R.; Hallett, J. P.; Haszeldine, R. S.; Heptonstall, P.; Lyngfelt, A.; Makuch, Z.; Mangano, E.; Porter, R. T. J.; Pourkashanian, M.; Rochelle, G. T.; Shah, N.; Yao, J. G.; Fennell, P. S. Carbon Capture and Storage Update. *Energy Environ. Sci.* **2014**, *7*, 130-189.

(27) Yang, Z.; Zhang, J.; Kinter-Meyer, M. C. W.; Lu, X.; Choi, D.; Lemmon, J. P.; Liu, J. Electrochemical Energy Storage for the Green Grid. *Chem. Rev.* **2011**, *111*, 3577-3613.

(28) Hayner, C. M.; Zhao, X.; Kung, H. H. Materials for Rechargeable Lithium-Ion Batteries. *Annu. Rev. Chem. Biomol. Eng.* **2012**, *3*, 445-471.

(29) Linden, D.; Reddy, T. B. Principles of Operation. In *Linden's Handbooks of Batteries*; 4th ed.; Reddy, T. B., Linden, D., Eds.; The McGraw-Hill Companies: New York, NY, 2010.

(30) Reddy, T. B. An Introduction to Secondary Batteries. In *Linden's Handbook of Batteries*; 4th ed.; Reddy, T. B., Linden, D., Eds.; The McGraw-Hill Companies: New York, NY, 2010.

(31) Choi, N.-S.; Chen, Z.; Freunberger, S. A.; Ji, X.; Sun, Y.-X.; Amine, K.; Yushin, G.; Nazar, L. F.; Cho, J.; Bruce, P. G. Challenges Facing Lithium Batteries and Electrical Double-Layer Capacitors. *Angew. Chem. Int. Ed.* **2012**, *51*, 9994-10024.

(32) Etacheri, V.; Marom, R.; Elazari, R.; Salitra, G.; Aurbach, D. Challenges in the Development of Advanced Li-Ion Batteries: A Review. *Energy Environ. Sci.* **2011**, *4*, 3243-3262.

(33) Goodenough, J. B.; Park, K.-S. The Li-Ion Rechargeable Battery: A Perspective. *J. Am. Chem. Soc.* **2013**, *135*, 1167-1176.

(34) Goodenough, J. B.; Kim, Y. Challenges for Rechargeable Li Batteries. *Chem. Mater.* **2010**, *22*, 587-603.

(35) Maier, J. Thermodynamics of Electrochemical Lithium Storage. *Angew. Chem. Int. Ed.* **2013**, *52*, 4998-5026.

(36) Winter, M.; Brodd, R. J. What Are Batteries, Fuel Cells, and Supercapacitors? *Chem. Rev.* **2004**, *104*, 4245-4269.

(37) Goodenough, J. B. Evolution of Strategies for Modern Rechargeable Batteries. *Acc. Chem. Res.* **2012**, *46*, 1053-1061.

(38) Verma, P.; Maire, P.; Novák, P. A Review of the Features and Analyses of the Solid Electrolyte Interphase in Li-Ion Batteries. *Electrochim. Acta* **2010**, *55*, 6332-6341.

(39) Park, M.; Zhang, X.; Chung, M.; Less, G. B.; Sastry, A. M. A Review of Conduction Phenomena in Li-Ion Batteries. *J. Power Sources* **2010**, *195*, 7904-7929.

(40) Salomon, M. Electrochemical Principles and Reactions. In *Linden's Handbook of Batteries*; 4th ed.; Reddy, T. B., Linden, D., Eds.; The McGraw-Hill Companies: New York, NY, 2010.

(41) Bard, A. J.; Faulkner, L. R. *Electrochemical Methods: Fundamentals and Applications*; John Wiley & Sons, Inc.: New York, NY, 2000.

(42) Reddy, M. V.; Subbo Rao, G. V.; Chowdari, B. V. R. Metal Oxides and Oxysalts as Anode Materials for Li Ion Batteries. *Chem. Rev.* **2013**, *113*, 5364-5457.

(43) Wagemaker, M.; Mulder, F. M. Properties and Promises of Nanosized Insertion Materials for Li-Ion Batteries. *Acc. Chem. Res.* **2013**, *46*, 1206-1215.

(44) Simon, P.; Gogotsi, Y.; Dunn, B. Where Do Batteries End and Supercapacitors Begin?0 *Science* **2014**, *343*, 1210-1211.

(45) Conway, B. E. Transition from "Supercapacitor" to "Battery" Behavior in Electrochemical Energy Storage. *J. Electrochem. Soc.* **1991**, *138*, 1539-1548.

(46) Augustyn, V.; Simon, P.; Dunn, B. Pseudocapacitive Oxide Materials for High-Rate Electrochemical Energy Storage. *Energy Environ. Sci.* **2014**, *7*, 1597-1614.

(47) Park, C.-M.; Kim, J.-H.; Kim, H.; Sohn, H.-J. Li-Alloy Based Anodes Materials for Li Secondary Batteries. *Chem. Soc. Rev.* **2010**, *39*, 3115-3141.

(48) Zhang, W.-J. Lithium Insertion/Extraction Mechanism in Alloy Anodes for Lithium-Ion Batteries. *J. Power Sources* **2011**, *196*, 877-885.

(49) Cabana, J.; Monconduit, L.; Larcher, D.; Palacín, M. R. Beyond Intercalation-Based Li-Ion Batteries: The State of the Arts and Challenges of Electrode Materials Reacting Through Conversion Reactions. *Adv. Mater.* **2010**, *22*, E170-E192.

(50) Li, L.; Meng, F.; Jin, S. High-Capacity Lithium-Ion Battery Conversion Cathodes Based on Iron Fluoride Nanowires and Insights into the Conversion Mechanism. *Nano Lett.* **2012**, *12*, 6030-6037.

(51) Melot, B. C.; Tarascon, J.-M. Design and Preparation of Materials for Advanced Electrochemical Storage. *Acc. Chem. Res.* **2013**, *46*, 1226-1238.

(52) Bruce, P. G.; Scrosati, B.; Tarascon, J.-M. Nanomaterials for Rechargeable Lithium Batteries. *Angew. Chem. Int. Ed.* **2008**, *47*, 2930-2946.

(53) Vu, A.; Qian, Y.; Stein, A. Porous Electrode Materials for Lithium-Ion Batteries - How to Prepare Them and What Makes Them Special. *Adv. Energy Mater.* **2012**, *2*, 1056-1085.

(54) Wang, Y. G.; Wang, Y. R.; Hosono, E. J.; Wang, K. X.; Zhou, H. S. The Design of a $LiFePO_4$/Carbon Nanocomposite with a Core-Shell Structure and Its Synthesis by an In Situ Polymerization Restriction Method. *Angew. Chem. Int. Ed.* **2008**, *47*, 461-465.

(55) Eberke, U.; Felderhoff, M.; Schüth, F. Chemical and Physical Solutions for Hydrogen Storage. *Angew. Chem. Int. Ed.* **2009**, *48*, 6608-6630.

(56) de Bruijn, F. The Current Status of Fuel Cell Technology for Mobile and Stationary Applications. *Green Chem.* **2005**, *7*, 132-150.

(57) Wachsman, E. D.; Marlowe, C. A.; Lee, K. T. Role of Solid Oxide Fuel Cells in a Balanced Energy Strategy. *Energy Environ. Sci.* **2012**, *5*, 5498-5509.

(58) Yilmaz, M.; Krein, P. T. Review of Battery Charger Topologies, Charging Power Levels, and Infrastructure for Plug-In Electric and Hybrid Vehicles. *IEEE Trans. Power Electron.* **2012**, *28*, 2151-2169.

(59) Chaubey, R.; Sahu, S.; James, O. O.; Maity, S. A Review on Development of Industrial Processes and Emerging Techniques for Production of Hydrogen from Renewable and Sustainable Sources. *Renewable Sustainable Energy Rev.* **2013**, *23*, 443-462.

(60) Joshi, A. S.; Dincer, I.; Reddy, B. V. Solar Hydrogen Production: A Comparative Performance Assessment. *Int. J. Hydrogen Energy* **2011**, *36*, 11246-11257.

(61) Graves, C.; Ebbesen, S. D.; Mogensen, M.; Lackner, K. S. Sustainable Hydrocarbon Fuels by Recycling CO_2 and H_2O with Renewable or Nuclear Energy. *Renewable Sustainable Energy Rev.* **2011**, *15*, 1-23.

(62) Zhang, Q.; Kang, J.; Wang, Y. Development of Novel Catalysts for Fischer-Tropsch Synthesis: Tuning the Product Selectivity. *ChemCatChem* **2010**, *2*, 1030-1058.

(63) Holladay, J. D.; Hu, J.; King, D. L.; Wang, Y. An Overview of Hydrogen Production Technologies. *Catal. Today* **2009**, *139*, 244-260.

(64) Roy, S. C.; Varghese, O. K.; Paulose, M.; Grimes, C. A. Toward Solar Fuels: Photocatalytic Conversion of Carbon Dioxide to Hydrocarbons. *ACS Nano* **2010**, *4*, 1259-1278.

(65) Rosenberg, J. N.; Oyler, G. A.; Wilkinson, L.; Betenbaugh, M. J. A Green Light for Engineered Algae: Redirecting Metabolism to Fuel a Biotechnology Revolution. *Curr. Opin. Biotechnol.* **2008**, *19*, 430-436.

(66) Kwietniewska, E.; Tys, J. Process Characteristics, Inhibition Factors and Methane Yields of Anaerobic Digestion Process, with Particular Focus on Microalgal Biomass Fermentation. *Renewable Sustainable Energy Rev.* **2014**, *34*, 491-500.

(67) Kodama, T.; Gokon, N. Thermochemical Cycles for High-Temperature Solar Hydrogen Production. *Chem. Rev.* **2007**, *107*, 4048-4077.

(68) Romero, M.; Steinfeld, A. Concentrating Solar Thermal Power and Thermochemical Fuels. *Energy Environ. Sci.* **2012**, *5*, 9234-9245.

(69) Ozalp, N.; Kogan, A.; Epstein, M. Solar Decomposition of Fossil Fuels as an Option for Sustainability. *Int. J. Hydrogen Energy* **2009**, *34*, 710-720.

(70) Piatkowski, N.; Wieckert, C.; Weimer, A. W.; Steinfeld, A. Solar-Driven Gasification of Carbonaceous Feedstock- A Review. *Energy Environ. Sci.* **2011**, *4*, 73-82.

(71) Barlev, D.; Vidu, R.; Stroeve, P. Innovation in Concentrated Solar Power. *Sol. Energy Mater. Sol. Cells* **2011**, *95*, 2703-2725.

(72) Zhang, H. L.; Baeyens, J.; Degrève, J.; Cacères, G. Concentrated Solar Power Plants: Review and Design Methodology. *Renewable Sustainable Energy Rev.* **2013**, *22*, 466-481.

(73) Siegel, N. P.; Miller, J. E.; Ermanoski, I.; Diver, R. B.; Stechel, E. B. Factors Affecting the Efficiency of Solar Driven Metal Oxide Thermochemical Cycles. *Ind. Eng. Chem. Res.* **2013**, *52*, 3276-3286.

(74) Kim, J.; Johnson, T. A.; Miller, J. E.; Stechel, E. B.; Maravelias, C. T. Fuel Production from CO_2 Using Solar-Thermal Energy: System Level Analysis. *Energy Environ. Sci.* **2012**, *5*, 8417-8429.

(75) Roeb, M.; Neises, M.; Säck, J.-P.; Rietbrock, P.; Monnerie, N.; Dersch, J.; Schmitz, M.; Sattler, C. Operational Strategy of a Two-Step Thermochemical Process for Solar Hydrogen Production. *Int. J. Hydrogen Energy* **2009**, *34*, 4537-4545.

(76) Miller, J. E.; Allendorf, M. D.; Ambrosini, A.; Coker, E. N.; Diver, R. B.; Ermanoski, I.; Evans, L. R.; Hogan, R. E.; McDaniel, A. H. *Development and Assessment of Solar-Thermal-Activated Fuel Production: Phase 1 Summary*, SAND2012-5658, Sandia National Laboratories, Albuquerque, NM, 2012.

(77) Vishnevetsky, I.; Epstein, M. Production of Hydrogen from Solar Zinc in Steam Atmosphere. *Int. J. Hydrogen Energy* **2007**, *32*, 2791-2802.

(78) Funk, J. E. Thermochemical Hydrogen Production: Past and Present. *Int. J. Hydrogen Energy* **2001**, *26*, 185-190.

(79) Fletcher, E. A.; Moen, R. L. Hydrogen and Oxygen from Water. *Science* **1978**, *197*, 1050-1056.

(80) Lange, M.; Roeb, M.; Sattler, C.; Pitz-Paal, R. T-S Diagram Efficiency Analysis of Two-Step Thermochemical Cycles for Solar Water Splitting under Various Process Conditions. *Energy* **2014**, *67*, 298-308.

(81) Kogan, A. Direct Solar Thermal Splitting of Water and On-Site Separation of the Products-II. Experimental Feasibility Study. *Int. J. Hydrogen Energy* **1998**, *23*, 89-98.

(82) Lede, J.; Villermaux, J.; Ouzane, R.; Hossain, M. A.; Ouahes, R. Production of Hydrogen by Simple Impingment of a Turbulent Jet of Steam upon a High Temperature Zirconia Surface. *Int. J. Hydrogen Energy* **1987**, *12*, 3-11.

(83) Ihara, S. On the Study of Hydrogen Production from Water Using Solar Thermal Energy. *Int. J. Hydrogen Energy* **1980**, *5*, 527-534.

(84) Ermanoski, I.; Miller, J. E.; Allendorf, M. D. Efficienct Maximization in Solar-Thermochemical Fuel Production: Challenging the Concept of Isothermal Water Splitting. *Phys. Chem. Chem. Phys.* **2014**, *16*, 8418-8427.

(85) Beghi, G. E. Development of Thermochemical and Hybrid Processes for Hydrogen Production. *Int. J. Hydrogen Energy* **1985**, *10*, 431-438.

(86) Abraham, B. M.; Schreiner, F. General Principles Underlying Chemical Cycles Which Thermally Decompose Water into the Elements. *Ind. Eng. Chem., Fundam.* **1974**, *13*, 305-310.

(87) Rosen, M. A. Advances in Hydrogen Production by Thermochemical Water Decomposition: A Review. *Energy* **2010**, *35*, 1068-1076.

(88) Smestad, G. P.; Steinfeld, A. Review: Photochemical and Thermochemical Production of Solar Fuels from H_2O and CO_2 Using Metal Oxide Catalysys. *Ind. Eng. Chem. Res.* **2012**, *51*, 11828-11840.

(89) Charvin, P.; Abanades, S.; Lemort, F.; Flamant, G. Hydrogen Production by Three-Step Solar Thermochemical Cycles Using Hydroxides and Metal Oxide Systems. *Energy Fuels* **2007**, *21*, 2919-2928.

(90) Xu, B.; Bhawe, Y.; Davis, M. E. Spinel Metal Oxide-Alkali Carbonate-Based, Low-Temperature Thermochemical Cycles for Water Splitting and CO_2 Reduction. *Chem. Mater.* **2013**, *2013*, 1564-1571.

(91) Miller, J. E.; McDaniel, A. H.; Allendorf, M. D. Considerations in the Design of Materials for Solar-Driven Fuel Production Using Metal-Oixde Thermochemical Cycles. *Adv. Energy Mater.* **2014**, *4*, 1300469(1-19).

(92) Meredig, B.; Wolverton, C. First-Principles Thermodynamic Framework for the Evaluation of Thermochemical H_2O- or CO_2-Splitting Materials. *Phys. Rev. B* **2009**, *80*, 245119(1-8).

(93) Venstrom, L. J.; Petkovich, N.; Rudisill, S.; Stein, A.; Davidson, J. H. The Effects of Morphology on the Oxidation of Ceria by Water and Carbon Dioxide. *J. Sol. Energy Eng.* **2012**, *134*, 011005(1-8).

(94) Furler, P.; Scheffe, J. R.; Steinfeld, A. Syngas Production by Simultaneous Splitting of H_2O and CO_2 *via* Ceria Redox Reactions in a High-Temperature Solar Reactor. *Energy Environ. Sci.* **2012**, *5*, 6098-6103.

(95) Furler, P.; Scheffe, J.; Marxer, D.; Gorbar, M.; Bonk, A.; Vogt, U.; Steinfeld, A. Thermochemical CO_2 Splitting *via* Redox Cycling of Ceria Reticulated Foam Structures with Dual-Scale Porosities. *Phys. Chem. Chem. Phys.* **2014**, *16*, 10503-10511.

(96) Gibbons, W. T.; Venstrom, L. J.; De Smith, R. M.; Davidson, J. H.; Jackson, G. S. Ceria-Based Electrospun Fibers for Renewable Fuel Production *via* Two-Step Thermal Redox Cycles for Carbon Dioxide Splitting. *Phys. Chem. Chem. Phys.* **2014**, *16*, 14271-14280.

(97) Chueh, W. C.; Haile, S. M. Ceria as a Thermochemical Reaction Medium for Selectively Generating Syngas or Methane from H_2O and CO_2. *ChemSusChem* **2009**, *2*, 735-739.

(98) Gokon, N.; Hasegawa, T.; Takahashi, S.; Kodama, T. Thermochemical Two-Step Water-Splitting for Hydrogen Production Using Fe-YSZ Particles and a Ceramic Foam Device. *Energy* **2008**, *33*, 1407-1416.

(99) Abanades, S.; Flamant, G. Thermochemical Hydrogen Production from a Two-Step Solar-Driven Water-Splitting Cycle Based on Cerium Oxides. *Sol. Energy* **2006**, *80*, 1611-1623.

(100) Lapp, J.; Davidson, J. H.; Lipiński, W. Efficiency of Two-Step Solar Thermochemical Non-Stoichiometric Redox Cycles with Heat Recovery. *Energy* **2012**, *37*, 591-600.

(101) Lapp, J.; Lipiński, W. Transient Three-Dimensional Heat Transfer Model of a Solar Thermochemical Reactor for H_2O and CO_2 Splitting Via Nonstoichiometric Ceria Redox Cycling. *J. Sol. Energy Eng.* **2014**, *136*, 031006(1-11).

(102) Hao, Y.; Yang, C.-K.; Haile, S. M. High-Temperature Isothermal Chemical Cycling for Solar-Driven Fuel Production. *Phys. Chem. Chem. Phys.* **2013**, *15*, 17084-17092.

(103) Bader, R.; Venstrom, L. J.; Davidson, J. H.; Lipiński, W. Thermodynamic Analysis of Isothermal Redox Cycling of Ceria for Solar Fuel Production. *Energy Fuels* **2013**, *27*, 5533-5544.

(104) Allendorf, M. D.; Diver, R. B.; Siegel, N. P.; Miller, J. E. Two-Step Water Splitting Using Mixed-Metal Ferrites: Thermodynamic Analysis and Characterization of Synthesized Materials. *Energy Fuels* **2008**, *22*, 4115-4124.

(105) Haltiwagner, J. F.; Davidson, J. H.; Wilson, E. J. Renewable Hydrogen from the Zn/ZnO Solar Thermochemical Cycle: A Cost and Policy Analysis. *J. Sol. Energy Eng.* **2010**, *132*, 041011(1-8).

(106) Nakamura, T. Hydrogen Production from Water Utilizing Solar Heat at High Temperatures. *Sol. Energy* **1977**, *19*, 467-475.

(107) Stamatiou, A.; Loutzenhiser, P. G.; Steinfeld, A. Solar Syngas Production via H_2O/CO_2-Splitting Thermochemical Cycles with Zn/ZnO and FeO/Fe_3O_4 Redox Reactions. *Chem. Mater.* **2010**, *22*, 851-859.

(108) Charvin, P.; Abanades, S.; Flamant, G.; Lemort, F. Two-Step Water Splitting Thermochemical Cycle Based on Iron Oxide Redox Pair for Solar Hydrogen Production. *Energy* **2007**, *32*, 1124-1133.

(109) Tamaura, Y.; Steinfeld, A.; Kuhn, P.; Ehrensberger, K. Production of Solar Hydrogen by a Novel, 2-Step, Water-Splitting Thermochemical Cycle. *Energy* **1995**, *20*, 325-330.

(110) Han, S. B.; Kang, T. B.; Joo, O. S.; Jung, K. D. Water Splitting for Hydrogen Production with Ferrites. *Sol. Energy* **2007**, *81*, 623-628.

(111) Fresno, F.; Fernández-Saavedra, R.; Gómez-Mancebo, M. B.; Vidal, A.; Sánchez, M.; Rucandio, M. I.; Quejido, A. J.; Romero, M. Solar Hydrogen Production by Two-Step Thermochemical Cycles: Evaluation of the Activity of Commercial Ferrites. *Int. J. Hydrogen Energy* **2009**, *34*, 2918-2924.

(112) Fresno, F.; Yoshida, T.; Gokon, N.; Fernández-Saavedra, R.; Kodama, T. Comparative Study of the Activity of Nickel Ferrites for Solar Hydrogen Production by Two-Step Thermochemical Cycles. *Int. J. Hydrogen Energy* **2010**, *35*, 8503-8510.

(113) Roeb, M.; Gathmann, N.; Neises, M.; Sattler, C.; Pitz-Paal, R. Thermodynamic Analysis of Two-Step Solar Water Splitting with Mixed Iron Oxides. *Int. J. Energy Res.* **2009**, *33*, 893-902.

(114) Bhosale, R. R.; Shende, R. V.; Puszynski, J. A. Thermochemical Water-Splitting for H_2 Generation Using Sol-Gel Derived Mn-Ferrite in a Packed Bed Reactor. *Int. J. Hydrogen Energy* **2012**, *37*, 2924-2934.

(115) Kodama, T.; Kondoh, Y.; Yamamoto, R.; Andou, H.; Satou, N. Thermochemical Hydrogen Production by a Redox System of ZrO_2-Supported Co(II)-Ferrite. *Sol. Energy* **2005**, *78*, 623-631.

(116) Scheffe, J. R.; Allendorf, M. D.; Coker, E. N.; Jacobs, B. W.; McDaniel, A. H.; Weimer, A. W. Hydrogen Production via Chemical Looping Redox Cycles Using Atomic Layer Deposition-Synthesized Iron Oxide and Cobalt Ferrites. *Chem. Mater.* **2011**, *23*, 2030-2038.

(117) Gokon, N.; Kodama, T.; Imaizumi, N.; Umeda, J.; Seo, T. Ferrite/Zirconia-Coated Foam Device Prepared by Spin Coating for Solar Demonstration of Thermochemical Water-Splitting. *Int. J. Hydrogen Energy* **2011**, *36*, 2014-2028.

(118) Coker, E. N.; Ambrosini, A.; Rodriguez, M. A.; Miller, J. E. Ferrite-YSZ Composites for Solar Thermochemical Production of Synthetic Fuels: *In Operando* Characterization of CO_2 Reduction. *J. Mater. Chem.* **2011**, *21*, 10767-10776.

(119) Scheffe, J. R.; McDaniel, A. H.; Allendorf, M. D.; Weimer, A. W. Kinetics and Mechanism of Solar-Thermochemical H_2 Production by Oxidation of a Cobalt Ferrite-Zirconia Composite. *Energy Environ. Sci.* **2013**, *6*, 963-973.

(120) Kaneko, H.; Miura, T.; Fuse, A.; Ishihara, H.; Taku, S.; Fukuzumi, H.; Naganuma, Y.; Tamaura, Y. Rotary-Type Solar Reactor for Solar Hydrogen Production with Two-Step Water Splitting Process. *Energy Fuels* **2007**, *21*, 2287-2293.

(121) Diver, R. B.; Miller, J. E.; Allendorf, M. D.; Siegel, N. P.; Hogan, R. E. Solar Thermochemical Water-Splitting Ferrite-Cycle Heat Engines. *J. Sol. Energy Eng.* **2008**, *130*, 041001(1-8).

(122) Gokon, N.; Mataga, T.; Kondo, N.; Kodama, T. Thermochemical Two-Step Water Splitting by Internally Circulating Fludized Bed of $NiFe_2O_4$ Particles: Successive Reaction of Thermal-Reduction and Water-Decomposition Steps. *Int. J. Hydrogen Energy* **2011**, *36*, 4757-4767.

(123) Steinfeld, A. Solar Hydrogen Production via a Two-Step Water-Splitting Thermochemical Cycle Based on Zn/ZnO Redox Reactions. *Int. J. Hydrogen Energy* **2002**, *27*, 611-619.

(124) Venstrom, L. J.; Davidson, J. H. The Kinetics of the Heterogeneous Oxidation of Zinc Vapor by Carbon Dioxide. *Chem. Eng. Sci.* **2013**, *93*, 163-172.

(125) Stamatiou, A.; Loutzenhiser, P. G.; Steinfeld, A. Solar Syngas Production from H_2O and CO_2 via Two-Step Thermochemical Cycles Based on Zn/ZnO and FeO/Fe_3O_4 Redox Reactions: Kinetic Analysis. *Energy Fuels* **2010**, *24*, 2716-2722.

(126) Loutzenhiser, P. G.; Meier, A.; Steinfeld, A. Review of the Two-Step H_2O/CO_2-Splitting Solar Thermochemical Cycle Based on Zn/ZnO Redox Reactions. *Materials* **2010**, *3*, 4922-4938.

(127) Abanades, S. Thermogravimetry Analysis of CO_2 and H_2O Reduction from Solar Nanosized Zn Powder for Thermochemical Fuel Production. *Ind. Eng. Chem. Res.* **2012**, *51*, 741-750.

(128) Wegner, K.; Ly, H. C.; Weiss, R. J.; Pratsinis, S. E.; Steinfeld, A. In Situ Formation and Hydrolysis of Zn Nanoparticles for H_2 Production by the 2-Step ZnO/Zn Water-Splitting Thermochemical Cycle. *Int. J. Hydrogen Energy* **2006**, *31*, 55-61.

(129) Perkins, C.; Lichty, P. R.; Weimer, A. W. Thermal ZnO Dissociation in a Rapid Aerosol Reactor As Part of a Solar Hydrogen Production Cycle. *Int. J. Hydrogen Energy* **2008**, *33*, 499-510.

(130) Schunk, L. O.; Haeberling, P.; Wepf, S.; Wuillemin, D.; Meier, A.; Steinfeld, A. A Receiver-Reactor for the Solar Thermal Dissociation of Zinc Oxide. *J. Sol. Energy Eng.* **2008**, *130*, 021009(1-6).

(131) Chueh, W. C.; Haile, S. M. A Thermochemical Study of Ceria: Exploiting an Old Material for New Modes of Energy Conversion and CO_2 Mitigation. *Phil. Trans. R. Soc. A* **2010**, *368*, 3269-3294.

(132) Chueh, W. C.; Falter, C.; Abbott, M.; Scipio, D.; Furler, P.; Haile, S. M.; Steinfeld, A. High-Flux Solar-Driven Thermochemical Dissociation of CO_2 and H_2O Using Nonstoichiometric Ceria. *Science* **2010**, *330*, 1797-1801.

(133) Rudisill, S. G.; Venstrom, L. J.; Petkovich, N. D.; Quan, T.; Hein, N.; Boman, D. B.; Davidson, J. H.; Stein, A. Enhanced Oxidation Kinetics in Thermochemical Cycling of CeO_2 through Templated Porosity. *J. Phys. Chem. C* **2013**, *117*, 1692-1700.

(134) Scheffe, J. R.; Li, J.; Weimer, A. W. A Spinel Ferrite/Hercynite Water-Splitting Redox Cycles. *Int. J. Hydrogen Energy* **2010**, *35*, 3333-3340.

(135) Arifin, D.; Aston, V. J.; Liang, X.; McDaniel, A. H.; Weimer, A. W. $CoFe_2O_4$ on a Porous Al_2O_3 Nanostructure for Solar Thermochemical CO_2 Splitting. *Energy Environ. Sci.* **2012**, *5*, 9438-9443.

(136) Muhich, C. L.; Evanko, B. W.; Weston, K. C.; Lichty, P.; Liang, X.; Martinek, J.; Musgrave, C. B.; Weimer, A. W. Efficient Generation of H_2 by Splitting Water with an Isothermal Redox Cycle. *Science* **2013**, *341*, 540-542.

(137) Stølen, S.; Bakken, E.; Mohn, C. E. Oxygen-Deficient Perovskite: Linking Structure, Energetics and Ion Transport. *Phys. Chem. Chem. Phys.* **2006**, *8*, 429-447.

(138) Scheffe, J. R.; Weibel, D.; Steinfeld, A. Lanthanum-Strontium-Manganese Perovskites as Redox Materials for Solar Thermochemical Splitting of H_2O and CO_2. *Energy Fuels* **2013**, *27*, 4250-4257.

(139) McDaniel, A. H.; Miller, E. C.; Arifin, D.; Ambrosini, A.; Coker, E. N.; O'Hayre, R.; Chueh, W. C.; Tong, J. Sr- and Mn-Doped $LaAlO_{3-\delta}$ for Solar Thermochemical H_2 and CO Production. *Energy Environ. Sci.* **2013**, *6*, 2424-2428.

(140) Demont, A.; Abanades, S.; Beche, E. Investigation of Perovskite Structures as Oxygen-Exchange Redox Materials for Hydrogen Production from Thermochemical Two-Step Water-Splitting Cycles. *J. Phys. Chem. C* **2014**, *118*, 12682-12692.

(141) Peña, M. A.; Fierro, J. L. G. Chemical Structures and Performance of Perovskite Oxides. *Chem. Rev.* **2001**, *101*, 1981-2017.

Chapter Two

Controlling Macro- and Mesostructures through Hard and Soft Templating

---

Parts of this chapter are from: Petkovich, N. D.; Stein, A. Controlling Macro- and Mesostructures with Hierarchical Porosity through Combined Hard and Soft Templating. *Chem. Soc. Rev.* **2013**, *42*, 3721-3739. – These parts are reproduced by permission of The Royal Society of Chemistry. Available at: http://dx.doi.org/10.1039/C2CS35308C

2.1. Introduction to Templated Porous Materials

For most of recorded history, humanity was completely unaware of the impressive variety of complex, microscopic structures that exist in the natural world. Only in the last 400 years, starting with the advent of the optical microscope, have we been able to glimpse the intricate architectures of the materials that surround us. What has been found during that time is nothing short of astonishing, and perhaps taken for granted, since microscopy is now commonplace. A block of wood contains aligned networks of porous cells whose function is to transport water. Certain species of algae, diatoms, have porous, silica-containing shells that function as protective cell walls. With the development of electron microscopy, researchers have gained the ability to resolve natural structures at even smaller length scales. For instance, the wing of the *Morpho* butterfly is composed of periodic nanometer-sized scales that were determined to be the source of its iridescent coloration. Minerals, such as aluminosilicate zeolites, possess a crystalline framework with pores that are on the Å-scale.

While there are many examples of hierarchical complexity in nature, the focus of this chapter is how to synthesize materials with complex pore architectures at the μm- and nm-scale. These hierarchically-porous materials are an exciting new frontier for materials research. For a variety of compounds and composites, it is now possible to simultaneously realize the advantages provided by multiple pore size regimes.[1] Mesopores (2–50 nm in diameter) and micropores (<2 nm in diameter) help impart a high surface area and pore volume in a material, providing numerous reactive sites, size-selectivity for molecules, and a substantial interfacial area. These small pores can then be coupled with larger macropores (>50 nm in diameter) that can improve mass transport through a structure, offsetting any diffusion limitations present in purely micro-/mesoporous materials. Owing to their structure, hierarchical materials provide substantial performance boosts in numerous applications: energy storage, energy conversion, catalysis, catalytic supports, filtration, sensing, medical diagnostics, and medical therapies.[1] Well-controlled "self-assembly" approaches, wherein a host of interactions direct spontaneous equilibrium structure formation (or the formation of kinetically-stable states), are elegant pathways for the synthesis of hierarchically-porous materials that would be difficult or expensive to generate otherwise. Of course, this is all provided that one can find suitable conditions and design the proper compounds for self-assembly processes.

Every synthesis of porous materials described in this thesis uses some type of rigid or semi-rigid material as a "hard template." A good way to understand this type of templating is through an analogy to the millennia-old technique of metal casting. In hard templating, one first finds a

rigid, porous object with nm- or μm-scale features.[2] This is the template or "mold." Then one must find a precursor, generally a liquid, which either adheres to the surface of the template or fills the void spaces within the template. After a series of processing steps, the precursor is transformed into a solid material. Keeping with the analogy, this solid can be considered the "cast" in the "mold." Finally, one removes the template, liberating the cast. If the precursor was coated on the template surface, a hollow replica of the template is obtained.[2] Alternately, if the precursor fills the void spaces of the template, the negative replica of the template is obtained.[1]

Another form of templating, soft templating, is a useful pathway for the formation of materials with ordered mesopores. The building blocks of soft templates are amphiphilic molecules known as surfactants, which contain both hydrophilic and hydrophobic domains. In water or polar solvents, these surfactants can self-assemble into supramolecular aggregates called micelles. By altering certain variables (temperature, pressure, surfactant concentration), it is possible for the micelles to organize even further, undergoing a phase transition to a lyotropic liquid crystalline state.[3] True to the name, a lyotropic liquid crystal possesses crystal-like orientational order and a liquid-like mobility of the constituent surfactants.[4] Researchers discovered that certain inorganic precursors can co-assemble with surfactants and form a solid structure surrounding a liquid crystalline phase. Unlike hard templating, the precursor actively participates in the self-assembly of the liquid crystalline template.[5] After processing and removal of the liquid crystal, a porous mesostructured material, the negative replica of the liquid crystal template, is formed. Further research has increased the flexibility of this process far beyond the mesoporous SiO_2 materials first synthesized in the 1990s, including new syntheses that combine hard and soft templating.[5]

The next two sections are a more comprehensive discussion of hard and soft templating for the synthesis of porous materials. These sections serve as a framework for an extended discussion of the great diversity of porous materials that can be synthesized through multiple templating. The discussion on multiple templating is limited to specific examples from the past few years. The examples illustrate how pore architectures can be tuned and how different types of compounds can be templated. Key examples are also given of how these materials have already shown excellent performance in many different applications.

2.2 The Fundamentals of Hard Templating

Hard templating pathways for the production of porous materials offer an opportunity for the accurate replication of a template structure. The mold and cast analogy from the introduction works well for these materials. That being said, the analogy slightly breaks down in actual syntheses. Different factors, including interactions between the precursor and the template, can change the pore architecture present in the final porous material. In other cases, hard templates are formed during the course of a synthesis. Ultimately, the product may not be an exact inverse replica of the mold. But to understand why that is the case, a description of the possible materials that can be used as hard templates and then general steps of hard templating must be presented.

2.2.1 Types of Hard Template

Many types of rigid structures with μm- or nm-scale features can be used as templates (Figure 2.1). Some of these hard templates could be considered mundane, including some materials that might not even seem suitable for advanced nanochemistry. For example, a piece of filter paper contains a network of μm-sized cellulose fibers that can serve as a template for hollow tubes of SiO_2.[6] Other templates are more exotic, and allow for the production of intricate porous structures. Going over every possible template is beyond the scope of this chapter. However, key families of hard templates can be identified. For the purposes of this section, three distinct groups of hard templates are discussed: extended structures, *in situ* templates, and discrete particles. The rationale for this division lies in differences between the general synthesis steps for each of these groups, and this point is further discussed in Section 2.2.2.

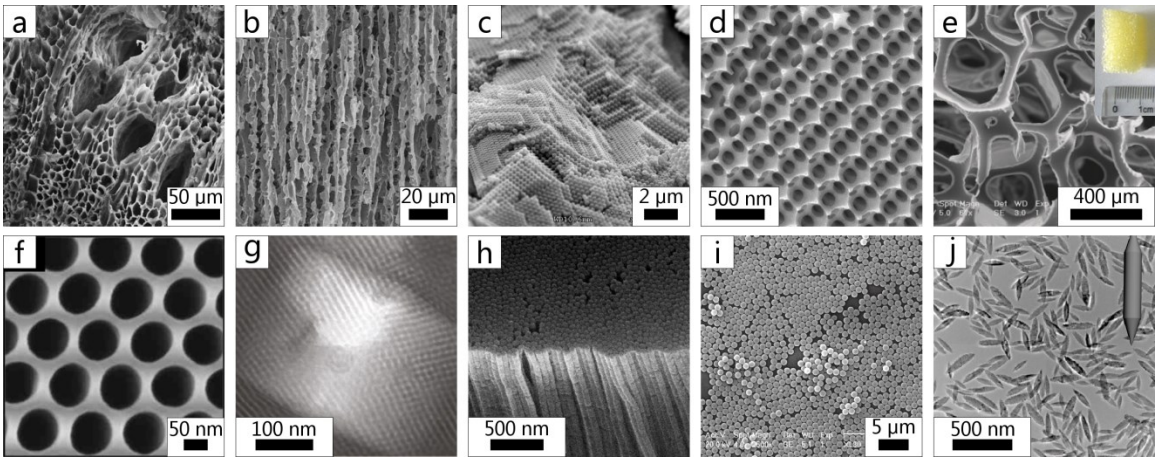

Figure 2.1 A compilation of images that show representative examples for certain categories of hard templates. The following materials are presented: a plant stem (a), freeze-dried starch (b), a polymeric colloidal crystal (c), a three-dimensionally ordered macroporous structure (d), a polyurethane foam (e), an AAO membrane (f), an *in situ* NaCl crystal template (g), a polymer produced from an AAO membrane (h), individual colloidal spheres (i), and rod-shaped nanoparticles (j). Adapted with permission from [29] (a) ©2010 Springer; from [32] (b) and [48] (inset) ©2010, 2012 Elsevier; from [39] (c), [47] (e), [8] (g), [33] (i), and [12] (j) ©2009, 2010, 2011 American Chemical Society; from [26] (f) ©2010 John Wiley and Sons; and from [54] (f) ©2010 Royal Society of Chemistry.

2.2.1.1 Macroscopic Structures

Many different preassembled hard templates can be used for the synthesis of porous materials with spatial dimensions that are resolvable (or nearly resolvable) by the human eye. These "macroscopic structures," as they are referred to in this chapter, include films, fibers, powders (up to hundreds of µm), and monolithic objects with dimensions greater than one mm. Certain kinds of hard template are only available as a single type of macroscopic structure. For instance, sheets of aluminium can be electrooxidized, producing anodized Al_2O_3 (AAO) membranes with cylindrical macropores normal to the surface (Figure 2.1 f).[7] The macroscopic morphology of this type of template is limited to a planar sheet. In contrast, other kinds of hard template have a far greater diversity of macroscopic structures. For instance, many different macroscopic morphologies are available when using templates derived from biological materials.[2] Similarly, a range of macroscopic structures can also be formed through deliberate changes to the synthesis of a hard template. Colloidal crystals are one such example. These templates typically consist of self-assembled face-centered cubic arrays of monodisperse polymer or SiO_2 spheres (Figure 2.1 c). To produce colloidal crystals, one typically starts with a suspension of colloidal spheres. Depending on how the suspension is processed, different macroscopic structures can be produced.

Sedimentation of a sphere suspension under gravity generally leads to the formation of monolithic colloidal crystals or powders, while controlled evaporation of the suspension onto a substrate leads to the formation of colloidal crystal films.[1]

2.2.1.2 *In Situ* Templates

Hard templates do not always have to be formed (or found) prior to a synthesis; a compound in the precursor can be transformed into a template. This compound can either be a solute intentionally added to the precursor solution, or even the solvent itself. Subsequent thermal processing induces physical or chemical transformations that convert the compound into the solid template. Many different materials can function as an *in situ* hard template. Salts (Figure 2.1 g),[8] carbon,[9] and ice crystals[10] are a few such examples that are encountered in a subsequent section. Carbon is used as an *in situ* template for several different porous materials discussed in Chapters 3, 4, and 6. In general, porous materials produced from *in situ* hard templates have a monolithic macroscopic structure.

2.2.1.3 Discrete Particles

For a variety of applications, discrete, colloidal particles (smaller than 10 μm in size) are favored over macroscopic structures. Different hard templates can be utilized for the formation of various templated particles, allowing for precise control over particle dimensions and shape. Monodisperse colloidal spheres, such as polymer or SiO_2 spheres, are fairly common templates for the synthesis of hollow spherical particles (Figure 2.1 i).[11] Additionally, hollow spheres containing encapsulated particles (yolk or rattle structures) are readily synthesized using these discrete particle templates. Other nm- or μm-scale particles can serve as hard templates. As an example, colloidal metal oxide particles[11,12] (Figure 2.1 j) can be employed as templates for hollow, non-spherical objects.

2.2.2 Synthesis Routes for Hard Templating

Once one has selected a hard template, the next step is to synthesize a templated porous material. The general schemes described herein are employed both in hard templating and combined hard and soft templating. While the general steps in any hard templating synthesis are fairly similar, each of the three groups of hard templates has unique requirements for their use. Templating using macroscopic structures serves a good starting point for the discussion of synthesis routes, since these types of hard template are frequently used in examples of multiple templating described later in this chapter and the rest of the thesis.

2.2.2.1 Templating with Macroscopic Structures

Four general steps are needed to synthesize a porous material from a hard template (Figure 2.2), starting with the synthesis of a precursor solution. While gas-phase molecules or solid particles can be used as precursors, solution-based precursors are principally used for multiple templating.[1] For the formation of a templated inorganic material, the simplest solution-based precursor is a salt dissolved in a polar solvent. Metal alkoxides dissolved in aliphatic alcohols are also commonly used as precursors. With metal alkoxides, formation of the final inorganic material needs to be catalyzed by acid or base. When SiO_2 is the targeted composition of the porous material, a common precursor solution is a mixture of the alkoxide tetraethyl orthosilicate (TEOS), aqueous hydrochloric acid, and ethanol.[1] The synthesis of templated carbon-containing materials can be accomplished through the use of low molecular weight phenol-formaldehyde oligomers (PF sol) dissolved in a polar solvent. An acidic catalyst is also added ensure cross-linking of the oligomers.[13]

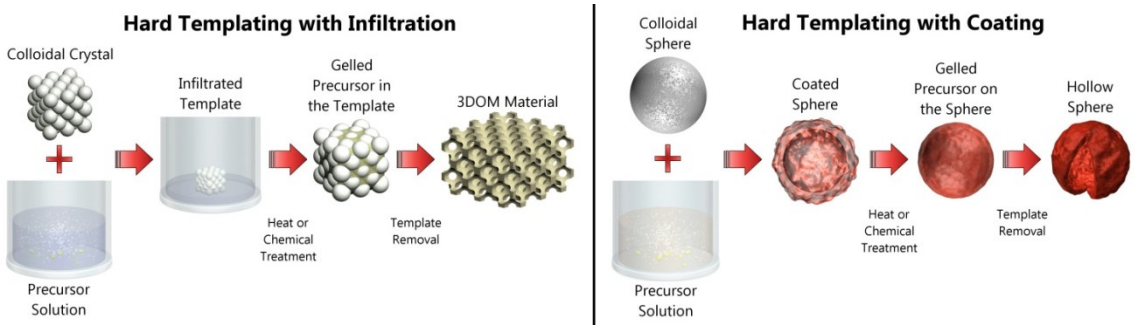

Figure 2.2 Schemes detailing the hard templating process. Left: An example of hard templating conducted using an infiltration process. Right: An example of hard templating conducted via a coating process.

Step two consists of filling or coating a hard template with a precursor. This is done by either letting a precursor solution infiltrate the void spaces of hard template via capillary action (Figure 2.2, left), or by soaking a hard template in the precursor solution (Figure 2.2, right).[2] Ensuring that the precursor uniformly fills or coats the template is a crucial part of this step. Several important things need to be considered in order to achieve this goal. First, the precursor solution should easily wet the template surface (i.e., have similar polarity). Second, the precursor needs to have sufficiently low viscosity so it can easily fill or coat the template. Additional solvent in the precursor often helps in this respect, provided the precursor does not become too dilute to adequately fill a template. Different methods that rely on the assistance of vacuum suction can also improve the infiltration of low viscosity precursors (and remove excess solvent).[1] Finally,

one must check that the precursor does not swell or dissolve the hard template.

After the template has been coated or filled, the precursor needs to be transformed into a solid-phase material. Chemical or thermal treatments are required for this step. Sol-gel chemistry is generally used to form templated inorganic oxides. In the initial step, hydrolysis of the salt (equation 2.1) or alkoxide (equation 2.2) takes place. Acid or base-catalyzed condensation occurs next, which produces oxo- (equation 2.3) or hydroxo- (equation 2.4) linkages between metal/metalloid atoms. Colloidal oxide clusters form during this process, producing a sol (a solid colloid dispersed in a liquid).[14]

$$M–X + H_2O \rightarrow M–OH + ROH,\ X = \text{Anion} \quad (2.1)$$

$$M–OR + H_2O \rightarrow M–OH + ROH \quad (2.2)$$

$$M–OH + XO–M \rightarrow M–O–M + X–OH,\ X = H \text{ or } R \quad (2.3)$$

$$M–OH + M–OX \rightarrow M–(OH)–M–OX,\ X = H \text{ or } R \quad (2.4)$$

Continued condensation, often at elevated temperatures, leads to the formation of a three-dimensional gel. Other non-hydrolytic sol-gel routes can be used, including routes that involve the condensation of metal carboxylates and alkoxides.[15] Citric acid or other polycarboxylic acids are capable of binding metal ions and can then undergo a condensation polymerization with various polyols.[16,17] A polyester gel that contains well-distributed metal ions is formed though this route, commonly known as the Pechini process. For templated organic or carbon materials, polymerization of PF polymeric sol takes place through a similar condensation route, leading to a cross-linked resin.[13] No matter what precursor is used for templating, it is essential that rapid gelation or uncontrolled precipitation is avoided. This can be challenging for certain precursors. Transition metal alkoxides, for instance, require highly acidic conditions, chelators, and/or inert gas environments to slow the rate of condensation.[18,19] Chelating agents and highly acidic conditions are used to stabilize precursors described in Chapters 3, 4, 5, and 6.

Further consolidation of the network of the templated material is often needed via high temperature (>300 °C) thermal treatment. This treatment increases the degree of condensation for the templated material and also help removes residual solvent from the structure. Crystallization of many metal oxides takes place at elevated temperatures, as does carbonization of PF resin.[13,18] Proper control of the temperature, heating rate and hold times is critical. Considerable shrinkage of the porous material (~20–40%) generally takes place, and uncontrolled evaporation (or combustion) of residual precursor can further exacerbate this phenomenon.[18] Also, a targeted crystalline polymorph may only form in a certain temperature range. Excessive temperatures or

prolonged thermal treatment can cause undesired solid-state reactions, sintering, and crystalline growth, leading to densification of the structure and closure of pores (if the template is already removed).[1] Removal of the template is the final and sometimes optional step. Chemical etching is a viable option for many different templates, including oxide templates. Templates containing SiO_2 are etched away in hot, concentrated alkali hydroxide or hydrofluoric acid (HF).[3] Other metal oxide templates, such as AAO membranes, can be dissolved in strong acids.[7] Suitable organic solvents are often used to dissolve polymeric templates. Unfortunately, it is difficult to remove all residual template material via etching and several cycles of etching may need to be performed. One must also make sure that the etching chemical does not dissolve the porous hard templated material. Plasma can also be employed to etch out polymeric templates.[20] A further advantage of this is that residual organic groups can be removed and infiltrated nanoparticles can be sintered together into a cohesive network.[20]

With polymeric templates, another common option for this final step is thermal treatment in either an O_2-containing environment (calcination) or an inert gas environment (pyrolysis). Calcination is quite effective at removing the template; however, appropriate temperature ramps should be used to avoid localized heating that can disrupt the structure during combustion.[1] Pyrolysis is used to depolymerize polymeric templates into monomers or oligomers. Flowing inert gas can be used to flush out these molecules and any other reaction products from a system.

2.2.2.2 *In Situ* Pathway

For syntheses that employ *in situ* templates, the infiltration or coating step is not required. The template is formed during a chemical or thermal processing step. Control over the amount of template and the location of the template are the key factors in determining pore morphology.[21] Template content is, in principle, easy to control, as one can increase the amount of template precursor in the reaction mixture. However, compatibility with the other precursor components must be ensured. Additionally, a high content of template can lead to fragile structures that collapse during template removal, whereas a low content of template can lead to isolated, closed pores.[21] Phase separation of the template during processing allows for the formation of extended, interconnected pore networks.[21] This process must be carefully controlled and optimized with respect to reaction temperature, concentration of precursors, and/or catalyst used for formation of the template.

2.2.2.3 Templating with Discrete Particles

The basic synthesis steps needed for the formation of porous materials via discrete particle templates are essentially outlined in the right side of Figure 2.2. However, a new challenge comes about that is directly tied to the small dimensions of the discrete particles. When a discrete particle template is dispersed in a precursor, that precursor must be directed to the particle surface and preferentially coat it. If this is not achieved, the precursor may coat other surfaces in the reaction vessel or precipitate without coating the template.[11] Formation of a contiguous shell can be achieved through modification of the exposed surfaces of the particle templates. One needs to have a good idea of what intermolecular interactions or reactions are sought to ensure a favorable coating. In many cases, electrostatic interactions can be used to draw a precursor to a surface and direct the coating process.[11] Polymer spheres often carry a charge from the initiator used in their formation, or can be functionalized with carboxylate groups.[1] Adsorption of polyelectrolytes, generally polystyrene sulfonate (negative charge) or poly(diallyldimethylammonium) salts (PDDA, positive charge), can also be used to tune surface charge on a template. SiO_2 spheres offer additional functionalization options, due to the presence of surface hydroxyls. These groups can undergo reactions with alkoxides that are bonded to organic functional groups, such as aliphatic amines.[22]

Once the appropriate modifications to the discrete particle template surface have been made, coating can take place. Salt or alkoxide precursors are added to solution, and these precursors precipitate or condense at the template surface.[11] Surface sites, such as the amines mentioned earlier, can initiate sol-gel processes.[23] Intermolecular forces can also be harnessed to chelate precursors or attract precursors of opposite charge.[22] It cannot be stressed enough that it is not trivial to prevent the precursor from precipitating, condensing, or aggregating away from the template surface. Strict control of the rate of precipitation/condensation is critical.

2.3 The Fundamentals of Soft Templating

The self-assembly that occurs during soft templating is a remarkable phenomenon that involves the structuring of surfactant, precursor, and solvent molecules. Comprehending the processes that govern self-assembly may seem daunting, but by understanding three interrelated topics, a solid foundation in soft templating can be gained. The first topic is the self-assembly of surfactants in solutions that do not contain inorganic or organic precursors. The second topic is types of surfactant molecules that are used in soft templating. The final topic is the soft-templating synthesis techniques themselves, including the processes that govern the formation of

a mesoporous material. Through a deeper understanding of the variables that impact mesostructure formation, better control can be established over the final architecture of the mesopore network. Much of this knowledge is the basis for attempts to control mesostructure formation in syntheses that employ multiple templates.

2.3.1 Self Assembly of Micelles and Liquid Crystals

Without question, the most important part of soft templating is ensuring that micelles and/or a liquid crystalline phase develop. Two conditions have to be met before micelles can form in any solution. First, micelles do not form below a given temperature range, the Krafft temperature.[4] The surfactant does not appreciably dissolve below that temperature and remains a hydrated solid. However, solubility increases dramatically once the Krafft temperature is reached.[4] The surfactant concentration can then be increased to a narrow concentration range at which micelles spontaneously form. This is the critical micelle concentration (cmc); the second condition mentioned above.[3] After reaching the cmc, any added surfactant is incorporated into micelles.

Once micelles form in solution, their shape dictates what liquid crystalline phases can form. The shape of a micelle depends on the structure of the surfactant molecule. A useful concept, the packing parameter (g), can be used to explain why certain liquid crystals form in solution.[24] Simply defined, the packing parameter is $g = v_o/(a_e l_o)$, where v_o is the volume of the hydrophobic tail, a_e is the equilibrium area of the headgroup on the micelle surface, and l_o is the chain length of the tail. Of these variables, a_e is the most complex because it depends on the equilibrium thermodynamics of the solution, including the interfacial tension and the repulsion between surfactant headgroups.[24] Table 1 shows how the packing parameter is related to the typical shape of the micelle. Low values of g imply that the interface between the micelle and solution is highly curved, while higher values mean the interface is less curved. In order of increasing g, spherical, rod-like, and disc-like micelles are found in solution.[3] While reversed micelles and liquid crystals can also be formed ($g > 1$), these structures will not be discussed. Even though new intermolecular interactions (precursor–surfactant) are present during soft templating, the packing parameter is still quite useful for understanding changes in micelle shape. However, the value of g may be considerably different for a surfactant dissolved in a precursor solution versus a surfactant dissolved in a solvent.[18]

In addition to determining micelle shape, the packing parameter can help determine what liquid crystalline phases form with the addition of more surfactant to solution.[3] Figure 2.3 shows models of various types of liquid crystals observed in a surfactant-containing solution. For this

section, the cubic, 2D hexagonal and lamellar structures are the most commonly encountered in templated materials. One set of cubic phases (I) are comprised of spherical micelles that are packed in cubic arrangements.[25] Another set of cubic phases (V_1) are composed of surfactant bilayers folded into complex cubic geometries. This structure is bicontinuous with a continuous surfactant and solvent phase.[3] The 2D hexagonal phase consists of extended cylindrical surfactant structures packed in a hexagonal arrangement.[25] For the lamellar phase, the surfactants are arranged in stacked bilayers. Typical phase changes observed upon increasing the wt% of surfactant in solution are listed in Table 2.1 for different *g* values. These phase changes generally hold in soft templating, but exceptions arise because of interactions between various components in the precursor solution.[5] More substantial changes can arise from liquid crystal confinement in nm-scale pores.[5] It is then best to thoroughly a characterize templated material for an accurate picture. Small-angle X-ray scattering (SAXS) and transmission electron microscopy (TEM) are particularly useful in this regard.[25]

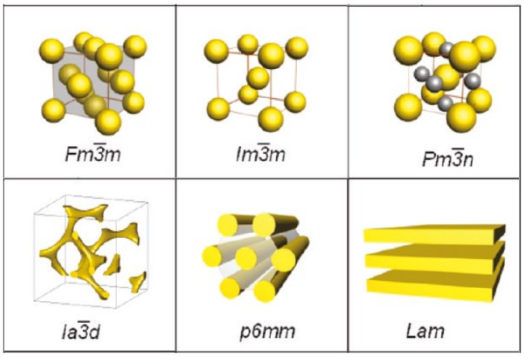

Figure 2.3 Computer generated images of common liquid crystalline phases. *Fm*-3*m*, *Im*-3*m* and *Pm*-3*n* are all cubic phases (I). *Ia*-3*d* is a bicontinuous cubic phase (V_1). *P6mm* is the 2D hexagonal phase and *Lam* is the lamellar phase. Adapted with permission from [25] ©2009 American Chemical Society.

Table 2.1 Changes in micelle shape and phase.

$g = v_o/(a_e l_o)$	<1/3	~1/3–1/2	~1/2	~1/2–1	1
Micelle Shape	Spherical Micelles	Elliptical Micelles	Rod-Like Micelles	Disc-Like Micelles	Bilayers
Phase Changes Upon Increasing Surfactant Concentration	Cubic (I) to 2D Hex. to Cubic (V_1) to Lamellar	2D Hex. to Cubic (V_1) to Lamellar	2D Hex. to Cubic (V_1) to Lamellar	Lamellar or Cubic (V_1) to Lamellar	Lamellar
Packing Shape[a]	Cone	Truncated Cone	Truncated Cone	Truncated Cone	Cylinder

[a] Shape of the surfactant in a micelle or liquid crystal.

Micelles and liquid crystals are dynamic structures that are readily altered when changes are made to the surrounding solution. Rapid shifts to new equilibria are possible, since surfactant molecules quickly exchange (hundreds to thousands of times per second) from micelles to solution and vice versa.[3] One simple change has already been described, the addition of more surfactant. This can increase micelle size or change the liquid crystalline phase.[14] Aromatic or aliphatic hydrocarbons dissolve in the dense hydrophobic cores of some micelles (up to a point).[4] This addition causes micelle cores to swell, and is one method to increase pore size in soft templating. Addition of salts into solution can impact the packing parameter, causing changes in micelle shape or liquid crystal phase. The exact effect of salt addition is highly dependent on both the cation/anion and the specific surfactant.[14]

2.3.2 Types of Surfactant

A considerable flexibility in synthesis conditions, mesopore size, and precursor compounds is possible in soft templating only by changing the surfactant. Fortunately, there are many surfactants that have been synthesized for their utility in consumer and industrial products. Amphiphilic molecules have many roles to play in commercial products, such as detergents for cleaning, emulsifiers (including those used in latex paints), and wetting agents.[4] While one may not be able to choose a soft template by reading the ingredients of a shampoo bottle, the rich chemistry of surfactant molecules is ready to be used in conjunction with inorganic and organic precursors.

Three major classes of surfactant molecules can be harnessed for soft templating: cationic, anionic, and non-ionic surfactants. These surfactants are named because of the charge the head group does or does not carry in neutral pH solution. Cationic surfactants are comprised of at least one amine functional group that serves as a hydrophilic head group and at least one hydrophobic tail.[4] A greater diversity of head groups available for anionic surfactants, including sulfates, sulfonates, carboxylates and phosphates (which are attached to a hydrophobic tail). In soft templating, ionic surfactants typically interact with precursors via electrostatic interactions, including interactions with intervening ions.[5,18] Electrostatic interactions are rarely important in the most popular class of surfactants, non-ionic surfactants. The structure of non-ionic surfactants varies widely from Brij surfactants—which contain a linear alkyl chain connected to a hydrophilic polyethylene oxide (-CH_2-CH_2-O-, PEO) chain—to a panoply of block copolymeric surfactants.[14] Tri-block poly(ethylene oxide)-*block*-poly(propylene oxide)-*block*-poly(ethylene oxide) surfactants (PEO_x-PPO_y-PEO_x), known as Pluronics® are commonly used. In water, the PPO block is sufficiently hydrophobic relative to the PEO block, allowing for micelle formation.[18] Self-assembly processes with non-ionic surfactants are primarily mediated by van der Waals interactions and hydrogen bonding.[5]

An important question may come to mind, "What surfactants should be used for a synthesis that involves soft templating?" While this depends on the specific synthesis, there are some general considerations that can be taken into account. First and foremost, the surfactant should be compatible with all compounds in the precursor solution. For instance, adjustments to the pH may be needed to allow for certain precursor–ionic surfactant interactions or to promote dissolution of certain surfactants.[4,18] Different surfactants are capable of templating different mesopore sizes. Ionic surfactants typically produce either micropores or small mesopores (2–4 nm), whereas non-ionics produce mesopores that range in diameter from a few nm to over 10 nm.[18] Brij surfactants produce small mesopores, and higher molecular weight Pluronics® can template mesopores around 4–7 nm in diameter.[14] Additionally, PEO blocks in block copolymeric surfactants tend to extend into the precursor, leading to the production of microporosity.[1] Certain mesostructures are commonly templated from specific surfactants, as would be predicted by their packing parameter. For instance, the cationic surfactant cetyltrimethylammonium bromide (CTAB) tends to produce 2D hexagonal mesostructures, whereas Pluronic® F127 (nominal composition: $HO(PEO)_{101}(PPO)_{56}(PEO)_{101}H$) tends to template body-centered cubic mesostructures (large head group, smaller *g*).[18,24]

2.3.3 Synthesis Routes for Soft Templating

Adding a precursor to a surfactant-containing solution can cause fairly substantial changes to the self-assembly process that leads to micelle/liquid crystal formation. These changes are a result of the new interactions between the precursor, surfactant, and solvent.[5] As a result, mesostructures that form during soft templating are not necessarily what would be predicted from surfactant–solvent phase diagrams. While basic considerations from surfactant science still apply, the mechanisms underlying soft templating add some new considerations. Pathways for the synthesis of mesoporous materials from soft templates are illustrated in Figure 2.4. The following subsection discusses these paths, the processing/template removal step common to all, and the factors that impact mesostructure formation.

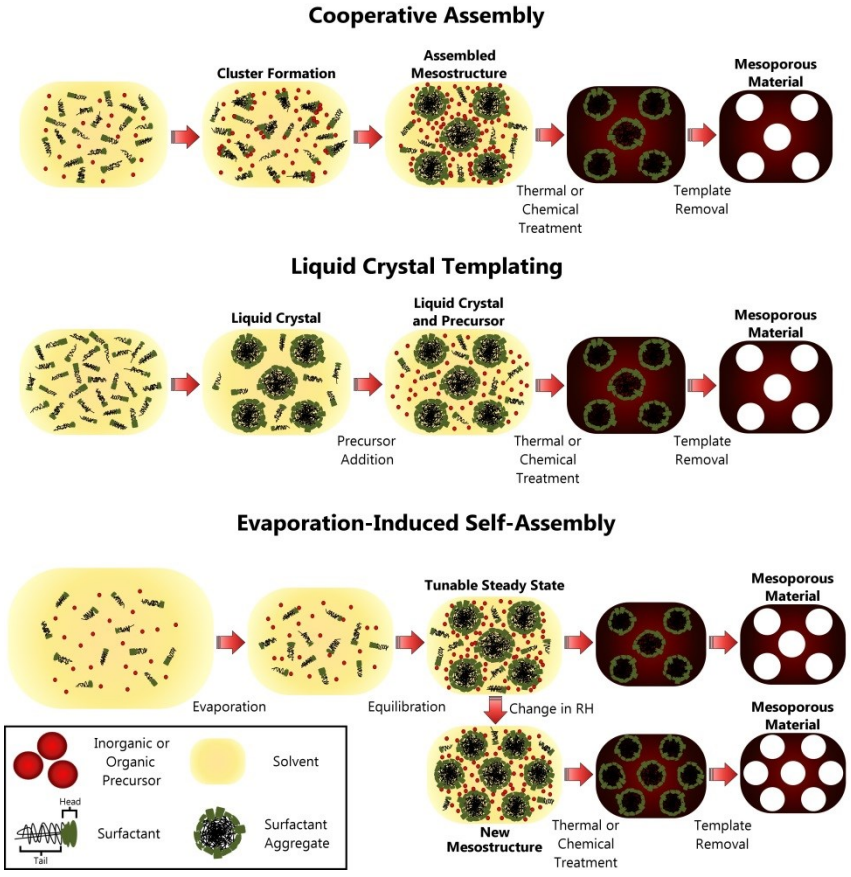

Figure 2.4 Schemes detailing the soft templating process. *Top*: The sequence of steps in cooperative assembly. *Middle*: The sequence of steps in liquid crystal templating. *Bottom*: The sequence of steps in evaporation-induced self-assembly.

2.3.3.1 Cooperative Assembly

For many hydrothermal syntheses of ordered mesoporous materials, formation occurs via the simultaneous assembly of the precursor and surfactant.[5] During this process, termed cooperative assembly (CA) or precipitation, small clusters of inorganic (or organic) precursors and surfactants initially develop in solution (Figure 2.4, top). These clusters are held together via the intermolecular interactions specified in the sections above, such as electrostatic interactions between ionic surfactants and hydrolyzed sol-gel precursors.[14] As the synthesis continues, the hybrid precursor–surfactant clusters coalesce into larger structures. Finally, a liquid crystalline phase that is surrounded by the precursor is formed, and this templated material precipitates out of solution. Throughout this process, it is essential that condensation of precursor does not occur rapidly. If condensation takes place to an appreciable extent before the liquid crystalline phase is formed, precipitation of an untemplated precursor may occur, or a disordered mesostructure could form.[5]

2.3.3.2 True Liquid Crystal Templating

In the mid-1990s, an alternate pathway for the formation of mesoporous materials via a soft template was demonstrated.[5] This process, "true liquid crystal templating" (LCT) involves the formation of a liquid crystalline phase before condensation of the inorganic network (Figure 2.4, middle). Much like hard templating, an inorganic material is "cast" around the "mold" of the liquid crystal template. However, special conditions are needed in LCT. LCT requires high concentrations of a non-ionic surfactant.[14] The high content of surfactant increases the viscosity of the precursor solution, which can complicate its use in multiple templating. However, certain precursors for noble metals, like chloroplatinic acid, are compatible with these solutions, making LCT a powerful method for the synthesis of mesoporous metals.[26] Just like in CA, it is essential that the precursor does not condense too rapidly or interfere with the self-assembly of the surfactants into a liquid crystal.

2.3.3.3 Evaporation-Induced Self-Assembly

An important route for the synthesis of many different mesoporous materials is evaporation-induced self-assembly or EISA. EISA is used extensively for the synthesis of mesoporous thin films and in multiple templating (Figure 2.4, bottom). While EISA can be understood to be closely related to LCT, there are additional interactions (like those at the solid–liquid interface) that arise due to the nature of the process.[25] To conduct an EISA synthesis, one

must use a dilute solution that contains a volatile solvent (like ethanol), an inorganic/organic precursor, and a surfactant. Nanoparticle precursors can also be used, provided that these crystals are small enough (<5 nm) to participate in self-assembly.[5] The solution is then spread over a large area and allowed to evaporate. During evaporation, the solution becomes more concentrated and the cmc is reached. By this point or after further loss of solvent, the water content reaches equilibrium with the atmosphere and a liquid crystalline phase forms.[14] Many inorganic/organic precursors are not fully condensed at this stage and the relative humidity (RH) of the surrounding atmosphere can potentially change the mesostructure.[25] This condition is called the tunable steady state.[18] Further condensation of the precursor around the liquid crystalline phase finally "locks-in" the final mesostructure. If condensation happens too rapidly, disordered worm-like mesopores may be templated or precipitation of untemplated material may occur.[5]

2.3.3.4 Further Processing and Template Removal

Much like hard templating, additional chemical and thermal processing is needed for soft templating. In many cases, further condensation of the precursor is desired and accomplished through heating at elevated temperatures.[18] This can also help remove residual solvent. After this processing step, the surfactant template can be removed by low-temperature chemical treatment. Alternately, the surfactant can be combusted or depolymerized during thermal treatment. For chemical treatments, ionic surfactants are removed via ion exchange, while non-ionics are extracted in hot ethanol.[14] Calcination or pyrolysis can be also used to remove the template and solidify/carbonize the mesoporous material. However, shrinkage of the mesopores can be expected with thermal treatment and alter the mesostructure present.[25] In mesoporous films, for instance, shrinkage normal to the substrate is responsible for the transition from a body-centered cubic mesostructure to an orthorhombic mesostructure.[25] High temperature treatment can also cause crystallites to sinter, grow and ultimately destroy pores. Due to the small size of the mesopores, retention of porosity is more difficult than for hard-templated macroporous materials. Various routes can be taken to avoid this issue, including lowering the calcination temperature, using rapid heating, or stabilizing the mesopores by synthesizing a carbon-containing composite (carbon can impede crystal growth).[14]

2.4 Multiple Templating and Morphological Control

Before exploring the different morphologies produced by multiple templating, a few general remarks need to be made. First, the general synthesis scheme for multiple templating (Figure 2.5) closely mirrors that of templating conducted with a single hard template. However, depending on the soft templating route chosen, certain additional steps may be required. For instance, solvent must be allowed to evaporate after infiltration when EISA is employed, so a liquid crystalline phase can be formed. Second, the combination of soft and hard templating can induce considerable changes in the templated mesostructure. If the liquid crystal template is confined in a hard template with nm-scale dimensions, packing constraints (geometrical frustration) will alter the structure of the liquid crystal.[5,7] Confinement also enhances interactions between hard and soft templates.[5] Illustrative examples are given to provide broad overview of the area and outline methods for tuning pore morphology.

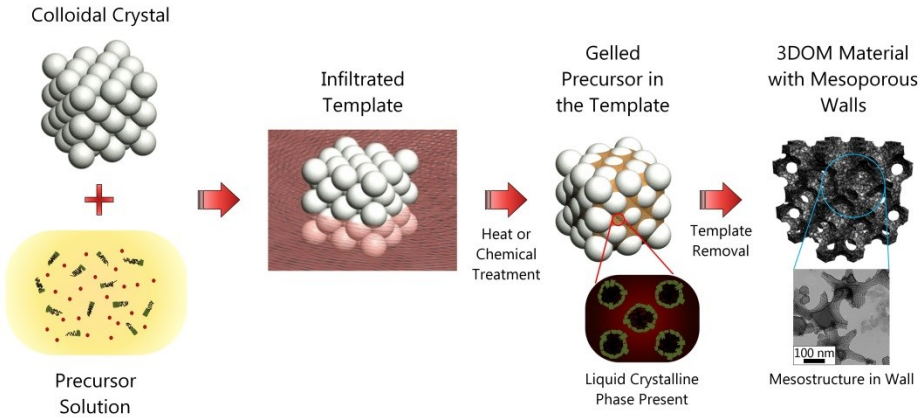

Figure 2.5 Scheme detailing a multiple templating approach. This particular example shows a combination of colloidal crystal templating and surfactant templating

Most of the materials formed through multiple templating possess structural hierarchy, and this section has its own hierarchy intended to aid the reader of this thesis. The six subsections that follow are divided by the category of hard template used in the multiple templating synthesis: macroscopic templates (biological, colloidal crystal, three-dimensionally ordered macroporous (3DOM) structure, foam, AAO membrane) and *in situ* templates. Discrete particles are not discussed, since these templates are not employed in this thesis. Additionally, the different compositions that can be formed via multiple templating are highlighted. For the certain subsections, especially when confinement effects are especially important (i.e., for colloidal crystals and AAO membranes), a focus is placed on the factors that influence mesopore

morphology. Whenever possible, applications for multiple templated materials are discussed to provide context for why one would want to synthesize these materials in the first place.

2.4.1 Biological Hard Templates and Soft Templates

This chapter opened with a description of the diversity of porous structures in the natural world, and it is only fitting to open the section on multiple templating by reintroducing some of these structures. Biological materials represent a massive category of templates that can be readily and inexpensively used to synthesize varied pore morphologies. These templates include unicellular organisms, complex tissues, and biomolecules.[2] A good starting point for this discussion is the use of viruses or unicellular organisms as templates. For instance, bacteriophages can align into filaments in solution via interactions mediated by the sol-gel SiO_2 precursor 3-aminopropyltriethoxysilane.[27] By then adding TEOS, the viral chains can be coated. Removal of the viruses via calcination produces hierarchical SiO_2 fibers with hollow, macroporous cores.[27] Microscopic cells can also be coated with a precursor and calcined, producing macropores with the same shape as the cell.[28] Freeze-dried suspensions of cells (bacteria or fungi) may be used for the production of macroscopic structures. In one example using multiple templates, these aggregated cells were coated with titanium ethoxide and polyethylene glycol (a soft template).[28] After calcination, TiO_2 structures with μm-sized macropores and worm-like mesopores were obtained. Macropore morphology was dictated by the type of cell used as the hard template.[28]

Highly structured, porous tissues offer another choice as a hard template. With respect to these tissues, plants possess a vast array of tissues with uniaxially-aligned pores (for water transport) that can be used and readily replicated via multiple templating. For example, a variety of plant peels and stems were soaked in an acidic solution of TEOS and the Pluronic® surfactant P123 (nominal composition: $HO(PEO)_{20}(PPO)_{70}(PEO)_{20}H$).[29] Calcination removed the templates, producing SiO_2 with ordered mesopores 3–5 nm in diameter. As expected, the morphology and size of the macropores (anywhere from ~10 μm to nearly 1mm) depended on the species of plant, but most of the samples possessed various configurations of uniaxially-aligned pores.[29] A different composition of templated material was made from bagasse, a fibrous cellulosic waste from sugar cane. In this case, an ethanolic solution of PF sol and F127 was used.[30] Heat treatment and pyrolysis (at 600 °C) of the coated bagasse generated a hierarchically porous carbon. This carbon possessed a replica of the macrostructure of bagasse; furthermore, the material had a 2D hexagonal mesostructure (with pores ~3 nm in size).[30]

Animals also have intricately structured tissues, like bones and exoskeletons, which can afford complex pore morphologies through multiple templating. Xia and his team developed a method to template the waste shells of several crab species.[31] The researchers immersed ground, calcined crab shells into an ethanolic solution of PF sol and P123. After this EISA process, the composites were pyrolyzed and the calcium carbonate crab shell was removed with an acid wash. Not only was a nanofibrous carbon structure produced from the original ~70 nm macropores in the shell, but large mesopores were also obtained (~11 nm in diameter) (Figure 2.6 a, 2.6 c).[31] If the shell was removed before pyrolysis, mesopore sizes were far smaller (~2.5 nm) (Figure 2.6 b, 2.6 d). It is thought that the PF sol precursor strongly interacts with the shell during the pyrolysis process, preserving large mesopores in samples that did not have the shell removed.[31] These mesoporous carbon nanofibers were also shown to have high capacitance in an organic solution, and are a potential catalytic support for methanol electrooxidation.

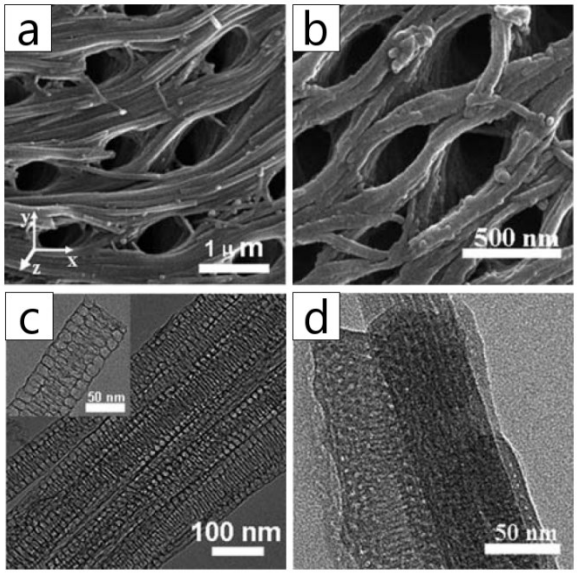

Figure 2.6 Electron micrographs of mesoporous carbon nanofibers templated from crab shells. The macrostructure (a) and mesostructure (c) of nanofibers made when the template was removed after pyrolysis is shown. The macrostructure (b) and smaller mesopores (d) of nanofibers made when the template was removed before pyrolysis is shown, as well. Adapted with permission from [31] © 2010 Royal Society of Chemistry.

All of the aforementioned biological templates are comprised of organic macromolecules that serve as essential structural elements responsible for the morphology of the template. These macromolecules can be used on their own for templating; fibers of cellulose from filter paper

were used by Huang and his team.[6] The cellulose was initially coated with TiO_2 via a sol-gel route, imparting a negative surface charge to the cellulose. Sequential adsorption of CTAB and then TEOS was performed, generating a mesostructured SiO_2 coating. Calcination and treatment in boiling sulfuric acid (to remove TiO_2) produced hollow tubes of silica with ~30–40 nm thick walls. The mesopore size was around 2 nm and the Brunauer-Emmett-Teller (BET) surface area (obtained from gas sorption) was 765 m^2/g.[6] By immersing an aqueous solution of starch and polyvinyl alcohol in liquid nitrogen, another type of template was synthesized (see Fig 2.1 b).[32] These templates contained uniaxially-aligned macropores (~3–12 μm in size) that were similar in appearance to the pores found in vascular plant templates. Subsequent soaking in an ethanolic solution of TEOS and a cationic surfactant produced a micro-/mesoporous SiO_2 replica of the starch structure. When the templates were soaked for a longer duration, the hierarchically porous SiO_2 had thicker walls and a higher surface area.[32]

2.4.2 Colloidal Crystal Templates and Soft Templates

Two different self-assembly routes can be coupled by first letting colloidal particles assemble into colloidal crystals (in the form of powders, fibers, films, or monoliths), and then infiltrating the colloidal crystal with a surfactant-containing precursor (Figure 2.5). This approach allows for the synthesis of hierarchical materials with an interconnected, face-centered cubic macropore network and a mesopore network, i.e., three-dimensionally ordered macroporous materials with mesoporous walls (3DOM/m materials).[1] Many different strategies exist for tailoring aspects of the 3DOM/m structure to meet specific goals for materials design. Since the diversity of available hard templates is no longer the focus, changes to the 3DOM structure generated from the colloidal crystal template are especially important. A rendering of this structure is shown in Figure 2.7. Several important structural features are highlighted in Figure 2.7. T_d and O_h denote the solid nodes generated by the inversion replication of the tetrahedral and octahedral holes of the parent colloidal crystal, respectively. The black arrow points the “walls” that connect the nodes, and the white arrow points to one of the twelve “windows” that connect the spherical macropores. Strategies to change the macropore size and alter the pore interconnectivity are covered in this section. Other aspects of the synthesis of 3DOM/m materials are discussed, including control of the micropore/mesopore morphology, changing the composition of 3DOM/m materials composition (including how that impacts morphology), and methods to convert the 3DOM/m structure into discrete nanoparticles.

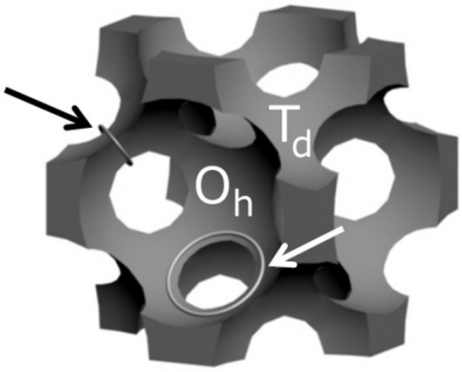

Figure 2.7 Computer rendering of the 3DOM structure. O_h denotes an octahedral node that was produced from an octahedral interstitial void in the parent colloidal crystal. T_d denotes a tetrahedral node that was produced from a tetrahedral interstitial void in the parent colloidal crystal. The black arrow points to a wall that connects the nodes (a ring is place around the wall). The white arrow points to a smaller pore window that connects the larger spherical macropores. Adapted with permission from [1] © 2012 John Wiley and Sons.

Several options exist for changing the diameter of the macropores present in a 3DOM/m structure. For instance, the diameter of the ordered macropores can be increased or decreased by changing the diameter of the spheres in the colloidal crystal template (from ~100 nm to a few μm).[1] The diameter of the windows that connect each macropore to its neighbors can be tuned, as well. This is done by sintering the spheres in the colloidal crystal together, forming necks that increase in diameter as the length of a thermal treatment is increased.[1] Sun *et al.* exploited this sintering strategy with a colloidal crystal of poly(styrene-co-3-(trimethoxysilyl)propyl methacrylate) that was infiltrated with a TEOS and P123-containing precursor solution.[33] This templating process produced a 3DOM/m SiO_2 structure without any interconnecting windows. It was hypothesized that co-polymer spheres swelled during infiltration and allowed the precursor to completely surround the spheres.[33] However, by sintering the spheres, the precursor could not enclose the spheres and interconnecting windows were observed. Interconnecting windows allowed for adsorption of proteins that would have otherwise been excluded from a closed structure.[33]

In addition to the macropore structure, morphological characteristics of the mesopores can be altered in a 3DOM/m structure. As is the case with purely mesoporous materials, the diameter of the mesopores in 3DOM/m materials can be tuned by changing the surfactant or through addition of a swelling agent.[34] The morphology of the liquid crystal (and resulting mesostructure) confined in a colloidal crystal can also be changed. Whereas cubic (I) mesostructures are typically

unaffected by confinement in a colloidal crystal, the pores in the 2D hexagonal mesostructure bend and curve along the precursor–hard template interface.[34] Additionally, the pores can be aligned perpendicular or parallel to the surface of the spheres. Stein and his team gained some insight into the factors that can impact the alignment of these pores via a combined computational and experimental study.[35] Dissipative particle dynamics was used to simulate triblock copolymer, solvent, and SiO_2 confined between two walls. If the walls had an affinity for the PEO block, vertically-aligned columnar mesostructures were formed. A mixture of parallel and perpendicular channels was generated if neither block has affinity for the walls.[35] To explore these results, the authors synthesized a monolayer of polystyrene (PS) hemispheres arranged a hexagonal array. When this template was spin-coated with a methanolic precursor solution of P123 and tetramethyl orthosilicate, the mesostructure in the calcined SiO_2 consists of hexagonally arranged pores running parallel to the substrate (Figure 2.8 a).[35] By increasing the water content in the precursor and thereby increasing the affinity of the PEO block for the wall, spherical and hexagonally arranged columnar pores were obtained (Figure 2.8 b, 2.8 c).

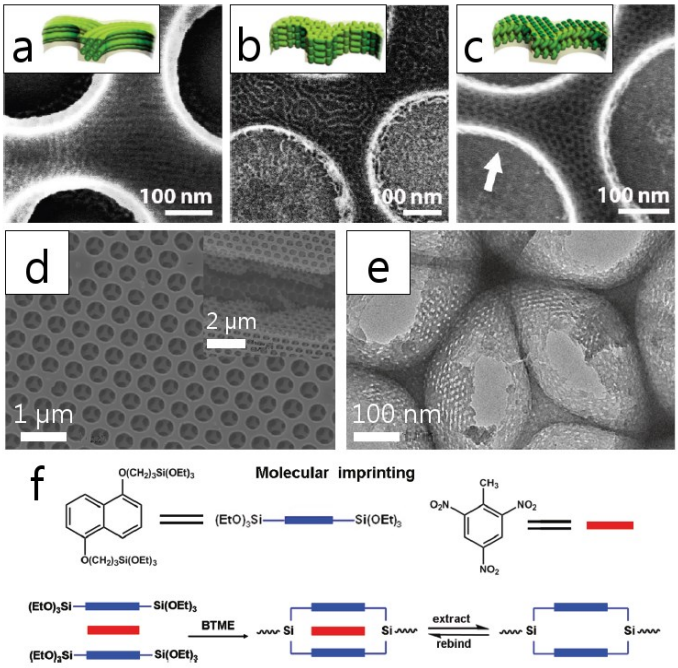

Figure 2.8 The top row shows TEM images and computer renderings of meso-/macroporous SiO_2. The mesopores were confined in a template of PS hemispheres. Water content in the precursor solution was increased from (a) to (c), inducing a transition to a columnar mesostructure. (d) Image of the macrostructure molecularly-imprinted 3DOM/m organosilica and the mesostructure (e). (f) Scheme detailing the molecular imprinting process. Adapted with permission from [35] (a–c) and [36] (d–f) ©2011, 2012 American Chemical Society.

Micropores are often present in 3DOM/m materials, but precise control over microporosity in these materials is difficult to achieve. Most carbon-containing 3DOM/m materials have significant microporosity that develops during the pyrolysis of phenolic resin-based precursors.[13] Aside from this, the synthesis of 3DOM/m organosilica with engineered, well-defined micropores was reported by Zhu *et al.* (Figure 2.8 d, 2.8 e).[36] To achieve this level of control, the authors synthesized 1,5-bis(3-(triethoxysilyl)propoxy)naphthane (BTPN) to be included in an ethanolic precursor solution of BTPN, 1,2-bis(trimethoxysilyl)ethane (BTME), F127 and 2,4,6-trinitrotoluene (TNT). This precursor was infiltrated into a colloidal crystal film, gelled, and the surfactant was then extracted. Micropore cavities were present in the material, formed through bonding between BTPN with BTME (Figure 2.8 f).[36] This molecularly-imprinted cavity provided high selectivity (as observed in time-resolved fluorescence studies) for TNT over its analogue, 2-dinitrotoluene, leading to potential use as a sensor for explosives.[36]

Research groups have also developed routes for the formation of several different 3DOM/m main group and transition metal oxides. One oxide, Al_2O_3, is amenable to dual templating, since it resists sintering and has stable alkoxide precursors.[1] Song and co-workers harnessed both of these properties to produce gamma-phase 3DOM/m Al_2O_3.[37] A precursor solution was made by mixing aluminum isopropoxide, concentrated hydrochloric acid, citric acid (for chelation), and P123 in ethanol. After infiltration of a template and calcination at 500 °C, 3DOM/m γ-Al_2O_3 with mesopores 3.6 nm in diameter was produced. When the authors increased the calcination temperature to 900 °C, the hierarchical structure of the material was maintained. However, crystallite growth disrupted the mesopore network, lowering the surface area and broadening the distribution of mesopore sizes.[37]

Hierarchically porous 3DOM/m transition metal oxides are more prone to sintering and mesopore collapse than Al_2O_3; however, that has not hindered research on these materials. Zhao *et al.* synthesized 3DOM/m TiO_2 by infiltrating a PS colloidal crystal film with an ethanolic solution of concentrated HCl, titanium butoxide, P123, and a chelator, 2,4-pentanedione.[38] When the infiltrated film was calcined at 350 °C or 400 °C, 3DOM/m TiO_2 was obtained that had a 2D hexagonal mesostructure with ~7 nm pores (Figure 2.9 a). However, calcination at 500 °C caused considerable crystallite growth that destroyed ordered mesoporosity in the 3DOM/m TiO_2.[38] Nanostructured iron oxides have even lower thermal stability than TiO_2, but Dai and co-workers were able to synthesize 3DOM/m α-Fe_2O_3.[39] Poly(methyl methacrylate) (PMMA) colloidal crystals were soaked in an ethanolic solution of iron nitrate and P123, and then calcined at a low temperature (550 °C). Large disordered mesopores were present in the 3DOM/m structure (Figure

2.9 b), tripling the surface area of the 3DOM/m material when compared to 3DOM α-Fe_2O_3.[39] An explanation for these voids was put forward by the authors, who proposed that Fe^{3+} ions were chelated by the PEO blocks of the surfactant, which organized into disordered micelles during drying.[39]

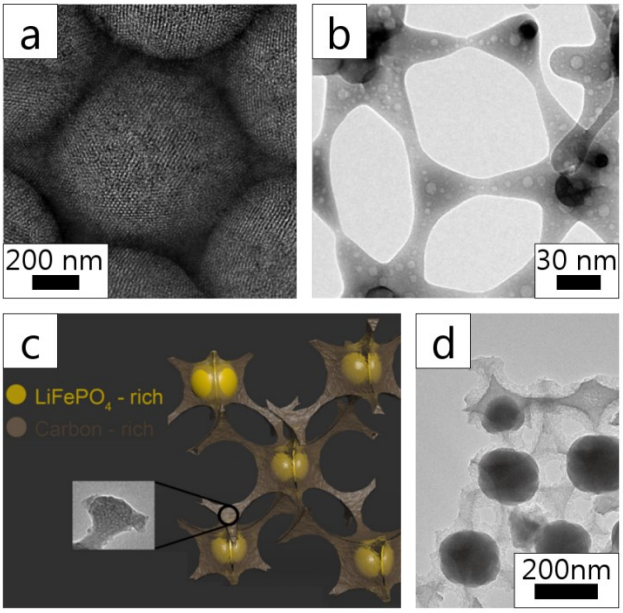

Figure 2.9 Images of 3DOM/m materials that contain transition metal ions. (a) A 2D hexagonal ordered mesostructure was present in 3DOM/m TiO_2. (b) Large, disordered mesopores were present in 3DOM/m α-Fe_2O_3. Phase separation of $LiFePO_4$ and carbon occurred in a 3DOM/m $LiFePO_4$/C composite, as shown in a computer rendering (c) and a TEM image (d). Adapted with permission from [38] (a) ©2011 Elsevier; and from [39] (b) and [40] ©2011 American Chemical Society.

Various properties of 3DOM/m transition metal oxides (and other materials) can be improved through the formation of a carbon-containing composite. This includes improved thermal stability and electrical conductivity. Vu and Stein utilized those advantages in 3DOM/m $LiFePO_4$/C for use as a Li^+ battery cathode.[40] This complex composition was made by infiltrating PMMA colloidal crystals with a PF sol-containing, multi-constituent precursor. It was determined that significant phase segregation after pyrolysis, with the $LiFePO_4$ phase located in the octahedral nodes of the 3DOM structure (Figure 2.9 c, 2.9 d).[40] The non-conductive $LiFePO_4$ crystals were "wired" together by the surrounding electronically conductive carbon matrix, allowing for excellent specific capacities at high charge/discharge rates.[40] Another composite, 3DOM/m TiO_2/C, was synthesized by Du *et al.*[41] Instead of using PF sol to produce amorphous carbon, they dispersed graphite oxide (GO) in an ethanolic solution of P123, TTIP and titanium tetrachloride.

The final templated porous film contained randomly-oriented 2D hexagonal mesopores. Both the hierarchical porosity and the presence of graphene improved the ability of the 3DOM/m TiO_2/C to photocatalytically degrade methylene blue.[41]

Although 3DOM/m materials are typically macroscopic structures, the disassembly of the ordered framework into individual parts is possible. During heat treatment, octahedral particles and smaller tetrahedral particles can be produced from the nodes of the 3DOM/m network.[42] This is accomplished when the mesoporous walls of the 3DOM/m network are mechanically weak enough to fracture. Many of the aspects of this pathway for morphological control were studied by Stein and his team for first-row transition metal oxides and phosphates.[42] The precursor solution used in the syntheses was a combination of a metal acetate, short-chain alcohol, Brij 56, and triethyl phosphate. Condensation of the precursors continued during calcination of the infiltrated template, inducing the stresses necessary for disassembly. In most cases, uniform rounded cubes were obtained after calcination due to the combined effects of Ostwald ripening (tetrahedral particles merge with octahedral ones) and surface energy minimization.[42] These rounded cubes were also found to self-assemble into a low-energy configuration, a simple cubic lattice. Capillary forces originating from the evaporation of the phosphate precursor were hypothesized to drive this process.[42]

2.4.3 3DOM Templates and Soft Templates

Not only are colloidal crystals a versatile hard template for multiple templating, but their inverse replicas, 3DOM materials (Figure 2.1 d), are also useful in multiple templating. Both 3DOM materials filled with a mesoporous material (Figure 2.10 a) and hierarchical colloidal crystal structures can be synthesized via this route. A good example of a filled 3DOM structure was reported by Bein and his team. They synthesized this material by dropping a minimal volume of a P123 and titanium ethoxide solution, onto a 3DOM TiO_2 film.[43] Two confinement effects were observed in the material. First, 3DOM template restricted mesopore shrinkage, which resulted in a larger mesopore diameter than in similarly-made TiO_2 thin films.[43] Second, the orientation of the cubic mesopore network changed from macropore to macropore (Figure 2.10 b). Beyond the morphological investigations, this material was tested as an anode in a dye-sensitized solar cell and provided a ten-fold higher efficiency when compared 3DOM TiO_2.[43]

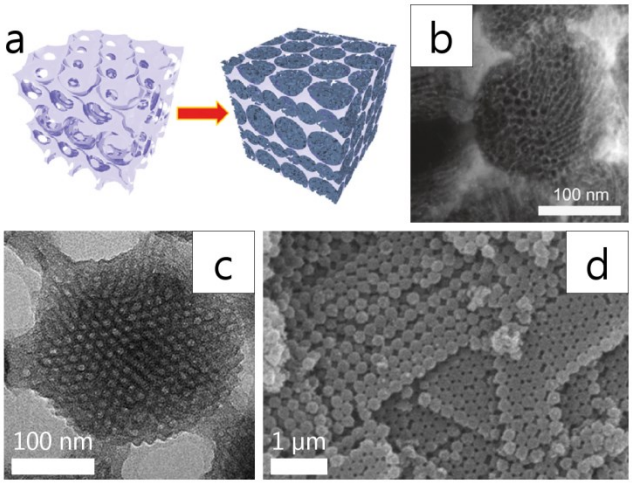

Figure 2.10 (a) Illustrates 3DOM TiO_2 structure before/after it is filled with mesoporous TiO_2. (b) High-angle annular dark-field scanning transmission microscopy of the filled TiO_2 structure. (c) The ordered mesostructure present in a hierarchically porous carbon colloidal crystal. (d) The opaline macrostructure of the same material from (c). Adapted with permission from [43] (a, b) ©2011 American Chemical Society; and from [45] (c, d) ©2012 Royal Society of Chemistry.

In other cases, removal of the 3DOM template is preferred in multiple templating, allowing for the formation of hierarchical colloidal crystals. Ozin and his team were the first to utilize 3DOM materials in such a fashion, and called the process micromolding in inverted polymer opals (MIPO).[44] First, a SiO_2 colloidal crystal was infiltrated with a styrene monomer solution that contained a radical initiator. After heat-treatment and HF etching, a 3DOM PS template was formed. To infiltrate the 3DOM PS, a solution of tetramethyl orthosilicate, hydrochloric acid, and the surfactant $C_{12}H_{25}(OCH_2CH_2)_{10}OH$ was prepared. In this case, vacuum suction was needed to help infiltration and remove excess solvent. After calcination, a hierarchical SiO_2 colloidal crystal was formed. A 2D hexagonal mesostructure was formed in the colloidal crystal, with mesopore channels running parallel to the original 3DOM template.[44] MIPO was more recently used for synthesis of a micro-, meso-, and macroporous carbon colloidal crystal. Xia and his team infiltrated 3DOM PMMA with F127, titanium citrate, and PF sol.[45] Carbothermal reduction of TiO_2 was conducted in an inert gas at 900 °C, producing a carbon and TiC composite. A further step, chlorination at 500 °C, removed all the TiC, generating additional micropores. Both 8 nm mesopores ordered in a hexagonal arrangement (Figure 2.10 c) and a well-ordered colloidal crystal structure were present (Figure 2.10 d). Additional micropores helped increase the surface area in the final hierarchical material, which boosted its capacitance (~150 F/g) by a factor of three when compared to the hierarchical carbon and TiC composite colloidal crystal.[45]

2.4.4 Foam Templates and Soft Templates

The hierarchical 3DOM/m and colloidal crystal structures described above contain macropores no larger than a few μm; however, large, interconnected macropores, up to hundreds of μm in size, are accessible by using various foam templates (see Figure 2.1 e). Large macropores, such as the ones afforded by polyurethane (PU) foams, allow for the confinement of large guests, like cells. Not surprisingly, hierarchical bioactive glass made via PU foam templates is being studied as an implantable scaffold for the regrowth of bone tissue.[46] A PU foam with a precursor solution containing TEOS, P123, calcium nitrate, triethyl phosphate, and another metal salt (one that has Zr, Sr, or Mg cations). Addition of other metal ions slightly decreased the observed surface area, but all calcined samples had a 2D hexagonal mesostructure with pores ~4 nm in diameter. Zr ions significantly inhibited the leaching of Si into a solution of simulated body fluid, and improved cell proliferation on the scaffold.

Pure SiO_2 and carbon hierarchical structures have also been synthesized using PU foams. Zhao and his team produced hierarchical SiO_2 via an EISA pathway, using an ethanolic coating solution of TEOS and P123.[47] Two different types of macrostructures were formed after calcination. At a ratio of 1:4 (precursor to foam), the resultant SiO_2 was shaped like the PU foam and contained a hollow core (Figure 2.11 a).[47] When a 1:2 ratio was used, the precursor coated the perimeter of each cell in the foam, producing closed SiO_2 polyhedra (Figure 2.11 b). Despite changes in the macrostructure, the mesopore size was similar in both samples. Another publication from the same research team further investigated the closed polyhedral morphology.[48] EISA was performed using an ethanolic PF sol and F127 precursor. Instead of combusting the PU foam, the PU was dissolved solvothermally in triethyl phosphate. This process liberated individual phenolic resin polyhedra that were carbonized. Addition of TEOS to the precursor improved the mesostructure, reinforcing it against collapse.[48] Polyhedral carbon pieces with a BET surface area of 1384 m^2/g and good adsorptive properties were then obtained.

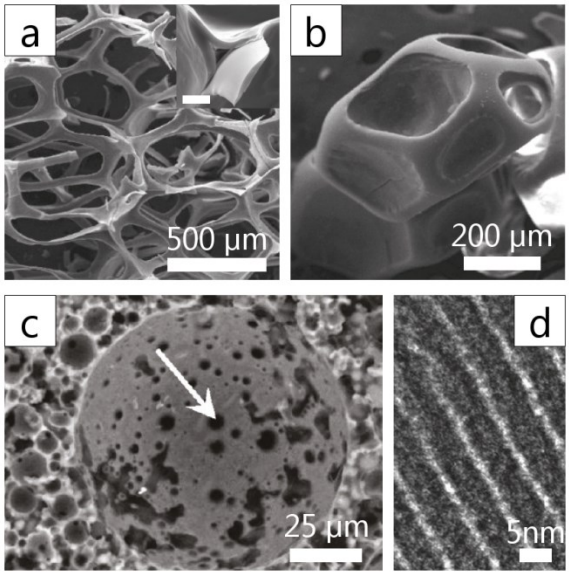

Figure 2.11 (a) A hollow replica of PU foam made from mesoporous SiO_2. The bar in the inset represents 20 µm. (b) Closed, mesoporous SiO_2 polyhedra made from the same templates as in (a). (c) The macrostructure of carbon templated by Si(HIPE). The white arrow points to an interconnecting window. (d) The mesostructure of the Si(HIPE) templated carbon. Adapted with permission from [47] (a, b) and [49] (c, d) ©2010, 2012 American Chemical Society.

Polyurethane foams are perhaps the most popular foams for use in multiple templating (again, stemming from biomedical applications), but other foam templates can be used for the production of different macropore morphologies. High internal phase emulsions—where the droplet phase takes up >74% of the emulsion—can be used to make SiO_2 foams, Si(HIPE).[49] Brun *et al.* used Si(HIPE), made from an emulsion of TEOS, dodecane, and a cationic surfactant, as a hard temple for meso-/macroporous carbon (Figure 2.11 c, d).[49] The Si(HIPE) was infiltrated with an ethanolic solution of phenolic resin and P123 or F127. One key factor in determining the morphology of the final sample was whether the Si(HIPE) was etched out before or after carbonization. Better order in the mesostructure was obtained by etching out the Si(HIPE) after carbonization, which is attributed to the stabilizing effect of the hard template.[49] However, in all cases the macrostructure was found to be similar, consisting of spherical macropores with a high variance of sizes connected by ~5–6 µm windows (Figure 2.11 c).[49]

2.4.5 AAO Membrane Templates and Soft Templates

Anodic Al_2O_3 (AAO) membranes are excellent platforms for studying mesostructures under confinement. The cylindrical channel morphology is responsible for a unique type of confinement that produces radially-symmetric mesostructures along the channel axis.[7] Multiple variables dramatically impact the formation and orientation of these mesostructures: the type of precursor, the precursor concentration, the channel diameter, and the affinity of the precursor for the channel wall.[5,7] Since this is a fairly well studied system, it is possible to identify key mesostructures and specific factors that can change the morphology of the confined mesostructures.

Much like the case in 3DOM/m materials, confinement of liquid crystalline phases within AAO membranes can radically alter their structure. By coupling SAXS and TEM, researchers have identified mesostructures that are present in these membranes.[7] Several of the mesostructures are closely related to the 2D hexagonal arrangement observed in non-confined systems (Figure 2.12 a).[7] In the circular hexagonal mesostructure, hexagonally-packed pores are arranged in a torus around the central axis of the AAO channel. The mesopores in this structure can also be tilted so that they are no longer parallel to the surface of the membrane, forming the helical phase. Another related mesostructure, the columnar structure, contains hexagonally-packed pores parallel to the central channel axis. A tubular lamellar mesostructure is also found that has pores arranged in concentric cylinders. Undistorted cubic mesostructures are sometimes observed, especially in templated carbons. In many cases, different mesostructures co-exist along the length of the channel.[7]

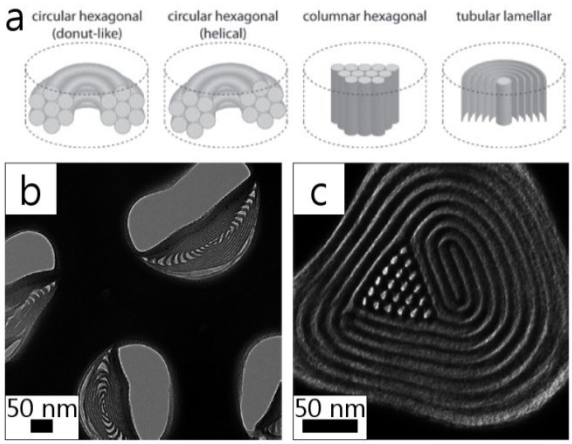

Figure 2.12 (a) Computer renderings of mesostructures found in AAO membranes. For a SiO_2 mesostructure produced using a THF solvent, a distorted lamellar phase was formed at low RH (b). When humidity was increased, circular hexagonal and columnar phases were formed (c). Adapted with permission from [7] (a) ©2011 John Wiley and Sons; and from [51] (b, c) ©2012 American Chemical Society.

Bein and his team conducted extensive investigations on the variables that control the mesostructure in confined SiO_2 made via an ethanolic EISA route.[50] As in any EISA-type synthesis, mesostructure evolution was found to be highly dependent on both the ratio of surfactant to TEOS and the relative humidity. Low concentrations of surfactant in the precursor favored circular hexagonal phases, while increasing the concentration of surfactant in the confined space led to the less curved (higher *g*) columnar and lamellar mesostructures.[50] The effect of humidity was more complex. Structural evolution was reported to be under kinetic control when Brij 56 is used a surfactant. Increasing the relative humidity slowed condensation and promoted partial conversion of the initially formed circular hexagonal mesostructure to the columnar phase. In contrast, structure formation was under equilibrium control for systems with P123.[50] The equilibrium water content was then increased at high relative humidity (RH) in the P123 system, which led to a larger, more hydrated surfactant head group (lower *g*). This promoted the highly curved circular hexagonal mesostructure at high RH, while domains of the columnar phase were also present at low RH.[50]

Changing the solvent from ethanol to tetrahydrofuran (THF) for this EISA synthesis can change how certain variables control the templated mesostructure.[51] Increasing the ratio of surfactant to TEOS precursor has the same effect as in the ethanolic system. A high concentration of the chosen surfactant, Brij 56 or P123, produced a greater fraction of the columnar phase and a larger *d*-spacing. The effect of relative humidity was explored with P123 as the surfactant. At

45% RH, a highly distorted mesostructure (possibly collapsed lamellar) was formed (Figure 2.12 b).[51] However, at 90% RH, a circular hexagonal mesostructure with some columnar phase (in the less curved center) was obtained (Figure 2.12 c). This difference between ethanol versus THF was attributed to lower water content in the THF system. Severe dehydration of the surfactant headgroups at low RH reduced the curvature of the mesostructure, resulting in the lamellar mesostructure.[51] High RH allowed for rehydration of the surfactant. Beyond the mesostructure characterization, the authors also demonstrated that the THF precursor could dissolve hydrophobic conjugated polymers, leading to their incorporation in the SiO_2.[51]

Researchers have also explored mesostructure formation in carbon-containing materials confined in AAO membranes. Holmes and co-workers investigated mesoporous organosilica in an AAO membrane using a precursor solution containing, 2-bis-(triethoxysilyl)ethane (BTME), TEOS, P123, and ethanol.[52] Much like what was observed in the ethanolic EISA system with TEOS, high RH (80%) led to the formation of the circular hexagonal mesostructure, while lower RH promoted the formation of the columnar phase. When the BTME content was increased in the precursor, formation of the circular hexagonal phase was favored.[52] In an even more carbon-rich material, mesostructured amorphous carbon, Bein and his team found several features that are (so far) unique to this type of system.[53] EISA was employed with a simple ethanolic precursor of PF sol and surfactant (P123 or F127). Changing the surfactant resulted in a circular hexagonal mesostructure for P123 and a body-centered cubic mesostructure for F127 (lower *g*). Interestingly, the cubic mesostructure had a different orientation near the edge versus the interior, due to confinement-induced interactions with the AAO membrane wall.[53] The other key finding was that structure formation in this system occurred only at the elevated temperature of the thermopolymerization process.

One of the most fascinating pathways for morphological control of confined mesostructures in these membranes is through adjustment of the diameter of the pore channels. This confinement can lead to interesting helical configurations or straight channels.[5] Kim *et al.* analyzed the effect of very strong confinement, using AAO membranes with 34, 50 and 83 nm pore diameters and a precursor solution that contained TEOS and F127.[54] Use of a hydrophilic membrane surface led to the formation of helical mesopore structures, culminating in a double-helix arrangement at 34 nm (Figure 2.13 a, 2.13 b). However, a functionalized, hydrophobic surface produced strong interfacial interactions with the PPO blocks that dominate at small diameters (34, 50 nm), leading to tubular pore structures (Figure 2.13 c, 2.13 d).[54] These confinement effects were also observed in SiO_2 nanotubes that were made by first infiltrating membrane pores with TEOS.[55] This was

followed by infiltration of a P123 solution that was spread on the membrane surface. Under the appropriate conditions most of the resulting nanotubes had hexagonally-packed pores perpendicular to the nanotube wall (Figure 2.13 e). In AAO and polycarbonate membrane channels with diameters smaller than 200 nm, hexagonally-packed arrangements could not be accommodated and disordered pores resulted (Figure 2.13 f).[55]

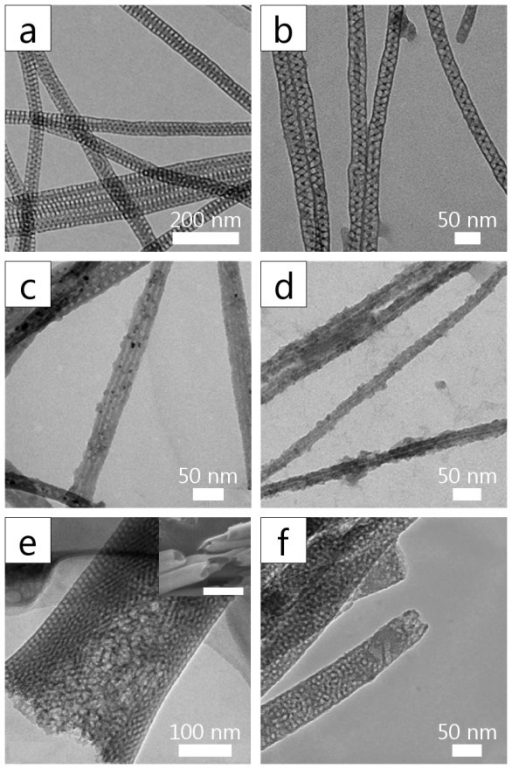

Figure 2.13 Helical mesostructures were formed in AAO membranes with hydrophilic walls (a, b). The diameter of the original AAO membrane channel was 50 nm in (a) and 34 nm in (b). Addition of a hydrophobic coating changed the mesostructure to a tubular lamellar arrangement (c, d). Again, the channel diameter for the original template was 50 nm in (c) and 34 nm in (d). Mesostructural disorder was increased with reduction in the PC membrane channel diameter from 200 nm (e) to 50 nm (f) for SiO_2 nanotubes. This nanotube morphology is highlighted in the inset in (e); scale bar is 500 nm. Adapted with permission from [54] ©2010 Royal Society of Chemistry (a–d) and [55] (e, f) ©2012 American Chemical Society.

These multiply-templated materials can be used for various applications. Some of the mesostructures present in these confined materials can serve as hard templates for nanowires, including metal nanowires synthesized via electrodeposition. For instance, μm-long helical Au wires were synthesized in mesoporous SiO_2 confined in 50 nm-wide AAO channels.[54] Filtration

or separation is an obvious application of these templated materials. El-Safty *et al.* demonstrated that organically-functionalized SiO_2 with a bicontinuous cubic (V_1) mesostructure effectively separated certain proteins.[56] The cubic mesostructure was produced through a microemulsion procedure, wherein Pluronic® F108 served as the surfactant and dodecane as the oil phase. Pore openings in the mesostructure were ~5 nm in diameter, reducing the apparent diffusion co-efficient for hemoglobin protein molecules versus smaller cytochrome *c* protein molecules.[56]

2.4.6 *In Situ* Templates and Soft Templates

Recently, *in situ* hard templates have been combined with soft templates. Hard templates made from either the solute or the solvent have been used, and each hard template has required special processing considerations. In terms of solutes, NaCl might not seem like an obvious choice. However, Innocenzi and his team discovered a method to control the crystallization of NaCl in a mesostructured SiO_2 film (formed via EISA).[8] To accomplish this, Na_2HPO_4 was added to an acidic solution of TEOS, methyltriethoxysilane, F127, NaCl and ethanol. The Na_2HPO_4 was essential to prevent uncontrolled precipitation of the NaCl. Within a certain concentration range for both salts, cubes of crystalline NaCl (~200 nm) were formed in a mesostructured SiO_2 matrix (Figure 2.1 g).[8] A key advantage was that removal of NaCl requires only washing in water.

Caruso and her team took a different approach for *in situ* templating, and used an organic polymer solute, polyfurfuryl alcohol (PFA), as a template.[9] They used a precursor solution that contained a metal chloride or alkoxide, F127, ethanol, acidified water, and furfuryl alcohol (FA). In an initial report, different porous materials were synthesized, including TiO_2, SiO_2, ZrO_2, and some mixed oxides.[9] The hard template was produced when FA polymerized in the ethanol/water solution, and then phase separated in the form of spherical colloids. During a subsequent evaporation step at 16–33 °C, sol-gel precursors and surfactant co-assembled around PFA colloids.[9] After calcination, small spherical macropores (~0.2–3 μm in diameter) were formed from the PFA colloids (Figure 2.14 a). Larger pore channels (10 μm wide) resulted from evaporated solvent. Mesopore sizes vary from composition to composition; however, templated mesopores were found in only one material, titanium zirconium oxide (Figure 2.14 b).[9] A later report detailed the key factors of morphological control for porous SiO_2.[21] First, macropores only formed if FA was present. Control over the acid concentration was critical, as well.[21] Lower acid concentration inhibited rapid condensation of the precursor, TEOS, allowing for co-assembly of condensing sol around micelles and swelling of the PFA with surfactant. At high acid concentration, condensation of silica and FA was rapid, so co-assembly could not take place.[21]

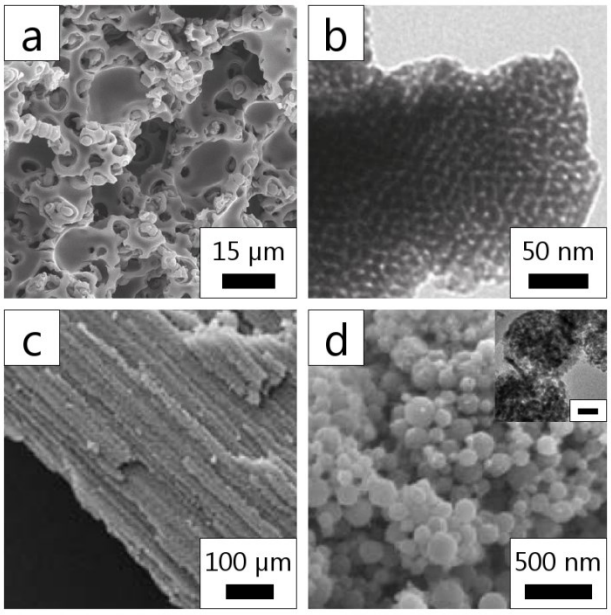

Figure 2.14 The top row highlights the macrostructure (a) and mesostructure (b) of titanium zirconium oxide made using a PFA *in situ* hard template. In (a) the spherical voids are formed from the PFA, while in (b) the mesopores are templated from F127 surfactant. Two types of ice templated materials are shown in the bottom row. (c) A meso-/macroporous SiO_2 material formed via uniaxial freezing. (d) Co_3O_4 templated with surfactant and ice crystals. The scale bar is 50 nm. Adapted with permission from [9] (a, b) and [57] (d) ©2010, 2012 American Chemical Society; and from [10] (c) ©2011 Royal Society of Chemistry.

The preceding discussion focused on *in situ* templates produced from a solute in some sort of precursor; however, water is also used as an *in situ* hard template. Rapid freezing of water produces ice crystals that can be removed by freeze-drying. With this ice templating it is possible to form cellular structures with uniaxially-aligned macropores that resemble those in plant tissue.[10] Zhang and his team prepared hierarchically porous SiO_2 using ice templating.[10] Aligned macropores were obtained by slowly dipping a suspension of mesoporous SiO_2 colloidal spheres in a bath of liquid N_2, and then freeze-drying the suspension. Additional porosity was obtained by soaking and thermally-treating the dried monolith in TEOS and surfactant (Figure 2.14 c). Bimodal mesoporosity was obtained from the mesoporous SiO_2 particles (CTAB-templated) and the coated mesoporous SiO_2.[10] Ice templating can also be used to make disordered porous structures. One example from Wang *et al.* involved freezing a mixture of P123, cobalt nitrate, and citric acid.[57] At an optimum pH of 3, mesoporous Co_3O_4 was obtained. This material was composed of spherical aggregates of mesoporous Co_3O_4 nanoparticles (Figure 2.14 d) that had excellent pseudocapacitive performance (742.3 F/g at 0.5 A/g).[57]

2.5 Conclusions

The simultaneous development of hard and soft templating methods unlocked a wealth of new possibilities for the synthesis of materials with a variety of morphologies. This is especially true for syntheses that combine both hard and soft templating to produce hierarchically structured materials with complex architectures. With multiple templating, any number of hard templates can be coated or filled with a surfactant-containing precursor solution. It is even possible to form the hard template *in situ*. While the morphology produced by a hard template is typically simple to predict, unexpected structures can result from multiple templating. For example, cubic nanoparticles can be made from the disassembly of 3DOM materials.[42] As for mesostructures formed from soft templates, structure prediction can be more challenging. Aspects of the chemistry of surfactants, such as the packing parameter and common liquid crystalline phase transformations, are useful for interpreting results from these often EISA-like syntheses. However, untangling the numerous factors that control the aspects of mesopore size, spacing, and morphology remains somewhat problematic in multiple templating, and an *ad hoc* approach predominates.

Despite limitations in the prediction of pore structures, hierarchically porous materials obtained from multiple templating possess structures that are beneficial for many different applications. For instance, in energy storage applications, the large surface area afforded by the presence of mesopores provides short diffusion lengths and a large electrode–electrolyte contact area.[40] Macropores in the structure can improve transport properties, assist in the infiltration of an electrolyte, and can act as reservoirs for electrochemically-active ions. In this manner, rate performance can be improved in capacitor and battery electrodes. These advantages are the motivation for the synthesis and testing of the lithium-ion battery anode materials described in the next four chapters. Hierarchical TiO_2/C composites were synthesized through a combination of colloidal crystal templating and surfactant templating. A carbon *in situ* template was also used for the synthesis of a 3DOM TiO_2 material with high specific surface area. As is seen in next chapter, actually achieving a boost in performance for the hierarchical electrodes is not as simple as it may initially appear.

References

(1) Petkovich, N. D.; Stein, A. Colloidal Crystal Templating Approaches to Materials with Hierarchical Porosity. In *Hierarchically Structured Porous Materials: From Nanoscience to Catalysis, Separation, Optics, Energy, and Life Science*; Su, B.-L., Sanchez, C., Yang, X.-Y., Eds.; Wiley-VCH Verlag GmbH & Co. KGaA: Weinheim, Germany, 2012.

(2) Caruso, R. A. Nanocasting and Nanocoating. *Top. Curr. Chem.* **2003**, *226*, 91-118.

(3) Hassan, S.; Rowe, W.; Tiddy, G. J. T. Surfactant Liquid Crystals. In *Handbook of Applied Surface and Colloid Chemistry*; Holmberg, K., Shah, D. O., Schwuger, M. J., Eds.; John Wiley & Sons Ltd: Chichester, England, 2002.

(4) Rosen, M. J.; Kunjappu, J. T. *Surfactants and Interfacial Phenomena*; 4th ed.; John Wiley & Sons, Inc.: Hoboken, NJ, 2012.

(5) Fan, J.; Boettcher, S. W.; Tsung, C.-K.; Shi, Q.; Schierhorn, M.; Stucky, G. D. Field-Directed and Confined Molecular Assembly of Mesostructured Materials: Basic Principles and New Opportunities. *Chem. Mater.* **2008**, *20*, 909-921.

(6) Zhang, Y.; Liu, X.; Huang, J. Hierarchical Mesoporous Silica Nanotubes Derived from Natural Cellulose Substance. *ACS Appl. Mater. Interfaces* **2011**, *3*, 3272-3275.

(7) Platschek, B.; Keilbach, A.; Bein, T. Mesoporous Structures Confined in Anodic Alumina Membranes. *Adv. Mater.* **2011**, *23*, 2395–2412.

(8) Falcaro, P.; Malfatti, L.; Kidchob, T.; Giannini, G.; Falqui, A.; Casula, M. F.; Amenitsch, H.; Marmiroli, B.; Grenci, G.; Innocenzi, P. Hierarchical Porous Silica Films with Ultralow Refractive Index. *Chem. Mater.* **2009**, *21*, 2055-2061.

(9) Drisko, G. L.; Zelcer, A.; Luca, V.; Caruso, R. A.; Soler-Illia, G. J. A. A. One-Pot Synthesis of Hierarchically Structured Ceramic Monoliths with Adjustable Porosity. *Chem. Mater.* **2010**, *22*, 4379-4385.

(10) Ahmed, A.; Clowes, R.; Myers, P.; Zhang, H. Hierarchically Porous Silica Monoliths with Tuneable Morphology, Porosity, and Mechanical Stability. *J. Mater. Chem.* **2011**, *21*, 5753-5763.

(11) Lou, X. W.; Archer, L. A.; Yang, Z. Hollow Micro-/Nanostructures: Synthesis and Applications. *Adv. Mater.* **2008**, *20*, 3987-4019.

(12) Chen, Y.; Chen, H.; Zeng, D.; Tian, Y.; Chen, F.; Feng, J.; Shi, J. Core/Shell Structured Hollow Mesoporous Nanocapsules: A Potential Platform for Simultaneous Cell Imaging and Anticancer Drug Delivery. *ACS Nano* **2010**, *4*, 6001-6013.

(13) Meng, Y.; Gu, D.; Zhang, F.; Shi, Y.; Yang, H.; Li, Z.; Yu, C.; Tu, B.; Zhao, D. Ordered Mesoporous Polymers and Homologous Carbon Framework: Amphiphilic Surfactant Templating and Direct Transformation. *Angew.Chem. Int. Ed.* **2005**, *44*, 7053-7059.

(14) Soler-Illia, G. J. A. A.; Azzaroni, O. Multifunctional Hybrid by Combining Ordered Mesoporous Materials and Macromolecular Building Blocks. *Chem. Soc. Rev.* **2011**, *40*, 1107-1150.

(15) Mutin, P. H.; Vioux, A. Nonhydrolytic Processing of Oxide-Based Materials: Simple Routes to Control Homogeneity, Morphology, and Nanostructure. *Chem. Mater.* **2009**, *21*, 582-596.

(16) Kakihana, M. Invited Review "Sol-Gel" Preparation of High Temperature Superconducting Oxides. *J. Sol-Gel Sci. Technol.* **1996**, *6*, 7-55.

(17) Rudisill, S. G.; Hein, N. M.; Terzic, D.; Stein, A. Controlling Microstructural Evolution in Pechini Gels through the Interplay between Precursor Complexation, Step-Growth Polymerization, and Template Confinement. *Chem. Mater.* **2013**, *25*, 745-753.

(18) Soler-Illia, G. J. A. A.; Sanchez, C.; Lebeau, B.; Patarin, J. Chemical Strategies to Design Textured Materials: From Microporous and Mesoporous Oxides to Nanonetworks and Hierarchical Structures. *Chem. Rev.* **2002**, *102*, 4093-4138.

(19) Boettcher, S. W.; Fan, J.; Tsung, C.-K.; Shi, Q.; Stucky, G. D. Harnessing the Sol-Gel Process for the Assembly of Non-Silicate Mesostructured Oxide Materials. *Acc. Chem. Res.* **2007**, *40*, 784-792.

(20) Ghadimi, A.; Cademartiri, L.; Kamp, U.; Ozin, G. A. Plasma within Templates: Molding Flexible Nanocrystal Solids into Multifunctional Architecture. *Nano Lett.* **2007**, *7*, 3864-3868.

(21) Drisko, G. L.; Zelcer, A.; Caruso, R. A.; Soler-Illia, G. J. A. A. One-Pot Synthesis of Silica Monoliths with Hierarchically Porous Structure. *Microporous Mesoporous Mater.* **2012**, *148*, 137-144.

(22) Van Gough, D.; Defino, J. L.; Braun, P. V. Programmed Size-Selected Permeation of ssDNA into ZnS Mesoporous Hollow Spheres. *Soft Matter* **2012**, *8*, 4396-4401.

(23) Su, Y.; Yan, R.; Dan, M.; Xu, J.; Wang, D.; Zhang, W.; Liu, S. Synthesis of Hierarchical Hollow Silica Microspheres Containing Surface Nanoparticles Employing the Quasi-Hard Template of Poly(4-vinylpyridine) Microspheres. *Langmuir* **2011**, *27*, 8983-8989.

(24) Israelachvili, J. N. *Intermolecular and Surface Forces*; 3rd ed.; Academic Press: Waltham, MA, 2011.

(25) Innocenzi, P.; Malfatti, L.; Kidchob, T.; Falcaro, P. Order–Disorder in Self-Assembled Mesostructured Silica Films: A Concepts Review. *Chem. Mater.* **2009**, *21*, 2555-2564.

(26) Zhang, X.; Lu, W.; Dai, J.; Bourgeois, L.; Hao, N.; Wang, H.; Zhao, D. Y.; Webley, P. A. Ordered Hierarchical Porous Platinum Membranes with Tailored Mesostructures. *Angew.Chem. Int. Ed.* **2010**, *49*, 10101-10105.

(27) Mao, C.; Wang, F.; Cao, B. Controlling Nanostructures of Mesoporous Silica Fibers by Supramolecular Assembly of Genetically Modifiable Bacteriophages. *Angew.Chem. Int. Ed.* **2012**, *124*, 6517-6521.

(28) Sun, X.; Zheng, C.; Qian, M.; Yan, J.; Wang, X.; Guan, N. Bioinspired Synthesis of Hierarchical Macro-Mesoporous Titania with Tunable Macoporous Morphology Using Cell-Assemblies as Macrotemplates. *Chem. Commun.* **2009**, 4750-4752.

(29) Li, X.; Jiang, J.; Wang, Y.; Nie, X.; Qu, F. Preparation of Multilevel Macroporous Materials Using Natural Plants as Templates. *J. Sol-Gel Sci. Technol.* **2010**, *56*, 75-81.

(30) Huang, C.-H.; Doong, R.-A. Sugarcane Bagasse as the Scaffold for Mass Production of Hierarchically Porous Carbon Monoliths by Surface Self-Assembly. *Microporous Mesoporous Mater.* **2012**, *147*, 47-52.

(31) Liu, H. J.; Wang, X. M.; Cui, W. J.; Dou, Y. Q.; Zhao, D. Y.; Xia, Y. Y. Highly Ordered Mesoporous Carbon Nanofiber Arrays From a Crab Shell Biological Template and Its Application in Supercapacitors and Fuel Cells. *J. Mater. Chem.* **2010**, *20*, 4223-4230.

(32) Zhang, Y.; Hu, L.; Han, J.; Jiang, Z.; Zhou, Y. Soluble Starch Scaffolds with Uniaxial Aligned Channel Structure for In Situ Synthesis of Hierarchically Porous Silica Ceramics. *Microporous Mesoporous Mater.* **2010**, *130*, 327-332.

(33) Sun, Z.; Deng, Y.; Wei, J.; Gu, D.; Tu, B.; Zhao, D. Y. Hierarchically Ordered Macro-Mesoporous Silica Monolith: Tuning Macropore Entrance Size for Size-Selective Adsorption of Proteins. *Chem. Mater.* **2011**, *23*, 2176-2184.

(34) Li, F.; Wang, Z.; Ergang, N. S.; Fyfe, C. A.; Stein, A. Controlling the Shape and Alignment of Mesopores by Confinement in Colloidal Crystals: Designer Pathways to Silica Monoliths with Hierarchical Porosity. *Langmuir* **2007**, *23*, 3996-4004.

(35) Li, F.; Wilker, M. B.; Stein, A. Simulation-Aided Design and Synthesis of Hierarchically Porous Membranes. *Langmuir* **2012**, *28*, 7484-7491.

(36) Zhu, W.; Tao, S.; Tao, C.-A.; Li, W.; Lin, C.; Li, M.; Wen, Y.; Li, G. Hierarchically Imprinted Porous Films for Rapid and Selective Detection of Explosives. *Langmuir* **2011**, *27*, 8451-8457.

(37) Bian, S.-W.; Zhang, Y.-L.; Li, H.-L.; Yu, Y.; Song, Y.-L.; Song, W.-G. γ-Alumina with Hierarchically Ordered Mesopore/Macropore from Dual Templates. *Microporous Mesoporous Mater.* **2010**, *131*, 289-293.

(38) Zhao, J.; Wan, P.; Xiang, J.; Tong, T.; Dong, L.; Gao, Z.; Shen, X.; Tong, H. Synthesis of Highly Ordered Macro-Mesoporous Anatase TiO_2 Film with High Photocatalytic Activity. *Microporous Mesoporous Mater.* **2011**, *138*, 200-206.

(39) Zhang, R.; Dai, H.; Du, Y.; Zhang, L.; Deng, J.; Xia, Y.; Zhao, Z.; Meng, X.; Liu, Y. P123-PMMA Dual-Templating Generation and Unique Physicochemical Properties of Three-Dimensionally Ordered Macroporous Iron Oxides with Nanovoids in the Crystalline Wall. *Inorg. Chem.* **2011**, *50*, 2534-2544.

(40) Vu, A.; Stein, A. Multiconstituent Synthesis of $LiFePO_4$/C Composites with Hierarchical Porosity as Cathode Materials for Lithium Ion Batteries. *Chem. Mater.* **2011**, *23*, 3237-3245.

(41) Du, J.; Lai, X.; Yang, N.; Zhai, J.; Kisailus, D.; Su, F.; Wang, D.; Jiang, L. Hierarchically Ordered Macro-Mesoporous TiO_2-Graphene Composite Films: Improved Mass Transfer, Reduced Charge Recombination and Thier Enhanced Photocatalytic Activities. *ACS Nano* **2011**, *5*, 590-596.

(42) Li, F.; Qian, Y.; Stein, A. Template-Directed Synthesis and Organization of Shaped Oxide/Phosphate Nanoparticles. *Chem. Mater.* **2010**, *22*, 3226-3235.

(43) Mandlmeier, B.; Szeifert, J. M.; Fattakhova-Rohlfing, D.; Amenitsch, H.; Bein, T. Formation of Interpenetrating Hierarchical Titania Structures by Confined Synthesis in Inverse Opal. *J. Am. Chem. Soc.* **2011**, *133*, 17274-17282.

(44) Yang, S. M.; Coombs, N.; Ozin, G. A. Micromolding in Inverted Polymer Opals (MIPO): Synthesis of Hexagonal Mesoporous Silica Opals. *Adv. Mater.* **2000**, *2000*, 1940-1944.

(45) Zhou, D.-D.; Liu, H.-J.; Wang, Y.-G.; Wang, C.-X.; Xia, Y.-Y. Ordered Mesoporous/Microporous Carbon Sphere Arrays Derived from Chlorination of Mesoporous TiC/C Composite and Their Application for Supercapacitors. *J. Mater. Chem.* **2012**, *22*, 1937-1943.

(46) Zhu, Y.; Li, X.; Yang, J.; Wang, S.; Gao, H.; Hanagata, N. Composition-Structure-Property Relationship of the CaO-M_xO_y-SiO_2-P_2O_5 (M = Zr, Mg, Sr) Mesoporous Bioactive Glass (MBG) Scaffolds. *J. Mater. Chem.* **2011**, *21*, 9208-9218.

(47) Xue, C.; Wang, J.; Tu, B.; Zhao, D. Y. Hierarchically Porous Silica with Ordered Mesostructure from Confinement Self-Assembly in Skeleton Scaffolds. *Chem. Mater.* **2010**, *22*, 494-503.

(48) Wang, J.; Xue, C.; Wu, Z.; Li, W.; Lv, Y.; Asiri, A. M.; Tu, B.; Zhao, D. Y. Hollow Micro-Mesoporous Carbon Polyhedra Produced by Selective Removal of Skeletal Scaffolds. *Carbon* **2012**, *50*, 2546-2555.

(49) Brun, N.; Prabaharan, S. R. S.; Surcin, C.; Morcrette, M.; Deleuze, H.; Birot, M.; Babot, O.; Achard, M.-F.; Backov, R. Design of Hierarchical Porous Carbonaceous Foams From a Dual-Template Approach and Their Use as Electrochemical Capacitor Li Ion Battery Negative Electrode. *J. Phys. Chem. C* **2012**, *116*, 1408-1421.

(50) Platschek, B.; Köhn, R.; Döblinger, M.; Bein, T. Formation Mechanism of Mesostructured Silica in Confined Space: An In Situ GISAXS Study. *ChemPhysChem* **2008**, *9*, 2059-2067.

(51) Keller, A.; Kirmayer, S.; Segal-Peretz, T.; Frey, G. L. Mesostructured Silica Containing Conjugated Polymers Formed with the Channels of Anodic Alumina Membranes from Tetrahydrofuran-Based Solution. *Langmuir* **2012**, *28*, 1506-1514.

(52) O'Callaghan, J. M.; Petkov, N.; Copley, M. P.; Arnold, D. C.; Morris, M. A.; Amenitsch, H.; Holmes, J. D. Time-Resolved SAXS Studies of Periodic Mesoporous Organosilicas in Anodic Alumina Membranes. *Microporous Mesoporous Mater.* **2010**, *130*, 203-207.

(53) Schuster, J.; Koehn, R.; Döblinger, M.; Keilbach, A.; Amenitsch, H.; Bein, T. In Situ SAXS Study on a New Mechanism for Mesostructure Formation of Ordered Mesoporous Carbon: Thermally-Induced Self-Assembly. *J. Am. Chem. Soc.* **2012**, *134*, 11136-11145.

(54) Kim, E.-M.; Jung, J.-S.; Chae, W.-S. Interfacial Interaction Induced Mesostructural Changes in Nanocylinders. *Chem. Commun.* **2010**, *46*, 1760-1762.

(55) Zhang, A.; Hou, K.; Gu, L.; Dai, C.; Liu, M.; Song, C.; Guo, X. Synthesis of Silica Nanotubes with Orientation Controlled Mesopores in Porous Membranes via Interfacial Growth. *Chem. Mater.* **2012**, *24*, 1005-1010.

(56) El-Safty, S.; Shahat, A.; Awual, M. R.; Mekawy, M. Large Three-Dimensional Mesocage Pores Tailoring Silica Nanotubes as Membrane Filter: Nanofiltration and Permeation Flux of Protein. *J. Mater. Chem.* **2011**, *21*, 5593-5603.

(57) Wang, X.; Sumboja, A.; Khoo, E.; Yan, C.; Lee, P. S. Cryogel Synthesis of Hierarchical Interconnected Macro-/Mesoporous Co_3O_4 with Superb Electrochemical Energy Storage. *J. Phys. Chem. C* **2012**, *116*, 4930-4935.

Chapter Three

Control of TiO_2 Grain Size and Positioning in Three-Dimensionally Ordered Macroporous TiO_2/C Composite Anodes for Lithium Ion Batteries

---

Parts of this chapter are from: Petkovich, N. D.; Rudisill, S.G.; Wilson, B. E.; Mukherjee, A.; Stein, A. Control of TiO_2 Grain Size and Positioning in Three-Dimensionally Ordered Macroporous TiO_2/C Composite Anodes for Lithium Ion Batteries *Inorg. Chem.* **2014**, *53*, 1100-1112. – These parts are reproduced by permission of The American Chemical Society. Available at: http://dx.doi.org/10.1021/ic402648f

3.1 Introduction and Motivation

Titanium is the second most abundant transition metal in the Earth's crust, and its oxide, TiO_2, finds use in a wide array of applications. Since TiO_2 is a wide band gap semiconductor, its electronic properties have been harnessed for photocatalysis,[1,2] electronic device fabrication,[3,4] and the creation of dye-sensitized solar cells.[5,6] TiO_2 also serves as an important component in many pigments[7] and in stable supports for catalytic materials.[8-10] While many of these applications for TiO_2 have been developed over decades, the emergence of TiO_2 as a material for lithium-ion battery anodes has happened only recently.[10] Despite limitations inherent to TiO_2, researchers have begun to utilize TiO_2 effectively in batteries. Some of the benefits of using TiO_2 are clear, e.g., its cost, low toxicity, and density, while others were discovered through the electrochemical testing of TiO_2. In many cases, these benefits can only be realized when modifications are made to the various polymorphs of TiO_2, as described below.

Huang et al. first reported on the use of anatase TiO_2 as an intercalation-based anode material that could potentially compete with graphite-based anodes used in lithium ion batteries.[11] As research into the electrochemistry of TiO_2 progressed from that point, two advantages of using TiO_2 were touted.[12-14] First, the lithium intercalation and deintercalation processes in TiO_2 take place at a higher voltage than in graphite (~1.4 to 1.8 V vs. Li/Li^+, depending on the polymorph).[10] While this operating potential does not necessarily eliminate irreversible capacity due to formation of the solid-electrolyte interphase,[15] it avoids the problems of lithium plating and dendrite formation. With continued concerns over lithium ion battery safety, especially in light of recent incidents in the transportation sector, this advantage is especially relevant.[16] Another key advantage of TiO_2 is that it can retain its capacity at fast charge/discharge rates, but only in TiO_2 materials with nanoscale features, not in their bulk counterparts.[17-20] Careful control of the overall morphology of TiO_2 is needed to obtain good rate performance and to obtain reasonable capacities that make TiO_2 competitive with graphite.[10,20]

The past decade of research into TiO_2 electrodes has been marked by a continued push to synthesize materials that can deliver good capacities at high rates. These efforts have focused on the synthesis of nanoporous TiO_2,[21-23] TiO_2 particles with extremely small crystallite sizes,[18,24,25] and intricate hierarchical structures of TiO_2.[26,27] Most of these engineered materials possess high surface areas and have an open morphology that allows the electrolyte to completely wet the active material. As a result of these morphologies, lithium ion diffusion distances are reduced and a large interfacial area can be utilized for insertion/extraction reactions. In addition, the extensive interface between the active material and the electrolyte helps contribute to pseudocapacitance

charge storage.[22,28] Pseudocapacitance becomes the dominant reversible charge storage mechanism for TiO_2 at high charge/discharge rates.[22] Significant reductions in the crystallite size of TiO_2 also assist in increasing the extent of lithium intercalation, leading to improvements in capacity.[22,29]

Moving beyond simply considering the morphology of pure TiO_2, substantial research has been performed on composite materials that contain TiO_2 and a secondary conductive phase. As a wide–band gap semiconductor, TiO_2 has low intrinsic electronic conductivity. The low electronic conductivity of TiO_2 can significantly reduce battery capacities at high rates when electron transport lengths are relatively long, as is the case for nanoporous materials that extend over micrometers in length. This limitation is overcome through doping with heteroatoms[30] or though the formation of composite materials.[10] Most TiO_2 electrodes are fairly "low-tech" composites, in which TiO_2 is mechanically mixed with a conductive additive, typically carbon black. Better "wiring" of the TiO_2 grains can be realized through the formation of a nanocomposite, wherein the active TiO_2 is intimately mixed with the conductive phase during materials synthesis.[31] Guo et al. accomplished this by using sol–gel-derived RuO_2 "wires" with a matrix of TiO_2 crystals.[32] Owing to the expense of RuO_2, other groups have focused on forming nanocomposites with conductive carbon allotropes. Various composites have been produced that exhibit a wide range of morphologies that are often determined by the type of carbon used. For instance, TiO_2 nanosheets have been grown on carbon nanotubes that easily transport electrons away from the sheets, thereby improving performance at fast charge/discharge rates.[33] The use of graphene in nanocomposites with TiO_2 has allowed for the generation of different morphologies. Graphene can be used to wrap TiO_2 crystallites in a conductive matrix[34,35] and has also been used to produce sandwich-like composites with TiO_2 sheets.[36] Amorphous carbon is another allotrope that can be combined with TiO_2 in a variety of syntheses.[37-40] Its versatility comes in part from the numerous compounds that can be pyrolyzed to form a conductive phase, and one such compound is critical in the study described herein.

This chapter describes an effort to improve the performance of TiO_2 for lithium ion battery anodes through the formation of nanostructured TiO_2/C composites. In addition, it explores the use of the carbon as a secondary template to minimize TiO_2 crystallite growth during thermal processing. To obtain a suitable morphology, a combination of colloidal crystal templating (CCT) and surfactant templating is employed. As described in Chapter 2, hierarchical materials can be synthesized via this dual-templating method.[41] For the preparation of the TiO_2/C composites discussed here, a multiconstituent precursor is used that contains titanium isopropoxide (TiO_2

source), a phenol-formaldehyde (PF) sol (amorphous carbon source), and a block copolymeric surfactant. Further processing at elevated temperatures removes the colloidal crystal template, crystallizes the TiO_2, and carbonizes the PF sol. Ultimately, a porous structure is formed that contains nanocrystals of TiO_2 in a conductive carbon matrix, allowing better utilization of TiO_2 as an anode material.

Specific alterations to the synthesis procedure have an impact on the performance of these materials as lithium-ion battery anodes. First, both the choice of chelating agent and the temperature used for pyrolysis influence the TiO_2 crystallite size. This translates into significant differences in the performance of the TiO_2/C composites. Second, removal of the carbon framework through combustion at low temperatures yields a three-dimensionally ordered macroporous (3DOM) TiO_2 with void spaces between crystallites (intrinsic mesopores). The carbon restricts TiO_2 crystallite growth prior to burnout and allows us to achieve good capacities with this particular material.

3.2 Experimental

3.2.1 Materials

Methyl methacrylate (99 %), titanium(IV) isopropoxide (>97%), 2,4-pentanedione (acac, 99+%), trifluoroacetic acid (TFA, 99 %), poly(ethylene oxide)–*block*–poly(propylene oxide)–*block*-poly(ethylene oxide) copolymer (molecular weight of 5800, P123), and sodium carboxymethyl cellulose (CMC, molecular weight of 250,000) were all purchased from Sigma-Aldrich. Phenol (ACS reagent grade), formaldehyde (37 wt% in water), and potassium persulfate (ACS reagent grade) were obtained from Fisher Scientific. Hydrochloric acid (37 wt% in water) and sodium hydroxide pellets (ACS reagent grade) were obtained from Macron Chemicals. A suspension of styrene–butadiene rubber (SBR, 50 wt% in water) was purchased from the MTI Corp. Ethanol (200 proof, USP grade) was purchased from Decon Laboratories. Aeroxide® P25 TiO_2 was provided by Evonik Industries. All chemicals were used without further purification. Deionized water was produced on-site using a Barnstead Sybron purification system (final resistivity >18 MΩ·cm).

3.2.2 Preparation of the PF Sol and PMMA Colloidal Crystals

To produce these materials, monodisperse colloidal spheres of poly(methyl methacrylate) (PMMA) were synthesized using a previously reported emulsifier-free emulsion polymerization.[42] Colloidal crystal templates were obtained by letting the sphere suspension

sediment under the force of gravity and then by allowing the supernatant to evaporate. Phenol-formaldehyde prepolymer sol was synthesized following a well-established literature procedure.[43] The final sol was produced by dispersing dried resol oligomers in an equal mass of ethanol, forming a 50 wt% ethanolic PF sol.

3.2.3 Preparation of the TFA-TiO_2/C Composites

After the PF sol was obtained, two separate solutions (solutions A and B) were made. In solution A, 3.5 g of titanium isopropoxide was mixed with 1.4 g of TFA. This solution was stirred, and 2 g of ethanol was then added. After 5 min of stirring, 0.6 g of concentrated HCl was added dropwise to it. P123 (0.75 g), gently heated to a liquid state, was then added to the solution. Solution A was stirred until complete dissolution of the P123 was achieved. In solution B, 0.3 g of PF sol was mixed with 2 g of ethanol. Water (0.88 g) and liquid P123 (1 g) were added to solution B. Solution B was stirred until the P123 completely dissolved. Once the P123 had dissolved in both solutions, solution B was added dropwise to solution A. The final precursor solution was allowed to stir overnight.

For infiltration, millimeter-sized monolithic colloidal crystal templates were first placed in 20 mL scintillation vials. The precursor solution was then injected into the vials up to half the height of the template monoliths. Capillary action drew the precursor into the templates over a period of 4–6 h. If all the precursor solution was taken up into the templates, a small amount of additional precursor was added to the vials. After infiltration was completed, excess precursor was wiped from the monoliths using laboratory wipes. Excess solvent was removed by placing the infiltrated templates under low vacuum at ambient temperature for 15 min. This was done to prevent destruction of the 3DOM structure during subsequent pyrolysis. The infiltrated monoliths were then thermally treated (in capped vials) at 100 °C for 24 h and then at 140 °C for 24 h to further condense and cross-link the components of the precursor. They were then placed in alumina boats in a quartz tube under Ar gas flow (0.7 L/min) to remove the template, crystallize the TiO_2, and carbonize the PF resin. Samples were heated in a tube furnace to 350 °C at 1 °C/min and held for 4 h and then to 500 °C, 600 °C, 700 °C, 800, or 900 °C at 1 °C/min and held for 2 h.

3.2.4 Preparation of the acac-TiO_2/C Composites

A similar procedure to the one described above was used for the precursor solutions that contained acac as a chelating agent. Once again, a 50 wt% PF sol in ethanol was used for this synthesis. Two solutions (A and B) were prepared. Solution A was made by first combining 3.5 g

of titanium isopropoxide with 1.23 g of acac. Shortly after these were mixed, 1.75 g of ethanol was added to solution A. After 5 min of stirring, 1 g of concentrated HCl was added dropwise while solution A was stirred. Liquid P123 (0.75 g) was then dissolved in solution A. For solution B, ethanol (1.75 g) and PF sol (0.27 g) were mixed. Subsequently, 0.75 g of water and 1 g of liquid P123 was added to the solution. Once P123 had dissolved in both solution A and B, solution B was added dropwise to solution A. The final precursor was allowed to stir overnight. Infiltration of the colloidal crystal templates and subsequent processing was conducted following the procedure detailed above for the TFA-TiO_2/C composites.

3.2.5 Preparation of Single-Phase 3DOM TiO_2

For the single-phase 3DOM TiO_2, a TFA-based composite was first prepared. Pyrolysis was conducted at 350 °C and 500 °C following the procedure detailed above. Carbon was removed from the composites by calcining them at 400 °C for 2 h in a tube furnace under static air. A ramp rate of 2 °C/min was used.

3.2.6 Product Characterization

All the of samples were characterized by powder X-ray diffraction (PXRD) using a PANalytical X'Pert PRO diffractometer operated with a Co anode at 45 kV and 40 mA and an X'Celerator detector. The Scherrer equation was used to estimate crystallite sizes via line broadening in the PXRD patterns. Further characterization of the crystal structures present in the samples was performed using a WITec Alpha300R confocal Raman microscope fitted with a 514.5 nm Ar^+ laser (operated at 15 mW). Raman scattering was detected using a DV401 CCD thermoelectric-cooled detector. Multiple spectra were collected for a given area and then averaged to give the final, reported spectrum. A 10× aperture was used for all measurements. Morphological information was obtained via scanning electron microscopy (SEM) performed with a JEOL 6700 instrument operated at 5 kV. Samples were mounted on Al stubs covered with double-sided sticky carbon tape. A 5-nm layer of Pt was deposited on the samples prior to imaging. Additional morphological information was obtained by transmission electron microscopy (TEM). An FEI Technai T12 operated at 120 kV with LaB_6 filament was used for TEM imaging. Samples were prepared by bath sonicating powders suspended in ethanol for 5 min. The suspensions were dropped onto Cu grids coated with Formvar. Small-angle X-ray scattering (SAXS) patterns were collected on a Rigaku RU-200BVH instrument equipped with a rotating copper anode and a Siemens Hi-Star multiwire area detector. Gas sorption isotherms

were obtained using a Quantachrome Autosorb IQ_2 with N_2 gas at 77 K. Samples were outgassed at 200 ºC and 0.001 Torr for 12 h prior to measurement. Surface areas were calculated using the Brunauer-Emmitt-Teller (BET) method. Pore volumes were calculated from the point P/P_0 = 0.995 on the adsorption branch. Micropore volumes were estimated using a quenched solid density functional theory (QSDFT) kernel supplied by Quantachrome Instruments. Thermogravimetric analysis was conducted using a Netzsch STA 409 PC Luxx Instrument to determine the TiO_2 content. Analyses were carried out in flowing air using a 10 ºC/min ramp up to 1000 ºC. Fluorine content in the TFA composite samples was determined via a combination of flask combustion and ion chromatography carried out by Atlantic Microlab (Norcross, GA).

3.2.7 Electrochemical Characterization

Electrodes were assembled by mixing ground, ultrasonicated active material, Timcal Super P carbon black, and the aqueous binder suspensions. This electrode paste was spread onto carbon-coated aluminum foil (provided by Exopack® Advanced Coatings), dried overnight at ambient conditions, and finally under vacuum at 105 °C for 24 h. The composition of the dried electrode film was 84 wt% active material, 10 wt% conductive additive, 4 wt% CMC binder, and 2 wt% SBR binder. Disks with a diameter of 0.5 in were punched out of the film. Typically, the mass of active material in the electrodes was between 1 and 1.5 mg cm^{-2}. The electrode disks were placed in 2032 coin cells in a half-cell configuration with metallic lithium as the counter electrode. A Celgard® 3501 polypropylene membrane was used as the separator. A commercial electrolyte (1 M $LiPF_6$ in a 1:1:1 mixture by volume of ethylene carbonate, dimethyl carbonate, and diethyl carbonate) purchased from the MTI Corporation was used in the cells. Coin cell assembly was performed in a glovebox filled with helium gas. Cells were tested using an Arbin Instruments BT-2000. Cycling was conducted between 1 and 3 V vs. Li/Li^+. The C-rate was set so that 1 C = 335 mA per g of TiO_2 in the electrode.

Impedance spectroscopy was carried out on the coin cells by using a Solartron 1255B frequency response analyzer with an attached SI1287 electrochemical interface. The electrode film served as the active electrode, while lithium foil served as the reference and counter electrodes. A frequency range of 50 kHz to 50 mHz was used, along with an AC signal of 20 mV. During the measurement, a constant potential of 2.1 V vs. Li/Li^+ was applied. The impedance spectra were fitted to equivalent circuits using Wolfram Mathematica 9.

3.3 Results and Discussion

3.3.1 Structural Characterization of TFA-TiO_2/C and acac-TiO_2/C

Numerous variables can be altered in the synthesis of the composite materials, but three variables are the main focus of this section: the type of chelating agent used in the synthesis, the pyrolysis temperature attained by the composite, and the use of carbon as a secondary template.

Two different chelating agents were used to stabilize the titanium isopropoxide in the multiconsitituent precursor. Without chelation, TiO_2 quickly precipitates out of the precursor prior to complete infiltration of the template. Trifluoroacetic acid had previously been used for arresting the condensation of a precursor that contained titanium alkoxide, allowing for the successful synthesis of mesoporous TiO_2 and 3DOM TiO_2.[44,45] 2,4-Pentanedione is another chelating agent commonly used to prevent rapid condensation of titanium alkoxides.[46] Both agents yielded precursors stable enough for the infiltration process. The overall TiO_2 content in the pyrolyzed composites was also similar: TFA-TiO_2/C pyrolyzed at 800 °C was 74 wt% TiO_2, while acac-TiO_2/C pyrolyzed at 800 °C was 71.5 wt% TiO_2. In addition to the TiO_2 content, elemental analysis was used to calculate fluorine content for the TFA-TiO_2/C pyrolyzed at 800 °C. Within the detection limits of the technique (0.25 wt%), no fluorine was found in the samples. While this does not completely eliminate possible low-level fluorine ion doping in the materials made via the TFA precursor, we postulate that fluorine does not play a significant role in the overall electrochemical properties.

Figure 3.1 shows PXRD patterns of both TFA- and acac-TiO_2/C composites together with the temperature reached during the final pyrolysis step. Carbon and four polymorphs of TiO_2 are observed in the patterns. While no strong peak exists for the amorphous carbon, a broad shoulder (essentially, a sloping background) is observed below 40 °2θ for all samples. Unlike the carbon, the TiO_2 present in both TFA-TiO_2/C and acac-TiO_2/C undergoes several phase transformations at different pyrolysis temperatures. At the lowest pyrolysis temperatures, anatase co-exists with the monoclinic TiO_2-B phase. Identification of TiO_2-B is fairly uncomplicated due to the appearance of two overlapping peaks near 52 °2θ (Figure 3.1). In syntheses with TiO_2 sol-gel precursors and surfactants, TiO_2-B can appear as a minor phase when the resulting materials are thermally treated at temperatures from 400 to 600 °C.[13,47,48] This is also observed with the TFA- and acac-TiO_2/C. Even the relatively featureless pattern for acac-TiO_2/C pyrolyzed at 500 °C contains a very broad peak between 50 and 55 °2θ (Figure 3.1 b). This feature is the result of several overlapping TiO_2-B reflections. It is important to note that the thermal stability of the TiO_2-B phase is quite high for these materials,[48] with acac-TiO_2/C retaining the phase at 600 °C.

This stability is likely enhanced from the carbon matrix that impedes crystal growth and consequent transformation to the anatase phase.

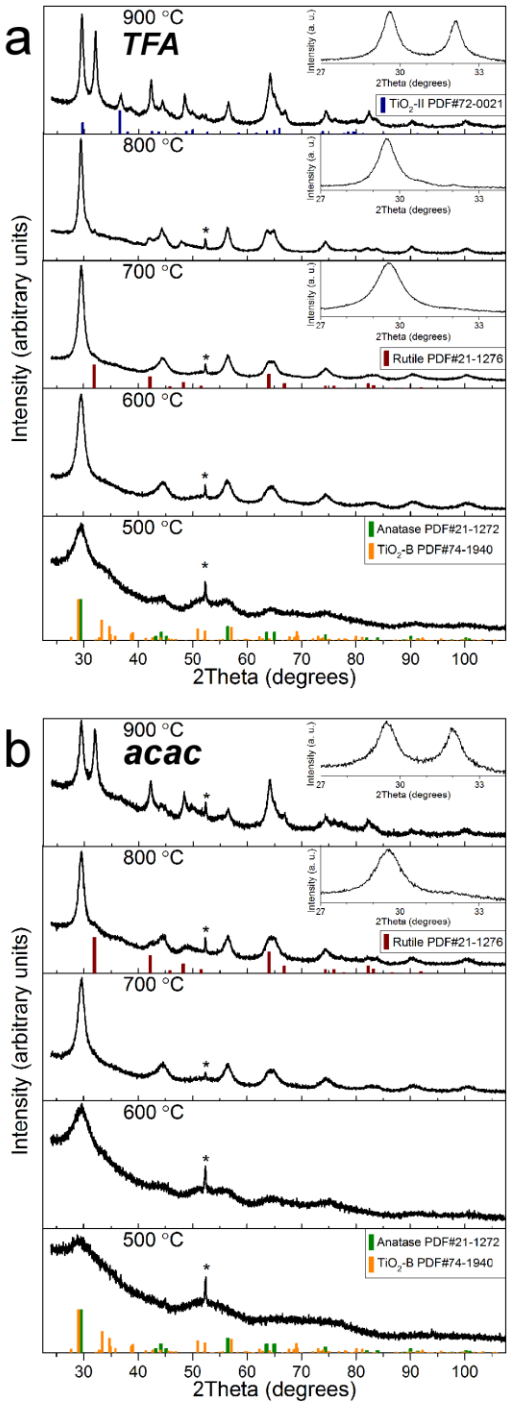

Figure 3.1 PXRD patterns of (a) TFA-TiO_2/C and (b) acac-TiO_2/C composites. The temperature reached in the final pyrolysis step is given. Reference patterns are presented underneath the collected patterns. The insets highlight the main reflections of anatase and rutile. The asterisk indicates a reflection from the Al sample holder.

As stated above, both TFA-TiO_2/C and acac-TiO_2/C contain the reflections characteristic of anatase TiO_2 (Figure 3.1). The main (101) reflection is clearly observed at ~29.4 °2θ for all samples. Anatase is the majority phase detected in sol-gel syntheses when TiO_2 first crystallizes during thermal treatment, especially with syntheses conducted at low pH.[49,50] This can be ascribed to the fact that anatase is the thermodynamically stable polymorph for high-surface-area TiO_2 crystallites below ~14 nm in size.[51,52] As the pyrolysis temperature increases, transformation from the anatase to the rutile polymorph accompanies an increase in crystallite size, since rutile is the thermodynamically stable phase for bulk TiO_2.[49] In TFA-TiO_2/C, the rutile (110) peak at ~31.9 °2θ appears when the final pyrolysis temperature reaches 700 °C. Rutile remains a very minor phase until the pyrolysis temperature reaches 900 °C, when rutile becomes the majority phase. For acac-TiO_2/C, a similar sequence of phase transformation with respect to temperature is observed; however, the pyrolysis temperature has to reach 800 °C before rutile peaks appear. Both the acac- and TFA-TiO_2/C composite materials clearly stabilize the anatase phase at high temperatures, consistent with other reports on TiO_2/C composites.[37,39,53,54] A delay in the phase transformation is caused by the carbon matrix that confines the TiO_2 crystallites and prevents diffusion of ions/vacancies. Grain growth is therefore lessened and the crystallites do not grow to the diameter required for the transformation from anatase to rutile. Also, nucleation of the rutile phase at the interface of anatase crystallites is limited due to confinement.[55]

Estimates of crystallite size were made using the line broadening of the PXRD reflections (Table 3.1). TiO_2-B reflections were too weak to be adequately fit and were not analyzed. Unsurprisingly, crystallite size increases for the anatase grains as pyrolysis temperature increases. The crystallite growth is more pronounced for TFA-TiO_2/C samples. This can be observed starting with samples pyrolyzed at 500 °C. With acac-TiO_2/C, the reflections are so broad that it is not possible to accurately assess crystallite size. In contrast, TFA-TiO_2/C has an estimated grain size of 3.0 nm after pyrolysis at 500 °C. For acac-TiO_2/C, pyrolysis temperatures have to be increased by 100 °C to obtain an estimated crystallite size that corresponds to those in TFA-TiO_2/C (e.g., the crystallites in TFA-TiO_2/C at 700 °C are similar in size to acac-TiO_2/C at 600 °C). Larger crystallites negatively impact overall electrode performance, an important point that will be quite relevant in the subsequent discussion of these materials. By 900 °C, both samples contain anatase crystallites over 10 nm in size. Again, this is close to the predicted size range where rutile becomes the thermodynamically stable phase;[51] therefore, it is understandable that rutile is the major phase for samples pyrolyzed at 900 °C. Rutile also exhibits a larger crystallite

size for both types of composite; this is consistent with observations that rutile crystallites grow faster than anatase crystallites.[56]

Table 3.1. Structural and textural parameters of 3DOM TiO_2/C and 3DOM TiO_2 samples.

sample	anatase crystallite size (nm)	rutile crystallite size (nm)	BET surface area (m^2/g)	pore volume (cm^3/g)	QSDFT micropore S.A. (m^2/g)[a]
TFA-TiO_2/C, 500 °C	3.0		261	0.24	172
TFA-TiO_2/C, 600 °C	5.8		332	0.46	222
TFA-TiO_2/C, 700 °C	8.5	[b]	394	0.44	244
TFA-TiO_2/C, 800 °C	11.5	[b]	451	0.46	232
TFA-TiO_2/C, 900 °C	14.0	15.8	505	0.63	304
acac-TiO_2/C, 500 °C	[c]		262	0.75	86.7
acac-TiO_2/C, 600 °C	3.0		272	0.56	144
acac-TiO_2/C, 700 °C	5.8		378	0.86	252
acac-TiO_2/C, 800 °C	8.4	[b]	428	0.50	277
acac-TiO_2/C, 900 °C	10.3	10.8	490	0.94	276
3DOM TiO_2	7.8		126	0.32	[d]

[a] Calculated using a QSDFT kernel for adsorption of N_2 on carbon at 77 K.
[b] Rutile (110) peak too weak to accurately fit.
[c] Anatase (101) line width too broad to accurately fit. Crystallite size is below 2 nm.
[d] Sample devoid of carbon, so QSDFT was not used.

One final note should be made about the PXRD patterns: a set of anomalous peaks are present in the TFA-TiO_2/C composite pyrolyzed at 900 °C. An intense peak is clearly observed near 36.5 °2θ, and others can be found in the pattern (Figure 3.1 a). In the presence of carbon, TiO_2 can undergo carbothermic reduction to form various Magnelí phases with ordered defect structures.[53] Titanium carbide can also be formed.[57] None of the reduced phases of TiO_2 or TiC have a diffraction pattern that matches the additional peaks. Instead the peaks match an orthorhombic phase of TiO_2 (TiO_2-II) that is generally synthesized by subjecting TiO_2 to high pressures.[58] The presence of TiO_2-II cannot fully explained, but it may be related to the reduction of TiO_2. The high temperature form of Ti_3O_5, β-Ti_3O_5, has an orthorhombic lattice (related to the pseudo-brookite structure).[59] It may be possible that a phase transition occurred from the Ti_3O_5 form to TiO_2-II when the sample was exposed to oxygen. Alternately, stresses induced by the confinement of TiO_2 in the 3DOM framework that contains carbon might induce the shear necessary for transformation to TiO_2-II.

More information concerning the crystal polymorphs present in the composite materials was obtained through confocal Raman microscopy. As is shown in Figure 3.2, characteristic vibrational modes for certain TiO_2 crystal structures can be found in TFA- and acac-TiO_2/C samples.[60] TiO_2-B modes, albeit extremely weak (Figure 3.2, orange arrows), are present in the spectra of composites that have TiO_2-B reflections in their PXRD patterns. The anatase E_g mode centered near 150 cm^{-1} is generally the strongest mode in any given spectrum, a typical observation when examining nanocrystalline anatase that has long-range order.[61] Since the grain size for the anatase is below 20 nm in the samples, no sharp peaks were observed in the spectra of any of the samples. This can be explained by phonon confinement that results in broadening of Raman modes for small crystallites.[61]

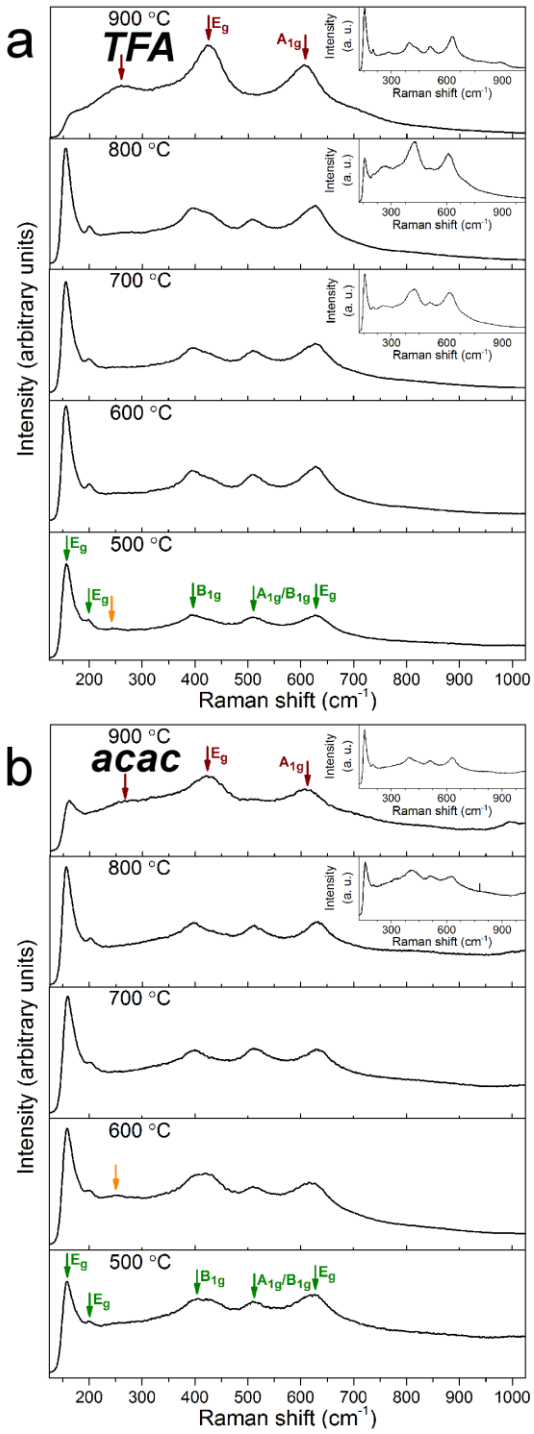

Figure 3.2 Raman spectra of (a) TFA-TiO_2/C and (b) acac-TiO_2/C. These spectra are from the region where TiO_2 lattice vibrations can be observed. Pyrolysis temperatures are given next to corresponding spectra. Arrows have been placed over some of the characteristic modes for anatase, rutile, and TiO_2-B in the spectra. The insets show the variation in the crystal polymorphs observed across a sample.

At high pyrolysis temperatures, the anatase modes, most notably the E_g mode, lose intensity. Rutile vibrational modes, especially the E_g and A_{1g} modes, appear as the transformation from anatase to rutile begins. For TFA-TiO_2/C, rutile vibrational modes are found in various areas of the composite starting at 700 °C (Figure 3.2 a). By 900 °C, the rutile modes dominate most spectra, and only weak peaks are observed that correspond to anatase modes. Some areas contain fairly intense anatase modes (top inset in Figure 3.2 a), which might be indicative of regions with low TiO_2 content and consequently less sintering. Alternately, local variations in temperature during pyrolysis might contribute to the heterogeneity. Rutile peaks and heterogeneities in the observed polymorphs are also observed for acac-TiO_2/C composites. However, the pyrolysis temperature has to reach 800 °C before rutile modes are observed. The peak near 400 cm^{-1} shifts and a shoulder appears for some spectra due to the rutile E_g peak (see inset in Figure 3.2 b). Even then, rutile remains a minor phase. Scanning a specific area, it was determined that acac-TiO_2/C pyrolyzed at 900 °C contains rutile, and the modes are most intense on the surface of the monolithic pieces (see inset in Figure 3.2 a). Any excess precursor left on the sample forms an untemplated surface "crust" after processing. Sintering can be quite severe in these regions, since large clusters of TiO_2 are aggregated on the surface. These observations all serve to largely confirm the data gathered from the XRD patterns. Furthermore, they indicate that the relative abundance of anatase vs. rutile is not uniform for samples pyrolyzed at high temperatures.

In addition to providing information on the structure of TiO_2, Raman spectroscopy was conducted on the *D*/*G* bands for the carbon framework. These bands are related to specific vibrational modes in aromatic six membered rings. The *G* band is found in pristine graphite (or planar sp^2 carbon) and comes from bond stretching. In contrast, the *D* band comes from a breathing mode that can only occur in carbon materials that contain disorder.[62] Figure 3.3 shows, for all of the samples, the region of the Raman spectra that contains the *D*/*G* bands. The same general trend is observed for both TFA-TiO_2/C and acac-TiO_2/C. As the pyrolysis temperature increases, the intensity of the *D* band increases relative to the *G* band (Table 3.2). This may seem surprising at first glance, since the conductivity of hard, amorphous carbon derived from phenolic resins is known to increase with increasing temperature.[63,64] However, the intensity of the *G* peak has been reported to decrease with increasing pyrolysis temperature below 1000 °C for carbonized phenolic resins.[65] Ferrari and Robertson note that for small (< 2 nm) clusters of aromatic rings in amorphous carbon, the *D* band intensity increases as the cluster size becomes larger.[62] In this case, the observed increase in *D* band intensity is simply a reflection of the presence of more aromatic rings in the minute clusters that make up the amorphous carbon.

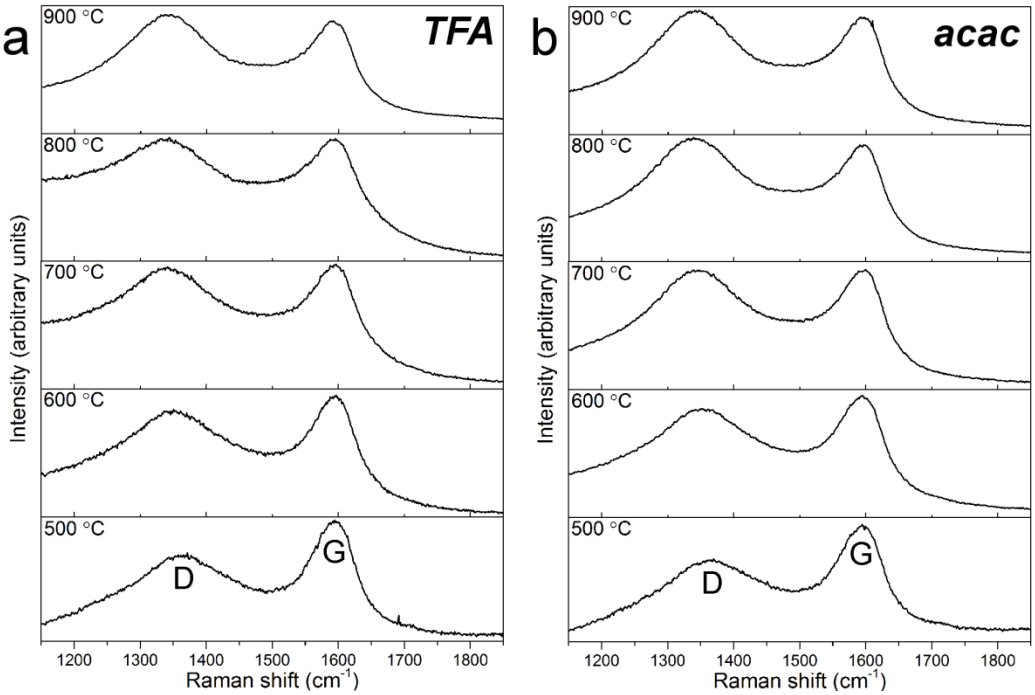

Figure 3.3 The *D*/*G* Raman bands are shown for (a) TFA-TiO_2/C and (b) acac-TiO_2/C. The two bands are labeled, along with the final pyrolysis temperature reached during processing. The *D* band intensity increases as pyrolysis temperature increases, indicating a growth in carbon cluster size.

Table 3.2 Relative Intensities of the *D*/*G* Raman Bands for the 3DOM TiO_2/C samples.

Sample	I_D/I_G
TFA-TiO_2/C, 500 °C	0.76
TFA-TiO_2/C, 600 °C	0.90
TFA-TiO_2/C, 700 °C	0.82
TFA-TiO_2/C, 800 °C	1.0
TFA-TiO_2/C, 900 °C	1.1
acac-TiO_2/C, 500 °C	0.81
acac-TiO_2/C, 600 °C	1.0
acac-TiO_2/C, 700 °C	1.1
acac-TiO_2/C, 800 °C	1.3
acac-TiO_2/C, 900 °C	0.97

3.3.2 Morphology and Textural Properties of TFA-TiO_2/C and acac-TiO_2/C

An assessment of the structure of the 3DOM network was conducted using SEM. Figure 3.4 contains a panel of SEM images for all TFA- and acac-TiO_2/C pyrolyzed at different temperatures. In all of the images, the face-centered cubic (fcc) lattice of macropores is clearly visible. Interconnecting windows are present between the large macropores, but unlike the case for the larger macropores, there is variation in the diameter of the windows.

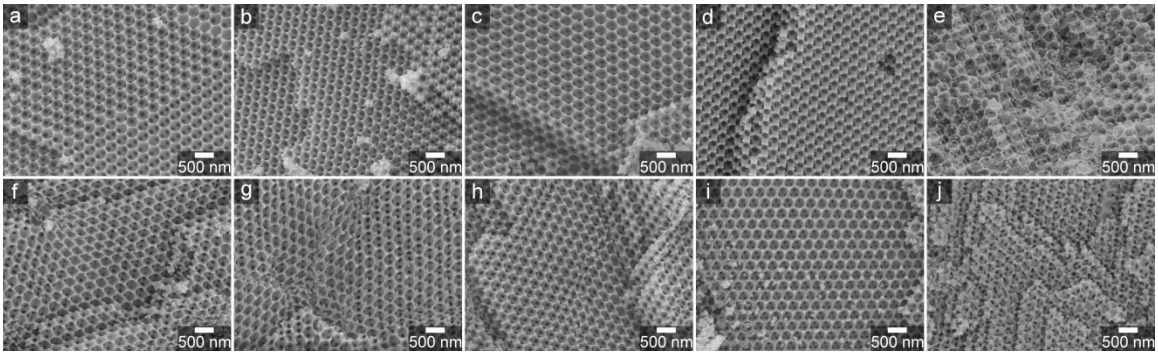

Figure 3.4 SEM images of TFA-TiO_2/C (a–e, 500–900 °C, 100 °C increments) and acac-TiO_2 composites (f–j, 500–900 °C, 100 °C increments). The 3DOM morphology is present in all of the materials processed. A well-ordered 3DOM morphology is observed across the majority (>50%) of any given sample.

Differences in crystallite size and location can also be ascertained using SEM for some of the composites. Figure 3.5 highlights the significant difference in crystallite size between TFA- and acac-TiO_2/C in the materials pyrolyzed at 800 °C. The aggregation is more pronounced in TFA-TiO_2/C, as is expected from the PXRD patterns. This trend continues at higher temperatures, as well. SEM micrographs also suggest that a substantial fraction of the TiO_2 exists on the surface of TFA-TiO_2/C samples.

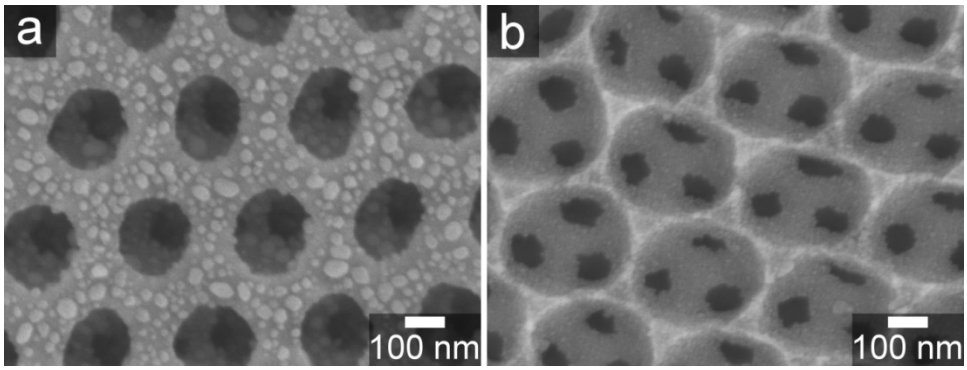

Figure 3.5 Two high-magnification SEM images are shown for (a) TFA-TiO_2/C and (b) acac-TiO_2/C pyrolyzed at 800 °C. The size of the TiO_2 aggregates is clearly larger in the TFA-TiO_2/C composite.

More information concerning the textural properties of the composites can be determined using N_2 sorption. This includes information concerning the presence of any mesopores created by the surfactant present in the precursor. The sorption isotherms for TFA- and acac-TiO_2/C are presented in Figure 3.6. An analysis of the general shape of the isotherms yields several insights into the porosity present in the composites. First, the hysteresis that is characteristic of mesoporous materials is absent for the majority of the isotherms. Weak hysteresis is observed for the samples pyrolyzed at 500 °C/600 °C, and also at 900 °C. The hysteresis at 900 °C is clearly not related to the surfactant template. Second, a sharp rise in the isotherm at $P/P_0 > 0.9$ reflects the presence of macroporosity. Third, another sharp rise is present at very low P/P_0 that comes from microporosity in the amorphous carbon matrix.[66] Finally, closure of the isotherms does not occur for the samples pyrolyzed at 500 °C. Many polymeric materials (like the PF resin) have isotherms that do not close,[66] which would explain why this phenomenon happens only at low temperatures.

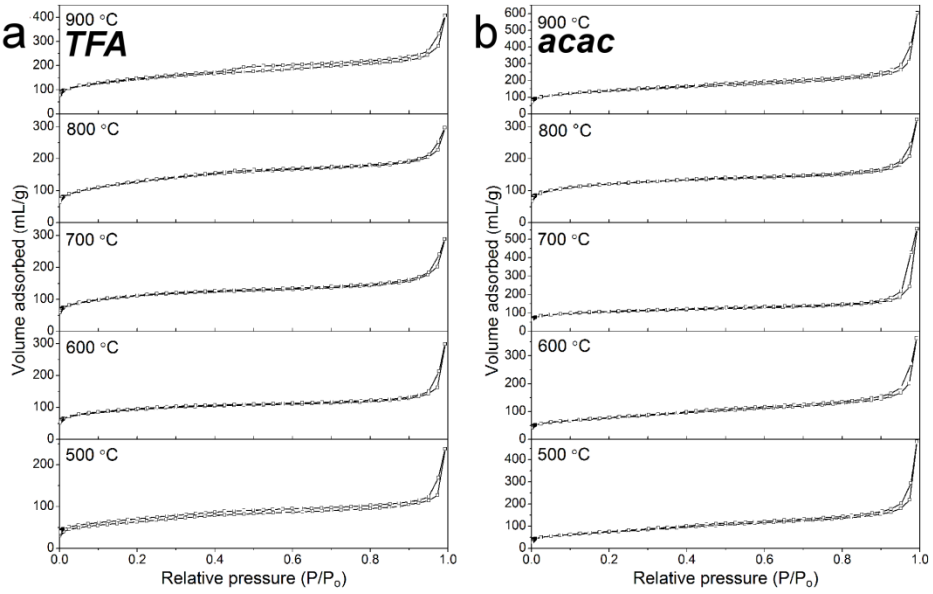

Figure 3.6 Nitrogen gas sorption isotherms of the TFA- and acac-TiO_2/C composites. Sharp rises in the isotherms are observed at both low and high P/P_0. This is characteristic of a material containing both micropores and macropores.

Table 3.1 presents additional information derived from the isotherms. Examining the BET surface areas first, an increase in surface area is observed as the pyrolysis temperature increases. This is in line with reports on mesoporous TiO_2/C composites derived using PF sol.[37,53] Much of

this increase can be attributed to the development of microporosity in the carbon phase. An estimate of the micropore area was found via a quenched state density functional theory (QSDFT) kernel for carbon. While the fits to the isotherms are good, this can only be considered an estimate due to differences in surface energetics between carbon and TiO_2. In general, the surface area due to microporosity increases for both TFA- and acac-TiO_2/C at higher pyrolysis temperatures, which can be attributed to the carbon in the composites. It is likely that the majority of the BET surface area increase is from the carbon, but mesoporosity that arises from the spaces between TiO_2 grains may also contribute. Since micropores in the carbon will not greatly increase the capacity of the composite material in the 1–3 V range,[54] the enhanced surface areas are not a major factor in the electrochemical performance of these composites. Pore volume does not follow a clear trend with increasing pyrolysis temperature for either TFA- or acac-TiO_2/C. At high P/P_0, there is a sharp increase in the volume adsorbed. Some factor other than the geometry of the 3DOM network may be responsible, including breakdown of the material into smaller particles.

Since only limited evidence of mesoporosity was found with gas sorption, SAXS was used to obtain evidence that a mesostructure exists in some of the composites. Before pyrolysis, the infiltrated, thermally-treated TFA- and acac-TiO_2/C both have a broad peak in their SAXS patterns (Figure 3.7). The peak in the patterns comes from a disordered mesostructure that arises from the co-assembly of surfactant molecules with other components of the precursor. Differences in *d*-spacing are observed between peaks in the patterns for TFA- and acac-TiO_2/C (10.0 nm versus 12.3 nm). Even though the same block-co-polymer was used as the soft template for both syntheses, the type of chelating agent and amounts of solvent used were changed. This change could result in a difference in the swelling of any P123 micelles and explain the altered *d*-spacing.[41] Once the samples are pyrolyzed, the disordered mesopore network disappears (Figure 3.8). Weak scattering peaks are observed for TFA-TiO_2/C at 6.9 nm (the contraction is due to condensation and shrinkage of the 3DOM network) until pyrolysis at 600 °C. The acac-TiO_2/C material fares better with regards to mesostructural stability; a weak scattering peak at 8.9 nm does not disappear until pyrolysis at 800 °C. Mesostructural collapse in both types of composite is likely a result of the sintering of TiO_2 crystallites. If pores are present in the TiO_2 phase, thermally-induced densification will ultimately close them. Pores present in the carbon phase can undergo collapse as growing TiO_2 crystallites pierce through their sides. Since acac-TiO_2/C has a consistently smaller crystallite size than TFA-TiO_2/C, better mesostructural stability is expected.

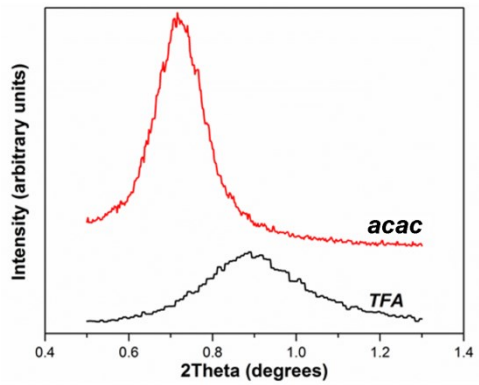

Figure 3.7 SAXS patterns of unpyrolyzed TFA-TiO_2/C and acac-TiO_2/C. Both types of material have single diffraction peaks indicative of a disordered mesostructure formed from the P123 surfactant.

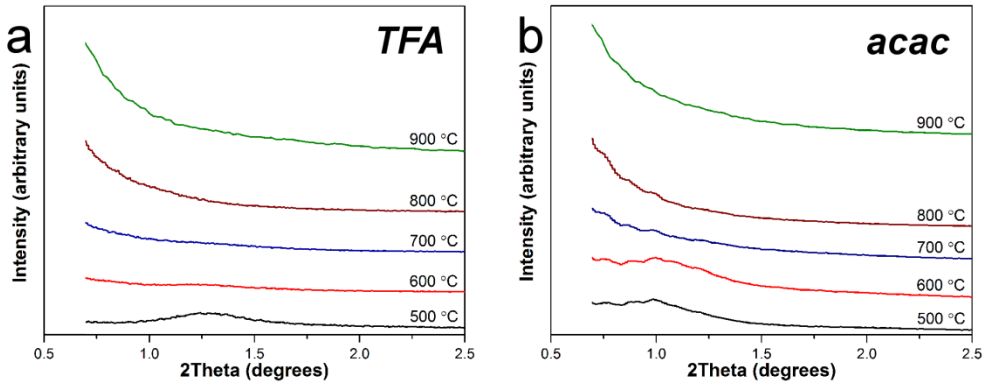

Figure 3.8 SAXS patterns of (a) pyrolyzed TFA-TiO_2/C and (b) acac-TiO_2/C. Diffraction peaks are fairly weak, if present at all, in the patterns. The position of the peak is shifted to high angles relative to the unpyrolyzed samples. This is a result of the contraction in the 3DOM structure during thermal treatment.

TEM analysis of the TiO_2/C composites further confirms these experimental results. TiO_2 crystallites contained within the walls of the 3DOM structure gradually increase in size as the pyrolysis temperature increases, due to thermally-induced grain growth. Figure 3.9 shows this effect, and also demonstrates the impact of chelating agent; crystallites present in acac-TiO_2/C are considerably smaller than crystallites in TFA-TiO_2/C. Additionally, as the pyrolysis temperature exceeds ~700 °C for TFA-TiO_2/C, the crystallites become larger than the confines of the walls. With increasing temperature, the TiO_2 grows outward, no longer contained by the carbon framework (Figure 3.10). This may result in poorer performance due to loss of carbon/TiO_2 interfacial area. Finally, low pyrolysis temperatures are associated with retention of disordered mesoporosity within the walls of the structure, offering confirmation of the SAXS results (Figure 3.11).

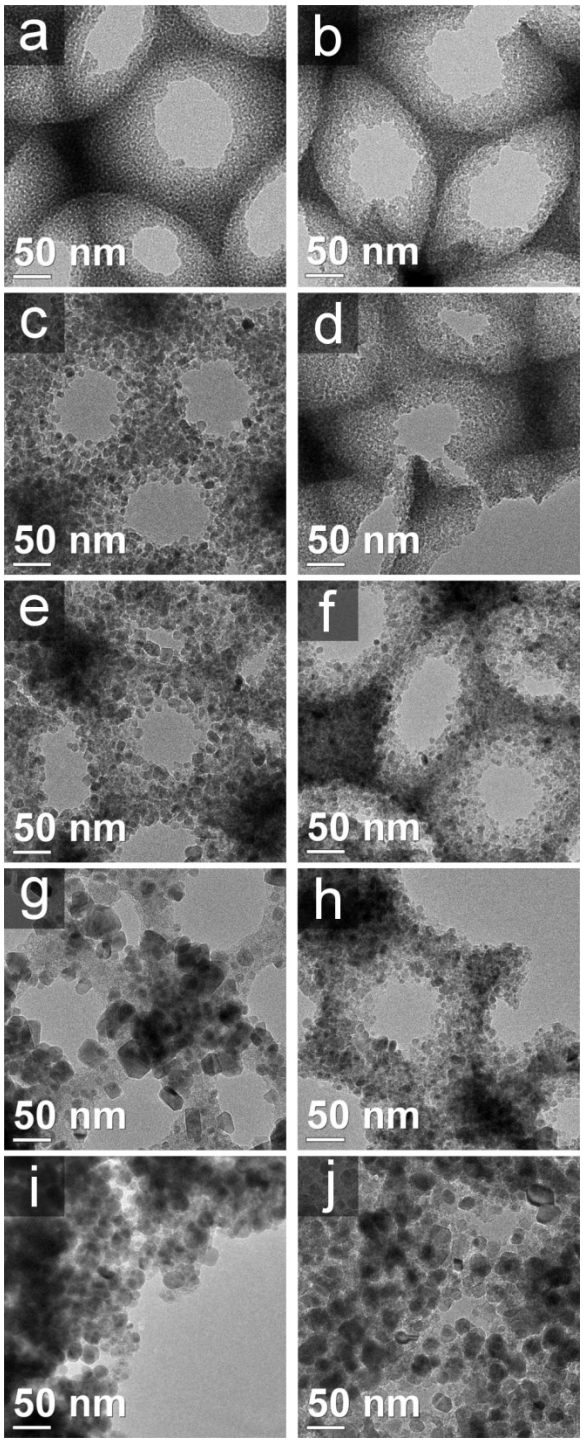

Figure 3.9 TEM images of TFA-TiO_2/C (a, c, e, g, and i, 500–900 °C, 100 °C increments) and acac-TiO_2/C (b, d, f, h, and j, 500–900 °C, 100 °C increments) composites. The TiO_2 crystallite size increases as the pyrolysis temperature is increased. At higher temperatures, the substantially larger TiO_2 crystallites present in TFA-TiO_2/C are clearly observed in comparison to images from acac-TiO_2/C. TEM images taken by Stephen Rudisill.

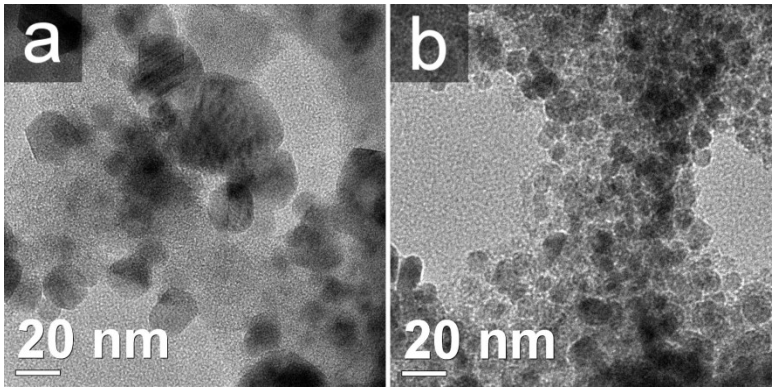

Figure 3.10 TEM images of (a) TFA-TiO_2/C and (b) acac-TiO_2/C, both pyrolyzed at 800 °C. These higher magnification images highlight the disparity in crystallite size between the TFA-TiO_2/C and acac-TiO_2/C samples. TEM images taken by Stephen Rudisill.

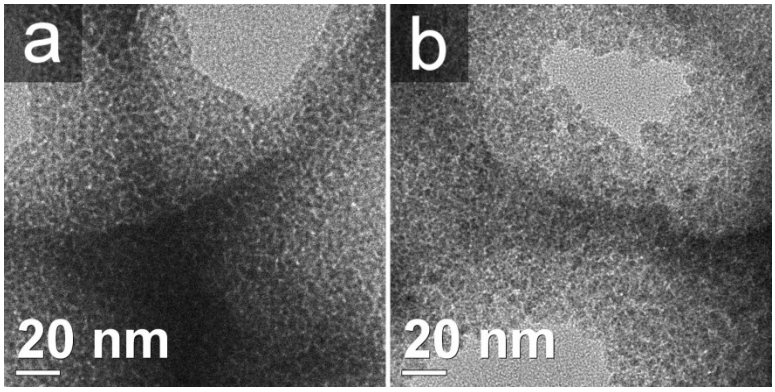

Figure 3.11 TEM images of (a) TFA-TiO_2/C pyrolyzed at 500 °C and (b) acac-TiO_2/C at 600 °C. These images show that disordered mesoporosity remains, as long as the pyrolysis temperature is sufficiently low. TEM images taken by Stephen Rudisill.

3.3.3 Discussion of the Differences Caused by Changing the Chelating Agent

From the structural analysis conducted above, there are clear differences caused by the use of trifluoroacetic acid vs. 2,4-pentanedione as a chelating agent. No matter what chelating agent is used, TiO_2 crystallites can be found embedded in the carbon phase. However, TEM and SEM imaging reveals that the TiO_2 crystallites in TFA-TiO_2/C are concentrated on the exterior surface of the 3DOM network. This localization also results in enhanced sintering and crystal growth of TiO_2, despite the fact that TFA-TiO_2/C has carbon content nearly identical to that of acac-TiO_2/C. The origin of the pronounced differences in the distribution of TiO_2 lies in the compatibility of the chelated complex with the other components of the precursor. When trifluoroacetic acid is used to chelate titanium isopropoxide (in a 1:1 molar ratio), the resulting complex contains

numerous trifluoromethyl groups.[44] Most of the other components of the precursor (water, alcohols, and the resol clusters) contain O–H moieties that can participate in hydrogen bonding. Interactions between the hydrophobic titanium-containing complex and the rest of the precursor should be unfavorable for TFA-TiO_2/C. Separation of the complex to the relatively hydrophobic surface of the PMMA template should then occur, in line with what we observe. A far different result should be expected for the acac-TiO_2/C precursor. Prior studies in the literature have determined that various monomers and dimers form when 2,4-pentanedione and titanium alkoxides are combined in solution.[46,67] No matter what particular complexes are found in the precursor, these titanium-containing complexes will contain aquo- and hydroxo- groups that can participate in hydrogen-bonding. Since the complexes in the acac-TiO_2/C precursor are relatively hydrophilic, they should be well-distributed throughout the other components of the precursor. Ultimately, this would lead to a situation where TiO_2 condenses and nucleates throughout the interstitial space of the colloidal crystal template. The surrounding carbon can more effectively restrict the growth of TiO_2 crystals and impede sintering, explaining the reduced crystal size for acac-TiO_2/C.

TFA-TiO_2/C and acac-TiO_2/C exemplify two possible distributions of an active material in a secondary matrix for a 3DOM/m nanocomposite. Taking these materials and a 3DOM/m $LiFePO_4$/C composite described by Vu and Stein into consideration,[68] three distinct types of 3DOM/m metal oxide/phosphate and carbon composites can be identified. Figure 3.12 offers computer renderings highlighting the difference in the distribution of the active phase in the three composites. In Figure 3.12 a, the active material is confined in confined in the octahedral nodes, as in the case for the 3DOM/m $LiFePO_4$/C. The precursors for $LiFePO_4$ are more ionic and minimize interactions with the nonpolar PMMA template by aggregating in the octahedral nodes.[68] Figure 3.12 b shows an intermediate distribution where the active material is distributed throughout the composite. This is observed for acac-TiO_2/C, owing to the favorable interaction between the titanium complex and the other components of the precursor. Finally, Figure 3.12 c is the other extreme case, where the active material is primarily localized on the outer surface. Unfavorable interactions between the titanium complex and the other precursor components lead to the situation shown in Figure 3.12 c for TFA-TiO_2/C. It is clear that the structure of the metal complex can dictate overall positioning of the active material in the carbon composite. Future work on templated composites should consider optimization of the interactions between any metal-containing complex, the solvent, additional precursors, and a hard template to achieve a distribution of active material favorable for the application at hand.

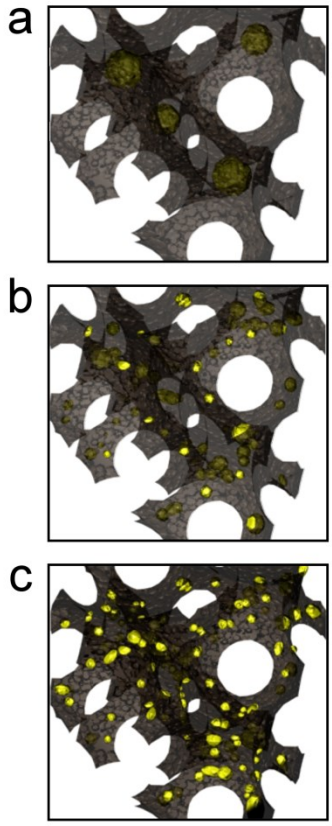

Figure 3.12 Computer renderings of three different distributions of an active material (yellow) in a secondary matrix (brown) for 3DOM/m composites. In (a) the active material is localized in the octahedral nodes, in (b) the active material is well-distributed through the structure, and in (c) the active material is localized on the exterior surface.

3.3.4 Structural and Morphological Characterization of 3DOM TiO_2

Before moving on to a discussion of the anodes made from the composites, one other material needs to be discussed: the 3DOM TiO_2 produced using carbon as a secondary template. This material was obtained by calcination of TFA-TiO_2/C pyrolyzed at 500 °C. The choice of TFA-TiO_2/C was made due to its slightly higher TiO_2 content than acac-TiO_2/C. In this initial step, the crystallite size was minimized both by the low pyrolysis temperature and the presence of a confining partially carbonized phase. Burnout of the partially carbonized PF resin increased the crystallite size of the anatase phase, as shown by the clear decrease in the line width of the XRD peaks (Figure 3.13 a and Table 3.1). Also, the shoulder below 40 °2θ from the PF component disappeared. The material retained a BET specific surface area of 126 m^2/g (Figure 3.13 b and Table 3.1), which is a value similar to that obtained in mesoporous TiO_2 made using soft

templating.[10] SEM micrographs reveal that the 3DOM structure is preserved after the combustion of the carbon matrix (Figure 3.13 c). Some variation in the size of interconnecting windows is present in the 3DOM structure and likely arose from the original composite. Finally, TEM imaging (Figure 3.13 d) reveals that the walls and nodes of the 3DOM network are comprised of aggregated TiO_2 crystallites. Textural mesoporosity exists between the crystals (enhanced by removal of the carbon phase), but no ordered mesoporosity can be found.

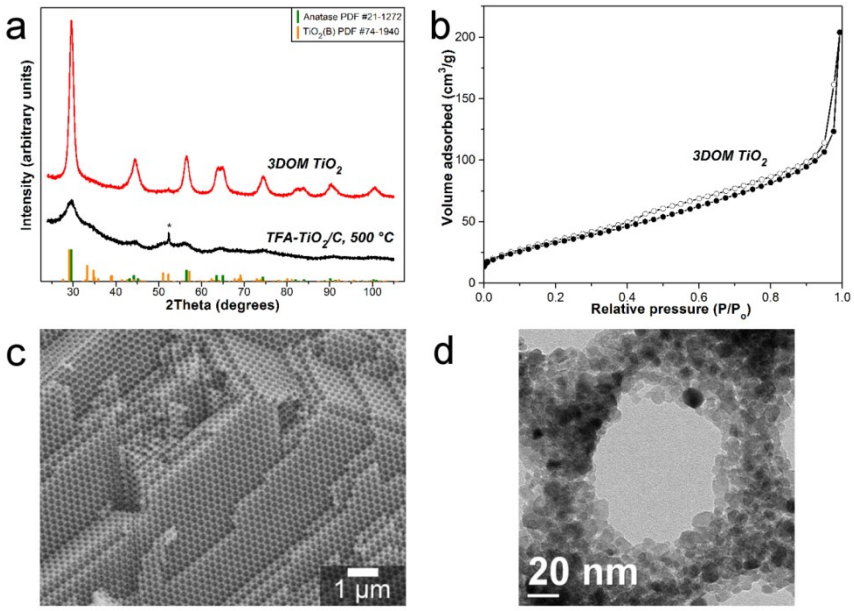

Figure 3.13 The characterization of the 3DOM TiO_2 produced from TFA-TiO_2/C pyrolyzed at 500 °C. (a) PXRD patterns of the original composite and 3DOM TiO_2. (b) Nitrogen sorption isotherm for the 3DOM TiO_2. (c) SEM and (d) TEM images show the 3DOM network that is made from fused TiO_2 crystallites. TEM image taken by Stephen Rudisill.

3.3.5 Electrochemical Characterization and Analysis

The TFA- and acac-TiO_2/C composites pyrolyzed at 800 °C and the 3DOM TiO_2 were selected for electrochemical tests and processed into electrodes for the half cells. The choice for the pyrolysis temperature was made by taking two factors into consideration. First, the PF resin needs to be brought to a sufficiently high temperature to adequately carbonize that particular component of the composite. As observed in Figure 3.3, the Raman *D*-band intensity increases at higher temperatures for the composites, indicating that the degree of graphitization increases. It is also known from DC conductivity testing using carbonized phenolic resin and carbonized 3DOM resorcinol-formaldehyde that temperatures in excess of 700 °C are needed to obtain

conductivities near 10 $S \cdot m^{-1}$.[63,64] However, the crystallite size increases substantially as the pyrolysis temperature increases (Table 3.1). As a compromise, 800 °C was chosen for a comparison between the capacity of TFA-TiO_2/C and acac-TiO_2/C at different rates.

Figure 3.14 a shows the results of electrochemical lithiation and delithiation cycles at different rates for the composites pyrolyzed at 800 °C and 3DOM TiO_2. At all rates, the capacity of acac-TiO_2/C is significantly higher than that of TFA-TiO_2/C. Clearly, the decreased TiO_2 crystallite size in acac-TiO_2/C can account for most of the capacity boost. Aside from crystal size, another contributing factor could be the location of the TiO_2 crystallites in the matrix. In TFA-TiO_2/C, crystallites are observed in sizable clusters on the surface. Electronic and ionic transport through the TiO_2 aggregates is then constrained to the contact points with the carbon matrix.[31] In contrast, acac-TiO_2/C contains many TiO_2 crystallites embedded in the carbon matrix, which might lead to better "wiring" for the TiO_2. The voltage profiles of the materials cycled in Figure 3.14 a are also shown in Figure 3.15. A characteristic plateau is observed in the profiles that results from the coexistence of a lithium-poor tetragonal and lithium-rich orthorhombic phase.[29] For the two composites, a greater contribution comes from a voltage range below the plateau region. This could be from small crystallites that can undergo primarily solid solution storage[22] or from intercalation into the carbon phase itself.

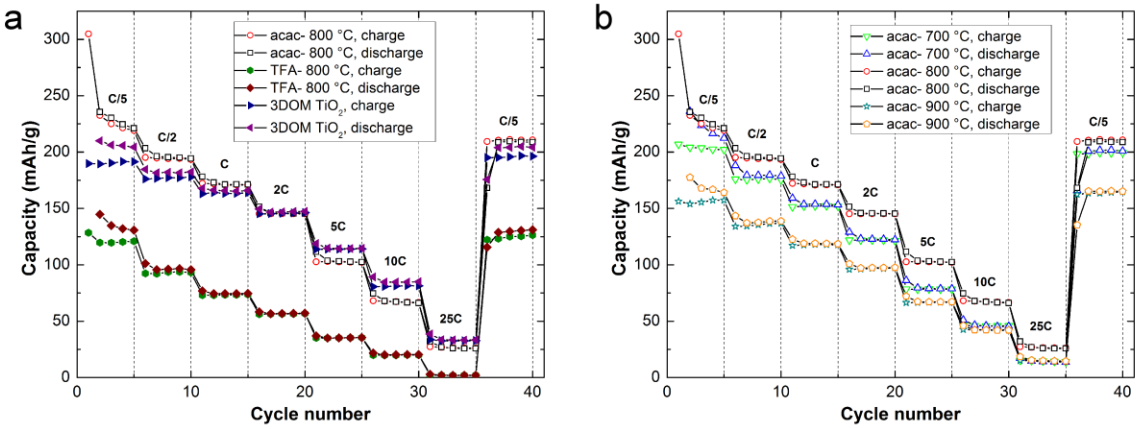

Figure 3.14 (a) rate performance data for various samples including, TFA-TiO_2/C pyrolyzed at 800 °C, the acac-TiO_2/C pyrolyzed at 800 °C, and 3DOM TiO_2. In (b), the rate performance data for the acac-TiO_2/C pyrolyzed at 700 °C, 800 °C, and 900 °C are shown. All specific capacities are plotted with respect to the mass of TiO_2 in the electrode.

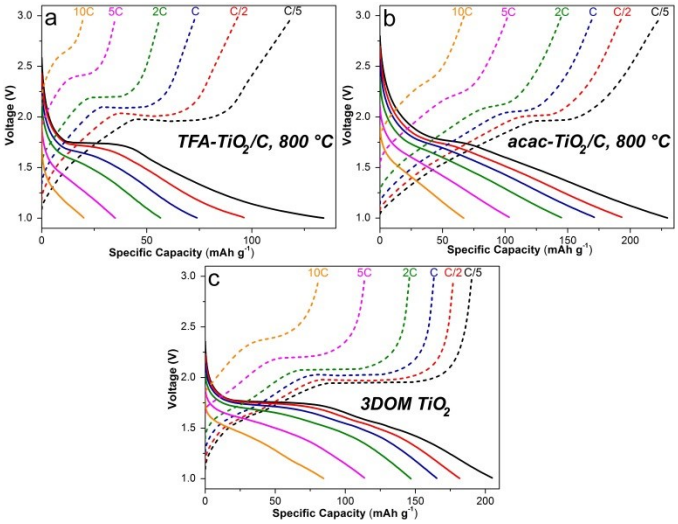

Figure 3.15 Voltage profiles for the three different 3DOM materials, the TFA-chelated composite pyrolyzed at 800 C (a), the acac-chelated composite pyrolyzed at 800 C (b), and the 3DOM TiO_2 (c). The expected plateau indicative of a two-phase intercalation is found in all the samples.

Perhaps the most surprising result in Figure 3.14 a is the excellent capacity of the 3DOM TiO_2 relative to the composites. At high rates, the capacity of 3DOM TiO_2 is greater than that of both composites. When the total mass of the electrode is taken into account (active and inactive components), 3DOM TiO_2 has the highest capacity, even at slow charge/discharge rates. The capacity boost in this compositionally simpler material may originate from several factors. First,

crystallite size in 3DOM TiO_2 is smaller (7.8 nm) than TiO_2 crystallites in the composites (11.4 nm for the TFA-TiO_2/C and 8.5 nm for the acac-TiO_2/C) due to the lower temperatures needed for processing. Second, burnout of the secondary carbon template produces numerous void spaces. These pores allow for penetration of the electrolyte throughout the structure, shortening diffusion lengths. With acac-TiO_2/C, numerous TiO_2 particles are buried in the carbon network, which restricts lithium ion transport. Finally, the only conductive additive in the 3DOM TiO_2 electrode is Super P carbon black. This carbon black has an electronic conductivity higher than the amorphous carbon present in the composites. Electronic transport through the amorphous carbon network may be a hindrance during rapid charging/discharging.

To further investigate the effects of the pyrolysis temperature, acac-TiO_2/C materials pyrolyzed at 700 °C, 800 °C, and 900 °C were processed into electrodes and tested. The results are shown in Figure 3.14 b. These pyrolysis temperatures are within the range in which carbon should be suitably conductive for cycling.[64] Pyrolysis at 800 °C results in the highest capacities at all rates, validating the choice of pyrolysis temperature made earlier. However, acac-TiO_2/C pyrolyzed at 700 °C exhibits similar capacities, especially upon the return to cycling at a rate of C/5. Overall, Figure 3.14 b demonstrates a major tradeoff that must be considered when using these composites as anode materials. While it is necessary to carbonize the PF resin at high temperatures, thereby increasing its conductivity, this necessity comes with a price. Crystallite size increases to the point at which diffusion through the large grains offsets any gains in carbon conductivity (i.e., acac-TiO_2/C at 900 °C).

The capacities of TFA-TiO_2/C, acac-TiO_2/C, and 3DOM TiO_2 after extended cycling at C/2 are shown in Figure 3.16. Coulombic efficiencies are good for the materials and exceed 99 % after ca. 20 cycles. The order of charge/discharge capacities for the materials is the same as that observed in Figure 3.14 a. The acac-TiO_2/C material has the highest capacities over all cycles, followed closely by 3DOM TiO_2, and TFA-TiO_2/C has the lowest capacity by a considerable margin. While acac-TiO_2/C has the best capacity, it suffers from a decay in capacity of roughly 25% when cycle 2 is compared to cycle 100. This decay in capacity has been observed in TiO_2/C composite systems;[69] thus, it is possible that the volume expansion and contraction during lithiation of TiO_2 (albeit small)[20] is damaging the contact between the carbon framework and the TiO_2. In contrast, the capacity of the 3DOM TiO_2 is fairly constant and the capacity of TFA-TiO_2/C increases. Any increases in capacity may be related to a more complete diffusion of electrolyte through a prepared electrode.[69]

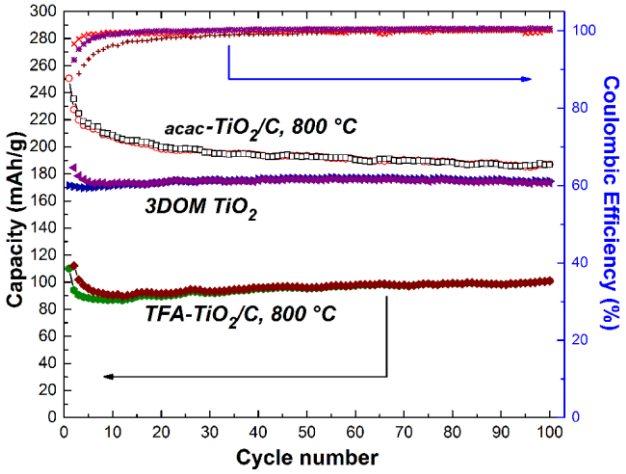

Figure 3.16 Cycle performance of TFA-TiO_2/C pyrolyzed at 800 °C, acac-TiO_2/C pyrolyzed at 800 °C, and 3DOM TiO_2 are shown over 100 cycles. Coulombic efficiencies are also plotted for the materials (brown pluses are from TFA-TiO_2/C, purple asterisks are from 3DOM TiO_2, and red "x"s are from acac-TiO_2/C). The rate was set at C/2.

Taking all of the cycling results into consideration, the materials attain capacities equal to or greater than that of the mass-produced, fumed TiO_2 Aeroxide® P25. Capacities for the nanocrystalline P25 are comparable to those for TFA-TiO_2/C (Figure 3.17); however, the carbon phase present in the composite appears to improve its performance at high rates. Both acac-TiO_2/C and 3DOM TiO_2 have significantly elevated capacities in comparison to P25 owing to reduced crystal sizes and interconnected porosity.

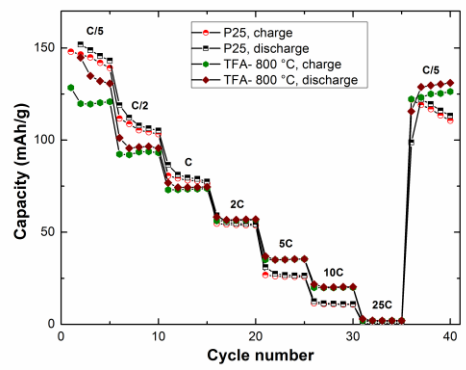

Figure 3.17 Comparison of the capacities of the TFA-TiO_2/C composite pyrolyzed at 800 °C and a similarly-made electrode that contains Aeroxide® P25. Capacities for both materials are similar, but the TFA-TiO_2/C has higher capacities at high rates and better capacity retention.

The two materials with the highest capacities, 3DOM TiO_2 and acac-TiO_2/C pyrolyzed at 800 °C, possess lithium-ion intercalation behavior that matches similar materials. With regard to the composite, for instance, equivalent capacities were reported for mesoporous, hollow TiO_2 spheres coated with amorphous carbon.[40] At a C/2 rate, some of these spheres composites have capacities of ~200 mAh/g, similar to that of acac-TiO_2/C (198 mAh/g). Additionally, acac-TiO_2/C compares favorably to ordered mesoporous TiO_2/C, when cycled at a rate of 2C (both have capacities of ~150 mAh/g).[54] It should also be noted that a larger voltage window was used for the mesoporous TiO_2/C (0–3 V vs. Li^+/Li). 3DOM TiO_2 also has capacities that exceed those of many other nanostructured TiO_2 materials. For instance, Jiang et al. synthesized 3DOM TiO_2 without a secondary template and achieved a capacity of 125 mAh/g at ~2 C.[70] Even with a lower wt% of carbon black in the electrode (10 wt% versus 15 wt%), the 3DOM TiO_2 prepared in this report has a capacity of 145 mAh/g. However, when more conductive carbon materials are used, such as graphene or carbon fibers, greater capacities are attainable at high rates (i.e. <100 mAh/g at 30 C).[71,72] The 3DOM TiO_2 also has capacities that match those of several different mesoporous TiO_2 materials at a rate of 1 C. Both mesoporous anatase[69,73] and rutile[74] have been produced that have capacities slightly lower than the ~160 mAh/g achieved by 3DOM TiO_2. When TiO_2 crystallite size is decreased further than what is observed in 3DOM TiO_2 or porous TiO_2-B is used as an anode, it is possible to achieve even higher rates.[22,75,76] Still, it appears that the small crystallites and disordered pores that are present in the 3DOM TiO_2 structure are sufficient to allow for shortened diffusion lengths. This structure provides good performance at moderate cycling rates.

To further study the effect of the pyrolysis temperature and chelating agent on the electrochemical properties and kinetic processes of the electrode reaction, electrochemical impedance spectroscopy (EIS) was used, both before and after 10 cycles at C/2. The impedance spectra (Figure 3.18) show a depressed semicircle in the high- to medium-frequency regions and a linear section in the low-frequency region, as would be expected for a lithium insertion/de-insertion mechanism.[77] The spectra were fitted to the equivalent circuit shown in Figure 3.18 c (see Table 3.3 for the calculated parameters). This circuit is comprised of a series resistor and capacitor (R_s and C_s, respectively), two elements each comprised of a parallel capacitor and resistor (R_1, R_2, C_1, and C_2), and a modified Randles cell (comprised of R_3, C_3, and Warburg impedance): a model similar to those used for other TiO_2-based anodes.[77,78] Moving across the circuit, the series resistor models the electrical resistance of the cell casing, testing apparatus, electrodes, and electrolyte, while the series capacitor models reversible ion sorption on exposed,

non-electrode surfaces inside the cell. A series capacitor is not needed in all cases, specifically TFA-TiO_2/C and acac-TiO_2/C samples pyrolyzed at 800 °C. Both of the next capacitor/resistor elements model surfaces at the electrode within the cell. R_1 and C_1 model the SEI layer, electrode roughness, and ion transport across the surface, while R_2 and C_2 model surfaces that are relatively inaccessible to the electrolyte and have a high resistance (i.e. TiO_2 embedded in the carbon matrix, TiO_2 that suffers from poor electrolyte wetting).[77,79] In all samples except for the acac-TiO_2/C pyrolyzed at 700 °C, all of the resistances dropped, consistent with improved electrolyte wetting allowing for improved ionic conductivity. The anomaly may be a result of an SEI layer blocking access to the small, embedded crystallites of TiO_2. Overall, the sample with the best performance, acac-TiO_2/C pyrolyzed at 800 °C, has the lowest resistances.

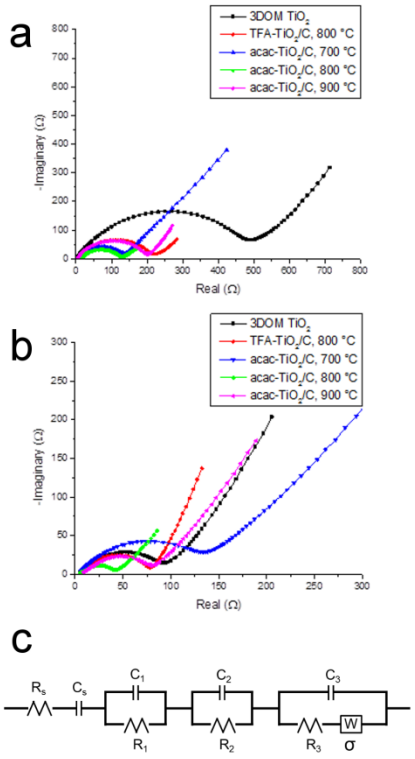

Figure 3.18 Nyquist plots of (a) as-made coin cells and (b) cells after 10 cycles at C/2. The equivalent circuit used to model the impedance spectra is shown in (c). Spectra fitted by Benjamin Wilson.

Table 3.3 Relevant parameters extracted from the electrochemical impedance spectra for the as-made samples and the samples cycled 10 times at C/2. Parameters calculated by Benjamin Wilson.

sample	R_s (Ω)	R_1 (Ω)	R_2 (Ω)	R_3 (Ω)	C_s (mF)	C_1 (μF)	C_2 (μF)	C_3 (μF)	Σ
As-made 3DOM TiO_2	7.5	64	210	184	60	3.3	8.4	36	140
Cycled 3DOM TiO_2	6.6	12	35	33	37	2.8	14	56	65
As-made TFA-TiO_2/C, 800 °C	8.1	51	110	43	n/a	3.5	12	190	36
Cycled TFA-TiO_2/C, 800 °C	6.1	8.1	25	33	39	4.9	19	5.4	31
As-made acac-TiO_2/C, 700 °C	6.7	9.2	30	71	36	16	2.2	7.2	150
Cycled acac-TiO_2/C, 700 °C	9.6	26	31	58	23	12	3.0	16	190
As-made acac-TiO_2/C, 800 °C	12	13	34	61	n/a	14	3.4	16	21
Cycled acac-TiO_2/C, 800 °C	6	5.5	14	14	34	4.7	28	125	24
As-made acac-TiO_2/C, 900 °C	9.4	35	94	54	92	2.7	6.7	56	44
Cycled acac-TiO_2/C, 900 °C	7.8	10	27	29	53	2.8	11	41	63

Looking beyond the resistances, it is seen that the Warburg coefficient (σ) decreases after electrochemical cycling of the samples made with TFA, indicating an increase in the Li^+ diffusion coefficient.[80] In contrast, the samples made with acac show an increase in σ, indicating a decrease in the Li^+ diffusion coefficient. This is consistent with the overall trends observed in Figure 3.16, where TFA-TiO_2/C and 3DOM TiO_2 show an increase in capacity after repeated cycling, while the capacity in the acac-TiO_2/C decays. Interestingly, the values for σ in the TFA-TiO_2/C compare favorably to acac-TiO_2/C, despite its poor performance during cycling. The lower-than-expected values for σ in TFA-TiO_2/C can be ascribed to the higher accessible TiO_2 surface area for this sample, since the grains are, in general, on the surface of the 3DOM network. However, while the Li^+ diffusion rate may be higher, the larger TiO_2 crystals found in that sample would limit the extent of discharge, leading to the overall lower capacity. This also explains why σ is lower for the acac-TiO_2/C pyrolyzed at 900 °C (a sample that has many crystallites protruding out of the carbon), when compared to the sample pyrolyzed at 700 °C.

3.4 Conclusions

Through the analysis of two types of 3DOM/m TiO_2/C materials, this chapter investigates several variables that control the structure of these porous composites. By influencing the structural features, lithium ion insertion properties for the porous anodes made from TiO_2/C were optimized. The chelating agent used to stabilize the titanium alkoxide in the precursor has a great impact on the resulting structure of the composite. The relatively hydrophobic trifluoroacetic acid causes the formation of a titanium complex that segregates to the surface of the PMMA colloidal crystal template. As a consequence, when the pyrolysis temperature is altered, TFA-TiO_2/C experiences severe TiO_2 crystallite growth from the clustering of TiO_2 on the surface of the 3DOM network. In contrast, the hydrophilic complexes produced using 2,4-pentanedione as a chelating agent allow for distribution of TiO_2 throughout the structure. These crystallites remain within the carbon phase, restricting overall crystallite growth. Ultimately, this results in a much higher capacity for reversible Li^+ intercalation than in the case of TFA-TiO_2/C. After pyrolysis at 800 °C, the acac-TiO_2/C displays excellent capacities (over 180 mAh/g at C/2), low resistances in the cell, and low Warberg impedance. However, burial of the TiO_2 grains in the carbon network may impede performance in certain cases. Removing the partially carbonized phase for TFA-TiO_2/C pyrolyzed at 500 °C results in the formation of 3DOM TiO_2 with additional porosity between TiO_2 crystallites. Since this material has an open structure with a fairly small crystallite size (< 8 nm) that reduces overall diffusion lengths, its capacity (<160 mAh/g) at moderate

lithiation and delithiation rates is comparable to that of the acac-TiO_2/C pyrolyzed at 800 °C. It can be envisioned that similar approaches to adjusting the chelating agent, pyrolysis temperature, and the presence of the carbon phase will allow for better structural control over other 3DOM/m composites. Improved performance for these materials in a wide range of applications (not just battery electrodes) could then be attained.

References

(1) Tachikawa, T.; Fujitsuka, M.; Majima, T. Mechanistic Insight into the TiO_2 Photocatalytic Reactions: Design of New Photocatalysts. *J. Phys. Chem. C* **2007**, *111*, 5259-5275.

(2) Chen, X.; Shen, S.; Guo, L.; Mao, S. S. Semiconductor-based Photocatalytic Hydrogen Generation. *Chem. Rev.* **2010**, *110*, 6503-6570.

(3) Kadoshima, M.; Hiratani, M.; Shimamoto, Y.; Torii, K.; Miki, H.; Kimura, S.; Nabatame, T. Rutile-type TiO_2 Thin Film for High-*k* Gate Insulator. *Thin Soild Films* **2003**, *424*, 224-228.

(4) Lee, M.-J.; Seo, S.; Kim, D.-C.; Ahn, S.-E.; Seo, D. H.; Yoo, I.-K.; Baek, I.-G.; Kim, D.-S.; Byun, I.-S.; Kim, S.-H.; Hwang, I.-R.; Kim, J.-S.; Jeon, S.-H.; Park, B. H. A Low-Temperature-Grown Oxide Diode as a New Switch Element for High-Density, Nonvolatile Memories. *Adv. Mater.* **2007**, *19*, 73-76.

(5) Hagfeldt, A.; Boschloo, G.; Sun, L.; Kloo, L.; Pettersson, H. Dye-Sensitized Solar Cells. *Chem. Rev.* **2010**, *110*, 6595-6663.

(6) Jung, H. S.; Lee, J.-K. Dye Sensitized Solar Cells for Economically Viable Photovoltaic System. *J. Phys. Chem. Lett.* **2013**, *4*, 1682-1693.

(7) Auer, G.; Griebler, W.-D.; Jahn, B. White Pigments. In *Industrial Inorganic Pigments*; 3rd ed.; Buxbaum, G., Pfaff, G., Eds.; Wiley-VCH Verlag GmbH & Co. KGaA: Weinheim, Germany, 2005.

(8) Comotti, M.; Li, W.-C.; Spliethoff, B.; Schüth, F. Support Effect in High Activity Gold Catalysts for CO Oxidation. *J. Am. Chem. Soc.* **2006**, *128*, 917-924.

(9) Cao, A.; Lu, R.; Veser, G. Stabilizing Metal Nanoparticles for Heterogeneous Catalysis. *Phys. Chem. Chem. Phys.* **2010**, *12*, 13499-13510.

(10) Fröschl, T.; Hörmann, U.; Kubiak, P.; Kučerová, G.; Pfanzelt, M.; Weiss, C. K.; Behm, R. J.; Hüsing, N.; Kaiser, U.; Landfester, K.; Wohlfahrt-Mehrens, M. High Surface Area Crystalline Titanium Dioxide: Potential and Limits in Electrochemical Energy Storage and Catalysis. *Chem. Soc. Rev.* **2012**, *41*, 5313-5360.

(11) Huang, S. Y.; Kavan, L.; Exnar, I.; Grätzel, M. Rocking Chair Lithium Battery Based on Nanocrystalline TiO_2 (Anatase). *J. Electrochem. Soc.* **1995**, *142*, L142-L144.

(12) Kavan, L.; Rathouský, J.; Grätzel, M.; Shklover, V.; Zukal, A. Surfactant-Templated TiO_2 (Anatase): Characteristic Features of Lithium Insertion Electrochemistry in Organized Nanostructures. *J. Phys. Chem. B* **2000**, *104*, 12012-12020.

(13) Kavan, L.; Rathouský, J.; Grätzel, M.; Shklover, V.; Zukal, A. Mesoporous Thin Film TiO_2 Electrodes. *Microporous Mesoporous Mater.* **2001**, *44-45*, 653-659.

(14) Leroux, F.; Dewar, P. J.; Intissar, M.; Ouvrard, G.; Nazar, L. F. Study of the Formation of Mesoporous Titania *via* a Template Approach and of Subsequent Li Insertion. *J. Mater. Chem.* **2002**, *12*, 3245-3253.

(15) Zampardi, G.; Ventosa, E.; La Mantia, F.; Schuhmann, W. *In Situ* Visualization of Li-Ion Intercalation and Formation of the Solid Electrolyte Interphase on TiO_2 Based Paste Electrodes Using Scanning Electrochemical Microscopy. *Chem. Commun.* **2013**, *49*, 9347-9349.

(16) Jacoby, M. Assessing the Safety of Lithium-Ion Batteries. *Chem. Eng. News* **2013**, *91*, 33-37.

(17) Armstrong, A. R.; Armstrong, G.; Canales, J.; García, R.; Bruce, P. G. Lithium-Ion Intercalation into TiO_2-B Nanowires. *Adv. Mater.* **2005**, *17*, 862-865.

(18) Hu, Y.-S.; Kienle, L.; Guo, Y.-G.; Maier, J. High Lithium Electroactivity of Nanometer-Sized Rutile TiO_2. *Adv. Mater.* **2006**, *18*, 1421-1426.

(19) Wang, K.; Wei, M.; Morris, M. A.; Zhou, H.; Holmes, J. D. Mesoporous Titania Nanotubes: Their Preparation and Application as Electrode Materials for Rechargeable Lithium Batteries. *Adv. Mater.* **2007**, *19*, 3016-3020.

(20) Yang, Z.; Choi, D.; Kerisit, S.; Rosso, K. M.; Wang, D.; Zhang, J.; Graff, G.; Liu, J. Nanostructures and Lithium Electrochemical Reactivity of Lithium Titanites and Titanium Oxides: A Review. *J. Power Sources* **2009**, *192*, 588-598.

(21) Ren, Y.; Hardwick, L. J.; Bruce, P. G. Lithium Intercalation into Mesoporous Anatase with an Ordered 3D Pore Structure. *Angew. Chem. Int. Ed.* **2010**, *49*, 2570-2574.

(22) Shin, J.-Y.; Samuelis, D.; Maier, J. Sustained Lithium-Storage Performance of Hierarchical, Nanoporous Anatase TiO_2 at High Rates: Emphasis on Interfacial Storage Phenomena. *Adv. Funct. Mater.* **2011**, *21*, 3464-3472.

(23) Saravanan, K.; Ananthanarayanan, K.; Balava, P. Mesoporous TiO_2 with High Packing Density for Superior Lithium Storage. *Energy Environ. Sci.* **2010**, *3*, 939-948.

(24) Szeifert, J. M.; Feckl, J. M.; Fattakhova-Rohlfing, D.; Liu, Y.; Kalousek, V.; Rathouský, J.; Bein, T. Ultrasmall Titania Nanocrystals and Their Direct Assembly into Mesoporous Structures Showing Fast Lithium Insertion. *J. Am. Chem. Soc.* **2010**, *132*, 12605-12611.

(25) Ren, Y.; Liu, Z.; Pourpoint, F.; Armstrong, A. R.; Grey, C. P.; Bruce, P. G. Nanoparticulate TiO_2(B): An Anode for Lithium-Ion Batteries. *Angew. Chem. Int. Ed.* **2012**, *51*, 2164-2167.

(26) Chen, S. C.; Tan, Y. L.; Li, C. M.; Cheah, Y. L.; Luan, D.; Madhavi, S.; Boey, F. Y. C.; Archer, L. A.; Lou, X. W. Constructing Hierarchical Spheres from Large Ultrathin Anatase TiO_2 Nanosheets with Nearly 100% Exposed (001) Facets for Fast Reversible Lithium Storage. *J. Am. Chem. Soc.* **2010**, *132*, 6124-6130.

(27) Zhao, B.; Shao, Z. From Paper to Paper-like Hierarchical Anatase TiO_2 Film Electrode for High-Performance Lithium-Ion Batteries. *J. Phys. Chem. C* **2012**, *116*, 17400-17447.

(28) Wang, J.; Polleux, J.; Lim, J.; Dunn, B. Pseudocapacitive Contributions to Electrochemical Energy Storage in TiO_2 (Anatase) Nanoparticles. *J. Phys. Chem. C* **2007**, *111*, 14925-14931.

(29) Wagemaker, M.; Mulder, F. M. Properties and Promises of Nanosized Insertion Materials for Li-Ion Batteries. *Acc. Chem. Rev.* **2012**, *46*, 1206-1215.

(30) Bi, Z.; Paranthaman, M. P.; Guo, B.; Unocic, R.; Meyer, H.; Bridges, C. A.; Sun, X.-G.; Dai, S. High Performance Cr, N - Codoped Mesoporous TiO_2 Microsphere Anodes for Lithium-ion Rechargeable Batteries. *J. Mater. Chem. A* **2014,** *2*, 1818-1824.

(31) Li, H.; Zhou, H. Enhancing the Performances of Li-Ion Batteries by Carbon-Coating: Present and Future. *Chem. Commun.* **2012**, *48*, 1201-1217.

(32) Guo, Y.-G.; Hu, Y.-S.; Sigle, W.; Maier, J. Superior Electrode Performance of Nanostructured Mesoporous TiO_2 (Anatase) through Efficient Hierarchical Mixed Conducting Networks. *Adv. Mater.* **2007**, *19*, 2087-2091.

(33) Ding, S.; Chen, J. S.; Lou, X. W. One-Dimensional Hierarchical Structures Composed of Novel Metal Oxide Nanosheets on a Carbon Nanotube Backbone and Their Lithium-Storage Properties. *Adv. Funct. Mater.* **2011**, *21*, 4120-4125.

(34) Chen, J. S.; Wang, Z.; Dong, X. C.; Chen, P.; Lou, X. W. Graphene-Wrapped TiO_2 Hollow Structures with Enhanced Lithium Storage Capabilities. *Nanoscale* **2011**, *3*, 2158-2161.

(35) Yu, S. X.; Yang, L. W.; Tian, Y.; Yang, P.; Jiang, F.; Hu, S. W.; Wei, X. L.; Zhong, J. X. Mesoporous Anatase TiO_2 Submicrospheres Embedded in Self-Assembled Three-Dimensional Reduced Graphene Oxide Networks for Enhanced Lithium Storage. *J. Mater. Chem. A* **2013**, *1*, 12750-12758.

(36) Yang, S.; Fang, X.; Müllen, K. Sandwich-Like, Graphene-Based Titania Nanosheets with High Surface Area for Fast Lithium Storage. *Adv. Mater.* **2011**, *23*, 3575-3579.

(37) Liu, R.; Ren, Y.; Shi, Y.; Zhang, F.; Zhang, L.; Tu, B.; Zhao, D. Controlled Synthesis of Ordered Mesoporous C-TiO_2 Nanocomposites with Crystalline Titania Frameworks from Organic-Inorganic-Amphiphilic Coassembly. *Chem. Mater.* **2008**, *20*, 1140-1146.

(38) Das, S. K.; Bhattacharyya, A. J. Influence of Mesoporosity and Carbon Electronic Wiring on Electrochemical Performance of Anatase Titania. *J. Electrochem. Soc.* **2011**, *158*, A705-A710.

(39) Liu, D.; Lei, J.-H.; Guo, L.-P.; Deng, K.-J. A Nanoparticle Assembly Method for the Production of Crystalline Ordered Mesoporous Titanium Oxide/Carbon Composites. *Microporous Mesoporous Mater.* **2011**, *139*, 87-93.

(40) Wang, W.; Sa, Q.; Chen, J. S.; Wang, Y.; Jung, H.; Yin, Y. Porous TiO_2/C Nanocomposite Shells As a High-Performance Anode Material for Lithium-Ion Batteries. *ACS Appl. Mater. Interfaces* **2013**, *5*, 6478-6483.

(41) Petkovich, N. D.; Stein, A. Controlling Macro- and Mesostructures with Hierarchical Porosity Through Combined Hard and Soft Templating. *Chem. Soc. Rev.* **2013**, *42*, 3721-3739.

(42) Josephson, D. P.; Popczun, E. J.; Stein, A. Effects of Integrated Carbon as a Light Absorber on the Coloration of Photonic Crystal-Based Pigments. *J. Phys. Chem. C* **2013**, *117*, 13585-13592.

(43) Meng, Y.; Gu, D.; Zhang, F.; Shi, Y.; Yang, H.; Li, Z.; Yu, C.; Tu, B.; Zhao, D. Ordered Mesoporous Polymers and Homologous Carbon Frameworks Amphiphilic Surfactant Templating and Direct Transformation. *Angew. Chem. Int. Ed.* **2005**, *44*, 7053-7059.

(44) Boettcher, S. W.; Bartl, M. H.; Hu, J. G.; Stucky, G. D. Structural Analysis of Hybrid Titania-Based Mesostructured Composites. *J. Am. Chem. Soc.* **2005**, *127*, 9721-9730.

(45) Galusha, J. W.; Tsung, C. K.; Stucky, G. D.; Bartl, M. H. Optimizing Sol-Gel Infiltration and Processing Methods for the Fabrication of High-Quality Planar Titania Inverse Opals. *Chem. Mater.* **2008**, *20*, 4925-4930.

(46) Schubert, U. Chemical Modification of Titanium Alkoxides for Sol-Gel Processing. *J. Mater. Chem.* **2005**, *15*, 3701-3715.

(47) Fattakhova-Rohlfing, D.; Wark, M.; Brezesinski, T.; Smarsly, B. M.; Rathouský, J. Highly Organized Mesoporous TiO_2 Films with Controlled Crystallinity: A Li-Insertion Study. *Adv. Funct. Mater.* **2007**, *17*, 123-132.

(48) Procházka, J.; Kavan, L.; Shklover, V.; Zukalová, M.; Frank, O.; Kalbáč, M.; Zukal, A.; Pelouchová, H.; Janda, P.; Mocek, K.; Klementová, M.; Carbon, D. Multilayer Films from Templated TiO_2 and Structural Changes during their Thermal Treatment. *Chem. Mater.* **2008**, *20*, 2985-2993.

(49) Chen, X.; Mao, S. S. Titanium Dioxide Nanomaterials: Synthesis, Properties, Modifications, and Applications. *Chem. Rev.* **2007**, *107*, 2891-2959.

(50) Isley, S. L.; Penn, R. L. Titanium Dioxide Nanoparticles: Effect of Sol−Gel pH on Phase Composition, Particle Size, and Particle Growth Mechanism. **2008**, *112*, 4469-4474.

(51) Zhang, H.; Banfield, J. F. Thermodynamic Analysis of Phase Stability of Nanocrystalline Titania. *J. Mater. Chem.* **1998**, *8*, 2073-2076.

(52) Ranade, M. R.; Navrotsky, A.; Zhang, H. Z.; Banfield, J. F.; Elder, S. H.; Zaban, A.; Borse, P. H.; Kulkarni, S. K.; Doran, G. S.; Whitfield, H. J. Energetics of Nanocrystalline TiO_2. *Proc. Natl. Acad. Sci. U.S.A.* **2002**, *99*, 6476-6481.

(53) Huang, C.-H.; Gu, D.; Zhao, D.; Doong, R.-A. Direct Synthesis of Controllable Microstructures of Thermally Stable and Ordered Mesoporous Crystalline Titanium Oxides and Carbide/Carbon Composites. *Chem. Mater.* **2010**, *22*, 1760-1767.

(54) Cheng, P.-Y.; Huang, C.-H.; Doong, R.-A. Ordered Mesoporous Carbon–TiO_2 Materials for Improved Electrochemical Performance of Lithium Ion Battery *Carbon* **2012**, *50*, 4259-4268.

(55) Zhang, J.; Li, M.; Feng, Z.; Chen, J.; Li, C. UV Raman Spectroscopic Study on TiO_2. I. Phase Transformation at the Surface and in the Bulk. *J. Phys. Chem. B* **2006**, *110*, 927-935.

(56) Hanaor, D. A. H.; Sorrell, C. C. Review of the Anatase to Rutile Phase Transformation. *J. Mater. Sci.* **2011**, *46*, 855-874.

(57) Yu, T.; Deng, Y. H.; Wang, L.; Liu, R. L.; Zhang, L. J.; Zhao, D. Ordered Mesoporous Nanocrystalline Titanium-Carbide/Carbon Composites from In Situ Carbothermal Reduction. *Adv. Mater.* **2007**, *19*, 2301-2306.

(58) Swamy, V.; Kuznetsov, A.; Dubrovinsky, L. S.; McMillan, P. F.; Prakapenka, V. B.; Shen, G.; Muddle, B. C. Size-Dependent Pressure-Induced Amorphization in Nanoscale TiO_2. *Phys. Rev. Lett.* **2006**, *96*, 135702(1-4).

(59) Grey, I. E.; Li, C.; Madsen, I. C.; Braunshausen, G. TiO_2-II. Ambient Pressure Preparation and Structure Refinement. *Mater. Res. Bull.* **1988**, *23*, 743-753.

(60) Balachandran, U.; Eror, N. G. Raman Spectra of Titanium Dioxide. *J. Solid State Chem.* **1982**, *42*, 276-282.

(61) Zhang, W. F.; He, Y. L.; Zhang, M. S.; Yin, Z.; Chen, Q. Raman Scattering Study on Anatase TiO_2 Nanocrystals. *J. Phys. D: Appl. Phys.* **2000**, *33*, 912-916.

(62) Ferrari, A. C.; Robertson, J. Interpretation of Raman Spectra of Disordered and Amorphous Carbon. *Phys. Rev. B* **2000**, *61*, 14095-14107.

(63) Bücker, W. Preparation and DC Conductivity of an Amorphous Organic Semiconducting System. *J. Non-Cryst. Solids* **1973**, *12*, 115-128.

(64) Fierke, M. A. The Utilization of Templated Porous Electrodes in Electrochemical Applications. Ph. D Thesis, University of Minnesota- Twin Cities, 2013.

(65) Ko, T.-H.; Kuo, W.-S.; Chang, Y.-H. Raman Study of the Microstructure Changes of Phenolic Resin During Pyrolysis. *Polym. Composites* **2000**, *21*, 745-750.

(66) Meng, Y.; Gu, D.; Zhang, F.; Shi, Y.; Cheng, L.; Feng, D.; Wu, Z.; Chen, Z.; Wan, Y.; Stein, A.; Zhao, D. A Family of Highly Ordered Mesoporous Polymer Resin Carbon Structures Organic-Organic Self-Assembly. *Chem. Mater.* **2006**, *18*, 4447-4464.

(67) Errington, R. J.; Ridland, J.; Clegg, W.; Coxall, R. A.; Sherwood, J. M. β-Diketoneate Derivatives of Titanium Alkoxides: X-Ray Crystal Structures and Solution Dynamics of the Binuclear Complexes $[\{Ti(OR)_3(dik)\}_2]$. *Polyhedron* **1998**, *17*, 659-674.

(68) Vu, A.; Stein, A. Multiconstituent Synthesis of $LiFePO_4$/C Composites wth Hierarchical Porosity as Cathode Materials for Lithium Ion Batteries. *Chem. Mater.* **2011**, *23*, 3237-3245.

(69) Zeng, L.; Zheng, C.; Xia, L.; Wang, Y.; Wei, M. Ordered Mesoporous TiO_2-C Nanocomposites as an Anode Material for Long-Term Performance Lithium-Ion Batteries. *J. Mater. Chem. A* **2013**, *1*, 4293-4299.

(70) Jiang, H.; Yang, X.; Chen, C.; Zhu, Y.; Li, C. Facile and Controllable Fabrication of Three-Dimensionally Quasi-Ordered Macroporous TiO_2 for High Performace Lithium-Ion Battery Applications. *New J. Chem.* **2013**, *37*, 1578-1583.

(71) Xin, X.; Zhou, X.; Wu, J.; Yao, X.; Liu, Z. Scalable Synthesis of TiO_2/Graphene Nanostructured Composite with High-Rate Performance for Lithium Ion Batteries. *ACS Nano* **2012**, *6*, 11035-11043.

(72) Zhao, B.; Jiang, S.; Su, C.; Cai, R.; Ran, R.; Tadé, M. O.; Shao, Z. A 3D Porous Arcitecture Composed of TiO_2 Nanotubes Connected with a Carbon Nanofiber Matrix for Fast Energy Storage. *J. Mater. Chem. A* **2013**, *1*, 12310-12320.

(73) Kubiak, P.; Geserick, J.; Hüsing, N.; Wohlfahrt-Mehrens, M. Electrochemical Performance of Mesoporous TiO_2 Anatase. *J. Power Sources* **2008**, *175*, 510-516.

(74) Wang, D.; Choi, D.; Yang, Z.; Viswanathan, V. V.; Nie, Z.; Wang, C.; Song, Y.; Zhang, J.-G.; Liu, J. Synthesis and Li-Ion Insertion Properties of Highly Crystalline Mesoporous Rutile TiO_2. *Chem. Mater.* **2008**, *20*, 3435-3442.

(75) Liu, H.; Bi, Z.; Sun, X.-G.; Unocic, R. R.; Paranthaman, M. P.; Dai, S.; Brown, G. M. Mesoporous TiO_2-B Microspheres with Superior Rate Performance for Lithium Ion Batteries. *Adv. Mater.* **2011**, *23*, 3450-3454.

(76) Myung, S.-T.; Takahashi, N.; Komaba, S.; Yoon, C. S.; Sun, Y.-K.; Amine, K.; Yashiro, H. Nanostructured TiO_2 and Its Application in Lithium-Ion Storage. *Adv. Funct. Mater.* **2011**, *21*, 3231-3241.

(77) Wang, J.; Zhou, Y.; Hu, Y.; O'Hayre, R.; Shao, Z. Facile Synthesis of Nanocrystalline TiO_2 Mesoporous Microspheres for Lithium-Ion Batteries. *J. Phys. Chem C* **2011**, *115*, 2529-2536.

(78) Yoon, S.; Manthiram, A. Hollow Core-Shell Mesoporous TiO_2 Spheres for Lithium Ion Storage. *J. Phys. Chem. C* **2011**, *115*, 9410-9416.

(79) Zhou, Y.-K.; Cao, L.; Zhang, F.-B.; He, B.-L.; Li, H.-L. Lithium Insertion into TiO_2 Nanotube Prepared by the Hydrothermal Process. *J. Electrochem. Soc.* **2003**, *150*, A1246-A1249.

(80) Ho, C.; Raistrick, I. D.; Huggins, R. A. Application of A-C Techniques to the Study of Lithium Diffusion in Tungsten Trioxide Thin Films. *J. Electrochem. Soc.* **1980**, *127*, 343-350.

Chapter 4

Addition of Extra Carbon and Dopant Cations to 3DOM TiO_2/C Materials: Impacts on Structural Features and Lithium Ion Capacity

4.1 Introduction and Motivation

It is well-understood that the addition of dopants into TiO_2 has profound effects on the properties of the resultant material. Many different elements can be incorporated into the various polymorphs of TiO_2, albeit to varying extents due to differences in ionic radius and preferred coordination environment.[1,2] When solid solutions of TiO_2 and dopants can be synthesized, it is possible to tailor the structure and a host of properties of these materials. While this is by no means an exhaustive list, researchers have been able to change (relative to undoped TiO_2): the crystallite size,[3] the temperature of polymorphic transformations,[4] the electronic conductivity,[5,6] the ionic conductivity,[7] the electronic band gap,[8,9] the optical absorption spectra,[10,11] the ability of the lattice to gain/lose oxygen,[12] and the reactivity of surface sites.[13,14] The impact on the structure/properties of the doped material is, not surprisingly, highly dependent on the heteroatom incorporated into the crystal lattice and its concentration.[15] Considerable research activity in doping TiO_2 continues, in order to optimize the properties of the material for a host of applications. While it would be beyond the scope of this chapter to provide a comprehensive review of the many facets of doping TiO_2 with heteroatoms, an effort is instead made to address salient points required for understanding results presented in this chapter. The main questions are how doping can impact TiO_2 crystallite size/polymorph, and how doping impacts lithium ion insertion and extraction into TiO_2.

As research into ceramics has progressed, methods to control the structure of the crystals that comprise these materials have received considerable research attention. With the increasing technological relevance of nanocrystalline and nanostructured ceramics, one crucial aspect of structural control for these materials is to ensure that the constituent crystallites retain small dimensions.[16,17] For nanocrystalline ceramics, including nanocrystalline TiO_2, the same strategies used to regulate crystal growth in coarser grained materials are employed.[2] Since the growth of crystallites is controlled by the movement of grain boundaries, it is critical to restrict the movement of these planar defects.[18,19] This task is often a bit more complicated in nanocrystalline ceramics because of a high density of grain boundaries. Doping offers a means to suppress the movement of grain boundaries through a variety of effects.[19,20] Most notably, dopants tend to either segregate towards or away from grain boundaries.[18] The diffusion of a dopant results in a concentration gradient that extends normal to the plane of the grain boundary. This imposes a kinetic limitation on grain boundary movement that is known as solute drag.[19,21] With doped TiO_2, this phenomenon has been observed for several different cationic dopants, such as calcium,[22] niobium,[23] zirconium,[23] lanthanum,[24] and iron.[25] In other cases, the dopant can alter the

concentration, identity, or diffusion rate of a slowly-diffusing defect that controls the movement of the grain boundary (essentially the rate-limiting defect).[18] Ideally, if diffusion is slowed by these changes, crystal growth can also be suppressed. Beyond changes to the kinetics of crystallite growth, the presence of a dopant can alter the energetics of a grain boundary.[19] A large enough change to the thermodynamics of the grain boundary can lead to cessation of grain boundary movement and the formation of stable grain boundary interfaces. Finally, the dopant can even segregate as a secondary phase that can pin grain boundaries in place.[21] In TiO_2, addition of more than 0.1 mol% of yttrium results in the precipitation of $Y_2Ti_2O_7$ at grain boundaries, alongside the enrichment of the grain boundaries with yttrium.[26]

One brief aside should also be made concerning a method to control crystallite growth. For most of the materials discussed in this chapter, a secondary phase of carbon is present alongside the oxide phase. This secondary phase is capable of isolating crystals from one another. Since the number of oxide crystal-to-oxide crystal contacts is very limited, sintering and crystal growth is retarded.[27] Chapter 3 explores this point for the TFA- and acac-TiO_2/C composites, and this method to restrict crystal growth is revisited in the current chapter. One other important feature of the secondary phase is that it releases gases during pyrolysis that can act as reducing agents. Though it was not mentioned explicitly in the paragraph above, the gaseous atmosphere surrounding a ceramic material undergoing thermal treatment has a substantial impact on its sintering and crystal growth.[27] After all, the concentration and identity of defects in a ceramic material can be changed by the partial pressures of reactive gases (such as O_2, CO, H_2, etc.) in the atmosphere.[28] Several materials studied in this chapter are impacted by the atmosphere, most noticeably changing the relative amounts of the anatase and rutile polymorphs present in the oxide phase.

Establishing ways to control the transformation of one polymorph to another in ceramic materials is frequently crucial for obtaining desirable material properties. While the focus in this introduction is on the use of dopants, other means are available to either induce or prevent changes in a crystalline polymorph. For instance, if crystallites are confined in a secondary phase, transformations that require a critical crystallite size (i.e. transformations that are surface energy dependent) can be suppressed.[29] With TiO_2, the anatase-to-rutile phase transition is commonly encountered in the thermal treatment of TiO_2 initially synthesized at low temperatures (via sol-gel, hydrothermal, precipitation, solvothermal, or other methods).[2] Many dopants have been used in TiO_2 to influence the temperature at which the anatase-rutile transition occurs. Hanaor and Sorrell reviewed the literature and presented a comprehensive listing of the dopants that can

either promote or inhibit the phase transformation from anatase to rutile.[30] The defect chemistry of the dopant in TiO_2 plays a pivotal role in determining whether or not it promotes the transition. Dopants with a lower valance (< 4) than Ti^{4+} promote the transition from anatase to rutile, while those with a higher valence inhibit the transition.[30] Compensating oxygen vacancies are formed upon incorporation of lower valence dopants in the anatase lattice. These vacancies allow for either easier structural rearrangement from anatase to rutile[30,31] or better mass transport during this process.[32] When oxygen vacancies are not formed, high valence cationic dopants generate strain in the anatase lattice and make the phase transformation less favorable.[30] This point is extremely important for understanding the structural characteristics of materials analyzed in this chapter. As discussed above, dopants also impact the growth of TiO_2 crystallites. Since the transformation from anatase to rutile occurs once TiO_2 crystals reach a certain critical size, dopants that facilitate crystal growth can make the transition occur at lower temperature and vise-versa.[32] However, some evidence indicates that the critical size for the anatase-to-rutile transformation does not change upon addition of certain dopants, suggesting that changes to the diffusion of cations/anions in the lattice are crucial.[32]

Since the maintenance of nanoscale dimensions in crystallites and nanoporosity is critical for achieving good capacities in TiO_2, it is no shock that many researchers have investigated doped TiO_2 for use in LIBs. Crystal growth can be curtailed via the use of dopants, preserving the structural features required to obtain adequate performance from TiO_2 anodes. Moreover, as was stated in Chapter 3, doping frequently changes the electronic and ionic conductivity of TiO_2, which (in the best case) improves capacities across a wide range of charge/discharge rates.[33] While dopants that can replace oxygen in the lattice are not a focus of this chapter, other research teams have investigated their use in TiO_2 anode materials. Nitrogen doping,[34] sulfur doping,[35] fluorine doping,[36] carbon/nitrogen co-doping,[37] and nitrogen/sulfur co-doping[35] have all been used to improve the capacities of TiO_2 anode materials relative to their undoped counterparts. More directly applicable to this chapter are the studies conducted using aliovalent cationic dopants. Dopants with a lower valence than Ti^{4+} (acceptors) and those with a higher valence than Ti^{4+} (donors) have proven to be effective at increasing the capacity of the resulting doped electrodes. For some doped TiO_2 anodes, an increase in electronic conductivity is thought to contribute to the improvement in capacity. This improvement has been postulated to originate from the formation of electrons[38,39] or titanium vacancies.[40] The higher surface areas and smaller crystallite sizes attainable in these doped materials are also thought to contribute to the improved capacities.[41,42] Hutchings *et al.* postulated that the improvement in capacities observed in TiO_2

doped with cobalt or nickel is the result of increased interfacial storage.[43] A radically different mechanism was also considered by Das *et al.* for the improvement in the capacity of iron-doped TiO_2.[44] They provided evidence that the iron undergoes a conversion reaction, forming Fe and Li_2O in localized regions of the structure. As these studies demonstrate, dopants can be used to increase the capacity of TiO_2, providing a key motivation for the work detailed in this chapter.

Both of the main synthesis routes for TiO_2/C described in Chapter 3, TFA-TiO_2/C and acac-TiO_2/C, can be tailored to allow for the incorporation of heteroatoms into the TiO_2 phase. The remainder of this chapter concerns the characterization of different TFA- and acac-TiO_2/C materials that are synthesized with either increased carbon content or with dopants. Several promising doped materials are then tested in as lithium ion batteries in the half-cell configuration described in Chapter 3. While not strictly a dopant (though it is presumably present in the TiO_2 lattice at low levels), the carbon content of the final composites can be adjusted by changing the amount PF sol in the precursor. This chapter starts with an exploration of such an adjustment for the TFA-TiO_2/C system, where the weight percent of the carbon phase is increased. Notably, the material does not provide a reduction in TiO_2 crystal size that could be beneficial for the electrochemical performance. Efforts to dope the TiO_2 phase in the TFA-TiO_2/C system are also described. An initial discussion focuses on the use of several dopants (Nb, Cu, and Fe) to attempt to reduce the crystal size of TiO_2 and improve the degree of graphitization at a relatively low pyrolysis temperature. Subsequently, an in-depth study of the use of tantalum as a dopant for TFA-TiO_2/C is discussed, with a focus on the structural changes caused by doping when compared to undoped TFA-TiO_2/C. Since the acac-TiO_2/C showed improved lithium ion insertion/extraction capacities over TFA-TiO_2/C, the structural characterization and electrochemical performance of different doped acac-TiO_2/C samples are described. Finally, much like the 3DOM TiO_2 described in Chapter 3, TFA-TiO_2/C with two different levels of tantalum content are first pyrolyzed and then calcined. These 3DOM mixed oxides of titanium and tantalum are characterized and then electrochemically tested. Most doped materials described in this chapter have lower capacities for lithium ion insertion/extraction, and this point is also addressed.

4.2 Experimental

4.2.1 Materials

Methyl methacrylate (99 %), titanium isopropoxide (>97%), trifluoroacetic acid (99 %), 2,4–pentanedione (99+%), iron(III) chloride hexahydrate (ACS reagent, 97 %), tantalum(V) ethoxide (99.98%), poly(ethylene oxide)–*block*-poly(propylene oxide)–*block*-poly(ethylene oxide) copolymer (molecular weight of 5800, P123), sodium carboxymethyl cellulose (molecular weight of 250000), and lithium ribbon (0.75 mm thickness, 99.9%) were bought from Sigma-Aldrich. Phenol (ACS reagent grade), formaldehyde (certified ACS, 37 wt% in water), potassium persulfate (ACS reagent grade) and copper(II) chloride dihydrate (laboratory grade) were purchased from Fischer Scientific. Hydrochloric acid (ACS regent grade, 37 wt% in water) and sodium hydroxide pellets (ACS reagent grade) were obtained from Macron Chemicals. Niobium ethoxide (99.9%) was purchased from Alfa Aesar. Nickel(II) chloride hexahydrate (laboratory grade) was purchased Mallinckrodt. Ethanol (200 proof, USP grade) was obtained from Decon Labs. A suspension of styrene-butadiene rubber (50 wt% in water) was purchased from the MTI Corporation. Chemicals were used without any additional purification. Water was purified using a Barnstead Sybron purification system (final resistivity >18 MΩ·cm).

4.2.2 Preparation of PMMA Colloidal Crystal Templates and PF Sol

Both the PMMA colloidal crystal templates and the PF sol were synthesized following the procedures outlined in Chapter 3. Literature procedures were followed.[45,46]

4.2.3 Preparation of TFA2-TiO_2/C Composites

The synthesis of the TFA2-TiO_2/C precursor is similar to that of the TFA-TiO_2/C described in Chapter 3. Two solutions were first synthesized, solution A and solution B. For solution A, titanium isopropoxide (2.00 g) and trifluoroacetic acid (1.10 g) were combined in a scintillation vial. Ethanol (0.500 g) was immediately added to the vial and the solution was stirred for 5 minutes. While stirring was maintained, 0.350 g of concentrated HCl was added dropwise to solution A. Heated (at ~40 °C), liquid P123 (0.500 g) was then added to solution A, and this mixture was stirred until P123 fully dissolved. Solution B was prepared by mixing 1.00 g of PF sol into 2.00 g of ethanol and 0.400 g of water. This mixture was stirred briefly and 0.750 g of heated, liquid P123 was added. Stirring was continued in solution B until the P123 dissolved. When the surfactant had dissolved, stirring was maintained for solution A and solution B was added dropwise to it. The combined TFA2-TiO_2/C precursor was stirred overnight.

Infiltration of the TFA2-TiO_2/C precursor into PMMA colloidal crystals was performed next. As before, monolithic pieces of the colloidal crystal template were placed in scintillation vials. The precursor solution was slowly added to the vial until the level of the liquid precursor was at roughly half the thickness of the monoliths. If the volume of precursor added was not sufficient for full infiltration of the templates, extra precursor was added to the vials. Infiltration took approximately 4 to 8 h. After infiltration, excess TFA2-TiO_2/C precursor was wiped off the surface of the monoliths. The templates were then placed in a vacuum oven under low vacuum at ambient temperature for 30 minutes. Once excess solvent was removed, the infiltrated templates were heated at 100 °C for 24 h and 140 °C for 24 h. Composites were pyrolyzed in a tube furnace under flowing Ar (0.7 L/min). All samples were heated at a rate of 1 °C/min to 350 °C and held at 350 °C for 4 h. The temperature was then raised at 1 °C/min to 500 °C, 600 °C, 700 °C, or 800 °C and held at the chosen temperature for 2 h.

4.2.4 Preparation of Undoped, Nb, Cu, and Fe-Doped TFA3-TiO_2/C Composites

These composites were prepared in a manner similar to the undoped TFA-TiO_2/C, except that water was omitted from solution B. Again, two solutions were prepared, denoted solution A and solution B. In solution A, titanium isopropoxide and the dopant precursor were mixed. The number of moles of titanium ions plus the dopant ions was fixed at 0.0123 moles. For the undoped precursor 3.50 g of titanium isopropoxide was used. For the 6 mol% Nb-doped sample, 0.235 g of niobium(V) ethoxide and 3.29 g of titanium ispropoxide were combined. For the 5 mol% Fe-doped sample, 0.166 g of iron(III) chloride hexahydrate and 3.33 g of titanium isopropoxide were added. For the 10 mol% Cu-doped sample, 0.210 g of copper(II) chloride dihydrate and 3.15 g of titanium isopropoxide were mixed in solution A. All subsequent synthesis steps are similar to those described in Chapter 3 for TFA-TiO_2/C. Briefly, the dopant and titanium isopropoxide were combined with trifluoroacetic acid (1.40 g), absolute ethanol (2.00 g), concentrated hydrochloric acid (0.600 g) and P123 surfactant (0.750 g). Solution B was prepared by mixing PF sol (0.300 g), absolute ethanol (2.00 g), and P123 surfactant (1.00 g). Upon dissolution of all P123, solution B was added to solution A drop by drop. Stirring was continued overnight.

The precursors were then infiltrated into PMMA colloidal crystal templates. Again, these monolithic templates were placed in scintillation vials and the precursor was injected into each vial. Infiltration of the precursor was allowed to proceed in the capped vials for 4–6 h. Removal of solvent was accomplished by wiping the monoliths and then evacuating them (at ambient

temperature) for 15 min under low vacuum. Templates were treated at 100 °C for 24 h and then 140 °C for 24 h. Pyrolysis was performed in a tube furnace (using alumina boats and a quartz tube) under a flow of Ar (0.7 L/min). First, the temperature was ramped to 350 °C at 1 °C/min, and held there for 4 h. The temperature was then increased to 600 °C at a rate of 1 °C/min and held at that temperature for 8 h. These samples are denoted: TFA3-TiO_2/C, TFA3-Nb:TiO_2/C (6 mol%), TFA3-Fe:TiO_2/C (5 mol%), and TFA3-Cu:TiO_2/C (10 mol%). The mol% listed in parentheses is calculated based on the mol% of the dopant ion in the initial precursor. For example, 0.0123 moles of titanium/dopant are used in the TFA3-Cu:TiO_2/C precursor, and the 0.210 g of added copper(II) chloride dehydrate contains 0.00123 moles of Cu^{2+} ions. This is 10 mol% of the combined moles of titanium/dopant, hence the name of the sample.

4.2.5 Preparation of Ta-Doped TFA-TiO_2/C and TFA2-TiO_2/C Composites

A systematic study of the effects of dopant concentration was carried out for the tantalum system using a modified TFA-TiO_2/C precursor synthesis. As was the case for the previous materials, the number of moles of titanium ions plus the number of moles of dopant ions was fixed at 0.0123 moles, total. Four different levels of doping were targeted: 3.125 mol% Ta, 6.25 mol% Ta, 9.375 mol% Ta, and 12.5 mol% Ta. In these syntheses, tantalum(V) ethoxide was initially combined with titanium isopropoxide. The total amounts of the alkoxide precursors and other components of solution A are given in Table 4.1. For all precursors irrespective of doping level, solution B contains 0.300 g of PF sol, 2.00 g of ethanol, 0.880 g of water, and 1.00 g of P123. Once again, all of the other steps for the synthesis of the doped precursors were carried out identically to what was described in Chapter 3 for the synthesis of TFA-TiO_2/C.

Table 4.1. Contents of solution "A" for the Ta-doped TFA-TiO_2/C and TFA2-TiO_2/C precursors.

Sample	tantalum(V) ethoxide (g)	titanium(IV) isopropoxide (g)	TFA (g)	ethanol (g)	concentrated HCl (g)	P123 surfactant (g)
TFA-Ta:TiO_2/C, (3.125 mol%)[a]	0.156	3.39	1.40	2.00	0.600	0.750
TFA-Ta:TiO_2/C, (6.25 mol%)[a]	0.313	3.28	1.40	2.00	0.600	0.750
TFA-Ta:TiO_2/C, (9.375 mol%)[a]	0.469	3.17	1.40	2.00	0.600	0.750
TFA-Ta:TiO_2/C (12.5 mol%)[a]	0.625	3.06	1.40	2.00	0.600	0.750
TFA2-Ta:TiO_2/C, (6.25 mol%)[b]	0.179	1.88	1.10	0.500	0.350	0.500
TFA2-Ta:TiO_2/C, (12.5 mol%)[b]	0.357	1.75	1.10	0.500	0.350	0.500

[a] The precursor contains 0.0123 moles total of Ti^{4+} plus Ta^{5+} ions. The mol% given in parentheses is the mol% of Ta ions in the precursor relative to the total moles of Ti plus Ta.

[b] The precursor contains 0.00704 moles total of Ti^{4+} plus Ta^{5+} ions. The mol% given in parentheses is calculated the same as above.

Additionally, tantalum(V) ethoxide was added to the TFA2-TiO_2/C precursor to generate Ta-doped composites with a high wt% of carbon. For these syntheses, the number of moles of titanium and dopant was fixed at 0.00704 moles. The contents of solution A for these precursors are listed in Table 4.1. Solution B, irrespective of the concentration of dopant, contained 1.00 g of PF sol, 2.00 g of ethanol, 0.400 g of water, and 0.750 g P123 surfactant. Aside from the

aforementioned adjustment to the precursor composition, all other steps for these syntheses were identical to what was described for the undoped TFA2-TiO_2/C.

Both types of precursor, the tantalum-containing TFA-TiO_2/C and TFA2-TiO_2/C, were infiltrated into PMMA colloidal crystal templates. Infiltration took place over approximately 4–6 h, and extra precursor was wiped from the surface of templates. Solvent was removed under low vacuum for 15 min (TFA-Ta:TiO_2/C) or 30 min (TFA2-Ta:TiO_2/C). The templates were heated at 100 °C for 24 h and 140 °C for 24 h. All materials were pyrolyzed in a tube furnace under 0.7 L/min of flowing Ar. The temperature was ramped 1 °C/min to 350 °C (4 h hold) and 1 °C/min to 800 °C (2 h hold). These samples are denoted either TFA-Ta:TiO_2/C (*x* mol%) or TFA2-Ta:TiO_2/C (*x* mol%).

4.2.6 Preparation of Doped acac-TiO_2/C Composites

The other TiO_2/C precursor described in Chapter 3, acac-TiO_2/C, was also modified with several different dopants (Nb, Ta, and Ni). Two solutions were made, solution A and solution B. Solution A was prepared by first combining titanium isopropoxide and the precursor for the dopant. As was the case for the doped TFA-TiO_2/C precursors, the number of moles of titanium ions plus the moles of the dopant ions was fixed at 0.0123 moles, total. For the 6.5 mol% Nb-doped sample, 3.27 g of titanium isopropoxide was combined with 0.255 g of niobium(V) ethoxide. For the 6.5 mol% Ta-doped sample, 3.27 g of titanium isopropoxide was combined with 0.325 g of tantalum(V) ethoxide. Finally, for the 5 mol% Ni-doped sample, 3.33 g of titanium isopropoxide was combined with 0.146 g nickel(II) chloride hexahydrate. No matter what dopant was used, 1.23 g of 2,4-pentanedione and 1.75 g of ethanol was added to solution A, and the solution was stirred for 5 min. While solution A was stirred, 1.00 g of concentrated HCl was added dropwise to it. Liquid P123 (0.75 g) was dissolved in the solution afterward. In solution B, 0.27 g of PF sol, 1.75 g of ethanol, 0.75 g of water, and 1 g of liquid P123. This solution was stirred until the P123 was dissolved. Solution B was then added to solution A, and the combined precursor was stirred overnight.

All subsequent processing steps were the same as those described for acac-TiO_2/C in Chapter 3. The same pyrolysis procedure was used for all doped samples. First, the materials were loaded into a tube furnace under a flow of 0.7 L/min of Ar. Using a temperature ramp rate of 1 °C/min, the infiltrated templates were pyrolyzed at 350 °C for 4 h and 800 °C for 2 h. These samples are denoted acac-Nb:TiO_2/C (6.5 mol%), acac-Ta:TiO_2/C (6.5 mol%), and acac-Ni:TiO_2/C (5 mol%).

The mol% listed in parentheses is calculated based on the mol% of the dopant ion in the initial precursor. This is the same notation used for the other materials described in this chapter.

4.2.7 Preparation of 3DOM Ta:TiO_2

Two TFA-Ta:TiO_2/C precursor solutions (one with 6.25 mol% Ta and the other with 12.5 mol% Ta) were prepared and infiltrated into PMMA colloidal crystal as indicated above. After the samples were heat-treated 100 °C and 140 °C, they were pyrolyzed under flowing N_2 (0.7 L/min). The composites were heated at 1 °C/min to 350 °C and held at that temperature for 4 h. The temperature was then raised at 1 °C/min to 500 °C and held at that temperature for 2 h. Once pyrolysis was completed, the composites were calcined under static air at 2 °C/min to 400 °C with a 2 h hold. These samples are denoted 3DOM Ta:TiO_2 (6.25 mol%) and 3DOM Ta:TiO_2 (12.5 mol%).

4.2.8 Structural Characterization

SEM was conducted using a JEOL 6700 with a 5 kV accelerating voltage. Samples were placed on Al stubs coated with double-sided sticky carbon tape, and then coated with 5 nm of Pt. PXRD was carried out using a PANalytical X'Pert Pro fitted with a Co anode and an X'Celerator strip detector. A voltage of 45 kV and current of 40 mA was used for obtaining the patterns. Weight fractions of the anatase and rutile polymorphs were determined using an empirical method developed by Spurr and Meyers.[47] Nitrogen sorption isotherms were collected on a Quantachrome Autosorb IQ_2-MP. Samples were outgassed at 200 °C for 12 h under a pressure of 0.001 torr, and all isotherms were collected at 77 K. Specific surface areas were estimated using the BET method and total pore volumes were determined from the point P/P_o = 0.995. Thermogravimetry was used to determine oxide content. Samples were heated under flowing air at 10 °C/min to 1000 °C in a Netzsch STA 409 PC Luxx. Several other techniques were used for some groups of materials, but not others. For instance, confocal Raman microscopy was performed on a WiTec Alpha 300R using an Ar^+ ion laser with a wavelength of 514.5 nm and a power of 15 mW. This instrument was equipped with a DV401 CCD thermoelectric-cooled detector. An FEI T12 was used to collect TEM micrographs. This particular instrument was equipped with a LaB_6 filament and operated with an accelerating voltage of 120 kV. All samples were ground, placed in ethanol, and sonicated for 5 min. The ethanolic dispersions were dropped on Cu grids coated with holey carbon. SAXS patterns were gathered using a Rigaku RU-200BVH that had a rotating copper anode. A Siemens Hi-Star multiwire area detector was used with this instrument.

4.2.9 Electrochemical Characterization

Electrodes for galvanostatic charge/discharge experiments were prepared similarly to what was described in Chapter 3. Once again, the active material was ground and ultrasonicated prior to use. This material was combined with Timcal Super P® carbon black, CMC binder, and SBR binder. The weight percent of each solid component in the final paste was: 84 wt% active material, 10 wt% carbon black, 4 wt% CMC binder, and 2 wt% SBR binder. Carbon-coated aluminum foil (donated by Exopack® Advanced Coatings) was used as a current collector. A doctor blade was used to spread electrode pastes, and these films were dried overnight at ambient and then at 105 °C for 24 h under low vacuum. A 0.5 in punch was used to obtain electrode disks with a typical loading of active material of 1 to 1.5 mg/cm^2. The electrode disks, Celgard® 3501 polypropylene separator (donated by Celgard®), and lithium ribbon were assembled in a type 2032 casing. One molar $LiPF_6$ in a mixture (1:1:1 by mass) of ethylene carbonate, dimethyl carbonate, and diethyl carbonate was used as the electrolyte (solution purchased from MTI Corp.). All cells were assembled in a He-filled glove box. These half-cells were cycled on an Arbin Instruments BT-2000 testing system between 1 V and 3 V vs. Li/Li^+ at varying rates. The C-rate was set to 335 mA/g of the doped oxide. For half cells containing 3DOM Ta:TiO_2 (6.25 mol%) and the 3DOM Ta:TiO_2 (12.5 mol%), impedance spectroscopy was performed using a Solartron 1255B frequency response analyzer connected to a SI1287 electrochemical interface. All other relevant parameters are same as those listed in Chapter 3. Cells were tested both prior to cycling and after ten cycles at a rate of C/2.

4.3 Results and Discussion

Owing to the substantial differences between the syntheses and analyses performed for each material discussed in this chapter, this section is split into five parts. First, the TFA2-TiO_2/C materials are discussed with a focus on how changing the pyrolysis temperature changes the structure of the composites. Second, the structures of the TFA3-TiO_2/C materials are analyzed. Third, the effect of changing the concentration of Ta on the TFA- and TFA2-TiO_2/C materials pyrolyzed at 800 °C is studied with an emphasis how this affects the polymorph/crystallite size of the doped TiO_2. Fourth, the structural and electrochemical characterization of the doped acac-TiO_2/C materials is discussed. Finally, the 3DOM Ta:TiO_2 materials are discussed with a focus on the electrochemical properties of the two doped materials. Each subsection has its own set of conclusions and a brief, global summary is also given at the end of this chapter.

4.3.1 TFA2-TiO_2/C System

4.3.1.1 Composition and Morphology of Samples

Overall, the TFA2-TiO_2/C system is fairly similar to TFA-TiO_2/C with the key differences resulting from the enhanced carbon content. Since less titanium isopropoxide and more PF sol was used in the TFA2-TiO_2/C precursor, the final content of the carbonaceous phase in the composite is 50.7 wt% for the sample pyrolyzed at 800 °C. This is nearly 25 wt% more carbon than in the matching TFA-TiO_2/C material pyrolyzed at the same temperature. The TFA2-TiO_2/C precursor is also stable for weeks, like its counterpart, but efforts to increase the content of PF sol or lower the amount of titanium isopropoxide were unsuccessful (precipitation rapidly occurs). Even for the TFA2-TiO_2/C, the molar ratio of TFA to Ti has to be increased above one to prevent rapid condensation. It appears that the minimum weight percent of TiO_2 in composites attainable through this synthesis pathway is only around 50 wt%. Still, this difference in TiO_2 and carbon content does result in structural changes.

From the standpoint of the morphology, the TFA2-TiO_2/C contains an interconnected network of macropores. The colloidal crystal templating process clearly works as illustrated in Figure 4.1; however, some disorder is present in the 3DOM network. Despite the higher carbon content of the TFA2-TiO_2/C, sintering of TiO_2 crystallites is quite severe in the composite pyrolyzed at 800 °C (Figure 4.1 e, f). This level of sintering and crystallite growth is more extensive than what is observed in the TFA-TiO_2/C composites in Chapter 3. However, crystallites of TiO_2 are not visible in the micrographs of samples pyrolyzed at lower temperatures. This indicates that the TiO_2 was successfully confined by the carbonaceous phase at final pyrolysis temperatures of 700 °C or below. Returning to the sample pyrolyzed at 800 °C (Figure 4.1 d, e), it is also observed that the crystallites of TiO_2 are present on the surface of the 3DOM network. Once again, the use of hydrophobic TFA as a chelating agent leads to segregation of the Ti-containing precursor complex. As discussed in chapter 3, the TFA-chelated complex separates to the surface of the hydrophobic PMMA template, which leads to the localization of TiO_2 crystallites on the surface of the pyrolyzed 3DOM TiO_2/C materials.

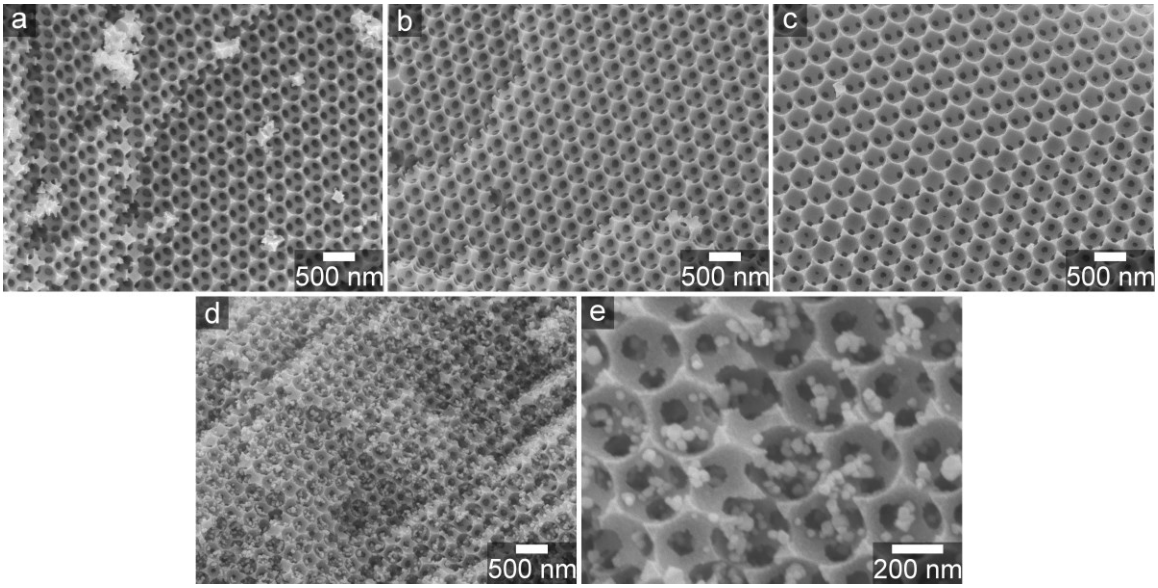

Figure 4.1 SEM micrographs of the TFA2-TiO_2/C pyrolyzed at (a) 500 °C, (b) 600 °C, (c) 700 °C, (d) 800 °C, and a higher magnification view of the sample pyrolyzed at (e) 800 °C. The 3DOM morphology is present in all micrographs. After pyrolysis at 800 °C, crystallites of sintered TiO_2 are noticeable on the surface of the composite.

Both TEM micrographs and SAXS patterns obtained from the TFA2-TiO_2/C composites highlight other features of the morphology, including similarities to the TFA-TiO_2/C composites. By examining the micrographs of the samples pyrolyzed at 500 °C and 600 °C (Figure 4.2), it is observed that the TiO_2 crystallites are so small that they cannot be resolved by TEM imaging. However, numerous bright spots do appear in the TEM images. These spots are from disordered mesopores that were produced from removal of the P123 soft template. Carbon appears to adequately confine any growing crystallites and allows for retention of a mesostructure at pyrolysis temperatures higher than what observed for TFA-TiO_2/C. SAXS patterns (Figure 4.3) offer further confirmation that a mesostructure is retained; a weak scattering peak with a *d*-spacing of ~6.8 nm is present for the TFA2-TiO_2/C patterns until the pyrolysis temperature hits 800 °C. Incidentally, this spacing is the same as the one measured for the TFA-TiO_2/C samples in Chapter 3. A peak with a similar *d*-spacing of ~10.0 nm is also shared by the unpyrolyzed TFA- and TFA2-TiO_2/C.

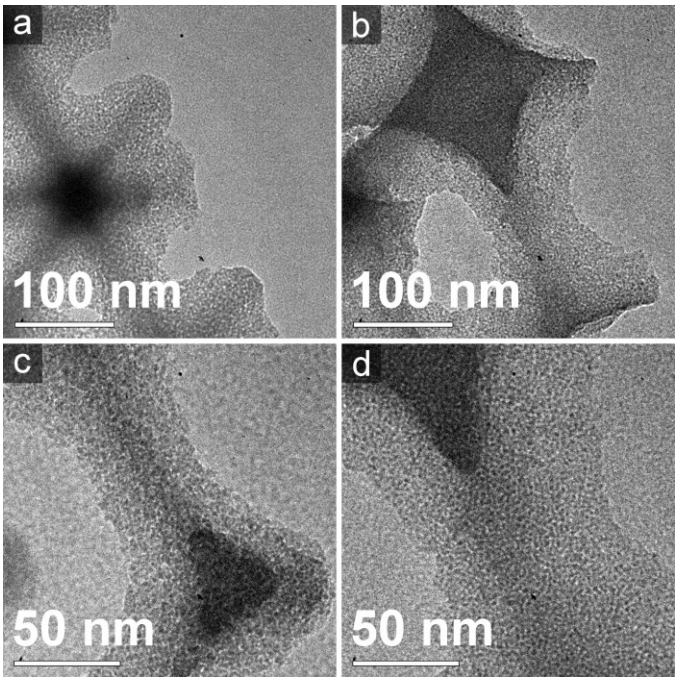

Figure 4.2 TEM micrographs of selected TFA2-TiO_2/C samples pyrolyzed at (a, c) 500 °C and (b, d) 600 °C. At low pyrolysis temperatures, crystallites are not resolvable. However, disordered mesopores are present in the 3DOM network. Images taken by Stephen Rudisill.

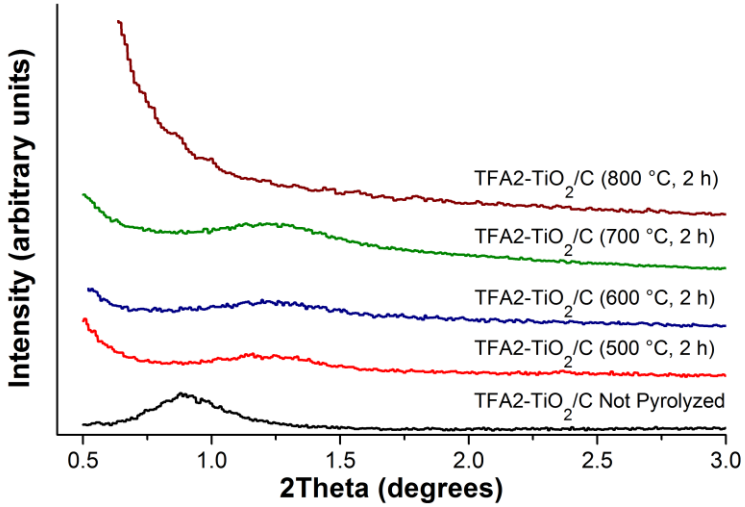

Figure 4.3 SAXS patterns for the TFA2-TiO_2/C pyrolyzed at different temperatures. Pyrolysis decreases the measured *d*-spacing due to contraction of the 3DOM structure. A remnant of the mesostructure exists in the TFA2-TiO_2/C samples until the pyrolysis temperature is increased to 800 °C.

4.3.1.2 PXRD Analysis and Textural Properties

Further information concerning both the TiO_2 crystallite size and the polymorphs present can be obtained from PXRD (Figure 4.4). As is the case for the TFA-TiO_2/C, the anatase phase crystalizes at low pyrolysis temperatures. At 500 °C, the crystallites of TiO_2 are so small that only peaks corresponding to the amorphous carbon are found near 30 and 52 °2θ.[48] Once the crystallites sinter and grow, the expected transformation to the thermodynamically stable (for grains <10 nm) rutile TiO_2 occurs.[30] Since 50 wt% amorphous carbon is in this material, the phase transition to rutile is delayed until 800 °C. The carbon phase prevents crystallites of TiO_2 from coming in contact with each other and sintering. Applying the Scherrer equation (as outlined in Chapter 3), the estimated anatase TiO_2 crystallite size for the TFA2-TiO_2/C is below 5 nm for composites pyrolyzed at temperatures below 800 °C (see Table 4.2). A transformation to rutile TiO_2 would not be expected for such small crystallites. Surprisingly, the anatase phase completely disappears when the pyrolysis temperature is raised to 800 °C. Strong rutile TiO_2 reflections are found, in addition to an unidentified minor phase that shares some reflections with reduced Magnelí TiO_2 phases.[49] The estimated crystallite size is also quite high, 35.2 nm for the rutile TiO_2/C. These observations stand in stark contrast to the case of the TFA-TiO_2/C. In that material, anatase remains the dominant phase at 800 °C and the average crystallite size of the anatase phase is one-third of that calculated for rutile TiO_2 in TFA2-TiO_2/C.

Table 4.2 TiO_2 crystallite sizes and textural properties of TFA2-TiO_2/C.

Sample	anatase crystallite size (nm)	rutile crystallite size (nm)	BET surface area (m^2/g)	pore volume (cm^3/g)
TFA2-TiO_2/C, 500 °C, 2 h	< 2	[a]	293	0.24
TFA2-TiO_2/C, 600 °C, 2 h	2.7	[a]	358	0.46
TFA2-TiO_2/C, 700 °C, 2 h	3.3	[a]	368	0.46
TFA2-TiO_2/C, 800 °C, 2 h	[b]	35.2	647	0.63

[a] Rutile polymorph is not found in these samples.

[b] Anatase polymorph has been completely transformed to rutile at this temperature.

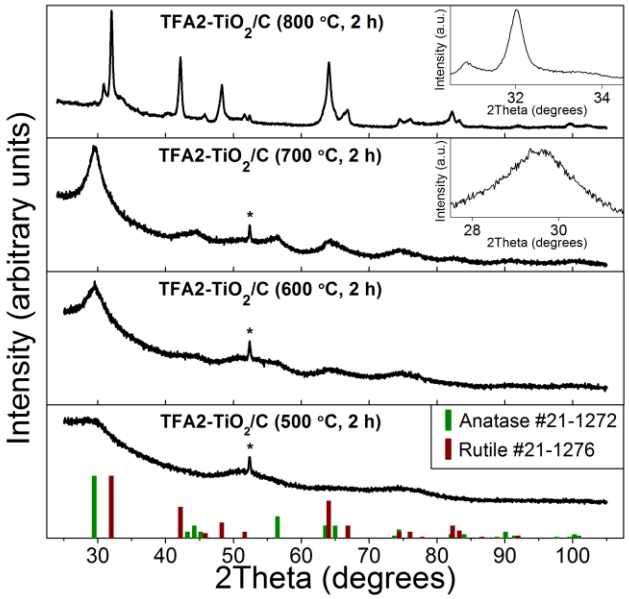

Figure 4.4 PXRD patterns of the TFA2-TiO_2/C composites pyrolyzed at different temperatures. The asterisk is above a peak originating from the Al sample holder.

More information concerning the types of pores present in the TFA2-TiO_2/C and other textural properties was obtained by using gas sorption (Figure 4.5). Unlike the TEM images and SAXS patterns, little evidence of mesoporosity is found in the gas sorption isotherms. These isotherms contain extremely narrow hysteresis loops. The disordered mesopores in the samples appear to contribute little to the overall sorption of N_2 gas. For high and low relative pressures, significant rises are noted in the volume of gas adsorbed. Macropores originating from the colloidal crystal template contribute to the rise near $P/P_o = 1$, whereas micropores from the carbon phase contribute at low P/P_o. Since amorphous carbon is the source of the micropores, the quantity of gas adsorbed at very low P/P_o increases with increasing pyrolysis temperature.[49] This also contributes to the rise in the BET surface area for samples pyrolyzed at higher temperatures (Table 4.2). Specific surface areas are greater than for TFA-TiO_2/C, which is likely a result of the increase in amorphous carbon content.

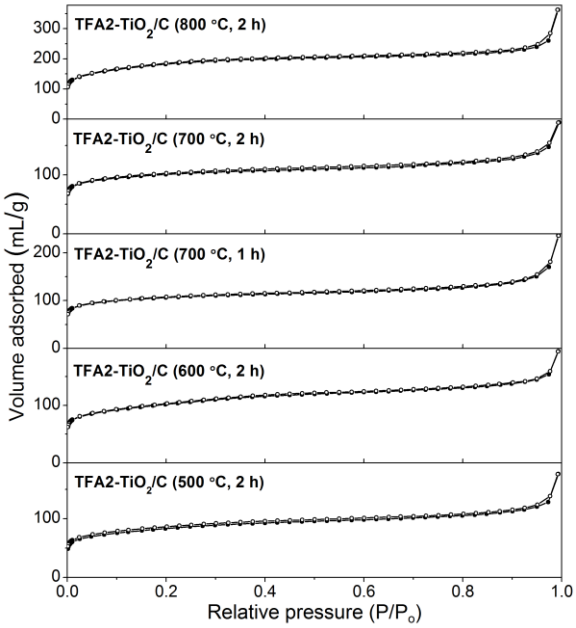

Figure 4.5 Nitrogen sorption isotherms for the TFA2-TiO_2/C samples. Hysteresis is limited for these materials, suggesting that little mesoporosity is present. Pressure rises occur at low and high P/P_o from micropores and macropores, respectively.

4.3.1.3 Concluding Remarks

One of the most intriguing features of this system is the dramatic change in the size and polymorph of TiO_2 crystallites when the final pyrolysis temperature is set to 800 °C. The change in crystallite size as the pyrolysis temperature is raised from 700 °C to 800 °C is far larger than in the case for TFA-TiO_2. It is possible that the changes to the precursor for TFA-TiO_2/C and TFA2-TiO_2/C, such as the higher content of TFA relative to the other components, induce a greater degree of phase separation. This could drive the increased sintering and crystal growth at 800 °C for the TFA2-TiO_2/C. Another possible reason for the extensive sintering could be the carbon phase. Pyrolysis of the carbonaceous phase releases reducing gases into the inert gas stream flowing over the samples.[50] For TFA2-TiO_2/C, this reducing environment should induce the formation of a substantial amount of oxygen vacancies, which can hasten the phase transformation.[31] Sintering of rutile is facile, leading to the sharp increase in crystallite size.[30] No matter what caused these changes, the substantial increase in crystallite size after pyrolysis at 800 °C makes TFA2-TiO_2/C a poor choice for an anode material. As a consequence, the TFA2-TiO_2/C composites were not electrochemically tested.

4.3.2 Structural Characterization of TFA3-TiO_2/C Materials

4.3.2.1 Compositional, PXRD, and Raman Analysis of the TFA3-TiO_2/C Materials

A variant of the TFA-TiO_2/C synthesis presented in Chapter 3, denoted TFA3-TiO_2/C was used as an initial test bed for studying doping of the TiO_2 phase. The principle difference between the TFA-TiO_2/C system and the TFA3-TiO_2/C system is that the latter contains 0.88 g less H_2O than the TFA-TiO_2/C. This change should assist in preventing hydrolysis of the niobium ethoxide precursor. Overall, the oxide content of the TFA3-TiO_2/C (Table 4.2) is similar to what is observed in the TFA-TiO_2/C, as reported in Chapter 3. All the doped materials have slightly lower oxide content, but the oxide content exceeds 65 % in the composites. For these materials, Nb was chosen as a potential dopant to improve electronic conductivity of TiO_2;[51] Fe was chosen to possibly act as an electrochemically active secondary phase and to enhance the degree of graphitization in carbon;[44,52,53] and Cu was chosen to improve the electronic conductivity of the carbon phase via catalytic graphitization.[54,55] A lower pyrolysis temperature (600 °C) was also used for the TFA3-TiO_2/C to observe if doping could substantially improve the degree of graphitization, while simultaneously allowing for the retention of small crystal sizes in the doped oxide phase. Owing to the differences between the TFA-TiO_2/C system and TFA3-TiO_2/C, the discussion will be limited to the four composites that were prepared for TFA3-TiO_2/C.

Table 4.3 Selected structural properties of the TFA3-TiO_2/C composites.

sample[a]	oxide content (wt %)	anatase crystallite size (nm)	BET surface area (m^2/g)	pore volume (cm^3/g)	ratio of I_d/I_g from Raman spectra
TFA3-TiO_2/C	71.5	5.3	288	0.43	1.0
TFA3-Nb:TiO_2/C (6 mol%)	69.1	5.5	203	0.29	1.0
TFA3-Fe:TiO_2/C (5 mol%)	68.1	5.8	250	0.39	0.98
TFA3-Cu:TiO_2/C (10 mol%)	66.9	5.1	233	0.35	0.82

[a] All materials pyrolyzed at 600 °C.

PXRD and Raman spectroscopy were used in tandem to determine if doping strategies worked for the TFA3-TiO_2/C system and to determine what impact these changes had on the crystal structure of both the TiO_2 and the carbon phase. Figure 4.6 shows the PXRD patterns obtained for the samples. Reflections that match anatase TiO_2 are found in all of the samples. For the TFA3-Nb:TiO_2/C (6 mol%) and TFA3-Fe:TiO_2/C (5 mol%), no evidence of a secondary phase is found and slight shifts are observed in the positions of the TiO_2 reflections. This provides evidence that doping into TiO_2 was successful for both Nb and Fe. Another indication that doping was achieved for TFA3-Fe:TiO_2/C (5 mol%) is that this particular material contains a greater concentration of the rutile polymorph. Compensating oxygen vacancies generated by doping with Fe^{3+} facilitate the change to rutile at lower temperatures.[30,56] In contrast to the aforementioned dopants, Cu separates from the TiO_2 and reflections from metallic Cu are found in TFA3-Cu:TiO_2/C (10 mol%). Pyrolysis of the phenolic resin causes the release of reducing gases (CO and CH_4) at intermediate temperatures (400 to 800 °C).[50] The reduction of copper oxide to copper metal in the presence of these gases occurs below 400 °C,[57] which explains the phase separation. Confocal Raman microscopy confirms that anatase is present in these samples, since the characteristic modes are observed (Figure 4.7 a).[58] Rutile TiO_2 vibrations are also found in some areas of the TFA3-Fe:TiO_2/C (5 mol%) samples, including the surface of the monoliths. Unfortunately, little enhancement can be observed in the intensity of the *G* band for any of the doped samples relative to TFA3-TiO_2/C (Figure 4.7 b and Table 4.3). For the Fe-doped sample, the dopant content may be too low to induce catalytic graphitization. In TFA3-Cu:TiO_2/C (10 mol%), the Cu phase separated and sintered. The *G* band is slightly stronger in this particular sample, which is an indication that graphitization progressed to a greater extent. However, both the *D* and *G* bands are broad in the case of TFA3-Cu:TiO_2/C (10 mol%), likely due to poor crystallinity.[59]

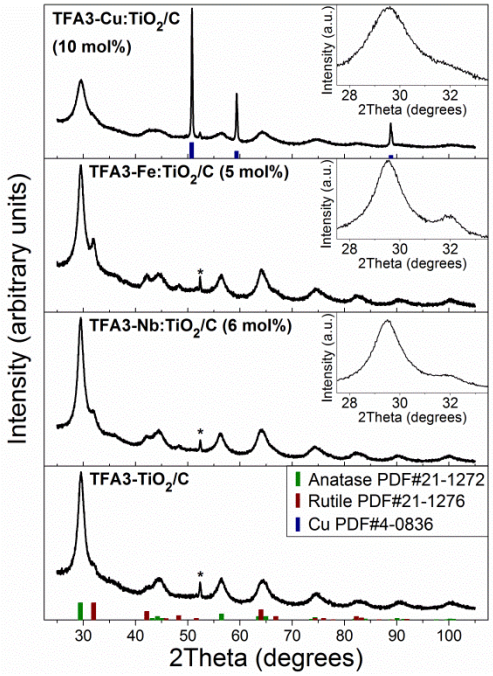

Figure 4.6 PXRD patterns of the undoped and doped TFA3-TiO_2/C samples. Rutile TiO_2 reflections intensify for the TFA3-Fe:TiO_2/C (5 mol%) and metallic copper is present in the TFA3-Cu:TiO_2/C (10 mol%). The asterisk denotes a peak originating from the Al sample holder.

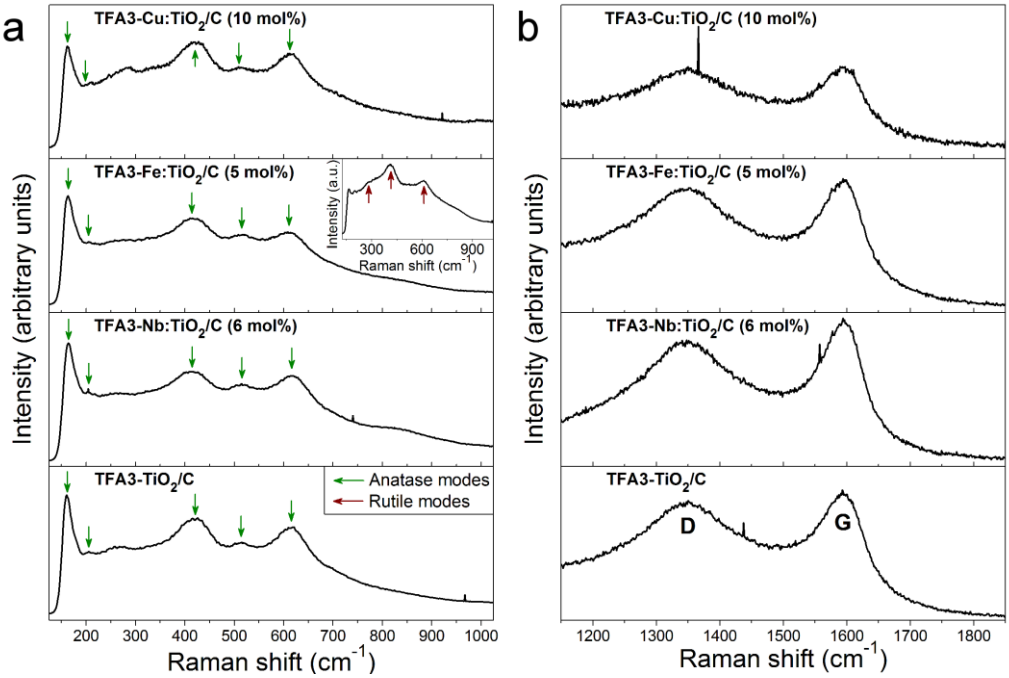

Figure 4.7 Raman spectra of the TFA3-TiO_2/C samples for both (a) the TiO_2 lattice vibration region and (b) the spectral region containing the *D*/*G* bands of amorphous carbon. Isolated regions of the TFA3-Fe:TiO_2/C (5 mol%) contain intense vibrational modes that correspond to rutile TiO_2 (a, inset). The intensity of the D/G bands only differs for the sample that contains Cu.

4.3.2.2 Analysis of Morphology and Surface Texture of the TFA3-TiO_2/C Materials

Analysis of the morphology via SEM yields insights into both the pore structure and the location of crystallites present in the TFA3-TiO_2/C materials. Figure 4.8 presents a set of lower magnification images that show the ordered network of macropores present in all the TFA3-TiO_2/C samples. Much like the cases of TFA- and TFA2-TiO_2/C, some distortions are present in the 3DOM network, but an interconnected pore structure exists throughout the sample. At higher magnifications (Figure 4.9), crystallites are spotted in the samples. These crystallites are observed on the surface of the 3DOM network in the TFA3 composites. Calculations of the anatase crystallite size using the Scherrer equation (Table 4.3) show that crystallite size in all the samples is similar. TFA3-Fe:TiO_2/C (5 mol%) has a slightly larger average anatase crystallite size (and also rutile crystals), and these grains are easily resolved in the SEM micrographs (see inset in Figure 4.10 c). For TFA3-Cu:TiO_2/C (10 mol%), spherical objects that extend over tens of nm and even micrometer-scale rods are found, albeit infrequently, across the sample. Judging from the narrow Cu reflections in PXRD pattern and the fact that Cu sinters readily at elevated temperatures,[57] these objects are Cu crystallites trapped in the 3DOM TiO_2/C network. It is unclear if the anisotropic rods were formed because the Cu melted (due to the small size of Cu nuclei) and underwent liquid phase sintering.[27] Even with the addition of 10 mol% Cu, it does not appear that a percolation threshold has been reached that could be beneficial for the transport of electrons through the structure.

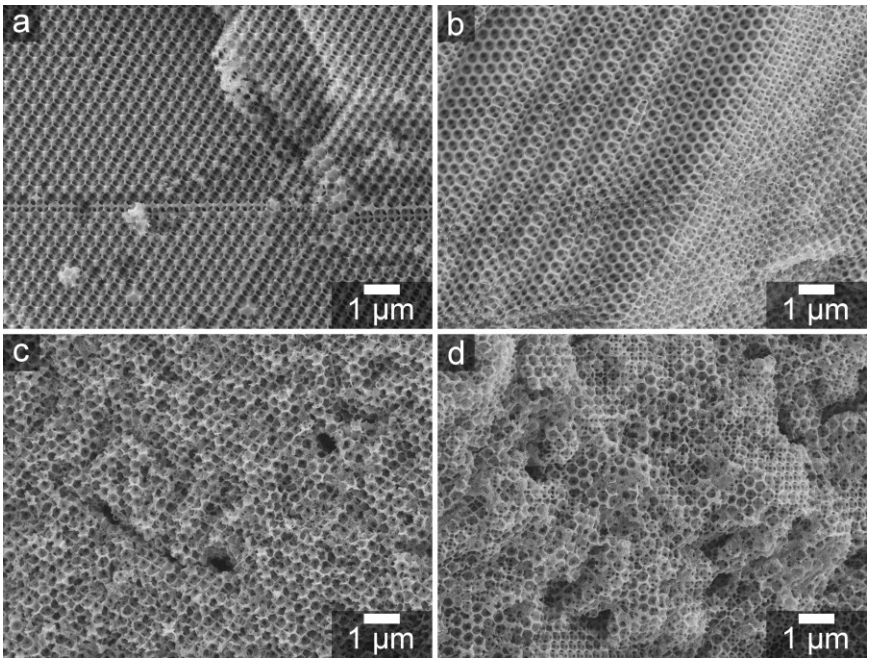

Figure 4.8 SEM micrographs of the TFA3-TiO_2/C (a), TFA3-Nb:TiO_2/C (b), TFA3-Fe:TiO_2/C (c), and TFA3-Cu:TiO_2/C (d). All samples possess a 3DOM structure, albeit with some disorder present.

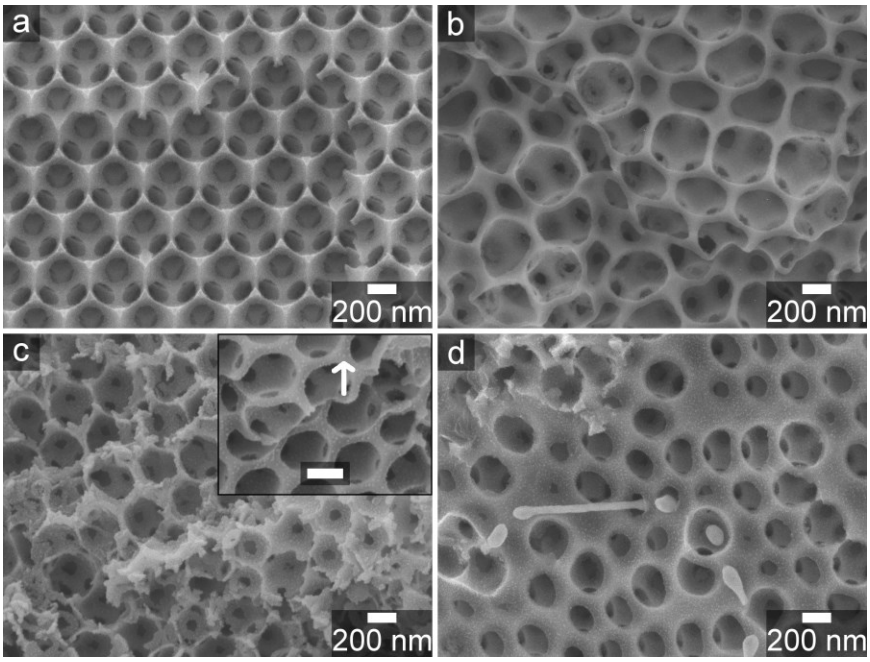

Figure 4.9 Higher magnification SEM micrographs of (a) TFA3-TiO_2/C, (b) TFA3-Nb:TiO_2/C, (c) TFA3-Fe:TiO_2/C, and (d) TFA3-Cu:TiO_2/C. Crystallites are not easily resolved for the TFA3-TiO_2/C and TFA3-Nb:TiO_2/C. Small crystallites are visible on the surface of TFA3-Fe:TiO_2/C (see white arrow in the inset). Much large crystals (the spoon-like structures in (d)) of Cu are scattered across the TFA3-Cu:TiO_2/C. The scale bar in the inset represents 200 nm.

Gas sorption isotherms were obtained for the TFA3-TiO_2/C samples, and these isotherms were used to determine BET surface areas and total pore volumes (Figure 4.10 and Table 4.3). The shape of the isotherms matches those of TFA- and TFA2-TiO_2/C. A very small hysteresis loop is observed for the isotherm from the undoped TFA3-TiO_2/C. Increases in the volume of gas adsorbed at low and high P/P_o (from micropores and macropores, respectively) are observed for all isotherms. Doping, at least in this case, does not lead to an increase the BET specific surface area or better preservation of the mesostructure when compared to the undoped sample. Since the size of the anatase TiO_2 changes little from sample to sample, this result is expected (Table 4.3).

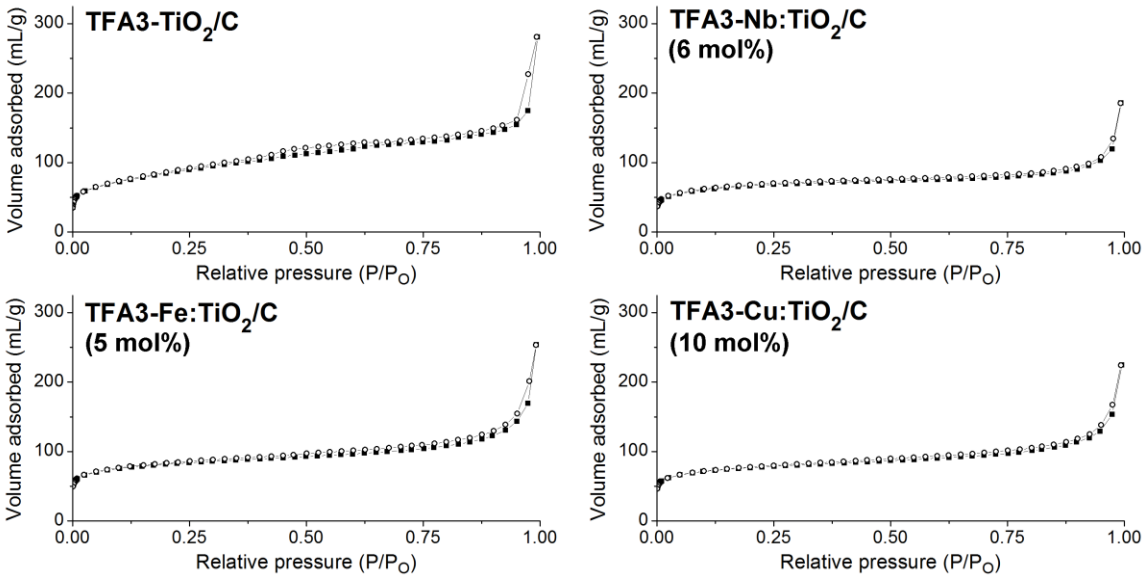

Figure 4.10 Nitrogen sorption isotherms for the undoped and doped TFA3-TiO_2/C samples. The isotherms resemble those of the TFA- and TFA2-TiO_2/C samples. Only limited hysteresis is observed.

4.3.2.3 Concluding Remarks

For the materials made using the TFA3-based precursor, no significant structural changes are observed in the doped composites that could potentially improve their lithium insertion/extraction properties. Consequently, these materials were not tested any further. For Fe and Cu, increases in the crystallite size and phase separation (respectively) are not favorable for any end use as an anode material. When this is coupled with the observation that the G band intensity is essentially unchanged with respect to the undoped material, continued studies are unwarranted. The use of Nb as a dopant is revisited later for the acac-TiO_2/C system. A related dopant, Ta, is explored for the TFA- and TFA2-TiO_2/C systems, and is discussed below.

4.3.3 Tantalum Doping of TFA-TiO_2/C and TFA2-TiO_2/C

Tantalum has, to the best of this author's knowledge, not been explored as a potential dopant for TiO_2 anodes in lithium ion battery applications. In many ways, this is fairly surprising. Studies have revealed that Ta can decrease the resistivity of TiO_2 by over two orders of magnitude through the generation of conducting electrons.[60] Since Ta-doped TiO_2 can be synthesized as a conductive, transparent film, it is a potential candidate to replace indium tin oxide.[60] Indeed, a recent computational study showed that doping with Ta steadily improves the electronic conductivity of TiO_2 up to 12.5 mol% Ta.[61] Coincidentally, this is close to the solubility limit of Ta in TiO_2, since $TiTa_2O_7$ begins to form at around 10 to 15 mol% doping.[62] TFA- and TFA2-

TiO_2/C precursors are stable (for many weeks) up to at least 12.5 mol% doping with Ta (by stoichiometry of the metal alkoxides), so these precursor systems serve as an excellent test bed for doping in porous TiO_2/C composites. Due to the relatively high levels of doping possible in the system, the hypothesis is that doping with Ta can also effectively limit crystal growth, which is quite severe in TFA- and TFA2-TiO_2/C. As is discussed in this section, the hypothesis is supported at certain doping levels, but not at others. The final pyrolysis temperature used for materials discussed in this section is fixed at 800 °C, which was the optimum for maximizing Li insertion/extraction in acac-TiO_2/C (see Chapter 3).

4.3.3.1 SEM Characterization of Ta-Doped Samples

Undoped TFA- and TFA2-TiO_2/C contains TiO_2 crystallites agglomerated on the surface of the 3DOM network, and unfortunately, the same problematic localization of crystallites occurs with the Ta-doped composites. However, some improvements are observed as a result of higher levels of doping. As was reasonably anticipated, colloidal crystal templating was successful when the TFA- and TFA2-Ta:TiO_2/C precursors were used. Figure 4.11 shows that all doped composites possess the 3DOM structure, irrespective of the amount of Ta added. At higher magnifications (Figure 4.12) it is clear that a high density of doped TiO_2 crystals is present on the surface of the 3DOM network. When qualitatively comparing the grain size for TFA-Ta:TiO_2/C (3.125 mol%) and TFA-Ta:TiO_2/C (12.5 mol%), it is observed in Figure 4.13 that the composite with higher mol% of dopant contains smaller grains. Generally, as the concentration of a dopant increases in an oxide, solute drag (or a change in grain boundary energetics) should increasingly restrict crystallite growth (as long as phase separation does not occur, see Chapter 7 for more examples).[19] By comparing TFA-Ta:TiO_2/C (12.5 mol%) and TFA2-Ta:TiO_2/C (12.5 mol%) the changes caused by an increase in the weight percent of carbon can be observed (Figure 4.13). Crystallites with dimensions greater than 10 nm are visible on the TFA-Ta:TiO_2/C (12.5 mol%), but crystallites of doped TiO_2 are barely visible in the TFA2-Ta:TiO_2/C (12.5 mol%). This is different from the undoped TFA- and TFA2-TiO_2/C, since crystal growth is far more severe in the latter. More on this contrasting situation is discussed below.

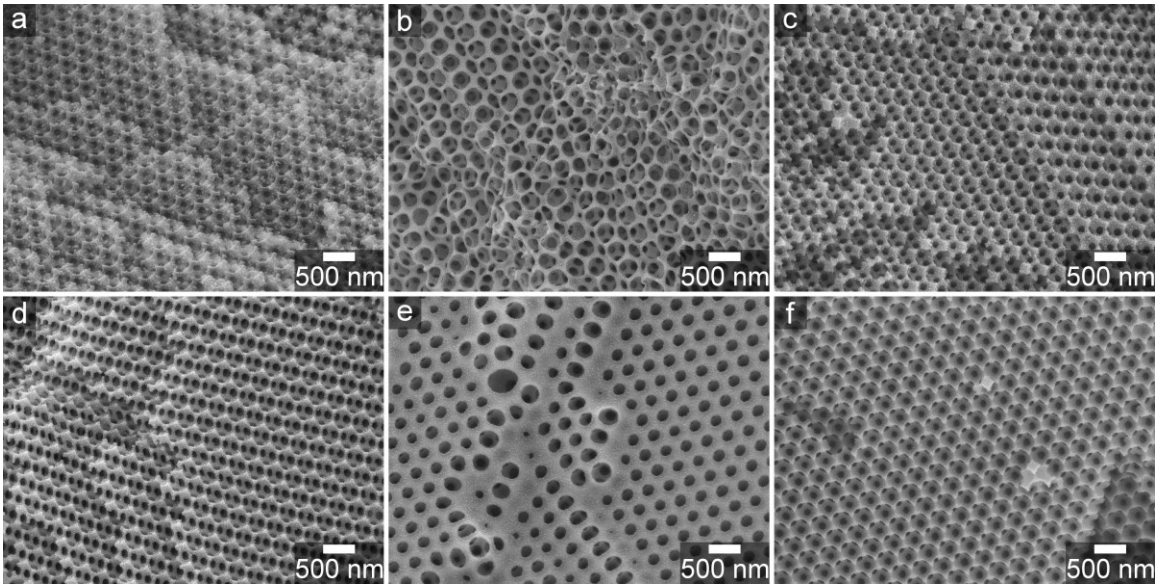

Figure 4.11 SEM micrographs for the six tantalum-doped composites investigated in this section: (a) TFA-Ta:TiO_2/C (3.125 mol%), (b) TFA-Ta:TiO_2/C (6.25 mol%), (c) TFA-Ta:TiO_2/C (9.375 mol%), (d) TFA-Ta:TiO_2/C (12.5 mol%), (e) TFA2-Ta:TiO_2/C (6.25 mol%), and (f) TFA2-Ta:TiO_2/C (12.5 mol%).

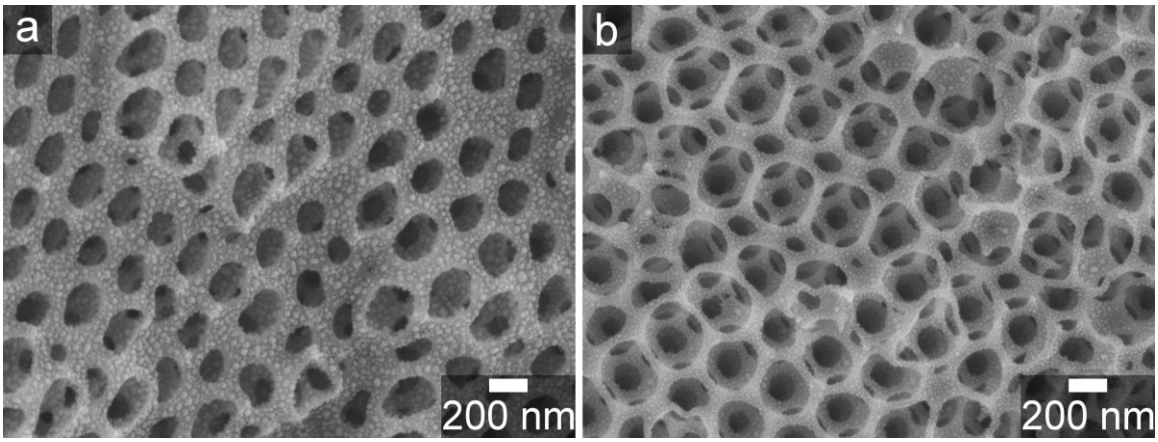

Figure 4.12 SEM micrographs of (a) TFA-Ta:TiO_2/C (3.125 mol%) and (b) TFA-Ta:TiO_2/C (12.5 mol%) at higher magnification than those shown above. The size of the doped TiO_2 crystallites decreases with increasing Ta content.

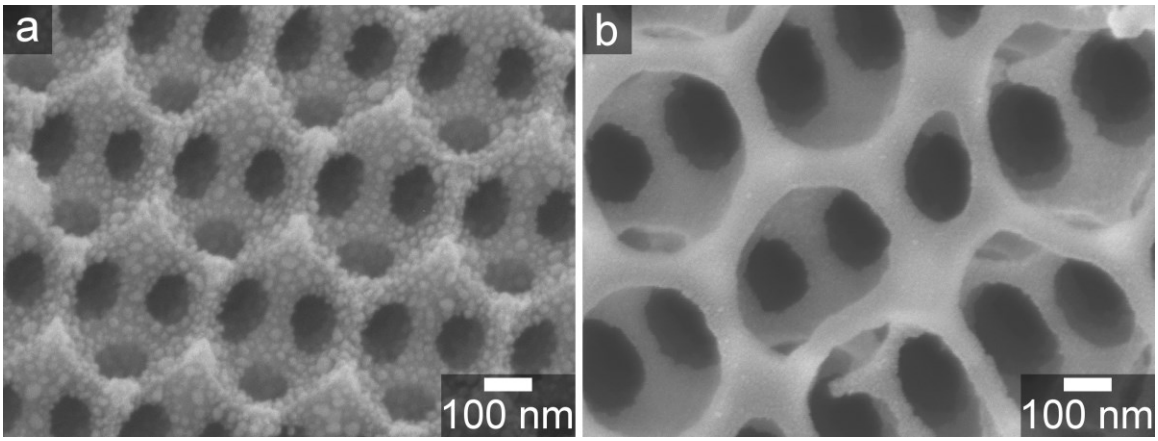

Figure 4.13 SEM micrographs of (a) TFA-Ta:TiO_2/C (12.5 mol%) and (b) TFA2-Ta:TiO_2/C (12.5 mol%) taken at high magnification to show the size/location of crystallites. In this case, the additional carbon content in the TFA2-Ta:TiO_2/C sample effectively stops crystallite growth.

4.3.3.2 Analysis of the Ta-Doped TiO_2 Phase by X-Ray Diffraction and Raman Spectroscopy

With the SEM micrographs revealing differences in crystallite size between samples, PXRD was conducted so that an average crystallite size could be calculated, and to identify the crystal polymorphs present in the materials. The latter aim of the analysis yielded a rather unexpected result. While the PXRD patterns (Figure 4.14) do not contain reflections that can be matched to pure Ta_2O_5 or $TiTa_2O_7$, these patterns contain relatively intense reflections that originate from rutile TiO_2. In Chapter 3, it was observed that the TFA-TiO_2/C pyrolyzed at 800 °C contains a limited amount of the rutile polymorph. Aliovalent dopants with a higher oxidation state than TiO_2 should delay the transformation of anatase to rutile, since these dopants should lead to the formation of reduced titanium or titanium vacancies as a primary defect, not oxygen vacancies.[30,62] Ruiz, et al. provided evidence that a similar dopant, Nb, segregates to the surface of doped anatase TiO_2, and this impedes both sintering and the ionic diffusion required for the transformation.[63] However, the complete opposite is observed here; the patterns for the heavily-doped TFA-Ta:TiO_2/C (12.5 mol%) and TFA2-Ta:TiO_2/C (12.5 mol%) contain a greater weight fraction of rutile than anatase (Table 4.4). Even samples with intermediate levels of the dopant contain much stronger rutile reflections than the undoped TFA-TiO_2/C.

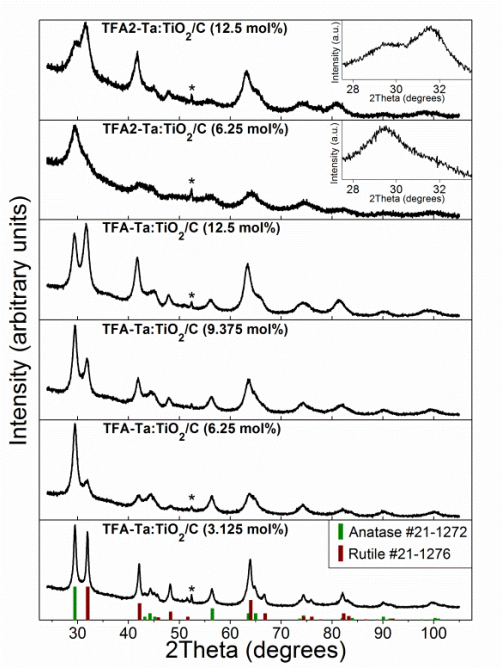

Figure 4.14 PXRD patterns of all the Ta-doped samples. The intensities of the rutile reflections generally increase as the content of Ta increases. The asterisk denotes a reflection from the Al sample holder.

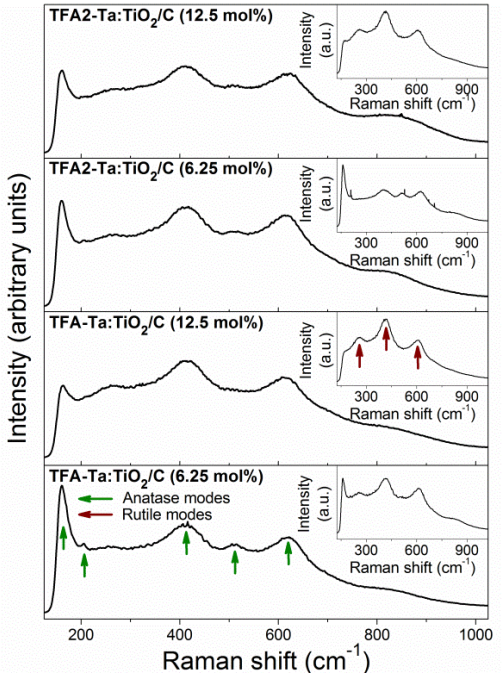

Figure 4.15 Raman spectra of the TFA- and TFA2-Ta:TiO_2/C doped at 6.25 mol% and 12.5 mol%. Anatase vibrational mode positions are indicated with green arrows and the rutile positions are indicated with red arrows. Insets show spectra that are found only in select areas across the samples.

Table 4.4 Selection of relevant structural parameters of the Ta-doped samples.

sample[a]	weight fraction anatase[b]	weight fraction rutile[c]	anatase crystallite size (nm)	rutile crystallite size (nm)	BET surface area (m^2/g)	pore volume (cm^3/g)
TFA-TiO_2/C, Undoped	[d]	[d]	11.5	[e]	451	0.46
TFA-Ta:TiO_2/C, (3.125 mol%)	0.46	0.537	11.9	16.8	461	0.63
TFA-Ta:TiO_2/C, (6.25 mol%)	0.775	0.225	8.8	11.7	430	0.60
TFA-Ta:TiO_2/C, (9.375 mol%)	0.597	0.403	8.5	12.8	331	0.57
TFA-Ta:TiO_2/C (12.5 mol%)	0.393	0.607	7.8	10.8	428	0.57
TFA2-TiO_2/C, Undoped	0	1.00	[e]	35.2	647	0.63
TFA2-Ta:TiO_2/C, (6.25 mol%)	0.673	0.327	4.2	5.3	451	0.43
TFA2-Ta:TiO_2/C, (12.5 mol%)	0.314	0.686	4.5	6.1	430	0.36

[a] All materials pyrolyzed at 800 °C for 2 h.

[b] Calculated using: $W_A = 1/[1+1.26\cdot(I_R/I_A)]$. W_A is the weight fraction of anatase, I_R is the intensity of the rutile (110) peak, and I_A is the intensity of the anatase (101) peak. Method from [47].

[c] Calculated using: $W_R = 1/[1+0.8\cdot(I_A/I_R)]$. W_R is the weight fraction of rutile, I_R is the intensity of the rutile (110) peak, and I_A is the intensity of the anatase (101) peak. Method from [47].

[d] Rutile is present as a minor phase, but the (110) peak cannot be adequately fit.

[e] Peaks cannot be adequately fit, so crystal size was not determined.

To explain this contradictory finding, it is necessary to consider the effect of the carbonaceous phase. As the PF sol is converted into amorphous carbon, reducing gases are released. In addition, the carbon phase itself can act as a reducing agent. While Ta can potentially delay the phase transformation from anatase to rutile in TiO_2, the reducing agents present during pyrolysis of the composite react with the doped TiO_2 to generate oxygen vacancies (equation 4.1).

$$O_O^x \rightleftarrows V_O^{\cdot\cdot} + 2e' + \frac{1}{2} O_2 \quad (4.1)$$

The appearance of rutile suggests that the Ta-doped TiO_2 is much easier to reduce than the undoped samples, leading to greater concentration of oxygen vacancies in the doped sample. Enhanced reducibility is also observed in Nb-doped TiO_2, since the equilibrium constant for oxygen vacancy formation substantially higher at 800 °C in Nb-doped versus undoped TiO_2.[64] In a severely reducing environment, like what should be present during pyrolysis of the Ta:TiO_2/C, the concentration of oxygen vacancies in Nb-doped TiO_2 steadily increases as $p(O_2)$ is decreased. From a standpoint of the oxidation state, preferred coordination, and ionic radius, Nb behaves quite similar to Ta, so it is reasonable to assume that a similar defect chemistry is present.[65,66] This bolsters the case that changes to the thermodynamics of defect formation are responsible for the increased fraction of rutile in the doped samples. It also explains why the weight fractions of rutile in the TFA2-Ta:TiO_2/C samples are greater than those of the corresponding TFA-Ta:TiO_2/C samples (Table 4.4). More carbon is present in the TFA2-Ta:TiO_2/C, which will lower the $p(O_2)$ and induce greater oxygen vacancy formation.

Returning to one of the original objectives of the PXRD analysis, the Scherrer equation was used to estimate the crystallite size of both the anatase and rutile phases in the doped samples (Table 4.4). As the dopant concentration is increased for the TFA-Ta:TiO_2/C materials, the crystal size of the anatase decreases. It appears that the presence of Ta interferes with the sintering of anatase crystallites, perhaps by solute drag, altered grain boundary energetics, or changes to the transport of species in the lattice.[18] For the TFA-Ta:TiO_2/C (12.5 mol%), the size of the crystallites approaches what is estimated for the acac-TiO_2/C, even though the crystallites are localized on the surface of the 3DOM network. Unfortunately, larger rutile crystallites are present in the TFA-Ta:TiO_2/C, as a consequence of the phase transformation. When the doping level is low in TFA-Ta:TiO_2/C (3.125 mol%), rutile crystal growth is fairly severe, and crystallites are larger than those present in the undoped TFA-TiO_2/C. The low level of Ta promotes the phase transformation to rutile, but the dopant cannot adequately restrict crystal growth of the rutile. The TFA2-Ta:TiO_2/C samples have smaller crystallites than the TFA-Ta:TiO_2/C, and have much smaller crystallites than those present in the undoped TFA2-TiO_2/C. Even though a

transformation to rutile is facilitated by Ta, the dopant restricts grain growth to a considerable extent. It may also be that the separation of the chelated metal alkoxide precursors to the interface with the hard template occurs to a lesser extent in this system. This would allow for greater confinement in the carbon phase, and much less sintering. One last fascinating observation is that the average crystal size for the rutile grains in TFA2-Ta:TiO_2/C (12.5 mol%) is below the critical size (~11 nm) at which point rutile becomes the thermodynamically stable polymorph. Currently, it is unclear if this occurs due to a change in the surface energetics of the Ta-doped TiO_2, or is perhaps induced by nanoscale phase separation at the surface of the crystallites (as is observed for Nb).[67]

Since the appearance of the rutile polymorph is a key structural difference between the doped and undoped composites, Raman microscopy was conducted on select samples to confirm the presence of this polymorph. This technique also provided more information on the heterogeneity of the two polymorphs, anatase and rutile, in the composites. Figure 4.15 shows spectra for four samples, TFA- and TFA2-Ta:TiO_2/C doped at either 6.25 mol% and 12.5 mol% with Ta. For the materials with only moderate levels of doping, the E_g, B_{1g}, and A_{1g}/B_{1g} of the anatase polymorph are fairly intense across the samples. There are areas where the strong E_g mode centered near 150 cm^{-1} decreases considerably in intensity. The vibration near 400 cm^{-1} also shifts due to the developing rutile E_g mode (see inset in Figure 4.15 for TFA-Ta:TiO_2/C (6.25 mol%)). These areas are far more common for the TFA2-Ta:TiO_2/C (6.25 mol%), which is expected since the weight percent of carbon is greater. It is clear that rutile is indeed present at 6.25 mol% doping with Ta, but is not a major phase and is not evenly distributed. When doping is increased to 12.5 mol%, the anatase modes lose intensity across the totality of the samples. Regions with extremely strong rutile vibrations are significantly more frequent (see insets in Figure 4.15). Again, this behavior is reflective of the increased amount of rutile that was also detected via PXRD.

4.3.3.3 Textural Properties of Ta-Doped Samples

Finally, a combination of gas sorption and SAXS was used to determine the impact that the dopant had on the textural properties of the composites, including the presence of any mesopores. The nitrogen sorption isotherms (Figure 4.16) do not provide evidence that the addition of Ta allows for retention of a mesostructure. Little or no hysteresis is observed in the isotherms; changes in volume adsorbed/desorbed are observed in pressure ranges that correspond to sorption in micro-/macropores. Since the crystallite sizes in the samples (via PXRD line broadening) are still above ~ 5 nm, it is not entirely surprising that hysteresis is not observed. Even for the

undoped TFA-TiO_2/C, hysteresis is weak for the composites pyrolyzed at 500 °C, and is non-existent at 700 °C (crystallite sizes are above 5 nm at this point). Growing crystallites appear to disrupt the mesopore network for these doped composites as well. However, the combination of micro- and (to a lesser extent) macroporosity affords these doped materials with BET specific surface areas in excess of 300 m^2/g (Table 4.4). These specific surface areas are fairly similar to undoped TFA-TiO_2/C and TFA2-TiO_2/C. No real pattern in the BET surface area of these materials can be discerned, suggesting that doping does little to change the surface area. It is likely that microporosity in the carbon phase is the major contributing factor to the surface area.[49] Pore volumes are also similar to the undoped composites. With this all taken into consideration, SAXS patterns were obtained for the TFA- and TFA2-Ta:TiO_2/C samples most likely to possess a mesostructure, e.g. those with 12.5 mol% of dopant. Figure 4.17 shows the patterns, and little evidence of a mesostructure is present. For the TFA2-Ta:TiO_2/C, the material with the smaller crystallite size, a very broad and weak feature is present from ~1 to 1.5 °2θ. This may be from a remnant of the mesopore network in this material.

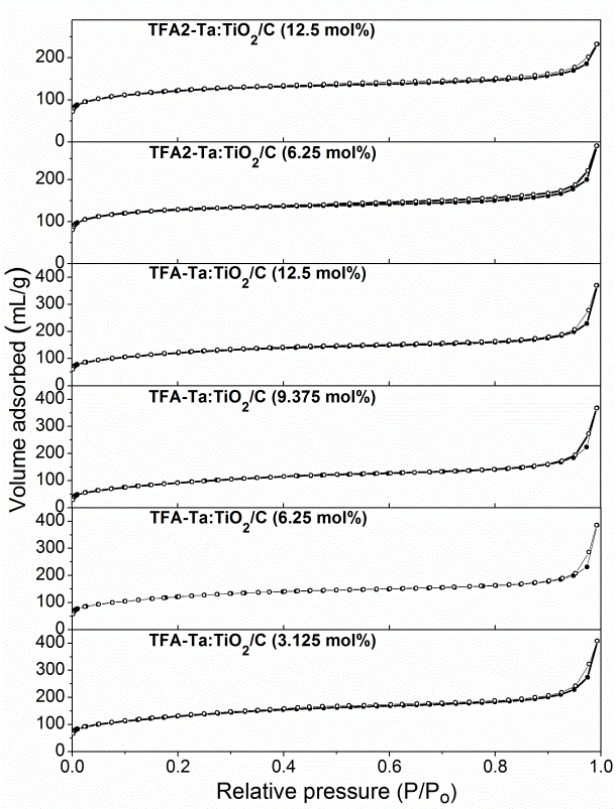

Figure 4.16 Nitrogen sorption isotherms for the Ta-doped samples. The isotherms obtained from the samples are similar to their undoped counterparts. Rises in the volume of N_2 adsorbed/desorbed occur at low and high relative pressure.

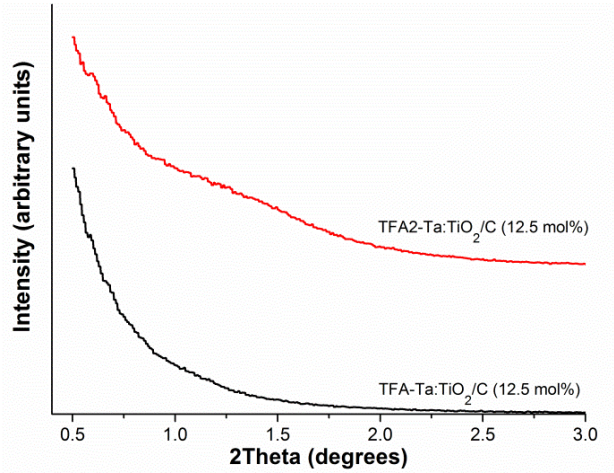

Figure 4.17 SAXS patterns for the most heavily-doped composites. No peak is observed for the TFA-Ta:TiO_2/C (12.5 mol%). A shoulder appears for the TFA2-Ta:TiO_2/C (12.5 mol%), but it has low intensity.

4.3.3.4 Concluding Remarks

While some advantages were realized through doping with Ta in the TFA-Ta:TiO_2/C, the doping does not change the location of the oxide crystallites in the composites and considerable sintering of the oxide phase still occurs. In the TFA-Ta:TiO_2/C composites, crystallites are located on the surface of the 3DOM network. By increasing the concentration of Ta in the precursor, the size of the crystallites is decreased and the amount of the rutile phase increases. For the TFA2-Ta:TiO_2/C composites, the synergistic effects of the confining carbon phase and the dopant are extremely effective at reducing crystallite size. Despite reductions in the size of the doped crystallites for both the TFA- and TFA2-Ta:TiO_2/C composites, the BET surface areas are unchanged. Mesoporosity is not detected for the composites. Nevertheless, these doped systems may have potential utility in other applications, and can also be calcined to form relatively high surface area 3DOM Ta:TiO_2 materials.

4.3.4 Structural and Electrochemical Characterization of Doped acac-TiO_2/C Composites

Due to the improved capacity for lithium ion insertion and extraction in the acac-TiO_2/C, as described in Chapter 3, a study of doping was undertaken for this precursor system. Nb and Ta were chosen as dopants to reduce crystallite size and improve electronic conductivity of the TiO_2 phase.[5,60] Ni was selected to improve capacities at high rates and to perhaps aid in the catalytic graphitization of the composite.[43,68] A pyrolysis temperature of 800 °C was selected, because the highest capacities were obtained for the acac-TiO_2/C pyrolyzed at that temperature. Although some of the hypothesized changes to the structure of the composites were realized, increases to insertion and extraction capacities were not realized. Capacities decrease for the Nb and Ta

samples and are essentially unchanged for the Ni doped sample. The structural features (and changes) in the doped composites are discussed first in this subsection, and this is followed by a discussion of their lithiation/delithiation properties.

4.3.4.1 Analysis of the Anatase and Rutile Polymorphs Present in the Doped acac-TiO_2/C Samples

Both the polymorphs of TiO_2 (and Ni) present in the composites and their estimated crystallite sizes were determined via PXRD (Figure 4.18). For both the Ta and Nb-doped composites, reflections that match the anatase and rutile polymorphs are present. As discussed in the previous section, doping with Nb changes the thermodynamics for oxygen vacancy formation.[64] In the reducing agent-rich environment generated during pyrolysis, oxygen vacancies are readily formed and the transformation to rutile can occur. Tantalum, with its similar oxidation state and ionic radius,[65] is presumed to have a similar effect on oxygen vacancy formation, and this is confirmed with the appearance of rutile TFA-/TFA2-Ta:TiO_2/C materials. Interestingly, the acac-Ta:TiO_2/C (6.5 mol%) has an increased content of the rutile polymorph when compared to the acac-Nb:TiO_2/C (6.5 mol%) (Table 4.5). This suggests that more oxygen vacancies develop in the Ta-doped sample than the Nb-doped sample, which may be from subtle differences between the defect thermodynamics in the materials. When compared to TFA-Ta:TiO_2/C (6.25 mol%), acac-Ta:TiO_2/C (6.5 mol%) has a greater weight percent of rutile because of both increased Ta and carbon content. While rutile is present in both acac-Nb:TiO_2/C (6.5 mol%) and acac-Ta:TiO_2/C (6.5 mol%), phase separation of a niobate/tantalate ($TiNb_2O_7$ or $TiTa_2O_7$) or another oxide (i.e. Nb_2O_5 or Ta_2O_5) does not occur. When nickel(II) chloride is added to the precursor, the pyrolyzed composite, acac-Ni:TiO_2/C (5 mol%), contains particles of nickel metal. Much like the copper-doped TFA3-Cu:TiO_2/C material described earlier and an earlier report on the inclusion of nickel in a carbon-containing 3DOM material,[68] the highly reducing conditions of pyrolysis are capable of causing phase separation. Crystallite sizes for the two successfully doped composites, acac-Nb:TiO_2/C (6.5 mol%) and acac-Ta:TiO_2/C (6.5 mol%) are slightly smaller than in the undoped composites (Table 4.5). Again, the crystallites of the rutile polymorph are larger than those of the anatase polymorph, mirroring what is observed for the TFA-Ta:TiO_2/C. These composites also provide evidence that doping with Nb and Ta can shift the phase transition from anatase to rutile below the critical crystallite size of 11 nm. For the acac-Ni:TiO_2/C (5 mol%), no change in the crystallite size is observed because the dopant phase separated.

Table 4.5 Selection of relevant structural parameters of the Ta-doped samples.

sample[a]	weight fraction anatase[b]	weight fraction rutile[c]	anatase crystallite size (nm)	rutile crystallite size (nm)	BET surface area (m^2/g)	pore volume (cm^3/g)
acac-TiO_2/C, undoped	[d]	[d]	8.4	[e]	428	0.50
acac-Nb:TiO_2/C, (6.5 mol%)	0.776	0.224	7.1	7.8	433	0.77
acac-Ta:TiO_2/C, (6.5 mol%)	0.670	0.330	7.2	7.6	421	0.76
acac-Ni:TiO_2/C, (5.0 mol%)	[d]	[d]	8.5	[e]	555	0.85

[a] All materials pyrolyzed at 800 °C for 2 h.

[b] Calculated via: $W_A = 1/[1+1.26\cdot(I_R/I_A)]$. W_A is the weight fraction of anatase, I_R is the intensity of the rutile (110) peak, and I_A is the intensity of the anatase (101) peak. Method from [47].

[c] Calculated using: $W_R = 1/[1+0.8\cdot(I_A/I_R)]$. W_R is the weight fraction of rutile, I_R is the intensity of the rutile (110) peak, and I_A is the intensity of the anatase (101) peak. Method from [47].

[d] Rutile is present as a minor phase, but the (110) peak cannot be adequately fit.

[e] Peaks cannot be adequately fit, so crystal size was not determined.

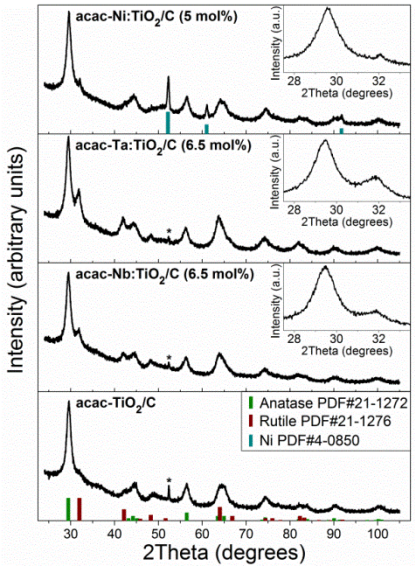

Figure 4.18 PXRD patterns for the doped acac-TiO_2/C samples and their undoped acac-TiO_2/C counterpart. All samples were pyrolyzed at 800 °C. The presence of Nb and Ta leads to the formation of an increasing amount of the rutile phase (see inset). In the doped composite containing Ni, Ni metal crystals phase separate from the TiO_2. As always, the asterisk denotes a peak from the Al sample holder.

Alongside the PRXD data, Raman spectra obtained via confocal Raman microscopy provide a better indication of the distribution of the crystal polymorphs in the doped acac-TiO_2/C samples. Not surprisingly, anatase vibrations are found across the acac-Ni:TiO_2/C (5 wt%), as shown in Figure 4.19. Since incorporation of Ni into TiO_2 did not occur for acac-Ni:TiO_2/C (5 wt%), the similarity of its Raman spectra to those of the undoped acac-TiO_2/C is expected. Vibrational modes belonging to rutile TiO_2 are present in the acac-Nb:TiO_2/C (6.5 mol%) and the acac-Ta:TiO_2/C (6.5 mol%) (see insets in Figure 4.19). However, areas with strong rutile modes are heterogeneously distributed across the composites. This finding is also observed in the undoped composite (see Chapter 3 for an analysis). Untemplated surface "crusts," or other defective regions that do not provide confinement may be responsible for the heterogeneity in the polymorph. Heterogeneities also may arise from subtle fluctuations in the concentration of the dopant.

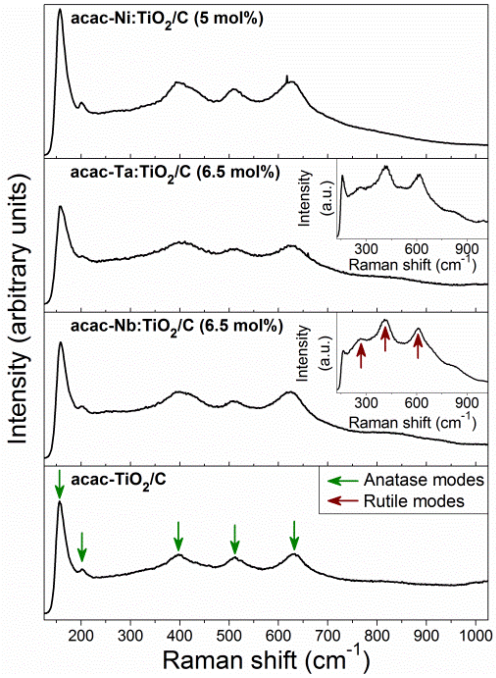

Figure 4.19 Raman spectra of the doped acac-TiO_2/C samples and their undoped acac-TiO_2/C counterpart. All samples were pyrolyzed at 800 °C. Spectra from both the acac-TiO_2/C and the acac-Ni:TiO_2/C (5 mol%) primarily display the characteristic vibrations of the anatase crystal structure. When Nb or Ta is used as a dopant, areas of the samples can be found that contain strong rutile vibrations.

4.3.4.2 Analysis of the Morphology and Crystallite Size of the Doped acac-TiO_2/C

While doping can impact the TiO_2 phase and even lead to the formation of a third phase (Ni) in the composite, electron micrographs show that little is changed from the standpoint of overall morphology. For example, SEM micrographs (Figure 4.20) show that with the exception of some disorder, which is typical for these syntheses, the 3DOM network is successfully produced in the doped acac-TiO_2/C composites. One difference can be observed in the acac-Ni:TiO_2/C (5 mol%), however. Figure 4.21 shows that spherical particles are distributed across the surface of the 3DOM structure. By examining the line broadening the peaks of Ni phase (or lack thereof) in the XRD, it is clear that the particles of Ni metal have a substantially larger size than the TiO_2. The particles observed in Figure 4.22 are from the Ni phase dispersed in the TiO_2/C. While particles of nickel can be easily visualized via SEM, TEM micrographs (Figure 4.23 and Figure 4.24) show the location of TiO_2 crystallites in the composites. When comparing the doped to the undoped samples, there is no discernable difference in the location of the crystallites. As explained in Chapter 3, the acac chelated transition metal precursors (Ti, Nb, and Ta) participate in intermolecular interactions with the solvents and other components present in the precursor. This allows the crystallites to be well-distributed throughout the 3DOM structure. The crystallites are all qualitatively similar in size (Figure 4.24), which matches the data gathered via Scherrer equation.

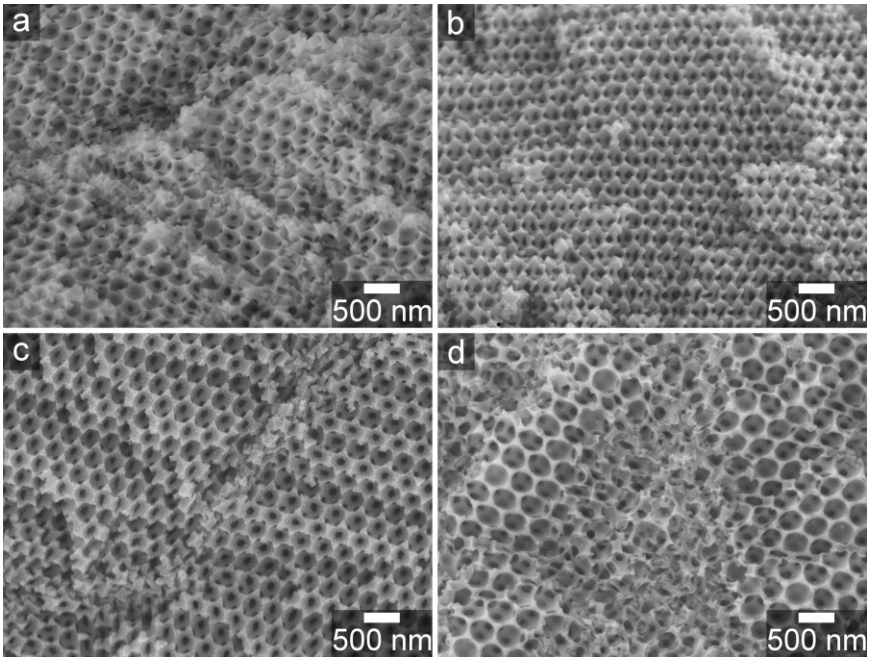

Figure 4.20 SEM micrographs of (a) undoped acac-TiO_2/C, (b) acac-Nb:TiO_2/C (6.5 mol%), (c) acac-Ta:TiO_2/C (6.5 mol%), and (d) acac-Ni:TiO_2/C (5 mol%).

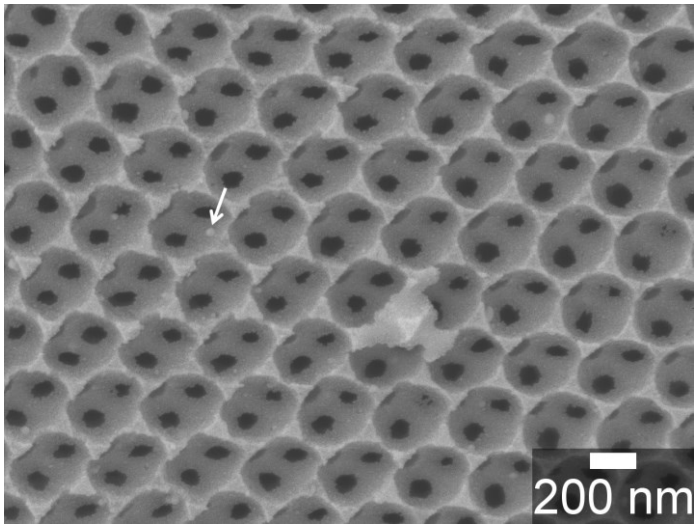

Figure 4.21 Higher magnification SEM micrograph of acac-Ni:TiO_2/C (5 mol%). The white arrow points at a nickel particle.

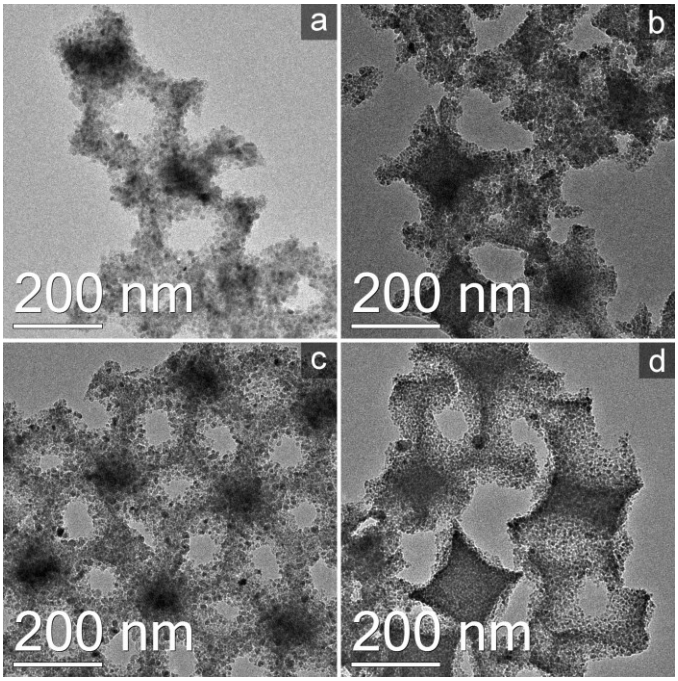

Figure 4.22 TEM micrographs of (a) undoped acac-TiO_2/C, (b) acac-Nb:TiO_2/C (6.5 mol%), (c) acac-Ta:TiO_2/C (6.5 mol%), and (d) acac-Ni:TiO_2/C (5 mol%). Crystallites are distributed throughout the 3DOM structure, since a relatively hydrophilic precursor for TiO_2 is present. Images taken by Stephen Rudisill.

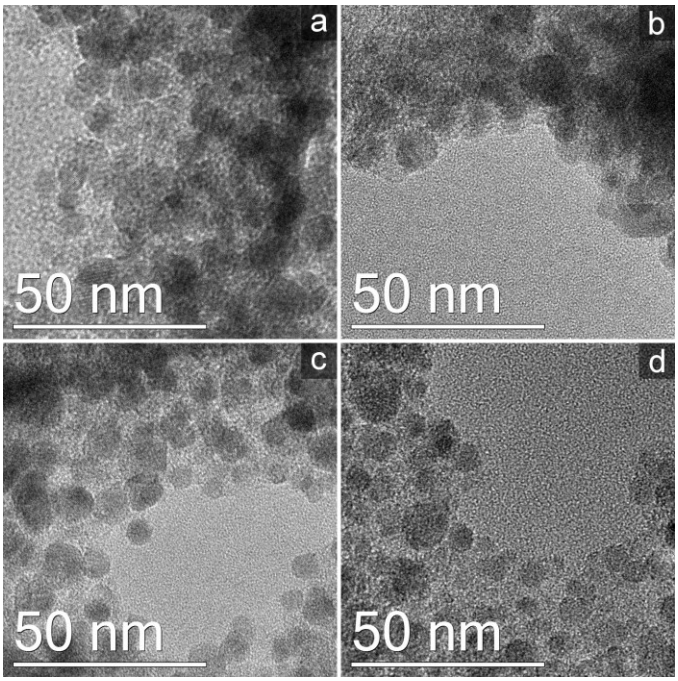

Figure 4.23 Higher magnification TEM micrographs of (a) undoped acac-TiO_2/C, (b) acac-Nb:TiO_2/C (6.5 mol%), (c) acac-Ta:TiO_2/C (6.5 mol%), and (d) acac-Ni:TiO_2/C (5 mol%). Crystallites sizes are around 10 nm, which matches well with the Scherrer equation estimates. Images taken by Stephen Rudisill.

4.3.4.3 Sorption Analysis and Additional Analysis of the Carbon Phase

Textural properties of the composites were also determined via gas sorption analysis. The isotherms obtained from the doped and undoped acac-TiO_2/C materials are shown Figure 4.24. Qualitatively, these isotherms are fairly similar, and show that the materials contain both macropores and micropores. Mesoporosity, if present at all in these materials, is fairly limited, since only narrow hysteresis loops are found. Decreasing the crystallite size via doping appears to have limited impact on the overall mesostructure, but then again, the size of the crystallites is only reduced by roughly 1 nm. It may be that the weak hysteresis observed comes from mesopores present between crystallites, since no indication of a mesostructure can be observed in TEM images. In terms of BET specific surface areas for the composites, the surface areas are similar for the Nb-doped, Ta-doped and undoped materials (Table 4.5). Pore volume is higher for the doped samples, but it is not clear why this is the case. One difference that can be reasonably explained is the higher surface area for the acac-Ni:TiO_2/C (5 mol%). This material should undergo at least a limited amount of catalytic graphitization.[54,68] In the acac-Ni:TiO_2/C (5 mol%), a greater fraction of micropores develop in the material (see the increased volume adsorbed at low P/P_o in Figure 4.24 d) relative to the other components. An increase in microporosity typically accompanies carbonization reactions (e.g. reactions that remove heteroatoms and lead to

the growth of graphitic domains) at pyrolysis temperatures below 1000 °C.[69] So, the acac-Ni:TiO_2/C (5 mol%) should have larger graphitic domains. Raman spectroscopy provides evidence that this increased graphitization occurs, at least to a minor extent (Figure 4.25). The ratio of the carbon *D* band intensity to the carbon *G* band intensity (I_d/I_g) is higher in the acac-TiO_2/C (1.3) and lower for the doped acac-Ni:TiO_2/C (1.1). This also matches the trend in chapter 3 for the undoped acac-TiO_2/C, since the intensity of the *G* band increases dramatically when the pyrolysis temperature is changed from 800 °C to 900 °C. Not surprisingly, there are indications in the electrochemical cycling data that improved graphitization was achieved.

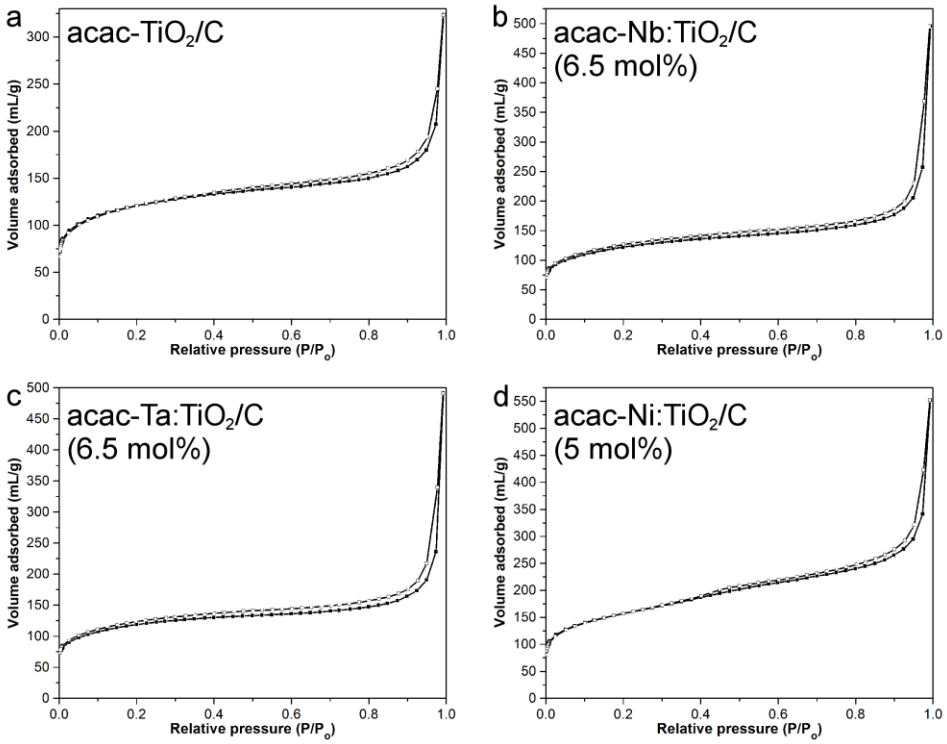

Figure 4.24 Nitrogen sorption isotherms for the acac-TiO_2/C materials (doped and undoped). Extremely narrow hysteresis loops are present in the isotherms. As is the case with the 3DOM TiO_2/C materials, steep rises in the volume of gas adsorbed occur at low and high relative pressures.

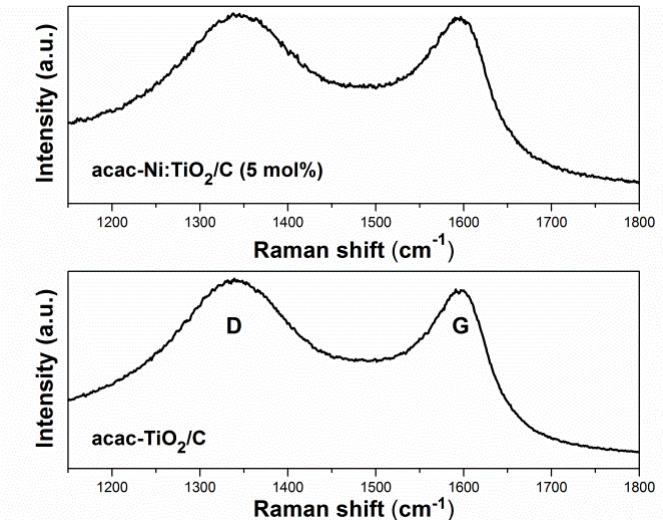

Figure 4.25 Raman spectra of the acac-TiO_2/C and acac-Ni:TiO_2/C (5 mol%) that show the *D*/*G* bands from amorphous carbon.

4.3.4.4 Characterization of the Li^+ Insertion/Extraction into Doped acac-TiO_2/C

While doping frequently leads to improvements in the insertion/extraction capacities for Li^+ relative to undoped electrode materials, the dopants explored in this study either cause a loss in capacity or improvements only at specific rates. Half cells containing the doped anode materials were assembled and then cycled following the same procedure used in Chapter 3 for the undoped acac-TiO_2/C. When comparing capacities of cells that contained the acac-Nb:TiO_2/C (6.5 mol%) and acac-Ta:TiO_2/C (6.5 mol%) with the acac-TiO_2/C, the cells with the doped composites had lower capacities than the undoped composite at all tested rates (Figure 4.26 a, b, c). For the acac-Ni:TiO_2/C (5 mol%), the capacity for Li^+ insertion/extraction exceeded that of the undoped material only at high rates. No obvious changes in the voltage profiles are noted from electrode material to electrode material (Figure 4.27). All these profiles contain plateaus centered near ~1.75 V vs. Li/Li^+ that originate from two phase intercalation into anatase, which during this process contains both a Li-rich orthorhombic phase and a Li-poor tetragonal phase.[33] The remainders of the profiles are sloped, which is most likely an overlay of lithiation/delithiation events in the carbon fraction and from a solid solution storage mechanism in small crystallites.[48,70] With the doped samples, the plateaus are noticeably smaller than undoped sample, which may indicate increased solid solution storage into the smaller crystallites and the rutile phase.[71]

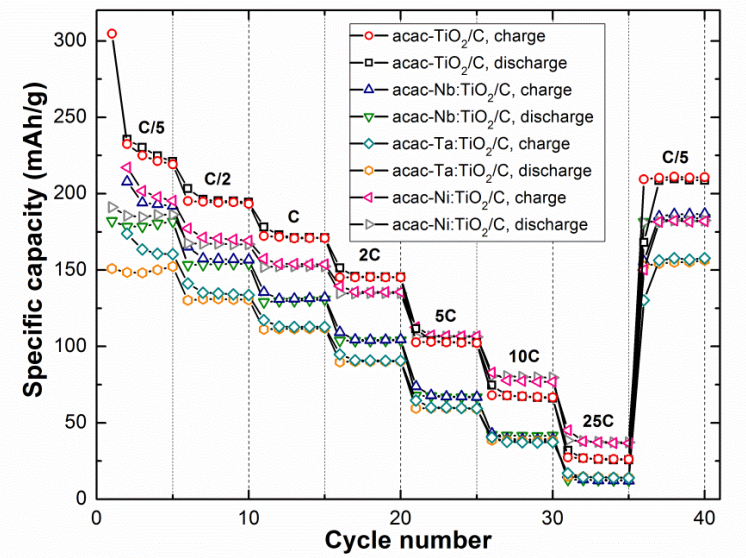

Figure 4.26 Rate performance data for the undoped and doped acac-TiO_2/C. The capacity of the composites doped with Nb or Ta are lower than the undoped acac-TiO_2/C. At high charge/discharge rates, the acac-Ni:TiO_2/C (5 mol%) has a greater capacity than the undoped acac-TiO_2/C. Specific currents and capacities were per the mass of the oxide present or per the mass of the TiO_2 and Ni.

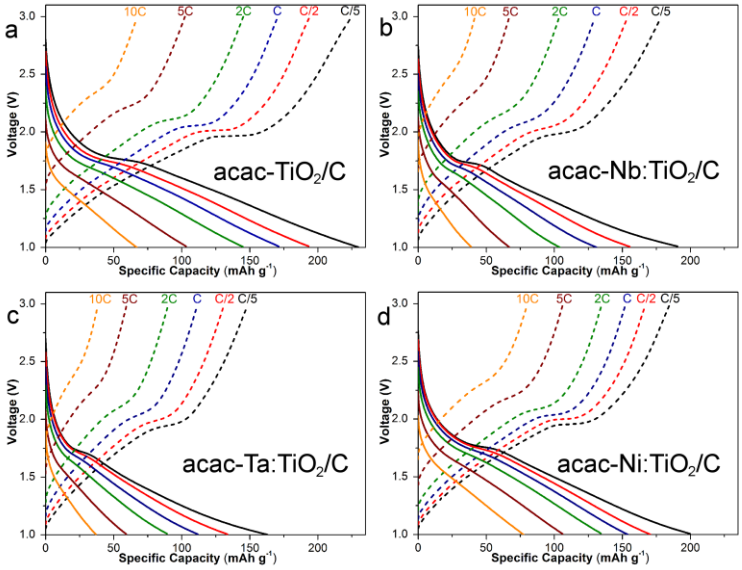

Figure 4.27 Voltage profiles for the undoped and doped acac-TiO_2/C. The profiles for all the electrodes made using these composites show small plateaus indicative of biphasic Li^+ insertion/extraction. A large solid solution regime is found in these profiles, as well.

A key question remains: why do the doped samples have lower capacity at most cycling rates? For the acac-Nb:TiO_2/C (6.5 mol%) and the acac-Ta:TiO_2/C (6.5 mol%), the appearance of rutile TiO_2 provides a clue as to the possible origin of the reduced capacity. As stated earlier, Nb and Ta should improve the electronic conductivity of the TiO_2 crystallites present in the electrodes. Unfortunately, the same phenomenon responsible for electronic conductivity improvement may have substantially curtailed the diffusion of Li ions.[72] In the case where the donor Nb or Ta dopant is added, electrons are generated as a compensating electronic defect via equation 4.2 or 4.3.

$$Nb_2O_5 + 2Ti \rightleftarrows 2Nb_{Ti}^{\cdot} + 2e' + \frac{1}{2}O_2 + TiO_2 \quad (4.2)$$

$$Ta_2O_5 + 2Ti \rightleftarrows 2Ta_{Ti}^{\cdot} + 2e' + \frac{1}{2}O_2 + TiO_2 \quad (4.3)$$

If hydrogen is used as a reductant for TiO_2, electrons are also produced. Maier and co-workers used hydrogen to reduce TiO_2 to differing extents.[73] His team subsequently checked the electronic conductivity and the lithium ion insertion/extraction capacity of TiO_2. When the reduction was carried out for a short time period (under 2 h in the conditions studied), electronic conductivity increased and so did the capacity. However, defect association reactions between Li^+ and e^- occur, which generates neutral lithium and curtails Li^+ diffusion (equation 4.4).[73]

$$Li_i^{\cdot} + e' \rightleftarrows Li_i^x \quad (4.4)$$

A balance is thus struck between the increasing electronic conductivity and the decreasing ionic mobility. For the reduction of TiO_2 with H_2, highly reduced samples have a low Li^+ ionic mobility.[73] This eliminates any advantage brought by the improved electronic conductivity, resulting in lower capacities for Li^+ insertion/extraction. The reduced capacity in the acac-Nb:TiO_2/C (6.5 mol%) and the acac-Ta:TiO_2/C (6.5 mol%) should come from a similar effect. During pyrolysis, the carbon component of the composite reduces the doped TiO_2 component. From prior analyses of the defect chemistry of Nb-doped TiO_2,[64] electrons should be generated in strongly reducing environments via incorporation of the dopant (equation 4.2 and 4.3) and also alongside oxygen vacancy formation (equation 4.1). While this improves electronic conductivity, lithium diffusivity is substantially reduced from combination of electrons with lithium ions (equation 4.4). Doping with Ta generates more intense reflections in the PXRD pattern from the rutile polymorph than does doping with Nb (Figure 4.19). This suggests a greater extent of reduction (more oxygen vacancies) in the case of doping with Nb. Since more electrons should be generated in this case, it is not surprising that the acac-Ta:TiO_2/C (6.5 mol%) has the lowest Li^+

insertion/extraction capacity of all materials tested. One final possibility for this behavior is that the rutile phase may be more resistive than the anatase phase, as reported by Zhang *et al*.[74]

In acac-Ni:TiO_2/C (5 mol%), an increase in capacity is observed at high charge/discharge rates relative to the undoped acac-TiO_2/C. After considering the structural differences between the two samples, it appears that an improvement in electronic conductivity of acac-Ni:TiO_2/C (5 mol%) contributed to the boost in capacities. Nickel separated from the TiO_2 and, as a consequence, the crystallite size of the TiO_2 fraction was not substantially altered. It is unlikely that structural changes to the TiO_2 are responsible for the improved Li^+ insertion/extraction behavior. Instead, the Raman and gas sorption data suggest that the carbonaceous component in acac-Ni:TiO_2/C (5 mol%) has a more graphitic character than the undoped composite. An additional minor component to capacity increase may come from the improved diffusion of Li^+ ions in the interface between the Ni crystals and the carbon framework.[75] Finally, it unclear why the capacity at low C-rates decreases more than expected for the acac-Ni:TiO_2/C (5 mol%) when compared to its undoped counterpart. A small drop should be expected in the capacity, since the inactive Ni phase is considered in the specific capacity. However, the capacity at C/5 is 10% lower in acac-Ni:TiO_2/C (5 mol%) when compared to the acac-TiO_2/C. Further research would be required to fully understand this discrepancy.

4.3.4.5 Concluding Remarks

Though two dopants (Nb and Ta) were successfully incorporated into the TiO_2 components of the composite materials, improvements in the Li^+ insertion/extraction capacities were not realized. The dopant (Ni) that phase separated, actually allowed for an improvement in the charge/discharge capacities at high rates. Structural characterization of the doped acac-TiO_2/C materials reveals similarities to the other composites described in this chapter and in Chapter 3. Donor dopants (Nb and Ta) accelerate the transformation to rutile and slightly reduce the crystallite size. Nickel, due to its phase separation, does little to change TiO_2 phase compared to the undoped acac-TiO_2/C. From a standpoint of morphology, the doped materials resemble the undoped acac-TiO_2/C. These materials contain a 3DOM structure, and also contain crystallites of TiO_2/doped TiO_2 that are well-distributed in the 3DOM network. Despite possessing favorable structural properties, the acac-Nb:TiO_2/C (6.5 mol%) and the acac-Ta:TiO_2/C (6.5 mol%) have lower capacities at all rates when compared to the undoped material. It is postulated that both the carbon component and the gases generated from it during pyrolysis cause the reduction of the Nb- and Ta-doped TiO_2. This reduction hinders the diffusion of Li^+ and lowers the capacity of the

doped electrodes. Improved graphitization of the carbon fraction in acac-Ni:TiO_2/C (5 mol%) is thought to cause the higher capacities attained at high charge/discharge rates for this anode material.

4.3.5 Structural and Electrochemical Characterization of 3DOM Ta:TiO_2

Since the 3DOM TiO_2 presented in Chapter 3 had the highest capacity at fast charge/discharge rate, it is logical to consider this electrode material for further improvement via doping. TFA-TiO_2/C can successfully and easily be doped with greater than 10 mol% of Ta, as is shown earlier in the chapter. By implementing the same pyrolysis and calcination procedures that were used for the 3DOM TiO_2, the Ta-doped counterparts to the 3DOM TiO_2 were synthesized. Restrictions to crystallite growth should occur, allowing for better retention of mesopore network. This procedure also avoids the problem of reducing the doped TiO_2, since the carbon phase is combusted during the calcination step. Interestingly, while the hypothesized changes to the structure of the doped 3DOM TiO_2 (denoted 3DOM Ta:TiO_2) are largely observed, the capacity of the half-cells that use the 3DOM Ta:TiO_2 are lower than the undoped 3DOM TiO_2. After a more detailed discussion of the characterization of the 3DOM Ta:TiO_2 (6.25 mol%) and 3DOM Ta:TiO_2 (12.5 mol%), this section closes with analysis of the electrochemical properties of these materials.

4.3.5.1 Characterization of the Crystal Structure of 3DOM Ta:TiO_2

As was the case with the TFA-Ta:TiO_2/C parent material, characterization of the crystal structure of the 3DOM Ta:TiO_2 samples was undertaken. From the PXRD patterns obtained from the doped materials (Figure 4.28), it is clear that the doping does not substantially change the observed pattern when compared to the 3DOM TiO_2. Neither $TiTa_2O_7$ or tantalum oxide phases are observed in the patterns of the 3DOM Ta:TiO_2. Tantalum is incorporated as a dopant and the resulting mixed oxides (either with 6.25 mol% or 12.5 mol% Ta, via the amount of precursor) display strong reflections characteristic of the tetragonal anatase phase. Spectra taken using a confocal Raman microscope also confirm the presence of anatase via the appearance of characteristic anatase vibrational modes (Figure 4.29). Since the final pyrolysis temperature is low for these materials and the carbon phase responsible for reduction is removed, rutile does not develop. However, reflections and vibrations from a TiO_2-B phase are present, and these are especially intense for the 3DOM Ta:TiO_2 (6.25 mol%). Considering that temperature for calcination is low, the presence of TiO_2-B is not unusual (see Chapter 3 for additional examples). The sizes of the crystallites in the doped TiO_2 materials are slightly smaller than their undoped

counterparts, as is expected from the results gathered from the Ta-doped composites. Raman spectra are also free of *D*/*G* bands (not shown) that emerge when amorphous carbon is present in the material.

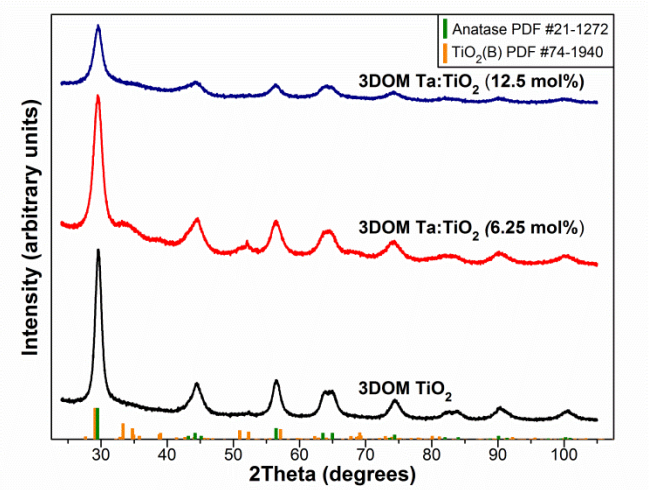

Figure 4.28 PXRD patterns of the two 3DOM TiO_2 samples doped with Ta. Reflections for TiO_2-B are stronger in the doped samples than for the undoped 3DOM TiO_2.

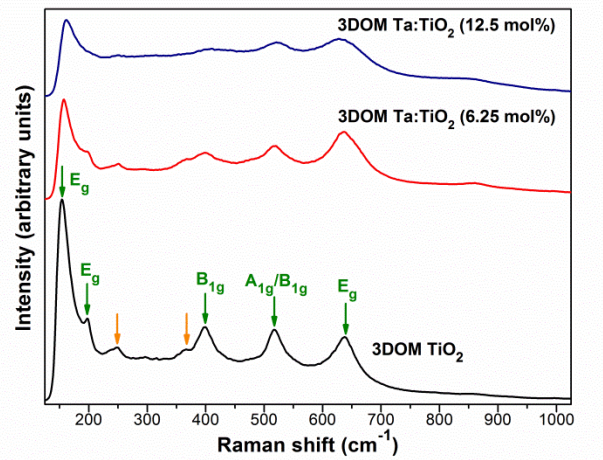

Figure 4.29 Raman spectra of 3DOM TiO_2 and the doped 3DOM TiO_2 materials. Both anatase vibrational modes (shown in green) and TiO_2-B vibrational modes (shown in orange) are present in these materials.

Table 4.6 Crystal sizes, BET surface areas, and pore volumes for the 3DOM Ta:TiO_2 materials.

sample[a]	anatase crystallite size (nm)	BET surface area (m^2/g)	pore volume (cm^3/g)
3DOM TiO_2, Undoped	7.8	126	0.32
3DOM Ta:TiO_2, (6.25 mol%)[b]	6.8	133	0.34
3DOM Ta:TiO_2, (12.5 mol%)[c]	6.5	207	0.35

[a] All materials calcined at 400 °C for 2 h.

[b] Parent material is TFA-Ta:TiO_2/C (6.25 mol%).

[c] Parent material is TFA-Ta:TiO_2/C (12.5 mol%).

4.3.5.2 Characterization of the Morphology of 3DOM Ta:TiO_2

Additional characterization of 3DOM Ta:TiO_2 was conducted using a combination of electron microscopy and gas sorption analysis. Through these techniques, a better understanding of the morphology of the 3DOM Ta:TiO_2 can be attained. Micrographs obtained via SEM (Figure 4.30) show that the addition of the Ta dopant does not change the morphology of the macropores. Even with removal of the carbon phase, the 3DOM morphology remains intact and a network of interconnected macropores suitable for infiltration with electrolyte is preserved. Much like the 3DOM TiO_2, the preservation of pore network is possible since the overall weight percent of the doped TiO_2 component is high. Via TEM micrographs, additional mesopores can be observed between crystallites in the walls and nodes (Figure 4.31). These pores (light spots in the images) are disordered and originate from the burnout of carbon. Lattice spacings measured from these images (see Figure 4.31 c, d) match that of anatase TiO_2 for the (101) plane, ~0.35 nm. The mesopores also have an impact on the N_2 gas sorption isotherms for the materials (Figure 4.32). Hysteresis is present in the isotherms owing to the textural mesoporosity. Both 3DOM Ta:TiO_2 materials have smaller crystallite sizes, which helps prevent closure of mesopores. As a consequence, BET specific surface areas and pore volumes increase with higher levels of Ta-doping (Table 4.6).

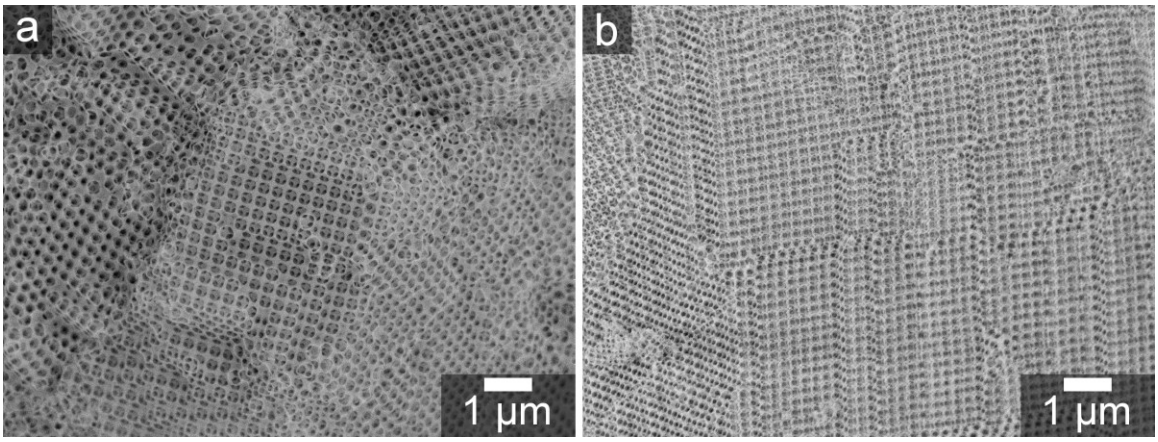

Figure 4.30 SEM micrographs of (a) 3DOM Ta:TiO_2 (6.25 mol%) and (b) 3DOM Ta:TiO_2 (12.5 mol%). The 3DOM structure is present in both materials.

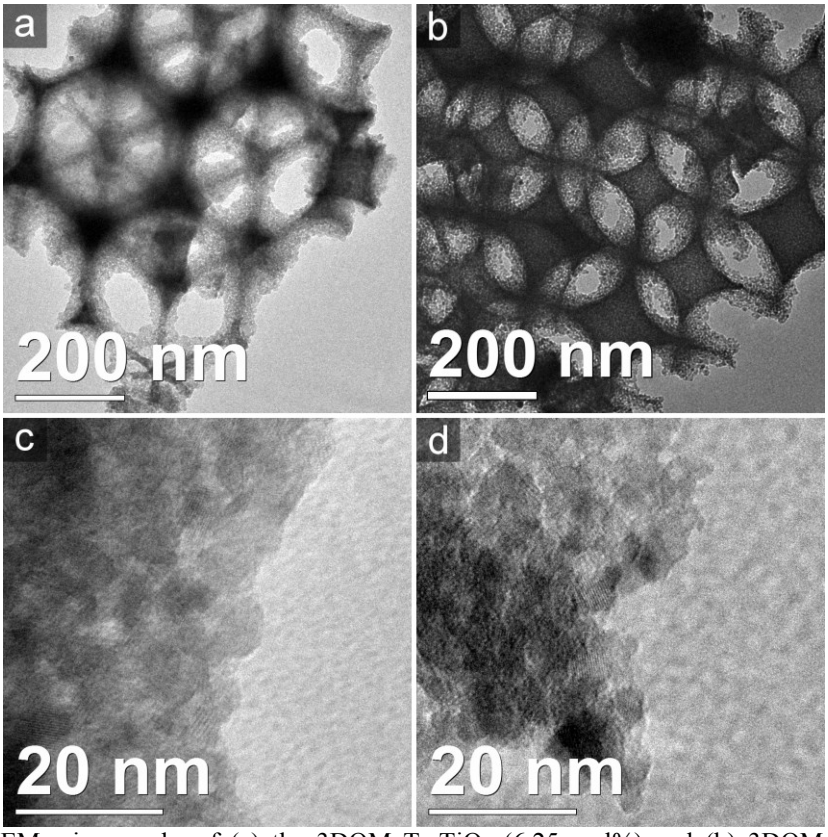

Figure 4.31 TEM micrographs of (a) the 3DOM Ta:TiO_2 (6.25 mol%) and (b) 3DOM Ta:TiO_2 (12.5 mol%) at low magnification. Higher magnification images of (c) 3DOM Ta:TiO_2 (6.25 mol%) and (d) 3DOM Ta:TiO_2 (12.5 mol%) show mesopores between crystallites. Images taken by Stephen Rudisill.

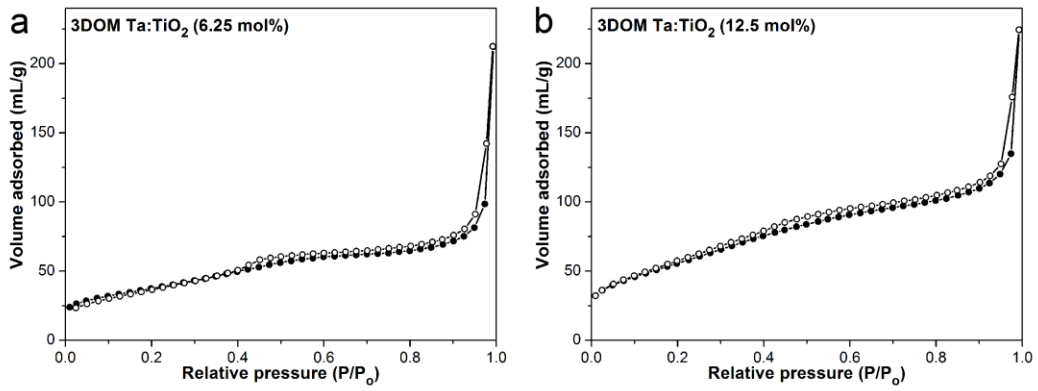

Figure 4.32 Nitrogen sorption isotherms of (a) the 3DOM Ta:TiO_2 (6.25 mol%) and (b) 3DOM Ta:TiO_2 (12.5 mol%). The isotherms contain hysteresis loops that arise from mesopores between crystallites of doped TiO_2.

4.3.5.3 Electrochemical Characterization of 3DOM Ta:TiO_2

While the 3DOM Ta:TiO_2 materials have structural features that should be beneficial for Li^+ insertion/extraction (including higher surface areas and smaller crystallite sizes), the charge/discharge capacity of these materials are lower than the undoped 3DOM TiO_2 (Figure 4.33). At the C/5 rate, the 3DOM Ta:TiO_2 (6.25 mol%) has ~155 mAh/g charge/discharge capacity and the 3DOM Ta:TiO_2 (12.5 mol%) has ~125 mAh/g charge/discharge capacity. The general trend continues for all rates, and the gap only begins to close at high rates (10 C and 25 C). In addition to plotting the final charge/discharge capacities for each cycle, the voltage profiles for 3DOM TiO_2 and 3DOM Ta:TiO_2 are shown in Figure 4.34. As the content of the dopant increases, the plateaus present in the profiles shrink and the sloped region expands. It is not entirely clear why this occurs for the 3DOM Ta:TiO_2. Part of the reason may be from the fact that the doped crystallites are smaller and Li^+ can be inserted into or extracted from the doped TiO_2 via a solid solution mechanism.[71] Surface areas are higher in the doped electrode materials, and this may also allow for a greater contribution from pseudocapacitance at interfaces.[71]

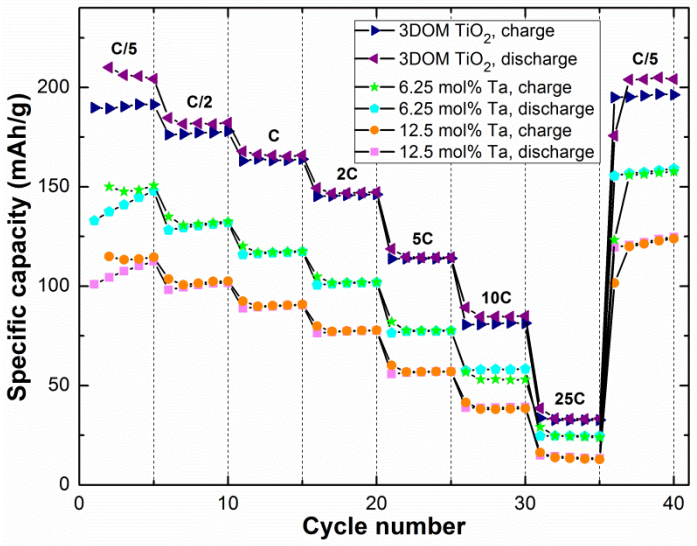

Figure 4.33 Rate performance comparison for the 3DOM TiO_2 and 3DOM Ta:TiO_2 materials. Charge/discharge capacities decrease as dopant content increases.

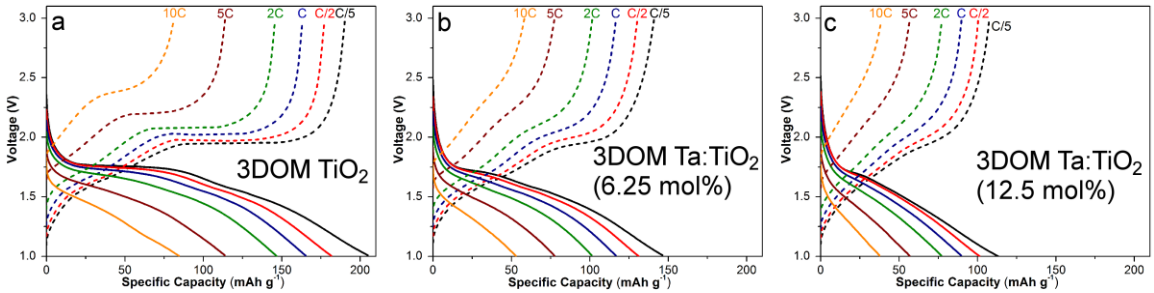

Figure 4.34 Voltage profiles for the 3DOM TiO_2 and the doped 3DOM Ta:TiO_2 materials. A plateau indicative of biphasic insertion/extraction is clearly visible for the 3DOM TiO_2. This plateau disappears with increasing Ta content.

Electrochemical impedance spectra were obtained for the doped 3DOM Ta:TiO_2 both as-made and after 10 charge/discharge cycles at a C/2 rate (Figure 4.25). As was observed for the 3DOM TiO_2 (see Chapter 3), conditioning occurs in the electrodes and resistances decrease after cycling (Table 4.7). Increased infiltration with electrolyte or subtle changes to the structure of the anode materials may occur. When comparing the 3DOM Ta:TiO_2 (6.25 mol%) and the 3DOM Ta:TiO_2 (12.5 mol%) spectra gathered after cycling, substantial differences are observed between the two electrode materials. Resistances are lower for the 3DOM Ta:TiO_2 (6.25 mol%), suggesting that electronic and ionic transport is easier in that cell than the cell made with the 3DOM Ta:TiO_2 (12.5 mol%). The lower Warburg impedance (σ) for the 3DOM Ta:TiO_2 (6.25 mol%) is also indicative of better Li^+ transport. Strangely, the resistances and Warburg impedance of the undoped 3DOM TiO_2 (fitted with the same model) are uniformly higher than that of the 3DOM

Ta:TiO_2 (6.25 mol%). This should suggest that the 3DOM Ta:TiO_2 (6.25 mol%) would have greater capacities than the 3DOM TiO_2, but this is not the case. However, the impedance spectra were taken at a fixed voltage (2.1 V vs. Li/Li^+), and they may change considerably during charge/discharge. A more detailed investigation may be warranted in this case.

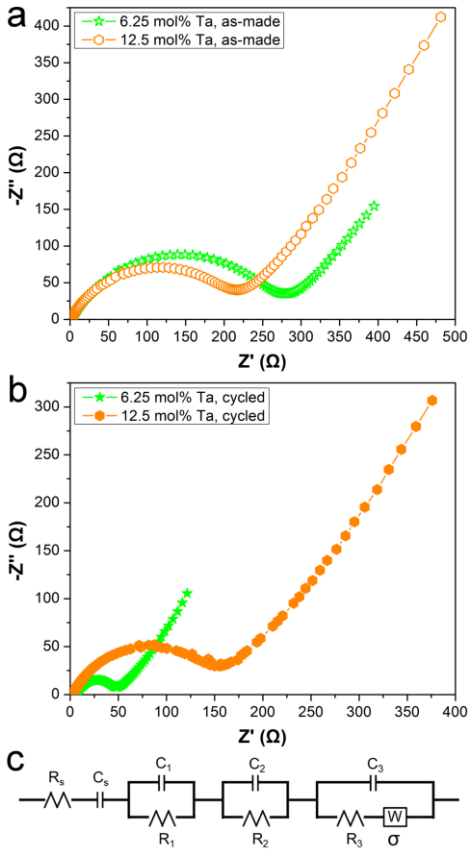

Figure 4.35 Impedance spectra for the 3DOM Ta:TiO_2 half cells. Spectra are shown for the half cells as-made (a) and after ten charge/discharge cycles at a rate of C/2 (b). The equivalent circuit used to model the spectra is shown in (c). It is the same model as the one used in Chapter 3. Equivalent circuit model developed by Benjamin Wilson.

Table 4.7 Relevant parameters obtained from the model fitted to the electrochemical impedance spectra for the 3DOM TiO_2 and 3DOM Ta:TiO_2 materials.[a]

sample	R_s (Ω)	R_1 (Ω)	R_2 (Ω)	R_3 (Ω)	C_s (mF)	C_1 (μF)	C_2 (μF)	C_3 (μF)	σ
As-made 3DOM TiO_2	7.5	64	210	184	60	3.3	8.4	36	140
Cycled 3DOM TiO_2	6.6	12	35	33	37	2.8	14	56	65
As-made 3DOM Ta:TiO_2 (6.25 mol%)	7.2	143	56	53	1.3	79	1300	27	30
Cycled 3DOM Ta:TiO_2 (6.25 mol%)	4.6	24	10	6.3	0.76	1400	1800	31	17
As-made 3DOM Ta:TiO_2 (12.5 mol%)	16	175	90	209	-	40	4200	550000	11
Cycled 3DOM Ta:TiO_2 (12.5 mol%)	7.2	77	26	56	0.19	17000	170000	29	46

[a] Modeling and analysis performed by Benjamin Wilson

While Nb-doping has been shown to improve the capacity of TiO_2 anodes (especially up to 10 mol% Nb),[39,51,72] the Ta-doped TiO_2 anodes prepared for this study did not show similar behavior. In fact, the capacity of the half cells decreases as the content of Ta is increased. Impedance spectra also indicate that the 3DOM Ta:TiO_2 (12.5 mol%) has higher resistances than the 3DOM Ta:TiO_2 (6.25 mol%). Reduction of the doped TiO_2 cannot be used to explain these findings because the carbon phase was combusted in air, leaving only doped TiO_2. An alternate explanation for low capacities in the 3DOM Ta:TiO_2 is that Li^+ is strongly trapped by any electrons present in the lattice (via equation 4.4). Shin explored the impact this could have on the diffusion of lithium ions for donor dopants (specifically Nb, but it is applicable to other

pentavalent dopants).[72] Provided that electronic mobility is higher in the lattice, the overall chemical diffusion co-efficient of lithium is controlled by the mobility of lithium ions. It may be that trapping of Li^+ is so effective in the mixed conducting 3DOM Ta:TiO_2 that the chemical diffusion co-efficient of lithium drops after only the addition of a few mol% of Ta. Or there may be a small window at a lower doping level where the trapping does not negate the boost in electronic conductivity. However, a combined computational and experimental study into the defect chemistry of the Ta-doped material would be required to fully explore this possibility.

4.3.5.4 Concluding Remarks

Unfortunately, the two doped materials studied in this section are not able to improve the capacities for lithium ion insertion/extraction over that of undoped 3DOM TiO_2. However, some potentially beneficial changes to the structure of the doped 3DOM Ta:TiO_2 were also observed. Once the carbon secondary template was removed, both the 3DOM Ta:TiO_2 (6.25 mol%) and the 3DOM Ta:TiO_2 (12.5 mol%) possessed a well-ordered network of interconnected macropores. Crystallite sizes are lower and BET specific surface areas are higher for the Ta-doped materials when compared to undoped 3DOM TiO_2. Despite this, doping with Ta decreases the capacity of the resulting electrodes and the capacity decreases with increasing dopant content. Significant differences in the impedance spectra for these materials are observed, as well. Trapping of Li^+ by e^- is postulated to be responsible for the decrease in capacities.

4.4 Overall Conclusions

Significant changes to both the structure and the electrochemical properties of 3DOM TiO_2/C composites can be induced by adding dopants or adjusting the carbon content for the TFA-TiO_2/C and acac-TiO_2/C precursors. In terms of carbon content, TFA2-TiO_2/C contains ~50 wt% carbon, which allowed for the reduction the TiO_2 crystallite size relative to TFA-TiO_2/C. However, pyrolysis at 800 °C causes both the conversion of TiO_2 to rutile and a significant increase in the crystal size of TiO_2. This appears to be driven by reduction of the TiO_2 component brought on by the increased carbon content in TFA2-TiO_2/C.TFA3-TiO_2/C (a slightly modified version of TFA-TiO_2/C) served as the first testing platform for the use of dopants. Niobium and iron were incorporated into the TiO_2 lattice, while Cu separated due to the reducing environment generated from the carbon phase during pyrolysis. A lower temperature was used for pyrolysis, but the changes to the structure of the TFA3-TiO_2/C brought on by doping were not enough to justify further testing. Tantalum was targeted next as dopant for both TFA-TiO_2/C and TFA2-TiO_2/C, and different doping concentrations were explored. In general, increasing the dopant

concentration causes the formation of more rutile and a smaller crystallite size for the TiO_2. Other characteristics, such as the BET surface area and the location of the doped TiO_2 phase, are not appreciably changed when compared to undoped TFA- and TFA2-TiO_2/C. While the TFA- and TFA2-Ta:TiO_2/C samples were not tested electrochemically, lithium insertion/extraction capacities were obtained for electrodes containing doped acac-TiO_2/C. Both Nb and Ta dopants were incorporated into the TiO_2 phase, resulting in smaller crystallites and more rutile. Capacities are lower for these materials, which are believed to trap diffusing Li^+ due to the generation of conducting electrons during pyrolysis. When Ni was used as a dopant, it phase-separated and caused catalytic graphitization. As a result, the capacities increase in the prepared electrodes at high rates. Finally, 3DOM Ta:TiO_2 materials were synthesized using the carbon component as a secondary template. While crystallite sizes and surface areas are favorable in these doped materials, the capacities for Li^+ insertion/extraction were lower than that of the 3DOM TiO_2

References

(1) Janisch, R.; Gopal, P.; Spaldin, N. A. Transition Metal-Doped TiO_2 and ZnO: Present Status of the Field. *J. Phys. Condens. Matter* **2005**, *17*, R657-R689.

(2) Chen, X.; Mao, S. S. Titanium Dioxide Nanomaterials: Synthesis, Properties, Modifications and Applications. *Chem. Rev.* **2007**, *107*, 2891-2959.

(3) Hirano, M.; Nakahara, C.; Ota, K.; Inagaki, M. Direct Formation of Zirconia-Doped Titania with Stable Anatase-Type Structure by Thermal Hydrolysis. *J. Am. Ceram. Soc.* **2002**, *85*, 1333-1335.

(4) Arbiol, J.; Cerdà, J.; Dezanneau, G.; Cirera, A.; Peiró, F.; Cornet, A.; Morante, J. R. Effects of Nb Doping on the TiO_2 Anatase-to-Rutile Phase Transition. *J. Appl. Phys.* **2002**, *92*, 853-861.

(5) Furubayashi, Y.; Hitosugi, T.; Yamamoto, Y.; Inaba, K.; Kinoda, G.; Hirose, Y.; Shimada, T.; Hasegawa, T. A Transparent Metal: Nb-doped Anatase TiO_2. *Appl. Phys. Lett.* **2005**, *86*, 252101(1-3).

(6) Osorio-Guillén, J.; Lany, S.; Zunger, A. Atomic Control of Conductivity Versus Ferromagnetism in Wide-Gap Oxides Via Selective Doping: V, Nb, Ta in Anatase TiO_2. *Phys. Rev. Lett.* **2008**, *100*, 036601(1-4).

(7) Fergus, J. W. Doping and Defect Association in Oxides for Use in Oxygen Sensors. *J. Mater. Sci.* **2003**, *38*, 4259-4270.

(8) Asahi, R.; Morikawa, T.; Ohwaki, T.; Aoki, K.; Taga, Y. Visible-Light Photocatalysis in Nitrogen-Doped Titanium Oxides. *Science* **2001**, *293*, 269-271.

(9) Nowotny, M. K.; Sheppard, L. R.; Bak, T.; Nowotny, J. Defect Chemistry of Titanium Dioxide. Application of Defect Engineering in Processsing of TiO_2-Based Photocatalysts. *J. Phys. Chem. C* **2008**, *112*, 5275-5300.

(10) Biedrzycki, J.; Livraghi, S.; Giamello, E.; Agnoli, S.; Granozzi, G. Fluorine- and Niobium-Doped TiO_2: Chemical and Spectroscopic Properties of Polycrystalline n-Type-Doped Anatase. *J. Phys. Chem. C* **2014**, *116*, 8462-8473.

(11) Chen, X.; Burda, C. The Electronic Origin of the Visible-Light Adsorption Properties of C-, N- and S-Doped TiO_2 Nanomaterials. *J. Am. Chem. Soc.* **2008**, *130*, 5018-5019.

(12) Mukri, B. D.; Waghmare, U. V.; Hedge, M. S. Platinum Ion-Doped TiO_2: High Catalytic Activity of Pt^{2+} with Oxide Ion Vacancy in $Ti^{4+1-x}Pt^{2+x}O_{2-x}$ Compared to Pt^{4+} without Oxide Ion Vacancy in $Ti^{4+1-x}Pt^{4+}O_2$. *Chem. Mater.* **2013**, *25*, 3822-3833.

(13) Kumar, S. G.; Devi, L. G. Review on Modified TiO_2 Photocatalysts under UV/Visible Light: Selected Results and Related Mechanisms on Interfacial Charge Carrier Transfer Dynamics. *J. Phys. Chem. A* **2011**, *115*, 13211-13241.

(14) Bingham, S.; Daoud, W. A. Recent Advances in Making Nano-Sized TiO_2 Visible-Light Active through Rare-Earth Metal Doping. *J. Mater. Chem.* **2011**, *21*, 2041-2050.

(15) McFarland, E. W.; Metiu, H. Catalysis by Doped Oxides. *Chem. Rev.* **2013**, *112*, 4391-4427.

(16) Suryanarayana, C. Nanocrystalline Materials. *Int. Mater. Rev.* **1995**, *40*, 41-64.

(17) Gleiter, H. Nanostructured Materials: Basic Concepts and Microstructure. *Acta. Mater.* **2000**, *48*, 1-29.

(18) Powers, J. D.; Glaeser, A. M. Grain Boundary Migration in Ceramics. *Interface Sci.* **1998**, *6*, 23-39.

(19) Liu, F.; Gong, M. Nano-Scaled Grain Growth. In *Sintering*; Castro, R. H. R., van Benthem, K., Eds.; Springer-Verlag: Berlin, 2013.

(20) Mayo, M. J. Processing of Nanocrystalline Ceramics from Ultrafine Particles. *Int. Mater. Rev.* **1994**, *41*, 85-115.

(21) Koch, C. C.; Scattergood, R. O.; Saber, M.; Kotan, H. High Temperature Stabilization of Nanocrystalline Grain Size: Thermodynamic Versus Kinetic Strategies. *J. Mater. Res.* **2013**, *28*, 1785-1791.

(22) Terwilliger, C. D.; Chiang, Y.-M. The Effect of Calcium Segregation on Grain Growth in Nanocrystalline TiO_2. *Nanostructured Mater.* **1994**, *4*, 651-661.

(23) Yan, M. F.; Rhodes, W. W. Effects of Solutes on the Grain Boundary Mobility of TiO_2. In *Ceramic Microstructures '86: Role of Interfaces*; Pask, J. A., Evans, A. G., Eds.; Plenum Press: New York, 1987; pp 519-532.

(24) Nair, J.; Nair, P.; Mizukami, F.; Oosawa, Y.; Okubo, T. Microstructure and Phase Transformation Behavior of Doped Nanostructured Titania. *Mater. Res. Bull.* **1999**, *34*, 1275-1290.

(25) Zhang, Y.-H.; Reller, A. Nanocrystalline Iron-Doped Mesoporous Titania and Its Phase Transition. *J. Mater. Chem.* **2001**, *11*, 2537-2541.

(26) Wang, Q.; Lian, G.; Dickey, E. C. Grain Boundary Segregation in Yttrium-Doped Polycrystalline TiO_2. *Acta. Mater.* **2004**, *52*, 809-820.

(27) German, R. M. *Sintering Theory and Practice*; John Wiley & Sons, Inc.: New York, 1996.

(28) Tilley, R. J. D. *Defects in Solids*; John Wiley & Sons, Inc.: Hoboken, NJ, 2008.

(29) Chraska, T.; King, A. H.; Berndt, C. C. On the Size-Dependent Phase Transformation in Nanoparticulate Zirconia. *Mater. Sci. Eng., A* **2000**, *286*, 169-178.

(30) Hanaor, D. A. H.; Sorrell, C. C. Review of the Anatase to Rutile Phase Transformation. *J. Mater. Sci.* **2011**, *46*, 855-874.

(31) Shannon, R. D. Phase Transformation Studies in TiO_2 Supporting Different Defect Mechanisms in Vacuum-Reduced and Hydrogen-Reduced Rutile. *J. Appl. Phys.* **1964**, *35*, 3414-3416.

(32) Reidy, D. J.; Holmes, J. D.; Morris, M. A. The Critical Size Mechanism for the Anatase to Rutile Transformation in TiO_2 and Doped-TiO_2. *J. Eur. Ceram. Soc.* **2006**, *26*, 1527-1534.

(33) Fröschl, T.; Hörmann, U.; Kubiak, P.; Kučerová, G.; Pfanzelt, M.; Weiss, C. K.; Behm, R. J.; Hüsing, N.; Kaiser, U.; Landfester, K.; Wohlfahrt-Mehrens, M. High Surface Area Crystalline Titanium Dioxide: Potential and Limits in Electrochemical Energy Storage and Catalysis. *Chem. Soc. Rev.* **2012**, *41*, 5313-5360.

(34) Zhang, Y.; Du, F.; Yan, X.; Jin, Y.; Zhu, K.; Wang, X.; Li, H.; Chen, G.; Wang, C.; Wei, Y. Improvements in the Electrochemical Kinetic Properties and Rate Capability of Anatase Titanium Dioxide Nanoparticles by Nitrogen Doping. *ACS Appl. Mater. Interfaces* **2014**, *6*, 4458-4465.

(35) Jiao, W.; Li, N.; Wang, L.; Wen, L.; Li, F.; Liu, G.; Cheng, H.-M. High-Rate Lithium Storage of Anatase TiO_2 Crystals Doped with Both Nitrogen and Sulfur. *Chem. Commun.* **2013**, *49*, 3461-3463.

(36) Jung, H.-G.; Yoon, C. S.; Prakash, J.; Sun, Y.-K. Mesoporous Anatase TiO_2 with High Surface Area and Controllable Pore Size by F^--Ion Doping: Applications for High-Power Li-Ion Battery Anode. *J. Phys. Chem. C* **2009**, *113*, 21258-21263.

(37) Ming, H.; Li, X.; Su, L.; Liu, M.; Jin, L.; Bu, L.; Kang, Z.; Zheng, J. One Step Synthesis of C&N Co-Doped Mesoporous TiO_2 with Enhanced Performance in a Lithium-Ion Battery. *RSC Advances* **2013**, *3*, 3836-3839.

(38) Wang, Y.; Chen, T.; Mu, Q. Electrochemical Performance of W-Doped Anatase TiO_2 Nanoparticles as an Electrode Material for Lithium-Ion Batteries. *J. Mater. Chem.* **2011**, *21*, 6006-6013.

(39) Wang, Y.; Smarsly, B. M.; Djerdj, I. Niobium Doped TiO_2 with Mesoporosity and Its Application for Lithium Insertion. *Chem. Mater.* **2010**, *22*, 6624-6631.

(40) Anh, L. T.; Rai, A. K.; Thi, T. V.; Gim, J.; Kim, S.; Shin, E.-C.; Lee, J.-S.; Kim, J. Improving the Electrochemical Performance of Anatase Titanium Dioxide by Vanadium Doping as an Anode Material for Lithium-Ion Batteries. *J. Power Sources* **2013**, *243*, 891-898.

(41) Ali, Z.; Cha, S. N.; Sohn, J. I.; Shakir, I.; Yan, C.; Kim, J. M.; Kang, D. J. Design and Evaluation of Novel Zn Doed Mesoporous TiO_2 Based Anode Material for Advanced Lithium Ion Batteries. *J. Mater. Chem.* **2012**, *22*, 17625-17629.

(42) Thi, T. V.; Rai, A. K.; Gim, J.; Kim, S.; Kim, J. Effect of Mo^{6+} Doping on Electrochemical Performance of Anatase TiO_2 as a High Performance Anode Material for Secondary Lithium-Ion Batteries. *J. Alloys Compd.* **2014**, *598*, 16-22.

(43) Hutchings, G. S.; Li, Q.; Jiao, F. Synthesis and Electrochemistry of Nanocrystalline M-TiO_2 (M = Mn, Fe, Co, Ni, Cu) Anatase. *J. Electrochem. Soc.* **2013**, *160*, A511-A515.

(44) Das, S. K.; Gnanavel, M.; Patel, M. U. M.; Shivakumara, C.; Bhattacharyya, A. J. Anamolously High Lithium Storage in Mesoporous Nanoparticulate Aggregation of Fe^{3+} Doped Anatase Titania. *J. Electrochem. Soc.* **2011**, *158*, A1290-A1297.

(45) Meng, Y.; Gu, D.; Zhang, F.; Shi, Y.; Yang, H.; Li, Z.; Yu, C.; Tu, B.; Zhao, D. Ordered Mesoporous Polymers and Homologous Carbon Frameworks Amphiphilic Surfactant Templating and Direct Transformation. *Angew. Chem. Int. Ed.* **2005**, *44*, 7053-7059.

(46) Josephson, D. P.; Popczun, E. J.; Stein, A. Effects of Integrated Carbon as a Light Absorber on the Coloration of Photonic Crystal-Based Pigments. *J. Phys. Chem. C* **2013**, *117*, 13585-13592.

(47) Spurr, R. A.; Myers, H. Quantitative Analysis of Anatase-Rutile Mixtures with an X-Ray Diffractometer. *Anal. Chem.* **1957**, *29*, 760-762.

(48) Zheng, T.; Zhong, Q.; Dahn, J. R. High-Capacity Carbons Prepared from Phenolic Resin for Anodes of Lithium-Ion Batteries. *J. Electrochem. Soc.* **1995**, *142*, L211-L214.

(49) Huang, C.-H.; Gu, D.; Zhao, D.; Doong, R.-A. Direct Synthesis of Controllable Microstructures of Thermally Stable and Ordered Mesoporous Crystalline Titanium Oxides Carbide/Carbon Composites. *Chem. Mater.* **2010**, *22*, 1760-1767.

(50) Trick, K. A.; Saliba, T. E. Mechanisms of the Pyrolysis of Phenolic Resin in a Carbon/Phenolic Composite. *Carbon* **1995**, *33*, 1509-1515.

(51) Fehse, M.; Cavaliere, S.; Lippens, P. E.; Savych, I.; Iadecola, A.; Monoconduit, L.; Jones, D. J.; Rozière, J.; Fischer, F.; Tessier, C.; Stievano, L. Nb-Doped TiO_2 Nanofibers for Lithium Ion Batteries. *J. Phys. Chem. C* **2013**, *117*, 13827-13835.

(52) Marsh, H.; Crawford, D.; Taylor, D. W. Catalytic Graphitization by Iron of Isotropic Carbon from Polyfurfuryl Alchol, 725-1090 K. A High Resolution Electron Microscopy Study. *Carbon* **1983**, *21*, 81-87.

(53) Sevilla, M.; Fuertes, A. B. Catalytic Graphitization of Templated Mesoporous Carbons. *Carbon* **2006**, *44*, 468-474.

(54) Ōya, A.; Ōtani, S. Catalytic Graphitization of Carbons by Various Metals. *Carbon* **1979**, *17*, 131-137.

(55) Yokokawa, C.; Hosokawa, K.; Takegami, Y. Low Temperature Catalytic Graphitization of Hard Carbon. *Carbon* **1966**, *4*, 459-465.

(56) Bally, A. R.; Korobeinikova, E. N.; Schmid, P. E.; Lévy, F.; Bussy, F. Structural and Electrical Properties of Fe-Doped TiO_2 Thin Films. *J. Phys. D: Appl. Phys.* **1998**, *31*, 1149-1154.

(57) Leventis, N.; Chandrasekaran, N.; Sadekar, A. G.; Sotiriou-Leventis, C.; Lu, H. One-Pot Synthesis of Interpenetrating Inorganic/Organic Networks of CuO/Resorcinol-Formaldehyde Aerogels: Nanostructured Energetic Materials. *J. Am. Chem. Soc.* **2009**, *131*, 4576-4577.

(58) Balachandran, U.; Eror, N. G. Raman Spectra of Titanium Dioxide. *J. Solid State Chem.* **1982**, *42*, 276-282.

(59) Ferrari, A. C.; Robertson, J. Interpretation of Raman Spectra of Disordered and Amorphous Carbon. *Phys. Rev. B* **2000**, *61*, 14095-14107.

(60) Hitosugi, T.; Furubayashi, Y.; Ueda, A.; Itabashi, K.; Inaba, K.; Hirose, Y.; Kinoda, G.; Yamamoto, Y.; Shimada, T.; Hasegawa, T. Ta-Doped Anatase TiO_2 Epitaxial Film as Transparent Conducting Oxide. *Jpn. J. Appl. Phys.* **2005**, *44*, L1063-L1065.

(61) Dy, E.; Hui, R.; Zhang, J.; Liu, Z.-S.; Shi, Z. Electronic Conductivity and Stability of Doped Titania ($Ti_{1-X}M_XO_2$, M = Nb, Ru, and Ta)-A Density Functional Theory-Based Comparison. *J. Phys. Chem. C* **2010**, *114*, 13162-13167.

(62) Balachandran, U.; Eror, N. G. Self-Compensation in Tantalum-Doped TiO_2. *J. Mater. Sci.* **1982**, *17*, 1207-1212.

(63) Ruiz, A. M.; Dezanneau, G.; Arbiol, J.; Cornet, A.; Morante, J. R. Insights into the Structural and Chemical Modifications of Nb Additive on TiO_2 Nanoparticles. *Chem. Mater.* **2004**, *16*, 862-871.

(64) Sheppard, L. R.; Bak, T.; Nowotny, J. Electrical Properties of Niobium-Doped Titanium Dioxide. 1. Defect Disorder. *J. Phys. Chem. B* **2006**, *110*, 22447-22454.

(65) Shannon, R. D. Revised Effective Ionic Radii and Systematic Studies of Interatomic Distances in Halides and Chalcogenides. *Acta. Cryst.* **1976**, *32*, 751-767.

(66) Stoklosa, A. Point Defect Diagrams for Pure and Doped Titanium (IV) Oxide $TiO_{2-\delta}$ in Temperature Range of 1073-1573 K. *Adv. Appl. Ceram.* **2012**, *111*, 44-61.

(67) Nakajima, T.; Sheppard, L. R.; Prince, K. E.; Nowotny, J.; Ogawa, T. Niobium Segregation in TiO_2. *Adv. Appl. Ceram.* **2007**, 82-88.

(68) Lei, Z.; Xiao, Y.; Dang, L.; You, W.; Hu, G.; Zhang, J. Nickel-Catalyzed Fabrication of SiO_2, TiO_2/Graphitized Carbon, andd the Resultant Graphitized Carbon with Periodically Macroporous Structure. *Chem. Mater.* **2007**, *19*, 477-484.

(69) Huang, C.-H.; Doong, R.-A.; Gu, D.; Zhao, D. Dual-Template Synthesis of Magnetically-Separable Hierarchically-Ordered Porous Carbons by Catalytic Graphitization. *Carbon* **2011**, *49*, 3055-3064.

(70) Maier, J. Thermodynamics of Electrochemical Lithium Storage. *Angew. Chem. Int. Ed.* **2013**, *52*, 4998-5026.

(71) Milne, N. A.; Skyllas-Kazacos, M.; Luca, V. Crystallite Size Dependence of Lithium Intercalation into Nanocrystalline Rutile. *J. Phys. Chem. C* **2009**, *113*, 12983-12995.

(72) Shin, J.-Y. Effects of Ionic and Electronic Charge Carriers in Nanostructured TiO_2 on Lithium Storage. Ph.D Thesis, Max Planck Institute for Solid State Research, 2012.

(73) Shin, J.-Y.; Joo, J. H.; Samuelus, D.; Maier, J. Oxygen Nonstoichiometric $TiO_{2-\delta}$ Nanoparticles *via* Hydrogen Reduction for High Rate Capability Lithium Batteries. *Chem. Mater.* **2012**, *24*, 543-551.

(74) Zhang, S. X.; Kundaliya, D. C.; Yu, W.; Dhar, S.; Young, S. Y.; Salamanca-Riba, L. G.; Ogale, S. B.; Vispute, R. D.; Venkatesan, T. Niobium Doped TiO_2: Intrinsic Transparent Metallic Anatase Versus Highly Resistive Rutile Phase. *J. Appl. Phys.* **2007**, *102*, 013710(1-4).

(75) Jamink, J.; Gaberscek, M. Li Ion Migration at the Interfaces. *MRS Bull.* **2009**, *34*, 942-948.

Chapter 5

Titania-Carbon Nanocomposite Anodes for Lithium-Ion Batteries– Effects of Confined Growth and Phase Synergism

---

Parts of this chapter are from: Petkovich, N. D.; Wilson, B. E..; Rudisill, S. G.; Stein, A. Titania-Carbon Nanocomposite Anodes for Lithium Ion Batteries– Effects of Confined Growth and Phase Synergism *ACS Appl. Mater. Interfaces* **2014**, *Accepted*. – These parts are reproduced by permission of The American Chemical Society. Available at: http://dx.doi.org/10.1021/am505210c

5.1 Introduction and Motivation

Many routes have been devised for the synthesis of carbon and TiO_2 composites that possess favorable electrochemical properties; however, few studies have specifically targeted means to minimize the toxicity of the synthesis precursors. Since an important motivation for the use of TiO_2 is to improve safety in batteries, it is logical to also consider the safety of syntheses for advanced electrode materials containing TiO_2. For instance, the introduction of amorphous carbon into a composite is commonly achieved using toxic organic molecules, such as phenol, formaldehyde, aniline, and furfural alcohol.[1,2] Other carbon sources, such as graphene and carbon nanotubes, present their own safety concerns that are still under intense investigation.[3,4] In addition, precursors used for the synthesis of TiO_2 are often hazardous, such as volatile and corrosive $TiCl_4$, or require stabilization through the use of chelating agents that are potentially harmful to human health.[5-7] Greener synthesis routes that use less dangerous precursors represent an important research direction for TiO_2 electrodes; including routes that produce materials with good capacity for lithium insertion and extraction.

The previous two chapters describe methods to synthesize porous TiO_2-containing anode materials for lithium ion batteries via a combination of colloidal crystal templating and surfactant templating. To stabilize the precursor, trifluoroacetic acid (TFA) or 2,4-pentanedione (acac) are used alongside a phenol-formaldehyde (PF) sol as carbon source. Unfortunately, those two chelating agents are hazardous to human health, and the synthesis of PF sol requires the use of toxic monomers. This chapter describes an investigation into the use of alternate precursors for the synthesis of 3DOM TiO_2/C. These new precursors employ a less hazardous chelating agent, citric acid; furthermore, some of the precursors used for the synthesis of 3DOM TiO_2/C contain relatively non-toxic carbon sources (sucrose and/or citric acid). While the toxicities of the precursors for 3DOM TiO_2/C are greatly reduced, structural and compositional changes (relative to TFA-TiO_2/C and acac-TiO_2/C) occur in the 3DOM TiO_2/C due to the use of these new precursor solutions. For instance, as a consequence of employing a carbon-rich chelating agent (citric acid), the content of carbon in the new 3DOM TiO_2/C composites is near 50 wt%. Before offering an outline of the research that is discussed in this chapter, some rationale behind a major change to cycling parameters needs to be provided. A key motivation for this change is the aforementioned abundance of carbon in the composite anodes.

Most TiO_2/C lithium-ion battery anodes are cycled so that the carbon phase functions purely as a conductive additive. However, lithium insertion and extraction into the carbon phase can be easily accomplished by changing the voltage window used for charging and discharging the

anode.[8-14] Specifically, the lower voltage limit needs to be set near 0 V vs. Li/Li^+ instead of ≥1 V vs. Li/Li^+ that is used when TiO_2 is the only active anode material. By expanding the voltage window, a greater capacity is attainable for TiO_2/C anodes. This advantage comes at a price, however. An extensive solid-electrolyte interphase (SEI) forms when cycling in this expanded window, and the potential for dangerous lithium plating returns.[10,15] While the cost-benefit analysis of this choice has not been fully explored, an extremely useful consequence of cycling in the larger voltage window has been discovered. For mesoporous TiO_2/C composites that contain amorphous carbon, cycling in the expanded voltage window allows the TiO_2/C composite materials to attain higher capacities than either pure TiO_2 or C with similar structures.[9,12-14] Interestingly, this same effect is not observed when TiO_2 and graphitic carbon are combined; however, this composite contains μm-scale domains.[8] Several explanations have been proposed for the capacity boost in the TiO_2/C composites: the carbon network accommodated volume changes in TiO_2, the carbon network functioned as a pathway for facile electron transport out of the TiO_2, and the high surface area of the composite materials facilitated insertion/extraction reactions.[12-14] Since the 3DOM TiO_2/C composites described in the chapter are carbon-rich and contain an amorphous carbon phase, the capacity of these anode materials can potentially be greatly increased by widening the voltage window. An exploration of the changing the voltage window thus forms a key component of the chapter, which is outlined below.

The remainder of this chapter describes a new synthesis of 3DOM TiO_2/C using a water-soluble, ammonium citratoperoxotitanate(IV) precursor for TiO_2 and different precursors (PF sol, sucrose, and citric acid) for amorphous carbon. Macropores in the 3DOM structure are templated from polymeric colloidal crystals. Colloidal crystals templates are infiltrated with a liquid precursor and thermally processed to obtain 3DOM TiO_2/C. A major focus of this work is an exploration on how the final pyrolysis temperature alters the structural and electrochemical properties of the composites. Another focus is the effect of changing the precursor from one that contains PF sol to a safer alternative that contains sucrose on the structure of these composite materials. In addition, 3DOM TiO_2/C made with slightly modified citric acid-based precursors are explored, including one without any added PF sol/sucrose and one prepared with half the citric acid used in the other syntheses. All of these 3DOM TiO_2/C materials were tested in lithium ion batteries in the half cell configuration. As stated in the paragraph above, the test cells were charged and discharged in two voltage windows: between 1 to 3 V vs. Li/Li^+ and in an expanded window between 0.05 to 3 V vs. Li/Li^+ that allows for insertion/extraction of lithium ions in the carbon phase. For the narrow voltage window, the 3DOM TiO_2/C composites are found to have

excellent capacities at low charge/discharge rates, but poor capacities at high charge/discharge rates. When charging and discharging in the wide voltage window, much higher capacities are obtained, and these capacities even exceed what can be obtained from similarly prepared 3DOM C anodes. These experiments have led to further evidence that composites of TiO_2 and C provide a considerably higher lithium ion capacity than similarly structured materials containing only carbon. Also, these results suggest that new hypotheses are required for why this synergistic phenomenon occurs.

5.2 Experimental Details

5.2.1 Materials

Methyl methacrylate (99 %), titanium metal (sponge, 3–19 mm, 99.5%), citric acid monohydrate (ACS regent grade, ≥99.0%), poly(ethylene oxide)–*block*-poly(propylene oxide)–*block*-poly(ethylene oxide) copolymer (molecular weight of 5800, P123), sodium carboxymethyl cellulose (CMC, molecular weight of 250000), lithium ribbon (0.75 mm thickness, 99.9%), and dimethyl carbonate (anhydrous, ≥99.0%) were purchased from Sigma-Aldrich. Phenol (ACS reagent grade), formaldehyde (certified ACS, 37 wt% in water), potassium persulfate (ACS reagent grade), and hydrogen peroxide (certified ACS, 30 wt% in water) were obtained from Fischer Scientific. Hydrochloric acid (ACS regent grade, 37 wt% in water), ammonium hydroxide (ACS regent grade, 28-30 wt% in water), and sodium hydroxide pellets (ACS reagent grade) were obtained from Macron Chemicals. Sucrose (ACS regent grade) was obtained from Mallinckrodt. Ethanol (200 proof, USP grade) was purchased from Decon Labs. A suspension of styrene-butadiene rubber (SBR, 50 wt% in water) was purchased from the MTI Corporation. All of the aforementioned chemicals were not further purified before use. Any deionized water used in these procedures was produced using a Barnstead Sybron purification system (final resistivity >18 MΩ·cm).

5.2.2 Synthesis of the Ammonium Citratoperoxotitanate(IV) Precursors

These complexes were synthesized following a procedure established in the literature,[16] but with a few modifications. To briefly summarize, 0.25 g of titanium metal was combined with 20 mL of 30 wt% of aqueous H_2O_2 and 5 mL of concentrated ammonium hydroxide. This mixture was stirred on ice for 1 h and then stirred at ambient temperature until all titanium dissolved. Citric acid monohydrate (1.10 g) was added to the solution. The mixture was heated to 40 °C

overnight and a yellow gel was formed (denoted: gel-1). If needed, further drying was conducted at 70 °C for 3 h.

Another gel (gel-2) was made similarly to the one described above. Again, 0.25 g of titanium metal was added to a mixture of 20 mL of H_2O_2 solution (30 wt% in water) and 5 mL of concentrated ammonium hydroxide solution. The titanium was dissolved under vigorous stirring first in an ice bath for 1 h and then at ambient temperature. Half the amount of citric acid monohydrate (0.55 g) relative to what was used above was then added to the solution. Finally, the mixture was gently heated to 40 °C and allowed to evaporate overnight.

5.2.3 Synthesis of 3DOM TiO_2/C Made with PF sol as a Carbon Source (PF-TiO_2/C)

For this composite and all others, colloidal crystal templates were used. Poly(methyl methacrylate) (PMMA) colloidal spheres were first synthesized using an emulsifier-free emulsion polymerization.[17] Once a suspension of spheres was obtained, a portion of the suspension was placed in a crystallization dish and allowed to sediment. The supernatant was removed via evaporation at ambient temperature. Phenol-formaldehyde (PF) prepolymer sol was also made following a procedure found in the literature.[18] The prepolymer was dried using rotary evaporation and redispersed in ethanol to form a 50 wt% ethanolic sol.

The precursor for 3DOM TiO_2/C was prepared by first mixing 1.5 g of water, 1.25 g of ethanol, and 1.25 g of concentrated HCl. P123 was then heated at 40 °C until it melted. Liquid P123 (0.8 g) was added to the precursor and stirred until it dissolved. Dried ammonium citratoperoxotitanate(IV) gel (1.6 g) was poured into the precursor, and the mixture was stirred for 15 min. More water (0.25 g) and concentrated HCl (0.25 g) were added to eliminate turbidity, and the precursor was stirred for 5 min. Finally, the precursor was combined with 0.1 g of PF sol and stirred overnight.

The colloidal crystal templates were broken into pieces with dimensions of several mm and infiltrated with the precursor. For infiltration, the pieces of template were placed at the bottom of a scintillation vial and precursor was pipetted into the vial. To reduce cracking, the liquid precursor was not allowed to cover the top of the templates. Infiltration via capillary action typically took between 2 and 6 h and caused the templates to turn partially translucent once completed. Once infiltration was complete, the templates were wiped clean of excess precursor. Additional solvent was removed by placing the templates in a vacuum oven under low vacuum for 30 minutes at ambient temperature. Thermal treatment of the templates was performed at 100 °C for 24 h and 140 °C for 24 h. Samples were then heated in a tube furnace under 0.7 L/min of

Ar at 1 °C/min to 350 °C and kept at that temperature for 4 h. Depending on the sample, the temperature was then increased at 1 °C/min to either 700 °C, 800 °C, or 900 °C and held at the target temperature for 2 h.

5.2.4 Synthesis of 3DOM TiO_2/C Made with Sucrose as a Carbon Source (Sucrose-TiO_2/C)

For the Sucrose-TiO_2/C, a precursor was prepared in fashion similar to the PF-TiO_2/C. Initially, 3.5 g of water, 1.25 g of concentrated HCl, and 0.8 g of liquid P123 were mixed until the P123 dissolved. The ammonium citratoperoxotitanate(IV) gel (1.6 g) was then added to the precursor, and the solution was stirred until it dissolved. If the solution remained slightly turbid, it was heated to 40 °C and was stirred until the turbidity disappeared. Sucrose crystals (0.1 g) were then poured into the precursor and the solution was stirred overnight. All subsequent processing steps were identical to those performed with the PF-TiO_2/C.

5.2.5 Modified Precursors

Two modified precursors were prepared that share similarities to the one made for Sucrose-TiO_2/C. A precursor without any additional carbon source, NAC (no added carbon)-TiO_2/C, was prepared. This precursor was prepared identically to the one used for Sucrose-TiO_2/C, but no sucrose crystals were dissolved in the NAC-TiO_2/C precursor. Processing was identical to what was conducted with the Sucrose-TiO_2/C, except the composite was pyrolyzed under Ar using a 1 °C/min ramp to 350 °C (4 h dwell) and 700 °C (2 h dwell). Another precursor, Sucrose2-TiO_2/C, was made using the ammonium citratroperoxotitanate(IV) gel-2 that contains reduced citric acid content. The gel, water, and hydrochloric acid content were altered in this synthesis. Only 1.05 g of gel-2 was added to a mixture of 3.5 g of water, 1.25 g of concentrated HCl, and 0.8 g of liquid P123. Once again, all subsequent processing was identical as described for Sucrose-TiO_2/C, except the composite was pyrolyzed under Ar using a 1 °C/min ramp to 350 °C (4 h dwell) and 700 °C (2 h dwell).

5.2.6 Synthesis and Characterization of the 3DOM C Reference Material

A 3DOM carbon material was prepared using a procedure slightly modified from one present in the literature.[19] In this synthesis, a precursor was made by stirring 2.0 g PF sol (50 wt% in ethanol), 1.0 g of 0.2 M HCl, and 1 g of F127 surfactant. After the precursor was stirred overnight, it was infiltrated into PMMA colloidal crystal templates. These infiltrated templates were evacuated for 2 h at 60 °C under low vacuum. The infiltrated templates were heat-treated at

100 °C for 24 h and 140 °C for 24 h. Pyrolysis of the material was done in a quartz tube furnace under flowing Ar (0.7 L/min) at 350 °C for 4 h and 700 °C for 2 h (a ramp rate of 1 °C/min was used).

5.2.7 Structural Characterization

All samples were analyzed using a variety of analytical techniques. TiO_2 content was determined using thermogravimetric analysis (TGA). Samples were loaded in a Netzsch STA 409 PC Luxx under air flow and heated at 10 °C/min to 1000 °C. Determination of C, H, and N content was done by Atlantic Microlab, Inc. (Norcross, GA) using automatic combustion analysis. Fourier-transform infrared (FTIR) spectra were obtained using a Nicolet Magna-IR 760 spectrometer. Solid samples for FTIR were ground with KBr and pressed into pellets prior to analysis. Raman measurements were carried out using a 514.5 nm Ar^+ laser attached to a WiiTech Alpha300R confocal Raman microscope with a DV401 CCD thermoelectric-cooled detector. For a given area, multiple spectra were collected and averaged to provide the final, reported spectrum. To prepare specimens for scanning electron microscopy (SEM), powders of the TiO_2/C samples were affixed to double-sided carbon tape placed on an Al stub. These samples were coated with 50 Å of Pt and imaged using a JEOL 6700 operated with an accelerating voltage of 5 kV. Specimens for transmission electron microscopy (TEM) were prepared by sonicating powders in ethanol (or dimethyl carbonate) for 5 min, and then dropping the suspension on Cu grids coated with holey carbon. Imaging was performed using a FEI Technai T12 equipped with a LaB_6 filament and operated at 120 kV. Powder X-ray diffraction (PXRD) was conducted using a PANalytical X'Pert Pro diffractometer that was outfitted with a cobalt anode (45 kV, 40 mA) and an X'celerator line detector. Line broadening in the patterns was used to estimate the crystal size via the Scherrer equation. A Rigaku RU-200BVH with a rotating copper anode was used to collect small-angle X-ray scattering (SAXS) patterns. Scattered X-rays were detected using a Siemens Hi-Star multiwire area detector. Nitrogen sorption isotherms at 77 K were obtained using a Quantachrome Autosorb-iQ_2-MP. Prior to analysis, all samples were outgassed for 12 h at 200 °C and 0.001 torr. The Brunauer-Emmett-Teller (BET) method was applied to obtain surface areas, and pore volumes were calculated using the point P/P_o=0.995 on the adsorption branch. Attenuated total reflectance FTIR (ATR-FTIR) spectra were collected using a Shimadzu IR Affinity-1 spectrometer fitted with a Specac Golden Gate single reflection diamond ATR accessory. Powders from electrodes (as-prepared and cycled) were scraped onto the diamond crystal and compacted under a stainless steel anvil.

5.2.8 Electrochemical Characterization

Before an electrode paste was made, the prepared 3DOM TiO_2/C composites were ground and ultrasonicated. This processed active material was mixed with Timcal Super P carbon black, aqueous sodium carboxymethyl cellulose (CMC), and aqueous styrene-butadiene rubber (SBR). In the final paste, the weight ratio of components was 84 wt% active material, 10 wt% carbon black, 4 wt% CMC, and 2 wt% SBR. Pastes were coated on either carbon-coated aluminum (kindly provided by Exopack® Advanced Coatings) or Cu foil. Electrode films were dried at ambient conditions overnight and then at 24 h at 105 °C. The loading of electrode paste per cm^2 ranged from 1 to 2 mg/cm^2. A punch with a 0.5 in diameter was used to cut out electrode disks. Half-cells were assembled using CR2032 cells purchased from MTI Corporation. Lithium ribbon served as the counter electrode in the cells and a coated polypropylene separator (Celgard® 3501, received as a gift) was utilized to prevent shorts. The electrolyte used in the cells was 1 M $LiPF_6$ dissolved in a 1:1:1 mixture (by mass) of ethylene carbonate, dimethyl carbonate, and diethyl carbonate (purchased from MTI Corporation). All cells were assembled in a glove box filled with He gas. Cycling was performed on an Arbin Instruments BT2000 from either 1 to 3 V vs. Li/Li^+ (using carbon-coated Al as a current collector) or from 50 mV to 3 V vs. Li/Li^+ (using copper as a current collector). Depending on the voltage range used, the C-rate was set so that 1 C = 335 mA per g of TiO_2 in the composite (1 to 3 V) or set at 1 C = 335 mA per g of the composite (0.05 to 3 V). Specific capacities were calculated in a similar fashion. Cyclic voltammetry (CV) curves were obtained using a Solartron 1287 electrochemical station. Scanning was conducted between 0.05 and 3 V vs. Li/Li^+ with a scan rate of 5 mV/s and a 1 s integration time.

5.3 Results and Discussion

Owing to the different types of 3DOM TiO_2/C synthesized for this work, the discussion is separated into several different topics. The first centers on the two ammonium citratoperoxotitanate(IV)-based syntheses designated PF-TiO_2/C and Sucrose-TiO_2/C. Both the ammonium citratoperoxotitanate(IV) precursor, and the processed composites are characterized. In the second, the additional composites are discussed along with the 3DOM C material that serves as a reference. A brief summary concerning of the composites is discussed, including a comparison to the types of 3DOM TiO_2/C composites shown in Chapter 3. Finally, the structural characterization of these materials is used to frame a discussion of their electrochemical lithium insertion/extraction properties.

5.3.1 Characterization of PF-TiO_2/C and Sucrose-TiO_2/C

For the PF- and Sucrose-TiO_2/C, the key foci of the investigation are exploring how changing the precursor to less toxic alternative impacts the structure, and how the composites change when the final pyrolysis temperature is altered. The characterization of these composites informs our understanding of their lithium insertion and extraction properties. Prior to that discussion, the characterization of the TiO_2 precursor common to both syntheses, the ammonium citratoperoxotitanate(IV) gel, is provided.

5.3.1.1 Characterization of the Ammonium Citratoperoxotitanate(IV) Gel (Gel-1)

While earlier research has typically concentrated on characterization of crystalline ammonium citratoperoxotitanate(IV),[16,20] only one research team has investigated a gel of this complex in any depth.[21,22] From Raman characterization of gel-1 (Figure 5.1 a), many bands are present that do not match the strong bands in the crystalline complex, suggesting that the structure of the gel is different from that of the crystalline complex. For instance, the crystalline ammonium citratoperoxotitanate(IV) contains a band that is located at ~610 cm^{-1} and is assigned to a vibration originating from a side-on peroxo ligand coordinated to Ti.[16] This band is absent (or obscured) by a much stronger band centered near 520 cm^{-1}. When only one peroxo group is coordinated to a metal center, a strong symmetric stretch is present near 520 cm^{-1}, which matches the spectrum in Figure 5.1 a.[23] It is also possible that there is a contribution to the band from Ti–O linkages between citric acid and the Ti cation.[21,24] Further complicating the analysis is that a Ti–O–Ti vibrational mode is also found in this spectral region for Ti-containing peroxy gels.[25] Some additional evidence for Ti–O–Ti linkages (from the condensation of the titanium complexes) can be observed in the spectrum. A peak near 420 cm^{-1} matches well with a Ti–O–Ti vibration identified by Tengvall *et al*. for a peroxy gel.[25] If all three contributions (from the peroxo linkages, Ti–O linkages, and Ti–O–Ti linkages) are present, that can explain the intensity of the band near 500 cm^{-1} in Figure 5.1 a. Vibrations from peroxo moieties, specifically the O–O symmetric stretch, can also be identified in a partially obscured band near 860 cm^{-1}.[16] Additional peaks near 1400 cm^{-1} (symmetric) and ~1600 cm^{-1} (asymmetric) arise from carboxylate groups present on deprotonated citric acid.[26] A split is observed in the asymmetric stretch near 1600 cm^{-1} (see inset in Figure 5.1 a). The higher intensity peak at 1625 cm^{-1} is likely from a Ti–O bonding mode as identified by Kakihana and co-workers,[24] and the other peak is from free carboxylate groups. Moieties on the citric acid are also responsible for bands near 3000 cm^{-1}, specifically vibrations near 2900 cm^{-1} from methylene bridges.[26]

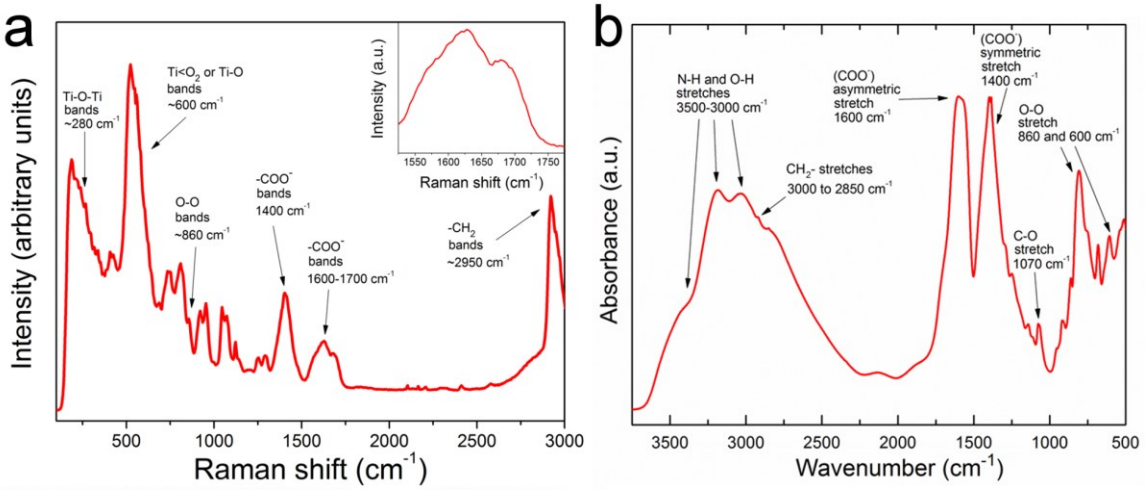

Figure 5.1 Raman (a) and IR (b) spectra obtained from the ammonium citratoperoxotitanate(IV) gel (gel-1) precursor. Characteristic vibrations for the bonds between the ligand and metal center and for bonds in the ligands themselves are labeled.

FTIR spectroscopy complements Raman spectroscopy for analysis of gel-1. An FTIR spectrum of a similar gel was reported by Truijen *et al.,* and it closely matches the spectrum in Figure 5.1 b.[22] The citric acid present in the gel is responsible for a number of absorption peaks present in the spectrum, including absorptions corresponding to the–OH stretch near 3000 cm^{-1} (broad), the $–CH_2–$ stretch slightly below 3000 cm^{-1}, and the C–O stretch from the alcohol functionality near 1070 cm^{-1}.[21] In addition, both peaks corresponding to the symmetric and asymmetric stretches of the carboxylate group can be found in the spectrum. Positions of the stretches are close to what has been reported for deprotonated trisodium citrate[27] and in the aforementioned ammonium citratoperoxotitanate(IV) gel.[22] A large difference in wavenumbers (Δ = 200 cm^{-1}) between the symmetric and asymmetric stretch of the carboxylate is observed. This is common for deprotonated carboxylic acids, which could be associated with ammonium cations in the gel.[26] Broadening is also observed for the asymmetric carboxylate peak that extends the plateau of the peak out to lower wavenumbers (~1570 cm^{-1} before a steep decline in absorbance). This is due to a contribution from a vibrational mode of a carboxylate chelated to titanium; a shoulder at a similar position was observed by Truijen *et al*. when evaluating the IR spectrum of a similar gel.[22] While ultimately judging the type of coordination (or lack thereof) that is adopted by the citrate ligands is difficult, it appears that some of the carboxylate groups participate in unidentate binding with Ti and some groups are not bound to the Ti cations. Since the difference in wavenumbers between the two carboxylate stretches for the gel is similar to trisodium citrate,

the carboxylate is unlikely to coordinate to Ti as a bidentate bridging or chelating ligand.[28] As for bound peroxo groups, several other vibrations in the spectrum can potentially be assigned to these ligands, including those near 910, 860 and 610 cm^{-1}.[23] Either the peak near 910 cm^{-1} or the one near 860 cm^{-1} is from the O–O stretching mode (or perhaps those peaks are from O–O mode in different coordination environments in the disordered gel), and the peak near 610 cm^{-1} is from a symmetric or asymmetric stretching vibration from the coordinated peroxo ligand.[21,23]

5.3.1.2 Elemental Analysis of PF-TiO_2/C and Sucrose-TiO_2/C

The chemical composition of PF-TiO_2/C and Sucrose-TiO_2/C pyrolyzed at 700 °C was determined using a combination of thermogravimetry and combustion analysis (Table 5.1). TGA revealed that the content of TiO_2 is slightly greater in PF-TiO_2/C than in Sucrose-TiO_2/C. This difference is most likely due to the fact that twice the mass of sucrose was used in the Sucrose-TiO_2/C precursor when compared to the mass of PF sol in the PF-TiO_2/C precursor. However, pyrolysis of citric acid contributes a substantial fraction of carbon in both the PF- and the Sucrose-TiO_2/C (ten times the number of moles of citric acid monohydrate is present relative to the PF sol/sucrose). While the carbon and hydrogen content is similar for both samples, the oxygen content is higher in the carbonaceous fraction of the Sucrose-TiO_2/C. Elevated oxygen content is expected since sucrose contains an atomic ratio of O to C of nearly one.[29] PF- and Sucrose-TiO_2/C contain similar amounts of hydrogen and nitrogen. The nitrogen content is significantly elevated in these composites when compared to 3DOM C prepared from the carbonization of resorcinol-formaldehyde resin.[30] Ammonium ions in the gel precursor for the TiO_2 appear to be responsible for the increased in nitrogen in the carbonaceous fraction.

Table 5.1. Compositions of the PF-TiO_2/C and Sucrose-TiO_2/C composites.

Sample	TiO_2 content (wt%)[a]	carbon content (wt%)[b]	carbonaceous oxygen content (wt%)[b]	hydrogen content (wt%)[b]	nitrogen content (wt%)[b]
PF-TiO_2/C, 700 °C	51.5	42.3	2.5	0.9	2.8
Sucrose-TiO_2/C, 700 °C	46.3	43.0	6.8	0.7	3.2

[a] Determined via thermogravimetric analysis.
[b] C/H/N of the determined via combustion analysis, oxygen by difference.

5.3.1.3 Electron Microscopy of the Pyrolyzed PF-TiO_2/C and Sucrose-TiO_2/C

To confirm that hard templating was successful, SEM images of the composites were obtained, and representative images are displayed in Figure 5.2 and Figure 5.3. All materials contain an interconnected, face-centered-cubic array of macropores that facilitates penetration of electrolyte throughout these materials. Some disorder (micrometer-scale voids, broken struts) is present in the network. While the 3DOM structure is similar for both PF- and Sucrose-TiO_2/C, a few differences can be observed. For the PF-TiO_2/C, many regions have interconnecting windows with a narrow diameter (see Figure 5.3 a). This is typical of surface-templated 3DOM materials synthesized with precursors that have more favorable interactions with the hard template. The ethanol in the PF-TiO_2/C can wet the PMMA colloidal crystal better than the purely water-based precursor for Sucrose-TiO_2/C, explaining the occurrence of surface templating. A more "skeletal" volume-templated structure with larger windows between adjacent macropores is present in the Sucrose-TiO_2/C (Figure 5.3 b) that likely arises from repulsive interactions between the highly polar precursor and the nonpolar template.[31]

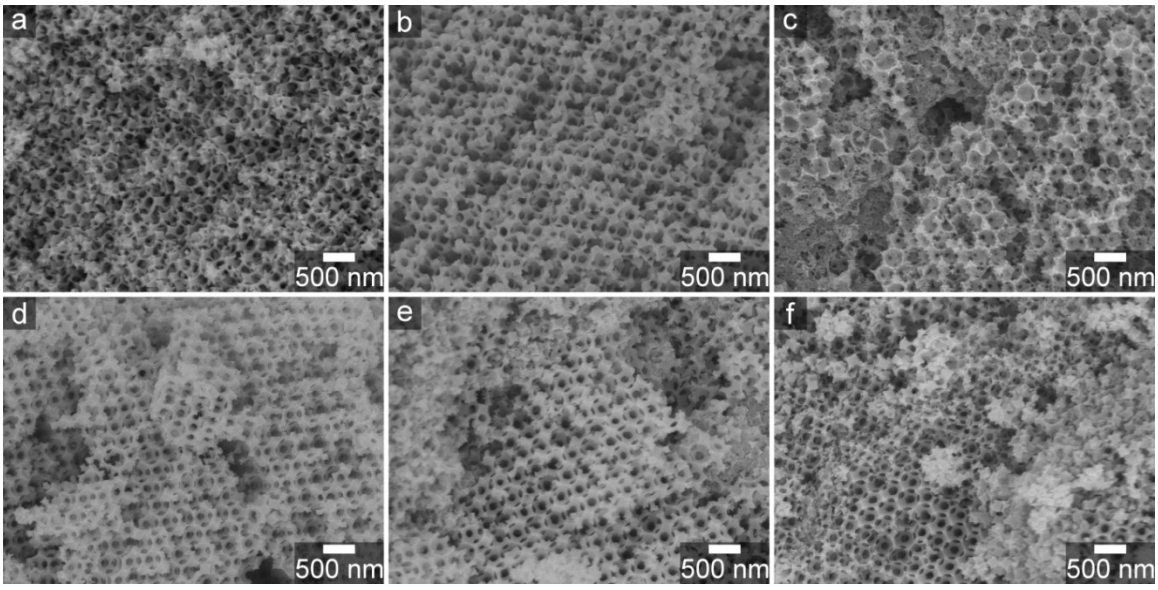

Figure 5.2 SEM micrographs of the 3DOM PF-TiO_2/C and Sucrose-TiO_2/C composites. The first row contains representative images of PF-TiO_2/C pyrolyzed at (a) 700 °C, (b) 800 °C, and (c) 900 °C. The second contains images of the Sucrose-TiO_2/C samples pyrolyzed at (d) 700 °C, (e) 800 °C, and (f) 900 °C. A 3DOM network, albeit with some disorder, is present in all samples.

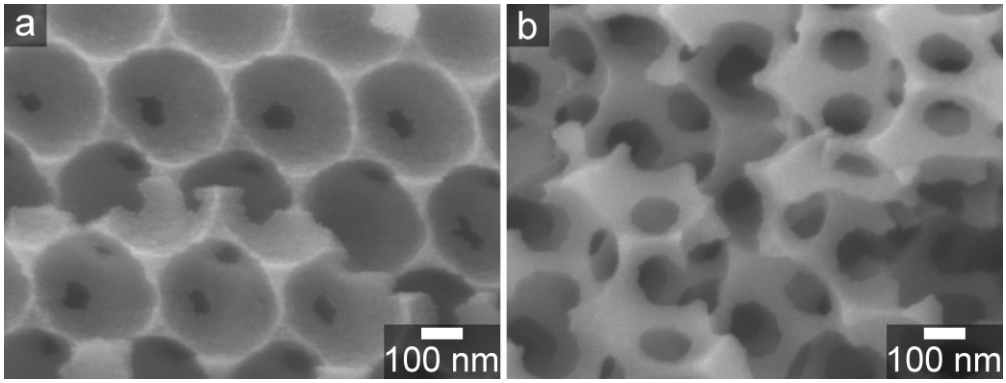

Figure 5.3 Higher magnification SEM images of (a) PF-TiO_2/C and (b) Sucrose-TiO_2/C composites pyrolyzed at 900 °C.

Transmission electron microscopy provides a more complete understanding of the morphology, including the location/size of TiO_2 crystallites and mesopores. From examination of Figure 5.4, TiO_2 crystallites are so small that they cannot be observed at moderate magnifications for composites pyrolyzed at 700 °C. Small, bright lines also snake across the composites at those temperatures, and result from disordered mesopores templated from P123 surfactant. Higher magnification images (Figure 5.5) reveal the crystallites via diffraction contrast. The sizes of these nuclei are smaller than 5 nm in both PF- and Sucrose-TiO_2/C. This is similar in size to the crystallites in TFA2-TiO_2/C, as described in Chapter 4. Since the TFA2-TiO_2/C has a similar content of carbon to the materials described in this chapter, this finding is to be expected. Increased carbon content in PF- and Sucrose-TiO_2/C samples leads to reduced sintering and crystallite growth, especially at 700 °C. Decomposition of the citric acid may also assist in inhibiting the sintering of TiO_2. Carboxylate groups of the citric acid are bound to Ti ions, and the citric acid can carbonize into shells that surround growing TiO_2 nuclei during pyrolysis. After pyrolysis at 800 and 900 °C, a distinct increase in the crystal size occurs, indicating that the temperature is sufficiently high to allow for sintering (Figure 5.4 c–f). At 800 °C, PF-TiO_2/C experiences more pronounced sintering than Sucrose-TiO_2/C, albeit in localized areas. For the PF-TiO_2/C sample pyrolyzed at 900 °C, many crystallites of TiO_2 are localized on the surface of the composite. In the case of the Sucrose-TiO_2/C, areas that suffer from extensive sintering contain crystallites conforming to the structure of the 3DOM network.

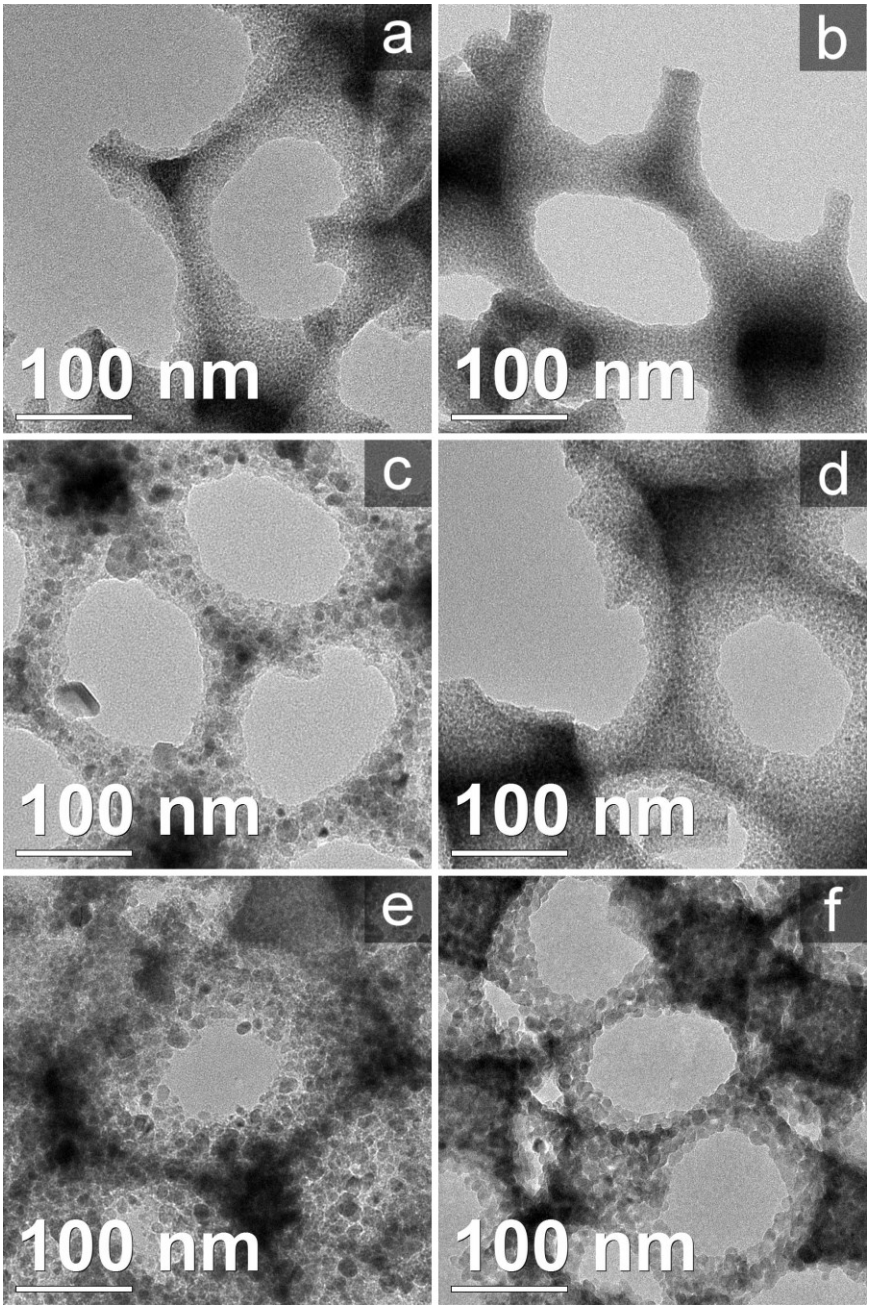

Figure 5.4 TEM micrographs of PF-TiO_2/C and Sucrose-TiO_2/C pyrolyzed at various temperatures. The first column shows PF-TiO_2/C pyrolyzed at (a) 700 °C, (c) 800 °C, and (e) 900 °C. The second column shows Sucrose-TiO_2/C pyrolyzed at (b) 700 °C, (d) 800 °C, and (f) 900 °C. Images taken by Stephen Rudisill.

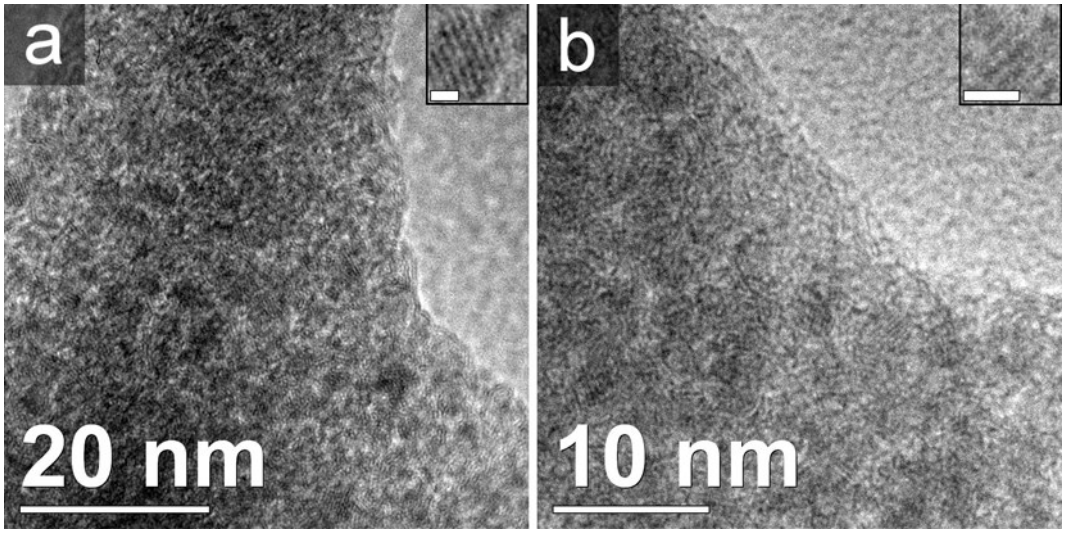

Figure 5.5 High magnification TEM micrographs of PF-TiO_2/C (a) and Sucrose-TiO_2/C (b) pyrolyzed at 700 °C. Insets show individual crystallites in the composite materials. The spacing of the lattice fringes in (a) matches that of the (110) planes in anatase, and the spacing of fringes in (b) matches that of the (101) planes in rutile. Scale bars in the insets are one nm in length. Images taken by Stephen Rudisill.

TEM imaging also reveals inhomogeneities in the location and size of TiO_2 crystallites in the composites (Figure 5.6). At higher pyrolysis temperatures (800 and 900 °C), there is a substantial non-uniformity in the size of the observed crystallites. Many regions contain crystals far smaller than those found adjacent regions (compare Figure 5.6 a–c with the counterparts in Figure 5.4). This variation is highlighted especially well by comparing the top right of Figure 5.6 a with the bottom center of the image. Areas with a high concentration of TiO_2 facilitate sintering and lead to larger crystallites. As shown later, titanium oxycarbide is also present in these composites. Regions with smaller crystallites contain a high concentration of the oxycarbide phase. Selected area electron diffraction (SAED) of these areas (specifically those shown in Figure 5.6 b, c), reveal diffraction rings that cannot be indexed to anatase or rutile TiO_2 (Figure 5.7). Instead, these rings match a titanium oxycarbide phase also found in the PXRD patterns discussed below.

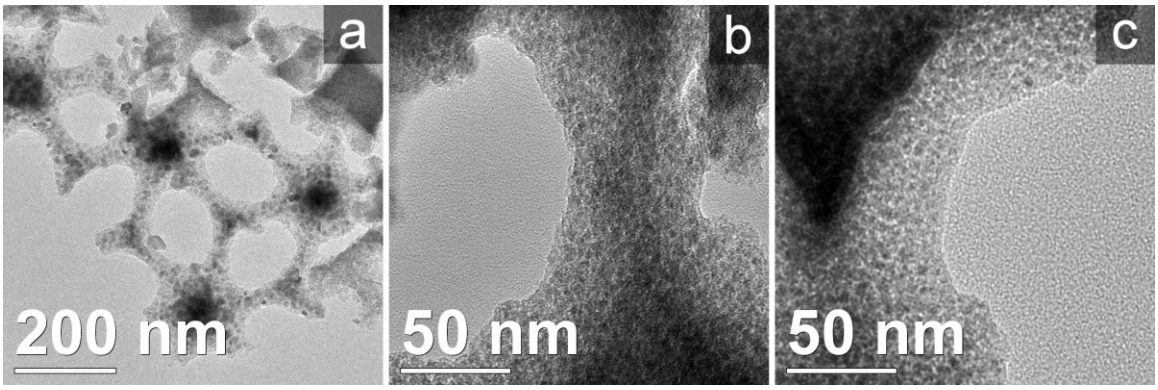

Figure 5.6 TEM micrographs highlighting inhomogeneities in the location/size of TiO_2 crystallites in the composites. (a) Regions with large and small crystallites of TiO_2, co-exist for the PF-TiO_2/C sample pyrolyzed at 800 °C. For the images of (b) PF-TiO_2/C and (c) Sucrose-TiO_2/C pyrolyzed at 900 °C, crystallites of TiO_2 (or titanium oxycarbide) are far smaller than those imaged in Figure 5.4. Images taken by Stephen Rudisill.

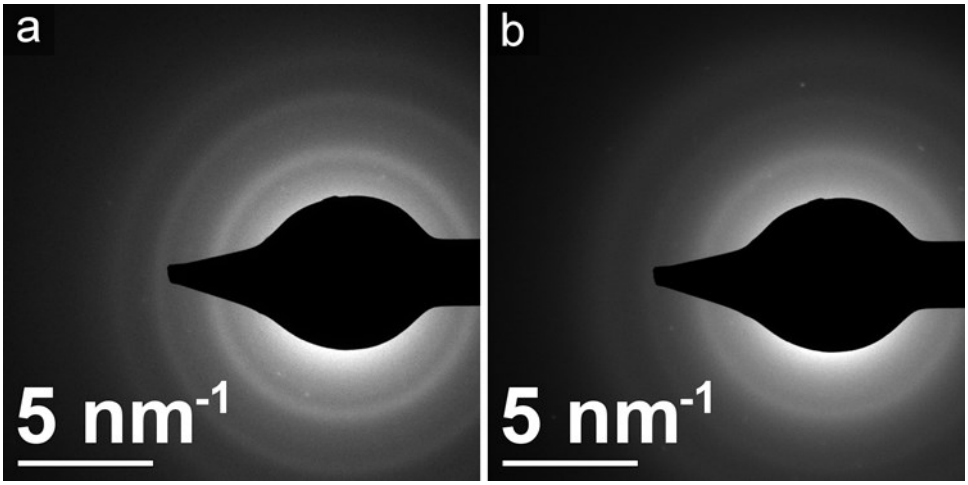

Figure 5.7 Selected area electron diffraction for PF- and Sucrose-TiO_2/C pyrolyzed at 900 °C. Broad diffraction rings are found in both patterns. Reflections that have similar *d*-spacings are observed in PXRD patterns (shown in the main text), and these reflections are from a titanium oxycarbide phase. The *d*-spacings of the rings (and their Miller indices) are approximately 0.21 nm (200), 0.15 nm (220), and 0.12 nm (311/222). Isolated diffraction spots are also present, which originate from TiO_2 crystals. Patterns collected by Stephen Rudisill.

5.3.1.4 Characterization of the Crystal Structures Present in PF-TiO_2/C and Sucrose-TiO_2/C

By examining the PXRD patterns of the composites (Figure 5.8), one can observe that similar series of phase transformations occur for both PF- and Sucrose-TiO_2/C. For composites pyrolyzed at 700 °C, strong peaks corresponding to anatase or rutile TiO_2 are absent. A broad peak near 29.4 °2θ matches the (101) reflection of anatase TiO_2 and is overlaid on a shoulder spanning from 22.5 to ~40 °2θ from amorphous carbon.[29] Another peak near 51 °2θ is most likely from the carbon framework produced from the various carbon-containing precursors (denoted with a cross in Figure 5.8).[29,32] Once the pyrolysis temperature is increased to 800 °C, anatase and rutile reflections appear in the patterns. Rutile is the major TiO_2 polymorph at 900 °C. This is expected since rutile is the thermodynamically stable phase for bulk TiO_2 and forms at high temperatures.[33] Several other peaks are observed in the patterns of materials pyrolyzed at 800 °C and 900 °C. Since these reflections are positioned between cubic TiC and TiO and follow the pattern of a face-centered cubic structure, it is likely that titanium oxycarbide (TiO_xC_y) is present.[34] All the *d*-spacings of the reflections shown in the PXRD patterns closely match those of the SAED patterns shown in Figure 5.7, which provides further confirmation that titanium oxycarbide is present in certain areas of the 3DOM composites. The titanium oxycarbide is formed from the carbothermic reduction of TiO_2,[35,36] and this process occurs at extremely low temperatures for the PF- and Sucrose-TiO_2/C.[37] Small crystallite sizes and the abundance of carbon facilitate the carbothermic reduction.[36-38] Indeed, this process occurs so quickly that the intermediate Magnelí phases that form during the reduction[34] are not even identified in the PXRD patterns. Since oxygen heteroatoms are present in the carbonaceous fraction, reflections for the titanium oxycarbide phase are shifted closer to TiO.[34] However, the lattice parameter increases (a shift to lower °2θ is observed, especially for the (220) peak near 75 °2θ) as the pyrolysis temperature is increased from 800 °C to 900 °C, and as oxygen is removed from the carbon fraction and the oxycarbide. PF-TiO_2/C patterns contain stronger reflections for the oxycarbide phase, which may be a consequence of the lower oxygen content in the carbon fraction of the composite.

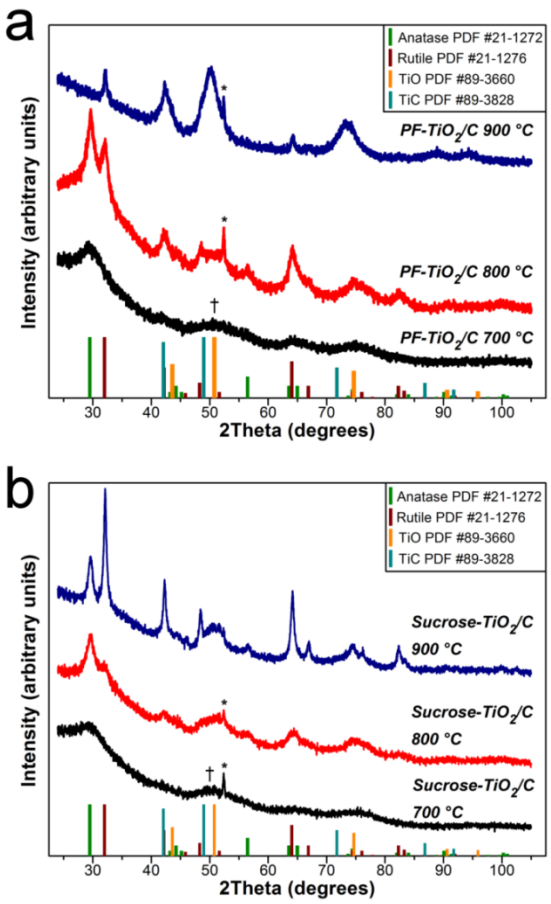

Figure 5.8 PXRD patterns for (a) PF-TiO_2/C and (b) Sucrose-TiO_2/C pyrolyzed at different temperatures. The cross marks the location of a peak from the carbon network and the asterisk marks a reflection from the Al sample holder.

Crystallite sizes of anatase TiO_2, rutile TiO_2, and titanium oxycarbide were estimated using the line width of sufficiently intense reflections in the PRXD patterns and are presented in Table 5.2. At 700 °C, the reflections are so weak that they cannot be satisfactorily fit. Once the pyrolysis temperature is increased to 800 °C, TiO_2 crystallite sizes can be determined. PF-TiO_2/C contains larger anatase TiO_2 crystallites than those in Sucrose-TiO_2/C. This difference may be from the increased proportion of the secondary carbon phase in Sucrose-TiO_2/C. However, both the PF- and Sucrose-TiO_2/C have much smaller crystallite sizes than the TFA2-TiO_2/C analyzed in Chapter 4. As observed in the TEM images (e.g. Figure 5.5), crystallites are confined within the carbon phase for the PF-TiO_2/C and Sucrose-TiO_2/C. The secondary carbon phase partially controls crystallite growth (similar to the acac-TiO_2/C), unlike TFA2-TiO_2/C that experiences phase separation of TiO_2 to the surface of the 3DOM structure. Even though confinement of TiO_2

by the carbonaceous fraction occurs in PF- and Sucrose-TiO_2/C, the size of TiO_2 crystallites exceeds 10 nm in all samples once pyrolysis is conducted 900 °C. Rutile TiO_2 grows more rapidly than anatase TiO_2,[39] and this is borne out by the larger rutile crystal size in Sucrose-TiO_2/C. Interestingly, larger rutile crystallites are found in Sucrose-TiO_2/C than in PF-TiO_2/C, but this may be from the increased conversion of TiO_2 to titanium oxycarbide in PF-TiO_2/C. A decreased content of TiO_2 in PF-TiO_2/C due to the conversion may limit sintering. Reflections from the titanium oxycarbide phase can be fitted for materials pyrolyzed at 900 °C. The average size of oxycarbide crystallites is 3.2 nm in PF-TiO_2/C and 3.9 nm in Sucrose-TiO_2/C, and these sizes are similar to TiC formed via carbothermic reduction in mesoporous TiO_2/C materials.[35,36] Titanium oxycarbide experiences slower sintering and grain growth kinetics than either TiO_2 polymorph.

Table 5.2 Structural and textural parameters of PF-TiO_2/C and Sucrose-TiO_2/C.

sample	anatase crystallite size (nm)	rutile crystallite size (nm)	titanium oxycarbide crystallite size (nm)	BET surface area (m^2/g)	pore volume (mL/g)
PF-TiO_2/C, 700 °C	[a]	[a]	[c]	226	0.44
PF-TiO_2/C, 800 °C	8.3	8.5	[b]	375	0.40
PF-TiO_2/C, 900 °C	[c]	10.3	3.2	412	0.60
Sucrose-TiO_2/C, 700 °C	[a]	[a]	[c]	225	0.43
Sucrose-TiO_2/C, 800 °C	6.7	8.8	[b]	281	0.47
Sucrose-TiO_2/C, 900 °C	10.0	16.3	3.9	326	0.65

[a] Reflections too weak to be analyzed via the Scherrer equation.
[b] Phase present, but too weak to be analyzed via the Scherrer equation.
[c] Phase not detected in PXRD pattern.

Since inhomogeneities were detected using TEM, confocal Raman microscopy was also used to investigate the spatial variations in the TiO_2 polymorph. Spectra of PF-TiO_2/C and Sucrose-TiO_2/C pyrolyzed at different temperatures are presented in Figure 5.9. Depending on the area of

sample analyzed, Raman modes corresponding to the anatase or rutile polymorph are found.[40,41] The appearance of peaks that match the position of rutile TiO_2 modes is unexpected, especially since the size of the crystallites is so small for the PF- and Sucrose-TiO_2/C pyrolyzed at 700 °C. Part of the contribution to these peaks in the Raman spectra comes from the unexpected formation of rutile TiO_2. It appears that rutile TiO_2 nucleates from ammonium citratoperoxotitanate(IV) or undergoes a phase transition (from either amorphous TiO_2 or anatase TiO_2) to rutile at extremely small crystallite sizes (below 5 nm). At that size, rutile is thermodynamically unstable relative to anatase.[39] When examining TEM images for Sucrose-TiO_2/C pyrolyzed at 700 °C (Figure 5.5 b), the spacing between lattice fringes of TiO_2 crystals is ~0.32 nm. This distance corresponds to the *d*-spacing for the (110) plane of rutile TiO_2. Anatase is found in other areas with a lattice spacing of ~0.35 nm (corresponding to the (101) plane), and this is shown for PF-TiO_2/C pyrolyzed at 700 °C (Figure 5.5 a). Another contribution to the vibrational modes that match rutile TiO_2 may be from titanium oxycarbide crystallites. While crystals of stoichiometric cubic TiC (and TiO) lack Raman-active modes, crystals with cationic vacancies display Raman modes at positions nearly identical to those of rutile TiO_2.[42,43] It is possible that conversion from TiO_2 to the oxycarbide would produce crystallites with defects.[43] This contribution would also fit the trend observed with regard to the commonality of particular TiO_2 modes. At lower pyrolysis temperatures, the characteristic modes of anatase are more common than rutile modes. Peaks corresponding to rutile are more prevalent when the pyrolysis temperature is increased. Both the continued phase transformation from anatase TiO_2 to rutile TiO_2 (see Figure 5.8) and the increased formation of titanium oxycarbide are likely responsible for the prevalence of the rutile modes at elevated pyrolysis temperatures.

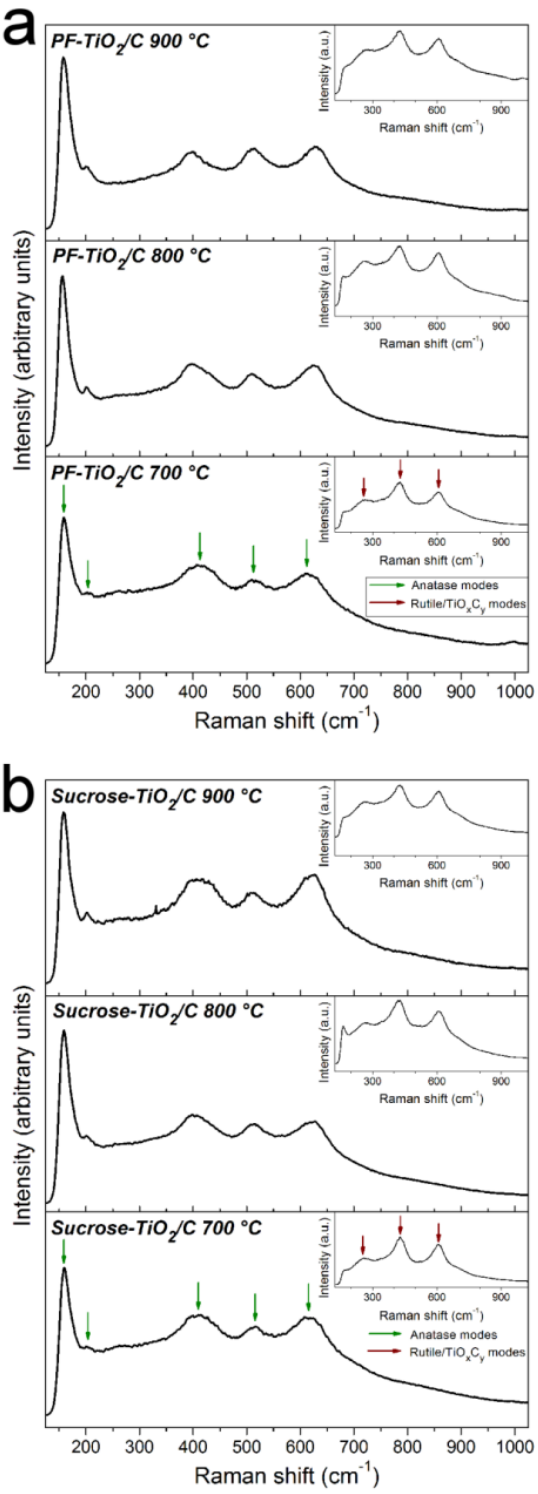

Figure 5.9 Raman spectra for (a) PF- TiO_2/C and (b) Sucrose-TiO_2/C in the spectral region that reveals TiO_2 lattice vibrations. Regions are found in all the samples that contain anatase and/or rutile modes (see insets). It is possible that vibrations from a defective TiO_xC_y phase overlap with rutile TiO_2 vibrations.

Confocal Raman microscopy was also used to analyze the carbonaceous components in these composites. The corresponding spectra are presented in Figure 5.10. Two characteristic bands are observed, both of which result from vibrations in the six-member carbon rings that are present in the amorphous carbon. Centered at ~1600 cm^{-1} is the *G* band, which arises from stretching of bonds between sp^2-hybridized carbon atoms.[44] At ~1350 cm^{-1} is the *D* band that results from a breathing mode in any sp^3-hybridized carbon atoms that are present in the ring.[44] Not surprisingly, the intensity of the *G* band relative to the *D* band increases as pyrolysis temperature is raised for both PF-TiO_2/C and Sucrose-TiO_2/C (see Table 5.3). This indicates that the fraction of sp^3-hybridized carbon atoms decreases at high pyrolysis temperatures, since higher temperatures allow for the removal of heteroatoms and the formation of extended aromatic (graphitic) domains. Intensity ratios are fairly similar for both types of composite at corresponding pyrolysis temperatures. While the *G* band intensity decreases for the TFA- and acac-TiO_2/C materials described in Chapter 3 with increasing pyrolysis temperature, the size of the graphitic clusters in the composites described here must be larger. For graphitic clusters larger than ~3 nm, *G* band intensity increases with increasing temperature.[44] It is understandable that the relatively high carbon content in the PF and Sucrose-TiO_2/C would yield sizeable graphitic domains (>3 nm) that grow in size with higher pyrolysis temperatures.

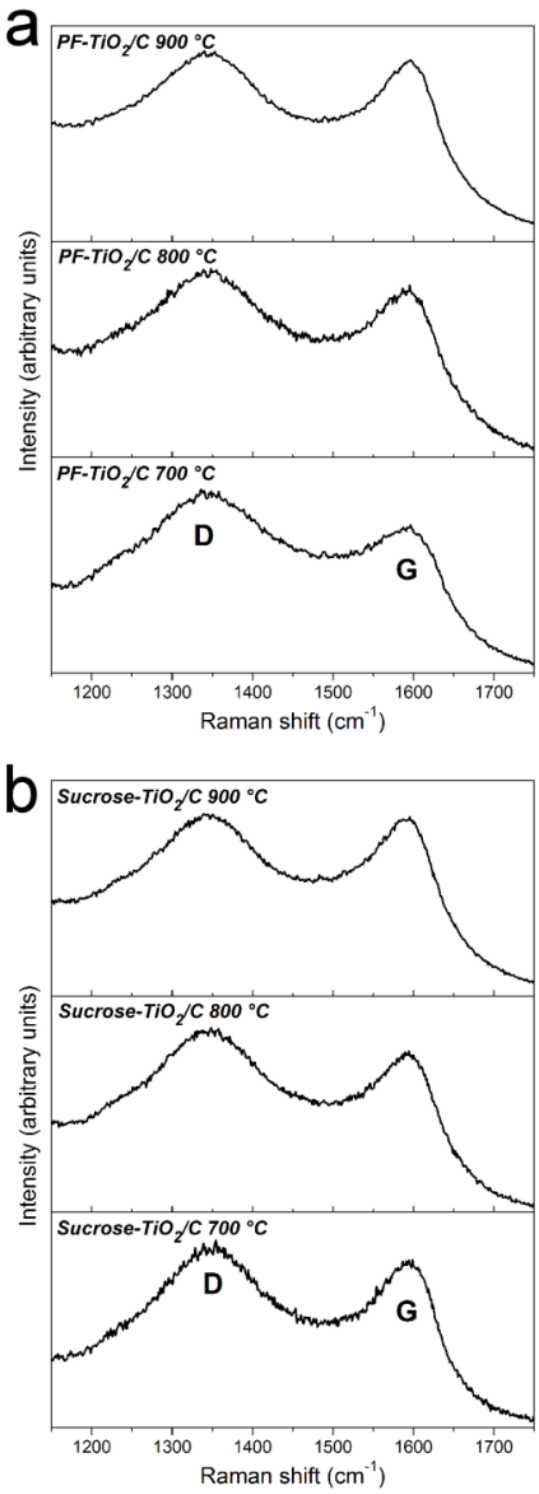

Figure 5.10 Raman spectra of (a) PF-TiO_2/C and (b) Sucrose-TiO_2/C from the region that shows the *D* and *G* bands from amorphous carbon. A significant fraction of sp^3-hybridized carbon is present in the carbon framework, as expected.

Table 5.3 Relative intensities of the *D*/*G* Raman bands for the composite samples.

sample	I_D/I_G	domain size (nm)
PF-TiO_2/C, 700 °C	1.32	3.3
PF-TiO_2/C, 800 °C	0.99	4.4
PF-TiO_2/C, 900 °C	0.92	4.8
Sucrose-TiO_2/C, 700 °C	1.15	3.8
Sucrose-TiO_2/C, 800 °C	1.14	3.9
Sucrose-TiO_2/C, 900 °C	0.95	4.6

5.3.1.5 Characterization of the Textural Properties of PF-TiO_2/C and Sucrose-TiO_2/C

The pore textures of the composite materials was analyzed by SAXS and by N_2 gas sorption to estimate the surface area of the various samples, determine pore volumes, and probe changes in meso-/microporosity. All of the N_2 sorption isotherms presented in Figure 5.11 reveal sharp rises in the volume of gas adsorbed at low ($P/P_o<0.001$) and high ($P/P_o>0.9$) relative pressures. Micropores present in the amorphous carbon are responsible for the rise at the low pressure range, and the templated macropores are responsible for the rise at high pressures. While P123 was present in the precursor, little hysteresis is present in the isotherms. For the PF-TiO_2/C, very narrow hysteresis loops are present in all samples. In contrast, the Sucrose-TiO_2/C only has a narrow hysteresis loop when pyrolyzed at 700 °C. However, TEM images show changes in contrast expected for disordered mesopores or perhaps isolated micelles (see Figure 5.4 and 5.5). It appears that either the concentration of surfactant was too low for the formation of any ordered mesostructure, or that the interactions between the surfactant and the other components of the precursor are insufficient or unfavorable for self-assembly. SAXS patterns of the composites suggest that a well-defined mesostructure is absent. These patterns are either free of scattering peaks or contain a very weak scattering peak near 1.5 °2θ (Figure 5.12). Even without substantial mesoporosity, all composites have BET specific surface areas greater than 200 m^2/g and high pore volumes (Table 5.2). As the pyrolysis temperature is brought higher, both the specific surface area and pore volume the composites increase. This increase is mainly from the continued formation of micropores in the amorphous carbon component (Figure 5.13); this phenomenon is also observed in the TiO_2/C composites studied in Chapter 3 and 4.

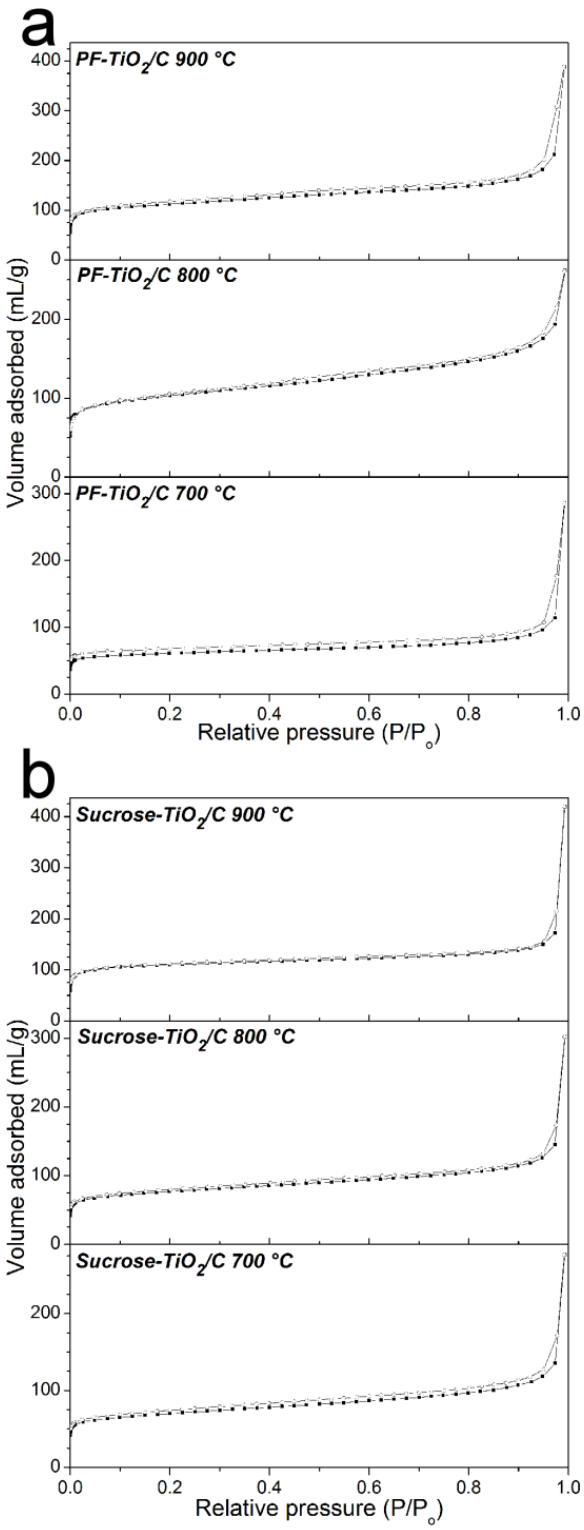

Figure 5.11 Nitrogen sorption isotherms for (a) PF-TiO_2/C and (b) Sucrose-TiO_2/C. All isotherms show pressure rises at low and high relative pressures originating from micropores and macropores, respectively.

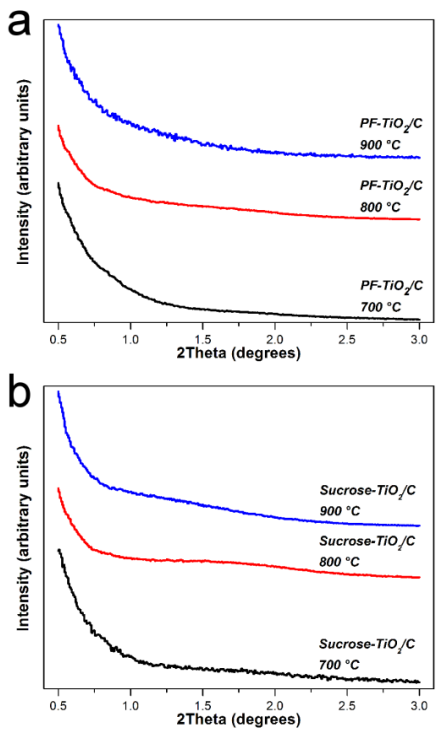

Figure 5.12 Small-angle X-ray scattering patterns for (a) PF-TiO_2/C and (b) Sucrose-TiO_2/C. Some composites, notably the Sucrose-TiO_2/C pyrolyzed at 700 °C or 800 °C, have weak scattering peaks near ~1.5 °2θ.

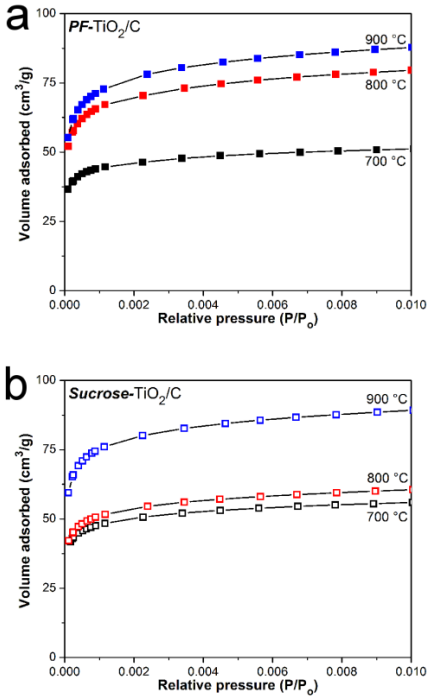

Figure 5.13 Enlarged view of the low relative pressure region of the adsorption branches of the sorption isotherms for (a) PF-TiO_2/C and (b) Sucrose-TiO_2/C.

5.3.1.6 Further Discussion Concerning the Location and Polymorph of TiO_2 Crystallites Present in PF-TiO_2/C and Sucrose-TiO_2/C

At this point, it is important to consider the location and polymorph of the TiO_2 crystallites in the composites in more detail. Based on results obtained from SEM and TEM images, TiO_2 crystallites are distributed throughout the carbon matrix in the walls and nodes of the 3DOM network. From studies of the citratoperoxotitanate(IV) complex, it has been determined that the complex is hydrophilic and carries a negative charge.[16] Even if that complex is different in the gel, functional groups on the citric acid ligands and the peroxo ligands themselves should be able to interact (via intermolecular bonding) with the water and other hydrophilic components in the precursor. Similar behavior is observed in the acac-TiO_2/C composites discussed in Chapter 3. In both the acac-TiO_2/C and the materials described here, the complex interacts with other components in the precursor and a fairly homogeneous distribution of TiO_2 is observed. Inhomogeneities may arise for the PF- and Sucrose-TiO_2/C if the Ti cations are bound extensively to carboxylate groups present on the citric acid and the peroxo ligands. In this case, the complexes are less likely to bond to hydroxyl functionalities present in the PF sol/sucrose, hindering the interaction of the various components. An alternate possibility is that excess ammonium citrate, which is not bonded to Ti cations, phase demixes from the other components of the precursor, and generates extensive carbon-rich domains. It is more likely this occurs, given that free carboxylate moieties are present in the gel precursor and only unidentate carboxylate binding is detected in the ammonium citratoperoxotitanate(IV) gel precursor (Figure 5.1). Rapid conversion of small TiO_2 grains to titanium oxycarbide (perhaps in carbon-rich areas) could also contribute to heterogeneities. Once TiO_2 is converted to titanium oxycarbide, the oxycarbide grains grow slowly, unlike the unconverted TiO_2. Slight differences in crystallite location between the PF- and Sucrose-TiO_2/C precursor systems may arise from the ethanol in the PF system. A less favorable interaction between the ionic precursor and the ethanol may result in more separation from the precursor, leading to more clustering of TiO_2 crystals near the surface, as is observed in PF-TiO_2/C electron microscopy images (Figure 5.4).

Another curious aspect of this system is that small rutile TiO_2 nuclei are present in the carbon matrix. As stated earlier, the transformation from anatase to rutile does not generally occur until anatase crystals reach roughly 11 nm in size.[33] Dopants can alter the point at which the phase transition occurs (as is discussed in Chapter 4), but the two likely dopants here, carbon and nitrogen, are known to suppress that transformation.[39] Additionally, the carbon matrix should limit crystal growth and reduce the number of interfaces between anatase crystallites that can

serve as nucleation sites for rutile.[45] The preferential nucleation of rutile at low temperatures has been observed in hydrothermal syntheses that use a titanium source and citric acid.[46] Researchers postulate that the octahedral complexes of titanium and citric acid undergo condensation to form linked edge-sharing units. Due to the structural similarity of this arrangement to the TiO_6 clusters in rutile, the rutile phase preferentially forms.[46] This could also occur in the composites studied herein. Another factor may be that reducing gases produced from pyrolysis of the citric acid and PF sol/sucrose generate oxygen vacancies in the TiO_2. As is discussed in Chapter 4, oxygen vacancies are known to assist in the transformation of anatase to rutile.[39,47] While these two explanations address the presence of rutile, they do not explain the co-existence of anatase TiO_2. It could be that some of the citratoperoxotitanate(IV) complexes condense at an earlier processing stage (as observed from Ti-O-Ti linkages shown in Figure 5.1) and form face-sharing octahedra. This is similar to the situation for TiO_6 clusters in anatase, leading to its preferential nucleation.[46]

5.3.2 Characterization of NAC-TiO_2/C and Sucrose2-TiO_2/C

Two other composites were synthesized to further explore certain aspects of the Sucrose-TiO_2/C system. One was produced without any added sucrose (NAC-TiO_2/C) and the other was made with half the citric acid used in the parent synthesis (Sucrose2-TiO_2/C). NAC-TiO_2/C has an identical precursor for TiO_2 to the samples analyzed above, but the ammonium citratoperoxotitanate(IV) precursor (gel-2) used for Sucrose2-TiO_2/C is prepared differently. Characterization of the gel-2 using a combination of Raman spectroscopy and IR spectroscopy (Figure 5.14) gives results that are similar to what is observed for gel-1. Strong peaks corresponding carboxylate vibrations, methylene groups and hydroxyl functionalities from the citric acid ligand are present in both spectra. An increase in intensity is observed in the Raman spectrum for wavenumbers between ~150 and 900 cm^{-1} when compared the similar region in gel-1 (compare Figure 5.1 with Figure 5.14). This is likely an overlay of numerous vibrations that occur due to the presence of Ti-O bonds and bound peroxo ligands.[21,23] Since the content of citric acid is lower than gel-1, it may be that there are fewer free molecules citric acid relative to those bound to Ti. Further evidence for this phenomenon can be observed in the asymmetric carboxylate stretch near 1600 cm^{-1} in the Raman spectrum (Figure 5.14 a). Relative to Figure 5.1, the peak from free carboxylate moieties (at 1675 cm^{-1}) is less pronounced for the gel-2 precursor.[24]

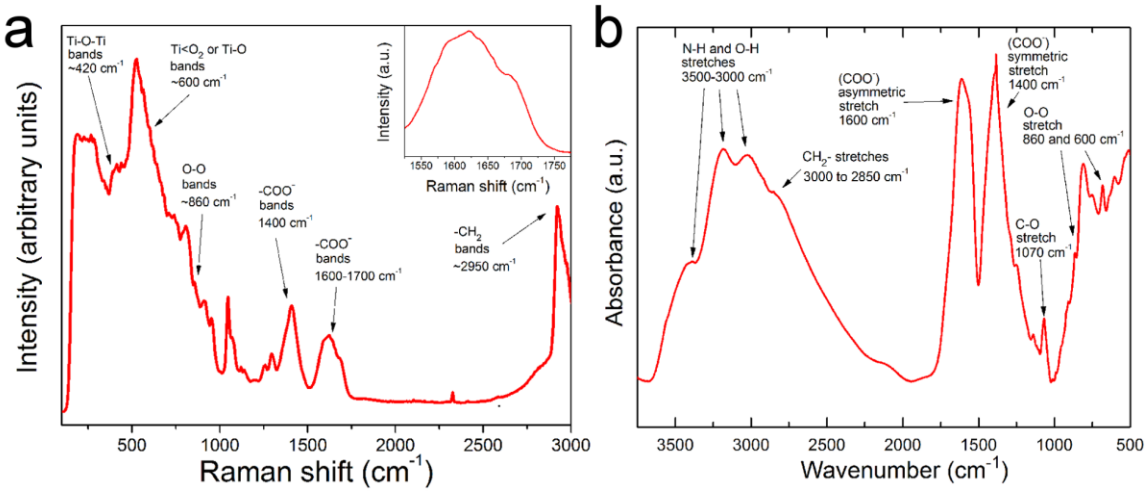

Figure 5.14 Raman (a) and IR (b) spectra of the modified ammonium citratoperoxotitanate(IV) gel that is designated gel-2. Features in the spectra closely match what is observed for gel-1 in Figure 5.1. More intense vibrations indicative Ti-O bonds (or a bound side-on peroxo ligand) are present in (a).

5.3.2.1 Compositional Analysis of NAC-TiO_2/C and Sucrose2-TiO_2/C

After performing thermogravimetric and elemental analyses, it was found that the NAC- and Sucrose2-TiO_2/C have a different carbon contents than the PF- and Sucrose-TiO_2/C composites described above (see Table 5.1 and Table 5.4). Oddly enough, the NAC-TiO_2/C has higher carbon content than the materials with added carbon. To explain this counter-intuitive result, it may be that the additional oxygen in the carbon precursors (e.g. PF sol and sucrose) allows for the formation of more volatile carbon-containing species. Another possibility is that the added carbon precursor disrupts tight binding of citric acid to the nuclei of TiO_2, allowing for greater loss of carbon during pyrolysis. For the Sucrose2-TiO_2/C, carbon content is decreased relative to Sucrose-TiO_2/C, which is expected since the amount of carbonizable citric acid is halved. Other elements (N, H, O) present in the carbonaceous fraction NAC-TiO_2/C are found to be present at similar levels to what is observed in the Sucrose-TiO_2/C. Sucrose2-TiO_2/C has a lower weight percent of N and O when compared to Sucrose-TiO_2/C. This may stem from the use of gel-2 as a TiO_2 precursor. If there are fewer free citric acid moieties, including those associated with ammonium cations, than are present in gel-1, then composites prepared from the gel-2 would incorporate fewer heteroatoms. The content of the various components of the modified composites are summarized in Table 5.4.

Table 5.4 Compositions of the NAC-TiO_2/C and Sucrose2-TiO_2/C composites.

Sample	TiO_2 content (wt%)[a]	carbon content (wt%)[b]	carbonaceous oxygen content (wt%)[b]	hydrogen content (wt%)[b]	nitrogen content (wt%)[b]
NAC-TiO_2/C, 700 °C	44.5	45.2	5.9	0.7	3.7
Sucrose2-TiO_2/C, 700 °C	53.6	40.0	3.4	1.1	1.9

[a] Determined via thermogravimetric analysis.
[b] C/H/N of the determined via combustion analysis, oxygen by difference.

5.3.2.2 Characterization of the Pyrolyzed NAC-TiO_2/C and Sucrose2-TiO_2/C

Beyond the differences in the overall composition of these two composite materials, the modified materials have a key difference in morphology present. SEM and TEM imaging show that the NAC-TiO_2/C has the 3DOM structure with some disorder present in certain regions (Figure 5.15 a, c). For the Sucrose2-TiO_2/C, extensive breakdown (~50 % of the sample) of the 3DOM structure occurs, and octahedral/tetrahedral particles are released (Figure 5.15 b). However, this process is not complete and regions containing the 3DOM structure remain (Figure 5.15 d). Disassembly of the 3DOM network, in the case of Sucrose2-TiO_2/C, may be related to a combination of two things. First, the concentration of the carbon-forming citric acid precursor is reduced, leading to a lower overall yield of carbon in the composite. Second, the surfactant content is higher relative to the content of citric acid. This relative surplus of surfactant can induce the formation of more pores in the wall network, which makes it easier for stresses to fracture the walls of the 3DOM structure during thermal treatment.[48,49]

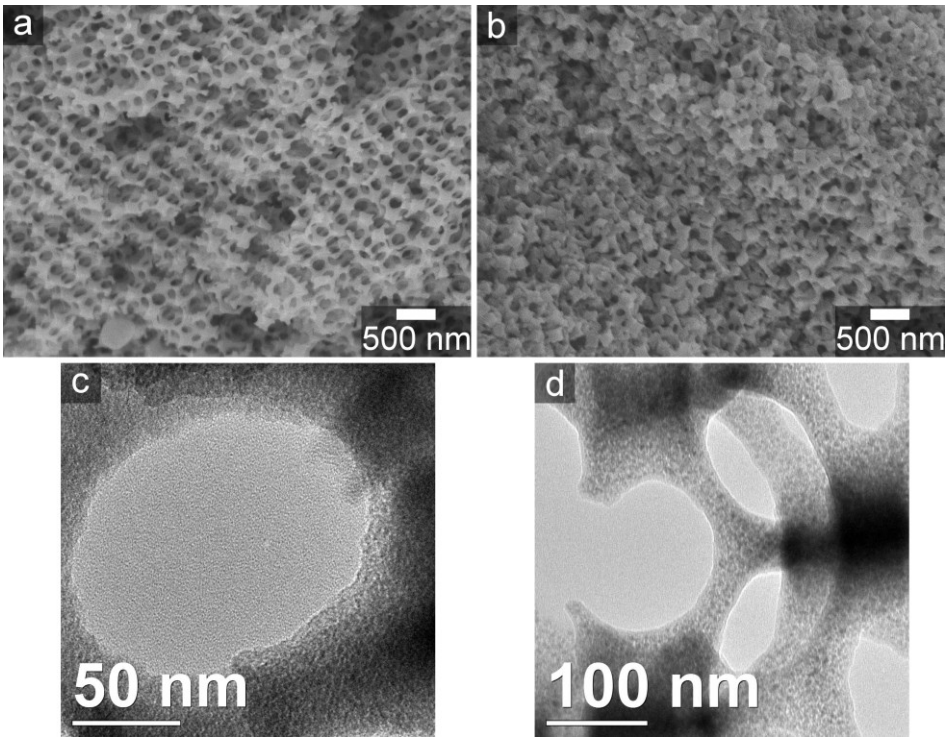

Figure 5.15 SEM and TEM images for the modified materials (a, c) NAC-TiO_2/C and (b, d) Sucrose2-TiO_2/C. These images are fairly similar to those taken of the Sucrose-TiO_2/C pyrolyzed at 700 °C. Disassembly of the 3DOM structure into cubic and tetrahedral nanoparticles is observed in (b). TEM images taken by Stephen Rudisill.

PXRD patterns obtained from the NAC- and Sucrose2-TiO_2/C (Figure 5.16 a) contain broad, poorly resolved peaks (near 29.4 °2θ) that correspond to anatase TiO_2. The small crystallite size is expected for these composites due to their high amorphous content. This phase is also associated with a peak near 51 °2θ. An additional peak in the Sucrose2-TiO_2/C pattern (denoted with a double cross) overlaps with a strong TiO_2-B reflection, and may be observable due to the higher TiO_2 content in the composite. From confocal Raman microscopy, it is revealed that both anatase and rutile TiO_2 co-exist in the NAC- and Sucrose2-TiO_2/C (Figure 5.16 b). This finding is similar to what was observed for Sucrose-TiO_2/C, and is expected since these composite materials share a common TiO_2 precursor. Again, it appears that the rutile phase nucleates at low pyrolysis temperatures. Finally, the ratio of the intensity of the disordered carbon Raman scattering band to that of the graphitic carbon Raman scattering band is given for the two modified materials in Table 5.5. The disordered carbon peak is extremely intense in both samples, as would be expected for amorphous carbon-containing materials pyrolyzed at low temperatures.

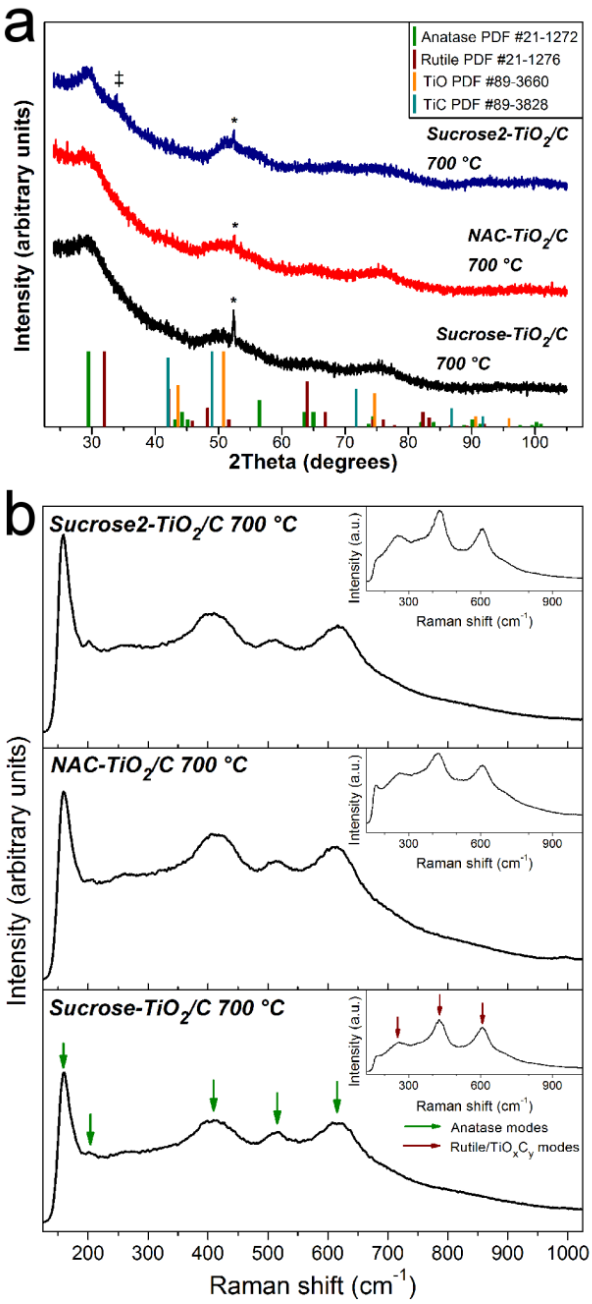

Figure 5.16 (a) PXRD and (b) Raman spectra from the modified materials. The closely related Sucrose-TiO_2/C is also included. All patterns and spectra provide evidence that anatase and rutile TiO_2 are present in the composites. TiO_2-B may be present and its presence in the pattern is marked with a double cross. Again, the asterisk denotes the peak from the Al sample holder.

Table 5.5 Raman and textural parameters of NAC-TiO_2/C and Sucrose2-TiO_2/C.

Sample	I_D/I_G	BET surface area (m^2/g)	pore volume (mL/g)
NAC-TiO_2/C, 700 °C	1.34	219	0.35
Sucrose2-TiO_2/C, 700 °C	1.39	182	0.63
Sucrose-TiO_2/C, 700 °C[a]	1.15	225	0.43

[a] Included for comparison.

Considering that the NAC- and Sucrose2-TiO_2/C share many characteristics with the Sucrose-TiO_2/C, it is expected that the textural properties should be similar. From the gas sorption isotherms and SAXS patterns, this expectation is mostly confirmed (Figure 5.17). Nitrogen sorption isotherms of the materials are closed, and show virtually no indication of hysteresis (Figure 5.17 a). This behavior is similar to the other composites. There are also rises in volume adsorbed at low/high relative pressures, which arise from micropores and mesopores, respectively. BET surface areas and total pore volumes are comparable to the other materials (Table 5.5). However, the Sucrose2-TiO_2/C has a slightly reduced surface area, which is from the increased TiO_2 content. Figure 5.17 b shows the SAXS patterns of the two modified composites. Both have a broad feature around 1.75 ° 2θ (d-spacing ~ 2.5 nm), and this is not present in the corresponding Sucrose-TiO_2/C. This peak may be related to disordered mesoporosity in the carbon network.

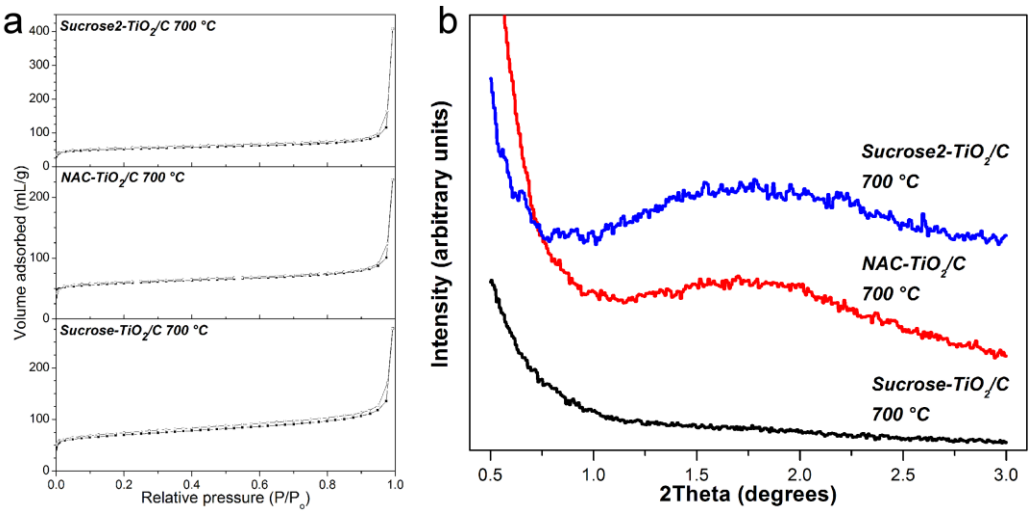

Figure 5.17 (a) Nitrogen sorption isotherms and (b) SAXS patterns for the modified materials. The isotherms are fairly similar and contain little hysteresis. A broad scattering peak is observed for the modified materials, which may be indicative of a limited amount of highly disordered mesoporosity.

5.3.3 Characterization of the 3DOM C Reference Sample

Overall, the morphology and textural properties of 3DOM C closely match those of the composites. This behavior was not expected, since the high concentration of F127 should have led to the formation of a confined, 2D-hexagonal mesostructure.[19] SEM imaging (Figure 5.17 a) shows that an interconnected set of macropores is present. Mesopores are not observed in TEM images (Figure 5.17 b) and the N_2 sorption isotherm has only the hallmarks of micropores and macropores (see the rises at low and high relative pressure in Figure 5.17 c). Alterations to the pyrolysis procedure may have resulted in the absence of mesoporosity; however, it led to the formation of a 3DOM material with a surface area closer in magnitude to the PF-TiO_2/C composite pyrolyzed at 700 °C. Significant microporosity results in the material having a BET surface area of 461 m^2/g (nearly double that of PF-TiO_2/C pyrolyzed at 700 °C) with 0.65 cm^3/g of total pore volume.

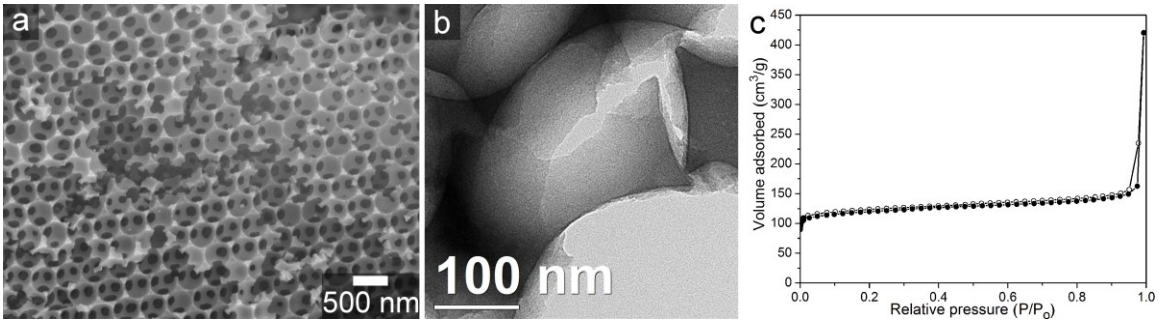

Figure 5.17 A (a) SEM micrograph, (b) TEM micrograph, and (c) gas sorption isotherm of the 3DOM C material. TEM image taken by Stephen Rudisill.

An evaluation of the graphitic structure of the 3DOM C was also undertaken using a combination of X-ray diffraction and Raman spectroscopy. Both techniques show features typical of amorphous carbon. The X-ray diffraction pattern consists of two main, extremely broad reflections centered at approximately 28 °2θ and 50 °2θ (Figure 5.18 a). Both of these are also present in the composite materials and originate from the amorphous carbon component.[29,32] *D*/*G* bands are observed in the Raman spectrum (Fig 5.18 b). Since the 3DOM C does not contain intervening TiO_2 crystallites, graphitic domains appear to be larger from the Raman spectral data. The size of these domains, L_a, was calculated using the equation $I_D/I_G = C(\lambda)/L_a$, where I_D = intensity of *D* band and I_G = intensity of *G* band, λ = wavelength of laser in Raman spectrometer (515.5 nm), and $C(\lambda = 515.5\text{ nm}) = 4.4$ nm.

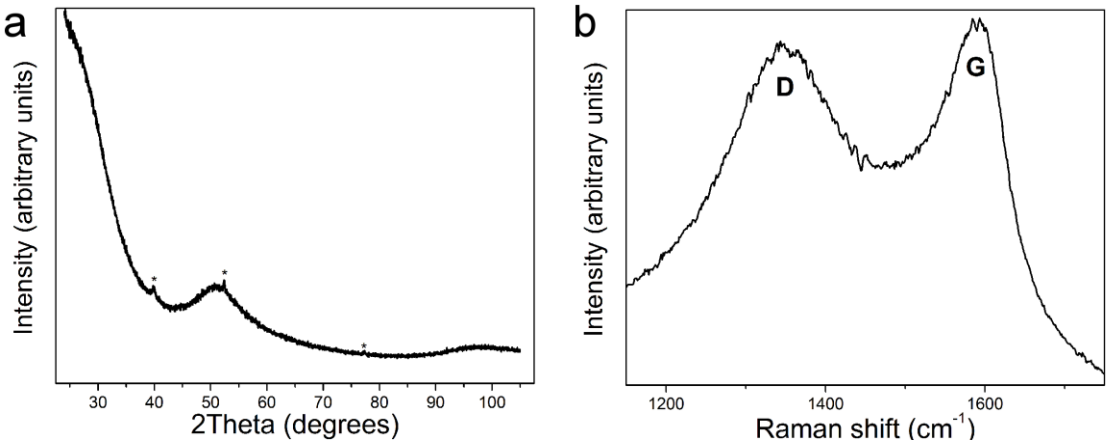

Figure 5.18 (a) PXRD pattern and (b) Raman spectrum of the 3DOM C material. Asterisks in (a) mark peaks from aluminum metal in the PXRD sample holder. *D*/*G* bands are labeled in (b).

5.3.4 Electrochemical Characterization and Analysis

5.3.4.1 Galvanostatic Charge/Discharge Testing of PF-TiO_2/C and Sucrose-TiO_2/C with a Comparison to 3DOM C

For electrochemical testing, PF- and Sucrose-TiO_2/C samples pyrolyzed at 700 and 800 °C were cycled in two different voltage windows. Due to increases in TiO_2 crystal size and widespread formation of titanium oxycarbide, samples pyrolyzed at 900 °C were not tested. This section first presents electrochemical cycling data in the window between 1 and 3 V vs. Li/Li^+, which should be dominated by insertion/extraction reactions in TiO_2. However, less than 50 wt% of any given electrode is TiO_2. Full utilization of the active material (TiO_2 and carbon) is explored by changing the voltage window to between 0.05 and 3 V vs. Li/Li^+, allowing for lithium insertion/extraction into amorphous carbon. Substantial improvements in the capacity of the composites are realized by using the wider window. A comparison is also made to 3DOM C synthesized using PF sol.

When cycling is limited to the window between 1 and 3 V vs. Li/Li^+, the impact of increased pyrolysis temperature and amorphous carbon content are observed. Figure 5.19 shows the capacities at different cycling rates, and Figure 5.20 shows extended cycling at a rate of C/2. Raising the pyrolysis temperature has a similar effect for both PF- and Sucrose-TiO_2/C; capacities decrease at 800 °C for all cycling rates when compared to electrode materials pyrolyzed at 700 °C. This is borne out in both the rate performance and the extended cycling data. Extensive crystallite growth occurs when pyrolysis temperatures are increased from 700 °C to 800 °C; moreover, the PXRD patterns (Figure 5.8) indicate that some titanium oxycarbide forms when the PF- and Sucrose-TiO_2/C are pyrolyzed at 800 °C. These processes counteract any benefit derived from the enhancement of the electronic conductivity of the carbon framework generated by higher pyrolysis temperatures.[50] The benefits of improved electronic conduction in the carbon framework are also partially negated in another fashion. While the amorphous carbon in the composites restricts crystal growth, it also blocks lithium ion transport to the active TiO_2 crystallites. An ideal composite of carbon and active material should contain either a minimal conformal coating of carbon[51] or (for an active material with slow ion conduction) as few contact points with carbon as possible.[52] Electronic conductivity is then facilitated and ionic transport is not hindered. This has been observed in multiple studies, including research conducted on lithium iron phosphate and on hollow TiO_2/C spheres.[53,54] Unfortunately, the PF- and Sucrose-TiO_2/C contain a large fraction of carbon that blocks ion transport to TiO_2 crystallites confined deep in the 3DOM network. As a consequence, capacities deteriorate at high charge/discharge rates.

However, the capacities for insertion/extraction of Li^+ at low rates are quite good, and exceed 0.5 Li^+ per unit of TiO_2.

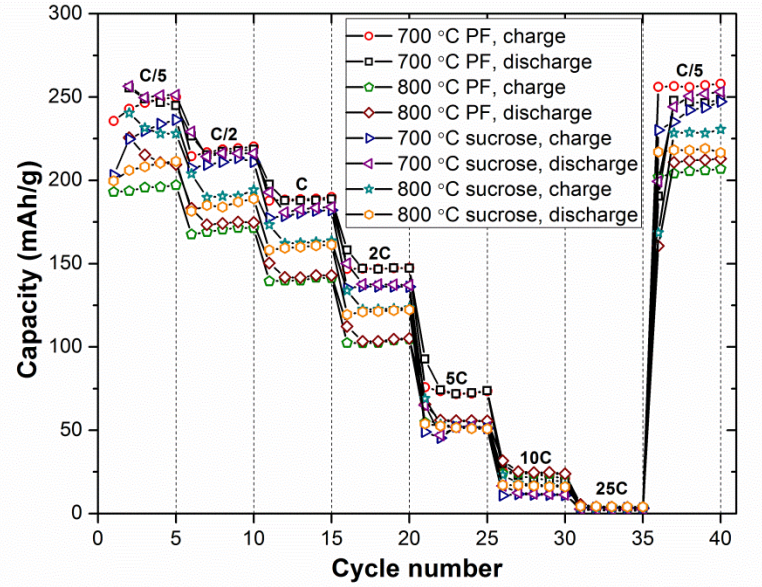

Figure 5.19 Capacities at different C-rates for the PF-TiO_2/C and Sucrose-TiO_2/C pyrolyzed at 700 °C and 800 °C. Specific capacities and currents are per gram of TiO_2 in the electrode. The voltage window extends between 1 and 3 V vs. Li/Li^+ for the tests.

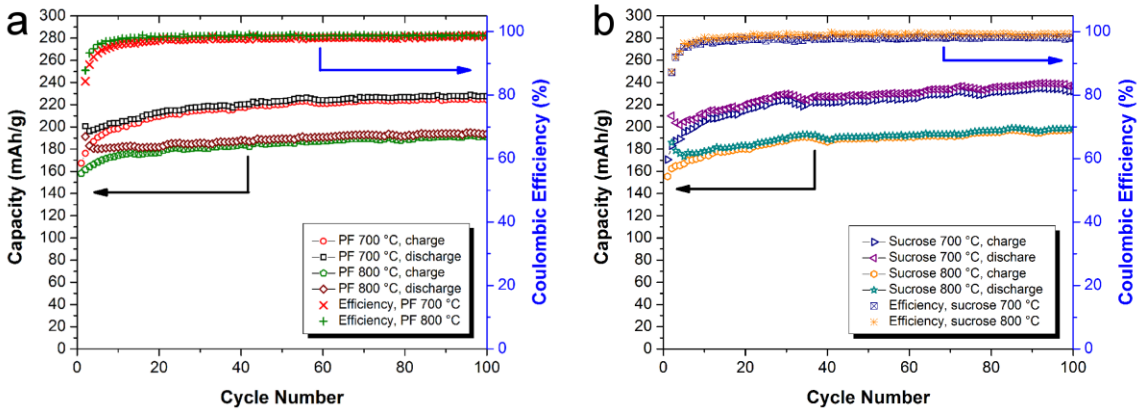

Figure 5.20 Extended cycling (100 cycles) conducted at a rate of C/2 for (a) PF-TiO_2/C and (b) Sucrose-TiO_2/C. Coulombic efficiencies are shown for all of the materials. The voltage window extends between 1 and 3 V vs. Li/Li^+ for the tests.

Changing the precursor to the less toxic one used for Sucrose-TiO_2/C induces minor changes in the observed capacities when compared to PF-TiO_2/C. Capacities are generally higher for PF-TiO_2/C than for Sucrose-TiO_2/C after these composites are pyrolyzed at 700 °C. This reverses

when pyrolysis is conducted at 800 °C. Sucrose-TiO_2/C has higher capacities than its counterpart until 2C (at which point they are about equal). Similar to what is discussed above, these differences in capacity stem from variations in carbon content and TiO_2 crystallite size. At 700 °C, both types of composite have extremely small crystallites, but the composite with PF-TiO_2/C contains more TiO_2 than the Sucrose-TiO_2/C. Extra carbon can impede Li^+ transport through Sucrose-TiO_2/C, causing the decreased capacity at high rates. Greater oxygen content in the carbonaceous phase of the Sucrose-TiO_2/C might also result in lower electronic conductivity and lower capacities. For composites pyrolyzed at 800 °C, the material with smaller anatase crystallites (Sucrose-TiO_2/C) has higher capacities at high rates. It should be noted that the maximum difference in capacities is about 30% for materials pyrolyzed at 700 °C and about 20% for 800 °C (see Figure 5.19). From the standpoint of the lithium-ion insertion/extraction, there are no substantial drawbacks to using the safer precursor for 3DOM TiO_2/C.

Possible mechanisms for insertion/extraction into the composite electrode can be explored for the composites via analysis of their voltage profiles (Figure 5.21). Easy resolution of a biphasic intercalation mechanism versus solid solution or interfacial charge storage is possible. For instance, the voltage profiles show a sloping profile without a noticeable plateau (Figure 5.21). The plateau for two-phase intercalation in anatase should occur at ~1.7 V at low C rates,[55] but it is absent in Figure 9a–d. Since the anatase crystallites are so small, the emergence of two phases (and an associated phase boundary) is postulated to be energetically unfavorable, leading to Li^+ solid solution insertion/extraction.[56] A sloping profile occurs in this solid solution case. Another contribution can be attributed to intercalation into rutile TiO_2, which also displays a sloped voltage at small crystallite sizes.[57] Either intercalation into a rutile-like lithiated form of TiO_2 with an extended solid solution range may contribute to this behavior,[58] or a phase change may have occurred early on in cycling.[57,59] Once an irreversible phase change from rutile TiO_2 to a lithiated hexagonal titanate takes place, insertion and extraction of Li^+ only occurs in the hexagonal phase via a solid solution mechanism.[59] Carbon should contribute a little capacity to the cells cycled between 1 and 3 V vs. Li/Li^+ because certain sites in the amorphous matrix can undergo insertion/extraction in this range (see discussion below).[15,29] However, the precise contribution of the carbon phase is difficult to isolate.

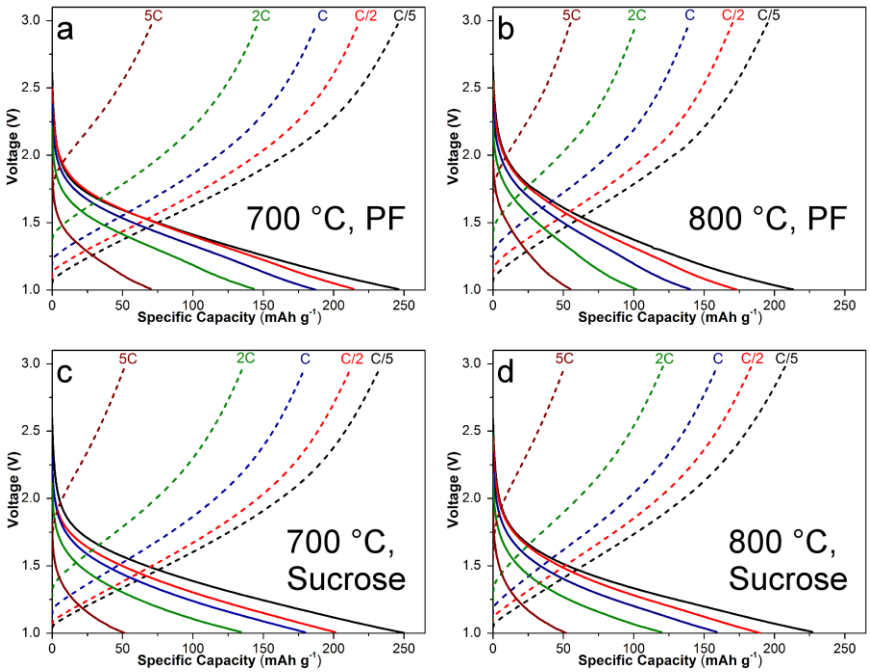

Figure 5.21 Voltage profiles for charging and discharging at various rates (using a window from 1 to 3 V vs. Li/Li^+). Graphs for the PF-TiO_2/C composites for pyrolysis at (a) 700 °C and (b) 800 °C are shown at the top, and graphs for the Sucrose-TiO_2/C composites for pyrolysis at (c) 700 °C and (d) 800 °C are shown at the bottom. Sloping profiles are observed for all of the composites tested.

Since amorphous carbon comprises a substantial fraction of these composites, better utilization of the entire mass of the electrode is possible by cycling the electrodes down to 0.05 V vs. Li/Li^+. A sloping profile found when the composites are cycled in this range (Figure 5.22). A large percentage (over 50% for all rates) of the capacity comes from the region below 1 V vs. Li/Li^+, which includes Li^+ insertion/extraction events into amorphous carbon. Staging behavior typical of graphitic carbon is not present,[15] instead the voltage profile is sloped. Amorphous carbon, with its abundance of different intercalation environments, displays a sloping voltage profile like what is observed in Figure 5.22.[15] Similarly, part of the capacity in Figure 10 comes from TiO_2, especially in the range of 1 to 3 V vs. Li/Li^+. Changing to a larger voltage window may also overcome any kinetic barriers (e.g. an overpotential) to intercalation into highly confined TiO_2 crystallites, allowing for better utilization of the active material. Even in unconfined TiO_2, higher capacities are obtained by extenting the window.[60]

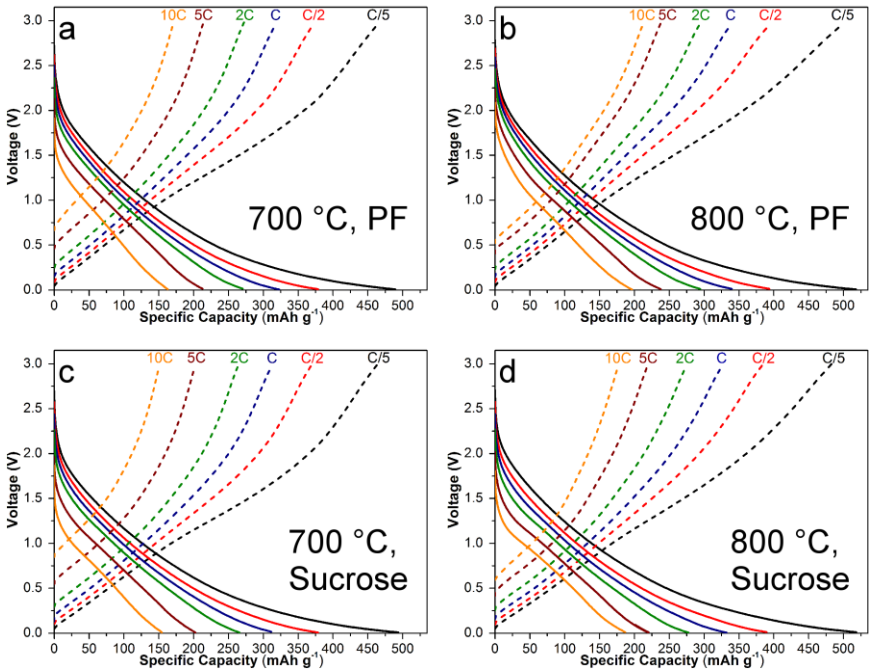

Figure 5.22 Voltage profiles for charging and discharging in an extended voltage window from 3 V vs. Li/Li^+ to 0.05 V vs. Li/Li^+. Graphs for the PF-TiO_2/C composites for pyrolysis at (a) 700 °C and (b) 800 °C are shown at the top, and graphs for the Sucrose-TiO_2/C composites for pyrolysis at (c) 700 °C and (d) 800 °C are shown at the bottom. Specific capacities and currents are per mass of all active material (carbon and TiO_2) in the composite.

A clearer picture of the changes induced by cycling in a wider voltage window can be obtained by examining rate performance data vs. cycle number and the morphology of the cycled electrodes. Capacities for the electrodes cycled between 0.05 V and 3 V vs. Li/Li^+ are considerably higher than those for electrodes cycled in a narrow voltage window (Figure 5.23). This boost in overall capacity is especially noticeable at high rates, with the PF- and Sucrose-TiO_2/C electrodes retaining roughly 150 to 200 mAh/g of capacity at 10C. Since the specific currents/capacities are per 84 wt% of the active mass of the electrode, the overall improvement in capacity is even greater than what is shown in Figure 5.23 when compared to those electrodes cycled in the narrower window. In contrast to electrodes cycled between 1 and 3 V vs. Li/Li^+, capacities for all the PF- and Sucrose-TiO_2/C electrodes are similar when they are cycled in the wide window. Increasing the pyrolysis temperature results in a slight improvement in capacities at high rates (25 C), perhaps due to better electronic conductivity in the amorphous carbon. Another key difference between cycling in the two ranges is that decomposition of the electrolyte should occur in the lower voltage range, leading to formation of a stable solid-electrolyte interface (SEI).[61] Formation of this SEI layer is responsible for the large drop in the initial cycling

capacity (see cycle 1 and 2 in Figure 5.23), as electrolyte degradation takes place. When comparing TEM micrographs of electrodes (washed in dimethyl carbonate to preserve the SEI) taken after cycling, a conformal SEI is found on the surface of the electrode materials cycled in the wide voltage window (Figure 5.24 a, b). In contrast, the SEI is absent (or extremely thin) in the electrodes cycled between 1 and 3 V vs. Li/Li^+ (see Figure 5.24 c). The SEI is comprised of light elements (Li, C, O and F), which explains why little contrast is observed between the SEI and the composite.[61] Despite the poor contrast, it is still clear that the SEI does not block the macropore windows, preserving the interconnected pore structure. ATR FT-IR was also conducted on these washed electrodes to attempt to determine some of the components present in the SEI (Figure 5.25). By comparing the spectra of the cycled PF- and Sucrose-TiO_2/C electrodes with the pristine Sucrose-TiO_2/C (pyrolyzed at 700 °C) electrode, peaks can be found that roughly correspond to C=O, C-O, CH_2-, and CO_3 vibrations. Decomposition of the carbonates (especially ethylene carbonate),[61] leads to the formation of deprotonated carboxylic acids ($LiOOR_1$) and $LiCO_3$. Peaks present in the collected spectra match vibrations that would be expected for the decomposition products. It is also highly likely that LiF is a component of the SEI (since $LiPF_6$ is present in the electrolyte), but this compound lacks IR-active vibrational modes.[61]

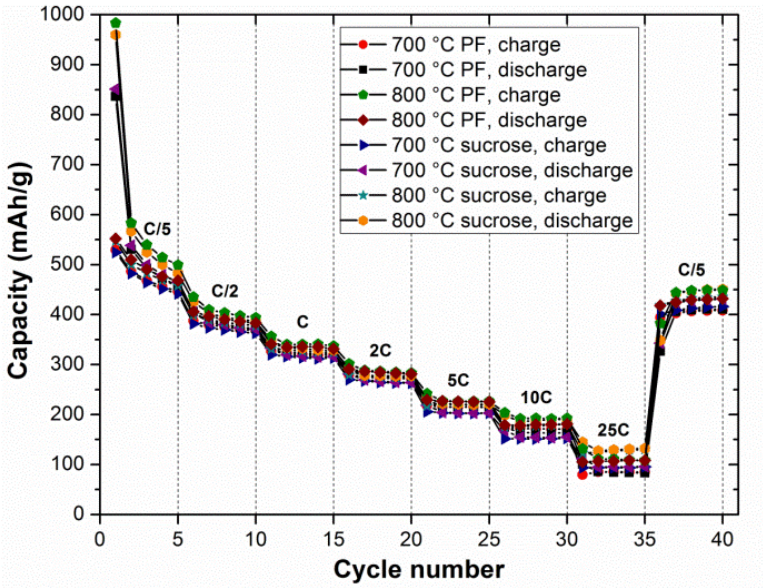

Figure 5.23 Capacities for the PF-TiO_2/C and Sucrose-TiO_2/C materials cycled at different rates. The voltage window used for these tests extends from 0.05 to 3 V vs. $Li/Li.^+$ Specific currents and capacities are per mass of composite in the electrode.

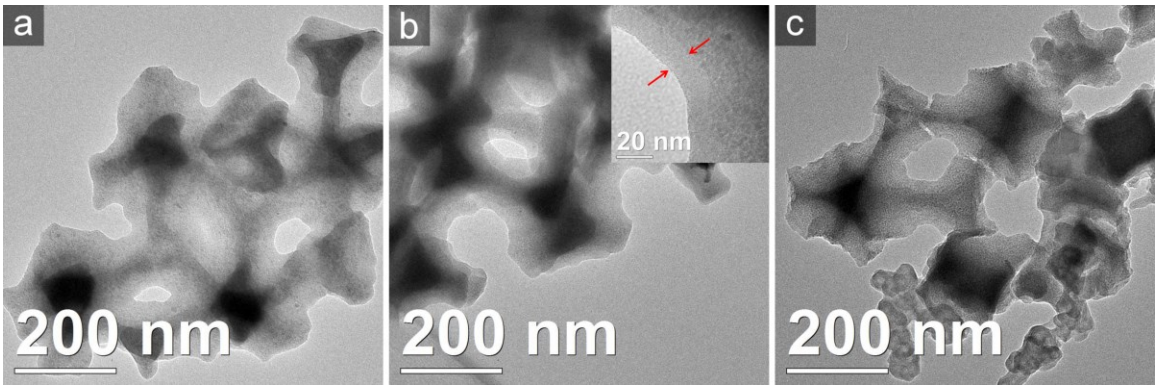

Figure 5.24 TEM micrographs of cycled electrodes that have been washed using dimethyl carbonate to preserve the SEI layer (if present). The (a) PF-TiO_2/C and (b) Sucrose-TiO_2/C composites were pyrolyzed at 700 °C, and cycled in the wider voltage window between 0.05 V and 3 V vs. Li/Li^+. An SEI layer covers the 3DOM network, but the interconnecting macropore windows remain open. The inset in (b) provides a clearer view of the SEI, which is ca. 10 to 15 nm in thickness. In (c), the PF-TiO_2/C (pyrolyzed at 700 °C) shown was cycled between 1 and 3 V vs. Li/Li^+. No conformal SEI can be observed on the surface of this sample, since the lower limit of the voltage window was capped at 1 V vs. Li/Li^+. Images taken by Stephen Rudisill.

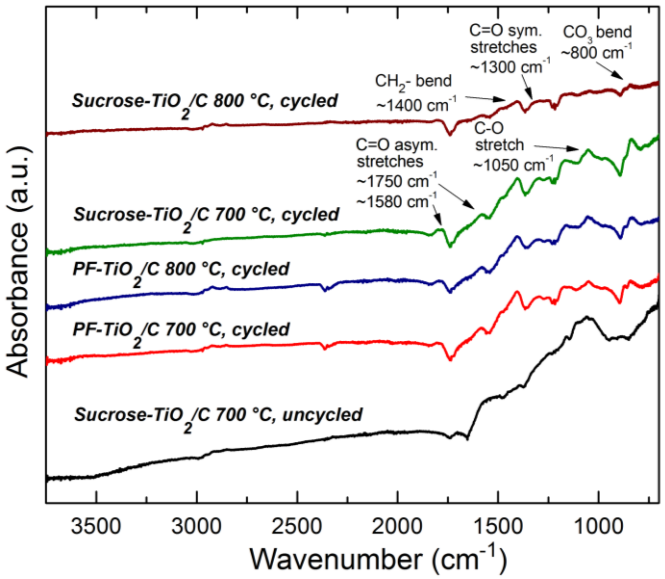

Figure 5.25 ATR FT-IR spectra for an uncycled electrode film (Sucrose-TiO_2/C, pyrolyzed at 700 °C) and the cycled electrode films. Multiple features are present that correspond to C=O, C-O, CH_2-, and CO_3 vibrations. Spectra collected by Professor Melissa Fierke.

Finally, the 3DOM carbon reference sample was cycled in the voltage window from 0.05 to 3 V vs. Li/Li^+. When compared to PF- and Sucrose-TiO_2/C in Figure 5.26 a, 3DOM C has lower

capacities than the composites at all rates. The difference in capacities is especially pronounced at moderate charge/discharge rates; the capacity of the composites outstrips that of the 3DOM C by ~100 mAh/g. This is akin to what has been observed for mesoporous TiO_2/C composites when compared to mesoporous C.[12,13] Additionally, the PF- and Sucrose-TiO_2/C composites have comparable[9,13] or greater capacities[12,14] at high charge/discharge rates when compared to mesoporous TiO_2/C composites pyrolyzed at higher temperatures. Returning to the reference material used in this study, from a voltage profile for the 3DOM carbon (Figure 5.26 b), the contribution to the charge/discharge capacity in the range from 1 to 3 V vs. Li/Li^+ is lower than for the composites, as indicated by the steep slope in this range. Again, this is a telling sign that the TiO_2 contributes to the overall capacity, especially at high rates. A substantial advantage is then achieved by the use of TiO_2 for the anode material. For rates greater than 1 C, PF- and Sucrose-TiO_2 deliver greater capacities than 3DOM carbon with mesoporous walls,[62] and lignin-derived carbon.[63] Even compared to highly conductive nanocarbon materials, i.e., carbon nanotube/mesoporous carbon composites[64] and graphene/carbon nanofiber composites,[65] the TiO_2/C composites provide similar capacities at high rates (10 C).

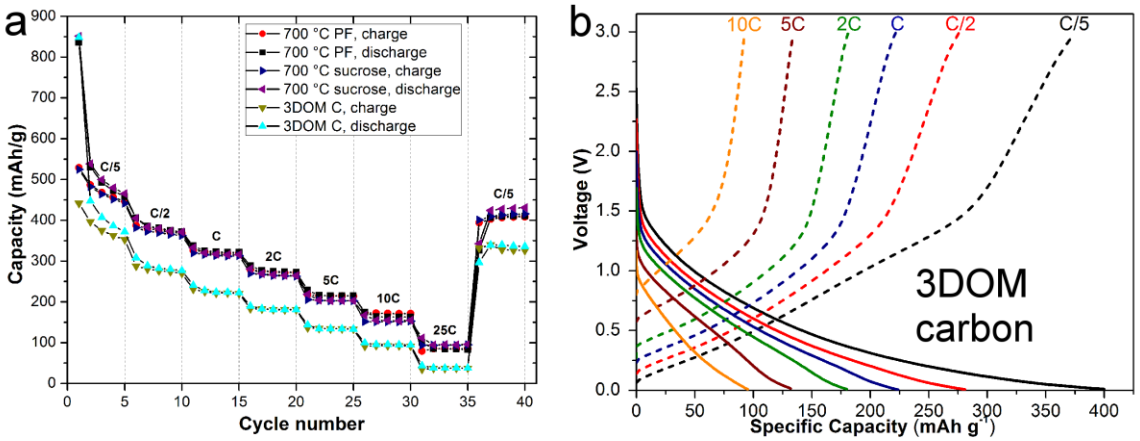

Figure 5.26 Comparison of the rate performance of the PF-TiO_2/C and Sucrose-TiO_2/C pyrolyzed at 700 °C versus the 3DOM C reference material (a). The voltage profile of the 3DOM C for several charge/discharge rates is shown in (b). The potential window extends from 0.05 to 3 V vs. Li/Li^+. Specific currents and capacities are per mass of composite in the electrode.

5.3.4.2 Cycling Voltammetry of PF-TiO_2/C, Sucrose-TiO_2/C, and 3DOM C

Cyclic voltammetry was conducted in conjunction with the galvanostatic testing to gain further understanding of the lithium ion insertion/extraction events (including the contribution of carbon vs. TiO_2) that occur during cycling in the wide voltage window. It is observed for the PF- and Sucrose-TiO_2/C electrodes (Figure 5.27) that the anodic peak current (for the peak near 0 V vs. Li/Li^+) is greater for the first cycle when compared to subsequent cycles. This difference is due to the formation of the SEI layer; however, SEI formation should also be accompanied by a peak in the anodic sweep at ~0.5 V vs. Li/Li^+.[64] The relatively quick scan rate of 5 mV/s may obscure the peak, but it is not entirely known why that peak is not found. For subsequent cycles, there is a broad peak on the cathodic sweep near 0.9 V vs. Li/Li^+ from lithium extraction out of non-graphitic, disordered sites in amorphous carbon.[64] Unlike electrodes that contain solely amorphous carbon (Figure 5.27 e), the current for the composites does not rapidly collapse to zero on either sweep in the range of 1.25 to 3 V vs. Li/Li^+. A contribution from TiO_2 is clearly present; however, no sharp peaks are observed. Since the voltage profiles (Figure 5.22) do not contain well-defined plateaus corresponding to biphasic insertion/extraction into TiO_2, it can be expected that the corresponding redox events in the CVs are not found. However, there is an ill-defined shoulder in some of the CVs near 1.9 V vs. Li/Li^+ on the cathodic sweep, which could originate from extraction of Li^+ out of anatase and rutile TiO_2.[66] The electrode composites with higher TiO_2 content, PF-TiO_2/C, generate larger currents in this region of the cathodic sweep, as well. Both PF- and Sucrose-TiO_2/C also have a broad peak near 1 V vs. Li/Li^+ in the anodic sweep. In amorphous carbon electrodes the redox peak is not as well-resolved,[64] so this feature is likely an overlay of insertion events into carbon and TiO_2. Indeed, insertion into rutile TiO_2 occurs near 1.3 V vs. Li/Li^+ at slower scan rates.[67] Finally, the CV for the 3DOM C reference is shown in Figure 5.27 e. Only a limited current flows from ~1.5 to 3 V vs. Li/Li^+ on either sweep, since no TiO_2 is present. Features from carbon intercalation/deintercalation are present in both the cathodic and anodic sweeps in the range from ~0.05 to 1.2 V vs. Li/Li^+.

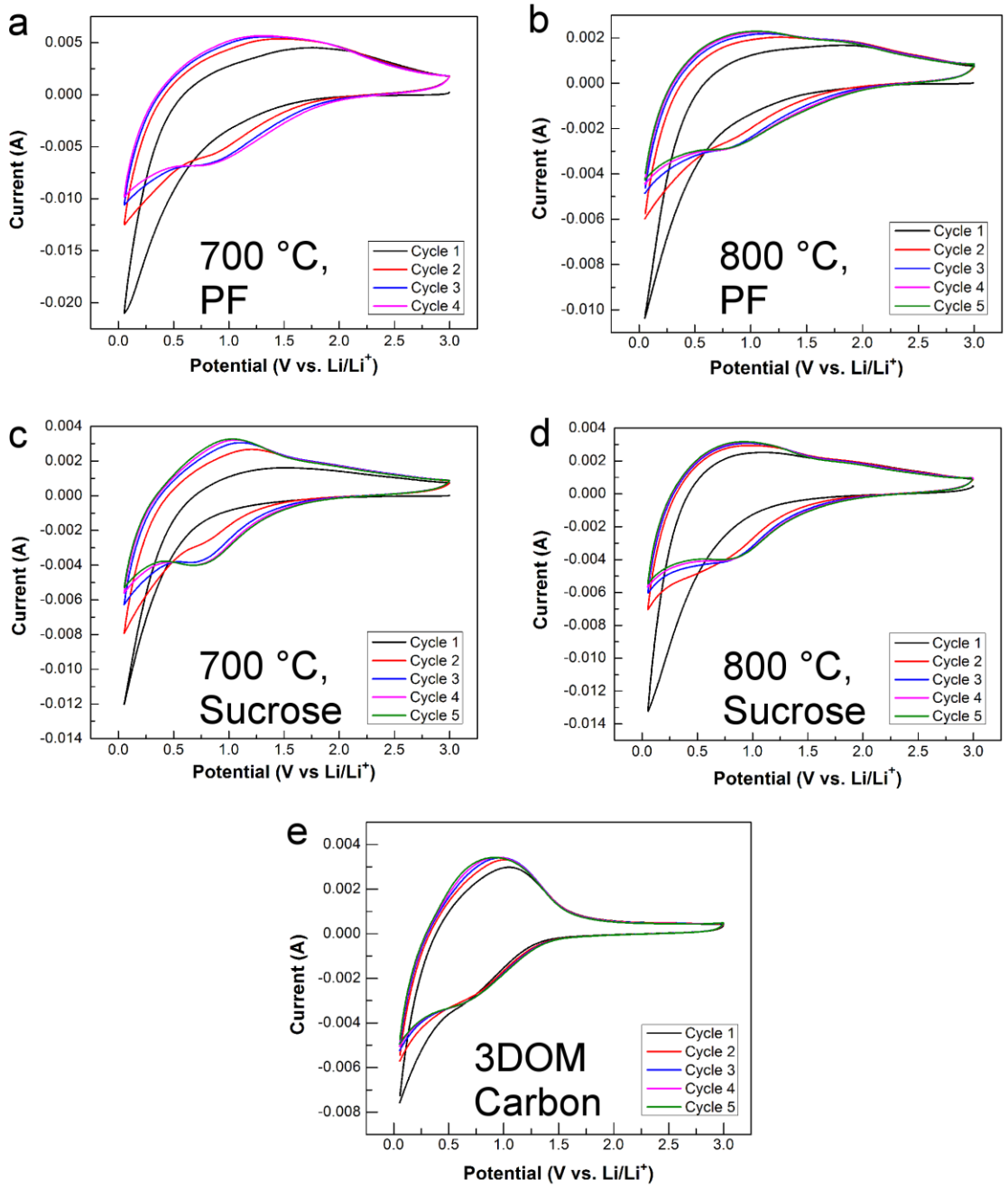

Figure 5.27 Cyclic voltammograms of (a, b) PF-TiO_2/C, (c, d) Sucrose-TiO_2/C, and (e) 3DOM C (all pyrolyzed at 700 °C). Evidence of lithium insertion/extraction into both carbon and TiO_2 is observed for the composites. For 3DOM C, little current flow (aside from a capacitive contribution) is recorded between 1 and 3 V vs. Li/Li^+. Voltammograms collected by Benjamin Wilson.

5.3.4.3 Electrochemical Testing of NAC-TiO_2/C and Sucrose2-TiO_2/C

Two other materials, NAC- and Sucrose2-TiO_2/C were also cycled in various voltage ranges. Both NAC- and Sucrose2-TiO_2/C were cycled in the range between 1 and 3 V vs. Li/Li^+. When these materials are compared to the Sucrose-TiO_2/C pyrolyzed at 700 °C, key differences are observed between the two modified materials (Figure 5.28). While Sucrose-TiO_2/C and Sucrose2-TiO_2/C exhibit similar capacities at different rates, the NAC-TiO_2/C has a substantially reduced capacity at moderate rates. This is a bit unexpected, due to the similar composition of the material when compared to Sucrose-TiO_2/C. It is possible that the pure citric acid forms amorphous carbon with conductivity that is lower carbon produced when PF sol/sucrose is also incorporated in a synthesis. Another possibility is that the carbon additives (PF sol or sucrose) slightly alters the location of TiO_2 crystallites and decreases the amount of intervening carbon; however, this is exceedingly difficult to determine via SEM imaging. Rate performance data for cycling between 0.05 V and 3 V vs. Li/Li^+ for the Sucrose-TiO_2/C, Sucrose2-TiO_2/C, and NAC-TiO_2/C is shown in Figure 5.28 b. In this voltage range, the Sucrose2-TiO_2/C has the greatest departure from the capacities of the Sucrose-TiO_2/C. Capacities for the Sucrose2-TiO_2/C exceed those of both the NAC- and Sucrose-TiO_2/C at rapid charge/discharge rates. Two aspects of the structure of Sucrose2-TiO_2/C may play a role in this difference. First, the carbon content is lower, which may allow for more facile access to TiO_2. Second, disassembly of the Sucrose2-TiO_2/C may also shorten diffusion lengths and allow for better high rate performance.

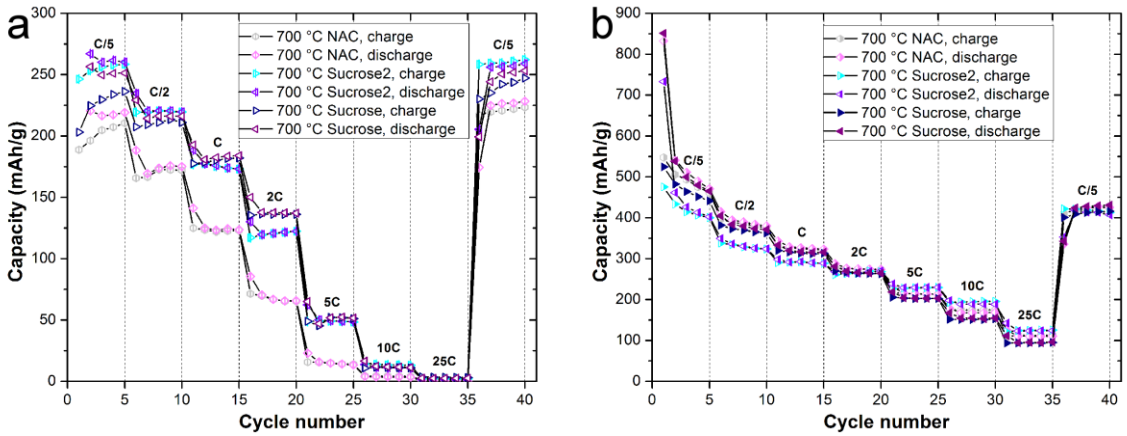

Figure 5.28 Capacities at different rates for the two modified materials (NAC- and Sucrose2-TiO_2/C) compared against Sucrose-TiO_2/C. cycled between (a) 1 and 3 V vs. Li/Li^+ and between (b) 0.05 and 3 V vs. Li/Li^+.

For these modified materials, cyclic voltammograms were also collected using the same parameters as used for the PF- and Sucrose-TiO_2/C (Figure 5.31). The voltammogram obtained from the NAC-TiO_2/C electrode is similar to those obtained from the Sucrose-TiO_2/C electrodes. Sucrose2-TiO_2/C, in contrast, possesses a peak near 2 V vs. Li/Li^+ that likely originates from lithium extraction from anatase TiO_2. Considering that Sucrose2-TiO_2/C has an elevated TiO_2 content, this finding is expected.

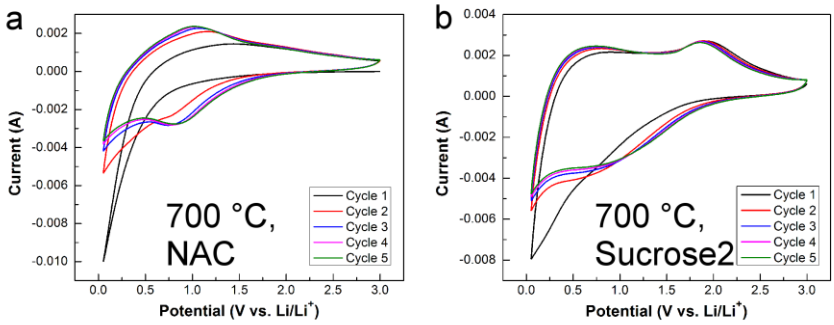

Figure 5.29 Cyclic voltammograms of the (a) NAC-TiO_2/C and the (b) Sucrose2-TiO_2/C electrodes. The voltammogram for the NAC-TiO_2/C is similar to those shown in Figure 5.27. For the Sucrose2-TiO_2/C, a peak is observed in the anodic sweep (centered just shy of 2 V vs. Li/Li^+) that likely arises from removal of lithium ions from TiO_2. Voltammograms collected by Benjamin Wilson.

5.3.4.4 A Note on Cycling TiO_2 and Carbon Nanocomposites in the Wide Voltage Window

Why is the capacity of the composites greater than that of the 3DOM carbon anode? Several explanations have been put forward for capacity boost observed mesoporous TiO_2/C in the literature, including that the high surface area of the composites facilitates insertion/extraction reactions.[12-14] Interestingly, the surface areas for the 3DOM TiO_2/C composites presented in this chapter are lower than what is attained in mesoporous TiO_2/C,[13] yet the 3DOM materials have equivalent or greater capacities at high rates. We posit two possibilities for the increase in capacities when the 3DOM TiO_2/C is cycled in an extended voltage window. First, a synergistic improvement in capacity in TiO_2/C nanocomposites may arise from the numerous interfaces that exist in these materials. Diffusion of lithium is easier through grain boundary defects, and possible storage of lithium can take place at the interfaces (much like the situation with amorphous carbon).[68] Second, extending the window may simply provide a driving force for greater utilization of the TiO_2 phase, as has been observed by Pfanzelt *et al*. for rutile TiO_2.[60] Future studies that determine lithium ion diffusion rates in the composites, determine at what

voltages specific insertion events occur, and determine the bonding environment around inserted lithium ions may assist in resolving this open question.

5.4 Conclusions

In this chapter, the influence of a porous carbon matrix on grain growth and polymorphism of confined TiO_2 was demonstrated and related to electrochemical lithium insertion/extraction properties of TiO_2/C composites, synthesized by hard templating using ammonium citratoperoxotitanate(IV) as a TiO_2 precursor and different carbon sources (PF sol or sucrose). One synthesis route developed, for the Sucrose-TiO_2/C composites, uses a low-toxicity, water-based precursor. Both the pyrolysis temperature used during processing and, to a lesser extent, the carbon source in the precursor influence the final structure of the composite. While the PF- and Sucrose-TiO_2/C retained a 3DOM structure dictated by the colloidal crystal template, irrespective of pyrolysis temperature, changes occur in the Ti-containing fraction of the material. After pyrolysis at 700 °C, extremely small anatase and rutile crystallites are present. Further, inhomogeneities in the crystallite size and the crystalline polymorph arise at higher pyrolysis temperatures. Widespread conversion of TiO_2 to titanium oxycarbide occurs at 800 °C and 900 °C, alongside considerable growth of both anatase and rutile TiO_2. Since crystal growth and conversion to titanium oxycarbide is substantial for materials pyrolyzed at 900 °C, testing of the PF- and Sucrose-TiO_2/C was restricted to samples pyrolyzed at 700 °C and 800 °C. Electrodes made from these composites (and cycled between 1 to 3 V vs. Li/Li^+) have high capacities at low and moderate charge/discharge rates. During extended cycling at C/2, samples pyrolyzed at 700 °C have capacities that exceed 200 mAh/g. However, capacities collapse rapidly at high charge/discharge rates. Once the voltage window is extended to 0.05 to 3 V vs. $Li/Li,^+$ both the carbon and TiO_2 phases can be utilized, and capacities increase substantially at all rates. The capacities of the composites materials are greater than what can be obtained from similarly-processed 3DOM C and compare favorably with other high-performing anode materials. Using a precursor with low toxicity, e.g. the one for Sucrose-TiO_2/C, does not adversely affect capacities. While the exact origin of the increase in capacity requires further study, changing the voltage window for the 3DOM TiO_2/C is an effective means to substantially increase the Li^+ insertion/extraction capacity for these nanostructured electrodes.

Modifications to the Sucrose-TiO_2/C precursor were made, and two additional materials, NAC-TiO_2/C and Sucrose2-TiO_2/C, were also investigated. The NAC-TiO_2/C, contained only carbon derived from citric acid and is, in most respects, similar to the corresponding Sucrose-

TiO_2/C material. NAC-TiO_2 has a slightly elevated carbon content and a slightly reduced electrochemical performance in the voltage window from 1 to 3 V vs. Li/Li^+. Sucrose2-TiO_2/C has an elevated content of TiO_2, since the citric acid content used in the ammonium citratroperoxotitanate(IV) gel is reduced. As a consequence, the size of the TiO_2 crystallites increases relative to the Sucrose-TiO_2/C. Although disassembly is observed in the structure, the Sucrose2-TiO_2 does show that TiO_2 content can be adjusted upward. From an electrochemical standpoint, Sucrose2-TiO_2/C is similar to the Sucrose-TiO_2/C.

References

(1) Wang, H.; Yao, J. Use of Poly(furfuryl alcohol) in the Fabrication of Nanostructured Carbons and Nanocomposites. *Ind. Eng. Chem. Res.* **2006**, *45*, 6393-6404.

(2) Stein, A.; Wang, W.; Fierke, M. A. Functionalization of Porous Carbon Materials with Designed Pore Architecture. *Adv. Mater.* **2009**, *21*, 265-293.

(3) Yang, K.; Li, Y.; Tan, X.; Peng, R.; Liu, Z. Behavior and Toxicity of Graphene and Its Functionalized Derivatives in Biological Systems. *Small* **2013**, *9*, 1492-1503.

(4) Liu, Y.; Zhao, Y.; Sun, B.; Chen, C. Understanding the Toxicity of Carbon Nanotubes. *Acc. Chem. Res.* **2013**, *46*, 702-713.

(5) Schubert, U. Chemical Modification of Titanium Alkoxides for Sol-Gel Processing. *J. Mater. Chem.* **2005**, *15*, 3701-3715.

(6) Boettcher, S. W.; Bartl, M. H.; Hu, J. G.; Stucky, G. D. Structural Analysis of Hybrid Titania-Based Mesostructured Composites. *J. Am. Chem. Soc.* **2005**, *127*, 9721-9730.

(7) Petkovich, N. D.; Rudisill, S. G.; Wilson, B. E.; Mukherjee, A.; Stein, A. Control of TiO_2 Grain Size and Positioning in Three-Dimensionally Ordered Macroporous TiO_2/C Composite Anodes for Lithium Ion Batteries. *Inorg. Chem.* **2014**, *53*, 1100-1112.

(8) Choi, M. G.; Lee, Y.-G.; Song, S.-W.; Kim, K. M. Anode Properties of Titanium Oxide Nanotube and Graphite Composites for Lithium-Ion Batteries. *J. Power Sources* **2010**, *195*, 8289-8296.

(9) Zhou, Y.; Kim, Y.; Jo, C.; Lee, J.; Lee, C. W.; Yoon, S. A Novel Mesoporous Carbon-Silica-Titania Nanocomposite as a High Perfomance Anode Material in Lithium Ion Batteries. *Chem. Commun.* **2011**, *47*, 4944-4946.

(10) Bresser, D.; Paillard, E.; Binetti, E.; Krueger, S.; Striccoli, M.; Winter, M.; Passerini, S. Percolating Networks of TiO_2 Nanorods and Carbon for High Power Lithium Insertion Electrodes. *J. Power Sources* **2012**, *206*, 301-309.

(11) Cai, D.; Lian, P.; Zhu, X.; Liang, S.; Yang, W.; Wang, H. High Specific Capacity of TiO_2-Graphene Nanocomposite as an Anode Material for Lithium-Ion Batteries in an Enlarged Potential Window. *Electrochim. Acta* **2012**, *74*, 65-72.

(12) Cheng, P.-Y.; Huang, C.-H.; Doong, R.-A. Ordered Mesoporous Carbon–TiO_2 Materials for Improved Electrochemical Performance of Lithium Ion Battery *Carbon* **2012**, *50*, 4259-4268.

(13) Ma, J.; Xiang, D.; Li, Z.; Li, Q.; Wang, X.; Yin, L. TiO_2 Nanocrystal Embedded Ordered Mesoporous Carbons as Anode Materials for Lithium-Ion Batteries with Highly Reversible Capacity and Rate Performance. *CrystEngComm* **2013**, *15*, 6800-6807.

(14) Zhang, C.; Zhang, Q.; Kang, S.; Li, X. A Novel Route for the Facile Synthesis of Hierarchically Porous TiO_2/Graphitic Carbon Microspheres for Lithium Ion Batteries. *J. Mater. Chem. A* **2014**, *2*, 2801-2806.

(15) Kaskhedikar, N. A.; Maier, J. Lithium Storage in Carbon Nanostructures. *Adv. Mater.* **2009**, *21*, 2664-2680.

(16) Kakihana, M.; Tada, M.; Shiro, M.; Petrykin, V.; Osada, M.; Nakamura, Y. Structure and Stability of Water Soluble $(NH_4)_8[Ti_4(C_6H_4O_7)_4(O_2)_4]\cdot 8H_2O$. *Inorg. Chem.* **2001**, *40*, 891-894.

(17) Josephson, D. P.; Popczun, E. J.; Stein, A. Effects of Integrated Carbon as a Light Absorber on the Coloration of Photonic Crystal-Based Pigments. *J. Phys. Chem. C* **2013**, *117*, 13585-13592.

(18) Meng, Y.; Gu, D.; Zhang, F.; Shi, Y.; Yang, H.; Li, Z.; Yu, C.; Tu, B.; Zhao, D. Ordered Mesoporous Polymers and Homologous Carbon Frameworks Amphiphilic Surfactant Templating and Direct Transformation. *Angew. Chem. Int. Ed.* **2005**, *44*, 7053-7059.

(19) Wang, Z.; Kiesel, E. R.; Stein, A. Silica-Free Syntheses of Hierarchically Ordered Macroporous Polymer and Carbon Monoliths with Controllable Mesoporosity. *J. Mater. Chem.* **2008**, *18*, 2194-2200.

(20) Dakanali, M.; Kefalas, E. T.; Raptopoulou, C. P.; Terzis, A.; Voyiatzis, G.; Kyrikou, I.; Mavromoustakos, T.; Salifoglou, A. A New Dinuclear Ti(IV)-Peroxo-Citrate Complex from Aqueous Solutions. Synthetic, Structural, and Spectroscopic Studies in Relevance to Aqueous Titanium(IV)-Peroxo-Citrate Speciation. *Inorg. Chem.* **2003**, *42*, 4632-4639.

(21) Hardy, A.; D'Haen, J.; Van Bael, M. K.; Mullens, J. An Aqueous Solution-Gel Citraperoxo-Ti(IV) Precursor: Synthesis, Gelation, Thermo-Oxidative Decomposition and Oxide Crystallization. *J. Sol-Gel Sci. Technol.* **2007**, *44*, 65-77.

(22) Truijen, I.; Hardy, A.; Van Bael, M. K.; Van den Rul, H.; Mullens, J. Study of the Decomposition of Aqueous Citratoperoxo-Ti(IV)-gel Precursors for Titania by Means of TGA-MS and FTIR. *Thermochim. Acta* **2007**, *456*, 38-47.

(23) Chaudhuri, M. K.; Das, B. Direct Synthesis of Alkali-Metal and Ammonium Pentafluoroperoxytitanates(IV), $A_3[Ti(O_2)F_5]$, and First Synthesis and Structural Assessment of Alkali-Metal and Ammonium Difluorodiperoxytitanates(IV), $A_2[Ti(O_2)_2F_2]$. *Inorg. Chem.* **1986**, *25*, 168-170.

(24) Kakihana, M.; Arima, M.; Nakamura, Y.; Yashima, M.; Yoshimura, M. Spectroscopic Characterization of Precursors Used in the Pechini-Type Polymerizable Complex Processing of Barium Titanate. *Chem. Mater.* **1999**, *11*, 438-450.

(25) Tengvall, P.; Vikinge, T. P.; Lundström, I.; Liedberg, B. FT-Raman Spectroscopic Studies of the Degradation of Titanium Peroxy Gels Made from Metallic Titanium and Hydrogen Peroxide. *J. Colloid Interface Sci.* **1993**, *160*, 10-15.

(26) Lin-Vien, D.; Colthup, N. B.; Fateley, W. G.; Grasselli, J. G. *Handbook of Infrared and Raman Characteristic Frequencies of Organic Molecules*; Academic Press: San Diego, **1991**.

(27) Max, J.-J.; Chapados, C. Infrared Spectroscopy of Aqueous Carboxylic Acids: Comparison between Different Acids and Their Salts. *J. Phys. Chem. A* **2004**, *108*, 3324-3337.

(28) Deacon, G. B.; Phillips, R. J. Relationships Between the Carbon-Oxygen Stretching Frequencies of Carboxylato Complexes and the Type of Carboxylate Coordination. *Coord. Chem. Rev.* **1980**, *33*, 227-250.

(29) Fey, G. T.-K.; Kao, Y.-C. Synthesis and Characterization of Pyrolyzed Sugar Carbons under Nitrogen or Argon Atmospheres as Anode Materials for Lithium-Ion Batteries. *Mater. Chem. Phys.* **2002**, *73*, 37-46.

(30) Fierke, M. A.; Lai, C.-Z.; Bühlmann, P.; Stein, A. Effects of Architecture and Surface Chemistry of Three-Dimensionally Ordered Macroporous Carbon Solid Contacts on Performance of Ion-Selective Electrodes. *Anal. Chem.* **2010**, *82*, 680-688.

(31) Petkovich, N. D.; Stein, A. Colloidal Crystal Templating Approaches to Materials with Hierarchical Porosity. In *Hierarchically Structured Porous Materials: From Nanoscience to Catalysis, Separation, Optics, Energy, and Life Science*; Su, B.-L., Sanchez, C., Yang, X.-Y., Eds.; Wiley-VCH Verlag GmbH & Co. KGaA: Weinheim, Germany, **2012**.

(32) Liu, G.; Liu, Y.; Wang, Z.; Liao, X.; Wu, S.; Zhang, W. F.; Jia, M. Direct Synthesis of Porous Carbon via Carbonizing Precursors of Aluminum Phosphate Containing Citric Acid. *Microporous Mesoporous Mater.* **2008**, *116*, 439-444.

(33) Zhang, H.; Banfield, J. F. Thermodynamic Analysis of Phase Stability of Nanocrystalline Titania. *J. Mater. Chem.* **1998**, *8*, 2073-2076.

(34) Shin, Y.; Li, X. S.; Wang, C.; Coleman, J. R.; Exarhos, G. J. Synthesis of Hierarchical Titanium Carbide from Titania-Coated Cellulose Paper. *Adv. Mater.* **2004**, *16*, 1212-1215.

(35) Yu, T.; Deng, Y. H.; Wang, L.; Liu, R. L.; Zhang, L. J.; Tu, B.; Zhao, D. Y. Ordered Mesporous Nanocrystalline Titanium-Carbide/Carbon Composites from In Situ Carbothermal Reduction. *Adv. Mater.* **2007**, *19*, 2301-2306.

(36) Huang, C.-H.; Gu, D.; Zhao, D.; Doong, R.-A. Direct Synthesis of Controllable Microstructures of Thermally Stable and Ordered Mesoporous Crystalline Titanium Oxides and Carbide/Carbon Composites. *Chem. Mater.* **2010**, *22*, 1760-1767.

(37) Koc, R. Kinetics and Phase Evolution During Carbothermal Synthesis of Titanium Carbide from Ultrafine Titania/Carbon Mixture. *J. Mater. Sci.* **1998**, *33*, 1049-1055.

(38) Bae, S.-T.; Shin, H.; Jung, H. S.; Hong, K. S. Synthesis of Titanium Carbide Nanoparticles with a High Specific Surface Area from a TiO_2 Core-Sucrose Shell Precursor. *J. Am. Ceram. Soc.* **2009**, *92*, 2512-2516.

(39) Hanaor, D. A. H.; Sorrell, C. C. Review of the Anatase to Rutile Phase Transformation. *J. Mater. Sci.* **2011**, *46*, 855-874.

(40) Zhang, W. F.; He, Y. L.; Zhang, M. S.; Yin, Z.; Chen, Q. Raman Scattering Study on Anatase TiO_2 Nanocrystals. *J. Phys. D: Appl. Phys.* **2000**, *33*, 912-916.

(41) Balachandran, U.; Eror, N. G. Raman Spectra of Titanium Dioxide. *J. Solid State Chem.* **1982**, *42*, 276-282.

(42) Klein, M. V.; Holy, J. A.; Williams, W. S. Raman Scattering Induced by Carbon Vacancies in TiC_x. *Phys. Rev. B* **1978**, *17*, 1546-1556.

(43) Lohse, B. H.; Calka, A.; Wexler, D. Raman Spectroscopy as a Tool to Study TiC Formation During Controlled Ball Milling. *J. Appl. Phys.* **2005**, *97*, 114912(1-17).

(44) Ferrari, A. C.; Robertson, J. Interpretation of Raman Spectra of Disordered and Amorphous Carbon. *Phys. Rev. B* **2000**, *61*, 14095-14107.

(45) Zhang, J.; Li, M.; Feng, Z.; Chen, J.; Li, C. UV Raman Spectroscopy Study on TiO_2. I. Phase Transformation at the Surface and in the Bulk. *J. Phys. Chem. B* **2006**, *110*, 927-935.

(46) Yin, H.; Wada, Y.; Kitamura, T.; Kambe, S.; Murasawa, S.; Mori, H.; Sakata, T.; Yanagida, S. Hydrothermal Synthesis of Nanosized Anatase and Rutile TiO_2 Using Amorphous Phase TiO_2. *J. Mater. Chem.* **2001**, *11*, 1694-1703.

(47) Shannon, R. D. Phase Transformation Studies in TiO_2 Supporting Different Defect Mechanisms in Vacuum-Reduced and Hydrogen-Reduced Rutile. *J. Appl. Phys.* **1964**, *35*, 3414-3416.

(48) Wang, Z.; Li, F.; Stein, A. Direct Synthesis of Shaped Carbon Nanoparticles with Ordered Cubic Mesostructure. *Nano Lett.* **2007**, *7*, 3223-3226.

(49) Wang, Z.; Stein, A. Morphology Control of Carbon, Silica, and Carbon/Silica Nanocomposites: From 3D Ordered Macro-/Mesoporous Monoliths to Shaped Mesoporous Particles. *Chem. Mater.* **2008**, *20*, 1029-1040.

(50) Bücker, W. Preparation and DC Conductivity of an Amorphous Organic Semiconducting System. *J. Non-Cryst. Solids* **1973**, *12*, 115-128.

(51) Li, H.; Zhou, H. Enhancing the Performances of Li-Ion Batteries by Carbon-Coating: Present and Future. *Chem. Commun.* **2012**, *48*, 1201-1217.

(52) Yu, J.; Sushko, M. L.; Kerisit, S.; Rosso, K. M.; Liu, J. Kinetic Monte Carlo Study of Ambipolar Lithium Ion and Electron Polaron Diffusion into Nanostructured TiO_2. *J. Phys. Chem. Lett.* **2012**, *2*, 2076-2081.

(53) Dominko, R.; Bele, M.; Gaberscek, M.; Remskar, M.; Hanzel, D.; Pejovnik, S.; Jamnik, J. Impact of the Carbon Coating Thickness on the Electrochemical Performance of $LiFePO_4$/C Composites. *J. Electrochem. Soc.* **2005**, *152*, A607-A610.

(54) Wang, W.; Sa, Q.; Chen, J. S.; Wang, Y.; Jung, H.; Yin, Y. Porous TiO_2/C Nanocomposite Shells As a High-Performance Anode Material for Lithium-Ion Batteries. *ACS Appl. Mater. Interfaces* **2013**, *5*, 6478-6483.

(55) Chen, Z.; Belharouak, I.; Sun, Y.-K.; Amine, K. Titanium-Based Anode Materials for Safe Lithium-Ion Batteries. *Adv. Funct. Mater.* **2013**, *23*, 959-969.

(56) Wagemaker, M.; Borghols, W. J. H.; Mulder, F. M. Large Impact of Particle Size on Insertion Reactions. A Case for Anatase Li_xTiO_2. *J. Am. Chem. Soc.* **2007**, *129*, 4323-4327.

(57) Milne, N. A.; Skyllas-Kazacos, M.; Luca, V. Crystallite Size Dependence of Lithium Intercalation into Nanocrystalline Rutile. *J. Phys. Chem. C* **2009**, *113*, 12983-12995.

(58) Borghols, W. J. H.; Wagemaker, M.; Lafont, U.; Kelder, E. M.; Mulder, F. M. Impact of Nanosizing on Lithiated Rutile TiO_2. *Chem. Mater.* **2008**, *20*, 2949-2955.

(59) Kubiak, P.; Pfanzelt, M.; Geserick, J.; Hörmann, U.; Hüsing, N.; Kaiser, U.; Wohlfahrt-Mehrens, M. Electrochemical Evaluation of Rutile TiO_2 Nanoparticles as Negative Electrode for Li-Ion Batteries. *J. Power Sources* **2009**, *194*, 1099-1104.

(60) Pfanzelt, M.; Kubiak, P.; Wohlfahrt-Mehrens, M. Nanosized TiO_2 Rutile with High Capacity and Excellent Rate Capability. *Electrochem. Solid State Lett.* **2010**, *13*, A91-A94.

(61) Verma, P.; Maire, P.; Novák, P. A Review of the Features and Analyses of the Solid Electrolyte Interphase in Li-Ion Batteries. *Electrochim. Acta* **2010**, *55*, 6332-6341.

(62) Kang, D.-Y.; Kim, S.-O.; Chae, Y. J.; Lee, J. K.; Moon, J. H. Particulate Inverse Opal Carbon Electrodes for Lithium-Ion Batteries. *Langmuir* **2013**, *29*, 1192-1198.

(63) Wang, S.-X.; Yang, L.; Stubbs, L. P.; Li, X.; He, C. Lignin-Derived Fused Electrospun Carbon Fibrous Mats as High Performance Anode Materials for Lithium Ion Batteries. *ACS Appl. Mater. Interfaces* **2013**, *5*, 12275-12282.

(64) Guo, B.; Wang, X.; Fulvio, P. F.; Chi, M.; Mahurin, S. M.; Sun, X.-G.; Dai, S. Soft-Templated Mesoporous Carbon-Carbon Nanotube Composites for High Performance Lithium-Ion Batteries. *Adv. Mater.* **2011**, *23*, 4661-4666.

(65) Fan, Z.-J.; Yan, J.; Wei, T.; Ning, G.-Q.; Zhi, L.-J.; Liu, J.-C.; Cao, D.-X.; Wang, G.-L.; Wei, F. Nanographene-Constructed Carbon Nanofibers Grown on Graphene Sheets by Chemical Vapor Deposition: High-Performance Anode Materials for Lithium Ion Batteries. *ACS Nano* **2011**, *5*, 2787-2794.

(66) Fröschl, T.; Hörmann, U.; Kubiak, P.; Kučerová, G.; Pfanzelt, M.; Weiss, C. K.; Behm, R. J.; Hüsing, N.; Kaiser, U.; Landfester, K.; Wohlfahrt-Mehrens, M. High Surface Area Crystalline Titanium Dioxide: Potential and Limits in Electrochemical Energy Storage and Catalysis. *Chem. Soc. Rev.* **2012**, *41*, 5313-5360.

(67) Hong, Z.; Wei, M.; Lan, T.; Jiang, L.; Cao, G. Additive-Free Synthesis of Unique TiO_2 Mesocrystals with Enhanced Lithium-Ion Intercalation Properties. *Energy Environ. Sci.* **2012**, *5*, 5408-5413.

(68) Jamink, J.; Gaberscek, M. Li Ion Migration at the Interfaces. *MRS Bull.* **2009**, *34*, 942-948.

Chapter 6

Conversion of 3DOM TiO_2 to High-Surface Area Titante and TiO_2 Materials via Treatment in Alkali Solutions: Morphological Transformations, Crystal Structure Analysis, and Li^+ Capacities

6.1 Introduction and Motivation

In the late 1990s, multiple routes for the synthesis of nanoporous titanium dioxide (TiO_2) and various titanates were discovered by research teams across the globe.[1-8] These initial breakthroughs led to a flurry of subsequent research, as teams studied how variables in the syntheses could be adjusted to influence the morphology and composition of the TiO_2 or titanates.[9-13] As greater control was attained and the mechanistic underpinnings of these methods were postulated, investigators began to test these materials for various applications that could benefit from engineered porosity. Reports have evaluated the use of nanoporous TiO_2 and titanates as components for improved dye-sensitized solar cells,[14] photocatalysts for a variety of reactions,[15,16] heterogeneous catalysts,[17-19] sorbents for metal ions and organic molecules,[20,21] catalyst supports,[22] hydrogen storage materials,[23] fuel cell components,[24] and anodes for lithium ion batteries.[17,25-27] In this chapter, I describe the combination of two synthesis techniques–colloidal crystal templating and the treatment of TiO_2 in alkali solutions–to produce titanate and TiO_2 materials with a novel, interconnected pore morphology, extremely high surface areas, and anisotropic crystallites with sub-10 nm dimensions. Before continuing, a brief discussion of the aforementioned synthesis methods is presented as a scaffold for understanding novel titanates/TiO_2 materials that are the focus of this work. An additional discussion is presented on the use of titanates and pyrolyzed titanates as anodes for lithium ion batteries.

As stated in Chapter 2, templating offers the potential for the reproducible synthesis of complex porous structures. Hard templates have an edge over soft templates in this respect, provided that the template can be adequately filled/coated, and that the template can be easily removed.[12] This method allows for precise replication of a structure or its inverse replica. When mesoporous carbon or silica is utilized as a template, researchers are able to synthesize mesoporous transition metal oxides that are often difficult to template using surfactants.[28] For instance, silica with a cubic bicontinuous mesopore network was used as the template for the synthesis of mesoporous TiO_2 with the inverse structure.[29] Larger macropores can also be produced by templates with feature sizes greater than 50 nm. As described earlier, hierarchical porosity is achieved in 3DOM TiO_2 through infiltration of a precursor that contains an additional porogen (or a secondary phase) that can be removed. Several teams have produced 3DOM TiO_2 that contains mesopores within the wall network that are templated from soft, surfactant templates present in the precursor.[30-34] Chapter 3 details the synthesis of the 3DOM material TFA-TiO_2/C. Burnout of the carbon phase (a secondary hard template) allows for the formation of 3DOM TiO_2 with a high surface area and disordered mesoporosity. While the BET surface area of that 3DOM

material is comparable to that of soft-templated, mesoporous TiO_2, even higher surface areas for TiO_2 are attainable through conversion to titanate materials.

The hydrothermal and, as was also discovered, ambient pressure treatment of TiO_2 in basic solutions is a facile means to produce layered titanates and TiO_2-B.[10,35] Fortuitously for researchers, the conversion process also produces different types of nanostructures, such as nanosheets, nanotubes, and nanowires.[36] Through control of the reaction time,[37-39] reaction temperature,[40-42] concentration of the basic solution,[38,43] concentration of TiO_2,[44,45] and the starting TiO_2 material,[46,47] it is possible to synthesize nanostructured titanate/TiO_2 that contains mesopores and even macropores. The prevailing theory is that a dissolution-reprecipitation mechanism underlies these syntheses and allows for the production of various nanostructures.[10,37,40,42,44] Dissolution of TiO_2 generates hydroxylated Ti^{4+} that is associated with a cationic counter ion, such as Na^+ when NaOH is used.[10,39] These species condense and crystallize, which results in the formation of multilayer nanosheets only a few nm thick.[40,42] Nanotubes can subsequently form via a scrolling mechanism that likely arises from mechanical stresses present in multilayer titanate nanosheets.[45] Scrolling occurs provided that sufficient energy is imparted to overcome the activation barrier for this process.[41] Given sufficiently forcing conditions, the excess surface energy of the titanate nanotubes is minimized through a transformation to nanowires/nanorods.[10] It is believed that this takes place through a combination of oriented attachment of nanotubes into bundles and Ostwald ripening of the titanate structures.[40] Depending on the treatment, various polymorphs of alkali titanate are formed from the treatment in base.[41,48,49] Subsequent ion exchange in an acid leads to the formation of hydrated/protonated titante polymorphs (or even conversion back to TiO_2),[50] and structural changes.[51-53] Hydrogen titanates produced via ion exchange can typically be converted to monoclinic TiO_2-B upon heating to 350–500 ºC[54] and then to anatase at higher temperatures.[55] This conversion occurs via the removal of hydroxyls and crystal water from the layered hydrogen titanate phases and then via phase transformation from TiO_2-B to anatase.[54,56] However, direct conversion to anatase is possible.[55,57] Monoclinic TiO_2 and anatase TiO_2 with exceedingly high specific surfaces areas can be attained via the procedures described above. Not surprisingly, these hierarchically porous materials have attracted a great deal of attention for electrochemical applications, including LIBs.

Several years after the discovery of the hydrothermal synthesis of titanate nanomaterials, multiple research teams began to investigate the use of those materials as LIB anodes. These studies were motivated by the discovery that nanostructuring/nanosizing is essential to enhance the capacity and rate performance of TiO_2 electrodes.[26] Hydrothermal syntheses offered a means

to readily produce nanostructured hydrogen titanate and TiO_2 that could be readily tested in LIBs.[58-62] At a time when the reported capacities of TiO_2 anodes were low, these nanostructured electrodes offered unparalleled capacities and rate performance. Part of the reason for the improved electrochemistry was the transformation (via pyrolysis) of hydrogen titanate to TiO_2-B.[26,60,61] High surface area materials containing the TiO_2-B polymorph mainly store charge via an intercalative pseudocapacitive mechanism near the electrolyte–electrode interface.[63] This avoids the kinetic limitation of slow solid-state diffusion, enhancing rate performance. A similar mechanism is postulated to be responsible for the boost in capacities of hydrogen titanate.[64] Even diffusion-controlled intercalation processes into larger-grained TiO_2-B are not limited to the reversible insertion/extraction of 0.5 Li^+ per formula unit of TiO_2 like anatase, but can reach ~0.6 Li^+ per unit of TiO_2.[26]

After initial research was conducted on hydrothermally prepared titanates/TiO_2 for LIBs, various groups have experimented with methods to tailor the structure of electrode materials to alter their electrochemical properties. Substantial optimization of the structure of the anode materials has been conducted by altering synthesis parameters used for the reaction of TiO_2 in basic solutions. Nanoribbons,[65] nanosheets,[66] and nanorods[67] have all been investigated in such a fashion. For instance, Myung *et al.* found that pyrolyzed anatase nanorods formed after 11 h of reaction at 170 °C had a substantially better capacity than TiO_2-B wires formed using longer reaction times.[67] To mitigate the poor electronic conductivity of these nanostructured TiO_2 materials, methods to combine these materials with carbon have been devised.[68,69] Flexible electrodes produced by growing TiO_2-B sheets on activated carbon fibers are just one example, and these electrodes attained 100 mAh/g of capacity at 30 C.[69] Conversion of the titanates to anatase nanostructures is an effective method for improving overall capacities.[57,70] Gentili, *et al.* showed that by adjusting ion-exchange and pyrolysis procedures used after formation of sodium titanate nanotubes, small-grained anatase nanotubes could be synthesized.[57] These nanotubes provided 175 mAh/g of capacity at a rate of ~5 C. Other research teams have continued to focus on hydrogen titanates.[56,71] Most importantly for this chapter, changing the morphology of the parent TiO_2 has been an extremely useful method for producing electrodes. Hierarchical structures have been synthesized using AAO-templated TiO_2 nanotubes,[72] nanotubes of TiO_2 generated via electrochemical anodization of Ti,[73] and TiO_2 coated on silica spheres.[74] However, researchers have yet to marry colloidal crystal templated TiO_2 with an additional alkaline treatment step, until now.

This chapter describes an investigation into the various transformations that occur when 3DOM TiO_2 is treated in alkali solution, ion-exchanged, and pyrolyzed. Additionally, selected materials were processed into electrodes and tested to determine their lithium insertion/extraction capacities at various rates. A major focus of this chapter is determining how the templated source material impacts the resulting morphology of the alkali-treated titanates. Using a variety of characterization techniques (electron microscopy, gas sorption and X-ray diffraction), both the crystal structure and structure of the pore/solid network are tracked as the 3DOM TiO_2 is processed. Remarkably, the 3DOM morphology is partially conserved after treatment in aqueous NaOH, albeit with nanosheets protruding into the macropores. Sufficient order exists in the titanate and pyrolyzed TiO_2-containing materials for photonic stop bands to be detected. The remnant 3DOM network prevents nanosheets from fully scrolling, resulting in extremely high BET specific surface areas that can even exceed 500 m^2/g. Surface areas were further increased by drying the titanate materials in supercritical CO_2. Pyrolysis dehydrates the lepidocrocite-like hydrogen titanate, transforming the crystals to TiO_2-B and finally anatase. Unfortunately, the high surface areas and high pore volumes do not translate into improved electrochemical capacities for lithium ion insertion and extraction. This point is discussed at the end of the chapter.

6.2 Experimental

6.2.1 Materials

Methyl methacrylate (99 %), titanium(IV) isopropoxide (>97%), trifluoroacetic acid (99 %), poly(ethylene oxide)–*block*-poly(propylene oxide)–*block*-poly(ethylene oxide) copolymer (molecular weight of 5800, P123), hydrochloric acid (volumetric, 0.1 N), sodium carboxymethyl cellulose (CMC, molecular weight of 250,000), and 1-methyl-2-pyrrolidone (99.5%, anhydrous) were all purchased from Sigma-Aldrich. Formaldehyde (37 wt% in water, certified ACS), phenol (ACS reagent grade), and potassium persulfate (ACS reagent grade) were purchased from Fischer Scientific. Hydrochloric acid (37 wt% in water, ACS reagent grade) and sodium hydroxide pellets (ACS reagent grade) were obtained from Macron Chemicals. Styrene-butadiene rubber (SBR, 50 wt% in water) and polyvinylidene fluoride (molecular weight of 600,000, ≥99.5%) were bought from the MTI Corporation. Ethanol (200 proof, USP grade) was purchased from Decon Labs. AEROXIDE® TiO_2 P25 was obtained as a gift from Degussa (now Evonik Industries). All chemicals listed were used without further purification. In addition, all water used in the syntheses was deionized on-site using a Barnstead Sybron purification system (final resistivity >18 MΩ·cm).

6.2.2 Preparation of 3DOM TiO_2

Poly(methyl methacrylate) (PMMA) colloidal crystals were synthesized to serve as the hard template for the 3DOM TiO_2. The polymer spheres that comprise the colloidal crystals were produced following a well-established emulsifier-free emulsion polymerization procedure.[75] A suspension of spheres with a diameter of ~450 nm was prepared for this chapter. These spheres were made using a fixed concentration of persulfate (0.6 g/L) in the emulsion. Polymer spheres were allowed to settle out of the suspension under the force of gravity. During sedimentation, the PMMA spheres self-assembled into face-centered cubic arrays. Once this process was complete, the supernatant was allowed to evaporate in ambient conditions.

3DOM TiO_2 was not directly synthesized, but made via a 3DOM composite of carbon and TiO_2. This composite was produced following the procedure for TFA-TiO_2/C detailed in Chapter 3. Pyrolysis was conducted under flowing N_2 (0.7 L/min) at 350 °C (4 h) and 500 °C (2 h) using a 1 °C/min ramp rate. Partially-carbonized PF sol was removed from the 3DOM TiO_2/C by calcining it under static air at 400 °C for 2 h using a 2 °C/min ramp.

6.2.3 Preparation of Titanate Materials and Their Derivatives

All titanate materials were synthesized through a similar procedure. 3DOM TiO_2 was combined with an 8 M aqueous solution of NaOH in a perfluoroalkoxy alkane round bottom flask (RBF). The concentration of 3DOM TiO_2 in the solution was fixed at 6 mg/mL. Once the 3DOM TiO_2 was added to the NaOH solution, the RBF was immersed in a bath of silicone oil and it was fitted with a water jacketed condenser. The oil bath was heated to 70 °C, 100 °C, or 125 °C (reflux), and the suspension was stirred at 120 RPM for 72 h.

After the treatment of the TiO_2 in alkali solution was completed, several additional processing steps were carried out. First, the suspension was poured onto cellulose filter paper in a Buchner funnel attached to a vacuum flask. The titanate material was washed with copious amounts of water (while vacuum was applied), placed in a ~20 mL scintillation vial, and immersed in 15 mL of DI water. This water was exchanged multiple times until the pH of the supernatant reached 10. After the pH had been lowered through washing, an ion-exchange procedure was undertaken. A solution of 0.1 M HCl (20 mL) was added to the scintillation vial containing the titanate. The solution was stirred for 1 h, the solution of HCl was exchanged with DI water, and the suspension was allowed to sit overnight. Multiple washes with DI water were then carried out until the pH of the supernatant reached ~6. At this point, the DI water was exchanged with ethanol, and an ethanolic suspension of hydrogen titanate was obtained. A sample was also prepared without the

ion-exchange procedure; in this case the sodium titanate was directly washed with water, and then suspended in ethanol prior to additional processing.

Once the ethanolic suspension was prepared, it was dried through one of two routes. In the first route, the supernatant was partially drained. The titanate was then poured out onto a Petri dish and allowed to dry in ambient conditions. Materials prepared through this route are denoted as 3DOM-[reaction temp]-H-EtOH. In the second route, the supernatant was exchanged with fresh 200 proof ethanol, the suspension was mixed briefly, and the solid titanate was dropped in polymeric foam buckets. These buckets were placed in a Tousimis Samdri-780A critical point drier and dried in supercritical CO_2. Following the scheme detailed above, materials prepared through this route are denoted as 3DOM-[reaction temp]-H/Na-CO_2. H/Na indicates if the material is hydrogen titanate or sodium titanate.

Samples of 3DOM-100 °C-H-EtOH were also pyrolyzed in a tube furnace under flowing Ar (1.0 L/min). These samples were heated at 2 °C/min to either 400 °C for 1 h or 500 °C for 1 h. The resulting materials are designated 3DOM-100 °C-H-EtOH-400 °C or 3DOM-100 °C-H-EtOH-500 °C, respectively.

Another related material was prepared using AEROXIDE® P25 as the source for TiO_2. All processing steps are identical to those for the preparation of titanates from 3DOM TiO_2. The reaction temperature used was 100 °C. This material was dried under ambient conditions from an ethanolic suspension. The sample is denoted as P25-100 °C-H-EtOH in the text. P25-100 °C-H-EtOH was also pyrolyzed at 400 °C for 1 h in a similar fashion to the samples prepared from 3DOM TiO_2. This pyrolyzed titanate is denoted as P25-100 °C-H-EtOH-400 °C.

6.2.4 Structural Characterization

A variety of characterization techniques were utilized to understand the structural changes caused by the treatment of the TiO_2 in alkali and from subsequent steps. Morphological analysis of the samples was conducted using scanning electron microscopy (SEM) using a JEOL 6700 operated at 5 kV. Prior to analysis, the TiO_2/titanates were placed on double-sided sticky carbon tape that was affixed to Al stubs. All stubs were coated with 50 Å of Pt. Transmission electron microscopy (TEM) was carried out using a Technai T12 equipped with a LaB_6 filament. The accelerating voltage used in the instrument was 120 kV. Samples were prepared by sonicating (for 10 min) the material to be analyzed in a minimal volume of ethanol. These suspensions were dropped onto copper grids covered with holey carbon. Diffuse reflectance UV spectra were collected using a Thermo Scientific Evolution 220 spectrophotometer equipped with an ISA-220

integrating sphere. Powder X-ray diffraction (PXRD) was performed using a PANalytical X'Pert PRO diffractometer outfitted with an Empyrean Co anode (operated at 45 kV and 40 mA). A complementary technique for crystal structure analysis, confocal Raman microspectroscopy, was performed using a WITec Alpha 300R confocal Raman microscope. Spectra were collected using an Ar^+ laser with a wavelength of 514.5 nm (output power of 15 mW) and DV401 CCD thermoelectric-cooled detector. A 10× Olympus lens was used in the microscope and integrated spectra were taken from multiple points on a given sample. Nitrogen sorption isotherms were collected (at 77K) using a Quantachrome Autosorb IQ_2-MP. Every sample was evacuated at 0.001 torr and 200 °C for 12 h prior to analysis. Surface areas were calculated using the Brunauer-Emmitt-Teller (BET) method, and pore size distributions were obtained using the Barrett-Joyner-Halenda (BJH) method on the adsorption branch of the isotherms. Specific pore volumes were calculated from the point P/P_o=0.995 on the adsorption branch. Finally, a Netzsch STA 409 PC Luxx was used for thermogravimetric analysis. Samples were calcined under flowing air up to 1000 °C using a (10 °C/min ramp).

6.2.5 Electrochemical Testing

Electrode films were prepared using the 3DOM-100 °C-H-EtOH-400 °C, 3DOM-100 °C-H-EtOH-500 °C, or P25-100 °C-H-EtOH-400 °C with copper as a current collector. Electrode pastes were prepared by first hand-grinding the active material and then grinding the active material with Timcal Super P carbon black. Two aqueous binders, SBR and CMC, were stirred into mixture. The final composition of the pastes were 75 wt% active material, 10 wt% carbon black, 5 wt% SBR, and 5 wt% of CMC. Pastes were spread onto the current collector using a doctor blade set to 300 μm, and dried for 24 h under ambient conditions. Further drying was done at 105 °C under low vacuum for 24 h. Electrode disks with a diameter of 0.5 in were punched out from the films; the loading of active material on the disks was 2–3 mg/cm^2. Half cells were assembled using CR 2032 cans, the disks with active material, lithium ribbon as the counter electrode, and a coated polypropylene separator (Celgard® 3501, kindly provided by Celgard LLC). Assembly of the coin cells was conducted in a helium-filled glove box. The electrolyte used in the cells was 1 M $LiPF_6$ dissolved in a 1:1:1 mixture (by mass) of ethylene carbonate, dimethyl carbonate, and diethyl carbonate (purchased from MTI Corporation). Cells were then cycled using an Arbin Instruments BT2000. The voltage window was selected from 1 to 3 V vs. Li/Li^+ and the C-rate was set at 335 mA per gram of active material. One film was also prepared using an Al/C current collector (donated by ExoPack Coatings), using a paste containing 84 wt%

3DOM-100 °C-H-EtOH-400 °C, 10 wt% carbon black, 4 wt% CMC, and 2 wt% SBR. All additional processing steps were the same. Cyclic voltammetry (CV) curves were obtained using a Solartron 1287 electrochemical station. Scanning was conducted between 0.05 and 3 V vs. Li/Li^+ with a scan rate of 5 mV/s and a 1 s integration time.

6.3 Results and Discussion

Owing to the large number of samples analyzed and discussed in this chapter, the following section is broken into three parts for the sake of readability. At first, a discussion is presented that centers around the characterization of the titanate/TiO_2 materials prepared using 3DOM TiO_2 as a precursor. This section also covers the pyrolyzed titanates and control materials made using unstructured P25 TiO_2. An extended analysis of the morphological transformation is then provided along with an evaluation of the crystal polymorphs present in the titanate and pyrolyzed titanates. Finally, the lithium insertion/extraction behavior of several alkali-treated materials is discussed.

6.3.1 Characterization of the Parent 3DOM TiO_2

The 3DOM TiO_2 used as a starting material was prepared following the procedure outlined in Chapter 3, so the structural properties will only be briefly discussed. As shown in Figure 6.1a, the PXRD pattern of the 3DOM TiO_2 contains peaks that can be matched to anatase TiO_2. Raman spectroscopy (Figure 6.1b) confirms the presence of anatase and a minimal amount of TiO_2-B. SEM micrographs show that the material contains an interconnected, face-centered cubic lattice of macropores (Figure 6.1c). These spherical macropores are ca. 245 nm in diameter and are connected by pore windows of varying diameter. Surrounding the macropore network are the connected octahedral and tetrahedral nodes of TiO_2 that are the replicas of interstitial sites present in the parent colloidal crystal. Since the 3DOM structure contains a multitude of pore channels that extend through the as-made granules, the alkali solution can permeate throughout the structure. Some isolated defects, such as closed pores resulting from grain boundaries in the PMMA colloidal crystal template, are also present.

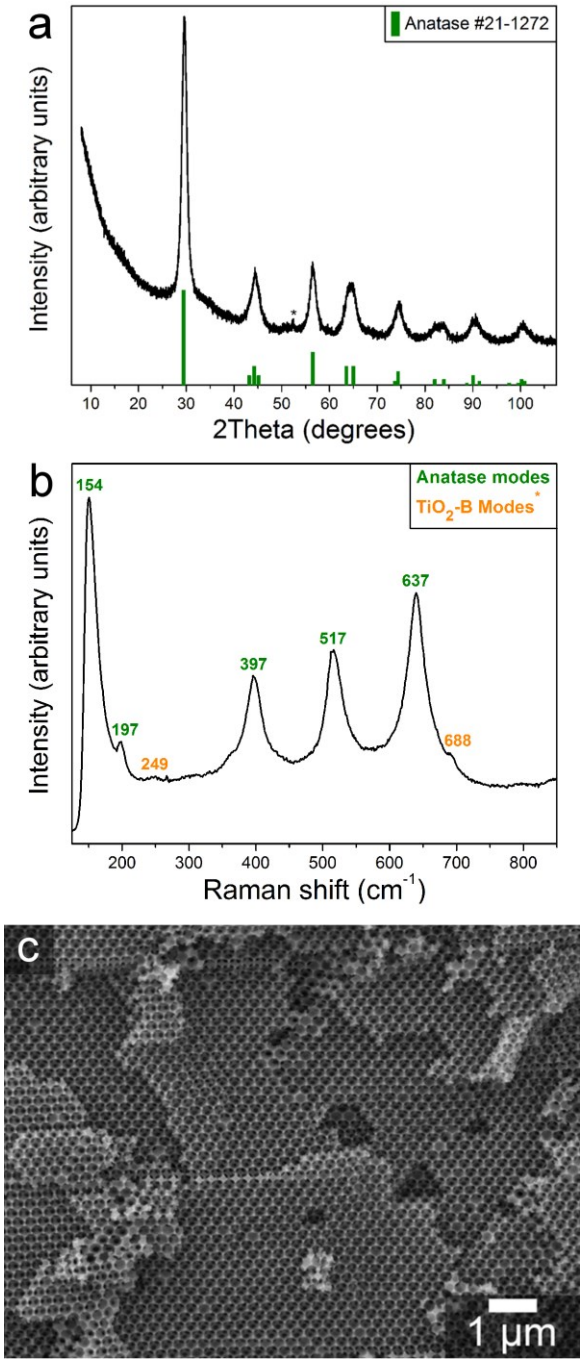

Figure 6.1 A compilation of characterization data from the 3DOM TiO_2 including (a) a PXRD pattern, (b) a Raman spectrum, and (c) a representative SEM image of the ordered macroporous structure. Anatase and TiO_2-B are detected in the material.

6.3.2 Microscopy Studies of the Alkali-Treated Materials

Once the starting 3DOM TiO_2 was converted to hydrogen titanate and dried, electron microscopy was first used to determine the morphological changes induced through the alkali/ion-exchange treatment. Examining the SEM micrographs first (Figure 6.2), the morphology of the 3DOM network is clearly altered for the hydrogen titanate materials. For samples prepared at 70 °C and 100 °C, numerous filament-like projections are present throughout more than half of the region that was comprised of the 3DOM structure (Figure 6.2 a–d). These disordered filaments are only a few tens of nm in size and appear to coarsen slightly as the reaction temperature is increased. Countless mesopore-sized, interconnected void spaces exist between filaments. There are also areas (comprising 30 to 50 % of a given sample) that contain much finer projections and large, roughly circular mesopores (Figure 6.3 a, b). Upon close inspection, the larger mesopores are aligned in a periodic pattern that matches the parent 3DOM structure. Both aforementioned regions contain a small fraction of larger-diameter wires that can stretch up to tens of micrometers in length (highlighted by Figure 6.2 b, c). Comparing the samples dried in ambient conditions versus the samples dried using supercritical CO_2, it is observed that a more open network of filaments is preserved when supercritical CO_2 is used (as shown in the right column of Figure 6.2). Without any drying stresses, the collapse of the nanostructures into bundles is inhibited, and a finer, gossamer structure is maintained. By increasing the reaction temperature to 125 °C, structural changes accelerate. Wires are found that extend for micrometers and have diameters around 100 nm (Figure 6.2 e, f). Regions are present that contain ordered pores and fine filaments (Figure 6.3 c), but are less prevalent (< 30 % of a given sample).

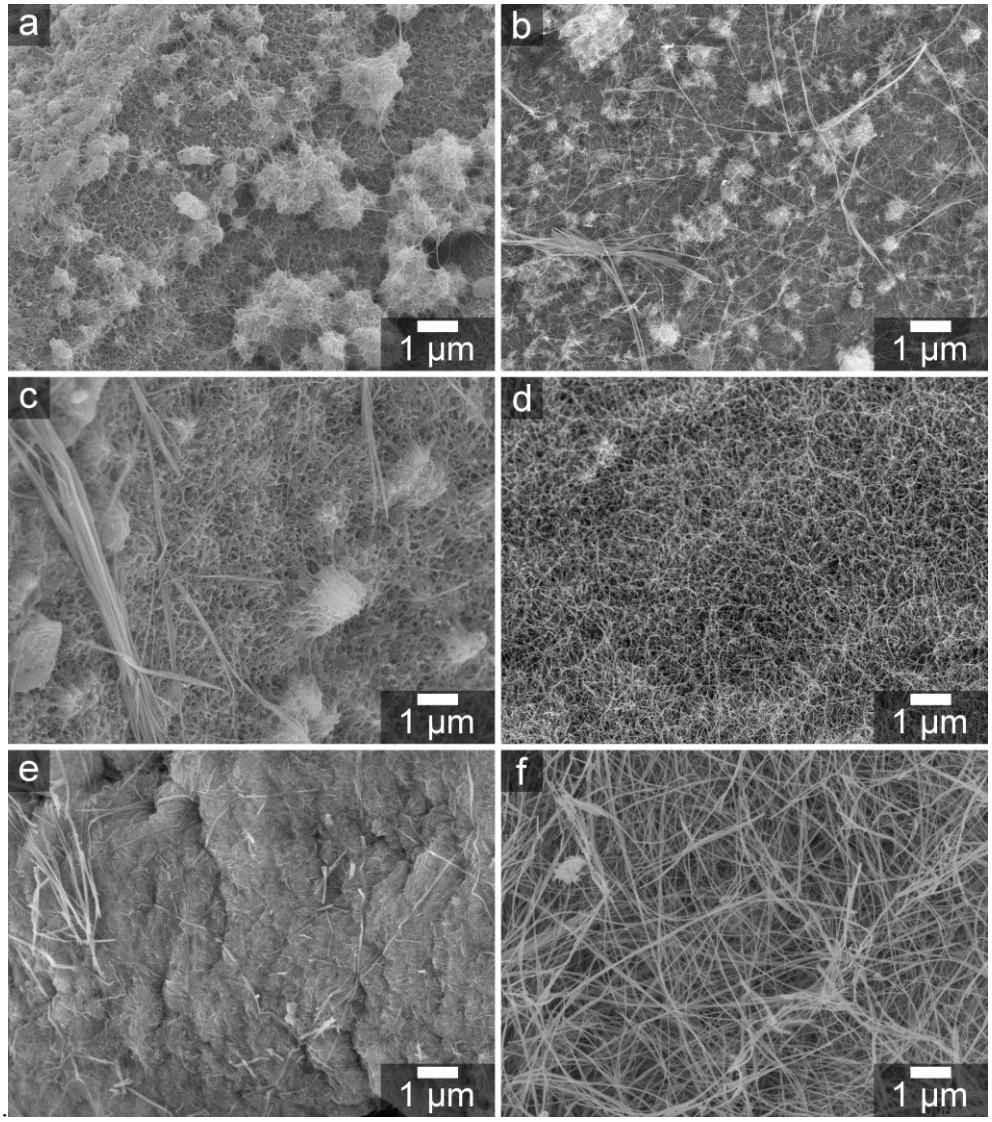

Figure 6.2 A compilation of SEM micrographs for various hydrogen titanate samples. The following samples are shown: (a) 3DOM-70 °C-H-EtOH, (b) 3DOM-70 °C-H-CO_2, (c) 3DOM-100 °C-H-EtOH, (d) 3DOM-100 °C-H-CO_2, (e) 3DOM-125 °C-H-EtOH, and (f) 3DOM-125 °C-H-CO_2. Anywhere from 50 to 70 % of a given sample resembles what is shown in these images.

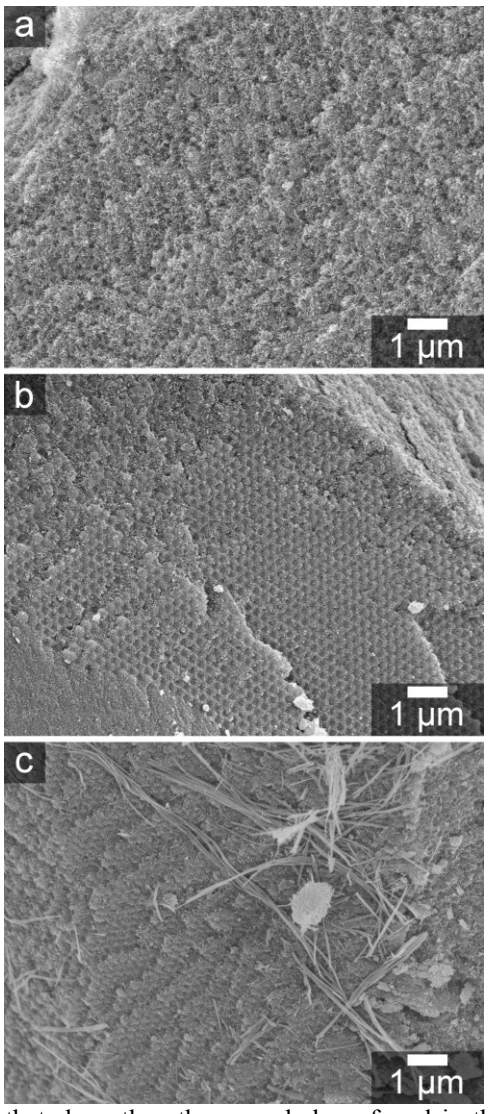

Figure 6.3 SEM micrographs that show the other morphology found in the hydrogen titanate materials. Examples are given for each of the reaction temperatures: (a) 3DOM-70 °C-H-CO_2, (b) 3DOM-100 °C-H-EtOH, and (c) 3DOM-125 °C-H-CO_2. The image in (b) is also an example of how this morphology is found in samples irrespective of the drying procedure used.

Better resolution of the overall morphology and the nanostructures present in the hydrogen titanate materials was accomplished through TEM imaging. When examining the micrographs of the samples, several things become immediately apparent. Most notably, a remnant of the 3DOM network exists, despite the dissolution-reprecipitation mechanism that occurs during the treatment of the 3DOM TiO_2 in NaOH solution. When viewed at lower magnification, the hexagonal tiling of large macropores along the (111) plane can be observed (Figure 6.4 a, b, d). Other regions (see Figure 6.4 e for an example) possess periodic stripes of light and dark resulting from planes of

aligned macropores and planes filled with hydrogen titanate. Unlike the parent 3DOM TiO_2, the contrast between the pore spaces and the network of connected nodes is less pronounced for the sample shown in Figure 6.4. This is due to the transformation of the TiO_2 crystals into nanosheets. In the hydrogen titanate materials, numerous crumpled nanosheets extend into what used to be the spherical macropores of the unconverted 3DOM structure (Figure 6.5). Nanosheets (and any other nanomaterials) are far more numerous in the octahedral and tetrahedral nodes of the former 3DOM structure (see Figure 6.5 e for a good example). The partially-scrolled nanosheets are the small "filaments" that are observed in the SEM micrographs in Figure 6.2 and 6.3, and the aligned dark spots in Figure 6.3 are from the low-density regions at the core of what used to be the spherical macropores. It also should be noted that some areas imaged in the hydrogen titanate samples lack any evidence that the 3DOM structure existed. Only a disordered network of crumpled nanosheets and nanowires is found in these regions (Figure 6.4 c, f). Unlike what is observed in the SEM images, the disordered morphology is fairly uncommon in the TEM specimens. SEM, which provides topographical information from surfaces, does not reveal that a substantial fraction of the underlying material retains a "memory" of the 3DOM network. Finally, the materials treated at 125 °C contain more nanowires and tubes than the other materials, as is observed in SEM images.

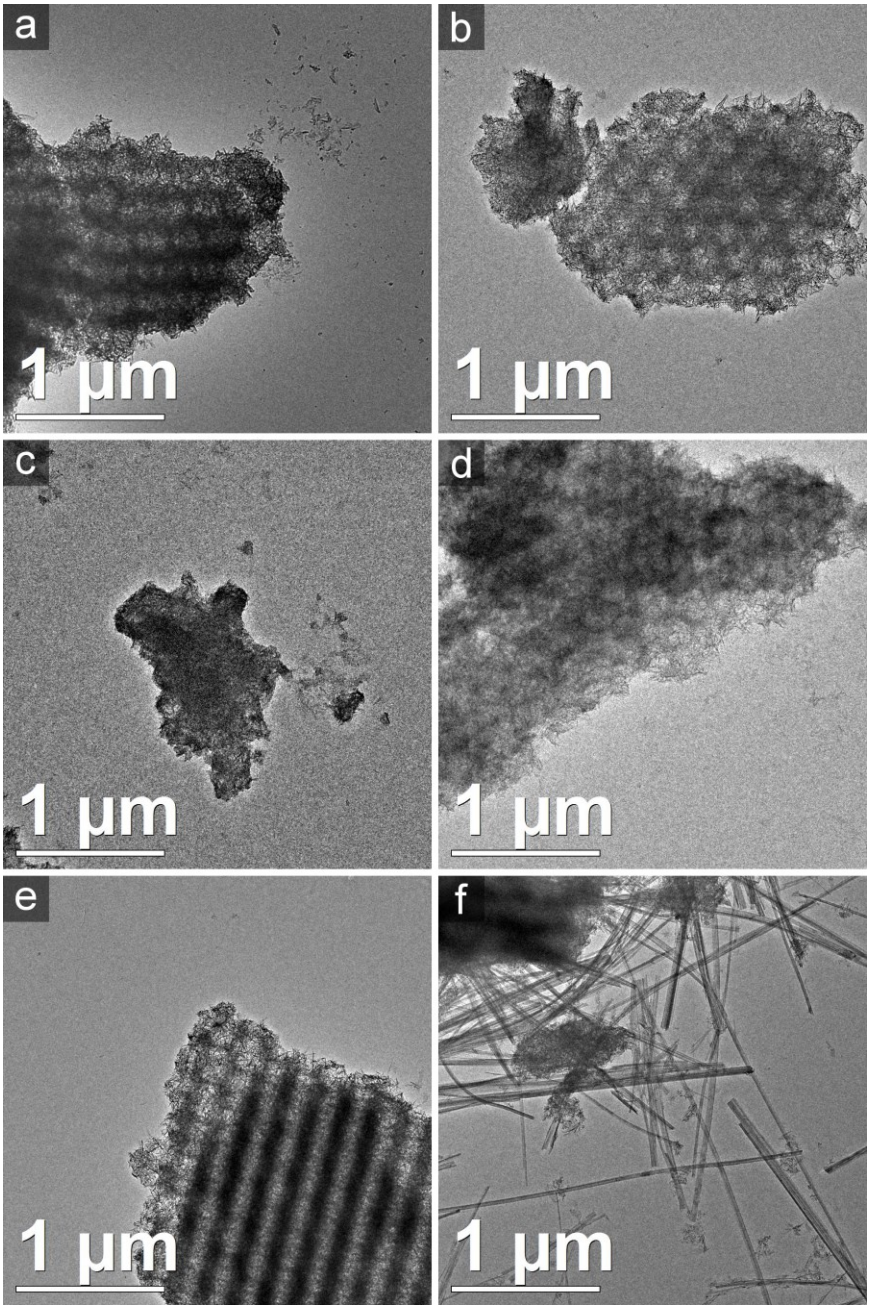

Figure 6.4 A series of TEM images of the hydrogen titanate materials taken at a low magnification. The following samples are shown: (a) 3DOM-70 °C-H-EtOH, (b) 3DOM-70 °C-H-CO_2, (c) 3DOM-100 °C-H-EtOH, (d) 3DOM-100 °C-H-CO_2, (e) 3DOM-125 °C-H-EtOH, and (f) 3DOM-125 °C-H-CO_2. Evidence of the ordered 3DOM network is observed in all of the materials; however, there are areas (c, f) that lack any remnant 3DOM structure. Nanowires are fairly prevalent in the materials treated at 125 °C. Images taken by Stephen Rudisill.

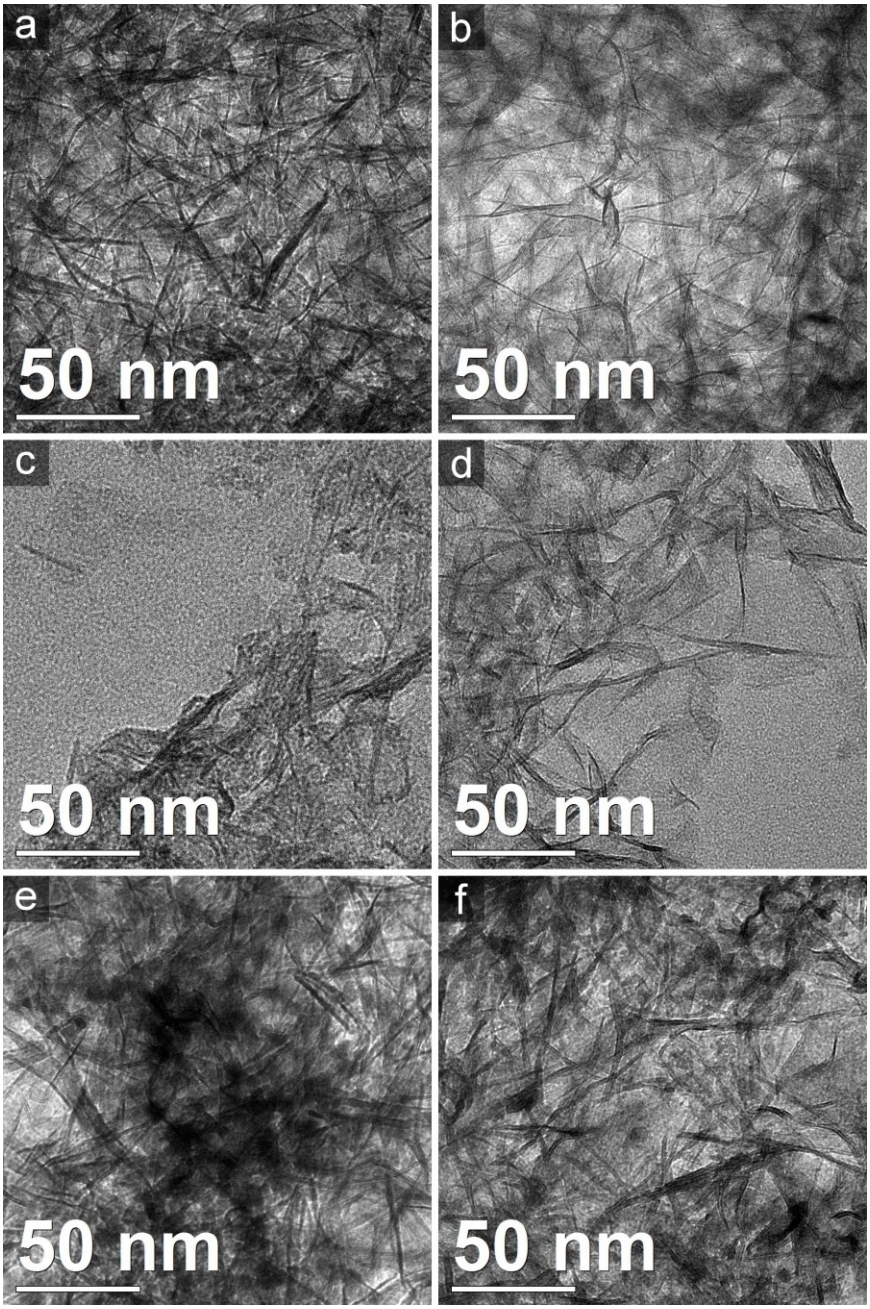

Figure 6.5 TEM images of the hydrogen titanate materials taken at a higher magnification. The following samples are shown: (a) 3DOM-70 °C-H-EtOH, (b) 3DOM-70 °C-H-CO_2, (c) 3DOM-100 °C-H-EtOH, (d) 3DOM-100 °C-H-CO_2, (e) 3DOM-125 °C-H-EtOH, and (f) 3DOM-125 °C-H-CO_2. The partially scrolled nanosheets that comprise the overwhelming majority of these materials are highlighted in the images. In some of the images, especially (e), the dense cores of the octahedral and tetrahedral nodes are clearly observed via thickness contrast. Images taken by Stephen Rudisill.

Tracing morphological changes through the ion-exchange and pyrolysis processes is also important for understanding the structural changes occurring in the treated 3DOM TiO_2. Prior to ion-exchange, the 3DOM TiO_2 is converted first into sodium titanate. One such sodium titanate material, 3DOM-100 °C-Na-CO_2, was washed with DI water, dried in supercritical CO_2, and analyzed. As expected from earlier research studies, the initial conversion from 3DOM TiO_2 to sodium titanate at relatively low reaction temperatures produces nanosheets (presumably via dissolution-reprecipitation).[37,41] 3DOM-100 °C-Na-CO_2 has a similar structure to its proton-exchanged counterpart as observed in SEM images (Figure 6.6), and has both ordered and disordered regions. The 3DOM network remnant can be resolved in low magnification TEM images (Figure 6.7 a) for 3DOM-100 °C-Na-CO_2. Higher magnification images (Figure 6.7 b, c) show that partially-scrolled nanosheets extend into the macropore spaces. Ion-exchange with H^+ is thought to alter the structure of alkali titanate nanosheets and nanotubes, but electron microscopy does not provide any conclusive evidence that structural changes occur during ion exchange (compare Figure 6.7 with Figures 6.4 and 6.5). However, changes induced by ion exchange with H^+ are notoriously difficult to visualize using microscopy[51,76] and are more easily resolved by sorption analyses.

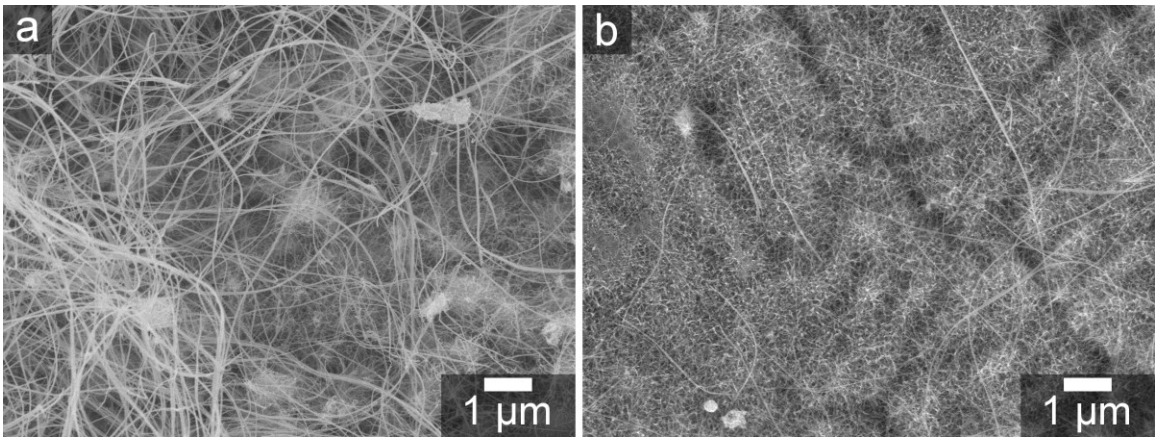

Figure 6.6 SEM images of 3DOM-100 °C-Na-CO_2. In (a) an area that contains a fair amount of nanowires and a more disordered morphology is shown. In contrast, in (b), finer filaments are present, and a remnant of the 3DOM structure is observed in at the upper left-hand side of the image.

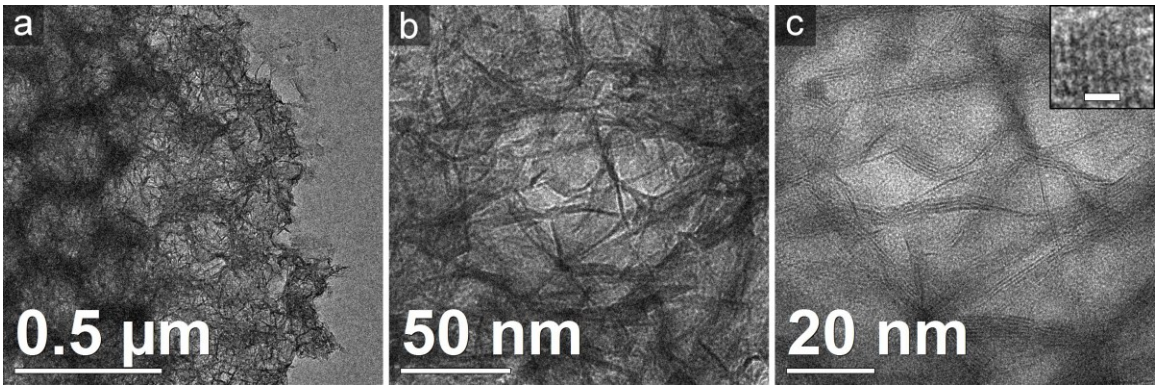

Figure 6.7 TEM images of 3DOM-100 °C-Na-CO_2 taken at various magnifications. At relatively low magnification, the outline of the original macropore network is observed in (a). When the magnification is increased, nanosheets can be clearly observed in the pore spaces of images (b) and (c). Scattered nanoparticles with a lattice spacing of (~0.63 nm) are found in the samples (see inset in c). The length of the scale bar in the inset is 2 nm. Images taken by Stephen Rudisill.

Although structural changes induced by ion exchange are not especially clear via analysis by microscopy, the changes induced by altering the pyrolysis temperature are readily apparent. Pyrolysis of 3DOM-100 °C-H-EtOH at 400 °C does not cause any substantial changes to the overall morphology. SEM images show the characteristic filament-like structure that is found in the unpyrolyzed materials (Figure 6.8). Some regions show evidence of the underlying parent periodic 3DOM structure (Figure 6.8 b). TEM images reveal the presence of numerous partially-scrolled nanosheets typical of the parent hydrogen titanate material (Figure 6.9 a, b). Structural changes have been reported to be fairly limited after pyrolysis at 400 °C,[10,77,78] mirroring what is observed here. Once the pyrolysis temperature for the 3DOM-100 °C-H-EtOH is increased to 500 °C, another situation arises. While SEM and low magnification TEM images show a structure that closely resembles the non-pyrolyzed material (Figure 6.8 c, d and Figure 6.9 c), higher magnification TEM images reveal substantial changes. These images show that the nanosheets and nanotubes are converted into sub-10 nm crystallites, and that the crystallites are fused together in filament-like projections (Figure 6.9 d). As is discussed later, these crystallites are formed as a result of sintering processes as hydrogen titanate/TiO_2-B is converted to anatase TiO_2.

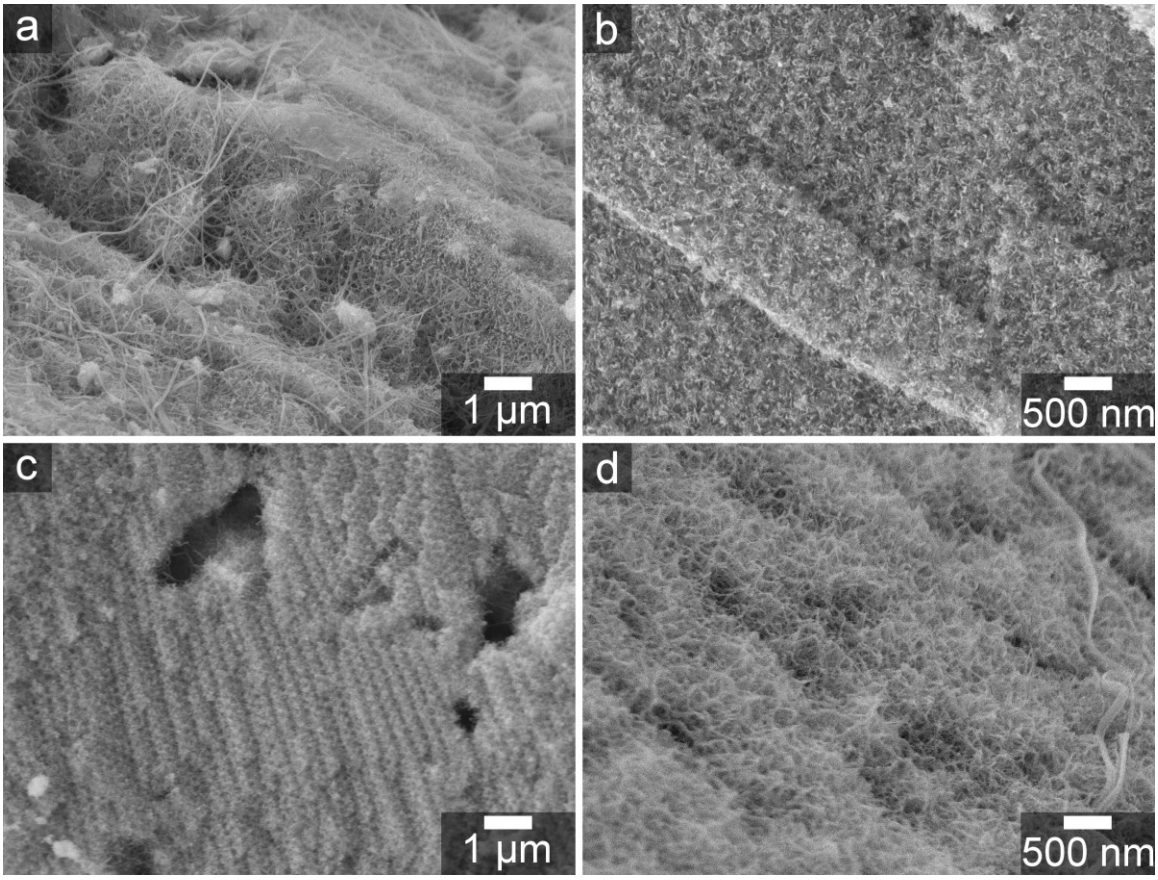

Figure 6.8 SEM images of (a, b) 3DOM-100 °C-H-EtOH-400 °C and (c, d) 3DOM-100 °C-H-EtOH-500 °C. Regions with more disorder (a, d) (similar to those in Figure 6.2) and regions that retain evidence of the ordered macropore structure (b, c) are displayed.

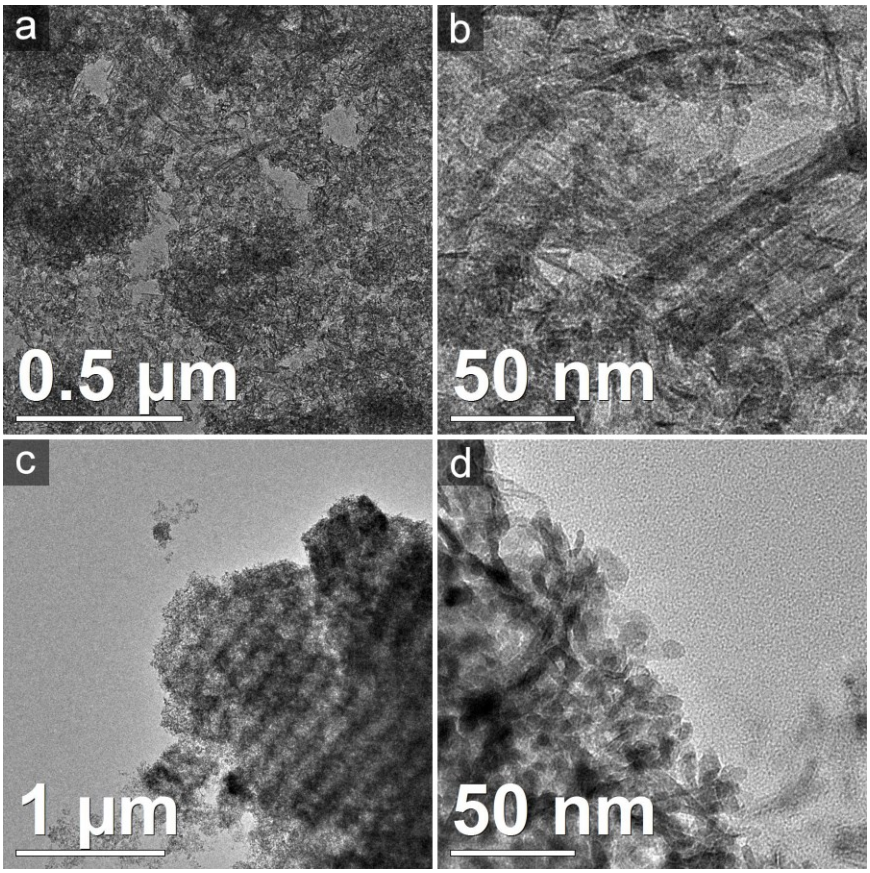

Figure 6.9 TEM micrographs of (a, b) 3DOM-100 °C-H-EtOH-400 °C and (c, d) 3DOM-100 °C-H-EtOH-500 °C. Nanosheets can still be observed in 3DOM-100 °C-H-EtOH-400 °C (b). While the periodic pattern indicative of the transformed 3DOM structure is visible for 3DOM-100 °C-H-EtOH-500 °C in (c), widespread conversion of the nanosheets to nanoparticles is observed in (d). Images taken by Stephen Rudisill.

Since the conditions used are fairly mild, it is not surprising that nanosheets are the dominant nanostructure found in the materials prepared using 3DOM TiO_2 (except for the material pyrolyzed at 500 °C). In a morphological diagram compiled by Bavykin *et al*., nanosheets were observed for materials treated at 70 °C in 10 M NaOH (under ambient pressure), and nanotubes were found at 100 °C.[41] Nanotubes/wires are also present in the 3DOM-70 °C/100 °C-H samples, albeit at a much lower frequency than the nanosheets (see Figure 6.2, for instance). Confinement of the nanosheets is afforded by the spherical macropores present in the 3DOM structure, leading to the bird's nest-like structure observed in the TEM micrographs. Complete scrolling of the sheets is not possible in the pores, which allows for nanosheets to be the prevalent nanostructure. Nanosheets are preserved after treatment in reflux conditions, even though these conditions generally lead to the formation in nanotubes and nanowires of sodium titanate.[41,43,65] However, it

appears that the kinetic barrier for complete scrolling is breached for a fraction of the multilayer sheets. Nanotubes and nanowires become also more numerous as the reaction temperature for the alkali treatment is increased, owing in large part to the increased energy supplied to the system. The origin of the differences between regions that retain a 3DOM remnant structure even at high temperatures versus those that do not is not fully clear. Hydrothermal syntheses of hydrogen titanate do contain heterogeneities, but this issue is frequently not discussed in the literature.[52] In this case, surfaces and defects in the 3DOM TiO_2 should enable scrolling, since the effects of confinement are limited in these regions. For instance, SEM images show that numerous nanotubes (or possibly nanowires) grow from the exterior surface of the hydrogen titanate granules (Figure 6.10 a). Cracks or grain boundaries in the original colloidal crystal template can also produce defective, non-porous, and unconfined surfaces. However, replication of terraces from the grain boundaries that are in the 3DOM structure is also observed (Figure 6.10 b). A possible reason for these heterogeneities is rapid dissolution of small particles, and this point is discussed below.

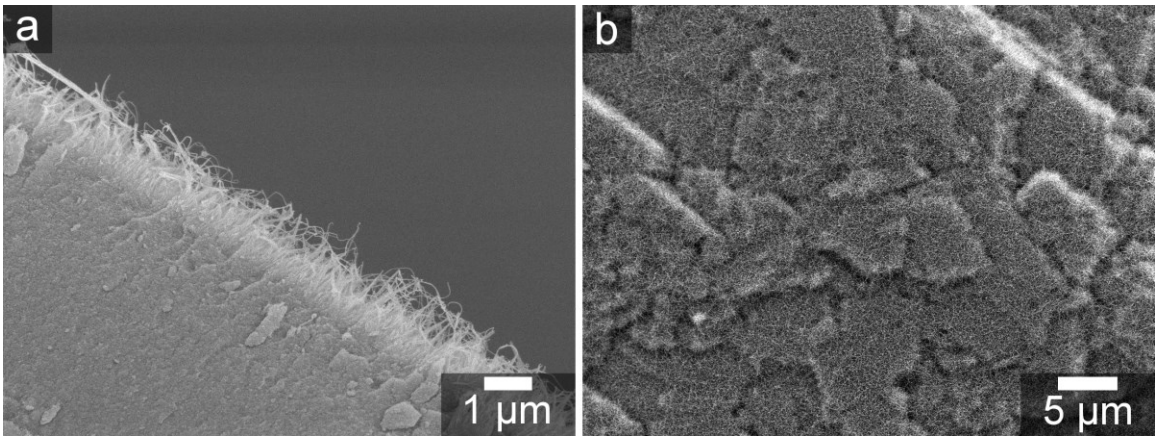

Figure 6.10 Two SEM images from 3DOM-100 °C-H-CO_2. The image in (a) shows an example of nanotubes that form on the exterior surfaces of granules. In (b), fractures along close-packed layers of the original 3DOM structure are preserved even after conversion and ion-exchange.

6.3.3 Proposed Structural Transformation Sequence

With the information obtained via microscopy, a further discussion of a possible sequence of transformation steps from 3DOM TiO_2 to the titanate nanostructure is warranted at this point. As seen in Figures 6.3 and 6.4, periodicity is clearly retained throughout the transformed 3DOM TiO_2. However, confined nanosheets fill most of the volume in the spherical macropores of the original 3DOM structure. With higher magnification images, the regions that used to be

octahedral and tetrahedral nodes are more clearly observed. Either small crystallites or highly crumpled nanosheets lie at the center of the darker nodes, which are encased in multi-layer nanosheets (see Figure 6.5 e). The arrangement suggests that TiO_2 progressively dissolves from the surface of the 3DOM structure, and then the soluble Ti^{4+} clusters begin to condense/crystallize in the alkali solution that fills the spherical macropores. Layered sodium titanate nucleates (as nanosheets) on TiO_2 crystals that remain undissolved in the shrinking 3DOM skeleton. Localized nucleation of sodium titanate nanosheets onto undissolved TiO_2 has also been observed in other studies.[37,42] As the reaction progresses, nanosheets begin to scroll, which is possibly driven by mechanical stresses caused by uneven lateral sizes of the individual layers of the nanosheets.[45,79] Alternately, it may be that multiple layers exfoliate from thicker nanosheets and begin to scroll.[37] In either case, scrolling nanosheets should impact TiO_2 crystallites and other nanosheets in the macropore spaces. This prevents further scrolling, resulting in the crumpled morphology observed in the microscopy images. Dissolution continues as more anatase TiO_2 is exposed to the solution through the voids between deposited titanate sheets. These titanate sheets, after ion-exchange, contribute to the diffraction rings observed in the selected area electron diffraction (SAED) patterns (Figure 6.12). Due to the substantial disorder encountered in the nanosheets,[44] diffraction rings are quite broad and weak. A more complicated situation arises at the core of the octahedral and tetrahedral nodes. At lower reaction temperatures (i.e. 70 °C), anatase crystallites remain in the 3DOM network. This is evidenced by a diffraction ring in SAED patterns that can be indexed to the anatase (004) plane (Figure 6.12 b) and, as is shown later, the presence of anatase vibrational modes in collected Raman spectra. Difficulties in transporting the aqueous alkali solution through the tortuous (and growing) titanate sheet network may impede the transformation. Interestingly, nanoparticles are present with a spacing between lattice fringes of ~0.63 nm (Figure 6.11 a). This spacing corresponds well with the (110) plane of TiO_2-B and the (031) plane in $NaTi_2O_4(OH)$.[48] It is not clear if these particles are residual TiO_2-B from the 3DOM TiO_2, or converted sodium titanate that was incapable of transforming into nanosheets due to extreme confinement. Particles with similar spacings are also found in 3DOM-100 °C-Na-CO_2 (Figure 6.6 c).

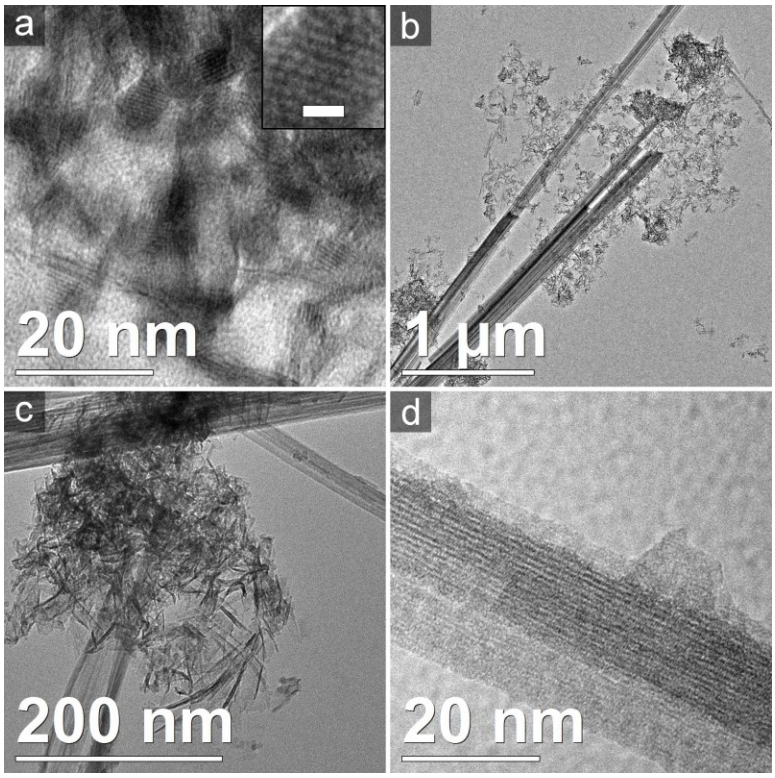

Figure 6.11 Four TEM micrographs of the 3DOM-125 °C-H samples. In (a), nanocrystals present in 3DOM-125 °C-H-EtOH are shown. The lattice spacing is ~0.63 nm in the crystals. Multi-µm long nanowires are shown in (b) for 3DOM-125 °C-H-EtOH. A partially unrolled nanotube can be observed in the center of (c), alongside a cluster of nanosheets. A close-up of a nanowire is given in (d) for 3DOM-125 °C-H-CO_2. The length of the scale bar in the inset is 2 nm. Images taken by Stephen Rudisill.

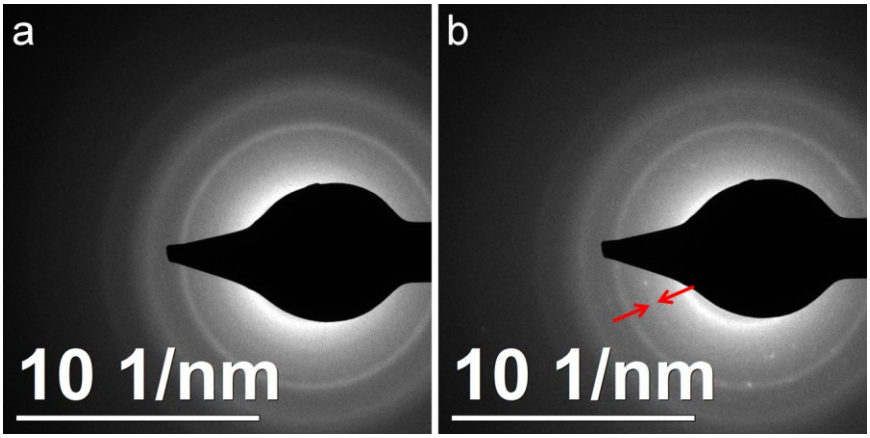

Figure 6.12 Selected area electron diffraction pattern of (a) 3DOM-70 °C-H-EtOH and (b) 3DOM-70 °C-H-CO_2. Four rings with *d*-spacings of 0.36 nm, 0.19 nm, 0.15 nm and 0.12nm are present in the diffraction patterns. These match what is reported for lepidocrocite-like hydrogen titanate nanotubes,[80] and match the diffraction peaks in PXRD patterns given later. The red arrows surround a ring with a *d*-spacing of 0.24 nm that corresponds to the (004) plane of anatase TiO_2. Patterns collected by Stephen Rudisill.

Nanosheets are the primary nanostructure found in the converted materials, but it is also important to address the presence of nanotubes and nanowires. Once most remaining TiO_2 crystals are dissolved (or the remaining 3DOM skeleton contains only a few extremely confined titanate crystals), the scrolling of nanosheets may accelerate near unconfined surfaces. Both the presence of 1-D nanostructures at the surface of monoliths (Figure 6.10 a) and the coarser, disordered nanostructures found in SEM images (Figure 6.2) may be a consequence of this phenomenon. The appearance of 1D nanostructures that are not obviously connected to the underlying granules of titanate, also warrants a further discussion. When the reaction temperature is at reflux (125 °C), scrolling is facilitated[41] and disordered regions are more prevalent. Both nanotubes and, far more frequently, solid nanowires (Figure 6.11 c-d) are found in greater frequency for these materials when compared to materials processed at lower temperatures. Lattice spacings in the nanowires are around 0.84 nm, which is typical for 1D nanostructures of hydrogen titanate (Figure 6.11 d).[53] Other researchers have observed that higher reaction temperatures promote dissolution of TiO_2, provide adequate energy to scroll nanosheets into nanotubes, and allow for the filling of the nanotubes (which leads to the formation of nanowires).[38,39,41] Beyond a temperature increase, stirring a reaction mixture has been shown to facilitate dissolution of TiO_2, nucleation of sodium titanate throughout the mixture (via enhanced mass transport), and formation of nanowires.[81] In the case of the 3DOM TiO_2 processed at reflux, all these effects should come into play. For instance, larger particles of 3DOM TiO_2 stay intact during processing, but smaller particles (sub-10 μm) appear to dissolve completely (they are not detected in the samples dried in ambient conditions). During the dissolution of the small 3DOM TiO_2 particles (a process that may also occur quickly due to the small size of the anatase grains),[39] scrolling nanotubes can be released from the particles into the solution. It is also possible that mechanical stirring can dislodge nanowires and nanotubes from the lager granules of 3DOM material. Free nanotubes can aggregate in the reaction solution, and further transform into wires. Cao and co-workers found evidence that that nanotubes bundle during reaction in alkali solution (also observed here), and the inner spaces fill with additional deposited titanate.[40] Aggregation and filling of the nanotubes, in the case of the 3DOM TiO_2-based materials, should also lead to the formation of nanowires.

6.3.4 Electron Microscopy-Based Characterization of Alkali-Treated P25 TiO_2

A final note should be made concerning the morphology of materials prepared using P25 TiO_2 instead of 3DOM TiO_2. P25 consists of crystals of anatase and rutile TiO_2 with grain sizes around 20 to 30 nm.[46] These grains can aggregate into larger clusters, but nothing exists that is equivalent to the fully-connected, mm-scale granules present in 3DOM TiO_2. As a consequence, the P25-100 °C-H-EtOH is comprised of irregular particles that range in size from several micrometers to several hundreds of micrometers (Figure 6.13 a). Each particle is comprised of aggregated nanosheets that have partially scrolled during the synthesis procedure (Figure 6.13 c). Since the P25 powder lacks an ordered macropore structure, there is no evidence of a periodic nanostructure in the P25-100 °C-H-EtOH. The nanosheets in this material also appear to have larger lateral dimensions, which is probably from the absence of any confinement afforded by a larger structure (as is the case for materials prepared with 3DOM TiO_2). Pyrolysis at 400 °C does not cause any significant changes to the morphology found in P25-100 °C-H-EtOH (Figure 6.13 b, d).

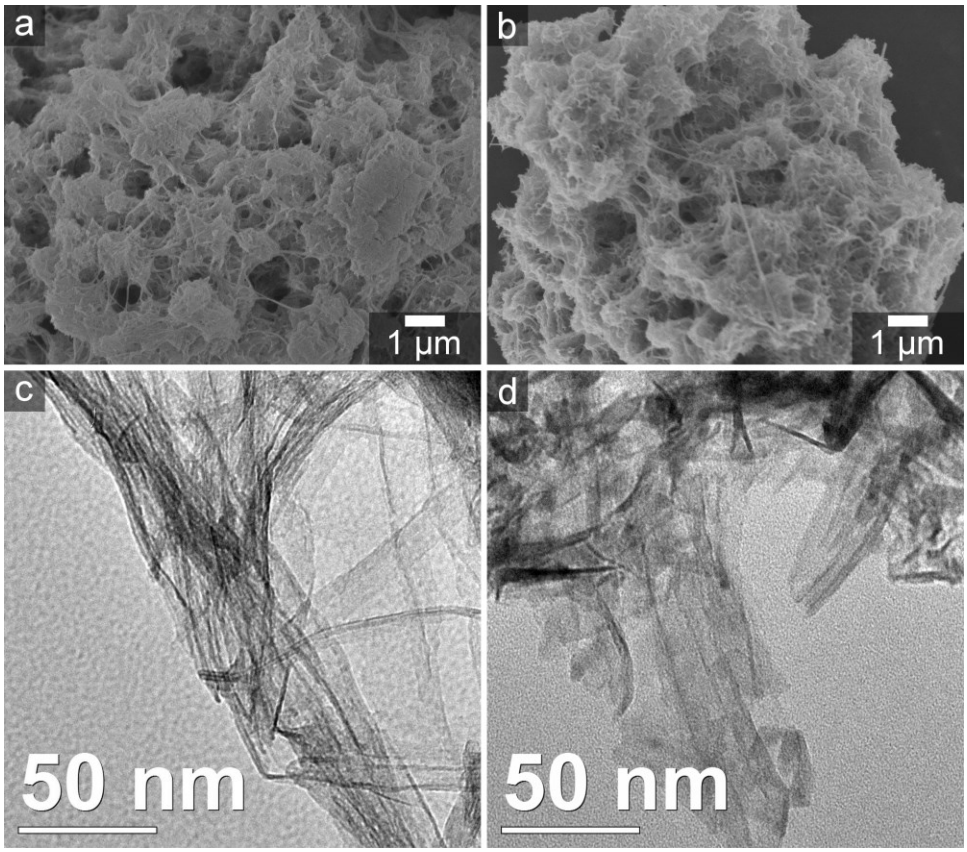

Figure 6.13 SEM (a, b) and TEM (c, d) micrographs of the materials prepared using P25 TiO_2. P25-100 °C-H-EtOH (a, c) and P25-100 °C-H-EtOH-400 °C (b, d) are both shown. The morphologies of the two materials are similar. TEM images taken by Stephen Rudisill.

6.3.5 UV-Visible Spectroscopy of Selected Titanate and Pyrolyzed Titanate Materials

Despite the structural transformations induced in the titanate materials prepared using 3DOM TiO_2, UV-visible spectroscopy reveals the unmistakable hallmarks of photonic stop bands (Figure 6.14). Since TEM images show a clear difference in the amount of nanosheets present in the former macropore spaces versus the densely-packed octahedral/tetrahedral nodes (i.e. Figure 6.5), a periodic difference in the refractive index exists in the 3DOM TiO_2-based materials. As a result, photonic peaks are expected in the UV-visible spectra.[82] To show that any peaks in the reflectance spectra originate from photonic stop bands, the pore spaces were filled with ethanol. Ethanol has a higher refractive index than air (1.36 vs. 1), and should alter the stop band position.[83] A sample that was not pyrolyzed, the white-colored 3DOM-100 °C-H-EtOH, shows high reflectance across the visible spectral range (Figure 6.14 a). Though it is somewhat difficult to resolve, a shoulder/peak is present at ~470 nm that shifts to ~565 nm with addition of ethanol. Since the average refractive index increases when ethanol fills the pore network, the redshift is expected. Once the samples are pyrolyzed, reflectance decreases substantially, and the samples appear bluish purple. While it is not completely clear why the reflectance decreases (it may be from Ti^{3+} ions that form during the heating of hydrogen titanate),[84,85] a similar decrease in reflectance is also observed for non-photonic P25-100 °C-H-EtOH-400 °C (Figure 6.14 b). When a 3DOM material absorbs more incoming light, its structural color is significantly enhanced.[75] This is observed for the spectra of the pyrolyzed materials, which contain distinct peaks from photonic stop bands (presumably originating from the (111) planes). Similar to what is observed for the non-pyrolyzed sample, filling the pores with ethanol causes a red-shift in the stop bands and produces green coloration (see Table 6.1 for positions). The photonic stop band for the material pyrolyzed at 500 °C is blue-shifted relative to the material pyrolyzed at 400 °C. Shrinkage of the structure from sintering is probably the cause of the blue-shift; however, refractive index changes in the solid may also have an impact.[75] Finally, when non-structured P25 is used as a starting material, no indication of photonic stop bands can be observed (Figure 6.14 b).

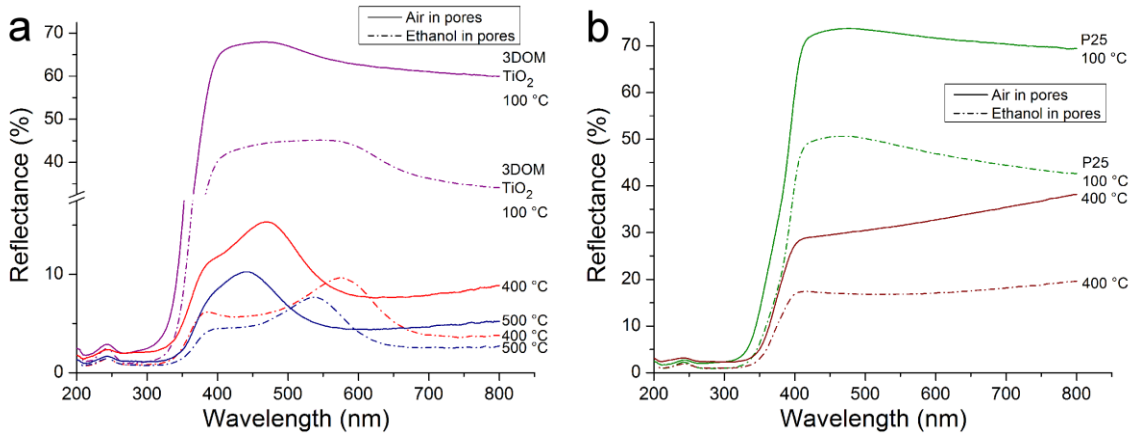

Figure 6.14 UV-visible spectra of various samples prepared from (a) 3DOM TiO_2 and (b) P25 TiO_2. 3DOM-100 °C-H-EtOH, 3DOM-100 °C-H-EtOH-400 °C, and 3DOM-100 °C-H-EtOH-500 °C are shown in (a). All these materials display photonic stop bands that shift upon infiltration with ethanol. These bands are absent in the spectra from P25-100 °C-H-EtOH and P25-100 °C-H-EtOH-400 °C shown in (b).

Table 6.1. Photonic and electronic band gap data determined from various samples.

Sample	ethanol in pores?	stop band center (nm)	reflectance at 800 nm (%)	band gap (eV)[a]
3DOM-100 °C-H-EtOH	No	469	69.0	3.50
3DOM-100 °C-H-EtOH	Yes	565	34.1	[b]
3DOM-100 °C-H-EtOH pyrolyzed at 400 °C	No	470	8.9	3.31
3DOM-100 °C-H-EtOH pyrolyzed at 400 °C	Yes	575	3.8	[b]
3DOM-100 °C-H-EtOH pyrolyzed at 500 °C	No	441	5.2	3.26
3DOM-100 °C-H-EtOH pyrolyzed at 500 °C	Yes	537	2.7	[b]
P25-100 °C-H-EtOH	No	[c]	69.4	3.51
P25-100 °C-H-EtOH	Yes	[c]	42.7	[b]
P25-100 °C-H-EtOH pyrolyzed at 400 °C	No	[c]	38.2	3.32
P25-100 °C-H-EtOH pyrolyzed at 400 °C	Yes	[c]	19.6	[b]

[a] Band gap estimated using a Kubelka-Munk transformation as discussed in the text.
[b] Only calculated for dry materials.
[c] Material is not photonic. A stop band is not present.

All UV-visible reflectance spectra presented contain a band edge that is typical of hydrogen titanate or anatase TiO_2. Estimated band gaps for the materials were determined by first applying the Kubelka-Munk transformation to the reflectance spectra. The band edge of the transformed spectra was fit with a linear function, and a band gap was extracted from the intersection of the fit line with the x-axis (Table 6.1). 3DOM-100 °C-H-EtOH has the largest estimated band gap, and this gap decreases as the pyrolysis temperature is raised. Other researchers have observed a similar red shift in the band edge of titanate nanomaterials as they are heated to increasing temperatures.[86] This is due to the conversion process from hydrogen titanate to TiO_2-B/anatase. The TiO_2 polymorphs have similar band gaps that are smaller than for hydrogen titanate.[86] For 3DOM-LG-100 °C-H-EtOH-500 °C, the estimated band gap is 3.27 eV, which is close to that of bulk anatase (~3.2 eV) and may be slightly elevated due to the small size of the crystallites. Also, that particular sample is comprised of a combination of TiO_2-B and anatase, which may contribute to the higher band gap. Band gaps for the P25-based materials are nearly identical to their counterparts made via 3DOM TiO_2 (Table 6.1).

6.3.6 Textural Properties of All Titanates and Pyrolyzed TiO_2 Materials

Further information concerning the morphology and textural properties of titanate materials and their derivatives was obtained via nitrogen sorption. All isotherms obtained from the 3DOM TiO_2-based hydrogen titanate materials possess clear hysteresis loops indicative of mesoporosity (Figure 6.15 a). These isotherms also show evidence of macroporosity in the materials, since the isotherms have a sharp rise in gas volume adsorbed near P/P_o=1. Both of these findings are consistent with what is observed in the micrographs collected using SEM/TEM. Macropores exist in the transformed remnant of the 3DOM network, in spaces between bundled nanotubes/wires, and between larger granules. Mesopores are present in scrolled nanotubes, but the majority of the pores lie between partially scrolled nanosheets. Since complete transformation of the nanosheets into nanotubes did not occur, the BET specific surface areas of the hydrogen titanate materials are extremely high (Table 6.2). Powders of hydrogen titanate nanotubes generally have BET surface areas between 200 to 300 m^2/g,[10] however the BET surface area of 3DOM samples exceed 500 m^2/g in some cases. Drying in supercritical CO_2 helps prevent aggregation from stresses induced from solvent evaporation. As a consequence, a slight increase in the BET specific surface area is observed in supercritically dried samples when compared to samples dried in ambient conditions (Table 6.2). BET surface areas decrease slightly when the reaction temperature is changed from 70 °C to 100 °C, and then the surface areas decline substantially when the reaction temperature is

set at 125 °C. Electron microscopy shows that many more nanotube/nanowires exist in the 3DOM-125 °C-H-EtOH/CO_2 and this leads to a lower BET surface area. This is similar to what has been observed other studies that used untemplated TiO_2 as a precursor.[38,51,87] Total pore volumes are very high for all materials studied, but do not appear to follow any trend.

To gain insight into the pore structure present in these materials, the BJH method was used to estimate mesopore size distributions (Figure 6.15 b). For samples treated at reaction temperatures of 70 °C and 100 °C, the calculated pore size distributions are very similar. The average pore size is close to 10 nm for the samples (see Table 6.2), and a secondary, partially cut-off peak is present near 2.5 nm. Titanate nanotubes should have a fairly narrow inner diameter, and are likely responsible for the peak below 3 nm the pore size distribution.[10,38] However, the primary peak in the distribution for all of the 3DOM-LG-70 °C/100 °C-H is from pores that lie between aggregated, partially-rolled nanosheets. These pores are responsible for much of the gas adsorbed onto the materials, and are the origin of the hysteresis loops. Similar behavior has been observed in other materials comprised of aggregated titanate nanotubes.[45,51] Increasing the reaction temperature to 125 °C causes the BJH pore size distribution to broaden significantly and causes the average pore size to increase (Table 6.2). Again, the materials processed at 125 °C contain a significant fraction of aggregated nanotubes and nanowires. The pore spaces between these nanostructures (separate from the nanosheets) contribute to the broadening of the pore size distribution, which is also observed in other studies.[45,87]

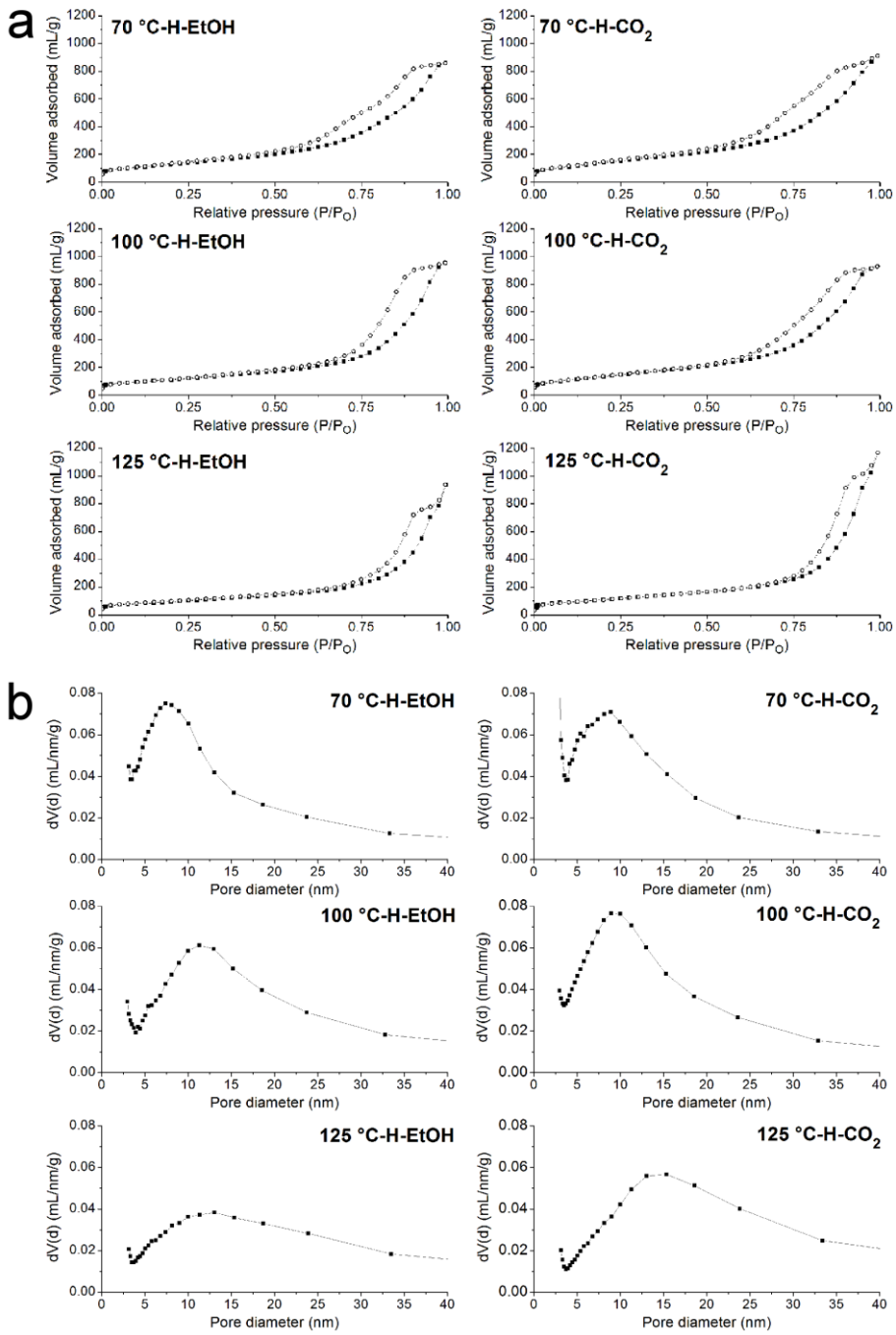

Figure 6.15 Nitrogen sorption isotherms (a) and Barrett-Joyner-Halenda pore size distributions (b) for the hydrogen titanate materials prepared from 3DOM TiO_2. All isotherms contain hysteresis characteristic of mesoporosity, and have a significant rise in volume adsorbed at high relative pressures, which is indicative of macroporosity. The pore size distributions tend to broaden and the average pore size increases as the reaction temperature is raised.

Table 6.2. Relevant textural properties obtained from sorption isotherms of the alkali-treated materials.

Sample	BET surface area (m^2/g)	total pore volume (mL/g)	average pore diameter (nm)
3DOM-70 °C-H-EtOH	472	1.3	7.4
3DOM-70 °C-H-CO_2	530	1.4	8.9
3DOM-100 °C-H-EtOH	481	1.4	11.2
3DOM-100 °C-H-CO_2	507	1.4	9.0
3DOM-125 °C-H-EtOH	338	1.5	13.0
3DOM-125 °C-H-CO_2	396	1.8	15.3
3DOM-100 °C-Na-CO_2	281	0.93	11.3
3DOM-100 °C-H-EtOH pyrolyzed at 400 °C	402	1.5	11.3
3DOM-100 °C-H-EtOH pyrolyzed at 500 °C	218	0.87	13.0
P25-100 °C-H-EtOH	344	1.5	3.0[a]
P25-100 °C-H-EtOH pyrolyzed at 400 °C	335	1.4	3.1[a]

[a] Pore size skewed to a low diameter due to the broadness of the distribution.

Additional isotherms and BJH pore size distributions were collected for 3DOM-100 °C-Na-CO_2 and the pyrolyzed samples (Figure 6.16). In terms of the textural changes induced by the processing steps, the observed behavior of the 3DOM materials is similar to other reports on alkali-treated TiO_2. 3DOM-100 °C-Na-CO_2 has a lower BET surface area than the materials that undergo ion-exchange with H^+ (see Table 6.2). Furthermore, the peak at ~2.5 nm in the BJH plot disappears for the sodium titanate. Different research groups have conducted studies on the changes induced in alkali titanates by ion exchange with H^+, and these studies have revealed that BET specific surface areas increase after that exchange. As discussed earlier, microscopy does not yield clues as to what morphological changes occur due to ion exchange. Morgado, *et al.* determined that exchanging Na^+ for H^+ in titanate materials causes both a decrease in density and a reduction in the wall thickness.[51] These changes can cause an increase in the surface area and alter the size of mesopores at the center of nanotubes. The same phenomenon occurs for the 3DOM-100 °C-Na-CO_2 and the 3DOM-100 °C-H-CO_2. Pyrolysis at 400 °C causes a decrease in BET surface area relative to the ion exchanged material; however, the pore size distribution and pore volume changes little from the 3DOM-100 °C-H-EtOH. Once the pyrolysis temperature is increased to 500 °C, substantial textural changes occur in the material. The BET surface area of the material plunges to ~200 m^2/g, and the pore size distribution changes. An important change in the distribution is the loss of the peak near 2.5 nm, which is attributed to the collapse of the

interior space of scrolled nanotubes. Conversion of the nanostructured titanates to TiO_2 crystallites, as observed in the micrographs (Figure 6.9), is undoubtedly responsible for these changes.

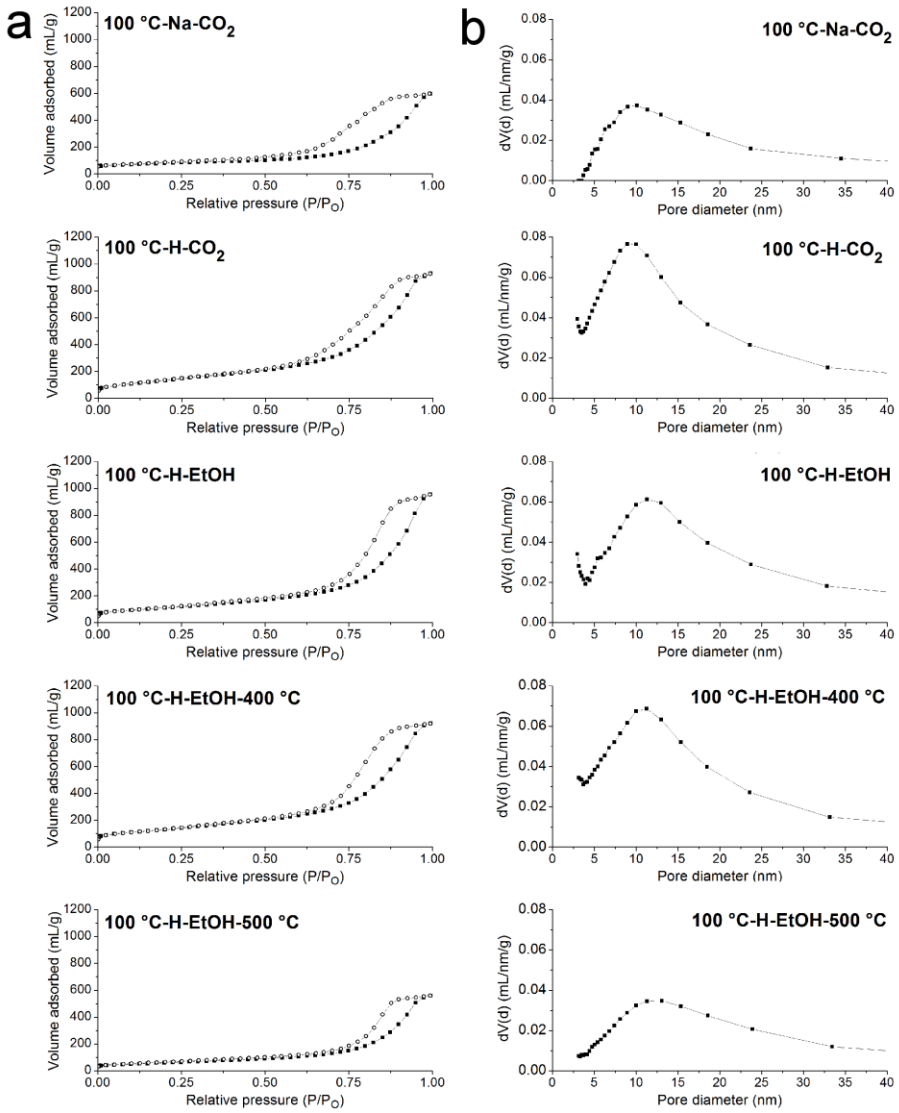

Figure 6.16 Nitrogen sorption isotherms (a) and Barrett-Joyner-Halenda pore size distributions (b) for various materials prepared from 3DOM TiO_2. This includes the sodium titanate material that was not ion-exchanged and the pyrolyzed samples. For the 3DOM-100 °C-Na-CO_2, the volume of gas adsorbed is lower than its ion-exchanged counterpart, and the hysteresis is not as pronounced. Pyrolysis of 3DOM-100 °C-H-EtOH at 400 °C does not result in a significant change to the isotherm. However, a substantial decrease in the volume adsorbed occurs after pyrolysis at 500 °C.

The textural properties of the two P25-based control materials are better understood in context of the prior discussion of the 3DOM TiO_2-based materials. Isotherms and BJH pore size distributions for materials prepared using P25 TiO_2 are shown in Figure 6.17. Additional information obtained from the isotherms is presented in Table 6.2. When comparing the similarly prepared samples 3DOM-100 °C-H-EtOH and P25-100 °C-H-EtOH, it can be observed that changing the parent TiO_2 material results in significant textural changes. The BET surface area is ~125 m^2/g lower for the material prepared using P25 TiO_2. Similar to the 3DOM-125 °C-H-EtOH, the pore size distribution for the P25-100 °C-H-EtOH is broad. Micrographs (discussed above, Figure 6.13) show that partially-scrolled nanosheets comprise the P25-100 °C-H-EtOH. Without the structural confinement provided by the spherical macropores of a 3DOM network, mesopores that lie between titanate nanostructures formed in the P25 aggregates take on a wide range of sizes. This results in the substantial broadening of the pore size distribution for the materials. In addition, the P25 TiO_2-based materials contain sheets that extend over a greater lateral area, which may contribute to a lowering of the surface area when compared to 3DOM TiO_2-based materials. The pore size distribution, BET surface area, and total pore volume all do not change much after pyrolysis at 400 °C.

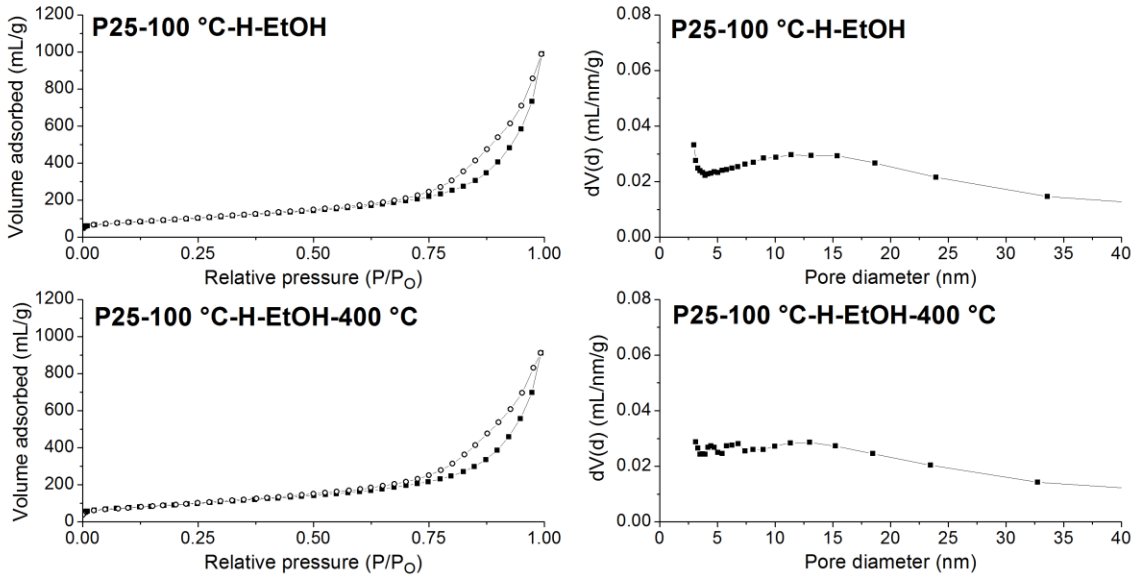

Figure 6.17 Nitrogen sorption isotherms (a) and Barrett-Joyner-Halenda pore size distributions (b) for the materials prepared from P25 TiO_2. Hysteresis loops are found in the isotherms, but these loops are narrower than those observed in materials prepared 3DOM TiO_2. As a consequence, a relatively broad pore size distribution is obtained. Pyrolysis at 400 °C causes little change to the isotherm/pore size distribution.

6.3.7 Crystalline Phases Present in the Prepared Titanates and TiO_2 Materials

Based on the morphological studies presented above, it is hardly surprising that the PXRD patterns obtained from the 3DOM TiO_2-based samples contain reflections that correspond to those found in titanate nanotubes/nanosheets (Figure 6.18). The literature pattern, reported by Hara and co-workers, is from a crystal structure that is closely related to lepidocrocite hydrogen titanate ($H_{0.7}Ti_{1.825}\square_{0.175}O_4 \cdot H_2O$, where □ is a vacancy) and found in hydrogen titanate nanotubes.[19] Other research groups have also obtained similar patterns, but peak positions shift slightly from report to report.[51,80,88] Intensities for the reflections of the "nanotube phase" are not frequently reported, but the reflections near 30 and 58 °2θ are often the two most intense peaks in the reported patterns.[51,80,88] Even though a good match with this lepidocrocite-phase is observed, the presence of anatase or TiO_2-B cannot be discounted due to overlap with high intensity peaks. It is likely that the 3DOM-LG-70 °C-H-CO_2 contains a minor contribution from anatase, since the peak near 29 °2θ is shifted relative to the other samples. One anomaly observed in the patterns shown in Figure 6.18 is the absence of the peak at ~11 °2θ from the (020) plane in the titanate crystal lattice. Only the pattern for the 3DOM-125 °C-H-CO_2 clearly contains this peak. Layers of edge-sharing TiO_6 units lie parallel to the (020) plane in the lepidocrocite-like crystal structure present in titanate nanotubes. These layers are stacked parallel to each other in nanosheets (and nanowires) or are curved in the case of nanotubes.[89] All of the titanate materials prepared from 3DOM TiO_2 contain highly distorted, partially-scrolled nanosheets and these sheets have varying lattice spacings for the (020) as observed in TEM microscopy. A greater fraction of completely-rolled nanotubes and nanowires are present in the 3DOM-125 °C-H-EtOH/CO_2 samples. Since more layers of TiO_6 octahedra are aligned and undistorted in these structures (see Figure 6.11 d), it is logical that the (020) reflection can be resolved. Subtle differences in the washing may contribute to the differences in the reflections of the samples prepared at reflux.[51] Finally, it should be noted that no systematic difference between the patterns for the -EtOH versus -CO_2 samples is found. This is to be expected, since changes in drying conditions should not alter the crystal structure.

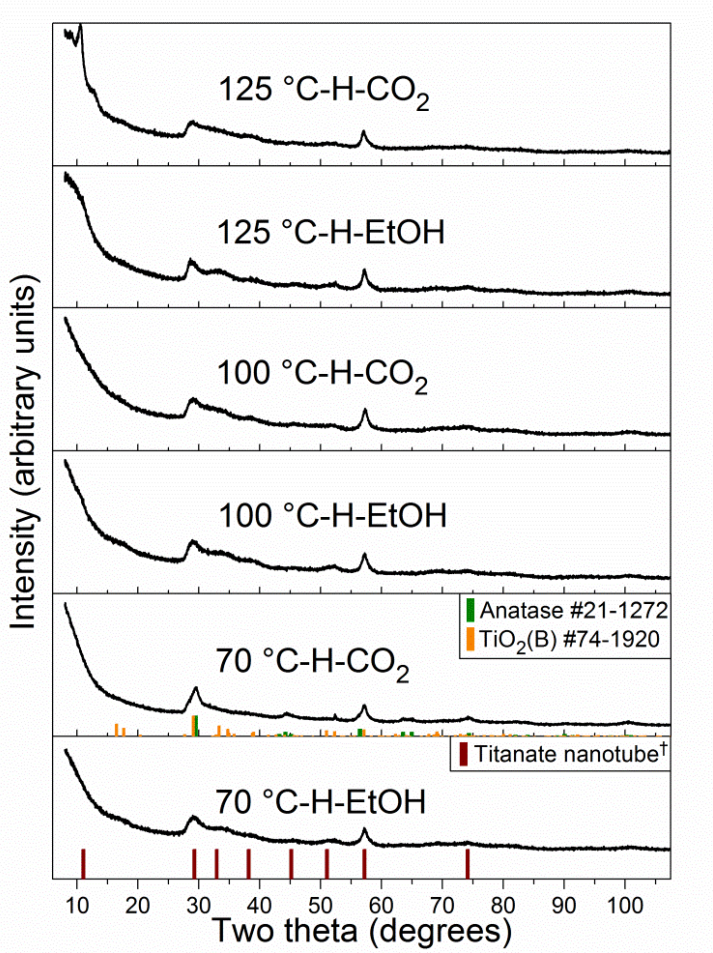

Figure 6.18 Powder X-ray diffraction patterns of the hydrogen titanate samples prepared from 3DOM TiO_2. All patterns contain reflections that match a previously reported hydrogen titanate phase found in nanotubes/nanosheets. †Pattern from [19].

With regards to the other samples prepared from 3DOM TiO_2, substantial changes in the crystal structure are tracked as the samples are processed and pyrolyzed (Figure 6.19). For 3DOM-100 °C-Na-CO_2, the PXRD pattern closely matches pseudolepidocrocite sodium titanate ($NaTi_2O_4(OH)$ as reported by Peng, C.-W. *et al.*).[48] This compound is comprised of infinite 1D chains of TiO_6 octahedra that share edges with other chains; the chains of TiO_6 exist as layers with the sodium ions present in between the layers. Slight distortions in the peak positions seen Figure 6.19, are from the fact that the pattern is obtained from a material primarily comprised of nanosheets and nanotubes. Since Na^+ is present in the material, the (020) peak near 11 °2θ is easily observed in the pattern.[51] Another lepidocrocite-like titanate is formed after ion-exchange (as described above), and this crystal structure retains the TiO_6 edge-sharing motif. A major crystallographic difference between the orthorhombic sodium versus hydrogen titanate is that the

sodium titanate is C-base-centered and the hydrogen titanate is body centered.[90] As the sample is heated, an expected series of compositional and crystal polymorph changes occurs. After the 3DOM-100 °C-H-EtOH is pyrolyzed at 400 °C, the pattern contains peaks that correspond to the reflections present in monoclinic TiO_2-B. Layered hydrogen titanates dehydrate and generally form TiO_2-B upon heating,[54] a phenomenon which is clearly observed here. The hydrogen titanate reflections and TiO_2-B reflections overlap, so it is difficult to determine the extent of remaining hydrogen titanate. However, any hydrogen titanate is clearly removed by pyrolysis at 500 °C. Most of the small crystallites spotted via electron microscopy are anatase TiO_2 (crystal size estimated at 7.8 nm), which co-exists alongside a small amount of untransformed TiO_2-B.

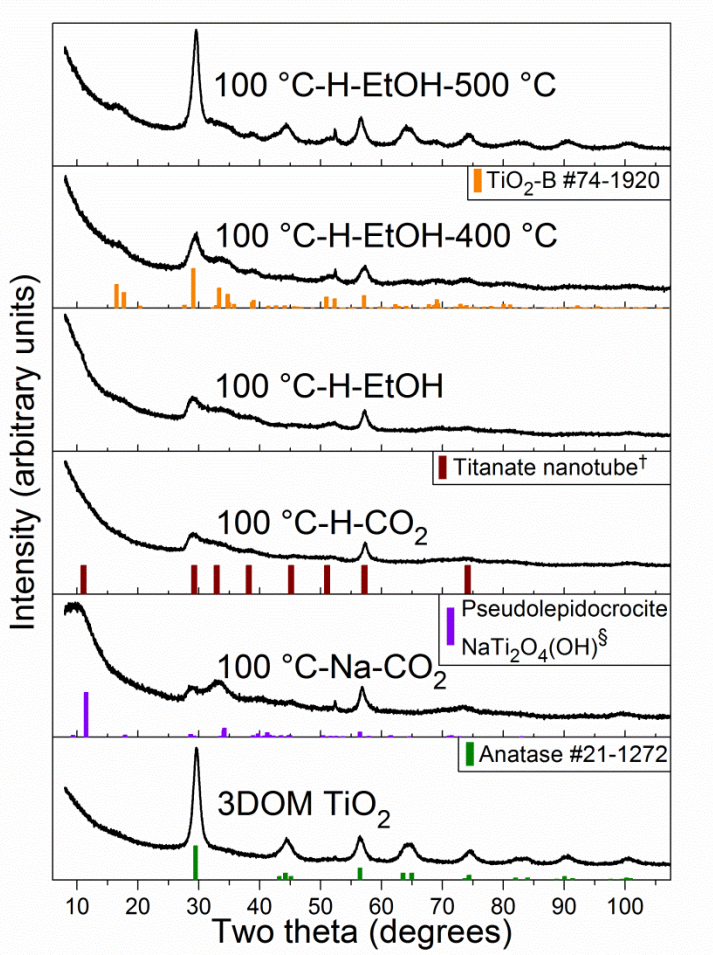

Figure 6.19 PXRD patterns of the sodium titanate and pyrolyzed materials prepared from 3DOM TiO_2 and several other patterns for comparison. The sodium titanate matches a previously reported pattern for $NaTi_2O_4(OH)$. As the pyrolysis temperature is increased for the 3DOM-100 °C-H-EtOH, hydrogen titanate is converted to TiO_2(B) and then to anatase TiO_2. †Pattern from [17]. §Pattern from [48].

Confocal Raman microscopy provided confirmation of the PXRD results, along with additional insight into the titanate and TiO_2 polymorphs in the samples. Analysis of the Raman spectra of titanate-containing materials can be complicated by the variations in the composition of titanates and by changes induced in the crystal structure by nanosheet scrolling.[88,91,92] Attempts have been made to identify the vibrational modes that should be found in spectra of nanostructured hydrogen titanate. Gao and co-workers conducted factor group analysis for two common hydrogen titanates, monoclinic $H_2Ti_3O_7$ (more than 14 modes) and an orthorhombic lepidocrocite phase (9 modes).[88,89] Experimental spectra of both phase pure hydrogen titanates were collected, and peaks were assigned to various Ti-O stretching vibration. Spectra obtained from titanate nanotubes and stacked nanosheets of hydrogen titanate contain similar vibrational modes to the lepidocrocite phase. Morgan *et al.* also reported on the Raman spectra of hydrogen titanate nanotubes, and found vibrational modes close to what was reported earlier by Gao's team.[46] The 3DOM-70 °C/100 °C/125 °C-H all contain modes that are indicative of nanostructured hydrogen titanate with the lepidocrocite-like structure (Figure 6.20), corroborating the PXRD results. Strong vibrations are present near 280 cm^{-1} (occasionally a doublet), 450 cm^{-1}, and 700 cm^{-1} in all spectra displayed in Figure 6.20. The three peaks correspond to symmetric A_g modes involving the Ti-O-Ti framework, and are found in the layered lepidocrocite structure.[88] Other peaks that correspond to Ti-O-Ti vibrations identified in earlier reports are present near 200 cm^{-1} and 380 cm^{-1} (the latter of which may arise from edge-sharing between TiO_6 units.[44,46] Weaker Ti-O vibrations that arise from surfaces and a possible overtone of the 450 cm^{-1} peak (at ~930 cm^{-1}) are found past 700 cm^{-1}.[46,92] However, two other vibrations (at roughly 550 and 660 cm^{-1}) that should exist in a lepidocrocite crystal structure are absent. This might be a result of overlap with the broad peaks generated from the nanocrystalline material or distortions in the crystal structure induced by scrolling; both possibilities that were discussed by Gao and co-workers.[88] Though the most intense mode of anatase (E_g at 144 cm^{-1}) is absent, the E_g vibration at 640 cm^{-1} is present. In the samples reacted at the lowest temperature, 3DOM-70 °C-H-EtOH/CO_2, a small fraction of regions analyzed contain far stronger anatase vibrations (Figure 6.21). Conversion appears to be impeded in certain regions (as observed in the SAED patterns shown in Figure 6.12), but strong anatase vibrations are not found in samples processed at 100 °C and 125 °C. It is reasonable to assume that the higher reaction temperature facilitates dissolution allows for further conversion of any residual anatase. The intensity of the vibration at 640 cm^{-1} also decreases with the increase in reaction temperature, and is nearly non-existent for samples treated at 125 °C. Finally, removal of moisture (via heating or freeze-drying has been observed to narrow

the width of Raman peaks; however, peaks of the hydrogen titanates prepared from 3DOM TiO_2 are all similarly broad.[92] This may indicate that re-hydration of the titanate materials is rapid, probably due to the high surface area of the material.

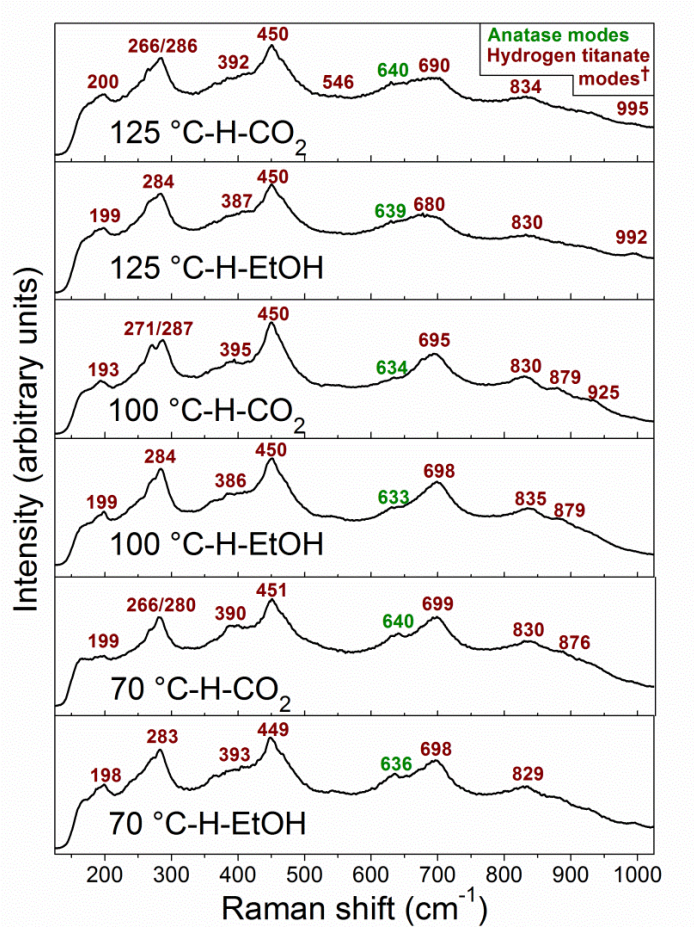

Figure 6.20 Representative Raman spectra of the hydrogen titanate samples collected using a confocal Raman microscope. Most peaks are matched to vibrations from a lepidocrocite crystal structure (brown); however, one of the E_g modes of anatase is also present (green). †Modes closely match those reported in [88].

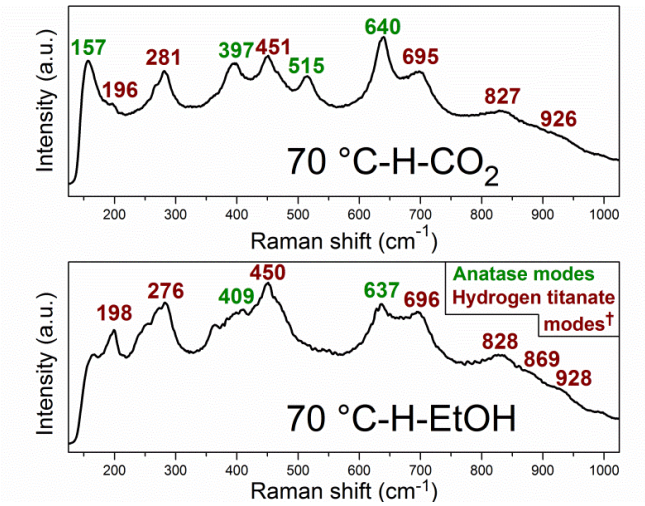

Figure 6.21 Additional Raman spectra of the 3DOM-70 °C-H-EtOH/CO_2 samples that contain relatively strong anatase vibrations. Typically, the vibrations for anatase are far weaker and a spectrum resembles Figure 6.20. †Modes closely match those reported in [88].

Raman spectroscopy can also serve as a means for probing crystal structure changes brought on by ion exchange/pyrolysis. In Figure 6.22, representative Raman spectra are presented for the 3DOM-100 °C-Na-CO_2, the corresponding hydrogen titanates, and the pyrolyzed TiO_2. The spectrum of the sodium titanate sample matches those of a previously reported pseudolepidocrocite crystal structure,[46,48] consistent with the PXRD pattern. As discussed above, ion exchange from an alkali titanate to hydrogen titanate generally does not cause substantial changes in the layered titanate structure.[48,90] For the hydrogen titanate materials, including 3DOM-100 °C-H-CO_2, the hallmarks of a distorted orthorhombic lepidocrocite phase (closely related to the pseudolepidocrocite phase) are present. Pyrolysis initially brings about conversion of hydrogen titanate to TiO_2-B, as is observed in the PXRD pattern. Multiple vibrational modes that belong to the TiO_2-B phase are identified;[93] however, the Raman spectra still contains vibrations that are typical of hydrogen titanate. It appears that conversion is not complete at 400 °C and a fraction of hydrogen titanate remains; this clarifies what is observed in the PXRD pattern since most TiO_2-B and hydrogen titanate peaks overlap. Dehydration and rearrangement of the titanate is not complete at 400 °C for this material.[48,54,94] By 500 °C, the same transformation observed in the PXRD pattern is observed in the Raman spectrum. The 3DOM-100 °C-H-EtOH-500 °C contains strong anatase modes and some residual TiO_2-B modes.

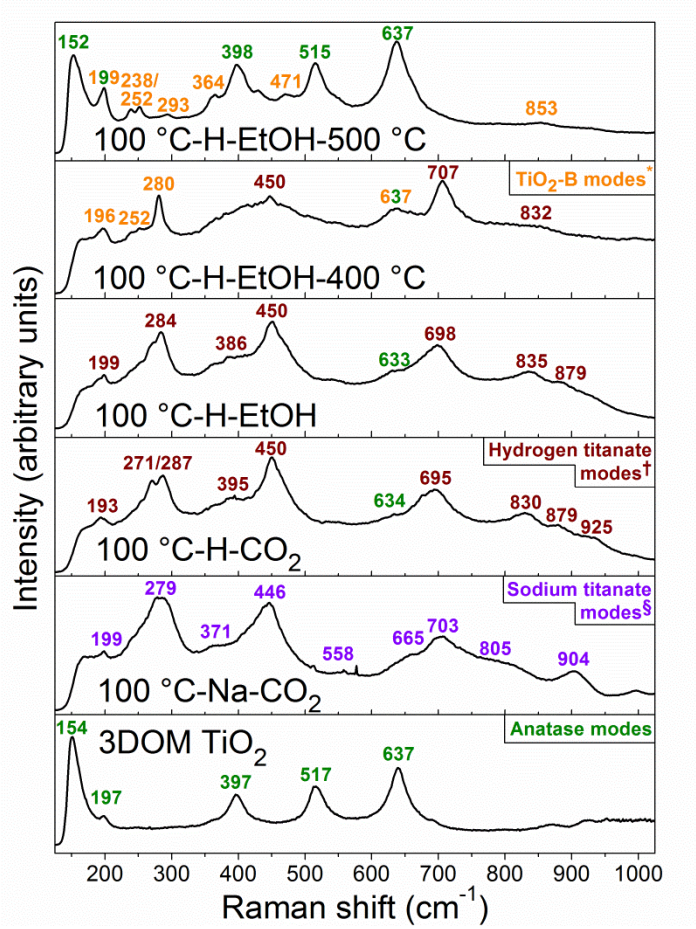

Figure 6.22 Representative Raman spectra for the sodium titanate and pyrolyzed samples. [§]Vibrations present in the sodium titanate material closely match those from a pseudolepidocrocite phase reported in [†]Modes match those reported in [46]. Pyrolysis of the hydrogen titanate leads to the formation of TiO_2-B and eventually anatase. *Modes match those reported in [93].

Finally, the P25-based materials were analyzed using a combination of PXRD and Raman spectroscopy. For the P25-100 °C-H-EtOH, both the PRXD patterns and Raman spectra reveal that hydrogen titanate is present (Figure 6.23). The peaks in the PXRD and Raman spectra match what is observed for the 3DOM-100 °C-H-EtOH, suggesting that the same lepidocrocite-like phase is present. Considering that the same reaction conditions are used for both samples, the formation of the same crystal structure is expected. One difference between the materials prepared from P25 TiO_2 versus the ones made from 3DOM TiO_2 is that anatase vibrations in the Raman spectra are stronger in the non-pyrolyzed material prepared from P25 TiO_2 (Figure 6.23 b). Problems with transport through the agglomerated P25 TiO_2 may preserve the anatase TiO_2 better than 3DOM TiO_2 precursor that contains an interconnected pore network. Another

difference is that an impurity phase is present in the transformed P25 TiO_2. This phase can be matched to rutile TiO_2, which did not convert into sodium titanate. The rutile TiO_2 has extremely narrow peaks, which means it has a large crystallite size. Both large crystallites of TiO_2 and rutile TiO_2 are known to require more forcing conditions for conversion to sodium titanate, so the rutile impurity remains in the P25-100 °C-H-EtOH.[39,44,51] Once the P25-based material is pyrolyzed at 400 °C, both anatase and TiO_2-B are present in the material. Unlike the 3DOM TiO_2-based counterpart, conversion of hydrogen titanate to TiO_2 is far more pronounced in P25-100 C-H-EtOH-400 °C. It may be that the non-ordered, aggregated structure of this material allows for a greater extent of sintering, which facilitates conversion to anatase. This pyrolyzed material also contains the rutile impurity, since rutile is the thermodynamically stable polymorph of TiO_2 for most grain sizes.[95]

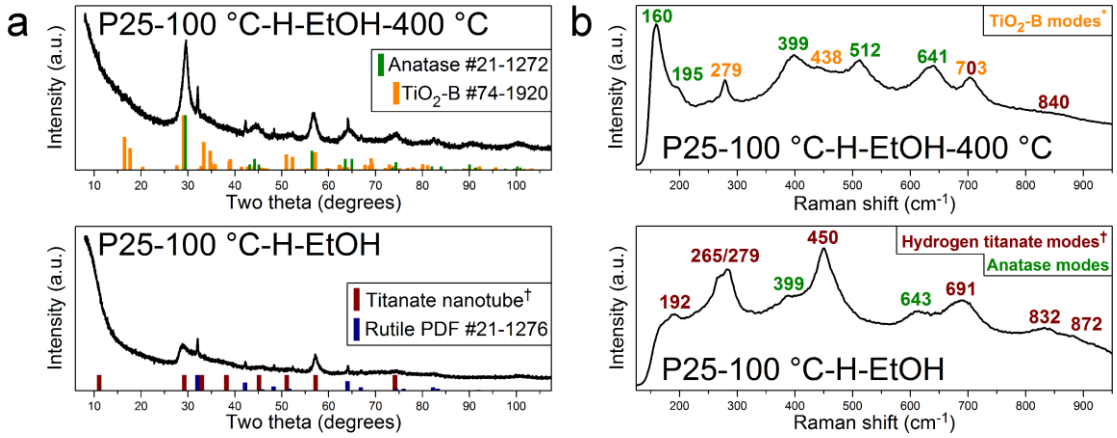

Figure 6.23 PXRD patterns (a) and Raman spectra (b) from hydrogen titanate materials prepared using P25 TiO_2. The non-pyrolyzed materials contains the same lepidocrocite-like hydrogen titanate phase observed in the materials prepared using 3DOM TiO_2. Pyrolysis at 400 °C results in the formation of TiO_2-B and a majority of anatase TiO_2. A crystalline rutile TiO_2 impurity is observed in the PXRD patterns.

6.3.8 Electrochemical Behavior of Selected Materials

Three materials characterized in the previous sections, 3DOM-100 °C -H-EtOH-400 °C, 3DOM-100 °C -H-EtOH-500 °C, and P25-100 °C-H-EtOH-400 °C, were subsequently tested as anode materials for lithium ion batteries. These specific materials were selected in order to explore questions about how structural and compositional changes impact the insertion/extraction of lithium ions. First, how does the choice of parent material (3DOM TiO_2 vs. P25) alter the capacity for lithiation? Second, does raising the pyrolysis temperature and producing the anatase polymorph, while sacrificing surface area in the process, result better capacities or capacity

retention? These questions are each addressed in this section. Finally, a discussion of extended cycling behavior and impact of binder content is presented at the end of this section.

The structures of materials prepared from 3DOM TiO_2 differ considerably from materials prepared from P25 TiO_2, so it should come as no surprise that the capacities of the prepared electrodes are different. By using 3DOM TiO_2, nanostructured TiO_2-B and anatase with extremely high surface areas and interconnected pore structures are produced. This morphology should allow for complete suffusion of the electrolyte within the material, short diffusion lengths, and a large interfacial area for electrochemical reactions. However, 3DOM-100 °C -H-EtOH-400 °C has much lower capacities at all tested rates than lower surface area P25-100 °C-H-EtOH-400 °C (Figure 6.24). Another difference is observed in the voltage profiles of the two materials (Figure 6.25 a, b), with the profiles of P25-based material displaying plateaus (at ~1.7 V vs. Li/Li^+) indicative of biphasic electrochemical insertion into anatase TiO_2.[96] Anatase is detected (Figure 6.19 and 6.22) in the PXRD pattern and Raman spectra from this material, so this is expected. After these plateaus, a sloping profile (Figure 6.25 a, b) is observed for both the 3DOM TiO_2 and P25-based materials that is typical for nanostructured TiO_2-B. In nanostructured TiO_2-B, a pseudocapacitive charge storage mechanism occurs, since lithiation/delithiation proceeds at a variety of surface/sub-surface sites generated by the disorder present in the TiO_2-B.[66] As a consequence, lithiation no longer occurs at a fixed potential and sloping profile is found.[26,63] The surface energy is also altered as lithiation proceeds in TiO_2-B nanomaterials.[17] Hydrogen titanate, which is also present in the 3DOM-100 °C-H-EtOH-400 °C, exhibits a similar pseudocapacitive mechanism that originates disorder in the nanostructures.[64] No plateaus are observed for 3DOM-100 °C-H-EtOH-400 °C, suggesting that charge storage occurs primarily through a pseudocapacitive charge storage mechanism in TiO_2-B and hydrogen titanate. This is in-line with the characterization of 3DOM-100 °C -EtOH-400 °C, which shows little evidence of anatase TiO_2.

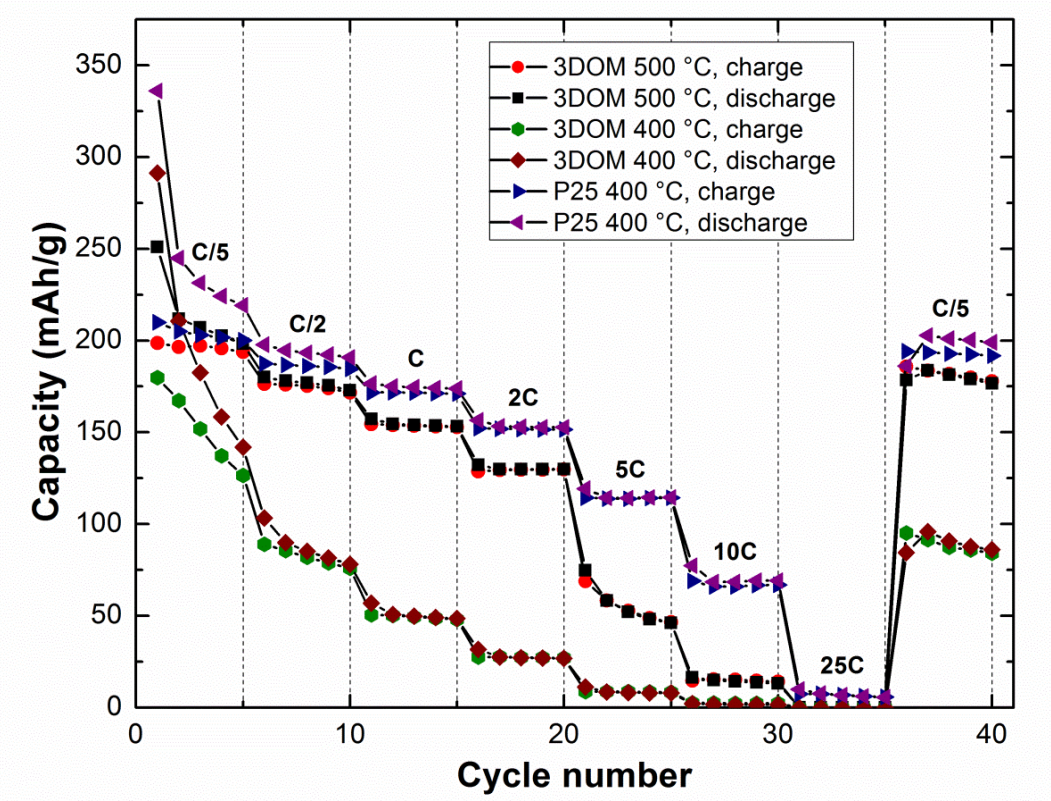

Figure 6.24 Rate performance data for 3DOM-100 °C-H-EtOH-400 °C, 3DOM-100 °C-H-EtOH-500 °C, and P25-100 °C-H-EtOH-400 °C. The electrodes that contain materials synthesized from 3DOM TiO_2 have lower capacities than the P25 control material. In addition, 3DOM-100 °C-H-EtOH-400 °C and 3DOM-100 °C-H-EtOH-500 °C lose capacity fairly precipitously from cycle to cycle.

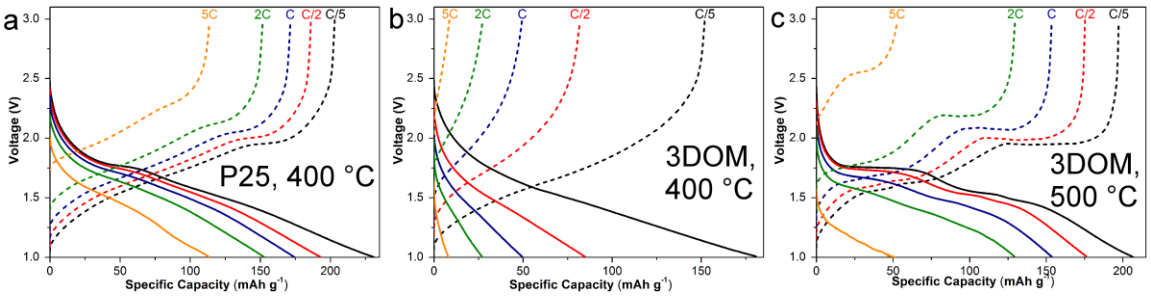

Figure 6.25 Voltage profiles for P25-100 °C-H-EtOH-400 °C (a), 3DOM-100 °C-H-EtOH-400 °C (b), and 3DOM-100 °C-H-EtOH-500 °C (c). Electrodes that contain anatase TiO_2 (a, c), also have plateaus that originate from biphasic lithium insertion/extraction.

While the presence of TiO_2-B and high surface areas usually leads to good anode performance, 3DOM-100 °C-H-EtOH-500 °C is found to have higher capacities at all rates than the corresponding material pyrolyzed at 400 °C (Figure 6.24 c). For 3DOM-100 °C -H-EtOH-500 °C, anatase is the major polymorph of TiO_2 detected. As the structure densifies during heat-treatment, the specific surface area also decreases by over 200 m^2/g. It would seem that these extensive changes, which at first glance appear to be detrimental, actually result in much higher capacities at moderate rates. The changes in the TiO_2 polymorph also generate substantial alterations to the voltage profile (Figure Figure 6.25 c). In the material pyrolyzed at 500 °C, a plateau appears near 1.75 V vs. Li/Li^+ (during insertion of Li^+ into the TiO_2) and 2 V vs. Li/Li^+ (during extraction) at low C-rates. This plateau is a result of the co-existence of a Li-poor tetragonal phase (similar to the parent anatase) and a Li-rich orthorhombic phase.[17,70] At low C-rates, there also is an indication that two phases related to TiO_2-B are formed during (de)lithiation. A shoulder is present near 1.5 V vs. Li/Li^+ in the discharge curve that corresponds to a two phase system for TiO_2-B.[26] With increasing C-rate, a fairly pronounced shift occurs in the voltage at which these plateaus are observed. Concentration overpotential is responsible for the shift, and the poor electronic transport properties of TiO_2 probably play a central role. Charge storage originating from a solid solution mechanism or interfacial charge storage takes place after the biphasic regime.[57]

Cyclic voltammetry provided more insight into the electrochemical properties of the materials tested in the half-cells was obtained through cyclic voltammetry (Figure 6.26). Unlike what was observed in chapter 5 for PF- and Sucrose-TiO_2/C, peaks in the anodic and cathodic sweeps can be easily resolved for most of the samples. Since the sweep rate (5 mV/s) is fairly rapid, the locations of peaks that result from biphasic insertion/extraction into TiO_2 are displaced from the voltages typically given for low rates (without any kinetic limitations). TiO_2-B and anatase TiO_2 are found in P25-100 °C-H-EtOH-400 °C (Figure 6.26 a) and 3DOM-100 °C-H-EtOH-500 °C (Figure 6.26 c), and four redox peaks (two on each sweep) can be identified. Insertion and extraction into TiO_2-B occurs at lower voltages than anatase TiO_2, so the peaks near 2 V vs. Li/Li^+ on the anodic sweep and near 1.15 V vs. Li/Li^+ on the cathodic sweep are from TiO_2-B.[77] The other peaks, at ~2.3 V vs. Li/Li^+ on the anodic sweep and at ~1.5 V vs. Li/Li^+ on the cathodic sweep, are from insertion/extraction of lithium into anatase TiO_2. Since the 3DOM-100 °C-H-EtOH-500 °C has larger crystallites than the materials pyrolyzed at lower temperature, the redox peaks are very well defined. A solid solution mechanism is unlikely to be encountered, so a biphasic mechanism is expected.[17] When the CVs from the cell containing P25-100 °C-H-EtOH-

400 °C are examined, the redox peaks from TiO_2-B and anatase TiO_2 are more difficult to distinguish. Pseudocapacitive charge storage likely obscures the redox peaks (owing to the multiple sites for lithiation,[66] since the crystallites are much smaller than 3DOM TiO_2-based material). The presence of this charge storage mechanism can also help explain why P25-100 °C-H-EtOH-400 °C performs better at high rates than any other material. It is interesting to note that even though PXRD and Raman spectroscopy data suggest that the anatase is the major polymorph of TiO_2 present in both of the aforementioned materials, the redox peaks for TiO_2-B and anatase TiO_2 have similar peak currents. This suggests that the TiO_2-B fraction may be more electrochemically active than the anatase TiO_2 fraction. For the 3DOM-100 °C-H-EtOH-400 °C, a set of peaks are observed whose location roughly corresponds to those found in TiO_2-B and hydrogen titanate.[77] These peaks are broad and indicative of pseudocapacitive charge storage, matching the results from galvanostatic cycling. One final item should be discussed, the peak current of the anodic peak near 1 V vs. Li/Li^+ is higher on the first cycle for both electrode materials synthesized from 3DOM TiO_2. Interactions of chemisorbed water and water within the crystal lattice with the electrolyte can cause an irreversible capacity loss, much like what is observed in Figure 6.26.[77]

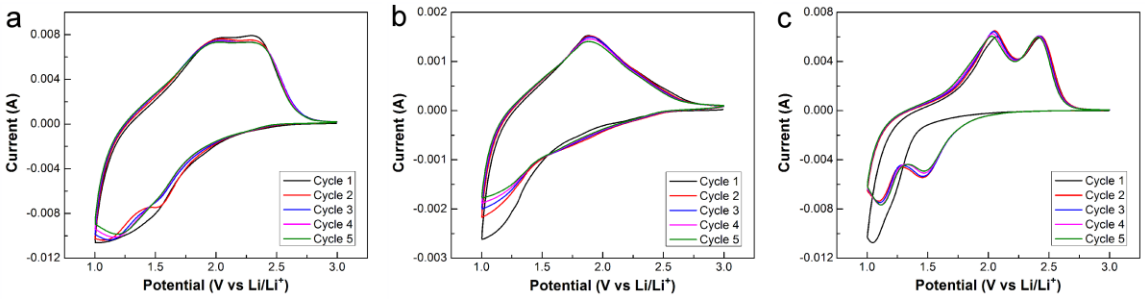

Figure 6.26 Cyclic voltammograms of (a) P25-100 °C-H-EtOH-400 °C, (b) 3DOM-100 °C-H-EtOH-400 °C, and (c) 3DOM-100 °C-H-EtOH-500 °C. Redox peaks that correspond to insertion/extraction into anatase and TiO_2-B are observed, depending on the polymorphs present in the electrode materials. Voltammograms collected by Benjamin Wilson.

One hundred charge-discharge cycles at C/2 were also conducted for the materials described in this section (Figure 6.27). While all electrodes attain high coulombic efficiencies (near 100 %) after a few tens of cycles, the cycle-to-cycle capacity losses vary considerably. As was also observed for the rate performance data, the P25-100 °C-H-EtOH-400 °C has fairly limited losses in capacity. It retains the ability to reversibly insert and extract more than 0.5 Li^+ after 100 cycles. Losses are more pronounced for cells made with the 3DOM TiO_2-based materials. The 3DOM-

100 °C -H-EtOH-500 °C has a capacity of only ~130 mAh/g after 100 cycles, and the material pyrolyzed at 400 °C retains only 50 mAh/g after 100 cycles. This also follows what is expected from the rate performance data; however, the loss of capacity in the anatase-rich material (3DOM-100 °C-H-EtOH-500 °C) is somewhat surprising. Typically, anatase TiO_2 electrodes have fairly stable capacities, which suggests that some sort of side-reaction is taking place.[17] These reactions may occur between the remaining TiO_2-B phase and the electrolyte.

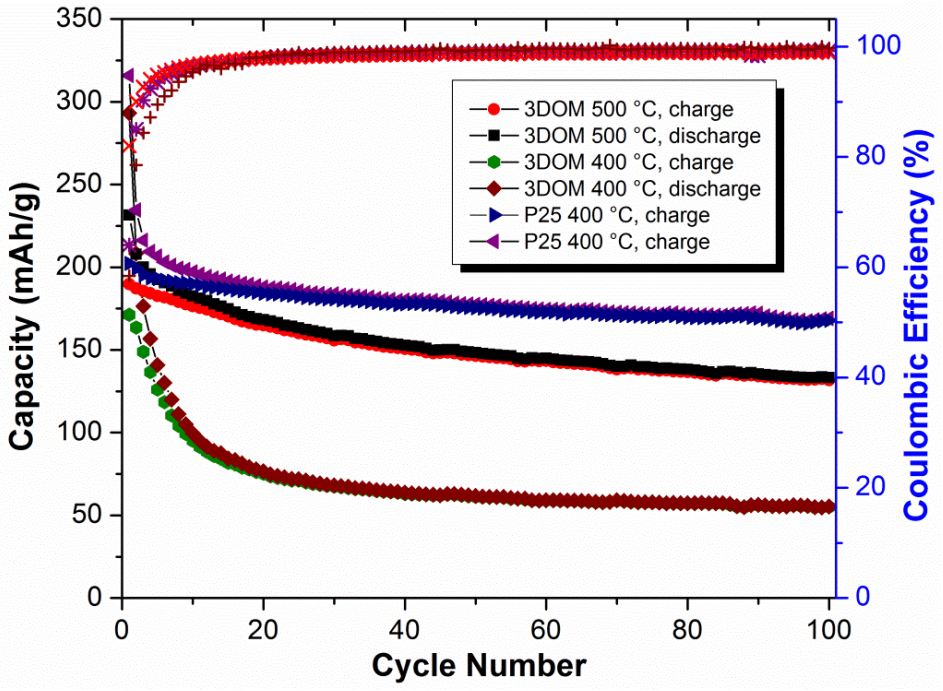

Figure 6.27 Extended cycling data and Coulombic efficiencies for P25-100 °C-H-EtOH-400 °C (purple asterisk, Coulombic efficiency), 3DOM-100 °C-H-EtOH-400 °C (brown plus), and 3DOM-100 °C-H-EtOH-500 °C (red "X") electrodes. Cycle-to-cycle losses are observed in all electrodes, but are worse for the 3DOM TiO_2-based materials. Coulombic efficiencies reach close to 100 % for all materials.

In many instances, it is advantageous to develop electrode materials with elevated surface areas; however, as in the case described here, these advantages are not always realized. One potential complication is that, while high surface areas facilitate electrochemically useful reactions, deleterious side reactions can also occur with increasing frequency. Hydrogen titanates and the TiO_2-B polymorph contain numerous surface hydroxyl functionalities and water of crystallization.[54] Computational studies also show that lepidocrocite hydrogen titanate preferentially crystallizes with hydronium ions between (020) planes.[94] These moieties can react

with the electrolyte, alongside any adventitious water that may have been picked up by the electrode.[97] The rate performance and extended cycling data for 3DOM-100 °C-H-EtOH-400 °C show a fairly precipitous cycle-to-cycle decay in capacity, and this may be tied to the presence of lepidocrocite-like hydrogen titanate and TiO_2-B. 3DOM-100 °C-H-EtOH-500 °C, in contrast, has a higher fraction of anatase and attains far greater capacities than the material pyrolyzed at lower temperatures. For this material, the reduced fraction of TiO_2-B may assist in allaying the deterioration in capacity. Strangely, the P25-based material contains TiO_2-B, but has a higher capacity than either 3DOM TiO_2-based material. The 3DOM TiO_2-based materials have a higher specific surface area than the P25-based material, so the 3DOM TiO_2-based materials have a greater available area over which side reactions with the electrolyte can take place. Extended cycling (Figure 6.27) shows that the capacity of the P25-100 °C-H-EtOH-400 °C decays from cycle-to-cycle, albeit less precipitously than the electrodes made from 3DOM-100 °C-H-EtOH-400 °C/500 °C. Voltammograms (Figure 6.26) also show a pronounced increase in current at low potentials for the first cycle, which indicates possible SEI formation due to reactions with the electrolyte.[77]

While side reactions with the electrolyte may play a critical role in the loss of capacity, the binder also has an impact on the overall capacity of 3DOM TiO_2-based materials. When an electrode is made using the 3DOM-LG-100 °C-H-EtOH-400 °C with only 6 wt% binder (4 wt% CMC and 2 wt% SBR), substantially higher capacities are attained for all charge/discharge rates (Figure 6.28). It is also interesting to consider that this electrode contains only 10 wt% carbon black, indicating that the electrode is sufficiently conductive even at a reduced carbon fraction. By examining SEM images of the low binder content electrode, particles of active material are clearly observed in the CMC/SBR matrix (Figure 6.29 a, b). This situation changes for the electrodes made using higher binder content; SEM images for the corresponding electrode made with 10 wt% binder shows that the active material is completely coated (Figure 6.29 c, d). Blockage of the pores with binder can substantially reduce the ability for electrolyte to access the active material. Any products from decomposing electrolyte are also more prone to block electrolyte access in this case. However, the electrodes prepared with reduced binder content still display significant cycle-to-cycle losses (Figure 6.28). Water present in the binder system may also cause side reactions to a greater extent in the 3DOM-based material than the more anatase-rich P25-based material. Still, further investigations may be warranted. It is unclear why the binder content does not adversely affect the capacity of P25-100 °C-H-EtOH-400 °C despite similar electrode film morphology (Figure 6.30).

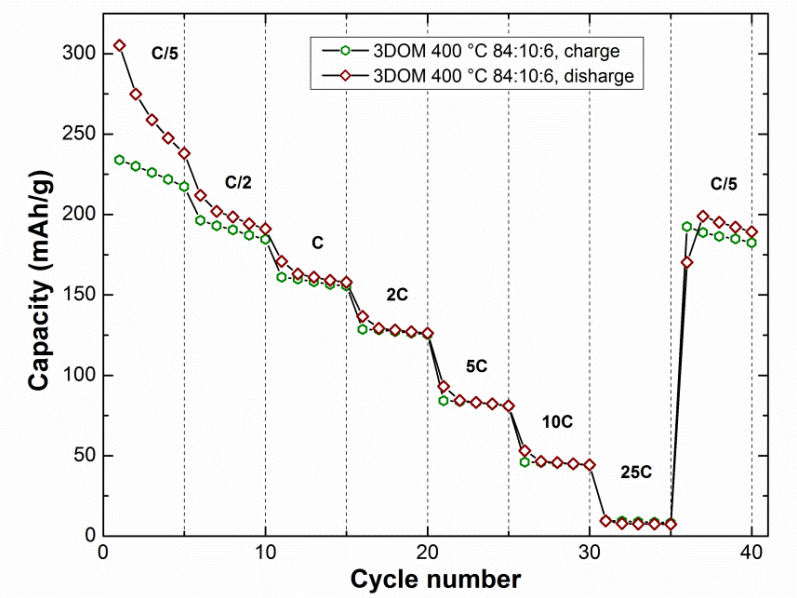

Figure 6.28 Rate performance data for a half-cell containing 84 wt% of 3DOM-100 °C-H-EtOH-400 °C, 10 wt% of carbon black, 4 wt% of CMC binder, and 2 wt% of SBR binder.

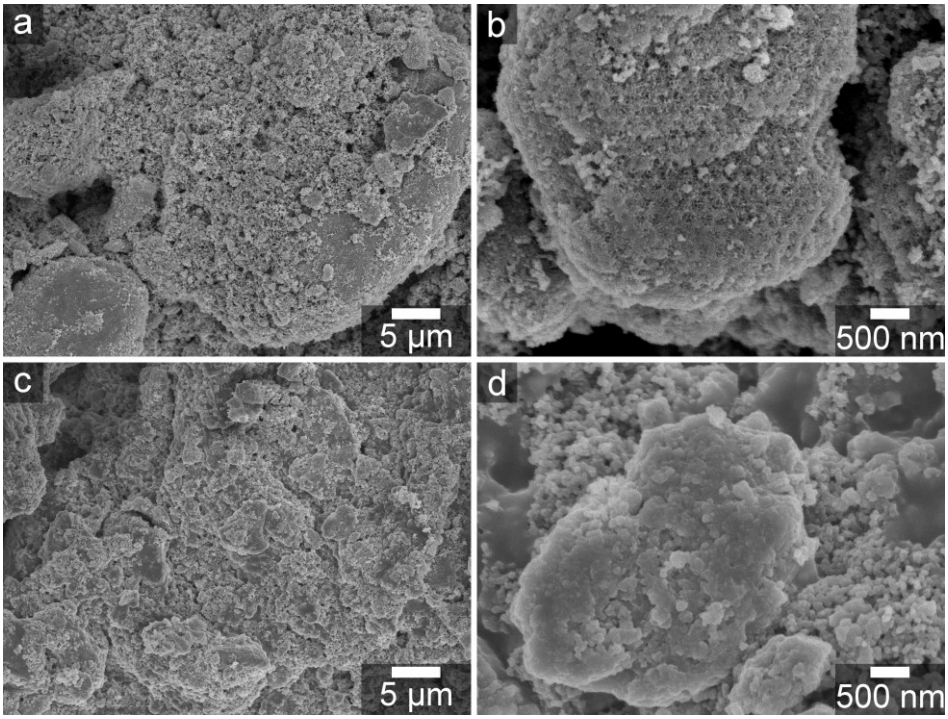

Figure 6.29 SEM micrographs of the uncycled electrode film with 84 wt% of 3DOM-100 °C-H-EtOH-400 °C, 10 wt% carbon black, and 6 wt% binder (a, b), and a cycled film containing 75 wt% 3DOM-100 °C-H-EtOH-400 °C, 15 wt% of carbon black, and 10 wt% of binder (c,d). Micrographs of the cycled and uncycled electrode films are similar, justifying the comparison. The cycled film was washed in dimethyl carbonate prior to imaging.

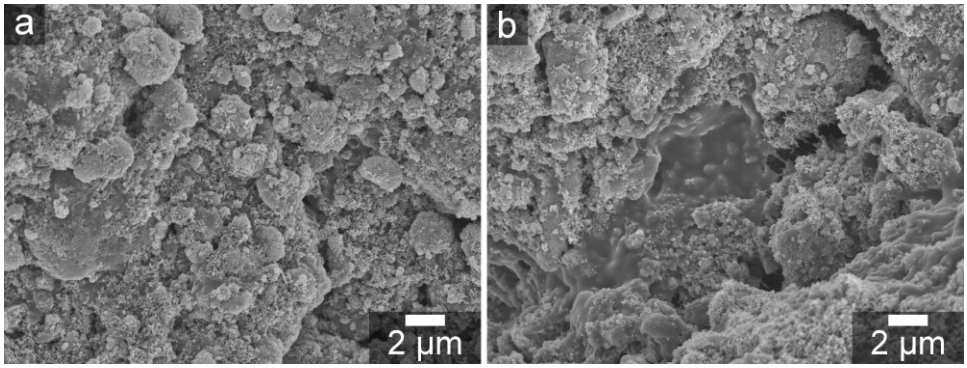

Figure 6.30 SEM micrographs of the uncycled P25-100 °C-H-EtOH-400 °C electrode film (a) and the uncycled 3DOM-100 °C-H-EtOH-400 °C (b).

6.4 Conclusions

A novel morphology for sodium titanate, hydrogen titanate and TiO_2 is explored in this chapter. To generate this morphology, the confinement provided by the macropore spaces of a 3DOM TiO_2 network is utilized. Treatment of 3DOM TiO_2 (prepared via TFA-TiO_2/C) in a sodium hydroxide solution at ambient pressure and at 70 °C, 100 °C or 125 °C results in the dissolution of TiO_2 and its reprecipitation as nanosheets of sodium titanate. Electron microscopy reveals that these materials contain numerous partially-scrolled nanosheets that fill the former spherical macropore space of the 3DOM network. Highly crumpled nanosheets and/or nanoparticles lie in the center of the original octahedral and tetrahedral nodes of the 3DOM structure. As a result, a remnant of the 3DOM structure is preserved. In this structure a periodic difference exists between the low density of nanosheets in the former macropores versus the high density present in the former nodes. Pyrolysis of the hydrogen titanates does not change the general morphology at 400 °C; however, crystallites of anatase do develop after pyrolysis at 500 °C. The periodicity present in these materials also results in a photonic stop band, despite massive structural changes from the original 3DOM TiO_2. However, heterogeneities are present in the materials including regions that lack the 3DOM remnant structure, and bundles of nanotubes/nanowires. With increasing reaction temperature, the presence of nanotubes and nanowires also increases, as is expected when sufficient energy is imparted to the system to cause these structures to scroll. Since the nanosheets do not fully scroll into nanotubes and lie crumpled in the macropores, very high BET specific surface areas are achieved for these materials. The hydrogen titanates can achieve surface areas over 400 m^2/g due (in large part) to the mesopores that lie between nanosheets. Supercritical drying of the titanates further increases the surface area up to 530 m^2/g. Diffraction (both SAED and PXRD) and Raman spectral data show that

pseudolepidocrocite sodium titanate ($NaTi_2O_4(OH)$) is initially formed, which transforms to a lepidocrocite-like ($H_{0.7}Ti_{1.825}\square_{0.175}O_4 \cdot H_2O$) upon ion-exchange with protons. Some residual anatase is present in the titanate, but it is nearly undetectable in the Raman spectra of 3DOM TiO_2 processed at 125 °C. Pyrolysis converts the hydrogen titanates first to TiO_2-B and then to anatase TiO_2. Finally, P25 TiO_2 was converted via a similar procedure, but it did not possess any evidence of an ordered structure. When tested in a half cell configuration for LIBs, the pyrolyzed 3DOM TiO_2-based materials display good initial capacities that quickly decay. It is believed that side reactions with the electrolyte eventually cripple the capacity of these materials for lithium ion insertion and extraction. These reactions are facilitated by the high surface areas of the active materials and by the high binder content in the materials.

References

(1) Antonelli, D. M.; Ying, J. Y. Synthesis of Hexagonally Packed Mesoporous TiO_2 by a Modified Sol-Gel Method. *Angew. Chem. Int. Ed.* **1995**, *34*, 2014-2017.

(2) Holland, B. T.; Blanford, C. F.; Stein, A. Synthesis of Macroporous Minerals with Highly Ordered Three-Dimensional Arrays of Spheroidal Voids. *Science* **1998**, *281*, 538-540.

(3) Imhof, A.; Pine, D. J. Ordered Macroporous Materials by Emulsion Templating. *Nature* **1997**, *389*, 948-951.

(4) Kasuga, T.; Hiramatsu, M.; Hoson, A.; Sekino, T.; Niihara, K. Formation of Titanium Oxide Nanotube. *Langmuir* **1998**, *14*, 3160-3163.

(5) Wijinhoven, J. E. G. J.; Vos, W. L. Preparation of Photonic Crystals Made of Air Spheres in Titania. *Science* **1998**, *281*, 802-804.

(6) Yang, P.; Deng, T.; Zhao, D.; Feng, P.; Pine, D.; Chmelka, B. F.; Whitesides, G. M.; Stucky, G. D. Hierarchically Ordered Oxides. *Science* **1998**, *282*, 2244-2246.

(7) Yang, P.; Zhao, D.; Margolese, D. I.; Chmelka, B. F.; Stucky, G. D. Generalized Syntheses of Large-Pore Mesoporous Metal Oxides with Semicrystalline Frameworks. *Nature* **1998**, *396*, 152-155.

(8) Zwilling, V.; Aucouturier, M.; Darque-Ceretti, E. Anodic Oxidation of Titanium and TA6V Alloy in Chromic Media. An Electrochemical Approach. *Electrochim. Acta* **1999**, *45*, 921-929.

(9) Chen, X.; Mao, S. S. Titanium Dioxide Nanomaterials: Synthesis, Properties, Modifications, and Applications. *Chem. Rev.* **2007**, *107*, 2891-2959.

(10) Bavykin, D. V.; Walsh, F. C. *Titanate and Titania Nanotubes: Synthesis, Properties and Applications*; Royal Society of Chemistry: Cambridge, UK, 2010.

(11) Roy, P.; Berger, S.; Schmuki, P. TiO_2 Nanotubes: Synthesis and Applications. *Angew. Chem. Int. Ed.* **2011**, *50*, 2904-2939.

(12) Petkovich, N. D.; Stein, A. Colloidal Crystal Templating Approaches to Materials with Hierarchical Porosity. In *Hierarchically Structured Porous Materials: From Nanoscience to Catalysis, Separation, Optics, Energy, and Life Science*; Su, B.-L., Sanchez, C., Yang, X.-Y., Eds.; Wiley-VCH Verlag GmbH & Co. KGaA: Weinheim, Germany, 2012.

(13) Li, W.; Wu, Z.; Wang, J.; Elzatahry, A. A.; Zhao, D. A Perspective on Mesoporous TiO_2 Materials. *Chem. Mater.* **2014**, *26*, 287-298.

(14) Hagfeldt, A.; Boschloo, G.; Sun, L.; Kloo, L.; Pettersson, H. Dye-Sensitized Solar Cells. *Chem. Rev.* **2010**, *110*, 6595-6663.

(15) Fujishima, A.; Zhang, X.; Tryk, D. A. TiO_2 Photocatalysis and Related Surface Phenomena. *Surf. Sci. Rep.* **2008**, *63*, 515-582.

(16) Aprile, C.; Corma, A.; Garcia, H. Enhancement of the Photocatalytic Activity of TiO_2 through Spatial Structuring and Particle Size Control: From Subnanometric to Submillimetric Length Scale. *Phys. Chem. Chem. Phys.* **2011**, *10*, 769-783.

(17) Fröschl, T.; Hörmann, U.; Kubiak, P.; Kučerová, G.; Pfanzelt, M.; Weiss, C. K.; Behm, R. J.; Hüsing, N.; Kaiser, U.; Landfester, K.; Wohlfahrt-Mehrens, M. High Surface Area Crystalline Titanium Dioxide: Potential and Limits in Electrochemical Energy Storage and Catalysis. *Chem. Soc. Rev.* **2012**, *41*, 5313-5360.

(18) Joo, J. B.; Dahl, M.; Li, N.; Zaera, F.; Yin, Y. Tailored Synthesis of Mesoporous TiO_2 Hollow Nanostructured for Catalytic Applications. *Energy Environ. Sci.* **2013**, *6*, 2082-2092.

(19) Kitano, M.; Wada, E.; Nakajima, K.; Hayashi, S.; Miyazaki, S.; Kobayashi, H.; Hara, M. Protonated Titanate Nanotubes with Lewis and Brønstad Acidity: Relationship between Nanotube Structure and Catalytic Activity. *Chem. Mater.* **2013**, *25*, 385-393.

(20) Li, N.; Zhang, L.; Chen, Y.; Fang, M.; Zhang, J.; Wang, H. Highly Efficient, Irreversible and Selective Ion Exchange Property of Layered Titanate Nanostructures. *Adv. Funct. Mater.* **2012**, *22*, 835-841.

(21) Wang, J.; Li, H.; Li, H.; Zou, C.; Wang, H.; Li, D. Mesoporous TiO_2 Thin Films Exhibiting Enhanced Thermal Stability and Controllable Pore Size: Preparation and Photocatalyzed Destruction of Cationic Dyes. *ACS Appl. Mater. Interfaces* **2014**, *6*, 1623-1631.

(22) Chang, Z.; Liu, J.; Liu, J.; Sun, X. Titanate Nanosheets and Nanotubes: Alkalinity Manipulated Snthesis and Catalyst Support Application. *J. Mater. Chem.* **2011**, *21*, 277-282.

(23) Bavykin, D. V.; Lapkin, A. A.; Plucinski, P. K.; Friedrich, J. M.; Walsh, F. C. Reversible Storage of Molecular Hydrogen by Sorption into Multilayered TiO_2 Nanotubes. *J. Phys. Chem. B* **2005**, *109*, 19422-19427.

(24) Matos, B. R.; Isidoro, R. A.; Santiago, E. I.; Linardi, M.; Ferlauto, A. S.; Tavares, A. C.; Fonseca, F. C. *In Situ* Fabrication of Nafion-Titanate Hybrid Electrolytes for High-Temperature Direct Ethanol Fuel Cell. *J. Phys. Chem. C* **2013**, *117*, 16863-16870.

(25) Hong, Z.; Wei, M. Layered Titanate Nanostructures and Their Derivatives as Negative Electrode Materials for Lithium-Ion Batteries. *J. Mater. Chem. A* **2013**, *1*, 4403-4414.

(26) Dylla, A. G.; Henkelman, G.; Stevenson, K. J. Lithium Insertion in Nanostructured TiO_2(B) Architectures. *Acc. Chem. Res.* **2013**, *46*, 1104-1112.

(27) Reddy, M. V.; Subba Rao, G. V.; Chowdari, B. V. R. Metal Oxides and Oxysalts as Anode Materials for Li Ion Batteries. *Chem. Rev.* **2013**, *113*, 5364-5457.

(28) Tiemann, M. Repeated Templating. *Chem. Mater.* **2008**, *20*, 961-971.

(29) Ren, Y.; Hardwick, L. J.; Bruce, P. G. Lithium Intercalation into Mesoporous Anatase with an Ordered 3D Pore Structure. *Angew. Chem. Int. Ed.* **2010**, *49*, 2570-2574.

(30) Du, J.; Lai, X.; Yang, N.; Zhai, J.; Kisailus, D.; Su, F.; Wang, D.; Jiang, L. Hierarchically Ordered Macro-Mesoporous TiO_2-Graphene Composite Films: Improved Mass Transfer, Reduced Charge Recombination, and Their Enhanced Photocatalytic Activities. *ACS Nano* **2011**, *5*, 590-596.

(31) Zhao, J.; Wan, P.; Xiang, J.; Tong, T.; Dong, L.; Guo, Z.; Shen, X.; Tong, H. Synthesis of Highly Ordered Macro-Mesoporous Anatase TiO_2 Film with High Photocatalytic Activity. *Microporous Mesoporous Mater.* **2011**, *138*, 200-206.

(32) Hu, Z.; Hua, Z.; Cai, S.; Chen, J.; Yan, Y.; Xu, L. Fabrication of Three-Dimensionally Ordered Macro-/Mesoporous Titania Monoliths by a Dual-Templating Approach. *MRS Proc.* **2011**, *1352*, 1-6.

(33) Sun, W.; Zhou, S.; You, B.; Wu, L. Facile Fabrication and High Photoelectric Properties of Hierarchically Ordered Porous TiO_2. *Chem. Mater.* **2012**, *24*, 3800-3810.

(34) Xin, Y.; Jiang, P.; Yu, M.; Gu, H.; Li, Q.; Zhang, Z. A Universal Route to Fabricate Hierarchically Ordered Macro/Mesoporous Oxides with Enhanced Intrinsic Activity. *J. Mater. Chem. A* **2014**, *2*, 6419-6425.

(35) Bavykin, D. V.; Cressey, B. A.; Light, M. E.; Walsh, F. C. An Aqueous, Alkaline Route to Titanate Nanotubes under Atmospheric Pressure Conditions. *Nanotechnology* **2008**, *19*, 275604(1-5).

(36) Bavykin, D. V.; Friedrich, J. M.; Walsh, F. C. Protonated Titanates and TiO_2 Nanostructured Materials: Synthesis, Properties, and Applications. *Adv. Mater.* **2006**, *18*, 2807-2824.

(37) Nakahira, A.; Kubo, T.; Numako, C. Formation Mechanism of TiO_2-Derived Titanate Nanotubes Prepared by the Hydrothermal Process. *Inorg. Chem.* **2010**, *49*, 5845-5852.

(38) Huang, J.; Cao, Y.; Wang, M.; Huang, C.; Deng, Z.; Tong, H.; Liu, Z. Tailoring of Low-Dimensional Titanate Nanostructures. *J. Phys. Chem. C* **2010**, *114*, 14748-14754.

(39) Morgan, D. L.; Triani, G.; Blackford, M. G.; Raftery, N. A.; Frost, R. L.; Waclawik, E. R. Alkaline Hydrothermal Kinetics in Titanate Nanostructure Formation. *J. Mater. Sci.* **2011**, *46*, 548-557.

(40) Huang, J.; Cao, Y.; Huang, Q.; He, H.; Liu, Y.; Guo, W.; Hong, M. High-Temperature Formation of Titanate Nanotubes and Transformation Mechanism of Nanotubes into Nanowires. *Cryst. Growth Des.* **2009**, *9*, 3632-3637.

(41) Bavykin, D. V.; Kulak, A. N.; Walsh, F. C. Metastable Nature of Titanate Nanotubes in an Alkaline Environment. *Cryst. Growth Des.* **2010**, *10*, 4421-4427.

(42) Wu, D.; Liu, J.; Zhao, X.; Li, A.; Chen, Y.; Ming, N. Sequence of Events for the Formation of Titanate Nanotubes, Nanofibers, Nanowires, and Nanobelts. *Chem. Mater.* **2006**, *18*, 547-553.

(43) Beuvier, T.; Richard-Plouet, M.; Brohan, L. Ternary Morphological Diagram for Nano(tube-ribbon-sphere) Sodium Titanate Deduced fro Raman Spectra Analysis. *J. Phys. Chem. C* **2010**, *114*, 7660-7665.

(44) Menzel, R.; Peiró, A. M.; Durrant, J. R.; Shaffer, M. S. P. Impact of Hydrothermal Processing Conditions on High Aspect Ratio Titanate Nanostructures. *Chem. Mater.* **2006**, *18*, 6059-6068.

(45) Bavykin, D. V.; Parmon, V. N.; Lapkin, A. A.; Walsh, F. C. The Effect of Hydrothermal Conditions on the Mesoporous Structure of TiO_2 Nanotubes. *J. Mater. Chem.* **2004**, *14*, 3370-3377.

(46) Morgan, D. L.; Liu, H.-W.; Frost, R. L.; Waclawik, E. R. Implications of Precursor Chemistry on the Alkaline Hydrothermal Synthesis of Titania/Titanate Nanostructures. *J. Phys. Chem. C* **2010**, *114*, 101-110.

(47) Nakahira, A.; Kato, W.; Tamai, M.; Isshiki, T.; Nishio, K.; Aritani, H. Synthesis of Nanotube from a Layer $H_2Ti_4O_9{\cdot}H_2O$ in a Hydrothermal Treatment Using Various Titania Sources. *J. Mater. Sci.* **2004**, *39*, 4239-4245.

(48) Peng, C.-W.; Richard-Plouet, M.; Ke, T.-Y.; Lee, C.-Y.; Chiu, H.-T.; Marhic, C.; Puzenat, E.; Lemoigno, F.; Brohan, L. Chimie Douce Route to Sodium Hydroxo Titanate Nanowires with Modulated Structure and Conversion to Highly Photoactive Titanium Dioxides. *Chem. Mater.* **2008**, *20*, 7228-7236.

(49) Yuan, Z.-Y.; Zhang, X.-B.; Su, B.-L. Moderate Hydrothermal Synthesis of Potassium Titanate Nanowires. *Appl. Phys. A* **2004**, *78*, 1063-1066.

(50) Mao, Y.; Wong, S. S. Size- and Shape-Dependent Transformation of Nanosized Titanate into Analogous Anatase Titania Nanostructures. *J. Am. Chem. Soc.* **2006**, *128*, 8217-8226.

(51) Morgado, E.; de Abreu, M. A. S.; Moure, G. T.; Marinkovic, B. A.; Jardim, P. M.; Araujo, A. S. Characterization of Nanostructured Titanates Obtained by Alkali Treatment of TiO_2-Anatases with Distinct Crystal Sizes. *Chem. Mater.* **2007**, *19*, 665-676.

(52) Papa, A.-L.; Millot, N.; Saviot, L.; Chassagnon, R.; Heintz, O. Effect of Reaction Parameters on Composition and Morphology of Titanate Nanomaterials. *J. Phys. Chem. C* **2009**, *113*, 12682-12689.

(53) Hernández-Alonso, M. D.; García-Rodríguez, S.; Sánchez, B.; Coronado, J. M. Revisting the Hydrothermal Synthesis of Titanate Nanotubes: New Insights on the Key Factors Affecting the Morphology. *Nanoscale* **2011**, *3*, 2233-2240.

(54) Bavykin, D. V.; Carravetta, M.; Kulak, A. N.; Walsh, F. C. Application of Magic-Angle Spinning NMR to Examine the Nature of Protons in Titanate Nanotubes. *Chem. Mater.* **2010**, *22*, 2458-2465.

(55) Kiatkittipong, K.; Scott, J.; Amal, R. Hydrothermally Synthesized Titanate Nanostructures: Impact of Heat Treatment on Particle Characteristics and Photocatalytic Properties. *ACS Appl. Mater. Interfaces* **2011**, *3*, 3988-3996.

(56) Zhu, G.-N.; Wang, C.-X.; Xia, Y.-Y. Structural Transformation of Layered Hydrogen Trititanate ($H_2Ti_3O_7$) to TiO_2(B) and Its Electrochemical Profile for Lithium-Ion Intercalation. *J. Power Sources* **2011**, *196*, 2848-2853.

(57) Gentili, V.; Brutti, S.; Hardwick, L. J.; Armstrong, A. R.; Panero, S.; Bruce, P. G. Lithium Insertion into Anatase Nanotubes. *Chem. Mater.* **2012**, *24*, 4468-4476.

(58) Zhou, Y.-K.; Cao, L.; Zhang, F.-B.; He, B.-L.; Li, H.-L. Lithium Insertion into TiO_2 Nanotube Prepared by the Hydrothermal Process. *J. Electrochem. Soc.* **2003**, *150*, A1246-A1249.

(59) Gao, X.; Zhu, H.; Pan, G.; Ye, S.; Lan, Y.; Wu, F.; Song, D. Preparation and Electrochemical Characterization of Anatase Nanorods for Lithium-Inserting Electrode Material. *J. Phys. Chem. B* **2004**, *108*, 2868-2872.

(60) Zukalová, M.; Kalbáč, M.; Kavan, L.; Exnar, I.; Graetzel, M. Pseudocapacitive Lithium Storage in TiO_2(B). *Chem. Mater.* **2005**, *17*, 1248-1255.

(61) Armstrong, A. R.; Armstrong, G.; Canales, J.; García, R.; Bruce, P. G. Lithium-Ion Intercalation into TiO_2-B Nanowires. *Adv. Mater.* **2005**, *17*, 862-865.

(62) Li, J.; Tang, Z.; Zhang, Z. Layered Hydrogen Titanate Nanowires with Novel Lithium Intercalation Properties. *Chem. Mater.* **2005**, *17*, 5848-5855.

(63) Augustyn, V.; Simon, P.; Dunn, B. Pseudocapacitive Oxide Materials for High-Rate Electrochemical Energy Storage. *Energy Environ. Sci.* **2014**, *7*, 1597-1614.

(64) Li, J.; Tang, Z.; Zhang, Z. Pseudocapacitive Characteristic of Lithium Ion Storage in Hydrogen Titanate Nanotubes. *Chem. Phys. Lett.* **2006**, *418*, 506-510.

(65) Beuvier, T.; Richard-Plouet, M.; Mancini-Le Granvalet, M.; Brousse, T.; Crosnier, O.; Brohan, L. TiO_2(B) Nanoribbons as Negative Electrode Material for Lithium Ion Batteries with High Rate Performance. *Inorg. Chem.* **2010**, *49*, 8457-8464.

(66) Dylla, A. G.; Xiao, P.; Henkelman, G.; Stevenson, K. J. Morphological Dependence of Lithium Insertion in Nanocrystalline TiO_2(B) Nanoparticles and Nanosheets. *J. Phys. Chem. Lett.* **2012**, *3*, 2015-2019.

(67) Myung, S.-T.; Takahashi, N.; Komaba, S.; Yoon, C. S.; Sun, Y.-K.; Amine, K.; Yashiro, H. Nanostructured TiO_2 and Its Application in Lithium-Ion Storage. *Adv. Funct. Mater.* **2011**, *21*, 3231-3241.

(68) Huang, H.; Fang, J.; Xia, Y.; Tao, X.; Gan, Y.; Du, J.; Zhu, W.; Zhang, W. Construction of Sheet-Belt Hybrid Nanostructures from One-Dimensional Mesoporous TiO_2(B) Nanobelts and Graphene Sheets for Advanced Lithium-Ion Batteries. *J. Mater. Chem. A* **2013**, *1*, 2495-2500.

(69) Liu, S.; Wang, Z.; Yu, C.; Wu, H. B.; Wang, G.; Dong, Q.; Qiu, J.; Eychmüller, A.; Lou, X. W. A Flexible TiO_2(B)-Based Battery Electrode with Superior Power Rate and Ultralong Cycle Life. *Adv. Mater.* **2013**, *25*, 3462-3467.

(70) Zakharova, G. S.; Jähne, C.; Popa, A.; Täschner, C.; Gemming, T.; Leonhardt, A.; Büchner, B.; Klingeler, R. Anatase Nanotubes as an Electrode Material for Lithium-Ion Batteries. *J. Phys. Chem. C* **2012**, *116*, 8714-8720.

(71) Zhang, Y.; Tang, Y.; Yin, S.; Zeng, Z.; Zhang, H.; Li, C. M.; Dong, Z.; Chen, Z.; Chen, X. Hierarchical Protonated Titanate Nanostructures for Lithium-Ion Batteries. *Nanoscale* **2011**, *3*, 4074-4077.

(72) Bae, C.; Yoon, Y.; Yoon, W.-S.; Moon, J.; Kim, J.; Shin, H. Hierarchical Titania Nanotubes with Self-Branched Crystalline Nanorods. *ACS Appl. Mater. Interfaces* **2010**, *2*, 1581-1587.

(73) Shin, K.; Kim, H. J.; Choi, J.-M.; Choi, Y.-M.; Song, M. S.; Park, J. H. Controlled Synthesis of Skein Shaped TiO_2-B Nanotube Cluster Particles with Outstanding Rate Capability. *Chem. Commun.* **2013**, *49*, 2326-2328.

(74) Liu, H.; Bi, Z.; Sun, X.-G.; Unocic, R. R.; Paranthaman, M. P.; Dai, S.; Brown, G. M. Mesoporous TiO_2-B Microspheres with Superior Rate Performance for Lithium Ion Batteries. *Adv. Mater.* **2011**, *23*, 3450-3454.

(75) Josephson, D. P.; Popczun, E. J.; Stein, A. Effects of Integrated Carbon as a Light Absorber on the Coloration of Photonic Crytal-Based Pigments. *J. Phys. Chem. C* **2013**, *117*, 13585-13592.

(76) Nakahira, A.; Kubo, T.; Numako, C. TiO_2-Derived Titanate Nanotubes by Hydrothermal Process with Acid Treatments and Their Microstructural Evaluation. *ACS Appl. Mater. Interfaces* **2010**, *2*, 2611-2616.

(77) Zhang, H.; Li, G. R.; An, L. P.; Yan, T. Y.; Gao, X. P.; Zhu, H. Y. Electrochemical Lithium Storage of Titanate and Titania Nanotubes and Nanorods. *J. Phys. Chem. C* **2007**, *111*, 6143-6148.

(78) Qu, J.; Gao, X. P.; Li, G. R.; Jiang, Q. W.; Yan, T. Y. Structure Transformation and Photoelectrochemical Properties of TiO_2 Nanomaterials Calcined from Titanate Nanotubes. *J. Phys. Chem. C* **2009**, *113*, 3359-3363.

(79) Bavykin, D. V.; Kulak, A. N.; Walsh, F. C. Control over the Hierarchical Structure of Titanate Nanotube Agglomerates. *Langmuir* **2011**, *27*, 5644-5649.

(80) Mao, Y.; Kanungo, M.; Hemraj-Benny, T.; Wong, S. S. Synthesis and Growth Mechanism of Titanate and Titania One-Dimensional Nanostructures Self-Assembled into Hollow Micrometer-Scale Spherical Aggregates. *J. Phys. Chem. B* **2006**, *110*, 702-710.

(81) Horváth, E.; Kukovecz, Á.; Kónya, Z.; Kiricsi, I. Hydrothermal Conversion of Self-Assembled Titanate Nanotubes into Nanowires in a Revolving Autoclave. *Chem. Mater.* **2007**, *19*, 927-931.

(82) Moon, J. H.; Yang, S. Chemical Aspects of Three-Dimensional Photonic Crystals. *Chem. Rev.* **2010**, *110*, 547-574.

(83) Schroden, R. C.; Al-Daous, M.; Blanford, C. F.; Stein, A. Optical Properties of Inverse Opal Photonic Crystals. *Chem. Mater.* **2002**, *14*, 3305-3315.

(84) Tokudome, H.; Miyauchi, M. Electrochromism of Titanate-Based Nanotubes. *Angew. Chem. Int. Ed.* **2008**, *44*, 1974-1977.

(85) Vittadini, A.; Schirmer, M.; Walz, M.-M.; Vollnhals, F.; Lukasczyk, T.; Steinrück, H.-P.; Marbach, H.; Riss, A.; Elser, M. J.; Schürer, B.; Diwald, O. Defects in Oxygen-Depleted Titanate Nanostructures. *Langmuir* **2012**, *28*, 7851-7858.

(86) Chatterjee, S.; Bhattacharyya, K.; Ayyub, P.; Tyagi, A. K. Photocatalytic Properties of One-Dimensional Nanostructured Titanates. *J. Phys. Chem. C* **2010**, *114*, 9424-9430.

(87) Tsai, C.-C.; Teng, H. Regulation of the Physical Characteristics of Titania Nanotube Aggregates Synthesized from Hydrothermal Treament. *Chem. Mater.* **2004**, *16*, 4352-4358.

(88) Gao, T.; Fjellvåg, H.; Norby, P. Crystal Structures of Titanate Nanotubes: A Raman Scattering Study. *Inorg. Chem.* **2009**, *48*, 1423-1432.

(89) Gao, T.; Fjellvåg, H.; Norby, P. Raman Scattering Properties of a Protonic Titanate $H_xTi_{2-x/4}\square_{x/4}O_4 \cdot H_2O$ (□, vacancy; x = 0.7) with Lepidocrocite-Type Layered Structure. *J. Phys. Chem. B* **2008**, *112*, 9400-9405.

(90) Tsai, C.-C.; Teng, H. Nanotube Formation from a Sodium Titanate Powder via Low-Temperature Acid Treatment. *Langmuir* **2008**, *24*, 3434-3438.

(91) Ma, R.; Fukuda, K.; Sasaki, T.; Osada, M.; Bando, Y. Structural Features of Titanate Nanotubes/Nanobelts Revealed by Raman, X-ray Adsorption Fine Structure and Electron Diffraction Characterizations. *J. Phys. Chem. B* **2005**, *109*, 6210-6214.

(92) Kim, S.-J.; Yun, Y.-U.; Oh, H.-J.; Hong, S. H.; Roberts, C. A.; Routray, K.; Wachs, I. E. Characterization of Hydrothermally Prepared Titanate Nanotube Powders by Ambient and In Situ Raman Spectroscopy. *J. Phys. Chem. Lett.* **2010**, *1*, 130-135.

(93) Aravindan, V.; Shubha, N.; Cheah, Y. L.; Prasanth, R.; Chuiling, W.; Prabhakar, R. R.; Madhavi, S. Extraordinary Long-Term Cycleability of TiO_2-B Nanorods as Anodes in Full-Cell Assembly with Electrospun PVdF-HFP Membranes. *J. Mater. Chem. A* **2013**, *1*, 308-316.

(94) Casarin, M.; Vittadini, A.; Selloni, A. First Principles Study of Hydrated/Hydroxylated TiO_2 Nanolayers: From Isolated Sheets to Stacks and Tubes. *ACS Nano* **2009**, *3*, 317-324.

(95) Hanaor, D. A. H.; Sorrell, C. C. Review of the Anatase to Rutile Phase Transformation. *J. Mater. Sci.* **2011**, *46*, 855-874.

(96) Kim, J.; Cho, J. Rate Characteristics of Anatase TiO_2 Nanotubes and Nanorods for Lithium Battery Anode Materials at Room Temperature. *J. Electrochem. Soc.* **2007**, *154*, A542-A546.

(97) Brutti, S.; Gentili, V.; Menard, H.; Scrosati, B.; Bruce, P. G. TiO_2-(B) Nanotube as Anodes for Lithium Batteries: Origin and Mitigation of Irreversible Capacity. *Adv. Energy Mater.* **2012**, *2*, 322-327.

Chapter 7

Control of Heterogeneity in Nanostructured $Ce_{1-x}Zr_xO_2$ Binary Oxides for Enhanced Thermal Stability and Water Splitting Activity

---

Parts of this chapter are from: Petkovich, N. D.; Rudisill, S.G.; Venstrom, L. J.; Boman, D. B.; Davidson, J. H.; Stein, A. Control of Heterogeneity in Nanostructured $Ce_{1-x}Zr_xO_2$ Binary Oxides for Enhanced Thermal Stability and Water Splitting Activity *J. Phys. Chem. C* **2011**, *115*, 21022-21033. – These parts are reproduced by permission of The American Chemical Society. Available at: http://dx.doi.org/10.1021/jp2071315

7.1 Introduction and Motivation

As stated in Chapter 1, finding pathways to renewable generation of fuels is a crucial step toward mitigating the ecological impacts of fossil fuel combustion. A renewable fuel source requires a sustainable energy input and abundant feedstocks. One promising route is through the use of concentrated solar energy to drive the thermochemical splitting of H_2O and CO_2. This chapter is focused on improving cerium oxide used for thermochemical fuel production via the two-step cycle. Before continuing, background information needs to be provided to set the stage for the rest of the chapter. A brief summary of the advantages of using cerium oxide is first given, and it is followed by a discussion of the two improvements–the synthesis of porous cerium oxide for fuel production and the addition of Zr^{4+} ions to the cerium oxide lattice.

Cerium oxide is an attractive material for two-step solar thermochemical fuel production. Both water splitting and CO_2 splitting with cerium oxide have been investigated, first in catalytic systems[1,2] and then as a solar thermochemical process.[3-9] Cerium oxide has found use in automotive three-way catalysis and other catalytic systems, due to its ability to reversibly store and release lattice oxygen.[10-12] This mechanism occurs due to the partial reduction of the Ce^{4+} cations in cerium oxide to Ce^{3+}, and it results in the formation of nonstoichiometric, cubic phases via the formation of oxygen vacancies without significant reorganization of the lattice.[12,13] When compared to the ferrites and zinc oxide materials that are used for fuel production, cerium oxide has a higher melting point (2400 °C), improved thermal stability, and lack of crystal reordering phase transitions in the operating temperature range.[8]

The rapid production of large quantities of H_2 and/or CO is critical to achieve an efficient reactor system for solar thermochemical fuel production.[14] Toward this end, 3DOM CeO_2 has been studied for use in fuel production.[15] Using a 3DOM material, it is possible to transport reactant and product gases easily through the pore network. Furthermore, the surface area of granules with the 3DOM structure is greater than that of bulk micrometer-sized granules, increasing the amount of surface sites available for heterogeneous reactions.[16,17] These advantages brought by the 3DOM structure improve the kinetics of the fuel production step.[15] There are further opportunities for improving kinetics, productivity, and thermal stability of 3DOM cerium oxide-based materials by adding dopant cations, such as Zr^{4+} to the lattice.

Ce–Zr mixed oxides are important catalytic materials that confer benefits over pure cerium oxide.[18-21] Zr^{4+} is an undersized cation that distorts the cubic fluorite lattice of CeO_2, induces defects and alters the redox properties of the mixed oxide, typically making reduction more favorable.[22-25] Even though the Zr^{4+} cations are redox inactive, the increase in the redox activity

of the cerium ions can often compensate for the addition of inactive cations.[26-28] Cerium oxide sinters at the temperatures required for thermochemical cycling; this results in a loss of surface area, hindering the ability of cerium oxide to gain and lose oxygen ions from its lattice.[29] Zirconium significantly improves resistance to sintering and limits growth of crystallites.[30,31] Retention of surface area is essential for both maintaining the nanostructured morphology in 3DOM materials and preserving the kinetic advantages.[15] There are still challenges present when investigating $Ce_{1-x}Zr_xO_2$ mixed oxides for catalytic applications, which necessitate careful control of synthetic pathways and thorough materials characterization. At the time this study was conducted, only cursory analyses had been carried out with $Ce_{1-x}Zr_xO_2$ for use in solar thermochemical fuel production.[6,7,32]

This chapter details the development of 3DOM $Ce_{1-x}Zr_xO_2$ for use in solar thermochemical production of hydrogen via the splitting of water. Two synthesis routes are investigated for the production of 3DOM $Ce_{1-x}Zr_xO_2$ and compared in terms of the homogeneity of the mixed oxide products (using X-ray diffractometry and Raman spectroscopy), morphology (using electron microscopy), and textural properties (using nitrogen sorption). The changes induced by cycling through a H_2 chemical reduction step and fuel production step (both conducted at 825 °C) are given special attention. Changes in kinetics and productivity in the fuel production step caused by increasing the Zr content are also studied. Structure–property relationships are considered in the behavior of the different materials with respect to fuel production.

7.2 Experimental

7.2.1 Materials

The following chemicals were used. Methyl methacrylate (MMA, 99%), $CeCl_3 \cdot 7H_2O$ (99.9%), $Ce(NO_3)_3 \cdot 6H_2O$ (99%), $ZrOCl_2 \cdot 8H_2O$ (98.5%), methanol (HPLC grade), and citric acid (99.5+%, ACS grade) were all obtained from Sigma Aldrich. Potassium persulfate (99.9%) was obtained from Fisher Scientific. Ethylene glycol (99+%) was obtained from Mallinckrodt Chemicals. No additional purification steps were performed for the chemicals listed. Deionized water was purified using a Barnstead-Sybron system to a resistivity of >18 MΩ·cm.

7.2.2 PMMA Template Synthesis

Colloidal crystal templates were synthesized by first producing monodisperse poly(methyl methacrylate) (PMMA) spheres via an emulsifier-free emulsion polymerization.[33] Briefly, MMA (400 mL) and water (1600 mL) were stirred together in a five-neck round-bottom flask to form an

emulsion. Potassium persulfate (1.0 g) was then added as a radical initiator. The polymerization was conducted at 70 °C under mechanical stirring. After polymerization, the colloidal dispersion of spheres was filtered through glass wool to remove aggregates. Monodisperse spheres with diameters of 485 ± 4 nm were obtained. Millimeter-sized colloidal crystals were prepared by gravity sedimentation.

7.2.3 Synthesis of 3DOM CeO_2 and 3DOM $Ce_{1-x}Zr_xO_2$ via Methanolic Salt Solutions (MSS)

Both CeO_2 and $Ce_{1-x}Zr_xO_2$ were synthesized through a facile process involving the infiltration of a methanolic solution of chloride salts into the colloidal crystal template. In a typical synthesis of 3DOM CeO_2, $CeCl_3 \cdot 7H_2O$ (2 g) was dissolved in methanol (2.5 g) and stirred for 15 min at room temperature (RT). This precursor was then infiltrated into PMMA colloidal crystal templates in a closed glass vessel at RT. The mass ratio of PMMA templates to the precursor was 3:2. After the PMMA templates became translucent and were completely infiltrated (a process that took 2–4 h), the infiltrated templates were dried for 24 h. The composites were then thermally treated by calcination under static air at 310 °C for 2 h and 450 °C for 2 h with a temperature ramp rate of 2 °C/min for all segments. A light yellow, opalescent powder was obtained and is designated 3DOM CeO_2-MSS.

In a similar fashion, 3DOM $Ce_{1-x}Zr_xO_2$ samples were synthesized through the use of methanolic precursors. $CeCl_3 \cdot 7H_2O$ and $ZrOCl_2 \cdot 8H_2O$ were mixed so that the total mass of the salts was 2 g and the stoichiometry of the metal ions matched the desired final material. These salts were dissolved in 2.5 g of methanol and stirred for 15 min at RT. All subsequent steps for infiltration, drying, and calcination were the same as those for 3DOM CeO_2-MSS. Yellow, opalescent powders were obtained and are designated 3DOM $Ce_{1-x}Zr_xO_2$-MSS.

7.2.4 Synthesis of 3DOM CeO_2 and $Ce_{1-x}Zr_xO_2$ via the Pechini Method (PM)

An alternate precursor was used to synthesize 3DOM CeO_2 by the Pechini gel method. The precursor was prepared by first dissolving 3.92 g (0.009 mol) of $Ce(NO_3)_3 \cdot 6H_2O$ in 3.11 g of water. Citric acid (1.5 g) was then added to the precursor and was dissolved under stirring. Finally, ethylene glycol (1 g) was added and the resultant solution was stirred for an additional 15 min. This precursor was then infiltrated into PMMA colloidal crystal templates in a closed glass vessel at RT. The mass ratio of PMMA templates to the precursor was 3:2. Infiltrated colloidal crystals were then heated to 90 °C for 1 h in closed vessels. After the heat treatment, samples were calcined under static air at 310 °C for 2 h with a ramp rate of 2 °C/min. These were then

heated at 2 °C/min up to 450 °C with a dwell time of 2 h. A yellow powder that exhibited blue-green structural color was obtained and is designated 3DOM CeO_2-PM.

The synthesis of the 3DOM $Ce_{1-x}Zr_xO_2$ via a Pechini precursor ($Ce_{1-x}Zr_xO_2$-PM) followed the same general route. Depending on the desired stoichiometry needed in the final material, the molar ratio of the metal ions was changed in the precursor. However, the total number of moles of the two metal ions was fixed at 0.009 mol, as in the synthesis for the 3DOM CeO_2.

7.2.5 Characterization of Materials

Scanning electron microscopy (SEM) was performed on a JEOL 6500 microscope operated at an accelerating voltage of 5 kV. Specimens were prepared by depositing powder on double-sided carbon sticky tape affixed to an Al stub. All specimens were coated with 75 Å of Pt before images were taken. For transmission electron microscopy (TEM), a Tecnai T12 microscope was used with a LaB_6 filament operating at 120 kV. The specimens were crushed into powder and immersed in a small volume of water. After sonicating the mixture for 10 min, a droplet of the suspension was allowed to dry on a holey carbon/Formvar-coated copper TEM grid. Powder X-ray diffraction (PXRD) patterns were obtained using a PANalytical X'Pert Pro diffractometer equipped with an X'Celerator detector. Co Kα radiation (λ = 1.790 Å) was used in the instrument with a generator voltage of 45 kV and a current of 40 mA. The Scherrer equation was used to calculate crystallite sizes from line broadening in the diffraction patterns. Contributions to line broadening were assumed to be Lorentzian. Raman spectroscopy of the powders was conducted using a Witec Alpha300R confocal Raman microscope with a DV401 CCD thermoelectric-cooled detector. The microscope was equipped with a 514.5 nm Ar ion laser operated at 20 mW. Scans were obtained by focusing the laser on a ~1 μm spot and then collecting multiple spectra that were averaged. Gas sorption analysis was conducted using a Quantachrome Autosorb iQ_2-MP with N_2 (at 77 K) as the adsorbate. Specimens were degassed at 300 °C for 1 h at 0.001 Torr. Brunauer–Emmett–Teller (BET) specific surface areas were determined using the adsorption branch from P/P_0 = 0.05 to 0.35. Pore volumes were calculated from P/P_0 = 0.995 on the adsorption branch, and pore size distributions were also obtained from the adsorption branch using the Barrett–Joyner–Halenda (BJH) method. X-ray photoelectron spectroscopy was done using a SSX-100 (Surface Science Instruments) that has a monochromated Al Kα anode operated at 200 W with a 1 × 1 mm^2 spot size. The instrument is also equipped with a hemispherical sector analyzer and a resistive anode detector. Samples were exposed to a 10 eV electron flux for charge

neutralization. Base pressure was 5.0×10^{-10} Torr, and survey scans were obtained with a 150 eV pass energy using a 0.5 eV/step.

7.2.6 Reactivity and Productivity Testing of 3DOM CeO_2 and 3DOM $Ce_{1-x}Zr_xO_2$ Materials

As-synthesized powder samples were studied in a fixed bed, vertical flow reactor comprised of an electric furnace (OMEGA CRFC-1512/120-C-A) and a cylindrical quartz column (Figure 7.1). The furnace is controlled using a type-K thermocouple probe placed between the quartz column and the hot furnace wall. The temperature measured by the control thermocouple was held at 800±2 °C. Due to the presence of axial temperature gradients, the sample temperature was 25 °C higher than the furnace set-point temperature, as verified in a separate experiment. Samples were sieved (<1.0 mm), weighed, and gravity fed into the column where they were held by a quartz frit (maximum pore diameter of 200 μm). Gas mixtures were delivered to the reactor via mass flow controllers with an accuracy of 1.5% of the desired flow rate. The composition of the product gas mixture was monitored with either a quadrupole mass spectrometer (Inficon Transpector CPM) or a Raman laser spectrometer (Atmosphere Recovery, Inc., RLGA-129a) to an accuracy of ≤0.02 mol %. These gas analyzers were calibrated using standard mixtures H_2 in Ar.

In each experiment, the 3DOM $CeO_2/Ce_{1-x}Zr_xO_2$ sample was reduced and oxidized six times. The reactor was first purged of air under a flow of Ar (99.999% purity). The sample was then chemically reduced for 50–70 min by a 100–300 mL min^{-1} flow of 5.0 ± 0.1 mol % H_2 in Ar. Upon completion of the chemical reduction, the reactor was purged by a flow of Ar. Oxidation was initiated by the delivery of a mixture of H_2O in Ar, created by saturating a 275–285 mL min^{-1} flow of Ar with water at RT. The total mass flow rate of gas through the fixed bed was maintained sufficiently high in all experiments to ensure that the bed behaved in a quasi-steady state fashion. The flow of reactants in the fixed bed was maintained for ~20 min. Finally, the reactor was again purged under a flow of Ar to remove all traces of the reactive H_2O. This reduction–purge–oxidation–purge procedure constituted a single chemical cycle and lasted approximately 90 min.

The amount of H_2 produced was calculated by integrating the instantaneous fuel production rate over the first 10 min of oxidation. Sample productivity is defined as the total H_2 production normalized by the total mass of oxide. H_2 production was also normalized (see Section 7.3.6) by the mass of cerium oxide when the sample was a mixed oxide (3DOM $Ce_xZr_{1-x}O_2$). This alternative normalization elucidates changes in the activity of the Ce ions in the mixture as a result of the addition of Zr. Process and systematic uncertainties in the measurements were

propagated to the productivity and H_2 production rates using the sequential perturbation method, and are reported at 95% confidence.

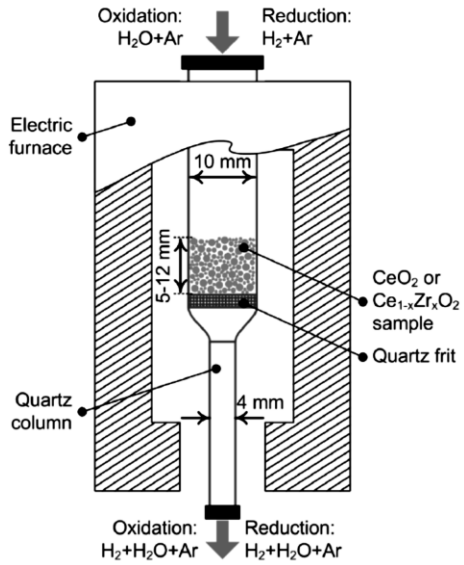

Figure 7.1 Vertical fixed bed tubular flow reactor for measuring H_2 production. The terms "oxidation" and "reduction" are used with respect to the cerium oxide-based material. Schematic created by Professor Luke Venstrom.

7.3 Results and Discussion

Changing certain properties of $Ce_{1-x}Zr_xO_2$ catalysts can have an impact on their performance in heterogeneous redox processes. These properties were changed by altering the synthesis methodology for the 3DOM $Ce_{1-x}Zr_xO_2$ and by altering the amount of Zr in $Ce_{1-x}Zr_xO_2$ (where x = 0, 0.1, 0.2, 0.3, 0.4, and 0.5). The synthesis method has a profound effect on the homogeneity of the final mixed oxide products. Various materials characterization techniques were used to determine the crystal polymorphs present and examine whether the material is homogeneous or segregated into Zr- and Ce-rich domains. The Pechini method yields single phase, homogeneous products (through chelation of metal ions in a polymer gel matrix), unlike the multiphase, inhomogeneous methanolic products. These results have important implications for fuel production and are discussed in a subsequent section. As mentioned in Section 7.1, addition of Zr to CeO_2 profoundly alters both the thermal stability and redox activity of the resultant $Ce_{1-x}Zr_xO_2$. For the 3DOM $Ce_{1-x}Zr_xO_2$, the improved stability was observed in changes to crystallite size after cycling at 825 °C. Electron microscopy and N_2 sorption showed that morphological and textural

changes in 3DOM $Ce_{1-x}Zr_xO_2$ from cycling were mitigated by increasing Zr content. In the last section, the effect of changing Zr content on fuel production is explored.

7.3.1 Assessment of the Crystallite Polymorph via Powder X-ray Diffraction

Before discussing the characterization of the nanocrystalline materials, it is important to give an overview of the crystal polymorphs present in the CeO_2–ZrO_2 system and any relevant polymorphic transformations that can occur. Several crystalline polymorphs in the CeO_2–ZrO_2 system are commonly seen in the study of these $Ce_{1-x}Zr_xO_2$ mixed oxides. For $x < 0.2$, a distorted cubic fluorite phase is generally observed, while, for $x > 0.9$, a monoclinic phase is detected.[34] Three metastable tetragonal phases have been identified in the composition range from $0.2 < x < 0.9$: t, t′, and t″.[35,36] These phases have a slightly lower ability to store and release oxygen when compared to the cubic phase.[37] The t″ phase cannot be detected with PXRD, since the tetragonal distortion is only present in the oxygen sublattice and requires alternate characterization techniques (such as Raman spectroscopy or neutron diffraction).[34,37] Both t′ and t phases have distortions in the cationic sublattice (with the t phase having a greater c/a ratio than t') that can be detected with PXRD. Depending on the initial homogeneity of the samples, the size of the crystallites, and the temperature used for thermal processing, combinations of cubic, tetragonal, and monoclinic phases have been observed in samples with compositions ranging from $0.2 < x < 0.9$.[34,37] Cubic pyrochlore and tetragonal phases that differ in cation ordering have been identified for the $Ce_{0.5}Zr_{0.5}O_{2-\delta}$ system as well.[38-40] Thermal treatment of as-made $Ce_xZr_{1-x}O_2$ under reducing and oxidizing conditions can generate further phase transformations and phase segregation.[31,41] Characterization of these changes is important because inhomogeneities have been shown to alter the catalytic activity of $Ce_{1-x}Zr_xO_2$.[42] Since the synthesized samples are subjected to high temperatures during the reduction and oxidation cycles, the complementary techniques of PXRD and Raman spectroscopy have been employed to characterize the polymorphs present in the samples and the size of the crystallites.

Assessment of the crystal polymorph and any gross structural heterogeneities was undertaken via PXRD. Patterns were obtained for samples of the as-synthesized 3DOM $Ce_{1-x}Zr_xO_2$-MSS (Figure 7.2 a). Considerable peak broadening is observed in these samples due to the small size of the crystallites that comprise the material. These patterns contain diffraction peaks corresponding to a cubic fluorite lattice. As the concentration of Zr increases in the mixed oxides, the positions of diffraction peaks are shifted to increasingly higher values of 2θ, corresponding to a decrease in the lattice parameter. This behavior is consistent with other studies and results from the

replacement of the larger Ce^{4+} cations (0.97 Å) with smaller Zr^{4+} cations (0.84 Å).[43,44] The 3DOM $Ce_{0.6}Zr_{0.4}O_2$-MSS and $Ce_{0.5}Zr_{0.5}O_2$-MSS both display partially resolved peaks corresponding to another mixed oxide phase with higher Zr content (Figure 7.2 a). It is unclear if the minor phase in the 3DOM $Ce_{0.6}Zr_{0.4}O_2$-MSS and $Ce_{0.5}Zr_{0.5}O_2$-MSS samples is cubic or tetragonal due to a high degree of peak broadening. Slight peak asymmetry is observed in the other 3DOM $Ce_{1-x}Zr_xO_2$-MSS samples, indicative of the presence of another minor phase that is slightly enriched in Zr content when compared to the major phase.[45]

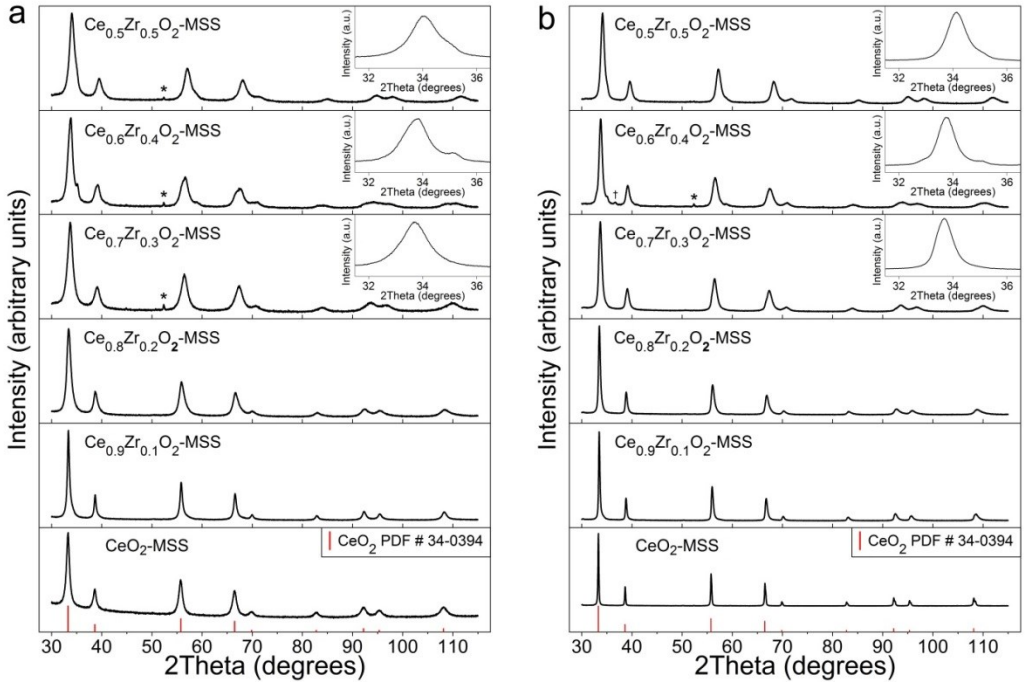

Figure 7.2 PXRD patterns obtained for the as-made (a) and cycled (b) 3DOM $Ce_{1-x}Zr_xO_2$-MSS, where $0 \leq x \leq 0.5$. All patterns have reflections that correspond to cubic fluorite phase. A shift in the peaks to higher 2θ values can be observed as Zr content increases. The insets show an additional peak appearing in the $Ce_{0.6}Zr_{0.4}O_2$ and $Ce_{0.5}Zr_{0.5}O_2$. This is attributed to phase demixing of the sample during synthesis, producing a Zr-rich phase. The materials retain the fluorite structure after 6 cycles at 825 °C. Inhomogeneities are still present and peak asymmetry is observed for mixed oxides with lower Zr content, like $Ce_{0.7}Zr_{0.3}O_2$ (see inset). The dagger in (b) marks a reflection of a monoclinic phase of $Ce_{1-x}Zr_xO_2$ (PDF #1-088-2392). Reflections marked with an asterisk are from the Al sample holder.

Thermochemical cycling did not cause significant changes in most of the patterns of the 3DOM $Ce_{1-x}Zr_xO_2$-MSS samples. Cycling led to crystallite growth, which narrowed the diffraction peaks and allowed for better resolution of compositional heterogeneities. The 3DOM

$Ce_{0.6}Zr_{0.4}O_2$-MSS sample was the only material in which new peaks were observed. These peaks can be closely matched to a calculated literature pattern for monoclinic $Ce_{1-x}Zr_xO_2$ (PDF #1-088-2392, Figure 7.2 b). While it is possible that the cycling may have induced phase segregation to produce the monoclinic polymorph, it may have been present in the original sample as small crystal nuclei undetectable by PXRD or as a phase with a low concentration. It is unusual for $Ce_{1-x}Zr_xO_2$ with values of $x < 0.5$ to have peaks corresponding to a monoclinic phase,[34,46] suggesting that widespread heterogeneities are present in the 3DOM $Ce_{0.6}Zr_{0.4}O_2$-MSS. Additional batches of 3DOM $Ce_{0.7}Zr_{0.3}O_2$, $Ce_{0.6}Zr_{0.4}O_2$, and $Ce_{0.5}Zr_{0.5}O_2$-MSS were synthesized through the methanolic route and had peaks corresponding to cubic, tetragonal, and monoclinic phases (see Figure 7.3 for an example). One extremely inhomogeneous sample, designated $Ce_{0.5}Zr_{0.5}O_2$-MSS-IH (Figure 7.3), was subsequently examined for H_2 productivity. It is unclear what causes such fluctuations in the homogeneity for the 3DOM $Ce_{1-x}Zr_xO_2$-MSS samples with higher Zr content. A possible source of the fluctuations is the segregation of the salts into Zr- and Ce-rich domains during the drying process.

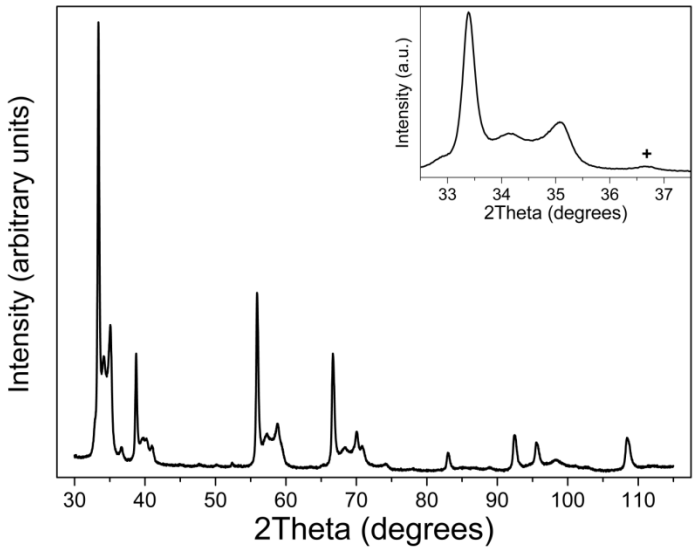

Figure 7.3 PXRD pattern of a highly inhomogeneous 3DOM $Ce_{0.5}Zr_{0.5}O_2$-MSS sample, designated 3DOM $Ce_{0.5}Zr_{0.5}O_2$-MSS-IH. Three cubic or tetragonal phases are observed, in addition to a series of reflections that match a monoclinic $Ce_{1-x}Zr_xO_2$ phase (PDF #1-088-2392, indicated by a plus in the inset). The most intense series of reflections are shifted to higher values of 2θ than the literature cubic fluorite pattern for CeO_2. This shift closely matches the shift and (111) d-spacing seen in $Ce_{0.9}Zr_{0.1}O_2$.

To achieve higher levels of compositional homogeneity, 3DOM samples were prepared using the Pechini method and analyzed with PXRD. Once again, patterns were obtained for both as-synthesized and cycled mixed oxides (Figure 7.4). Notably, the as-made samples only have diffraction peaks that match those of a cubic fluorite phase. Similar to the samples prepared by the methanolic route, the peaks in the patterns shifted to higher 2θ values as the concentration of Zr increased. After cycling, no new peaks were detected in the diffraction patterns of any Pechini samples. Asymmetry was also not observed in the peak shape of the cycled samples, indicating compositional homogeneity. However, PXRD cannot be used to fully assess the homogeneity of the Pechini samples, as line broadening can mask peaks from other phases. Confocal backscatter Raman spectroscopy was used for this purpose.[19,31]

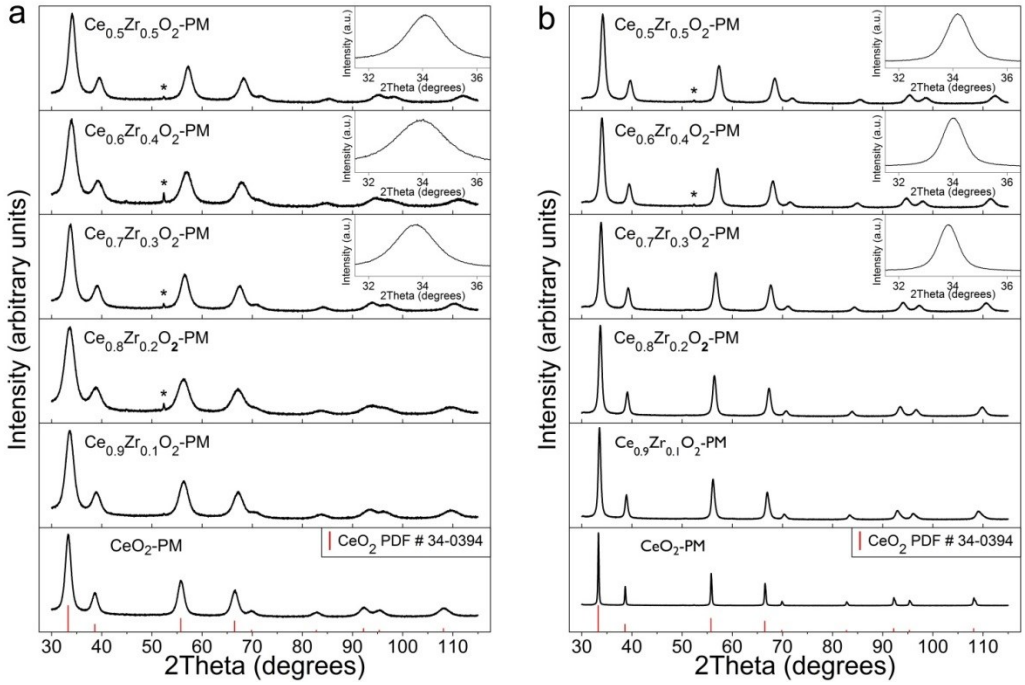

Figure 7.4 PXRD patterns obtained for the as-made (a) and cycled (b) 3DOM $Ce_{1-x}Zr_xO_2$-PM, where $0 \leq x \leq 0.5$. The reflections in the patterns for these samples correspond to a cubic fluorite lattice. These reflections are shifted to higher values of 2θ with increasing Zr content. All patterns are single phase, even for high Zr content samples (see inset). The samples undergo no phase changes after six cycles at 825 °C. Line broadening in this series of samples is greater than for the methanolic samples, which is indicative of a smaller grain size. The reflection marked with an asterisk is from the Al sample holder.

7.3.2 Further Assessment of Crystallite Polymorph and Homogeneity via Raman Spectroscopy

Raman spectroscopy is a complementary technique to PXRD in the characterization of $Ce_{1-x}Zr_xO_2$ and is effective at detecting the presence of tetragonal phases, including the t″ phase. With the use of a confocal backscatter Raman instrument, one can more effectively probe samples for localized inhomogeneities. While this technique does not yield localized information of crystal structure homogeneity on the nanoscale, it allows for examination of micrometer-sized spots across a sample. The spectra from 3DOM CeO_2-MSS had a single peak at 464 cm^{-1} from the T_{2g} vibrational mode of the cubic fluorite lattice. All of the 3DOM $Ce_{1-x}Zr_xO_2$-MSS samples had a peak present near 600 cm^{-1} indicative of distortions in the cubic lattice brought by addition of Zr.[46] When the Zr content is increased to $x > 0.3$ for 3DOM $Ce_{1-x}Zr_xO_2$-MSS, vastly dissimilar spectra are observed from focusing the laser on different areas of a particle of a given sample (Figure 7.5). These spectra show that widespread inhomogeneities are present in the samples, as was observed with PXRD. Furthermore, for a given high Zr-content sample, spectra can be obtained that contain Raman modes (i.e., near 300 cm^{-1}) corresponding to the tetragonal space group $P4_2/nmc$.[46] It seems that the t″ phase coexists with the cubic phase in these inhomogeneous samples.

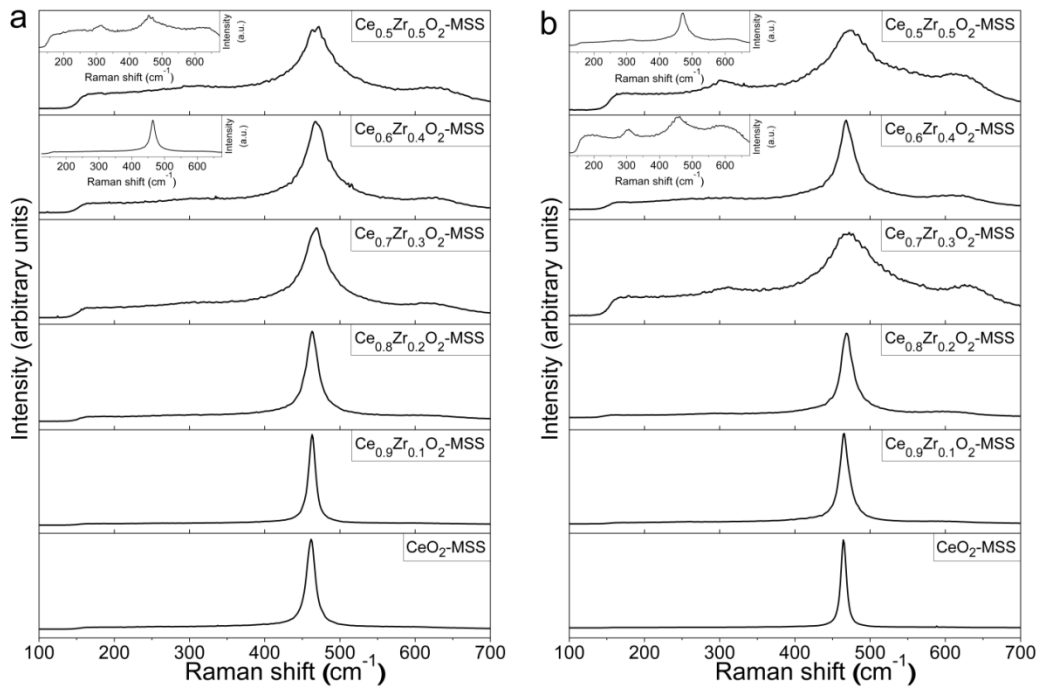

Figure 7.5 Raman spectra for the as-made (a) and cycled (b) 3DOM $Ce_{1-x}Zr_xO_2$-MSS samples. The insets shown for $x = 0.4$ and $x = 0.5$ are taken from different areas on the samples, showing that inhomogeneities are located throughout the sample. The peak that emerges in the mixed oxides at 600 cm^{-1} is indicative of a loss of symmetry in the cubic lattice resulting from Zr addition. Peaks corresponding to the t″ phase (131, 307, 626 cm^{-1}) begin to appear for $x > 0.2$, becoming more prominent as Zr content increases. However, as the insets show, some spectra are found in these inhomogeneous samples that are more Ce-rich and lack peaks corresponding tetragonal vibration modes. Inhomogeneities observed in the as-made samples are still present after cycling (b).

In contrast to the 3DOM materials synthesized with methanolic solutions, the as-synthesized and cycled 3DOM $Ce_{1-x}Zr_xO_2$-PM samples have a high degree of uniformity in obtained spectra (Figure 7.6). Spectra obtained across a given sample did not show any significant differences in peak positions or shapes, indicating improved homogeneity over the methanolic samples. In addition to the assessment of the homogeneity, determination of the polymorphs present in the Pechini samples was possible. A peak centered at 464 cm^{-1} was observed for both the as-made and cycled 3DOM CeO_2-PM, corresponding to the T_{2g} mode present in the cubic lattice. In the 3DOM $Ce_{0.9}Zr_{0.1}O_2$ and $Ce_{0.8}Zr_{0.2}O_2$-PM samples, the broad peak at around ~600 cm^{-1} indicates distortions in the cubic lattice due to the presence of the Zr. When the Zr content is $x > 0.2$ (in $Ce_{1-x}Zr_xO_2$), a new peak can be observed near 300 cm^{-1} that is associated with a tetragonal Raman mode.[36,46] The appearance of the new peak is indicative of the formation of the t″ crystal phase,

which cannot be resolved in the diffraction studies.[36] It is also interesting to note that cycling has little effect on the spectra, except for sharpened tetragonal peaks in the 3DOM $Ce_{0.5}Zr_{0.5}O_2$-PM sample (Figure 7.6).

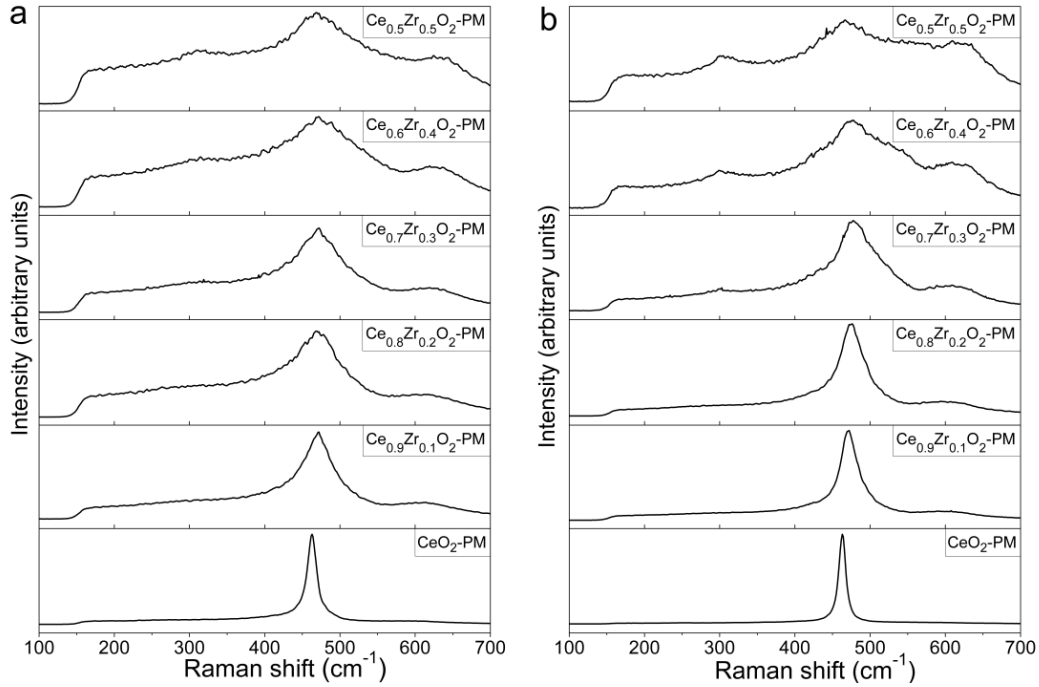

Figure 7.6 Raman spectra for the as-made (a) and cycled (b) 3DOM $Ce_{1-x}Zr_xO_2$-PM samples. Spectra were taken in different locations on a given sample. These Raman spectra for a given mixed oxide composition were all similar in appearance, indicating a high degree of homogeneity. Distortions in the cubic lattice generate the peak at 600 cm^{-1}. The appearance of a peak at 300 cm^{-1} is indicative of a tetragonal distortion present in the samples with $x > 0.2$ (the t″ phase). The patterns undergo little change after samples are cycled at 825 °C.

7.3.3 Crystallite Size Analysis

The Scherrer equation allowed for estimation of the crystallite size in 3DOM $Ce_{1-x}Zr_xO_2$ samples through the analysis of PXRD line broadening (Table 7.1). Crystallite sizes for the homogeneous as-made and cycled 3DOM $Ce_{1-x}Zr_xO_2$-PM samples were impacted by the presence of Zr. The beneficial property of Zr in mitigating the extent of grain growth at high temperatures is clearly observed in the cycled 3DOM $Ce_{1-x}Zr_xO_2$-PM samples. As seen in Table 7.1, the crystallite size decreases dramatically from 73.8 nm in 3DOM CeO_2-PM to only 9.7 nm in 3DOM $Ce_{0.5}Zr_{0.5}O_2$-PM. Solute drag caused by the Zr ions interfering with grain

boundary diffusion is a probable cause for the reduced crystal growth. Colón et al. also suggested the possibility that phase demixing could be responsible for the smaller crystallite sizes observed for $Ce_{1-x}Zr_xO_2$ samples with $0.3 < x < 0.5$.[31] However, both PXRD and Raman spectroscopy suggest that phase separation is not at work in this case. When compared to the 3DOM $Ce_{1-x}Zr_xO_2$-MSS materials, the as-made Zr-containing 3DOM $Ce_{1-x}Zr_xO_2$-PM samples have crystallite sizes smaller than those of the methanolic samples (Table 7.1). Crystallite sizes for the 3DOM $Ce_{1-x}Zr_xO_2$-PM materials are also consistently smaller than those of the MSS samples after cycling, especially for samples with lower amounts of Zr. This may be due to the smaller initial crystallite size of the Pechini samples or to the greater homogeneity in the samples relative to the methanolic samples.

Table 7.1 Crystallite sizes (before and after cycling) determined from the XRD analysis of 3DOM $Ce_{1-x}Zr_xO_2$-MSS and $Ce_{1-x}Zr_xO_2$-PM. Crystallite size was calculated using the Scherrer equation.

Material	crystallite size (nm)	
	as-made	Cycled
3DOM CeO_2-MSS	15.0	81.0
3DOM $Ce_{0.9}Zr_{0.1}O_2$-MSS	11.8	48.2
3DOM $Ce_{0.8}Zr_{0.2}O_2$-MSS	11.4	26.8
3DOM $Ce_{0.7}Zr_{0.3}O_2$-MSS	8.4	14.3
3DOM $Ce_{0.6}Zr_{0.4}O_2$-MSS	8.8	15.0
3DOM $Ce_{0.5}Zr_{0.5}O_2$-MSS	7.8	12.5
3DOM CeO_2-PM	7.4	73.8
3DOM $Ce_{0.9}Zr_{0.1}O_2$-PM	5.1	18.2
3DOM $Ce_{0.8}Zr_{0.2}O_2$-PM	4.1	14.8
3DOM $Ce_{0.7}Zr_{0.3}O_2$-PM	5.5	11.6
3DOM $Ce_{0.6}Zr_{0.4}O_2$-PM	4.4	10.6
3DOM $Ce_{0.5}Zr_{0.5}O_2$-PM	5.9	9.7

Overall, the Pechini method considerably aided homogeneity, allowed for the synthesis of products with a well-controlled crystal structure, and provided smaller average crystallite sizes. The Pechini method allowed for a homogeneous product through a polymer gel network containing well-distributed chelated (via citric acid) cations. These cations formed oxide nuclei

that underwent solid state reactions during the course of thermal treatment, forming the homogeneous 3DOM mixed oxides.[47] While the high degree of homogeneity did not further boost fuel productivity in the mixed oxides (as shown later), the use of the Pechini method allows for the rational synthesis of simple-to-characterize, single phase cubic or t″ $Ce_{1-x}Zr_xO_2$. It is then possible to assess the fuel production for a given composition of $Ce_{1-x}Zr_xO_2$, while avoiding the complications of determining the contributions to productivity from several different compositions present in a material. Finally, the 3DOM $Ce_{1-x}Zr_xO_2$-PM samples had a lower degree of crystal grain growth, which is essential for preservation of the 3DOM structure.

7.3.4 Analysis of Changes in Morphology Induced by Cycling

Structures and morphologies of the as-synthesized 3DOM $Ce_{1-x}Zr_xO_2$-PM samples were studied by scanning and transmission electron microscopy. The SEM images confirm that an open, macroporous framework was obtained in all cases (Figure 7.7) and that the 3DOM morphology was not altered by increasing Zr content. Features of the 3DOM $Ce_{1-x}Zr_xO_2$-PM were measured, in the interest of quantifying differences between the structures. Differences in the pore spacing (the repeat distance between adjacent pores), wall thickness (the solid material between adjacent pores), and window size (the open space between adjacent pores) were found to be minimal among the Pechini samples with different levels of Zr concentration (Table 7.2).

Table 7.2 Pore spacings (repeat distance from pore to pore), pore window sizes, and wall thicknesses for the $Ce_{1-x}Zr_xO_2$-PM materials before and after cycling. Measurements made by Stephen Rudisill.

	as-made			**cycled**		
Material	pore spacing (nm)	wall thickness (nm)	pore window diameter (nm)	pore spacing (nm)	wall thickness (nm)	pore window diameter (nm)
3DOM CeO_2-PM	301 ± 6	70 ± 6	73 ± 8	285 ± 4	37 ± 6	117 ± 10
3DOM $Ce_{0.9}Zr_{0.1}O_2$-PM	284 ± 3	47 ± 5	97 ± 12	274 ± 8	33 ± 5	110 ± 12
3DOM $Ce_{0.8}Zr_{0.2}O_2$-PM	311 ± 2	43 ± 5	104 ± 10	305 ± 2	39 ± 6	115 ± 13
3DOM $Ce_{0.7}Zr_{0.3}O_2$-PM	304 ± 3	62 ± 9	113 ± 10	271 ± 3	57 ± 6	137 ± 11
3DOM $Ce_{0.6}Zr_{0.4}O_2$-PM	283 ± 4	59 ± 6	93 ± 8	282 ± 3	48 ± 7	93 ± 6
3DOM $Ce_{0.5}Zr_{0.5}O_2$-PM	321 ± 2	67 ± 7	81 ± 6	290 ± 3	47 ± 7	101 ± 10

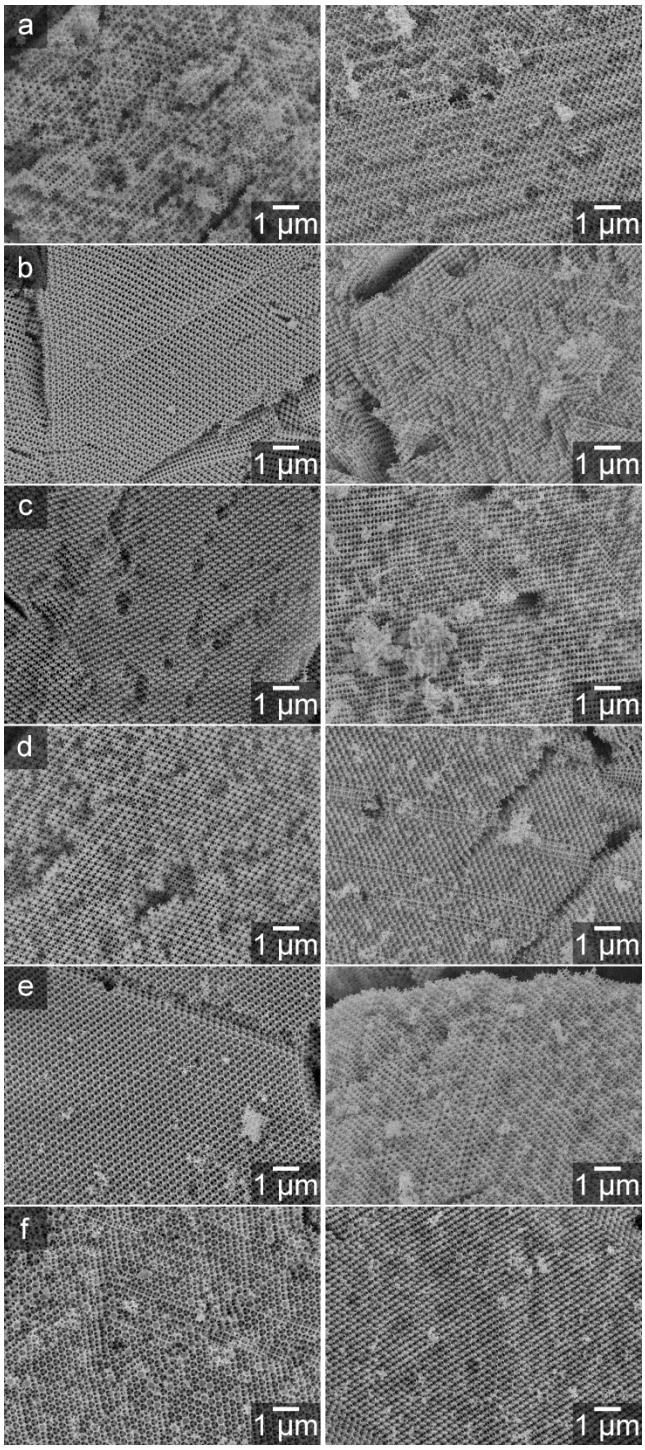

Figure 7.7 SEM images of 3DOM CeO_2-PM (a), $Ce_{0.9}Zr_{0.1}O_2$-PM (b), $Ce_{0.8}Zr_{0.2}O_2$-PM (c), $Ce_{0.7}Zr_{0.3}O_2$-PM (d), $Ce_{0.6}Zr_{0.4}O_2$-PM (e), and $Ce_{0.5}Zr_{0.5}O_2$-PM (f) before and after cycling. The 3DOM structure is retained throughout cycling. After cycling, the nodes of the 3DOM structure (formed from octahedral and tetrahedral holes in the parent template) grow more pronounced due to sintering, though this is less extensive in the samples with high Zr content.

When cycled, the 3DOM $Ce_{1-x}Zr_xO_2$-PM samples undergo structural changes which were particularly noticeable in the CeO_2, $Ce_{0.9}Zr_{0.1}O_2$, and $Ce_{0.8}Zr_{0.2}O_2$ samples. A thinning of the walls and wider windows between pores is observed, producing a more "open" structure. Despite these changes, the overall 3DOM structure is retained after cycling for all Zr concentrations. The changes in wall thickness and window width are quantifiable for the 3DOM CeO_2-PM sample (Table 7.2); however, whether this effect is present in the mixed oxide samples is harder to discern from the SEM data. Thus, the samples were further analyzed under the TEM, allowing for qualitative assessment of the individual features.

The effect of increasing Zr content with respect to postcycling morphology in 3DOM $Ce_{1-x}Zr_xO_2$-PM is evident from the TEM images. For the cycled 3DOM CeO_2-PM sample (Figure 7.8 a), the structure of the walls has been drastically altered. Single crystallites comprise the walls between nodes in the 3DOM structure, and the nodes themselves are composed of large, fused grains. However, as was noted in the SEM images, the macroporosity and ordering of the structure is still intact. In the samples that contain Zr, changes to wall thickness and window size are mitigated with increasing Zr content (Figure 7.8 b–f). This trend continues to the 3DOM $Ce_{0.5}Zr_{0.5}O_2$-PM sample, the structure of which undergoes very little morphological change after cycling. The changes in the wall structure are from sintering processes, which result in material being transported to the nodes (as observed in the SEM analysis) of the 3DOM skeleton at the expense of the walls. This Ostwald ripening-like effect has been observed in other 3DOM systems.[16,48] It is clear that incorporation of high levels of Zr is beneficial from a structural standpoint. For the reactions conducted at 825 °C, excellent retention of the 3DOM structure can be obtained through addition of Zr.

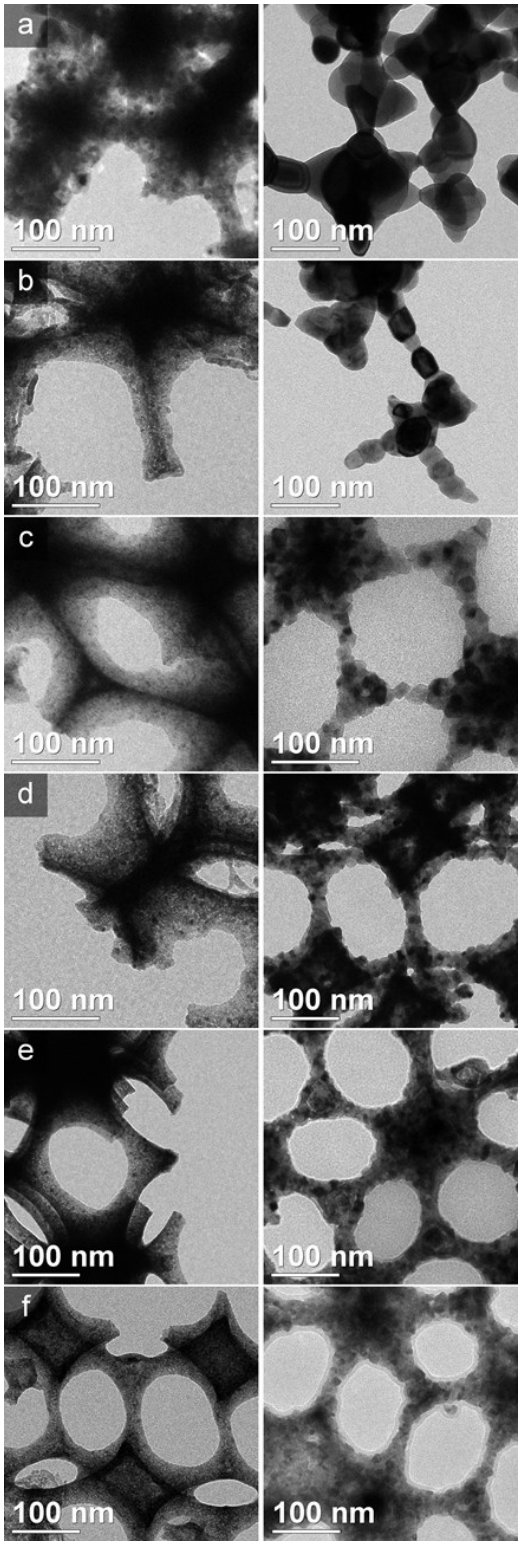

Figure 7.8 TEM images of 3DOM CeO_2-PM (a), $Ce_{0.9}Zr_{0.1}O_2$-PM (b), $Ce_{0.8}Zr_{0.2}O_2$-PM (c), $Ce_{0.7}Zr_{0.3}O_2$-PM (d), $Ce_{0.6}Zr_{0.4}O_2$-PM (e), and $Ce_{0.5}Zr_{0.5}O_2$-PM (f) before and after cycling. Images taken by Stephen Rudisill.

The 3DOM $Ce_{1-x}Zr_xO_2$-MSS samples were also studied under SEM and TEM. Comparing the two methods, it is notable that the 3DOM $Ce_{1-x}Zr_xO_2$-PM materials give a more faithful replication of the template than the 3DOM $Ce_{1-x}Zr_xO_2$-MSS samples. Pore spacings of the 3DOM $Ce_{1-x}Zr_xO_2$-PM materials were typically on the order of 300 nm, regardless of dopant level. However, the spacings for the 3DOM $Ce_{1-x}Zr_xO_2$-MSS samples were around 390 nm. Windows and walls were approximately 100 and 50 nm in the PM samples, respectively, and approximately 120 and 70 nm in the MSS.

Under the TEM, a significant degree of intergrain porosity in the walls of the 3DOM $Ce_{1-x}Zr_xO_2$-MSS can be observed; this porosity is not present in the 3DOM $Ce_{1-x}Zr_xO_2$-PM (Figure 7.9). In addition, the crystallite morphology and arrangement is different between the two synthesis methods. The crystallites of the methanolic samples have a wide range of shapes and sizes and are often separated by wormlike pores. Pechini samples contain largely spherical crystallites in close contact with one another. After cycling, the methanolic samples appear to undergo a greater degree of grain growth than the Pechini samples, in agreement with the XRD data.

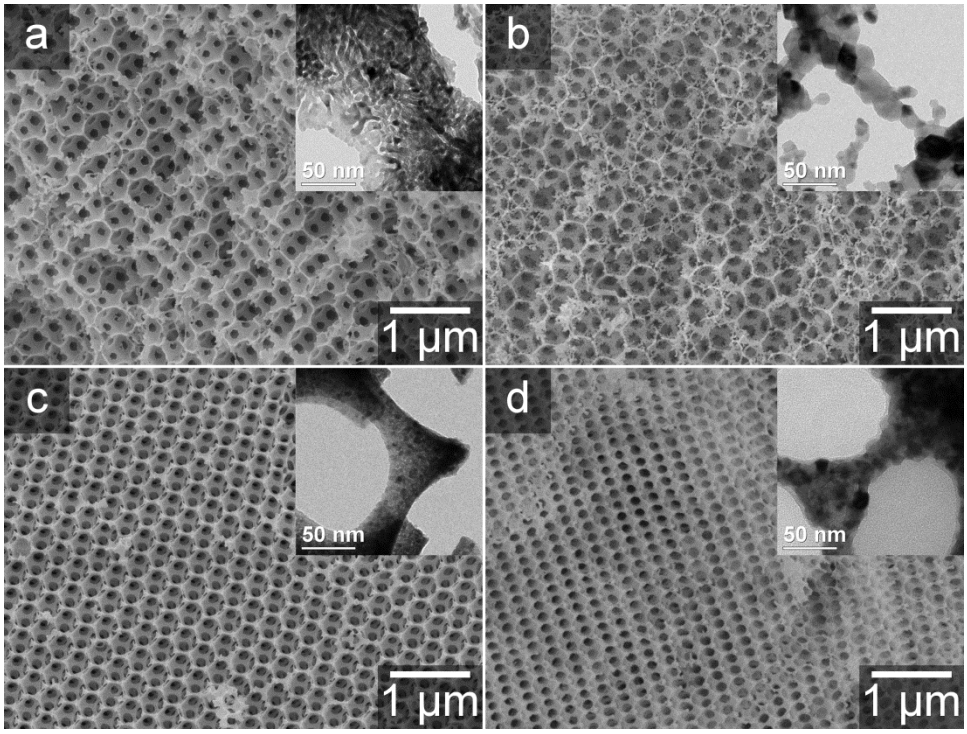

Figure 7.9 (a) SEM image of 3DOM $Ce_{0.6}Zr_{0.4}O_2$-MSS, as-synthesized. The TEM image in the inset shows grains of random size and shape, leading to significant textual mesoporosity within the walls of the structure. (b) SEM image of 3DOM $Ce_{0.6}Zr_{0.4}O_2$-MSS after cycling. The 3DOM structure is retained, but the mesoporosity (as seen in the inset) is lost, and the walls become thinner. (c) For 3DOM $Ce_{0.6}Zr_{0.4}O_2$-PM, the pores are smaller and more regular. Widespread mesoporosity is not observed. (d) After cycling, 3DOM $Ce_{0.6}Zr_{0.4}O_2$-PM undergoes little structural change, compared to the material synthesized via methanolic salt solutions. TEM images taken by Stephen Rudisill.

7.3.5 Textural Stability for As-Made and Cycled 3DOM CeO_2 and 3DOM $Ce_{1-x}Zr_xO_2$

Analysis of the textural stability of the 3DOM $Ce_{1-x}Zr_xO_2$-PM demonstrates that addition of Zr helps to preserve the surface area of the 3DOM nanostructure. Examining Table 7.3, it is clear that the Pechini samples with low Zr content (3DOM CeO_2 to $Ce_{0.8}Zr_{0.2}O_2$-PM) have limited retention of BET surface area upon cycling. The most dramatic losses are observed in the pure 3DOM CeO_2-PM sample. By further increasing the Zr content to $x > 0.2$, progressively better retention of surface area is achieved. This trend culminates with the 3DOM $Ce_{0.5}Zr_{0.5}O_2$-PM sample that retains the surface area it had before cycling. Considering the mean crystallite size of the samples and the obtained TEM images, the observed pattern of surface area change is to be expected. Samples with lower Zr content (3DOM $Ce_{0.9}Zr_{0.1}O_2$ and $Ce_{0.8}Zr_{0.2}O_2$-PM) experience more grain growth (Table 7.1) and greater narrowing of the wall structure of the 3DOM network

during cycling. In this case, intergrain porosity is more easily eliminated, as crystallites merge together to form lower numbers of larger crystallites. However, with the higher Zr content samples (3DOM $Ce_{0.7}Zr_{0.3}O_2$ to $Ce_{0.5}Zr_{0.5}O_2$-PM), crystallite growth is fairly limited. Morphologically, there is little change between as-made and cycled samples with both walls and nodes in the 3DOM structure containing numerous crystallites. It can be concluded that intergrain porosity is better retained.

Table 7.3 BET surface areas and pore volumes before and after cycling, showing increased retention of surface area and porosity with increased Zr content. A sample prepared by the methanolic method is listed for comparison.

	BET surface area ($m^2 \cdot g^{-1}$)		**pore volume ($cm^3 \cdot g^{-1}$)**	
material	as-made	Cycled	as-made	cycled
3DOM CeO_2-PM	19.6	9.7	0.085	0.067
3DOM $Ce_{0.9}Zr_{0.1}O_2$-PM	26.0	17.3	0.069	0.064
3DOM $Ce_{0.8}Zr_{0.2}O_2$-PM	26.7	17.8	0.067	0.060
3DOM $Ce_{0.7}Zr_{0.3}O_2$-PM	25.1	21.5	0.084	0.085
3DOM $Ce_{0.6}Zr_{0.4}O_2$-PM	27.2	24.1	0.077	0.094
3DOM $Ce_{0.5}Zr_{0.5}O_2$-PM	22.2	24.5	0.070	0.098
3DOM $Ce_{0.5}Zr_{0.5}O_2$-MSS	44.7	23.4	0.24	0.12

Pore volume and isotherm and pore size information support the BET surface area findings. Losses in pore volume are observed for the samples with low Zr content (Table 7.3). In contrast, pore volume remains approximately the same or increases after cycling for 3DOM $Ce_{0.7}Zr_{0.3}O_2$, $Ce_{0.6}Zr_{0.4}O_2$, and $Ce_{0.5}Zr_{0.5}O_2$-PM. The isotherms of the as-made and cycled 3DOM $Ce_{0.7}Zr_{0.3}O_2$, $Ce_{0.6}Zr_{0.4}O_2$, and $Ce_{0.5}Zr_{0.5}O_2$-PM are different from the isotherms of samples with lower Zr content. An example of each type is shown (high and low Zr content) in Figure 7.10. Isotherms for the as-made and cycled 3DOM $Ce_{1-x}Zr_xO_2$-PM samples with $x < 0.3$ are of type II, which is typical for macroporous materials.[49] The pore size distribution for these samples indicates that some intergrain mesoporosity (with a diameter of around 4 nm) exists within the as-made samples (Figure 7.10 a). Much of that porosity is lost during cycling, which can be explained by grain growth, as is revealed by TEM microscopy (Figure 7.11). Hysteresis is observed in the isotherms

for the as-made 3DOM $Ce_{0.7}Zr_{0.3}O_2$, $Ce_{0.6}Zr_{0.4}O_2$, and $Ce_{0.5}Zr_{0.5}O_2$-PM that closes at ~0.45P/P_0, probably due to the tensile strength effect.[50] BJH analyses of the adsorption branches for these as-made, high Zr content samples show a fairly wide range of pore sizes with a small peak centered at around 4 nm in diameter (Figure 7.10 b). It appears that these pores are partially eliminated upon cycling; however, some hysteresis remains present in the isotherm at higher partial pressures. From these data, it is clear that a high Zr content further increases the stability of the 3DOM morphology under reducing and oxidizing conditions at 825 °C. Aside from the application presently under investigation, this stability suggests that the 3DOM material holds considerable promise as a stable catalytic material, i.e., for the water gas shift reaction, at temperatures at or below 800–900 °C.

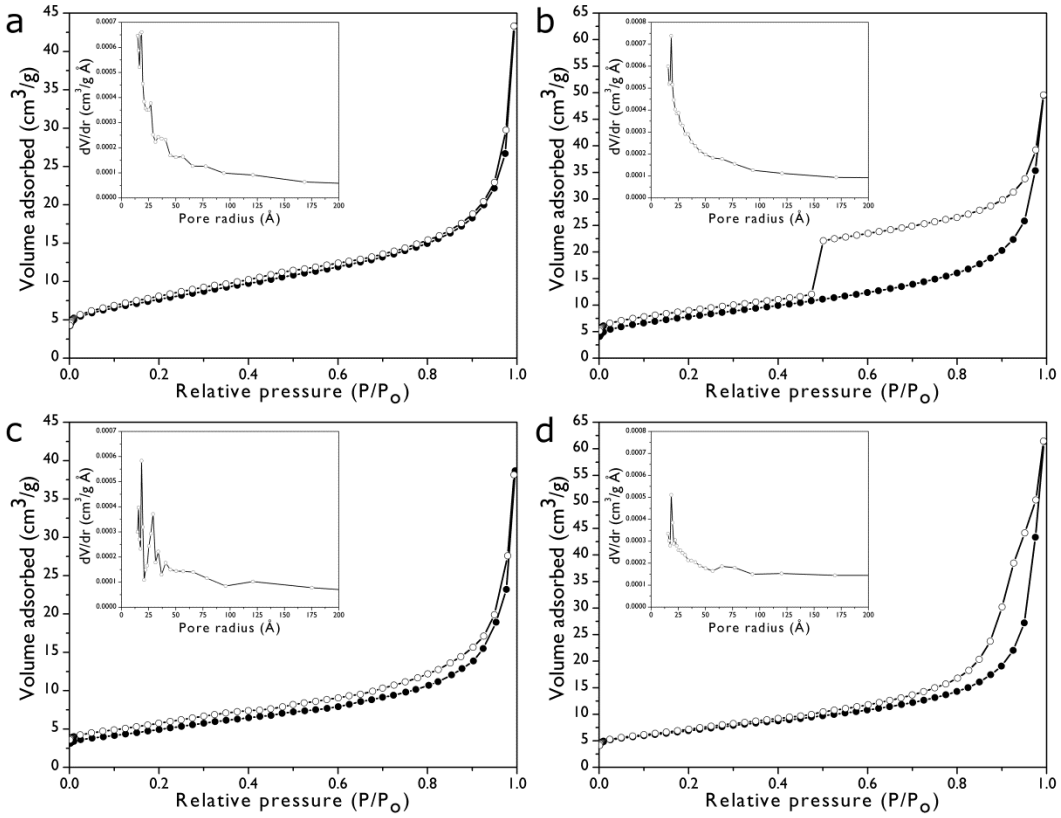

Figure 7.10 Compilation of isotherms and pore size distributions for as-made 3DOM $Ce_{0.8}Zr_{0.2}O_2$-PM (a) and $Ce_{0.6}Zr_{0.4}O_2$-PM (b) and for these materials after cycling (c and d). There is little change between the isotherms for the as-made and cycled $Ce_{0.8}Zr_{0.2}O_2$-PM. Mesopores around 4 nm in diameter are present in the as-made sample that are eliminated on cycling. More hysteresis is observed in the $Ce_{0.6}Zr_{0.4}O_2$-PM, as are pores 4 nm in diameter. Again, cycling eliminates the small mesopores, but some hysteresis remains.

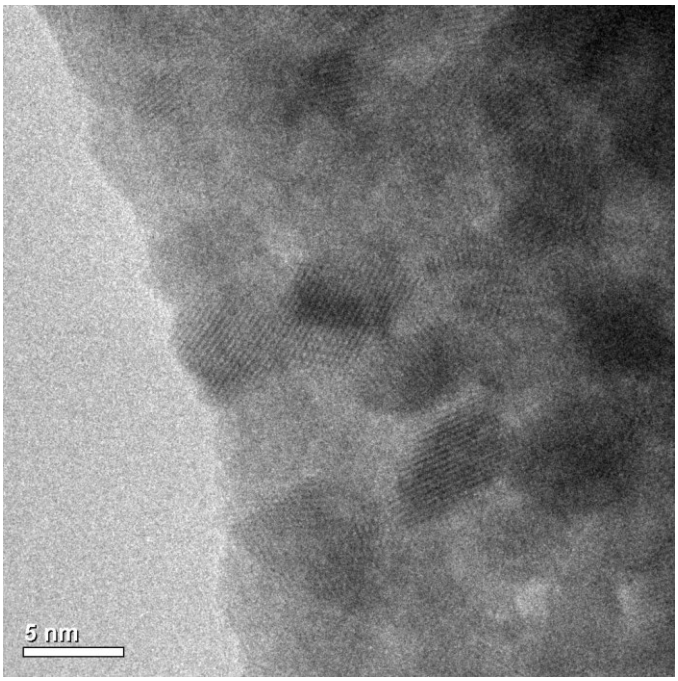

Figure 7.11 TEM image of a $Ce_{0.8}Zr_{0.2}O_2$-PM sample. Small, lighter regions can be observed between crystallites. These regions are from scattered intergranular pores that can also be observed in the BJH pore size distribution. Image taken by Stephen Rudisill.

A further useful comparison can be made between the 3DOM $Ce_{1-x}Zr_xO_2$-MSS and 3DOM $Ce_{1-x}Zr_xO_2$-PM samples in terms of pore volume and surface area. Samples prepared by the methanolic synthesis have higher initial surface areas and pore volumes than the Pechini samples. Much of this porosity is from the mesopore-sized void spaces between crystallites which are observed in TEM images (Figure 7.9). This intergrain porosity boosts BET surface areas to 40 to 60 m^2/g and pore volumes to greater than 0.01 cm^3/g for MSS samples, when compared to the lower surface areas (~20 m^2/g) and pore volumes (below 0.01 cm^3/g) for the Pechini samples. However, cycling eliminates the majority of this "extra" porosity present in the methanolic samples. When comparing the 3DOM $Ce_{0.5}Zr_{0.5}O_2$-MSS and PM samples (Table 7.3), it is apparent that the post-cycling BET surface areas and pore volumes of each are virtually identical. TEM and SEM images of the cycled methanolic and Pechini samples also show that their appearance is similar (Figure 7.9), with the 3DOM $Ce_{1-x}Zr_xO_2$-MSS intergrain porosity eliminated after cycling. The operational temperature of the fuel production step—let alone the thermal reduction step—is too high to permit the retention of porosity in the mesoporous regime. It therefore does not appear worthwhile to attempt to engineer additional mesoporosity in these

materials and form hierarchical macro-/mesoporous samples for high temperature applications. This is a conclusion that is in line with findings made in previous studies.[15,32]

7.3.6 3DOM CeO_2 and 3DOM $Ce_{1-x}Zr_xO_2$ Fuel Production

To understand the influence of the synthesis method and Zr content on the production of H_2 from 3DOM CeO_2 and 3DOM $Ce_{1-x}Zr_xO_2$, the materials were subjected to six redox cycles, measuring the H_2 production rate and the total amount of H_2 produced in each cycle. The results are summarized in Figure 7.12 and Table 7.4. Table 7.4 lists the maximum rate of H_2 production and the productivity (the amount of H_2 produced over 10 min) achieved for each sample in the first and sixth cycles. Figure 7.12 shows the rate of H_2 production as a function of time during the sixth cycle. In Figure 7.12 a, a comparison is made between samples of identical mixed oxide composition synthesized via the methanolic and Pechini methods, and it also includes the rate of H_2 production for low surface area, nonporous, commercially available CeO_2. The H_2 production rates from the single-phase 3DOM $Ce_{1-x}Zr_xO_2$-PM samples are compared in Figure 7.12 b. For all samples the H_2 production rate rose rapidly as H_2O flowed into the sample, reached a maximum, and then slowly decayed as oxygen vacancies were depleted.

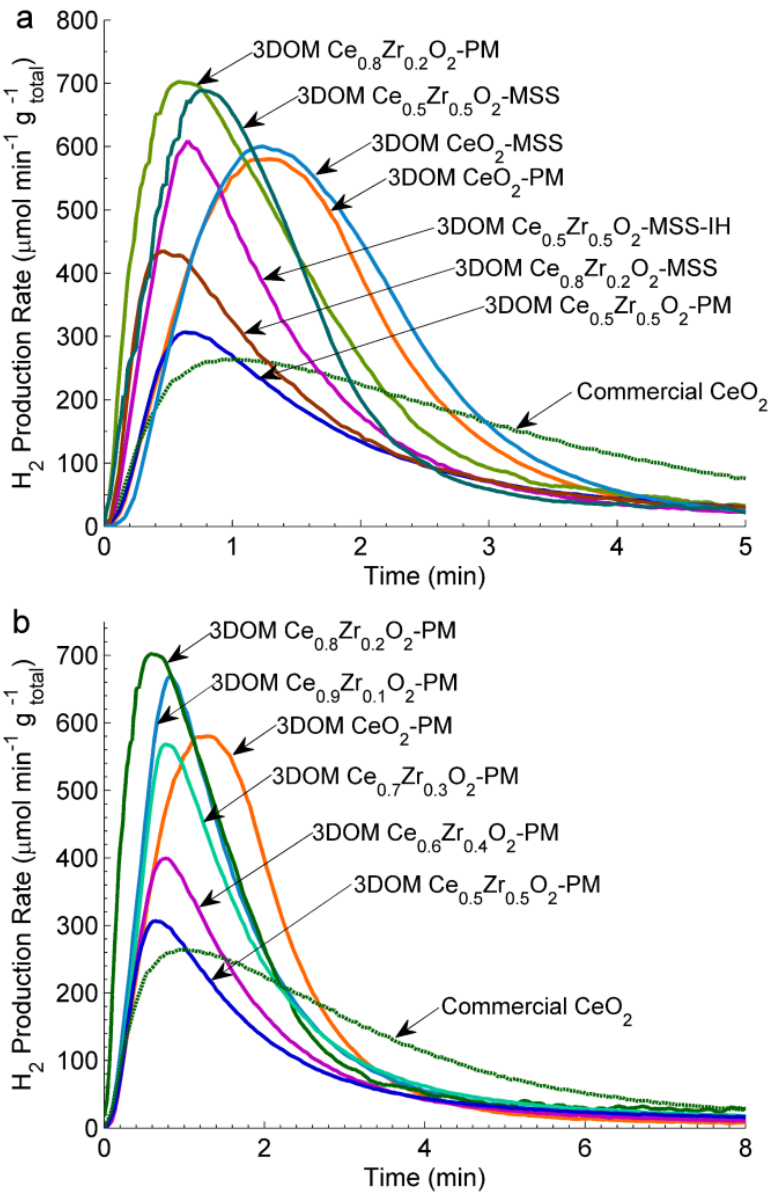

Figure 7.12 H_2 production rates from the sixth redox cycle over (a) 3DOM CeO_2-PM, 3DOM CeO_2-MSS, 3DOM $Ce_{0.8}Zr_{0.2}O_2$-PM, 3DOM $Ce_{0.8}Zr_{0.2}O_2$-MSS, 3DOM $Ce_{0.5}Zr_{0.5}O_2$-PM, 3DOM $Ce_{0.5}Zr_{0.5}O_2$-MSS-IH, and 3DOM $Ce_{0.5}Zr_{0.5}O_2$-MSS and (b) 3DOM CeO_2-PM, 3DOM $Ce_{1-x}Zr_xO_2$-PM, and commercial CeO_2 (T=825°C, y_{H2O} = 2.7 mol%, and Q_{total} = 275-285 mL·min^{-1}, except for the commercial CeO_2 sample for which Q_{total}=330 mL·min^{-1}). Data collected and plotted by Professor Luke Venstrom.

Table 7.4 The maximum rate of H_2 production and the productivity for the 3DOM $Ce_{1-x}Zr_xO_2$-PM and -MSS samples and the commercial CeO_2 sample in the oxidation step of the first and sixth H_2O-splitting cycles. The mass of the sample tested is also included. Data analysis performed by Luke Venstrom.

		peak production rate ($\mu mol \cdot min^{-1} \cdot g^{-1}$)		productivity ($\mu mol \cdot g^{-1}$)	
Material	**mass (g)**	cycle 1	cycle 6	cycle 1	cycle 6
3DOM CeO_2-PM	0.23	720 ± 20	580 ± 20	1460 ± 30	1220 ± 30
3DOM CeO_2-MSS	0.24	610 ± 20	600 ± 20	1440 ± 30	1310 ± 30
3DOM $Ce_{0.9}Zr_{0.1}O_2$-PM	0.24	660 ± 20	670 ± 20	1400 ± 30	1380 ± 30
3DOM $Ce_{0.8}Zr_{0.2}O_2$-PM	0.21	790 ± 20	730 ± 20	1530 ± 40	1330 ± 30
3DOM $Ce_{0.8}Zr_{0.2}O_2$-MSS	0.29	800 ± 20	690 ± 20	1220 ± 30	1180 ± 30
3DOM $Ce_{0.7}Zr_{0.3}O_2$-PM	0.20	590 ± 20	570 ± 10	1250 ± 30	1120 ± 30
3DOM $Ce_{0.6}Zr_{0.4}O_2$-PM	0.25	420 ± 10	400 ± 10	970 ± 20	780 ± 20
3DOM $Ce_{0.5}Zr_{0.5}O_2$-PM	0.27	300 ± 10	310 ± 10	760 ± 20	690 ± 20
3DOM $Ce_{0.5}Zr_{0.5}O_2$-MSS	0.22	500 ± 10	610 ± 10	930 ± 20	960 ± 20
3DOM $Ce_{0.5}Zr_{0.5}O_2$-MSS	0.11	460 ± 10	440 ± 10	930 ± 20	820 ± 20
Commercial CeO_2	1.27	250 ± 10	270 ± 10	1060 ± 20	1030 ± 20

The graphs in Figure 7.12 emphasize the improvement in H_2O-splitting kinetics that is provided by the moderate surface areas of the 3DOM $Ce_{1-x}Zr_xO_2$. The H_2 production rates of the 3DOM materials with specific surface areas of 10–25 $m^2\ g^{-1}$ are significantly faster than the rate of H_2 production of the commercial CeO_2 with a low specific surface area of $\leq$1.0 $m^2\ g^{-1}$. For example, the peak production rate was increased by a factor of 2.5 with the 3DOM CeO_2-PM when compared to the commercial sample (Figure 7.12). Given the importance of specific surface area for fuel production, one might expect changes in the specific surface area of the 3DOM samples during cycling to influence H_2O-splitting kinetics. There was, however, little statistically significant cycle-to-cycle variation in H_2 production rates (Table 7.4 and Figure 7.13). Thus, the difference in the specific surface areas of the 3DOM samples is not the distinguishing feature for fuel production. Similar behavior has been observed in $Ce_{1-x}Zr_xO_2$ soot oxidation catalysts with moderate surface area.[51] Increasing the BET surface areas of the catalysts to 30 m^2/g was shown to lower the temperature needed for soot oxidation, but further increases in surface area had no effect on the soot oxidation temperature. Since differences in surface area do not affect the 3DOM $Ce_{1-x}Zr_xO_2$ materials, it is the method of synthesis and the level of Zr doping that are the two factors with the greatest influence on H_2 production.

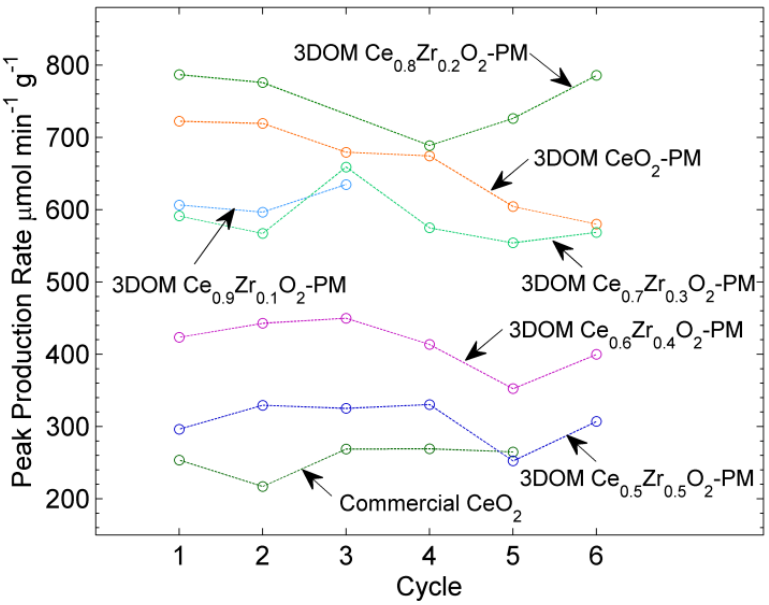

Figure 7.13 Peak hydrogen production rates over 6 cycles for the 3DOM $Ce_{1-x}Zr_xO_2$-PM and commercial CeO_2 samples. Little variability is observed in these data. (T = 825 °C, y_{H2O} = 2.7 mol% and Q_{total} = 275-285 mL min^{-1}, except for the commercial CeO_2 sample for which Q_{total} = 330 mL min^{-1}). Data collected and plotted by Luke Venstrom.

The similarities and differences between the MSS and Pechini samples are apparent from reactivity data for the samples shown in Figure 7.12. Both the 3DOM CeO_2-MSS and CeO_2-PM materials behaved identically (within measurement uncertainty), a result that was true for the majority of redox cycles (Figure 7.14). Since fuel production rates and productivity of the two pure samples are similar, this suggests that fuel production is independent of the synthesis method for a pure material. This result is further confirmed for the 3DOM $Ce_{0.8}Zr_{0.2}O_2$-MSS and -PM samples, which both have a high degree of homogeneity and have similar H_2 production rates and productivity.

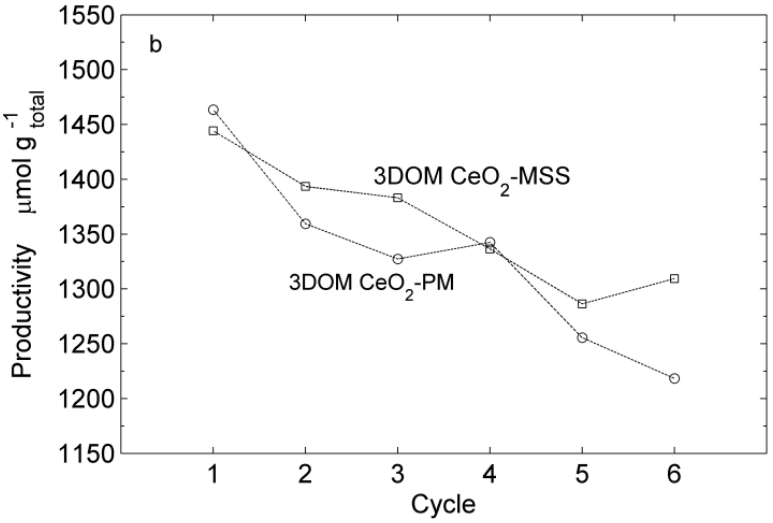

Figure 7.14 Peak rates of H_2 production (a) and productivity (b) for CeO_2-PM and CeO_2-MSS samples over 6 cycles (T = 825 °C, y_{H2O} = 2.7 mol% and Q_{total} = 275-285 mL min^{-1}). Data collected and plotted by Luke Venstrom.

There are differences in H_2 production for the 3DOM $Ce_{0.5}Zr_{0.5}O_2$-MSS and $Ce_{0.5}Zr_{0.5}O_2$-PM that highlight the importance of phase homogeneity. As seen in Figure 7.12 a and Table 7.4, increases in peak production and productivity correlate with increases in heterogeneity at high levels of Zr (x> 0.3). At these levels, the 3DOM $Ce_{1-x}Zr_xO_2$-MSS samples contain widespread inhomogeneities (see above). Both XRD and Raman spectra confirm the presence of Ce-rich distorted cubic domains and Zr-rich tetragonal domains in the methanolic samples. X-ray photoelectron spectroscopy, specifically analysis of the Ce 4d and Zr 3d peaks, allowed for a semiquantitative determination of the surface composition of the 3DOM $Ce_{0.5}Zr_{0.5}O_2$ samples.[52] This data shows that all the samples have roughly the same overall cationic composition (equimolar amounts of Ce and Zr). What is observed in the fuel production is that the overall redox properties depend on the phases present in the sample and not the overall composition, a finding in line with previous research.[28] The 3DOM $Ce_{0.5}Zr_{0.5}O_2$-MSS-IH contains a major phase with a similar (111) d-spacing (3.11 Å) to $Ce_{0.9}Zr_{0.1}O_2$ (Figure 7.3). A phase with that composition should enhance redox activity and peak production, functioning similar to a corresponding single-phase sample. Other Zr-rich phases would have lower peak rates and productivity. Similarly, the 3DOM $Ce_{0.5}Zr_{0.5}O_2$-MSS contains a minor Zr-rich phase and a major Ce-rich phase with diffraction peaks that are shifted to lower values for 2θ. This Ce-rich phase is more active than the phase present in the homogeneous $Ce_{0.5}Zr_{0.5}O_2$-PM. From a standpoint of a suitable material for fuel production, the use of the methanolic route is somewhat advantageous

for $Ce_{1-x}Zr_xO_2$ with $x > 0.3$. Analysis of the surface area and crystallite size for the 3DOM $Ce_{0.5}Zr_{0.5}O_2$-MSS and -PM shows that they have similar stability at 825 °C. However, controlling the extent of heterogeneity was not possible through the methanolic route.

In addition to improving H_2 production by altering the material synthesis methodology, H_2O-splitting kinetics can also be improved by Zr addition. The single phase 3DOM $Ce_{0.8}Zr_{0.2}O_2$-PM highlights this benefit, as it achieved the fastest rates of H_2 production. The substitution of Ce ions with Zr ions in the 3DOM $Ce_{1-x}Zr_xO_2$ increases the redox activity of the remaining Ce ions. This effect is directly observed when the H_2 production rates are normalized relative to the mass of CeO_2 in the mixed oxide. By analyzing the normalized H_2 production rates, the $Ce_{0.8}Zr_{0.2}O_2$-PM still produced H_2 faster than in any other sample (Figure 7.15). Increases in the redox activity of Ce ions in $Ce_{1-x}Zr_xO_2$ have been previously observed and have been attributed to the formation of domains of a pyrochlore phase or to the ability of Ce^{3+} ions to better accommodate undersized Zr^{4+} ions in the lattice.[24,53] It is important to note that the increase in the Ce ion redox activity also causes an increase in H_2 productivity for $Ce_{0.8}Zr_{0.2}O_2$-PM, which mirrors published results (Table 7.4).[32]

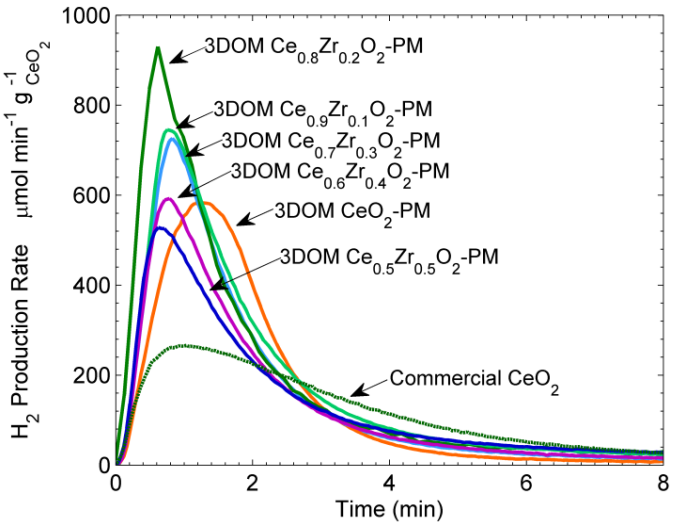

Figure 7.15 H_2 production rates normalized to the mass of CeO_2 present in the sample for sixth redox cycle. All 3DOM $Ce_{1-x}Zr_xO_2$-PM samples and the commercial CeO_2 sample are shown. (T=825°C, y_{H2O} = 2.7 mol%, and Q_{total} = 275-285 mL·min^{-1}, except for the commercial CeO_2 sample for which Q_{total}=330 mL·min^{-1}). Data collected and plotted by Luke Venstrom.

While the 3DOM $Ce_{0.8}Zr_{0.2}O_2$-PM material benefited the most from the addition of Zr, this benefit extended to other 3DOM $Ce_{1-x}Zr_xO_2$-PM samples as well. The H_2 production rates of 3DOM $Ce_{0.9}Zr_{0.1}O_2$-PM in the sixth cycle were greater than those of 3DOM CeO_2-PM, and the increase can be attributed to the activity of the Ce ions (Figure 7.15) and the improved stability of the Zr-doped material (Table 7.4). 3DOM $Ce_{0.7}Zr_{0.3}O_2$-PM produced H_2 at similar rates to 3DOM CeO_2-PM. With 3DOM $Ce_{0.7}Zr_{0.3}O_2$-PM, the enhancement in the Ce ion activity was balanced by the unfavorable effect of replacing chemically active CeO_2 with chemically inactive ZrO_2. The 3DOM $Ce_{0.6}Zr_{0.4}O_2$-PM and $Ce_{0.5}Zr_{0.5}O_2$-PM materials produced H_2 more slowly than 3DOM CeO_2-PM, and they are thus less effective fuel producers. These high Zr content materials are, however, structurally stable at 825 °C, and as was discussed, the introduction of heterogeneity into these materials improves H_2O-splitting kinetics.

7.4 Conclusions

3DOM $Ce_{1-x}Zr_xO_2$ was evaluated as a thermochemical water splitting catalyst. Two synthesis pathways for this 3DOM mixed oxide were explored: a methanolic salt solution method and a Pechini gel method. Samples with differing amounts of Zr were prepared to determine the effects on thermal stability and H_2 generation. The synthesis route had a profound impact on the homogeneity of the products. Samples from the methanolic synthesis contained Ce-rich and Zr-rich domains that became more prevalent with higher Zr content. In contrast, the Pechini method produced compositionally homogeneous samples. Increasing the Zr content for all 3DOM $Ce_{1-x}Zr_xO_2$ samples improved the thermal stability at 825 °C in terms of crystallite size, retention of the 3DOM morphology, and BET surface area. However, differences in H_2O-splitting kinetics did not directly correlate with changes in surface area of the 3DOM $Ce_{1-x}Zr_xO_2$ samples, suggesting that there is a threshold of available surface area beyond which appreciable returns in reactivity are diminished. Total fuel production and peak rates of production were affected by heterogeneity in composition present in the 3DOM $Ce_{0.5}Zr_{0.5}O_2$-MSS samples. These samples contained Ce-rich phases that performed significantly better than single-phase products. While addition of Zr to 3DOM $Ce_{1-x}Zr_xO_2$-PM with $x > 0.2$ did not improve fuel production or peak production rates over that of CeO_2, this did not hold true for the single-phase 3DOM $Ce_{0.9}Zr_{0.1}O_2$ and $Ce_{0.8}Zr_{0.2}O_2$-PM samples. Both materials exhibited better total productivity and higher peak production rates of H_2 than 3DOM CeO_2-PM. Furthermore, these materials were far more thermally stable during the cycling procedure. The enhancements detailed here can be readily implemented and exploited in other systems for high-temperature heterogeneous catalysis.

References

(1) Otsuka, K.; Hatano, M.; Morikawa, A. Hydrogen from Water by Reduced Cerium Oxide. *J. Catal.* **1983**, *79*, 493-496.

(2) Otsuka, K.; Wang, Y.; Nakamura, M. Direct Conversion of Methane to Synthesis Gas Through Gas-Solid Reaction Using CeO_2-ZrO_2 Solid Solution at Moderate Temperature. *Appl. Catal. A* **1999**, *183*, 317-324.

(3) Abanades, S.; Flamant, G. Thermochemical Hydrogen Production From a Two-Step Solar-Driven Water-Splitting Cycle Based on Cerium Oxides. *Solar Energy* **2006**, *80*, 1611-1623.

(4) Kaneko, H.; Miura, T.; Ishihara, H.; Taku, S.; Yokoyama, T.; Nakajima, H.; Tamaura, Y. Reactive Ceramics of CeO_2-MO_x (M=Mn, Fe, Ni, Cu) for H_2 Generation by Two-Step Water Splitting Using Concentrated Solar Thermal Energy. *Energy* **2007**, *32*, 656-663.

(5) Kang, K.-S.; Kim, C.-H.; Park, C.-S.; Kim, J.-W. Hydrogen Reduction and Subsequent Water Splitting of Zr-Added CeO_2. *J. Ind. Eng. Chem.* **2007**, *13*, 657-663.

(6) Miller, J. E.; Allendorf, M. D.; Diver, R. B.; Evans, L. R.; Siegel, N. P.; Stuecker, J. N. Metal Oxide Composites and Structures for Ultra-High Temperature Solar Thermochemical Cycles. *J. Mater. Sci.* **2008**, *43*, 4714-4728.

(7) Abanades, S.; Legal, A.; Cordier, A.; Peraudeau, G.; Flamant, G.; Julbe, A. Investigation of Reactive Cerium-Based Oxides for H_2 Production by Thermochemical Two-Step Water-Splitting. *J. Mater. Sci.* **2010**, *45*, 4163-4173.

(8) Chueh, W. C.; Haile, S. M. A Thermochemical Study of Ceria: Exploiting an Old Material for New Modes of Energy Conversion and CO_2 Mitigation. *Phil. Trans. R. Soc. A* **2010**, *368*, 3269-3294.

(9) Chueh, W. C.; Falter, C.; Abbott, M.; Scipio, D.; Furler, P.; Haile, S. M.; Steinfeld, A. High-Flux Solar-Driven Thermochemical Dissociation of CO_2 and H_2O Using Nonstoichiometric Ceria. *Science* **2010**, *330*, 1797-1801.

(10) de Leitenburg, C.; Trovarelli, A.; Llorca, J.; Cavani, F.; Bini, G. The Effect of Doping CeO_2 with Zirconium in the Oxidation of Isobutane. *Appl. Catal., A* **1996**, *139*, 161-173.

(11) Mogensen, M. Physical, Chemical and Electrochemical Properties of Pure and Doped Ceria. *Solid State Ionics* **2000**, *129*, 63-94.

(12) Trovarelli, A. Structural Properties and Nonstoichiometric Behavior of CeO_2. In *Catalysis by Ceria and Related Materials*; Trovarelli, A., Ed.; Imperial College Press: London, **2002**.

(13) Skorodumova, N. V.; Simak, S. I.; Lundqvist, B. I.; Abrikosov, I. A.; Johansson, B. Quantum Origin of the Oxygen Storage Capability of Ceria. *Phys. Rev. Lett.* **2002**, *89*, 166601(1-4).

(14) Kodama, T.; Gokon, N. Thermochemical Cycles for High-Temperature Solar Hydrogen Production. *Chem. Rev.* **2007**, *107*, 4048-4077.

(15) Venstrom, L. J.; Petkovich, N.; Rudisill, S.; Stein, A.; Davidson, J. H. The Effects of Morphology on the Oxidation of Ceria by Water and Carbon Dioxide. *J. Sol. Energy Eng.* **2012**, *134*, 011005(1-8).

(16) Sokolov, S.; Bell, D.; Stein, A. Preparation and Characterization of Macroporous α-Alumina. *J. Am. Ceram. Soc.* **2003**, *86*, 1481-1486.

(17) Stein, A.; Li, F.; Denny, N. R. Morphological Control in Colloidal Crystal Templating of Inverse Opals, Hierarchical Structures and Shaped Particles. *Chem. Mater.* **2008**, *20*, 649-666.

(18) Fornasiero, P.; Balducci, G.; Di Monte, R.; Kašpar, J.; Sergo, V.; Gubitosa, G.; Ferrero, A.; Graziani, M. Modification of the Redox Behaviour of CeO_2 Induced by Structural Doping with ZrO_2. *J. Catal.* **1996**, *164*, 173-183.

(19) Di Monte, R.; Kašpar, J. Nanostructured CeO_2-ZrO_2 Mixed Oxides. *J. Mater. Chem.* **2005**, *15*, 633-648.

(20) Atribak, I.; Bueno-López, A.; García-García, A.; Azambre, B. Contributions of Surface and Bulk Heterogeneities to the NO Oxidation Activities of Ceria-Zirconia Catalysts with Conposition $Ce_{0.76}Zr_{0.24}O_2$ Prepared by Different Methods. *Phys. Chem. Chem. Phys.* **2010**, *12*, 13770-13779.

(21) Kašpar, J.; Fornasiero, P.; Graziani, M. Use of CeO_2-Based Oxides in the Three-Way Catalysis. *Catal. Today* **1999**, *50*, 285-298.

(22) Balducci, G.; Islam, M. S.; Kašpar, J.; Fornasiero, P.; Graziani, M. Bulk Reduction and Oxygen Migration in the Ceria-Based Oxides. *Chem. Mater.* **2000**, *12*, 677-681.

(23) Mamontov, E.; Egami, T.; Brezny, R.; Koranne, M.; Tyagi, S. Lattice Defects and Oxygen Storage Capacity of Nanocrystalline Ceria and Ceria-Zirconia. *J. Phys. Chem. B* **2000**, *104*, 11110-11116.

(24) Shah, P. R.; Kim, T.; Zhou, G.; Fornasiero, P.; Gorte, R. J. Evidence for Entropy Effects in the Reduction of Ceria-Zirconia Solutions. *Chem. Mater.* **2006**, *18*, 5363-5369.

(25) Wang, H.-F.; Guo, Y.-L.; Lu, G.-Z.; Hu, P. Maximizing the Localized Relaxation: The Origin of the Outstanding Oxygen Storage Capacity of κ-$Ce_2Zr_2O_8$. *Angew. Chem. Int. Ed.* **2009**, *48*, 8289-8292.

(26) Daturi, M.; Finocchio, E.; Binet, C.; Lavalley, J. C.; Fally, F.; Perrichon, V. Study of Bulk and Surface Reduction by Hydrogen of $Ce_xZr_{1-x}O_2$ Mixed Oxides Followed by FTIR Spectroscopy and Magnetic Balance. *J. Phys. Chem. B* **1999**, *103*, 4884-4891.

(27) Martínez-Arias, A.; Fernández-García, M.; Hungría, A.-B.; C., C. J.; Munuera, G. Spectroscopic Characterization of Heterogeneity and Redox Effects in Zirconium-Cerium (1:1) Mixed Oxides Prepared by Microemulsion Methods. *J. Phys. Chem. B* **2003**, *107*, 2667-2677.

(28) Kim, T.; Vohs, J. M.; Gorte, R. J. Thermodynamic Investigation of the Redox Properties of Ceria-Zirconia Solid Solutions. *Ind. Eng. Chem. Res.* **2006**, *45*, 5561-5565.

(29) Giordano, F.; Trovarelli, A.; de Leitenburg, C.; Dolcetti, G.; Giona, M. Some Insight into the Effects of Oxygen Diffusion in the Reduction Kinetics of Ceria. *Ind. Eng. Chem. Res.* **2001**, *40*, 4828-4835.

(30) Colón, G.; Pijolat, M.; Valdivieso, F.; Vidal, H.; Kašpar, J.; Finocchio, E.; Daturi, M.; Binet, C.; Lavalley, J. C.; Baker, R. T.; Bernal, S. Surface and Structural Characterization of $Ce_xZr_{1-x}O_2$ CEZIRENCAT Mixed Oxides as Potential Three-Way Catalyst Promoters. *J. Chem. Soc., Faraday Trans.* **1998**, *94*, 3717-3726.

(31) Colón, G.; Valdivieso, F.; Pijolat, M.; Baker, R. T.; Calvino, J. J.; Bernal, S. Textural and Phase Stability of $Ce_xZr_{1-x}O_2$ Mixed Oxides Under High Temperature Oxidising Conditions. *Catal. Today* **1999**, *50*, 271-284.

(32) Le Gal, A.; Abanades, S. Catalytic Investigation of Ceria-Zirconia Solid Solutions for Solar Hydrogen Production. *Int. J. Hydrogen Energy* **2011**, *36*, 4739-4748.

(33) Schroden, R. C.; Al-Daous, M.; Sokolov, S.; Melde, B. J.; Lytle, J. C.; Stein, A.; Carbajo, M. C.; Fernández, J. T.; Rodríguez, E. E. Hybrid Macroporous Materials for Heavy Metal Ion Adsorption. *J. Mater. Chem.* **2002**, *12*, 3261-3267.

(34) Varez, A.; Garcia-Gonzalez, E.; Sanz, J. Cation Miscibility in CeO_2-ZrO_2 Oxides with Fluorite Structure. A Combined TEM, SAED and XRD Rietveld Analysis. *J. Mater. Chem.* **2006**, *16*, 4249-4256.

(35) Yashima, M. Crystal Structures of the Tetragonal Ceria-Zirconia Solid Solutions $Ce_xZr_{1-x}O_2$ Through First Principles Calculations ($0 \leq x \leq 1$). *J. Phys. Chem. C* **2009**, *113*, 12658-12662.

(36) Yashima, M.; Arashi, H.; Kakihana, M.; Yoshimura, M. Raman Scattering Study of Cubic-Tetragonal Phase Transition in $Zr_{1-x}Ce_xO_2$ Solid Solution. *J. Am. Ceram. Soc.* **1994**, *77*, 1067-1071.

(37) Trovarelli, A.; Zamar, F.; Llorca, J.; de Leitenburg, C.; Dolcetti, G.; Kiss, J. T. Nanophase Fluorite-Structured CeO_2-ZrO_2 Catalysts Prepared by High-Energy Mechanical Milling. *J. Catal.* **1997**, *169*, 490-502.

(38) Omata, T.; Kishimoto, H.; Otsuka-Yao-Matsuo, S.; Ohtori, N.; Umesaki, N. Vibrational Spectroscopic and X-Ray Diffraction Studies of Cerium Zirconium Oxides with Ce/Zr Composition Rato = 1 Prepared by Reduction and Successive Oxidation of *t'*-$(Ce_{0.5}Zr_{0.5})O_2$ Phase. *J. Solid State Chem.* **1999**, *147*, 573-583.

(39) Otsuka-Yao-Matsuo, S.; Omata, T.; Izu, N.; Kishimoto, H. Oxygen Release Behavior of $CeZrO_4$ Powders and Appearance of New Compounds κ and t*. *J. Solid State Chem.* **1998**, *138*, 47-54.

(40) Montini, T.; Hickey, N.; Fornasiero, P.; Graziani, M.; Bañares, A.; Martinez-Huerta, M. V.; Alessandri, I.; Depero, L. E. Variations in the Extent of Pyrochlore-Type Cation Ordering in $Ce_2Zr_2O_8$: a t'-κ Pathway to Low-Temperature Reduction. *Chem. Mater.* **2005**, *17*, 1157-1166.

(41) Yeste, M. P.; Hernández, J. C.; Trasobares, S.; Bernal, S.; Blanco, G.; Calvino, J. J.; Pérez-Omil, J. A.; Pintado, J. M. First Stage of Thermal Aging under Oxidizing Conditions of a $Ce_{0.62}Zr_{0.38}O_2$ Mixed Oxide with an Ordered Cationic Sublattice: A Chemical, Nanostructural, and Nanoanalytical Study. *Chem. Mater.* **2008**, *20*, 5107-5113.

(42) Hori, C. E.; Permana, H.; Simon Ng, K. Y.; Brenner, A.; More, K.; Rahmoeller, K. M.; Belton, D. Thermal Stability of Oxygen Storage Properties in a Mixed CeO_2-ZrO_2 System. *Appl. Catal., B* **1998**, *16*, 105-117.

(43) Kašpar, J.; Fornasiero, P.; Balducci, G.; Di Monte, R.; Hickey, N.; Sergo, V. Effect of ZrO_2 Content on Textural and Structural Properties of CeO_2-ZrO_2 Solid Solutions Made by Citrate Complexation Route. *Inorg. Chim. Acta* **2003**, *349*, 217-226.

(44) Shannon, R. D. Revised Effective Ionic Radii and Systematic of Interatomic Distances in Halides and Chalcogenides. *Acta Cryst.* **1976**, *A32*, 751-767.

(45) Bozo, C.; Gaillard, F.; Guilhaume, N. Characterisation of Ceria-Zirconia Solid Solution After Hydrothermal Ageing. *Appl. Catal., A* **2001**, *220*, 69-77.

(46) Zhang, F.; Chen, C.-H.; Hanson, J. C.; Robinson, R. D.; Herman, I. P.; Chan, S.-W. Phases in Ceria-Zirconia Binary Oxide (1-*x*)CeO_2-*x*ZrO_2 Nanoparticles: The Effecs of Particle Size. *J. Am. Ceram. Soc.* **2006**, *89*, 1028-1036.

(47) Kakihana, M. Invited Review "Sol-Gel" Preparation of High Temperature Superconducting Oxides. *J. Sol-Gel Sci. Technol.* **1996**, *6*, 7-55.

(48) Denny, N. R.; Han, S. E.; Norris, D. J.; Stein, A. Effects of Thermal Processes on the Structure of Monolithic Tungsten and Tungsten Alloy Photonic Crystals. *Chem. Mater.* **2007**, *19*, 4563-4569.

(49) Sing, K. S. W. Reporting Physisorption Data for Gas/Solid Systems with Special Reference to the Determination of Surface Area and Porosity. *Pure Appl. Chem.* **1985**, *57*, 603-619.

(50) Groen, J. C.; Peffer, L. A. A.; Pérez-Ramírez, J. Pore Size Determination in Modified Micro- and Mesoporous Materials. Pitfalls and Limitations in Gas Adsorption Data Analysis. *Micropor. Mesopor. Mater.* **2003**, *60*, 1-17.

(51) Aneggi, E.; de Leitenburg, C.; Dolcetti, G.; Trovarelli, A. Promotional Effect of Rare Earths and Transition Metals in the Combustion of Diesel Soot over CeO_2 and CeO_2-ZrO_2. *Catal. Today* **2006**, *114*, 40-47.

(52) Galtayries, A.; Sporken, R.; Riga, J.; Blanchard, G.; Caudano, R. XPS Comparative Study of Ceria/Zirconia Mixed Oxide: Powders and Thin Film Characterisation. *J. Electron Spectrosc. Relat. Phenom.* **1998**, *88-91*, 951-956.

(53) Mamontov, E.; Brezny, R.; Koranne, M.; Egami, T. Nanoscale Heterogeneities and Oxygen Storage Capacity of $Ce_{0.5}Zr_{0.5}O_2$. *J. Phys. Chem. B* **2003**, *107*, 13007-13014.

Chapter 8

Morphological/Structural Analysis, Thermal Stability and Thermochemical Fuel Production from Porous Cerium-Based Oxides, Prasedymium-Based Oxides, and Perovskite Oxides

8.1 Introduction and Motivation

A vast number of compounds are potential candidates for solar thermochemical fuel production, including many compounds that remain as solids during the course of cycling. Using the studies of CeO_2 and $Ce_{1-x}Zr_xO_2$ as a springboard, this chapter describes a broader investigation of compounds (including ones that do not rely on the Ce^{4+}/Ce^{3+} redox couple) that could be used for solar thermochemical fuel production. Since the 3DOM structure is extremely effective at improving the kinetics of fuel production from cerium oxide-based materials, all materials studied in this chapter possess that structure. While the general morphology of the materials discussed herein is the same, the chemical compositions of the studied materials are varied. These compositions are broken up into three main groupings for the purposes of this chapter. The first group discussed is cerium oxide-based compounds that contain lanthanoid or transition metal ions. All of these compounds primarily rely on the Ce^{4+}/Ce^{3+} redox couple for thermochemical fuel production; however, some added redox active metal ions may also participate. The second group discussed is praseodymium oxide-based compounds. Praseodymium oxide is one of the few lanthanoids, aside from cerium oxide, that possesses a readily accessible redox couple, Pr^{4+}/Pr^{3+}, which can potentially be used for solar thermochemical fuel production. The third and final group of materials is the pervoskite oxides. Many perovskites readily gain and lose oxygen in response to changes in oxygen partial pressure and temperature,[1] and this has attracted interest in the use of these materials for solar thermochemical fuel production.[2-4] To assist in the discussion of the results from the 3DOM materials under investigation, each of these groups are further described below. A special emphasis is placed on how these materials are (or can be) used in solar thermochemical cycling.

The addition of main group metal, transition metal and/or lanthanoid cations to CeO_2 has attracted the attention of various research groups working on catalysis at temperatures lower than 1000 °C.[5-17] This research has largely been motivated by the need to improve the performance of internal combustion engine pollution control devices.[18,19] CeO_2 and Ce-based mixed oxides can reversibly store and release O_2 in order to promote a wide range of catalytic reactions for pollution abatement.[19-21] Addition of metal cations can substantially alter the redox performance of the cerium ions, improving the capacity for oxygen storage and release.[12,22-24] An increase in reducibility is often observed for the mixed oxides relative to CeO_2.[25-28] Many Ce-based mixed oxides also have improved thermal resistance to sintering and surface area loss,[29,30] allowing for improved redox properties and kinetics during operation when compared to CeO_2.[31-36] Other compounds have improved stability with respect to phase segregation, allowing for the use of

these materials in a wide range of applications.[32,37-39] Unfortunately, the majority of these studies of Ce-based mixed oxides were restricted to temperatures no higher than approximately 1000 °C. Due in part to the positive results obtained from these investigations of the catalytic properties of Ce-based mixed oxides, these compounds have been studied for use in solar thermochemical fuel production.[40-54] These studies have focused on the critical need to understand the reactivity and stability of the mixed oxides under the conditions required for solar thermochemical fuel production. It has been found that some mixed oxides produce more fuel than pure cerium oxide. However, others do little to improve fuel production and can even harm fuel production kinetics.[50,53,54] There are conflicting reports on the impact that certain dopants have on fuel production, including Zr,[46,48,54,55] and Sc.[52,54] Some of these discrepancies arise from variations in the cycling conditions from study to study, including different reduction and oxidation times, temperatures, and environments.[55] In other cases, the concentration of the dopant is found to have a significant impact.[54] Overall, a better understanding is needed of how the identity and concentration of the added cations affect the redox thermodynamics and reaction kinetics of the material.

Praseodymium oxide is closely related to cerium oxide both in terms of its phase diagrams and its redox activity. Both cerium oxide and praseodymium oxide have cubic fluorite MO_2 and hexagonal M_2O_3 end members in their phase diagrams.[56] In addition, several non-stoichiometric oxides lie between these end members that can be accessed via reduction or oxidation treatments.[57-60] Similar to cerium oxide, some of these non-stoichiometric oxides are ordered polymorphs that can only be found for a specific degree of non-stiochiometry (Pr_nO_{2n-2m}). In addition, there are polymorphs that exist over a wide non-stoichiometric range at high temperatures.[56] Due to the similarities between Ce-based oxides and Pr-based oxides, studies have been conducted on their redox properties.[6,60-66] One recurring finding is that praseodymium oxide is far easier to reduce than cerium oxide.[57,59] Indeed, the product obtained from praseodymium salt decomposition in air is cubic fluorite Pr_6O_{11}.[56] Studies have also been conducted that focus on changing the redox properties of Pr-based oxides through the introduction of additional metal cations.[65,67-69] The ease of reduction of praseodymium oxide coupled with the array of possible mixed oxide composition have attracted researchers targeting applications in pollution control catalysis,[64,68] oxidative coupling reactions,[70] solid oxide fuel cells[71] and even hydrogen production from methane gas.[67] The application of praseodymium oxides has yet to be extended to solar thermochemical fuel production, despite the redox activity

of these materials. Possible two-step thermochemical reactions (with water used as an oxidant) for undoped praseodymium are given below (equation 8.1 and 8.2).

$$Pr_6O_{11} \rightleftarrows 3Pr_2O_3 + O_2 \quad (8.1)$$

$$3Pr_2O_3 + 2H_2O \rightleftarrows Pr_6O_{11} + 2H_2 \quad (8.2)$$

A vast number of oxide compounds have been identified that crystallize with a perovskite structure. The general formula for these compounds is ABO_3, where A denotes a 12-fold coordinated cation with a larger ionic radius than the six-fold coordinated B cation. While the prototypical cubic structure (Figure 8.1) is commonly described in textbooks, distorted structures are far more common in perovskites at ambient conditions.[72] In 1926, Victor Goldschmidt introduced a parameter now known as the Goldschmidt tolerance factor (*t*) that usually allows for the identification of a particular perovskite structure based on ionic radii of the A and B cation (equation 8.3).[73]

$$t = \frac{(r_A + r_O)}{\sqrt{2}(r_B + r_O)} \quad (8.3)$$

For the equation, r_A is the radius of the A cation, r_B is the radius of the B cation, and r_O is the radius of the oxide anion. Within a certain range for *t* (about 0.75 to a little over 1), perovskite crystal structures can form. Cubic structures only form in a limited range, roughly $0.9 < t < 1$.[1] Hexagonal perovskites are formed for $t > 1$, and the BO_6 octahedra in these structures share faces.[74] When *t* is between 0.7 and 0.9, the BO_6 octahedra tilt, owing to the small size of the A cation.[72] Orthorhombic and rhombohedral lattices are found in these perovskites. Many related structures are also found, including double perovskites and Brownmillerites that contain ordered oxygen vacancies.[1,74] Regardless of the space group of the perovskite, A and/or B cations can be substituted for other cations with a similar ionic radius. Many technologically important perovskite oxides incorporate substituted cations and have a general formula of $A_{1-x}A'_xBO_3$, $AB_{1-y}B'_yO_3$, or $A_{1-x}A'_xB_{1-y}B'_yO_3$ (where A′ and B′ are the substituted cationic species).[1] Substitution of cations can change the space group of the perovskite relative to the non-substituted ABO_3, and, more importantly, can substantially alter the redox properties of the perovskite materials.[75-77]

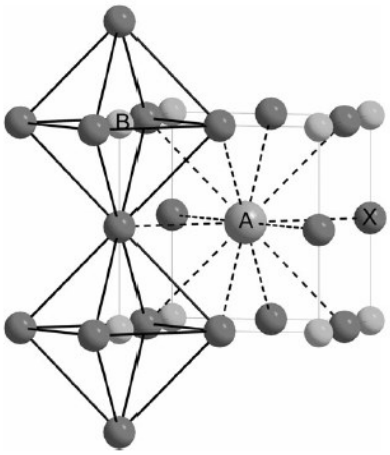

Figure 8.1 Ideal cubic perovskite structure, ABX_3. A is the larger, 12-coordinate cation. B is the smaller, 6-coordinate cation. X is an anion, such as O^{2-} for perovskite oxides. Image reproduced with permission from [76] © 2006 Royal Society of Chemistry.

Many perovskites exhibit oxygen nonstoichiometry to varying degrees,[76] and it is this ability for perovskites to gain and lose oxygen that can be harnessed for solar thermochemical fuel production. Perovskites can change their oxygen content in response to changes in $p(O_2)$ and temperature, as long as the A or (most likely) the B cation can adopt multiple oxidation states.[1] Most perovskites with variable oxygen stoichiometry exhibit an oxygen deficiency (oxygen vacancies); however, a few, such as $LaMnO_3$, can have an oxygen excess (via interstitial oxygen atoms or cationic vacancies). Another salient feature is that phase changes or outright decomposition can occur as the oxygen content changes, which can drastically alter the redox properties.[76,78-82] Efforts have been made to understand the equilibrium defect thermodynamics of these materials,[83-92] but a comprehensive summary is far beyond the scope of this thesis. These studies into both the redox properties and defect chemistry of perovskite oxides have been driven, in part, by the desire to engineer optimized perovskites (with different A′/B′ cations) for redox catalysis applications,[93-101] oxygen-permeable membranes,[102-106] and for use as solid oxide fuel cell components.[107-114] Research into the use of peroskite oxides for catalysis and fuel cells has taken place over multiple decades. However, it was not until 2013 and 2014, that reports on the use of perovskite oxides for solar thermochemical fuel production were first published.[2-4] The endothermic reduction step (equation 8.4) and exothermic oxidation/fuel production step (equation 8.5, shown for CO production) are similar to those same steps in the cycle for CeO_2.

$$ABO_3 \rightleftarrows ABO_{3-x} + x/2\ O_2 \qquad (8.4)$$

$$ABO_{3-x} + xCO_2 \rightleftarrows ABO_3 + xCO \qquad (8.5)$$

While a stoichiometric, non-substituted perovskite is shown, the same reactions can occur in perovskites that have substituents or are non-stoichiometric as-synthesized. Perovskites share many of the same advantages possessed by cerium oxide: certain perovskites can remain solid during the whole thermochemical cycle, oxygen ion conduction though certain perovskites is fast, and certain perovskites exhibit high thermal stability.[1,4] However, perovskites have the distinct advantage of occupying a much larger compositional space than CeO_2. One possibility is that certain perovskites produce more fuel than cerium oxide. McDaniel *et al.* were able to find such a perovskite, the double-substituted $Sr_xLa_{1-x}Mn_yAl_{1-y}O_{3-\delta}$, which was capable of producing nine times the amount of H_2 produced by CeO_2 that was cycled under similar conditions.[3] Demont *et al.* examined several different perovskite (and the related Ruddlesden-Popper) compositions, and found that $LaSrCoO_4$ and $La_{0.50}Sr_{0.50}MnO_{3-x}$ produced more H_2 than CeO_2 under similar conditions.[4] Another key finding was that many of the perovskites were reduced to a far greater extent than they were able to be reoxidized. It was proposed that the fast kinetics exhibited by the by these perovskites is caused by a substantial driving force for oxidation caused by the deep reduction. There is, however, some disagreement in the literature about the kinetics and maximum attainable process efficiency for $La_{1-x}Sr_xMnO_3$. Scheffe et al. reported that reduced $La_{1-x}Sr_xMnO_3$ requires more concentrated, faster flows of CO_2 than cerium oxide.[2] Under those oxidation conditions (unfavorable from a heat recovery standpoint) $La_{1-x}Sr_xMnO_3$ can produce more CO than CeO_2, but at a slower rate than CeO_2. Still, perovskite oxides remain relatively unexplored, and there is an unprecedented opportunity for optimizing these compounds for use in solar thermochemical fuel production.

Since many questions still remain concerning the suitability of particular compositions for solar thermochemical cycling, the remainder of this chapter is an exploration of porous candidate materials for that application. All the materials described have the 3DOM structure, which offers an advantage from the standpoint of kinetics. In terms of their composition, the materials studied in this chapter fall under the three groupings described above. A set of Ce-based mixed oxides that contain lanthanoid cations or Zr^{4+} were produced via a methanolic precursor. Most of these materials were treated at high temperatures to assess their thermal stability, and overall suitability for thermochemical cycling. Thermochemical cycling was conducted using the transition-metal doped 3DOM $Ce_{0.9}Mn_{0.1}O_{2-x}$, which was produced via a Pechini-type precursor. An evaluation of

that material and a similarly made 3DOM $Ce_{0.9}La_{0.1}O_{1.95}$ from a structural standpoint is also presented. For the Pr-based materials, two Pechini-method derived 3DOM compositions are analyzed: undoped 3DOM PrO_{2-x} and the 3DOM mixed oxide, $Pr_{0.6}Zr_{0.35}Y_{0.05}O_{2-x}$. Finally, six 3DOM perovskites oxides are synthesized, characterized, and one is cycled in chemical redox conditions. A short summary of the results is then given at the end of the chapter.

8.2 Experimental Details

8.2.1 Materials

Methyl methacrylate (99 %), 2,2′-azobis(2-methylpropionamide) dihydrochloride (97 %), methanol (≥99.8 %, ACS reagent grade) cerium(III) chloride heptahydrate (99.9 %), zirconyl chloride octahydrate (98 %), lanthanum(III) chloride heptahydrate (99.9 %), samarium (III) chloride hexahydrate (≥99 %), praseodymium (III) chloride hydrate (99.9 %), neodymium(III) chloride hexahydrate (99.9 %), gadolinium(III) chloride hexahydrate (99.9 %), yttrium chloride hexahydrate (99.99 %), citric acid monohydrate (≥99 %, ACS reagent grade), manganese(II) chloride tetrahydrate (≥99 %, ReagentPlus®), praseodymium nitrate hexahydrate (99.9 %), strontium nitrate (>99.0%, ACS reagent grade), iron(III) nitrate nonahydrate (certified ACS), manganese nitrate tetrahydrate (≥97 %, purum), and cobalt(II) nitrate hexahydrate (ACS reagent grade) were purchased from Sigma-Aldrich. Lanthanum nitrate hexahydrate (>99.0 %) was bought from Fluka. Potassium persulfate (ACS reagent grade) was obtained from Fischer Scientific. Ethylene glycol (99+%) was obtained from Mallinckrodt Chemicals. Ammonia solution (28 wt%–30 wt%, analytical reagent grade) was purchased from Macron Chemicals. These chemicals were used without any additional purification. Water was purified using a Barnstead Sybron purification system (final resistivity >18 MΩ·cm).

8.2.2 Preparation of PMMA Colloidal Crystal Templates

Polymethyl methacrylate (PMMA) spheres were synthesized via an emulsifier-free emulsion polymerization following a published procedure.[115,116] Two different batches were prepared. The first was prepared using potassium persulfate (KPS, 1.00 g) as an initiator. For the second, 2,2′-azobis(2-methylpropionamide) dihydrochloride (AMPA, 1.50 g) was used to initiate the polymerization. No matter what initiator was used, an emulsion of MMA (400 mL) and water (1575 mL) was initially stirred in a 3000 mL, five-neck round bottom flask. A slow N_2 flow was used to purge the system and it was stirred via a Teflon stir blade attached to an overhead mixer. The emulsion was brought to 70 °C. Once the temperature was stabilized, the initiator (either

KPS or AMPA) was dissolved in 25 mL of water and then poured into the emulsion. The N_2 flow was cut and the mixture was allowed to react for several hours. Glass wool was used to filter large aggregates from the suspension.

As outlined before, suspensions of the PMMA spheres were poured into crystallization dishes to prepare colloidal crystal templates. These spheres were allowed to sediment under the force of gravity in covered dishes. Once sedimentation was completed, the cover was partially removed and the supernatant was allowed to evaporate. Small, mm-sized pieces of the dried colloidal crystals were used as templates in the following syntheses.

8.2.3 Synthesis of Cerium-Containing Mixed Oxides via the Methanolic Salt Solution (MSS) Route

Similar to what was described in Chapter 7, precursor solutions of metal chloride salts in methanol were prepared. Table 8.1 lists the identities and amounts of the metal chloride salts required for the particular compositions explored in this chapter. As was the case for the doped/mixed metal oxides described in previous chapters, the designation for the mixed oxide samples is based off the molar ratios of the salt precursors dissolved in the methanol. All precursors contained 2.00 g of metal chloride salts. These salts were dissolved in 2.00 g of methanol and then stirred for an additional 30 min.

Once a given precursor was fully prepared, it was infiltrated into colloidal crystal templates containing AMPA-initiated PMMA spheres. For infiltration, colloidal crystal templates were placed into glass scintillation vials and the precursor was poured onto templates. Like the MSS syntheses outlined in Chapter 7, a mass ratio of approximately 3:2 (colloidal crystal template:precursor solution) was used. Capillary action drew the precursor into the interstitial spaces of the template, and this process was allowed to take place for 1 d. After infiltration, the cap of the scintillation vial was removed and the infiltrated templates were dried in ambient conditions for 1 d. The infiltrated templates were then placed in alumina boats and inserted into a tube furnace. To combust the PMMA spheres and crystallize the precursor, the materials were heated at 2 °C/min to 310 °C with a 2 h hold and then heated at 2 °C/min to 450 °C with a 2 h hold. Thermal treatment was conducted under static air.

Table 8.1 Identity and amount of metal chloride salts used for the MSS precursors.

sample[a]	amount of $CeCl_3 \cdot 7H_2O$ (g)	first dopant	amount (g)	second dopant	amount (g)
CeO_2-MSS	2.00	NA	NA	NA	NA
$Ce_{0.8}Zr_{0.2}O_2$-MSS	1.64	$ZrOCl_2 \cdot 8H_2O$	0.36	NA	NA
$Ce_{0.8}La_{0.2}O_{1.9}$-MSS	1.60	$LaCl_3 \cdot 7H_2O$	0.60	NA	NA
$Ce_{0.8}Pr_{0.2}O_{2-x}$-MSS	1.60	$PrCl_3 \cdot xH_2O$[b]	0.40	NA	NA
$Ce_{0.8}Nd_{0.2}O_{1.9}$-MSS	1.61	$NdCl_3 \cdot 6H_2O$	0.39	NA	NA
$Ce_{0.8}Sm_{0.2}O_{1.9}$-MSS	1.61	$SmCl_3 \cdot 6H_2O$	0.39	NA	NA
$Ce_{0.8}Gd_{0.2}O_{1.9}$-MSS	1.60	$GdCl_3 \cdot 6H_2O$	0.40	NA	NA
$Ce_{0.8}La_{0.1}Zr_{0.1}O_{1.95}$-MSS	1.62	$LaCl_3 \cdot 7H_2O$	0.20	$ZrOCl_2 \cdot 8H_2O$	0.18
$Ce_{0.8}Sm_{0.1}La_{0.1}O_{1.95}$-MSS	1.60	$SmCl_3 \cdot 6H_2O$	0.20	$LaCl_3 \cdot 7H_2O$	0.20
$Ce_{0.8}Sm_{0.1}Zr_{0.1}O_{1.95}$-MSS	1.63	$SmCl_3 \cdot 6H_2O$	0.20	$ZrOCl_2 \cdot 8H_2O$	0.18

[a] Total mass of metal salts is 2.00 g.

[b] Degree of hydration between 6 and 7, but assumed to be 7 for calculations.

Specimens from the doped 3DOM MSS materials were also subjected to an additional thermal treatment step. The thermal treatment was conducted in a Netzsch STA 409 PC Luxx thermogravimetric analyzer under an atmosphere of 99 vol% N_2 and 1 vol% O_2. A ramp of 10 °C/min used to bring the temperature of the specimens to 1350 °C, and the specimens were kept at that temperature for 1 h.

8.2.4 Synthesis of Cerium-Containing Mixed Oxides via the Pechini Method (PM)

An additional metal ion (Mn) was added to the cerium oxide lattice via the Pechini method. For this synthesis, 0.010 moles of total metal ions (Ce^{3+} and the dopant) were used. The metal salts were first combined in a scintillation vial. 3DOM $Ce_{0.9}Mn_{0.1}O_{2-x}$-PM was made by combining 3.35 g of $CeCl_3 \cdot 7H_2O$, 0.20 g of $MnCl_2 \cdot 4H_2O$, and 6.30 g of citric acid monohydrate. These solids were then dissolved in 6.70 g of H_2O. After this was completed, 1.24 g of ethylene glycol was added to the precursor, and the solution was stirred for 15 minutes.

Stirred precursors were subsequently infiltrated into PMMA colloidal crystal templates. The precursors were infiltrated into templates containing KPS-initiated PMMA spheres. A mass ratio of 3:4 (precursor to template) was used for the infiltration, and the infiltration was conducted in

closed glass scintillation vials kept at ambient temperature. Once infiltration was completed (a process that typically took 2–4 h), the infiltrated templates were placed in closed vessels and were kept at 90 °C for 24 h. All materials were then placed in a tube furnace and calcined under static air. The furnace was held at 310 °C for 2 h and 450 °C for 2 h. A temperature ramp rate of 2 °C/min was used.

8.2.5 Synthesis of 3DOM Praseodymium-Based Oxides via the Pechini Method

Undoped 3DOM PrO_{2-x} samples and 3DOM $Pr_{0.6}Zr_{0.35}Y_{0.05}O_{2-x}$ mixed oxide samples were made using Pechini-type precursor. For the undoped sample, 3.91 g of praseodymium nitrate hexahydrate and 1.50 g of citric acid monohydrate were combined in a scintillation vial. These solids were then dissolved in 3.11 g of water. After dissolution of the solids, 1.00 g of ethylene glycol was added and the solution was stirred for 15 min. The doped sample was produced by combining 2.61 g of praseodymium chloride heptahydrate, 1.31 g of zirconyl chloride octahydrate, 0.18 g of yttrium chloride hexahydrate and 2.00 g of citric acid monohydrate in a vial. Four g of water was then added to the vial and the solution was stirred until all solids were dissolved. At that point, 2.00 g of ethylene glycol was added to the solution. Stirring was continued for 15 min.

For the undoped Pr-containing precursor, pieces of the KPS-initiated PMMA colloidal crystal templates were placed in scintillation vials. The Pechini precursor was then added to the vials. As was the case in Chapter 7, a mass ratio of 3 to 2 (template to precursor) was used. Infiltration via capillary action took roughly 2 h, and then the capped vials were heated at 90 °C for 1 h. These infiltrated templates were placed in an alumina boats and calcined under static air in a tube furnace. A ramp rate of 2 °C/min was used, and the temperature was held at 310 °C for 2 h and 450 °C for 2 h.

The doped material was processed in a different fashion that relied on the assistance of a vacuum. Structurally colored materials were obtained using this method, while unassisted infiltration resulted in poor inverse replication of the structure. A few-mm layer of KPS-initiated, partially-crushed PMMA colloidal crystal templates was placed on a circle of cellulose filter paper. Both the filter paper and the colloidal crystals were placed in a Büchner funnel attached to a vacuum flask. Precursor was then dripped onto the templates via a pipette until the all the exterior surfaces of the PMMA templates were coated with precursor. Infiltration was allowed to take place over a period of roughly 15 min. Excess precursor was then removed by applying a low vacuum (>1 torr) for several min. A second cycle of infiltration (dripping precursor, waiting,

and applying vacuum) was then conducted. These infiltrated templates were thermally-treated at 90 °C for 1 h in a closed vessel. Calcination of the treated material was performed via the same procedure used above for the undoped material.

8.2.6 Preparation of 3DOM Perovskite Materials via the Pechini Method

Solution-based precursors were first prepared for the synthesis of the 3DOM perovskites. The components and amounts of each component in the precursors are listed in Table 8.2. Nitrate salts were used to supply the metal cations needed for the perovskites. The amount of certain components and the identity of the transition metal nitrate were varied from precursor to precursor. For instance, the precursor for 3DOM $La_{0.6}Sr_{0.4}MnO_{3-x}$ requires double the moles of citric acid monohydrate needed for precursors that contain iron or cobalt nitrate. For all precursors, the same sequence of steps was carried out to generate a stable solution suitable for infiltration into the colloidal crystal template. First, the metal nitrates (0.015 moles in total) and citric acid monohydrate were added to a scintillation vial. These solids were dissolved in water under rapid stirring (a process that can take up to 1 h). Ammonia solution was then added to the precursor, while it was stirred. Finally, ethylene glycol was added and the precursor was stirred for 15 min.

These Pechini precursors were infiltrated into AMPA-initiated PMMA colloidal crystal templates. For these infiltrations, 2.00 g of ground (roughly 1 to 2 mm) colloidal crystal templates were combined with 1.50 g of a given precursor in a closed vessel. Ambient conditions were used. Infiltration of the solution was facilitated by gently stirring the templates and the precursor or via the addition of ~0.20 to 0.30 g more precursor solution. Complete infiltration of the templates typically occurred within 3 h. The infiltrated templates were then placed in a sealed vessel and heated at 90 °C for 24 h. (CAUTION: Vessels were kept sealed and were only opened in a well-ventilated area. Nitrogen oxides are produced during the gelation step.) Once the curing step was complete, the infiltrated templates were placed in an alumina boat in a tube furnace. Samples were heated (in static air) to 600 °C using a 1 °C/min rate and held at 600 °C for 5 h.

Table 8.2. Contents of the precursor solutions for the 3DOM pervoskite samples.

Sample	$La(NO_3)_3 \cdot 6H_2O$ (g)	$Sr(NO_3)_2$ (g)	transition metal nitrate (g)[a]	citric acid (g)[b]	water (g)	ammonia solution (g)[c]	ethylene glycol (g)
$LaFeO_{3-x}$	3.25	NA	3.03	6.30	7.30	0.200	1.12
$La_{0.75}Sr_{0.25}FeO_{3-x}$	2.44	0.40	3.03	6.30	7.30	0.200	1.12
$SrFeO_{3-x}$	NA	3.17	3.03	6.30	7.30	0.200	1.12
$La_{0.6}Sr_{0.4}MnO_{3-x}$	1.94	0.64	1.40	3.15	7.30	0.200	1.24
$LaCoO_{3-x}$	3.25	NA	2.18	6.30	7.30	0.200	1.12
$La_{0.6}Sr_{0.4}CoO_{3-x}$	1.95	0.64	2.18	6.30	7.30	0.200	1.12

[a] Three different transition metal nitrates were used for these precursors. $Fe(NO_3)_3 \cdot 9H_2O$ was used for the Fe-containing perovskites, $Mn(NO_3)_2 \cdot 4H_2O$ was used for the Mn-containing perovskite, and $Co(NO_3)_2 \cdot 6H_2O$ is used for the Co-containing perovskites.

[b] The monohydrate was used for these precursors.

[c] Concentrated ammonia solution (28–30 wt%) was used.

8.2.7 Structural Characterization

Various methods of materials characterization and analysis of the obtained data were employed for this chapter. For materials made via the methanolic salt solution route (i.e., the MSS samples) and praseodymium oxide-based materials, SEM was conducted using a JEOL 6500 operated at 5 kV. All other materials were analyzed using a JEOL 6700 microscope also operated at 5kV. Irrespective of the instrument used, specimens for SEM were prepared by placing a portion of the powdered materials on double-sided sticky carbon tape affixed to an Al stub. A coating of 75 Å of Pt metal was applied to the specimens. PXRD diffraction patterns were obtained using PANalytical X'Pert Pro fitted with a Co anode (operated at 45 kV and 40 mA). TREOR90, supplied with PANalytical's HighScore Plus software, was used to index several patterns and obtain unit cell parameters. An internal LaB_6 (99 %, Sigma-Aldrich) standard was used to correct for instrumental errors. Crystallite sizes were determined using the Scherrer equation. Lorentizian functions were used to fit peaks for this purpose. Sorption isotherms were collected using a Quantachrome Autosorb IQ_2-MP. Nitrogen gas was used and the temperature was kept at 77 K. All samples were outgassed at 200 °C for 8 h under a pressure of 0.001 torr. As

before, the BET method was employed to determine specific surface areas. Total pore volumes were determined from the point $P/P_o = 0.995$.

8.2.8 Procedures for Testing Fuel Production Capabilities of Select Materials

For the praseodymium-based materials and the $La_{0.6}Sr_{0.4}MnO_{3-x}$, chemical redox cycling was conducted using the reactor set-up that is outlined in Chapter 7. Again, 3DOM powders were sieved to sizes between 180 and 840 μm, weighed, and placed in the reactor. Gas production was monitored using a Raman spectrometer (Atmosphere Recovery, Inc., RLGA-129a). Calibration of the mass flow controllers and the detector was carried out using the same procedures detailed in Chapter 7. The praseodymium-based materials were reduced and re-oxidized either three or six times at ~825 °C. For reduction, a stream of 5 mol% H_2 in Ar (99.999% purity, Airgas) was passed over the sample at a rate of ~200 mL/min. Reduction was conducted for 60 min. Samples were re-oxidized under flow of 300 mL/min of Ar that was saturated with water (0.02 atm). Oxidation was conducted for 20 min. Purge steps were conducted using pure Ar to flush out residual hydrogen and water. This is identical to the procedure used for the cerium zirconium oxide samples studied in Chapter 7.

Extensive changes to the chemical cycling procedure were carried out for the 3DOM $La_{0.6}Sr_{0.4}MnO_{3-x}$. The reduction temperature was fixed during these tests, but the oxidation temperature was changed. Only one reduction and oxidation step was performed for a given temperature. In these experiments, the 3DOM $La_{0.6}Sr_{0.4}MnO_{3-x}$ was first reduced at 500 °C in a stream of Ar that contains a mixture of water and hydrogen (680 mL/min). Overall content of the stream was 0.7 % ± 0.1 % H_2, 2.7 % H_2O and the balance being Ar. Hydrogen was produced via electrolysis, while the stream of Ar was saturated with water by bubbling though a column containing DI water. This reduction was carried out for 30 min. Based on an extrapolation of the redox thermodynamics of $La_{0.6}Sr_{0.4}MnO_{3-x}$,[91] this chemical reduction step should be equivalent to a thermochemical reduction at 1500 °C under $1 \cdot 10^{-5}$ atm of oxygen. Prior to oxidation, the reactor was flushed with a stream of pure Ar gas to remove hydrogen and water. The 3DOM $La_{0.6}Sr_{0.4}MnO_{3-x}$ was then oxidized in a stream of CO_2 (99.9 % purity, Airgas) using a flow rate of 300–330 mL/min. Oxidation was performed at 500 °C, 600 °C, 700 °C, 800 °C, 900 °C, 1000 °C, or 1100 °C.

A different set-up was used for determining the fuel productivity of the 3DOM $Ce_{0.9}Mn_{0.1}O_{2-x}$-PM. This material was thermochemically cycled in an infrared image furnace (Ulvac-Riko VHT-E44). A schematic for the system is shown in Figure 8.2. Due to the high temperatures attainable

in this set-up, an alumina process tube and alumina sheaths was used to protect the Pt–Pt/Rh thermocouples. The 3DOM materials were sieved between 180 and 840 μm and loaded into the process tube. To help hold the bed of 3DOM $Ce_{0.9}Mn_{0.1}O_{2-x}$-PM in place, a porous alumina plug was placed downstream of the bed. Two thermocouples were present in the reactor system. The thermocouple designated T2 was placed downstream from the bed and this particular thermocouple controlled the temperature of the reactor system. Since T2 was not is isolated from the 3DOM sample, a fixed amount of power can be sent into the reactor no matter what sample is present. This is similar to what can be easily achieved in a reactor linked to a concentrated solar power system.[117] Another thermocouple, T1 was embedded in the sample and can record its temperature. For the reduction step, the temperature was initially increased from 800 °C to 1100 °C (as monitored by T2) over a period of 18 sec. The temperature was kept at 1100 °C for an additional 60 sec. During reduction, a stream (100 mL/min) of N_2 containing 10.5±0.1 ppm O_2 was passed over the sample. For the oxidation step, the temperature was rapidly reduced to 800 °C and then held at that temperature for 120 sec. A stream (100 mL/min) of 25 mol% CO_2 (balance N_2) was used for the oxidation. As before, a Raman spectrometer was used to monitor the composition of the effluent gas stream (Atmosphere Recovery, Inc., RLGA-129a). Further details of the reactor system can be found in a report by Rudisill *et al*.[117]

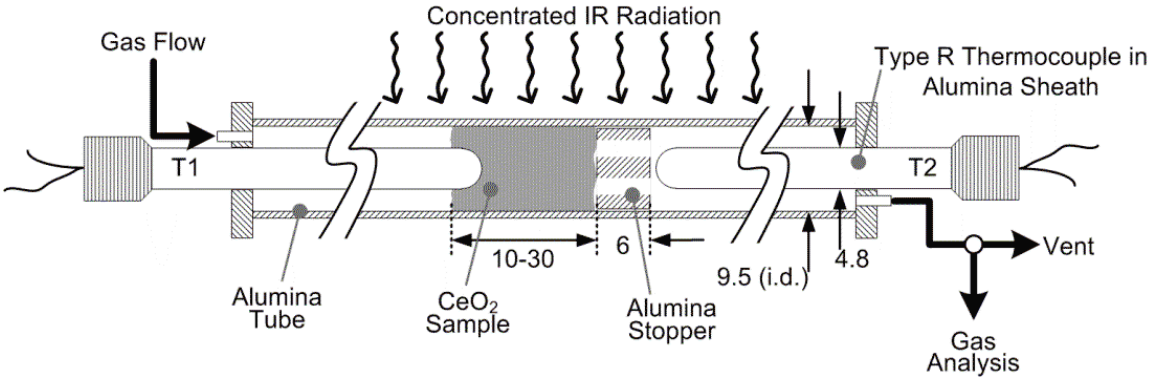

Figure 8.2 Diagram of the reactor system used for thermochemical cycling of 3DOM $Ce_{0.9}Mn_{0.1}O_{2-x}$-PM. All lengths are given in millimeters. Image reproduced with permission from [117] © 2013 American Chemical Society.

8.3 Results and Discussion

Similar to the structure of Chapter 4, the results in this chapter are divided into separate sections for each study. The first section details the analysis of the crystal structure, crystal size, and morphology of cerium-based mixed oxides made via the MSS route. A brief exploration of their thermal stabilities at 1350 °C is also presented. In the second section, two additional cations (Mn and La) are incorporated into the cerium oxide lattice via the Pechini method. One of these materials, 3DOM $Ce_{0.9}Mn_{0.1}O_{2-x}$ was also thermochemically cycled. A brief analysis of its structure after cycling is given, along with an analysis of its fuel production and fuel production kinetics. For the third section, the characterization of 3DOM PrO_{2-x} and 3DOM $Pr_{0.6}Zr_{0.35}Y_{0.05}O_{2-x}$ is discussed. Chemical redox cycling of these materials and induced structural changes are discussed. Finally, six perovskites are analyzed by PXRD, gas sorption, and electron microscopy. 3DOM $La_{0.6}Sr_{0.4}MnO_{3-x}$ was reduced (chemically) and oxidized in CO_2, and this study is discussed. Brief conclusions are given at the end of each section, and an overall summary is presented at the end of the chapter.

8.3.1 Extension of the MSS Route to Cerium-Based Mixed Oxides that Contain Other Lanthanoids

While some disagreement exists on whether lanthanoid dopants improve the conversion efficiencies for the thermochemical generation of H_2/CO using cerium oxide,[50,118,119] lanthanoids can improve the thermal stability of cerium oxide.[53] The MMS route is an extremely facile way to produce mixed oxides that contain cerium as the major cationic component. For that reason, the MSS route was chosen for this particular study on mixed oxides that contain lathanoids, especially since the lighter lanthanoids are fairly soluble in the fluoride lattice.[120] As is presented in Chapter 7, materials synthesized (via the MSS route) that contain higher concentrations of Zr, 30 mol% and above, are not phase pure. While the presence of multiple mixed oxide phases is not necessarily problematic (in Chapter 7, the H_2 fuel production was increased for a highly inhomogeneous sample relative to one that was phase pure), it can complicate analyses of the crystalline polymorphs present in a material. Also, the different phases can sinter at substantially different rates, which can make analysis of the thermal stability of a particular 3DOM material difficult. To avoid potential issues stemming from the formation of multiple phases, the content of cerium cations was fixed at 80 mol% (relative to the total content of cations). Data was mainly gathered to determine how the dopants change the structural characteristics of the crystalline phase and the morphological after thermal treatment. Each point is discussed in turn.

8.3.1.1 Characterization of As-Made MSS Samples via Powder X-Ray Diffraction

Mixed oxides that contain two cationic species (cerium and a dopant) or three cationic species (cerium and two dopants) were synthesized and analyzed via PXRD. The patterns for the singly-doped 3DOM materials are shown in Figure 8.3. All patterns for the 3DOM materials possess the characteristic reflections of a face-centered cubic fluorite lattice. However, the positions of the peaks are displaced from the literature pattern for CeO_2. Oxygen vacancies generated due to the small size of the crystallites[121] and the presence of the dopant cations contribute to the shifts in the locations of the peaks.[120] Due to the high content of the dopant in these samples, the latter is far more important. Zirconium lowers the lattice parameter and causes reflections to shift to higher °2θ, similar to what is observed in the 3DOM materials discussed in Chapter 7. Trivalent lanthanoid dopants shift the peaks to lower values of °2θ due to an expansion of the cubic fluorite lattice.[120] These dopants are larger than the Ce^{4+} (0.97 Å) that they replace in the lattice and tend to increase the unit cell parameter (*a*).[122] While expansion of the lattice is encountered for lighter lanthanoids, it is observed that heavier lanthanoids (like Yb) experience lattice contractions. This is due, in part, to the formation of oxygen vacancies that compensate for the addition of the acceptor dopants (equation 8.6, where Ln is a trivalent lanthanoid). Heavier lanthanoids have ionic radii closer to Ce^{4+} (0.97 Å), so the decreased O–O repulsion induced by widespread oxygen vacancy formation causes the contraction of the lattice.[120,123]

$$Ln_2O_3 + 2Ce_{Ce}^{X} + O_O^{X} \rightarrow 2Ln'_{Ce} + 2CeO_2 + V_O^{\cdot\cdot} \quad (8.6)$$

Table 8.3 provides the calculated unit cell parameters for the lanthanoid-doped 3DOM materials. To obtain these parameters, PXRD patterns of the relevant materials were indexed using the program TREOR90. An internal LaB_6 standard was used, as well. For the mixed oxides, the unit cell parameter is higher than the undoped 3DOM CeO_2. Since the ionic radius of the dopant decreases with increasing lanthanoid atomic number, the unit cell parameter typically decreases. These values are not what would be expected using Vegard's law, but match well with what has been reported in the literature.[123,124] Two anomalies to the general trend should be discussed. First, the lanthanum-containing mixed oxide has a lower unit cell parameter than what is reported in the literature. It is possible that the deliquescent $LaCl_3 \cdot 7H_2O$ adsorbed enough water to significantly change the number of moles of La^{3+} added to the precursor. Thermogravimetric analysis of the $LaCl_3 \cdot 7H_2O$, shows that it loses more mass than would be expected if it for a heptahydrate. This would lead to a lower than expected dopant concentration and a smaller unit cell parameter as is seen in Table 8.3 Other researchers have also encountered

anomalies in the observed unit cell parameter with lanthanum dopants potentially due to water uptake in the precursors.[120] Second, as stated in the introduction, praseodymium is found as both Pr^{3+} and Pr^{4+} under ambient conditions. Tetravalent praseodymium has a smaller ionic radius than trivalent praseodymium, so the tetravalent cation tends to decrease the unit cell parameter.[124]

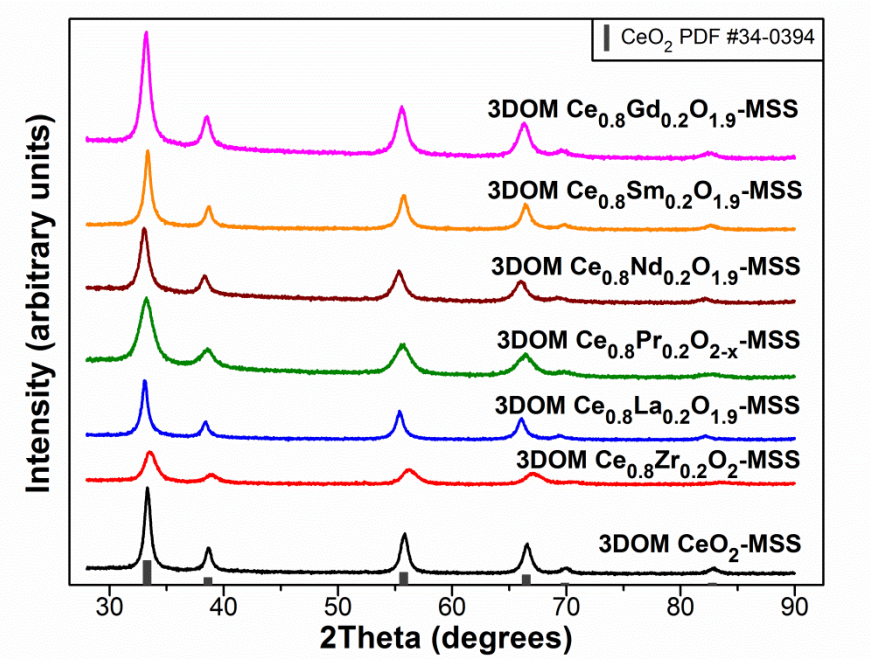

Figure 8.3 Powder X-ray diffraction patterns for the singly-doped cerium oxide materials made via the MSS route.

Table 8.3 Lattice parameters for MSS samples that contain cerium and an additional lanthanoid cation.

	None	La	Pr	Nd	Sm	Gd
a (Å), experiment	5.4111	5.445	5.426	5.452	5.438	5.427
a (Å), literature	5.4113[a]	5.47630[b]	5.423(3)[c]	5.44482[b]	5.43688[b]	5.42573[b]
dopant ionic radius (Å)[d]	NA	1.160	1.126	1.109	1.079	1.053

[a] From JCPDS #34-0394.

[b] From [123].

[c] From [124].

[d] From [122], values are for eight-fold coordination.

Three 3DOM mixed oxides were also synthesized that contain two cationic dopants. The PXRD patterns for these materials are shown in Figure 8.4. Again, the cubic fluorite crystal lattice is present in all of the samples. For the materials that contain a lanthanoid and zirconium,

the positions of the reflections are not appreciably displaced from that of pure CeO_2. This is due to the contrasting effects of the lanthanoid and zirconium when incorporated into the fluorite lattice. Both La^{3+} and Sm^{3+} are larger than Ce^{4+} (see Table 8.3) and increase the unit cell parameter; however, Zr^{4+} is smaller than Ce^{4+} and shrinks the fluorite lattice. Overall, little change in the unit cell parameter occurs. Trivalent samarium has a smaller ionic radius than trivalent lanthanum, so the dually-doped material containing Sm^{3+} has a pattern with reflections that are displaced toward higher °2θ. 3DOM $Ce_{0.8}Sm_{0.1}La_{0.1}O_{1.9}$ contains two lanthanoid dopants that are smaller than Ce^{4+} and as a consequence has reflections that are displaced to lower °2θ.

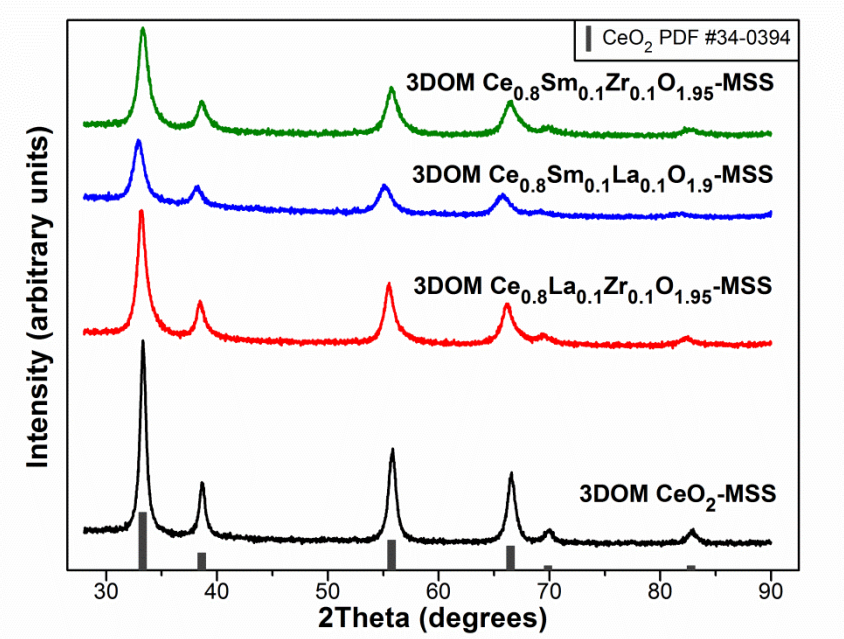

Figure 8.4 Powder X-ray diffraction patterns for the doubly-doped cerium oxide materials made via the MSS route.

Crystallite sizes were also determined using the Scherer equation (Table 8.4). All mixed metal oxides have smaller crystallite sizes than the pure 3DOM CeO_2-MSS. No clear relation exists between the properties of the dopants (ionic radius, charge, etc.) and the measured crystallite size. Even the dual-doped materials have no clear relation to their single-doped counterparts. For the dual-doped materials that contain lanthanum, addition of a second dopant significantly decreases crystallite size compared to the 3DOM $Ce_{0.8}La_{0.2}O_{1.9}$-MSS. However, the 3DOM $Ce_{0.8}Sm_{0.1}Zr_{0.1}O_{1.95}$-MSS has larger crystallites than either the 3DOM material doped only with Sm or only with Zr. Variations in crystallite size may be caused by small temperature fluctuations generated by variations in the position of the sample in the furnace or variations in the amount of material loaded in the boat.

Table 8.4 Crystallite sizes of the MSS samples estimated using the Scherrer equation.

Sample	crystallite size (nm)[a]
CeO_2-MSS	16.5
$Ce_{0.8}Zr_{0.2}O_2$-MSS	8.1
$Ce_{0.8}La_{0.2}O_{1.9}$-MSS	15.0
$Ce_{0.8}Pr_{0.2}O_{2-x}$-MSS	7.4
$Ce_{0.8}Nd_{0.2}O_{1.9}$-MSS	11.4
$Ce_{0.8}Sm_{0.2}O_{1.9}$-MSS	8.6
$Ce_{0.8}Gd_{0.2}O_{1.9}$-MSS	11.4
$Ce_{0.8}La_{0.1}Zr_{0.1}O_{1.95}$-MSS	10.3
$Ce_{0.8}Sm_{0.1}La_{0.1}O_{1.95}$-MSS	8.6
$Ce_{0.8}Sm_{0.1}Zr_{0.1}O_{1.95}$-MSS	9.7

[a] Lorentzian function used for fitting of (111) peak.

8.3.1.2 Morphological Characterization of the MSS Samples Before and After Thermal Treatment

Scanning electron micrographs were taken of all the as-made 3DOM MSS materials discussed in the prior subsection. These images are split in two parts, with 3DOM $Ce_{0.8}Pr_{0.2}O_{2-x}$-MSS and 3DOM $Ce_{0.8}Nd_{0.2}O_{1.9}$-MSS in Figure 8.5 and all other materials in Figure 8.6. The materials shown in Figure 8.5 were not treated at high temperatures, so they are presented in a separate image. All the materials synthesized via the MSS route contain interconnected macropores. Most regions of these samples contain the 3DOM structure, albeit with some larger voids that may have been generated from incomplete infiltration. Greater disorder is found in the dually-doped materials, but pore spaces remain interconnected.

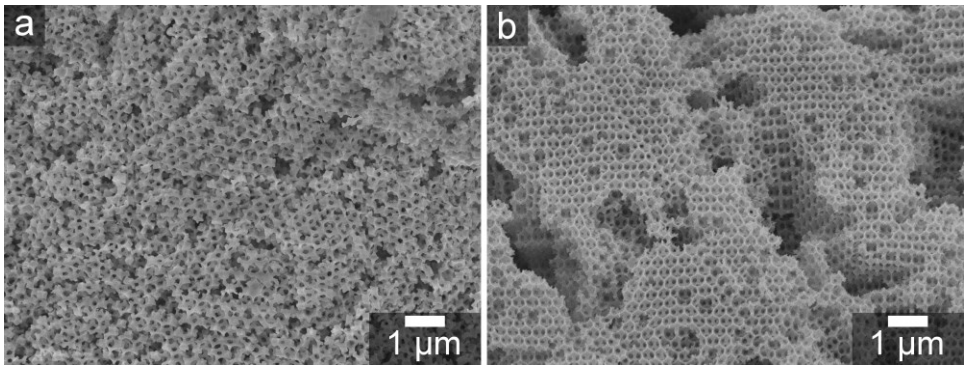

Figure 8.5 SEM micrographs of (a) 3DOM $Ce_{0.8}Pr_{0.2}O_{2-x}$-MSS and (b) 3DOM $Ce_{0.8}Nd_{0.2}O_{1.9}$-MSS.

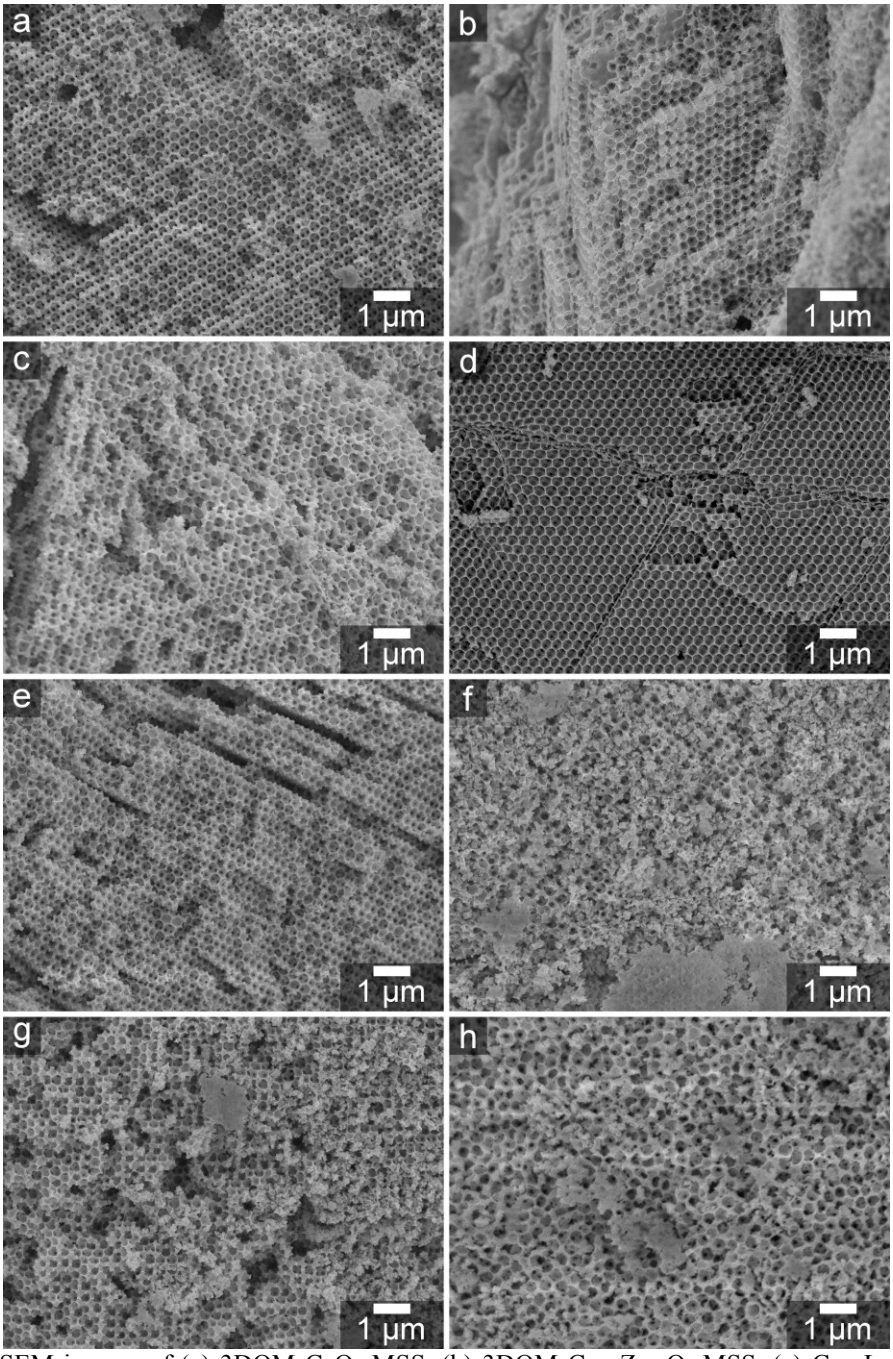

Figure 8.6 SEM images of (a) 3DOM CeO_2-MSS, (b) 3DOM $Ce_{0.8}Zr_{0.2}O_2$-MSS, (c) $Ce_{0.8}La_{0.2}O_{1.9}$-MSS, (d) $Ce_{0.8}La_{0.1}Zr_{0.1}O_{1.95}$-MSS, (e) $Ce_{0.8}Sm_{0.2}O_{1.9}$-MSS, (f) $Ce_{0.8}Sm_{0.1}La_{0.1}O_{1.95}$-MSS, (g) $Ce_{0.8}Sm_{0.1}Zr_{0.1}O_{1.95}$-MSS, and (h) $Ce_{0.8}Gd_{0.2}O_{1.9}$-MSS.

Considerable morphological changes occur upon thermal treatment of these macroporous materials at 1350 °C. Figure 8.7 provides representative images for eight of the 3DOM material after the thermal treatment step. The corresponding images of the as-made samples are shown in

Figure 8.6. Any semblance of an ordered pore network disappears due to extensive sintering. Both crystal growth and densification occur during heating; however, the densification of the material is easier to observe upon visual inspection of the power after thermal treatment. While the as-made 3DOM materials are fluffy, opalescent powders, the treated samples lose both their opalescence and well over 50 % of their volume. For all materials, the final sintered morphology resembles what has been reported by Rudisill *et al.* for 3DOM CeO_2 that underwent thermochemical cycling at ~1200 °C and at 800 °C.[117] Thermal treatment eliminates ordered macroporosity, but a disordered network of pores remains. This network coarsens and pores eventually become closed off from each other as sintering progresses. In these 3DOM materials, the macropores in the original 3DOM network provide a kinetic barrier for sintering.[125] This "pore drag" phenomenon is caused by the attachment of pores to grain boundaries. Moving grain boundaries drag attached pores along, provided the mobility of the pore and the boundary/attached pore are similar.[125] These pores coalescence and coarsen as grain boundaries migrate and merge into each other. For most of the sintered 3DOM materials, pores that are similar in size to the grains are formed. Numerous grains border these pores, so any reduction in the surface area of the pores causes a greater increase in the area of grain boundaries. Pores tend to be stable in these cases.[126] However, the undoped 3DOM CeO_2-MSS contains larger grains and lower coordination, which can facilitate further reduction of surface area.[126]

Addition of dopants, either Zr^{4+} or the lanthanoid cations, causes significant reductions in the crystal size relative to undoped CeO_2. Since the amount of dopant is 20 mol% for these samples, solute drag can be reasonably expected to contribute to the smaller crystallite size.[29,127] It cannot be ruled out that changes to the mobility of ionic species in the lattice (altering the volume diffusion) also lead to reductions in crystallite size (to hundreds of nm). At high levels of doping in CeO_2, defect associations are thought to slow various mass transport mechanisms.[128] Grain boundary energetics may also be changed. As was mentioned in the paragraph before, the doped 3DOM materials retain smaller pores surrounded by numerous crystallites. Reductions in the size of crystallites, also lead to lessened coarsening of pores.[126] Both pores and grains are fairly anisotropic in these sintered materials, which likely originates from anisotropy drag forces acting on the crystallites (via attached pores). While solute drag is likely responsible for inhibited sintering, the origin of the differences in crystallite size between particular samples is nebulous. Larger lanthanoid ions tend to cause greater reductions in crystallite size,[128,129] and this is observed here for the smaller grains in 3DOM $Ce_{0.8}La_{0.2}O_{1.9}$-MSS and 3DOM $Ce_{0.8}Sm_{0.2}O_{1.9}$-MSS. Unfortunately, that does not explain the substantial reduction in crystallite size for the

3DOM $Ce_{0.8}La_{0.1}Zr_{0.1}O_{1.95}$-MSS. A recent report provided information that co-doping with La/Zr and Sm/Zr produced materials with smaller crystallites, but a mechanism was not put forth.[130] However, with all of the doped materials, it remains to be seen if continued grain growth and densification occur at 1350 °C.

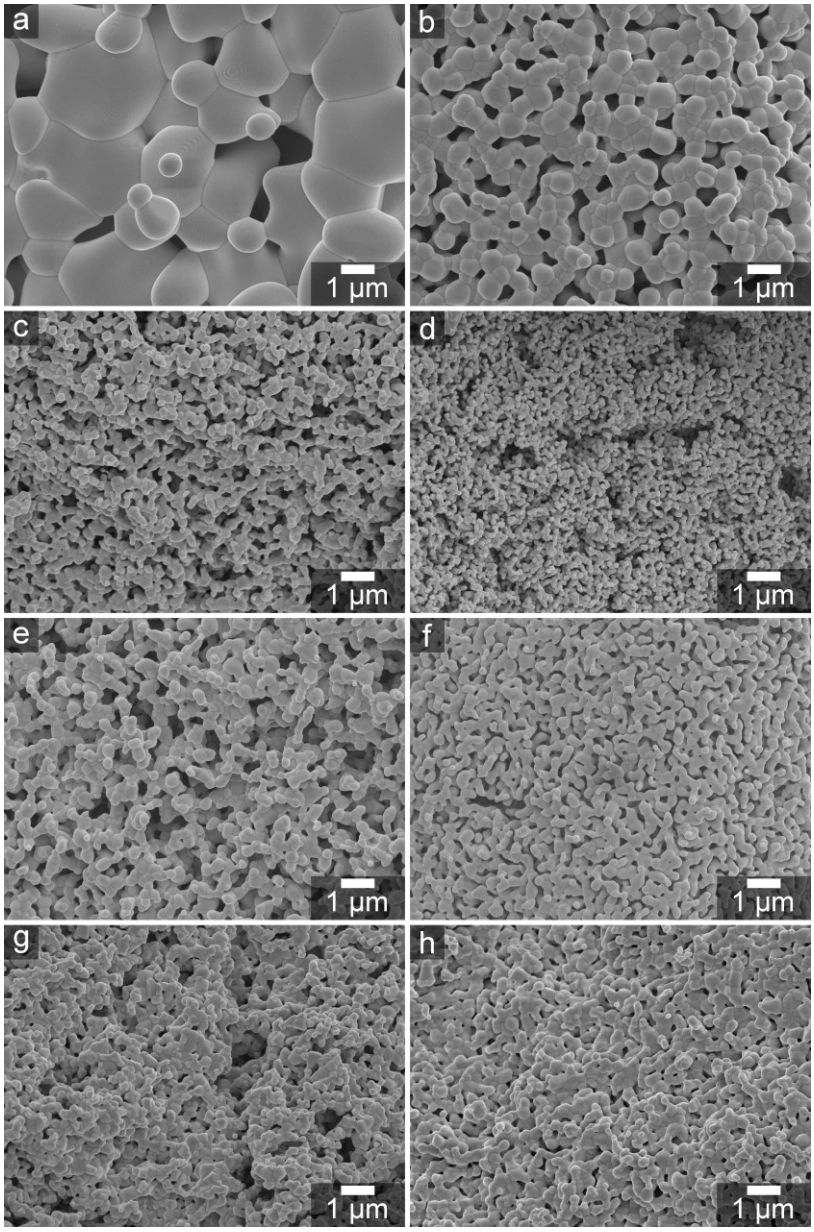

Figure 8.7 SEM images of various 3DOM materials thermally-treated at 1350 °C for 1 h. The specific materials are: (a) 3DOM CeO_2-MSS, (b) 3DOM $Ce_{0.8}Zr_{0.2}O_2$-MSS, (c) $Ce_{0.8}La_{0.2}O_{1.9}$-MSS, (d) $Ce_{0.8}La_{0.1}Zr_{0.1}O_{1.95}$-MSS, (e) $Ce_{0.8}Sm_{0.2}O_{1.9}$-MSS, (f) $Ce_{0.8}Sm_{0.1}La_{0.1}O_{1.95}$-MSS, (g) $Ce_{0.8}Sm_{0.1}Zr_{0.1}O_{1.95}$-MSS, and (h) $Ce_{0.8}Gd_{0.2}O_{1.9}$-MSS.

8.3.1.3 Conclusions

Ten cerium-based 3DOM materials made through the methanolic salt solution route were characterized via PXRD and electron microscopy. These analyses show that the dopants were successfully incorporated into the lattice. A cubic fluorite crystal structure is present in the materials. Trivalent lanthanoids increase the unit cell parameter for the materials, whereas Zr^{4+} decreases the unit cell parameter. Crystallite sizes for the doped as-made 3DOM materials are smaller than 3DOM CeO_2-MSS. More dramatic differences are observed in the crystallite size of the 3DOM materials after thermal treatment at 1350 °C. Dopants are found to considerably reduce the size of crystallites and pores in the sintered materials. 3DOM $Ce_{0.8}La_{0.1}Zr_{0.1}O_{1.95}$-MSS contains the smallest crystallites for all the samples.

8.3.2 Extension of the PM Route to $Ce_{0.9}Mn_{0.1}O_{2-x}$

For the rest of the chapter, the discussion centers on 3DOM materials created via the Pechini method. A good starting point is for this discussion is an extension of the Pechini method to a mixed oxide that contains cerium oxide. The general synthesis is slightly modified from what is described in Chapter 7, based on optimizations of the synthesis explored by Rudisill *et al.*[131] Manganese was chosen as dopant for cerium oxide, since it this mixed oxide has been used as a catalyst and as a material for solar thermochemical fuel production.[7,16,41] In addition, manganese can change oxidation states and potentially participate in the fuel production reactions. An especially promising finding comes from Janik and co-workers,[132] who found that manganese dopant reduces the energy needed for oxygen vacancy formation and does not significantly cripple the ability of the doped material to re-oxidize. However, this study was conducted for C–H bond activation, and, as is seen, its results do not necessarily translate to solar thermochemical fuel production.

8.3.2.1 Characterization of As-Made 3DOM $Ce_{0.9}Mn_{0.1}O_{2-x}$-PM

The transition metal-doped, 3DOM $Ce_{0.9}Mn_{0.1}O_{2-x}$-PM, was also characterized after its synthesis. As was expected, a 3DOM network is present in the material (Figure 8.8 a). Mn cations also cause the 3DOM material to absorb more incoming visible light, and consequently, the material exhibits a brilliant green structural color.[116] No impurity phases can be detected in the diffraction pattern of the material (Figure 8.8 b). A cubic fluorite structure is present and the estimated crystallite size is quite small at 4.4 nm. While the oxidation state of the Mn cations was not assessed, the positions of the reflections suggest that Mn^{2+} is present. The as-made material is tinged greenish-brown, which would be expected for the addition of Mn^{2+} cations. Reflections are

slightly shifted to higher °2θ, indicating a contraction of the lattice occurred. From Shannon, the ionic radius of eight coordinate Mn^{2+} (0.96 Å) is slightly smaller than that of Ce^{4+} (0.97 Å) cations.[122] This should lead to a slight contraction of the lattice (that may also be reinforced by the formation of oxygen vacancies), as is observed. However, additional characterization, such as XPS, is ultimately required to assess the valence state of the Mn cationic species. Unlike the 3DOM $Ce_{0.9}La_{0.1}O_{1.95}$-PM, hysteresis is not observed in the isotherm of the Mn-containing material (Figure 8.8 c). A sharp rise in the volume adsorbed/desorbed happens at high relative pressures due to the presence of macropores. The BET specific surface area of the material is 29.2 m^2/g, which is similar to as-made 3DOM cerium zirconium oxide materials.

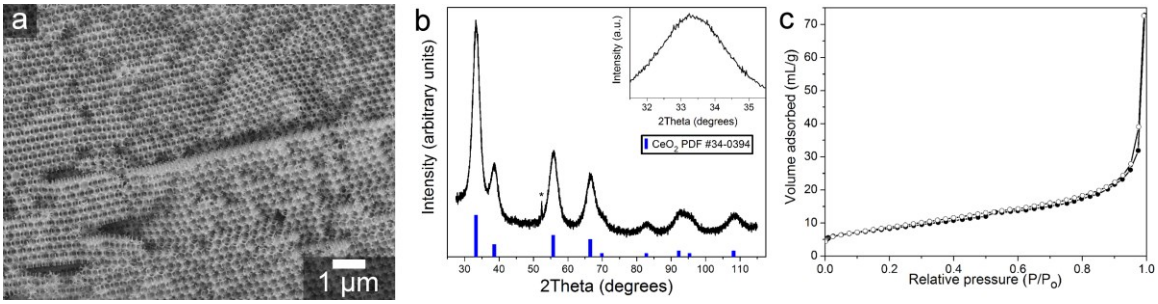

Figure 8.8 Results from characterization of 3DOM $Ce_{0.9}Mn_{0.1}O_{2-x}$-PM by several different techniques are shown. In (a) an SEM micrograph of the 3DOM network is given, (b) presents the PXRD pattern, and (c) is the N_2 sorption isotherm collected from the material.

8.3.2.2 Thermochemical Cycling of 3DOM $Ce_{0.9}Mn_{0.1}O_{2-x}$-PM

Thermochemical cycling (70 reduction/oxidation cycles) of the 3DOM $Ce_{0.9}Mn_{0.1}O_{2-x}$-PM results in massive structural changes. After the bed of 3DOM $Ce_{0.9}Mn_{0.1}O_{2-x}$-PM was removed from the reactor, it was easily observed that densification of the bed had occurred. The bed densified away from the process tube and formed a sintered cylinder around the T_1 thermocouple. Since the bed was broken during removal, a cross-section of the core was not available for imaging. Even though a cross-section was not obtained, different morphologies are observed in the SEM images of the post-cycled material (Figure 8.9 a). Rudisill *et al.* discovered that when undoped 3DOM CeO_2 was thermochemically cycled in the IR reactor set-up, a thermal gradient developed.[117] This thermal gradient results in considerable grain growth/densification of crystals near the process tube, and better retention of the 3DOM structure in center. However, 3DOM $Ce_{0.9}Mn_{0.1}O_{2-x}$-PM sinters more extensively than 3DOM CeO_2, and contains a high fraction of µm-size grains (~70 % of the specimen). Areas with disordered macropores and smaller crystallites are much rarer than in 3DOM CeO_2. Manganese cations have been reported to

facilitate sintering at high temperature,[133] and this is confirmed for the 3DOM $Ce_{0.9}Mn_{0.1}O_{2-x}$-PM. Even though some smaller crystallites are present, the line widths of the reflections in the PXRD pattern are so narrow that the $K_{\alpha 2}$ peaks are visible (Figure 8.9 b). Diffraction from μm-scale grains drowns out the smaller crystallites. Phase separation does not occur during cycling, and only reflections from a cubic fluorite phase can be identified.

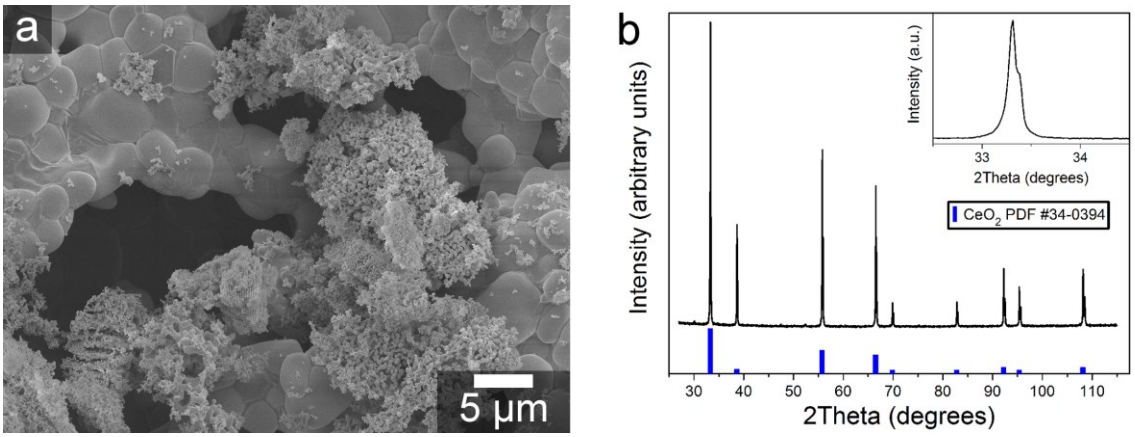

Figure 8.9 (a) SEM micrograph of the thermochemically cycled 3DOM $Ce_{0.9}Mn_{0.1}O_{2-x}$-PM sample that shows morphological variations in present the sample. Most of the scanned areas are heavily sintered. Peaks in the PXRD pattern (b) narrow considerably from the as-made sample, but remain single phase.

Unlike 3DOM CeO_2, the 3DOM $Ce_{0.9}Mn_{0.1}O_{2-x}$-PM does not produce any appreciable amounts of CO. Since only peaks from O_2 production were found, only the O_2 gas production from the reduction step is recorded (Figure 8.10). The temperature of the thermocouple embedded in the sample (T1) is also recorded (Figure 8.10). Though it is not shown, the O_2 production commences when the temperature is ramped to 1100 °C. Although the amount of O_2 produced exceeds that of pure 3DOM CeO_2 for the first two cycles, the oxygen production stabilizes at a low level (0.1 mL/g). It is likely that a combination of severe sintering (see Figure 8.9 a) and unfavorable changes to the redox properties of the material are responsible for the poor O_2 production. With regards to the latter point, the addition of Mn eases the reducibility of the of CeO_2 lattice. This leads to the high levels of O_2 production for the first two cycles. However, the 3DOM $Ce_{0.9}Mn_{0.1}O_{2-x}$-PM is much harder to oxidize, since it is easier to reduce.[134] Therefore, the use of CO_2 at 800 °C was insufficient to reoxidize the doped material to any appreciable extent, as evidenced by the lack of CO production. One curious finding also shown in Figure 8.10 is that the T1 temperature is significantly lower than what was reported by Rudisill *et al.* for 3DOM CeO_2.[117] It may be that poor positioning of the 3DOM $Ce_{0.9}Mn_{0.1}O_{2-x}$-PM or even shrinkage of the bed away from the thermocouple is responsible for this discrepancy.

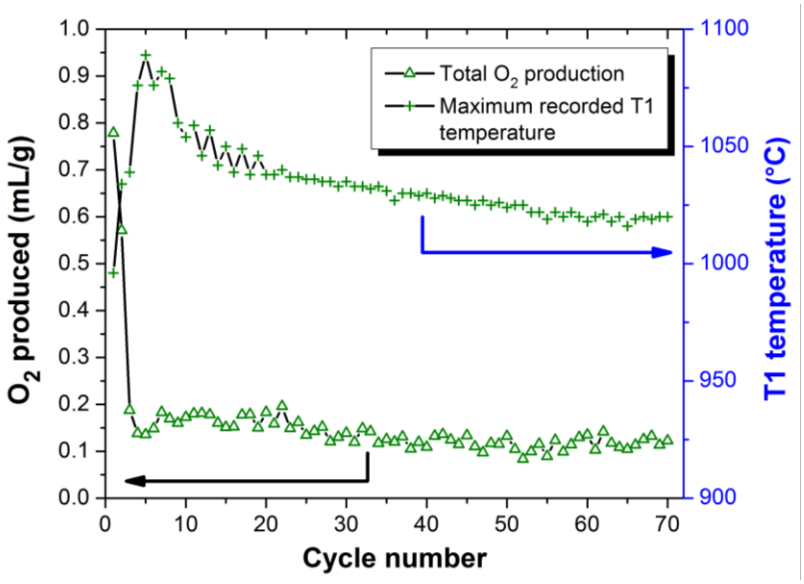

Figure 8.10 Both the highest temperature recorded by the sample thermocouple (T1) and the integrated cycle-to-cycle O_2 production are recorded. Data collected by Tingting Quan.

8.3.2.3 Conclusions

3DOM $Ce_{0.9}Mn_{0.1}O_{2-x}$-PM was characterized and thermochemically cycled in an IR furnace. The as-made 3DOM material contains the same cubic fluorite crystal structure found in undoped CeO_2, and crystallite sizes for the 3DOM $Ce_{0.9}Mn_{0.1}O_{2-x}$-PM are less than 5 nm. The specific surface area and pore volume obtained via gas sorption are similar to those obtained for other 3DOM materials synthesized via the Pechini method. These promising structural features do not lead to an increase the fuel production for the 3DOM $Ce_{0.9}Mn_{0.1}O_{2-x}$-PM compared to 3DOM CeO_2. Structural changes are severe due to thermochemical cycling, and the material cannot be oxidized under CO_2 at 800 °C.

8.3.3 3DOM Praseodymium-Based Oxides

Since the Pechini method allows for the synthesis of many different oxide and mixed oxide compositions, it was selected for the synthesis of the praseodymium-based oxide materials. For the undoped PrO_{2-x} material, a Pechini precursor was prepared that was similar in composition to the precursor for the cerium oxide-based materials described in Chapter 7. Modifications to the amount of citric acid, ethylene glycol, and water in the precursor were made for the doped oxide. In addition, a vacuum-infiltration method was used for the synthesis of this 3DOM material. These changes to the composition of the precursor and to the processing conditions were required for the colloidal crystal templating to be successful. Much like the prior section, a discussion of

the structure of both the 3DOM PrO_{2-x} and the 3DOM $Pr_{0.6}Zr_{0.35}Y_{0.05}O_{2-x}$ are first given, including structural changes induced by chemical redox cycling. Finally, the H_2 production of these two materials arising from redox cycling in the presence of steam is discussed in light of the structural characterization results.

8.3.3.1 Structural Characterization of 3DOM Praseodymium-Based Oxides

Due to the similarities in the crystal structures of lanthanoid oxides, a good starting point for the analysis of the praseodymium-containing materials is their PXRD patterns. Patterns collected before and after chemical redox cycling are shown in Figure 8.11. Focusing on the undoped material first (Figure 8.11 a), the as-made 3DOM PrO_{2-x} contains relatively few peaks. These reflections match those of cubic fluorite Pr_6O_{11}, a stable mixed valence phase that is commonly formed from sol-gel syntheses.[135] Table 8.5 provides the crystallite size of the sample. After cycling, the undoped PrO_{2-x} contains a different phase and much sharper peaks in the pattern. All of the reflections for the cycled 3DOM PrO_{2-x} match those of the hexagonal (A-type) praseodymium sesquioxide. Although Pr^{4+} is present in the as-made sample, the Pr^{4+} content is reduced during cycling. The hexagonal phase is only stable in a fairly narrow range that includes the end member Pr_2O_3 that contains solely Pr^{3+} cations. The crystallite size of the cycled sample is too large for application of the Scherrer equation (Table 8.5). A different situation arises for the doped 3DOM $Pr_{0.6}Zr_{0.35}Y_{0.05}O_{2-x}$. Figure 8.11 b shows the diffraction patterns for the doped material both before and after cycling. The as-made material is either amorphous or contains extremely small crystallites. A broad peak is found at ~35 °2θ, which does not match either of the highest intensity peaks for Pr_6O_{11} or Pr_2O_3. It could be that the peak is from nuclei of a doped Pr_6O_{11} phase. Once cycling is finished, the pattern from the 3DOM $Pr_{0.6}Zr_{0.35}Y_{0.05}O_{2-x}$ contains reflections from a cubic fluorite phase similar that reported for Pr_6O_{11}. Reflections are displaced to higher °2θ relative to the Pr_6O_{11} since the undersized Y^{3+} and Zr^{4+} cations contract the crystal lattice. Cycled 3DOM $Pr_{0.6}Zr_{0.35}Y_{0.05}O_{2-x}$ also contains peak shapes that can be better fit by two overlapping peaks with different full widths at half maximum height. If this bimodal distribution is accurate, then the smaller crystallites are around 8.4 nm in diameter and the size of the large ones cannot be estimated using Scherrer equation. Thermal gradients in the reactor may have made sintering anisotropic in this sample.

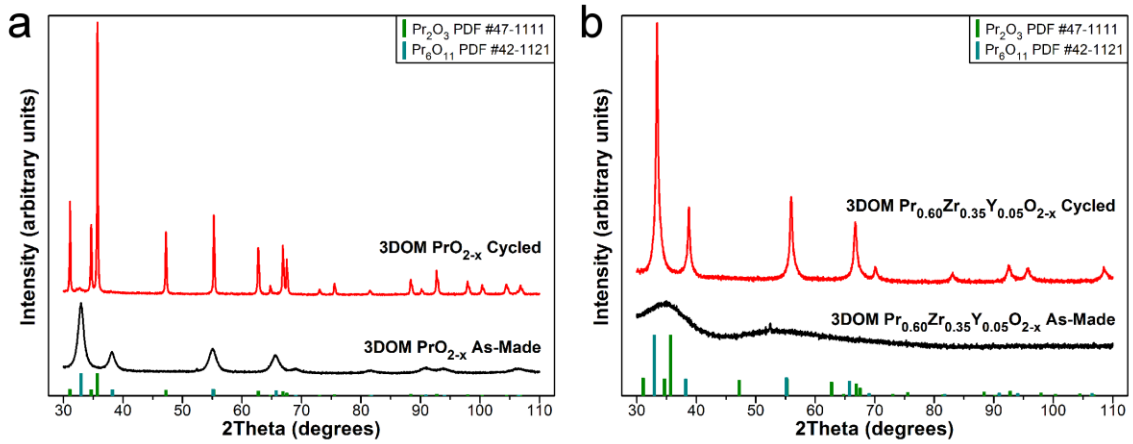

Figure 8.11 Diffraction patterns for the Pr-containing 3DOM materials both before and after cycling. The patterns from the undoped 3DOM PrO_{2-x} are shown in (a) and those from the doped material are shown in (b).

Table 8.5 Crystallite sizes, surface areas, and pore volumes for the Pr-based materials.

Sample	crystallite size (nm)	secondary crystallite size (nm)[a]	BET surface area (m^2/g)	pore volume (cm^3/g)
3DOM PrO_{2-x}, as-made	9.0	NA	16.1	0.063
3DOM PrO_{2-x}, Cycled	>100[b]	NA	7.3	0.022
3DOM $Pr_{0.60}Zr_{0.35}Y_{0.05}O_{2-x}$, as-made	[c]	NA	28.6	0.083
3DOM $Pr_{0.60}Zr_{0.35}Y_{0.05}O_{2-x}$, cycled	8.4	>100[b]	18.8	0.15

[a] Bimodal distribution of crystallites possibly present in one of the samples.

[b] Reflections too narrow to allow for application of the Scherrer equation.

[c] Peaks too broad to allow for accurate fitting.

To further explore the changes in the crystallite sizes caused by cycling and the resulting impact on the 3DOM morphology, SEM microscopy was used to image the materials. For the 3DOM PrO_{2-x}, a distinct change occurs during cycling. The 3DOM structure is clearly visible for this material after the template is removed via calcination (Figure 8.12 a, b). Treatment at 800 °C under alternating reducing/oxidizing gas streams causes considerable crystallite growth, as is also

detected in the PXRD pattern of the cycled material. A disordered macropore network remains after chemical redox cycling (Figure 8.12 c, d), and these macropores are still interconnected, despite extensive sintering. Compared to cerium oxide, the PrO_{2-x} has much lower thermal stability. The images shown in Figure 8.12 c and d have sintered far worse than the similarly cycled 3DOM CeO_2 described in Chapter 7. It is not completely clear if the gaseous atmosphere flowing over the 3DOM PrO_{2-x} impacts its sintering. However, the Pr is in its lowest oxidation state after cycling (and, as is later discussed barely produces H_2), so it is unlikely changes to the defect chemistry are a major contributing factor. By co-doping with Zr and Y, crystal growth is effectively suppressed. SEM micrographs from the 3DOM $Pr_{0.60}Zr_{0.35}Y_{0.05}O_{2-x}$ both prior to (Figure 8.13 a) and after cycling (Figure 8.13 b, c) are very similar. Chemical cycling does not disrupt the 3DOM network and ordered macropores remain in the structure. No evidence of crystallites that are larger than 100 nm can be found via SEM imaging. While that does not necessarily mean that large crystals do not exist (only a small specimen was analyzed), it may suggest that if this bimodal distribution of crystal sizes exists, large crystals are rare.

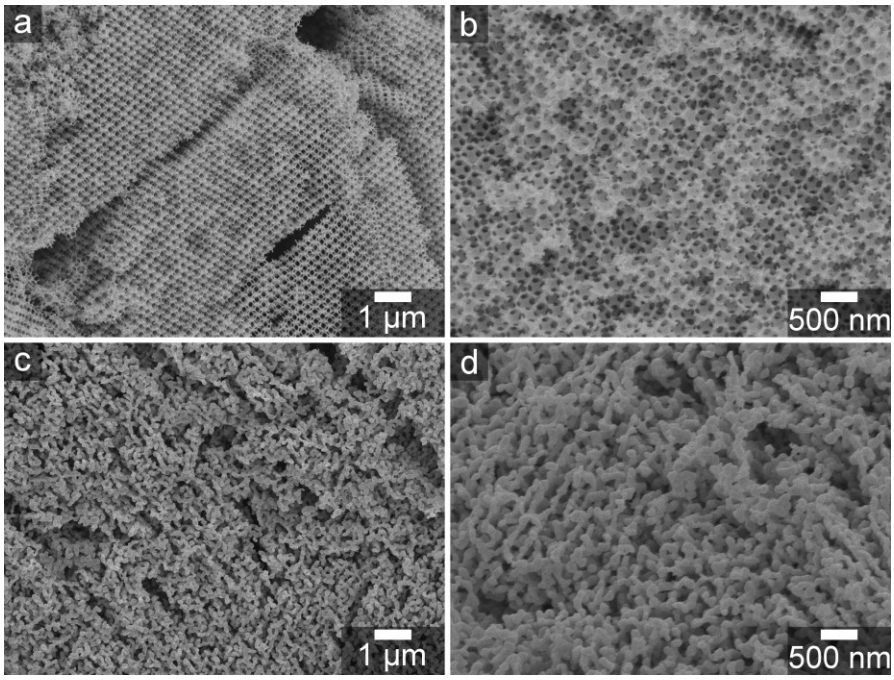

Figure 8.12 Representative SEM micrographs of the 3DOM PrO_{2-x} (a, b) before and (c, d) after chemical redox cycling at 825 °C.

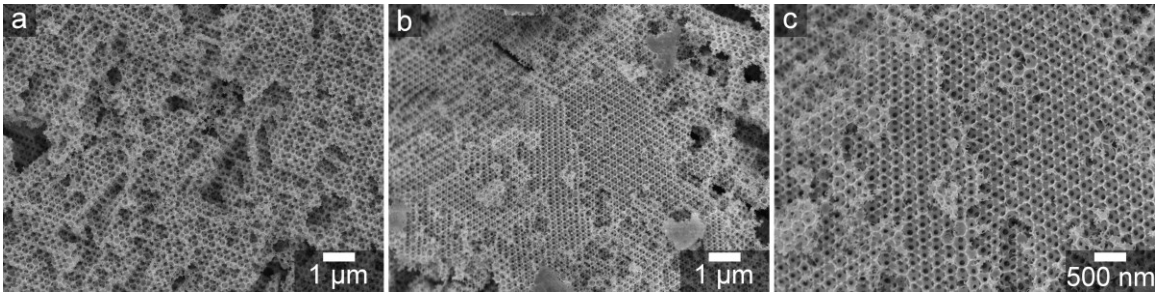

Figure 8.13 SEM micrographs of the 3DOM $Pr_{0.60}Zr_{0.35}Y_{0.05}O_{2-x}$ taken (a) before and (b, c) after cycling at 825 °C. No change in the morphology is observed.

The morphological changes caused by chemical redox cycling were also analyzed via nitrogen sorption. Isotherms collected from the as-made and cycled samples are shown in Figure 8.14. All isotherms contain a rise in volume adsorbed at high P/P_o that is from macropores in the materials. Limited hysteresis is also observed in the as-made 3DOM PrO_{2-x}. This is likely from pore spaces between crystallites. BET specific surface areas decrease after cycling (Table 8.5), and this change is more dramatic for the material that experiences the worst sintering, the 3DOM PrO_{2-x}. Doping leads to improvements in surface area both before and after cycling relative to the undoped material. Pore volumes decrease for the 3DOM PrO_{2-x}, but increase for the 3DOM $Pr_{0.60}Zr_{0.35}Y_{0.05}O_{2-x}$. It is possible that the increase in pore volume of the doped material is caused by grinding and sieving prior to redox cycling.

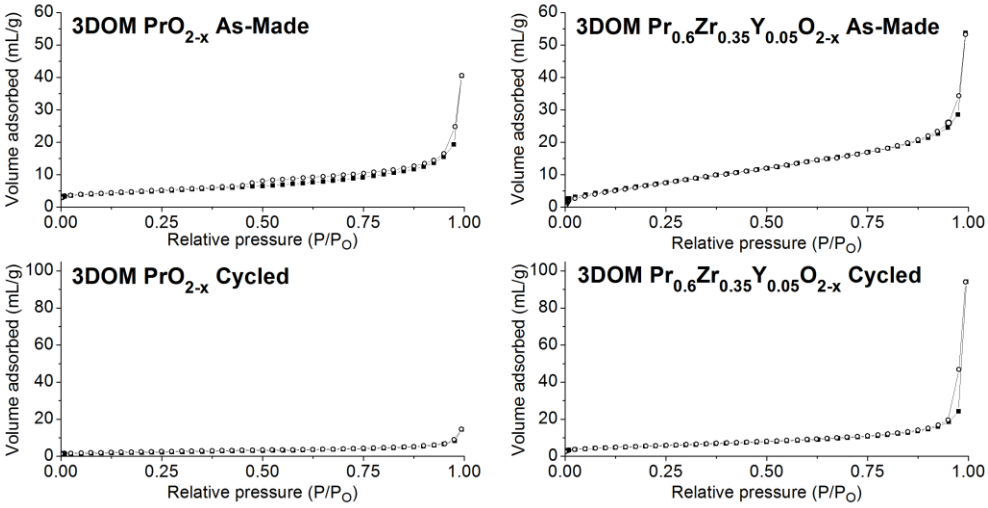

Figure 8.14 Gas sorption isotherms of the various as-made and cycled Pr-containing 3DOM materials. All materials are macroporous, but lose surface area after cycling.

8.3.3.2 Chemical Redox Cycling of the Pr-Containing Materials

While the structural characterization gave an indication that the 3DOM PrO_{2-x} has poor fuel production capabilities, both materials, the 3DOM PrO_{2-x} and the 3DOM $Pr_{0.6}Zr_{0.35}Y_{0.05}O_{2-x}$, produce much less H_2 than the cerium oxide-based materials discussed in Chapter 7. Fuel production curves for the 3DOM PrO_{2-x} are plotted in Figure 8.15. The initial cycles have a higher maximum H_2 flow rate, but maximum rates stabilize at around 0.50 $mL \cdot min^{-1} \cdot g^{-1}$ or 22 $\mu mol \cdot min^{-1} \cdot g^{-1}$ by cycle 4. Overall H_2 production for these latter cycles is only around 3.0 $mL \cdot min^{-1} \cdot g^{-1}$ or 130 $\mu mol \cdot min^{-1} \cdot g^{-1}$, a tenth of what was produced by the best materials in Chapter 7. Much like the 3DOM $Ce_{0.9}Mn_{0.1}O_{2-x}$-PM, the culprit for the poor production of H_2 in the 3DOM PrO_{2-x} is a combination of structural changes and an inability of the material to be reoxidized. Structural changes are more severe than for CeO_2, leading to less surface area available for heterogeneous reactions. In terms of the redox properties, praseodymium oxide is easier to reduce than cerium oxide.[57,63] Even the as-made 3DOM PrO_{2-x} contains both Pr^{3+} and Pr^{4+} cations. PXRD reveals that the cycled 3DOM PrO_{2-x} contains a pattern that matches the fully reduced Pr_2O_3 phase, and it is important to point out that the sample was removed after completion of an oxidation step. This ease of reduction comes at the price of making oxidation extremely difficult; a saturated stream of H_2O in Ar at 825 °C cannot oxide the 3DOM PrO_{2-x} sample to any appreciable extent. Increases in the oxidation temperature and a higher concentration of the oxidant in the gas stream may improve this situation. Doping improves the fuel production rates and overall productivity; however, the 3DOM $Pr_{0.60}Zr_{0.35}Y_{0.05}O_{2-x}$ still performs worse than 3DOM $CeO_2/Ce_xZr_{1-x}O_2$. Figure 8.16 shows the fuel production curves and Table 8.6 contains the cycle-to-cycle maximum fuel production rates and the total H_2 production. While these values are higher than what is observed for 3DOM PrO_{2-x}, a noticeable cycle-to-cycle decrease in the peak H_2 production rate occurs, and the overall production of H_2 also decreases. Since the morphology appears to be fairly stable (and far more stable than 3DOM PrO_{2-x}) to cycling at 800 °C, this loss of H_2 productivity may be connected with an inability of the material to oxidize. Again, the excellent reducibility is a detriment in these cycling conditions because oxidation is far more difficult.

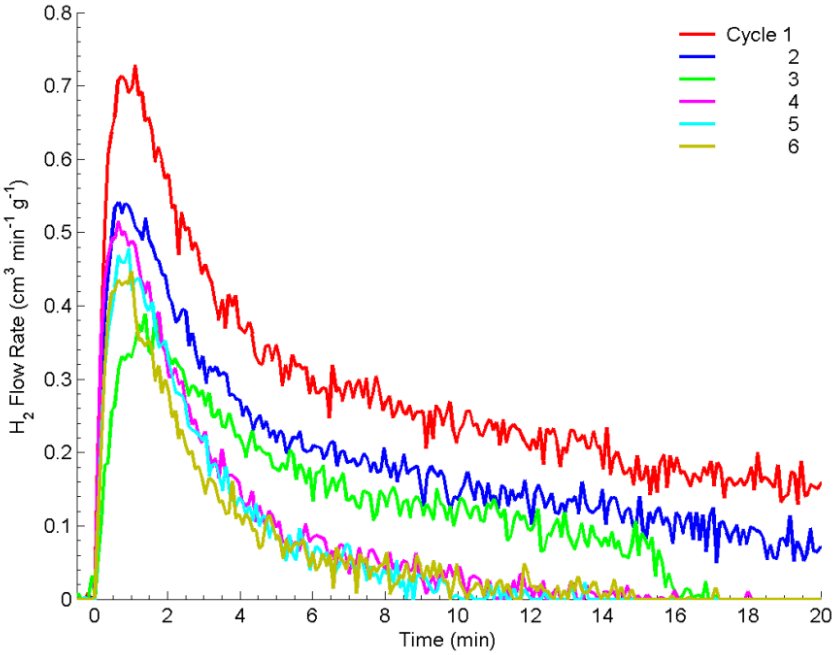

Figure 8.15 Production of H_2 gas from 3DOM PrO_{2-x} during the oxidation step of chemical redox cycling. Fuel production and the peak fuel production rate decrease for the first 3 cycles and then stabilize. Data collected and plotted by Luke Venstrom.

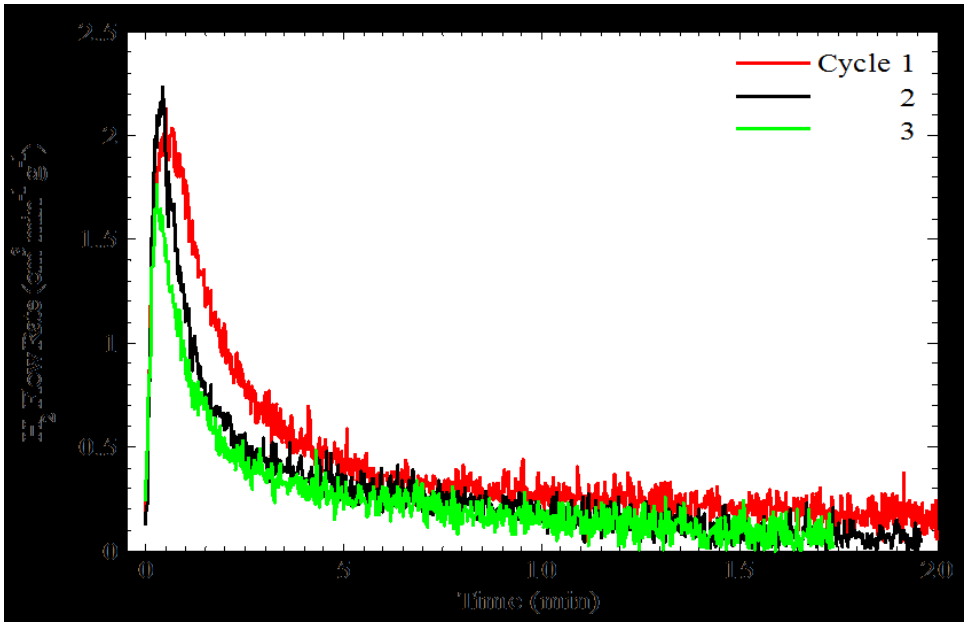

Figure 8.16 Production of H_2 gas from 3DOM $Pr_{0.60}Zr_{0.35}Y_{0.05}O_{2-x}$ during the oxidation step of chemical redox cycling. Data collected and plotted by Luke Venstrom.

Table 8.6 Production of H_2 from the 3DOM $Pr_{0.60}Zr_{0.35}Y_{0.05}O_{2-x}$ sample. Data collected by Luke Venstrom.

cycle	peak H_2 production rate ($mL \cdot min^{-1} \cdot g^{-1}$)	peak H_2 production rate ($\mu mol \cdot min^{-1} \cdot g^{-1}$)	total H_2 produced ($mL \cdot g^{-1}$)[a]	total H_2 produced ($\mu mol \cdot g^{-1}$)[a]
First	2.1±0.1	94±2	8.6±1	380±40
Second	2.2±0.1	98±2	5.9±1	260±40
Third	1.8±0.1	78±2	4.8±1	210±40

[a] Obtained by integration of the fuel production curve following the same procedure used in Chapter 7.

8.3.3.3 Conclusions

It has been shown that 3DOM PrO_{2-x} and doped 3DOM $Pr_{0.6}Zr_{0.35}Y_{0.05}O_{2-x}$ can be used for thermochemical cycling; however, the overall H_2 production rates and total productivity are significantly lower than those obtained using 3DOM CeO_2 under similar conditions. Doping does greatly improve the thermal stability of the PrO_{2-x}, allowing for retention of the 3DOM network and moderate surface areas. 3DOM $Pr_{0.6}Zr_{0.35}Y_{0.05}O_{2-x}$ also produces more fuel than 3DOM PrO_{2-x}. Still, the improvement is nowhere near what is needed to put it on par with 3DOM CeO_2. Further research with these materials will require rigorous experimental or theoretical/computational studies to determine appropriate cycling windows. Even then, the reducibility of Pr may preclude its use for thermochemical fuel production.

8.3.4 3DOM Perovskites Made via the Pechini Method

While 3DOM perovskites have been synthesized in prior studies,[136-141] the Pechini method has, to this author's knowledge, not been considered for the synthesis of these materials. As is seen in this section, Pechini precursors can be easily made that allow for the synthesis of a wide compositional range of perovskites. Complicated infiltration or thermal processing steps are not needed. This section focuses on characterizing six 3DOM perovskites that provide an indication of the broad applicability of this type of synthesis for 3DOM perovskites. It should be noted that some tailoring of the synthesis is required for certain transition metal ions. Manganese requires double the amount of citric acid compared to iron or cobalt-based perovskites, and this may be due to differences in the equilibrium constants for chelation to citric acid.[142] After the structural characterization these materials are discussed, the chemical redox cycling of the 3DOM $La_{0.6}Sr_{0.4}MnO_{3-x}$ is analyzed.

8.3.4.1 Structural Characterization of Six 3DOM Perovskite Materials

The 3DOM morphology was successfully obtained for six perovskite compositions: $LaFeO_{3-x}$, $La_{0.75}Sr_{0.25}FeO_{3-x}$, $SrFeO_{3-x}$, $La_{0.6}Sr_{0.4}MnO_{3-x}$, $LaCoO_{3-x}$, and $La_{0.6}Sr_{0.4}CoO_{3-x}$. SEM images of these materials are shown in Figure 8.17. An fcc macropore network is clearly visible in all these materials. Larger, μm-scale voids are also present in all of the structures that may be from poor infiltration. It is also possible that these voids are from phase separation in the polyester network, as reported by Rudisill *et al*.[131] A spinodal decomposition mechanism is thought to create bicontinuous networks (a μm-scale voids network and a 3DOM network) or isolated 3DOM microspheres for certain ratios of metal ions, citric acid, and ethylene glycol. In these Pechini-based 3DOM perovskite materials, a similar spinodal decomposition mechanism may be at work. To explore this possibility, additional precursors would need to be synthesized that have different ratios of metal ions, citric acid, and ethylene glycol. Aside from the presence of voids in the 3DOM network, another interesting morphological feature is observed when comparing the 3DOM $La_{0.75}Sr_{0.25}FeO_{3-x}$ and 3DOM $La_{0.6}Sr_{0.4}CoO_{3-x}$ to 3DOM $La_{0.6}Sr_{0.4}MnO_{3-x}$. Figure 8.18 shows the higher magnification images of the Sr-containing 3DOM perovskite materials. The 3DOM $La_{0.75}Sr_{0.25}FeO_{3-x}$ and $La_{0.6}Sr_{0.4}CoO_{3-x}$ (Figure 8.17 a, c) are both volume-templated and the solid network fills the totality of the interstitial space. However, the 3DOM $La_{0.6}Sr_{0.4}MnO_{3-x}$ is surface templated, and the octahedral nodes of the structure are hollow. This change may be a result of the enhanced organic content that reduces the overall concentration of metal ions. Nucleation of the perovskite may initially occur near the surface of the PMMA template, and continued growth in the metal ion poor environment may result in the hollow morphology.

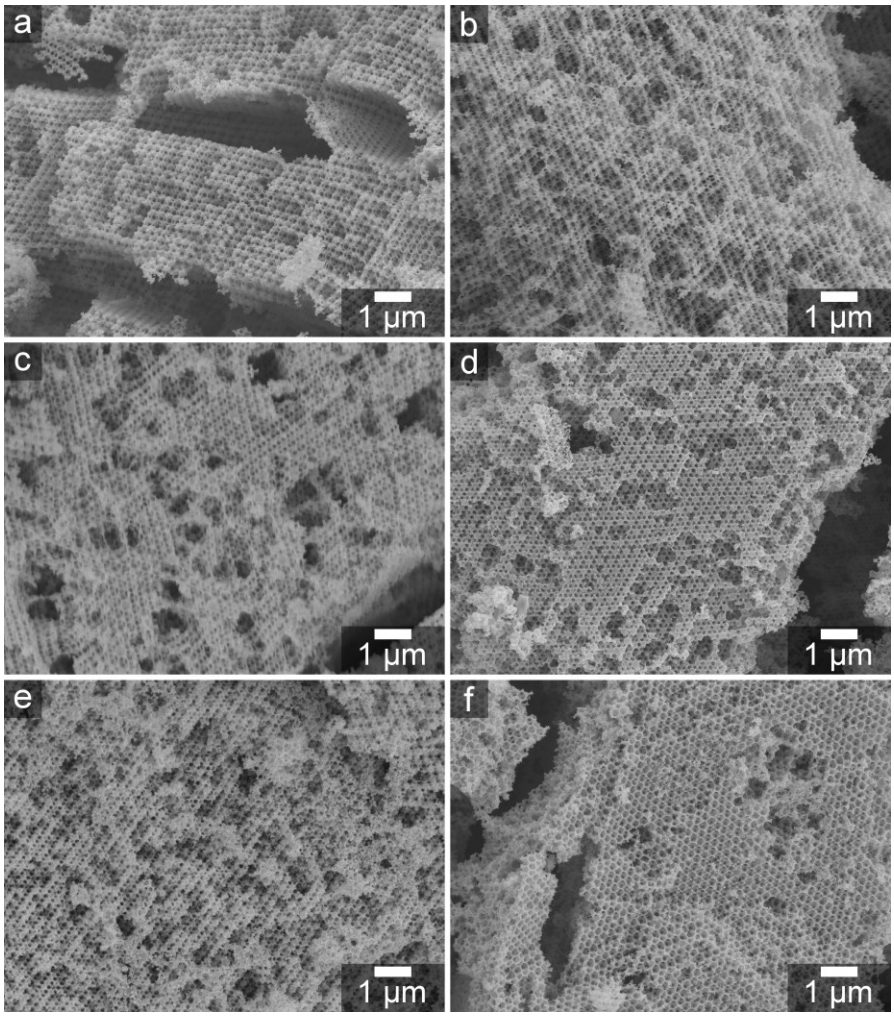

Figure 8.17 SEM images of (a) 3DOM $LaFeO_{3-x}$, (b) 3DOM $La_{0.75}Sr_{0.25}FeO_{3-x}$, (c) 3DOM $SrFeO_{3-x}$, (d) 3DOM $La_{0.6}Sr_{0.4}MnO_{3-x}$, (e) 3DOM $LaCoO_{3-x}$, and (f) 3DOM $La_{0.6}Sr_{0.4}CoO_{3-x}$.

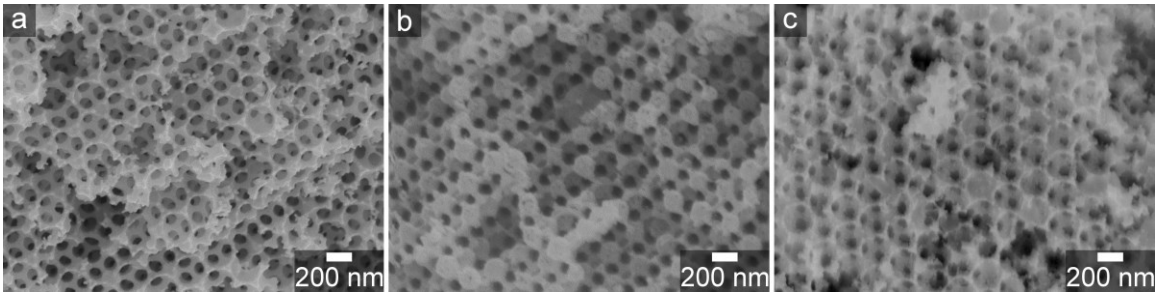

Figure 8.18 Higher magnification SEM images of the (a) 3DOM $La_{0.75}Sr_{0.25}FeO_{3-x}$, (b) 3DOM $La_{0.6}Sr_{0.4}MnO_{3-x}$, and (c) 3DOM $La_{0.6}Sr_{0.4}CoO_{3-x}$. The 3DOM $La_{0.6}Sr_{0.4}MnO_{3-x}$ is surface templated and contains hollow nodes.

Analysis of the crystal polymorphs present in the perovskite materials was conducted using PXRD. Diffraction patterns of the six 3DOM perovskite materials are shown in Figure 8.19. Reference patterns of the targeted perovskite compositions are also shown as sticks. No reference patterns are available for $La_{0.25}Sr_{0.75}FeO_{3-x}$ or $La_{0.6}Sr_{0.4}CoO_{3-x}$; however, reference sticks for two compositionally-similar perovskites ($La_{0.2}Sr_{0.8}FeO_{3-x}$ and $La_{0.5}Sr_{0.5}CoO_{3-x}$) are displayed. As can be observed in Figure 8.19, the reflections present in the 3DOM perovskites closely match those of the reference patterns. Based on the reference patterns, the iron-containing 3DOM perovskites have an orthorhombic lattice (space group 62, *Pnma*), and the other 3DOM perovskites have a rhombohedral lattice (space group 161, $R\bar{3}c$). In addition to the main perovskite phase, minor impurities are observed in some of the samples. These impurities likely arise from incomplete reactions between the various cationic components. 3DOM $SrFeO_{3-x}$ and 3DOM $La_{0.6}Sr_{0.4}CoO_{3-x}$ contain a minor $SrCO_3$ impurity (the highest intensity reflection is marked with an asterisk). Strontium carbonate is stable to temperatures in excess of 600 °C, which explains its presence in those Sr-rich perovskites.[131] Another impurity, La_2O_3, is present in the pattern for the 3DOM $LaCoO_{3-x}$ (two high intensity peaks are marked with by a cross).

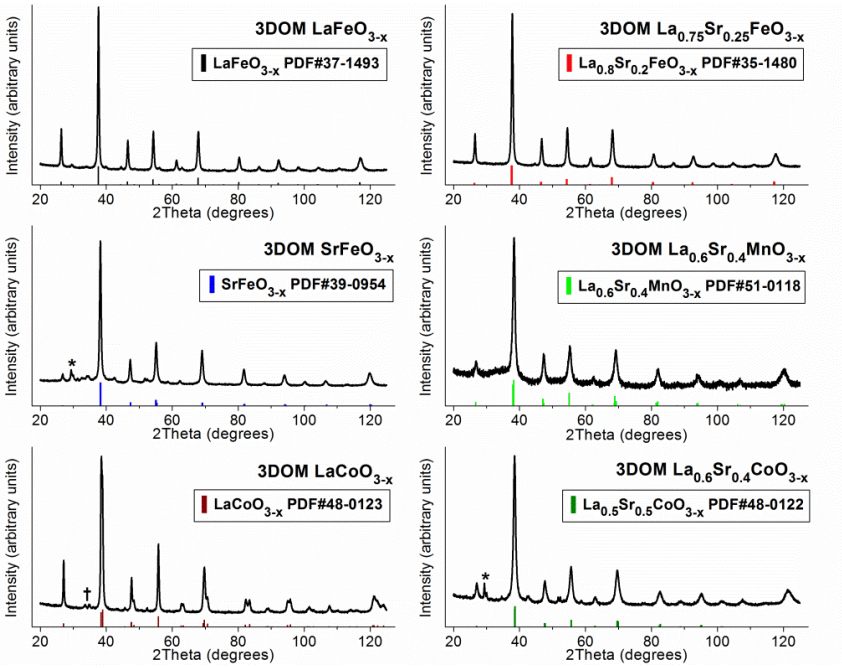

Figure 8.19 PXRD patterns are shown for the six 3DOM perovskite materials. The main reflections of these materials match the reference patterns (shown as sticks) given in each panel. Most reference patterns are for materials with the identical composition to the 3DOM perovskites or very similar compositions. Asterisks mark the (111) reflection of a $SrCO_3$ impurity (PDF #5-0418) and the cross marks two high intensity reflections from La_2O_3 (PDF #5-0602).

Crystallite sizes in the 3DOM perovskite materials (estimated using the Scherrer equation) vary considerably from sample to sample. Table 8.7 lists the crystallite sizes of the as-made materials. For the Fe- and Co-containing perovskites, the A-site substitution of Sr^{2+} for La^{3+} significantly reduces the size of the crystallites. The impact is most dramatic for the Co-containing perovskite, which is not surprising since the addition of Co is known to facilitate sintering in perovskites.[100] Addition of Sr^{2+} is known to increase the activation energy of the diffusion of cations through pervoskites resulting in a greater resistance to sintering.[143] 3DOM $La_{0.60}Sr_{0.40}MnO_{3-x}$, a Sr^{2+}-substituted material, has the smallest crystallite of any of the six 3DOM materials. It may be that the pores present in the nodes provide and addition kinetic barrier to sintering for the $La_{0.60}Sr_{0.40}MnO_{3-x}$.

Table 8.7 Crystallite sizes, surface areas, and pore volumes for the perovskite materials.

Sample	crystallite size (nm)	BET surface area (m^2/g)	pore volume (mL/g)
3DOM $LaFeO_{3-x}$, as-made	28.0	39.7	0.10
3DOM $La_{0.75}Sr_{0.25}FeO_{3-x}$, as-made	21.6	22.4	0.092
3DOM $SrFeO_{3-x}$, as-made	21.7	69.6	0.10
3DOM $La_{0.6}Sr_{0.4}MnO_{3-x}$, as-made	9.4	49.0	0.19
3DOM $La_{0.6}Sr_{0.4}MnO_{3-x}$, cycled at 500 °C	16.2	36.7	0.15
3DOM $La_{0.6}Sr_{0.4}MnO_{3-x}$, cycled at 1000 °C/1100 °C	21.3	17.4	0.079
3DOM $LaCoO_{3-x}$, as-made	32.6	19.2	0.091
3DOM $La_{0.6}Sr_{0.4}CoO_{3-x}$, as-made	11.6	29.3	0.099

[a] Bimodal distribution of crystallites possibly present in one of the samples.

[b] Reflections too narrow to allow for application of the Scherrer equation.

[c] Peaks too broad to allow for accurate fitting.

Interestingly, the crystallite size of the 3DOM perovskite does not correlate with the specific surface area of these materials determined via nitrogen sorption. The sorption isotherms are shown in Figure 8.20 and the BET specific surface areas/pore volumes are given in Table 8.7. All of the isotherms contain rises in the volume of gas adsorbed at high relative pressure. Again, this is indicative of the macropores present in the 3DOM network. Many of the isotherms also contain hysteresis loops originating from mesopore spaces between crystallites. This hysteresis loop is especially pronounced in the 3DOM $La_{0.60}Sr_{0.40}MnO_{3-x}$, which is a result of the pore spaces in the hollow nodes of the 3DOM structure. As a consequence, the pore volume of this material is high. In terms of the specific surface area, the addition of Sr^{2+} tends to improve the specific surface area. However, there are exceptions, such as the 3DOM $La_{0.25}Sr_{0.75}FeO_{3-x}$. A clear relationship is not found for the crystallite size and surface area, as stated above. It may be that the mesopore spaces between crystallite simply not correlated to the size of the crystallites.

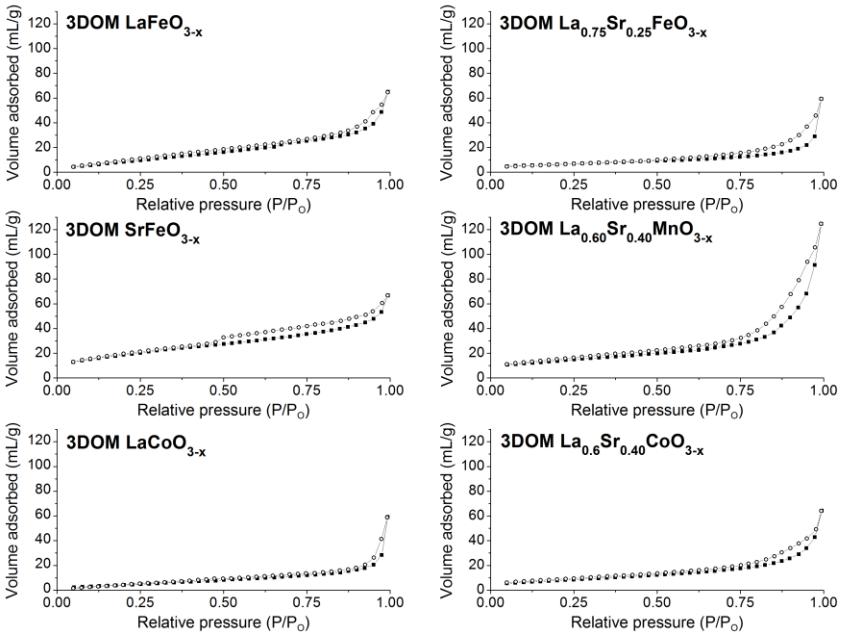

Figure 8.20 Nitrogen sorption isotherms of the 3DOM perovskite materials. All materials are macroporous and some contain hysteresis loops that arise from mesopores between crystallites.

8.3.4.2 Chemical Redox Cycling of 3DOM $La_{0.60}Sr_{0.40}MnO_{3-x}$

One perovskite composition, 3DOM $La_{0.60}Sr_{0.40}MnO_{3-x}$, was chosen for chemical redox cycling experiments. The selection of this material was based on the promising structural characteristics of the as-made material (e.g. the small crystal size and high surface area), and the potential for this material to produce more fuel than CeO_2 under certain cycling conditions.[2] To

explore the feasibility of using the 3DOM $La_{0.60}Sr_{0.40}MnO_{3-x}$ for two-step thermochemical fuel production with a temperature swing, the 3DOM material was reduced using an H_2/H_2O mixture at 500 °C. Given the thermodynamics for the $La_{0.60}Sr_{0.40}MnO_{3-x}$,[91] the atmosphere established by the gas mixture at 500 °C should be equivalent to a reduction at 1500 °C under $1 \cdot 10^{-5}$ atm of O_2. By using chemical reduction, the 3DOM structure can be retained along with its (potential) kinetic boost. Different oxidation temperatures (T_{ox}) were explored to see if production could be maximized by adjusting T_{ox}. As can be seen in Figure 8.21, CO production increases with increasing oxidation temperatures and so does the overall fuel production (Table 8.8). Fuel production initially is rapid in this material, similar to the cerium oxide-based materials discussed in Chapter 7. However, the fuel production rate drops off more quickly for $La_{0.60}Sr_{0.40}MnO_{3-x}$ than for cerium oxide-based materials. The fuel production does continue at a low level (< 0.8 $mL \cdot min^{-1} \cdot g^{-1}$) for ~15–20 min for $T_{ox} \geq 900$ °C before falling below the detection limit of the Raman spectrometer. This slow oxidation process has been reported for other perovskites,[2,3] but its origin has yet to be determined. Unfortunately, overall fuel production is still lower than what has been achieved for 3DOM CeO_2 using similar cycling conditions.[144] It may be that a high degree of reduction is achieved; however, complete re-oxidation does not occur within the timespan given for oxidation. An exceedingly slow oxidation (producing gas a rate below the detection limit of the instrument) may continue for a very long time. This would match what was observed by Scheffe *et al.* and Demont *et al.* who both reported reoxidation difficulties with this material.[2,4] Still, this material offers far better fuel productivity than that of the praseodymium oxides, and this study represents only one point in the massive compositional space of the non-stoichiometric perovskite oxides.

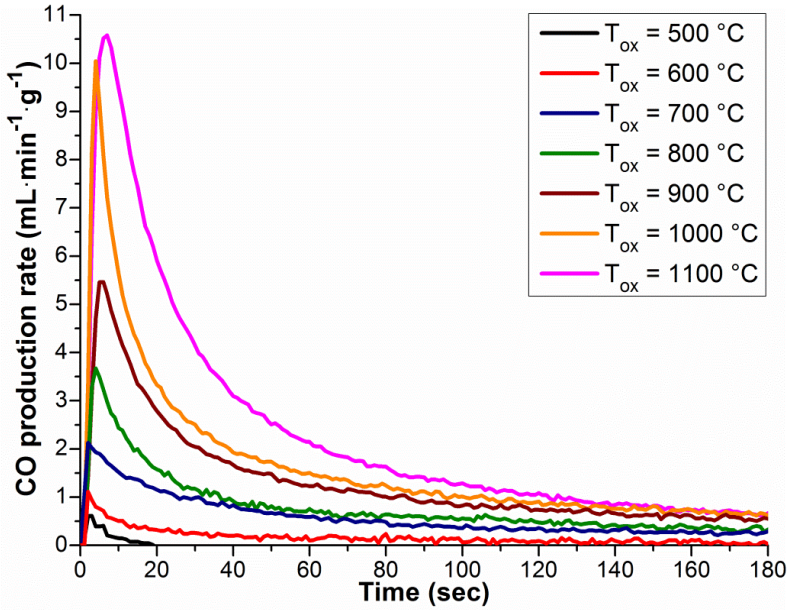

Figure 8.21 CO production curves for the 3DOM $La_{0.60}Sr_{0.40}MnO_{3-x}$ oxidized at different temperatures (T_{ox}). The production rate for CO increases with increasing oxidation temperature. Though most of the CO production is complete after 3 min, a "tail" is present for oxidations performed at high temperatures. Low levels (< 0.8 $mL \cdot min^{-1} \cdot g^{-1}$) of CO production continue for ~15 min for some runs. Data collected by Daniel Boman.

Table 8.8 Peak CO production rate and total CO produced for the oxidation of at different temperatures. Data collected by Daniel Boman and analyzed by Stacey Saba.

oxidation temperature	peak CO production rate ($mL \cdot min^{-1} \cdot g^{-1}$)	total CO produced ($mL \cdot g^{-1}$)[a]
500 °C	0.6±0.5	0.1<
600 °C	1.1±0.5	0.6±0.5
700 °C	2.1±0.5	2.5±0.5
800 °C	3.7±0.5	5.0±1
900 °C	5.5±1	7.9±1
1000 °C	10.0±1	10.9±1
1100 °C	10.6±1	10.4±1

[a] Estimated by integration of the fuel production curve.

Since structural changes are experienced by all 3DOM materials exposed to high temperatures, characterization of some of the post-cycled 3DOM $La_{0.60}Sr_{0.40}MnO_{3-x}$ samples was conducted. PXRD patterns are shown in Figure 8.22 of the as-made 3DOM $La_{0.60}Sr_{0.40}MnO_{3-x}$, a sample that had been oxidized at 500 °C, and a sample that had been oxidized at 1000 °C and 1100 °C (two reduction steps were carried out). Cycling does not cause the $La_{0.60}Sr_{0.40}MnO_{3-x}$ to phase separate, and the perovskite phase is retained. The reflections for the 3DOM $La_{0.60}Sr_{0.40}MnO_{3-x}$ cycled at T_{ox} = 500 °C are shifted to lower °2θ. An expansion of the lattice likely arises because this material was not completely reoxidized after exposure to CO_2 at 500 °C (production of CO is very limited for this sample, too). This shift is not observed for the material oxidized at higher temperatures, since the material undergoes more oxidation. With regards to thermal stability, the crystallite size increases from ca. 10 nm for the as-made material to 21 nm for the material cycled at the highest T_{ox} (based on the Scherrer equation, see Table 8.7). Changes are also observed in the gas sorption isotherms of the cycled materials, as well (Figure 8.23). Hysteresis disappears in the isotherms for the cycled, undoubtedly brought on by sintering of the $La_{0.60}Sr_{0.40}MnO_{3-x}$ crystallites. BET specific surface areas decrease as T_{ox} increases; however, the $La_{0.60}Sr_{0.40}MnO_{3-x}$ oxidized at 1000 °C/1100 °C is still macroporous and retains 17.4 m^2/g of surface area. SEM images taken of the 3DOM $La_{0.60}Sr_{0.40}MnO_{3-x}$ oxidized at 1000 °C/1100 °C reveal that the majority of the sample (~80 %) retains the 3DOM structure (Figure 8.24 a). Some areas have sintered far more than adjacent regions, and a disordered macropore structure is present in ~20 % of sample (Figure 8.24 b). It is possible that a thermal gradient is present in the furnace, but additional studies would need to be conducted to determine its extent.

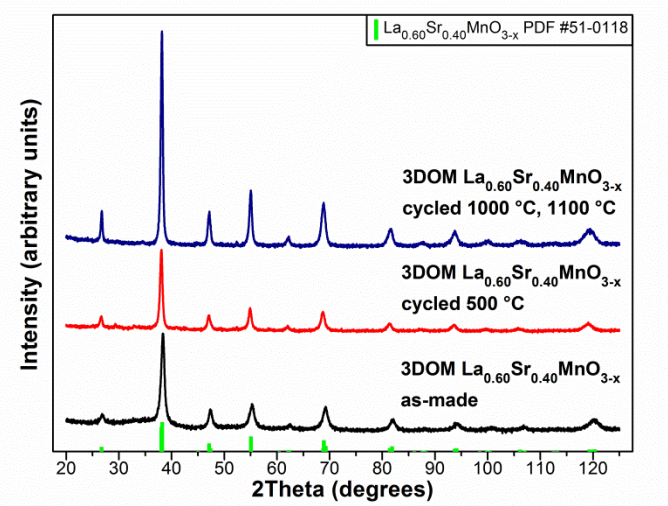

Figure 8.22 PXRD patterns of pristine 3DOM $La_{0.60}Sr_{0.40}MnO_{3-x}$, 3DOM $La_{0.60}Sr_{0.40}MnO_{3-x}$ oxidized at 500 °C, and 3DOM $La_{0.60}Sr_{0.40}MnO_{3-x}$ oxidized at 1000/1100 °C. All samples were reduced at 500 °C. A single perovskite phase was retained after cycling.

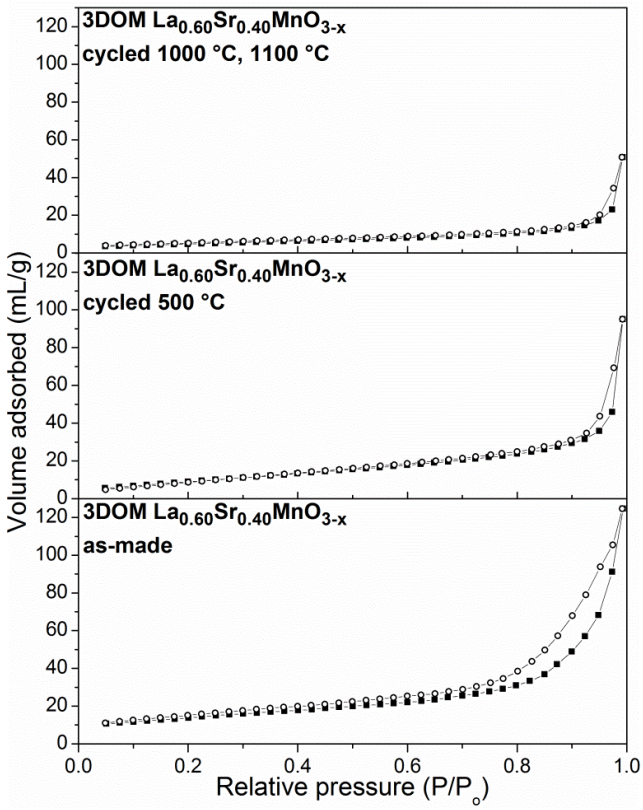

Figure 8.23 Nitrogen sorption isotherms of pristine 3DOM $La_{0.60}Sr_{0.40}MnO_{3-x}$, 3DOM $La_{0.60}Sr_{0.40}MnO_{3-x}$ oxidized at 500 °C, and 3DOM $La_{0.60}Sr_{0.40}MnO_{3-x}$ oxidized at 1000/1100 °C. All samples were reduced at 500 °C. The cycled samples lose surface area, but macropores remain in the structure.

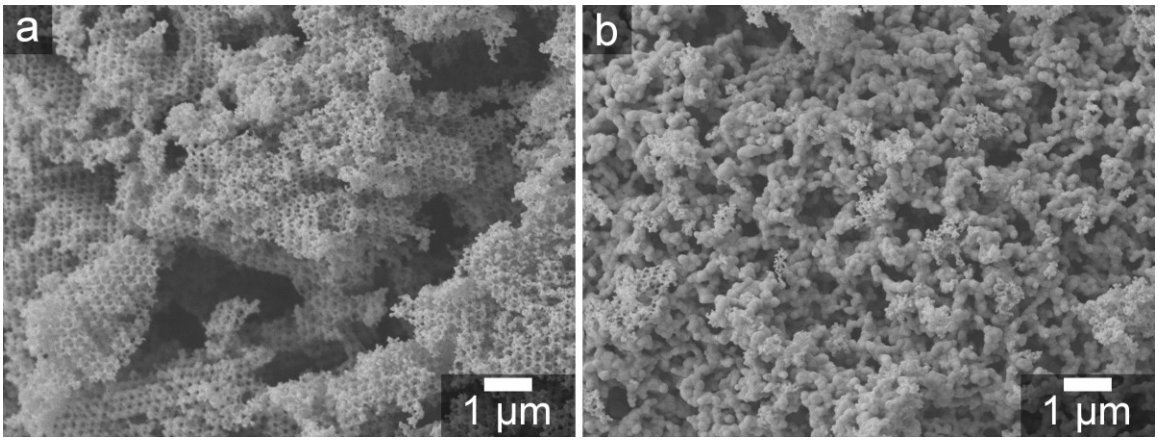

Figure 8.24 SEM micrographs of 3DOM $La_{0.60}Sr_{0.40}MnO_{3-x}$ oxidized at 1000/1100 °C. Approximately 80% of the sample resembles what is shown in (a). More heavily sintered regions, as shown in (b), are also found in the sample.

8.3.4.3 Conclusions

Six 3DOM perovskites were synthesized using a Pechini-based precursor solution, and one, 3DOM $La_{0.6}Sr_{0.4}MnO_{3-x}$, was cycled using a chemical reductant (a mixture of H_2 and H_2O) and CO_2. Three of the perovskite oxides are phase pure, as seen in the PXRD patterns. The other three contain impurity phases ($SrCO_3$ or La_2O_3) that produce PXRD reflections roughly twenty times less intense than those of the major pervoskite phase. All perovskites synthesized possess either rhombohedral or orthorhombic lattices. Crystallite size and BET specific surface areas vary greatly for the as-made perovskite oxides. However, the presence of Sr^{2+} is generally associated with a decrease in crystallite size and an increase in BET surface area. A slightly different morphology is obtained for the 3DOM $La_{0.6}Sr_{0.4}MnO_{3-x}$ in comparison to the other materials. 3DOM $La_{0.6}Sr_{0.4}MnO_{3-x}$ contains hollow nodes and additional mesopores between crystallites, which might be a consequence of the increased citric acid in the precursor used for that material. This composition was also chemically cycled. Overall, the production of CO is rapid in the 3DOM $La_{0.6}Sr_{0.4}MnO_{3-x}$, but a considerable "tail" is present in the fuel production curve. Production of CO is less than what is achieved for 3DOM CeO_2 cycled in similar conditions. It is postulated that reduction may be facile in the 3DOM $La_{0.6}Sr_{0.4}MnO_{3-x}$, but oxidation is more difficult.

8.4 Overall Conclusions

A series of investigations were carried out using several different types of candidate materials for solar thermochemical fuel production. All the materials analyzed possess the 3DOM structure. 3DOM Ce-based oxides that contain lanthanoid cations and/or Zr^{4+} were synthesized. These materials are single phase as-made and have a cubic fluorite crystal structure. Shifts in the lattice parameter of these Ce-based mixed oxides are also observed via PXRD that can be understood in terms of the ionic radii of the dopant cation. All the Ce-based oxides have improved thermal resistance, leading to smaller crystallite sizes in the as-made materials and in materials treated at 1350 °C. Another 3DOM Ce-based oxide, 3DOM $Ce_{0.9}Mn_{0.1}O_{2-x}$-PM, was synthesized via the use of a Pechini precursor. This material also has a cubic fluorite crystal structure. The 3DOM $Ce_{0.9}Mn_{0.1}O_{2-x}$-PM was cycled (reduced at elevated temperature in inert gas and oxidized under CO_2) in an infrared image furnace under conditions that simulate those in a CSP reactor. Unfortunately, CO production cannot be detected, which is believed to from the high reducibility of the material and its poor resistance to sintering. Similar problems are observed for the 3DOM PrO_{2-x} and the 3DOM $Pr_{0.6}Zr_{0.35}Y_{0.05}O_{2-x}$. For the 3DOM PrO_{2-x}, a single phase, nanocrystalline material was initially synthesized. Chemical redox cycling (using H_2) at 825 °C causes crystal growth that disrupts the 3DOM structure, and results in only limited production of H_2. Oxidation does not regenerate the original composition (Pr_6O_{11}), instead a hexagonal phase is found. While the doped 3DOM $Pr_{0.6}Zr_{0.35}Y_{0.05}O_{2-x}$ has a higher thermal stability than the undoped material, H_2 production is only slightly improved when compared to 3DOM PrO_{2-x}. Finally, a set of six 3DOM perovskites were synthesized using the versatile Pechini method. Most of the perovskites are single phase, but some contain minor $SrCO_3$ or La_2O_3 impurities. Sr-containing perovskites have a smaller crystal size and higher BET surface areas. Additionally, the 3DOM $La_{0.60}Sr_{0.40}MnO_{3-x}$ has a different type of 3DOM structure, a surface-templated structure with hollow octahedral nodes. 3DOM $La_{0.60}Sr_{0.40}MnO_{3-x}$ was cycled in a chemical redox set-up, and exhibits decent CO production kinetics. However, a temperature of 1000 or 1100 °C was needed to achieve the maximum CO production rate and overall CO productivity.

References

(1) Peña, M. A.; Fierro, J. L. G. Chemical Structures and Performance of Perovskite Oxides. *Chem. Rev.* **2001**, *101*, 1981-2017.

(2) Scheffe, J. R.; Weibel, D.; Steinfeld, A. Lanthanum-Strontium-Manganese Perovskites as Redox Materials for Solar Thermochemical Splitting of H_2O and CO_2. *Energy Fuels* **2013**, *27*, 4250-4257.

(3) McDaniel, A. H.; Miller, E. C.; Arifin, D.; Ambrosini, A.; Coker, E. N.; O'Hayre, R.; Chueh, W. C.; Tong, J. Sr- and Mn-Doped $LaAlO_{3-\delta}$ for Solar Thermochemical H_2 and CO Production. *Energy Environ. Sci.* **2013**, *6*, 2424-2428.

(4) Demont, A.; Abanades, S.; Beche, E. Investigation of Perovskite Structures as Oxygen-Exchange Redox Materials for Hydrogen Production from Thermochemical Two-Step Water-Splitting Cycles. *J. Phys. Chem. C* **2014**, *118*, 12682-12692.

(5) Gupta, A.; Hedge, M. S.; Priolkar, K. R.; Waghmare, U. V.; Sarode, P. R.; Emura, S. Structural Investigation of Activated Lattice Oxygen in $Ce_{1-x}Sn_xO_2$ and $Ce_{1-x-y}Sn_xPd_yO_{2-\delta}$ by EXAFS and DFT Calculations. *Chem. Mater.* **2009**, *21*, 5836-5847.

(6) Bernal, S.; Blanco, G.; Cauqui, M. A.; Corchado, P.; Pintado, J. M.; Rodriguez-Izquierdo, J. M. Oxygen Buffering Capacity of Mixed Cerium Terbium Oxide: A New Material with Potential Applications in Three-Way Catalysts. *Chem. Commun.* **1997**, 1545-1546.

(7) Murugan, B.; Ramaswamy, A. V.; Srinivas, D.; Gopinath, C. S.; Ramaswamy, V. Nature of Manganese Species in $Ce_{1-x}Mn_xO_{2-\delta}$ Solid Solutions Synthesized by the Solution Combustion Route. *Chem. Mater.* **2005**, *17*, 3983-3993.

(8) Baidya, T.; Gayen, A.; Hedge, M. S.; Ravishankar, N.; Dupont, L. Enhanced Reducibility of $Ce_{1-x}Ti_xO_2$ Compared to That of CeO_2 and Higher Redox Catalytic Activity of $Ce_{1-x-y}Ti_xPt_yO_{2-\delta}$ Compared to That of $Ce_{1-x}Pt_xO_{2-\delta}$. *J. Phys. Chem. B.* **2006**, *110*, 5262-5272.

(9) Djinović, P.; Batista, J.; Ćehić, B.; Pintar, A. Utilization of High Specific Surface Area CuO–CeO_2 Catalysts for High Temperature Processes of Hydrogen Production: Steam Re-forming of Ethanol and Methane Dry Re-forming. *J. Phys. Chem. A* **2010**, *114*, 3939-3949.

(10) Rossignol, S.; Descorme, C.; Kappenstein, C.; Duprez, D. Synthesis, Structure and Catalytic Properties of Zr–Ce–Pr–O Mixed Oxides. *J. Mater. Chem.* **2001**, *11*, 2587-2592.

(11) Bernal, S.; Blanco, G.; Calvino, J. J.; Gatica, J. M.; Omil, J. A. P.; Pintado, J. M. Characterization of Three-Way Automotive Aftertreatment Catalysts and Related Model Systems. *Top. Catal.* **2004**, *28*, 31-45.

(12) Kehoe, A. B.; Scanlon, D. O.; Watson, G. W. Role of Lattice Distortions in the Oxygen Storage Capacity of Divalently Doped CeO_2. *Chem. Mater.* **2011**, *23*, 4464-4468.

(13) Vidmar, P.; Fornasiero, P.; Kašpar, J.; Gubitosa, G.; Graziani, M. Effects of Trivalent Dopants on the Redox Properties of $Ce_{0.6}Zr_{0.4}O_2$ Mixed Oxide. *J. Catal.* **1997**, *171*, 160-168.

(14) Krishna, K.; Bueno-López, A.; Makkee, M.; Moulijn, J. A. Potential Rare-Earth Modified CeO_2 Catalysts for Soot Oxidation: Part III. Effect of Dopant Loading and Calcination Temperature on Catalytic Activity with O_2 and NO + O_2. *Appl. Catal., B* **2007**, *75*, 210-220.

(15) Otsuka, K.; Wang, Y.; Nakamura, M. Direct Conversion of Methane to Synthesis Gas Through Gas–Solid Reaction Using CeO_2–ZrO_2 Solid Solution at Moderate Temperature. *Appl. Catal., A* **1999**, *183*, 317-324.

(16) Tang, X.; Li, Y.; Huang, X.; Xu, Y.; Zhu, H.; Wang, J.; Shen, W. MnO_x–CeO_2 Mixed Oxide Catalysts for Complete Oxidation of Formaldehyde: Effect of Preparation Method and Calcination Temperature. *Appl. Catal., B* **2006**, *62*, 265-273.

(17) Bonnetot, B.; Rakic, V.; Yuzhakova, T.; Guimon, C.; Auroux, A. Preparation and Characterization of Me_2O_3–CeO_2 (Me = B, Al, Ga, In) Mixed Oxide Catalysts. 2. Preparation by Sol-Gel Method. *Chem. Mater.* **2008**, *20*, 1585-1596.

(18) Kašpar, J.; Fornasiero, P.; Graziani, M. Use of CeO_2-Based Oxides in the Three-Way Catalysis. *Catal. Today* **1999**, *50*, 285-298.

(19) Kašpar, J.; Fornasiero, P.; Hickey, N. Automotive Catalytic Converters: Current Status and Some Perspectives. *Catal. Today* **2003**, *77*, 419-449.

(20) Yao, H. C.; Yu Yao, Y. F. Ceria in Automotive Exhaust Catalysts: I. Oxygen Storage. *J. Catal.* **1984**, *86*, 254-265.

(21) Kašpar, J.; Fornasiero, P.; Graziani, M. Use of CeO_2-Based Oxides in the Three-Way Catalysis. *Catal. Today* **1999**, *50*, 285-298.

(22) Otsuka-Yao-Matsuo, S.; Omata, T.; Izu, N.; Kishimoto, H. Oxygen Release Behavior of $CeZrO_4$ Powders and Appearance of New Compounds κ and t*. *J. Solid State Chem.* **1998**, *138*, 47-54.

(23) Zhou, G.; Gorte, R. J. Thermodynamic Investigation of the Redox Properties for Ceria-Hafnia, Ceria-Terbia, and Ceria-Praseodymia Solid Solutions. *J. Phys. Chem. B* **2008**, *112*, 9869-9875.

(24) Gupta, A.; Waghmare, U. V.; Hedge, M. S. Correlation of Oxygen Storage Capacity and Structural Distortion in Transition-Metal-, Noble-Metal-, and Rare-Earth-Ion-Substituted CeO_2 from First Pinciples Calculation. *Chem. Mater.* **2010**, *22*, 5184-5198.

(25) Daturi, M.; Finocchio, E.; Binet, C.; Lavalley, J. C.; Fally, F.; Perrichon, V. Study of Bulk and Surface Reduction by Hydrogen of $Ce_xZr_{1-x}O_2$ Mixed Oxides Followed by FTIR Spectroscopy and Magnetic Balance. *J. Phys. Chem. B* **1999**, *103*, 4884-4891.

(26) Shah, P. R.; Kim, T.; Zhou, G.; Fornasiero, P.; Gorte, R. J. Evidence for Entropy Effects in the Reduction of Ceria-Zirconia Solutions. *Chem. Mater.* **2006**, *18*, 5363-5369.

(27) Zhou, G.; Shah, P. R.; Gorte, R. J. A Study of Cerium–Manganese Mixed Oxides for Oxidation Catalysis. *Catal. Lett.* **2008**, *120*, 191-197.

(28) Reddy, B. M.; Katta, L.; Thrimurthulu, G. Novel Nanocrystalline $Ce_{1-x}La_xO_{2-\delta}$ (x = 0.2) Solid Solutions: Structural Characteristics and Catalytic Performance. *Chem. Mater.* **2010**, *22*, 467-475.

(29) Chen, P.-L.; Chen, I.-W. Grain Growth in CeO_2: Dopant Effects, Defect Mechanism, and Solute Drag. *J. Am. Ceram. Soc.* **1996**, *79*, 1793-1800.

(30) Kašpar, J.; Fornasiero, P.; Balducci, G.; Di Monte, R.; Hickey, N.; Sergo, V. Effect of ZrO_2 Content on Textural and Structural Properties of CeO_2-ZrO_2 Solid Solutions Made by Citrate Complexation Route. *Inorg. Chim. Acta* **2003**, *349*, 217-226.

(31) Colón, G.; Pijolat, M.; Valdivieso, F.; Vidal, H.; Kašpar, J.; Finocchio, E.; Daturi, M.; Binet, C.; Lavalley, J. C.; Baker, R. T.; Bernal, S. Surface and Structural Characterization of $Ce_xZr_{1-x}O_2$ CEZIRENCAT Mixed Oxides as Potential Three-Way Catalyst Promoters. *J. Chem. Soc., Faraday Trans.* **1998**, *94*, 3717-3726.

(32) Colón, G.; Valdivieso, F.; Pijolat, M.; Baker, R. T.; Calvino, J. J.; Bernal, S. Textural and Phase Stability of $Ce_xZr_{1-x}O_2$ Mixed Oxides Under High Temperature Oxidising Conditions. *Catal. Today* **1999**, *50*, 271-284.

(33) Shigapov, A. N.; Graham, G. W.; McCabe, R. W.; Plummer Jr., H. K. The Preparation of High-Surface Area, Thermally-Stable, Metal-Oxide Catalysts and Supports by a Cellulose Templating Approach. *Appl. Catal., A* **2001**, *210*, 287-300.

(34) Bueno-López, A.; Krishna, K.; van der Linden, B.; Mul, G.; Moulijn, J. A.; Makkee, M. On the Mechanism of Model Diesel Soot-O_2 Reaction Catalysed by Pt-Containing La^{3+}-Doped CeO_2: A TAP Study Isotopic O_2. *Catal. Today* **2007**, *121*, 237-245.

(35) Fan, J.; Weng, D.; Wu, X. D.; Wu, X. D.; Ran, R. Modification of CeO_2–ZrO_2 Mixed Oxides by Coprecipitated/Impregnated Sr: Effect on the Microstructure and Oxygen Storage Capacity. *J. Catal.* **2008**, *258*, 177-186.

(36) Aneggi, E.; de Leitenburg, C.; Dolcetti, G.; Trovarelli, A. Promotional Effect of Rare Earths and Transition Metals in the Combustion of Diesel Soot over CeO_2 and CeO_2-ZrO_2. *Catal. Today* **2006**, *114*, 40-47.

(37) Wilkes, M. F.; Hayden, P.; Bhattacharya, A. K. Catalytic Studies on Ceria Lanthana Solid Solutions III. Surface Segregation and Solid State Studies. *J. Catal.* **2003**, *219*, 305-309.

(38) Si, R.; Zhang, Y.-W.; Wang, L.-M.; Li, S.-J.; Lin, B.-X.; Chu, W.-S.; Wu, Z.-Y.; Yan, C.-H. Enhanced Thermal Stability and Oxygen Storage Capacity for $Ce_xZr_{1-x}O_2$ (x = 0.4–0.6) Solid Solutions by Hydrothermally Homogenous Doping of Trivalent Rare Earths. *J. Phys. Chem. C* **2007**, *111*, 787-794.

(39) Sardar, K.; Playford, H. Y.; Darton, R. J.; Barney, E. R.; Hannon, A. C.; D., T.; Fisher, J.; Kashtiban, R. J.; Sloan, J.; Ramos, S.; Cibin, G.; Walton, R. I. Nanocrystalline Cerium–Bismuth Oxides: Synthesis, Structural Characterization, and Redox Properties. *Chem. Mater.* **2010**, *22*, 6191–6201.

(40) Gibbons, W. T.; Venstrom, L. J.; De Smith, R. M.; Davidson, J. H.; Jackson, G. S. Ceria-Based Electrospun Fibers for Renewable Fuel Production *via* Two-Step Thermal Redox Cycles for Carbon Dioxide Splitting. *Phys. Chem. Chem. Phys.* **2014**, *16*, 14271-14280.

(41) Kaneko, H.; Miura, T.; Ishihara, H.; Taku, S.; Yokoyama, T.; Nakajima, H.; Tamaura, Y. Reactive Ceramics of CeO_2-MO_x (M=Mn, Fe, Ni, Cu) for H_2 Generation by Two-Step Water Splitting Using Concentrated Solar Thermal Energy. *Energy* **2007**, *32*, 656-663.

(42) Kang, K.-S.; Kim, C.-H.; Park, C.-S.; Kim, J.-W. Hydrogen Reduction and Subsequent Water Splitting of Zr-Added CeO_2. *J. Ind. Eng. Chem.* **2007**, *13*, 657-663.

(43) Miller, J. E.; Allendorf, M. D.; Diver, R. B.; Evans, L. R.; Siegel, N. P.; Stuecker, J. N. Metal Oxide Composites and Structures for Ultra-High Temperature Solar Thermochemical Cycles. *J. Mater. Sci.* **2008**, *43*, 4714-4728.

(44) Kaneko, H.; Ishihara, T.; Taku, S.; Naganuma, Y.; Hasegawa, N.; Tamaura, Y. Cerium Ion Redox System in CeO_2–Fe_2O_3 Solid Solution at High Temperatures (1,273–1,673 K) in the Two-Step Water-Splitting Reaction for Solar H_2 Generation. *J. Mater. Sci.* **2008**, *43*, 3153-3161.

(45) Abanades, S.; Legal, A.; Cordier, A.; Peraudeau, G.; Flamant, G.; Julbe, A. Investigation of Reactive Cerium-Based Oxides for H_2 Production by Thermochemical Two-Step Water-Splitting. *J. Mater. Sci.* **2010**, *45*, 4163-4173.

(46) Kaneko, H.; Taku, S.; Tamaura, Y. Reduction Reactivity of CeO_2–ZrO_2 Oxide Under High O_2 Partial Pressure in Two-Step Water Splitting Process. *Sol. Energy* **2011**, *85*, 2321-2330.

(47) Meng, Q.-L.; Lee, C.; Ishihara, T.; Kaneko, H.; Tamaura, Y. Reactivity of CeO_2-Based Ceramics for Solar Hydrogen Production via a Two-Step Water-Splitting Cycle with Concentrated Solar Energy. *Int. J. Hydrogen Energy* **2011**, *36*, 13435-13441.

(48) Le Gal, A.; Abanades, S.; Flamant, G. CO_2 and H_2O Splitting for Thermochemical Production of Solar Fuels Using Nonstoichiometric Ceria and Ceria/Zirconia Solid Solutions. *Energy Fuels* **2011**, *25*, 4836-4845.

(49) Le Gal, A.; Abanades, S. Catalytic Investigation of Ceria-Zirconia Solid Solutions for Solar Hydrogen Production. *Int. J. Hydrogen Energy* **2011**, *36*, 4739-4748.

(50) Scheffe, J. R.; Steinfeld, A. Thermodynamic Analysis of Cerium-Based Oxides for Solar Thermochemical Fuel Production. *Energy Fuels* **2012**, *26*, 1928-1936.

(51) Le Gal, A.; Abanades, S. Dopant Incorporation in Ceria for Enhance Water-Splitting Activity during Solar Thermochemical Hydrogen Generation. *J. Phys. Chem. C* **2012**, *116*, 13516-13523.

(52) Lee, C.; Meng, Q.-L.; Kaneko, H.; Tamaura, Y. Solar Hydrogen Productivity of Ceria-Scandia Solid Solution Using Two-Step Water-Splitting Cycle. *J. Sol. Energy Eng.* **2012**, *135*, 011002(1-7).

(53) Le Gal, A.; Abanades, S.; Bion, N.; Le Mercier, T.; Harlé, V. Reactivity of Doped Ceria-Based Mixed Oxides for Solar Thermochemical Hydrogen Generation via Two-Step Water-Splitting Cycles. *Energy Fuels* **2013**, *27*, 6068-6078.

(54) Scheffe, J. R.; Jacot, R.; Patzke, G. R.; Steinfeld, A. Synthesis, Characterization and Thermochemical Redox Performance of Hf^{4+}, Zr^{4+}, and Sc^{3+} Doped Ceria for Splitting CO_2. *J. Phys. Chem. C* **2013**, *117*, 24104-24114.

(55) Ramos-Fernandez, E. V.; Shiju, N. R.; Rothenberg, G. Understanding the Solar-Driven Reduction of CO_2 on Doped Ceria. *RSC Adv.* **2014**, *4*, 16456-16463.

(56) Adachi, G.; Imanaka, N. The Binary Rare Earth Oxides. *Chem. Rev.* **1998**, *98*, 1479-1514.

(57) Hyde, B. G.; Bevan, D. J. M.; Eyring, L. On the Praseodymium+Oxygen System. *Phil. Trans. R. Soc. Lond. A.* **1966**, *259*, 583-614.

(58) Tuenge, R. T.; Eyring, L. On the Structures of the Intermediate Phases in the Terbium Oxide System. *J. Sol. State Chem.* **1982**, *41*, 75-89.

(59) Otsuka, K.; Kunitomi, M.; Saito, T. Oxidation and Reduction of Praseodymium Oxides at Low Temperatures. *Inorg. Chim. Acta* **1986**, *115*, L31-L32.

(60) Takasu, Y.; Yoko-o, T.; Matsui, M.; Matsuda, Y.; Toyoshima, I. Catalytic Reactivity of the Lattice Oxygen Atom of Terbium Oxide. *J. Catal.* **1982**, *77*, 485-490.

(61) Otsuka, K.; Nakajima, T. Effects of Additives on the Reduction and Oxidation of Terbium Oxides. *J. Catal.* **1987**, *103*, 216-219.

(62) Sinev, M. Y.; Graham, G. W.; Haack, L. P.; Shelef, M. Kinetic and Structural Studies of Oxygen Availability of the Mixed Oxides $Pr_{1-x}M_xO_y$ (M = Ce, Zr). *J. Mater. Res.* **1996**, *11*, 1960-1971.

(63) Ramdas, S.; Patil, K. C.; Rao, C. N. R. Thermodynamic and Kinetics of Oxidation Pr_2O_3 and Tb_2O_3 to Non-Stoichiometric Oxides. *J. Chem. Soc. A* **1970**, 64-68.

(64) Narula, C. K.; Haack, L. P.; Chun, W.; Jen, H.-W.; Graham, G. W. Single-Phase PrO_y–ZrO_2 Materials and Their Oxygen Storage Capacity: A Comparison with Single-Phase CeO_2–ZrO_2, PrO_y–CeO_2, and PrO_y–CeO_2–ZrO_2 Materials. *J. Phys. Chem. B* **1999**, *103*, 3634-3639.

(65) Kang, Z. C.; Eyring, L. Lattice Oxygen Transfer in Fluorite-Type Oxides Containing Ce, Pr, and/or Tb. *J. Solid State Chem.* **2000**, *155*, 129-137.

(66) Sonström, P.; Birkenstock, J.; Borchert, Y.; Schilinsky, L.; Behrend, P.; Gries, K.; Müller, K.; Rosenauer, A.; Bäumer, M. Nanostructured Praseodymium Oxide: Correlation Between Phase Transitions and Catalytic Activity. *ChemCatChem* **2010**, *2*, 694-704.

(67) Kang, Z.; Wang, Z. L. Novel Oxides for Cycled Hydrogen Production from Methane and Water Using a Temperature Swing. *Adv. Mater.* **2003**, *15*, 521-526.

(68) He, H.; Dai, H. X.; Wong, K. W.; Au, C. T. $RE_{0.6}Zr_{0.4-x}Y_xO_2$ (RE = Ce, Pr; x= 0, 0.05) Solid Solutions: An Investigation on Defective Structure, Oxygen Mobility, Oxygen Storage Capacity, and Redox Properties. *Appl. Catal., A* **2003**, *251*, 61-74.

(69) Bellakki, M. B.; Shivakumara, C.; Baidya, T.; Prakash, A. S.; Vasanthacharya, N. Y.; Hedge, M. S. Synthesis, Structure and Oxygen-Storage Capacity of $Pr_{1-x}Zr_xO_{2-\delta}$ and $Pr_{1-x-y}Pd_yZr_xO_{2-\delta}$. *Mater. Res. Bull.* **2008**, *43*, 2658-2667.

(70) Gaffney, A. M.; Jones, C. A.; Leonard, J. J.; Sofranko, J. A. Oxidative Coupling of Methane over Sodium Promoted Praseodymium Oxide. *J. Catal.* **1988**, *114*, 422-432.

(71) Tuller, H. L.; Stefanik, T. S. Nonstoichiometry and Defect Chemistry in Praseodymium-Cerium Oxide. *J. Electroceram.* **2004**, *13*, 799-803.

(72) Lufaso, M. W.; Woodward, P. M. Prediction of the Crystal Structures of Perovskites Using the Software Program *SPuDS*. *Acta Crystallogr., Sect. B: Struct. Sci.* **2001**, *57*, 725-738.

(73) Goldschmidt, V. M. Die Gesetze der Krystallochemie. *Naturwissenschaften* **1926**, *14*, 477-485.

(74) Stitzer, K. E.; Darriet, J.; zur Loye, H.-C. Advances in the Synthesis and Structural Description of 2H-Hexagonal Perovskite-Related Oxides. *Curr. Opin. Solid State Mater. Sci.* **2001**, *5*, 535-544.

(75) Bakken, E.; Norby, T.; Stølen, S. Redox Energetics of Perovskite-Related Oxides. *J. Mater. Chem.* **2002**, *12*, 317-323.

(76) Stølen, S.; Bakken, E.; Mohn, C. E. Oxygen-Deficient Perovskite: Linking Structure, Energetics and Ion Transport. *Phys. Chem. Chem. Phys.* **2006**, *8*, 429-447.

(77) Jacobson, A. J. Materials for Solid Oxide Fuel Cells. *Chem. Mater.* **2010**, *22*, 660-674.

(78) Nakamura, T.; Petzow, G.; Gauckler, L. J. Stability of the Perovskite Phase $LaBO_3$ (B = V, Cr, Mn, Fe, Co, Ni) in Reducting Atmosphere. *Mater. Res. Bull.* **1979**, *14*, 649-659.

(79) Fierro, J. L. G.; Tascón, J. M. D.; Tejuca, L. G. Surface Properties of $LaNiO_3$: Kinetic Studies of Reduction and of Oxygen Adsorption. *J. Catal.* **1985**, *93*, 83-91.

(80) Fierro, J. L. G.; Peña, M. A.; Tejuca, L. G. An XPS and Reduction Study of $PrCoO_3$. *J. Mater. Sci.* **1988**, *23*, 1018-1023.

(81) Mizusaki, J.; Okayasu, M.; Yamauchi, S.; Fueki, K. Nonstoichiometry and Phase Relationship of the $SrFeO_{2.5}$-$SrFeO_3$ System at High Temperature. *J. Solid State Chem.* **1992**, *99*, 166-172.

(82) Rørmark, L.; Wiik, K.; Stølen, S.; Grande, T. Oxygen Stoichiometry and Structural Properties of $La_{1-x}A_xMnO_{3\pm\delta}$ (A = Ca or Sr and $0 \leq x \leq 1$). *J. Mater. Chem.* **2002**, *12*, 1058-1067.

(83) Kuhn, M.; Hashimoto, S.; Sato, K.; Yashiro, K.; Mizusaki, J. Oxygen Nonstoichiometry, Thermo-Chemical Stability and Lattice Expansion of $La_{0.6}Sr_{0.4}FeO_{3-\delta}$. *Solid State Ionics* **2011**, *195*, 7-15.

(84) Yokokawa, H.; Horita, T.; Sakai, N.; Dokiya, M.; Kawada, T. Thermodynamic Representation of Nonstoichiometric Lanthanum Manganite. *Solid State Ionics* **1996**, *86-88*, 1161-1165.

(85) Rørmark, L.; Mørch, A. B.; Wiik, K.; Stølen, S.; Grande, T. Enthalpies of Oxidation of $CaMnO_{3-\delta}$, $Ca_2MnO_{4-\delta}$ and $SrMnO_{3-\delta}$ - Deduced Redox Properties. *Chem. Mater.* **2001**, *13*, 4005-4013.

(86) Cheng, J.; Navrotsky, A.; Zhou, X.-D.; Anderson, H. U. Thermochemistry of $La_{1-x}Sr_xFeO_{3-\delta}$ Solid Solutions ($0.0 \leq x \leq 1.0$, $0.0 \leq \delta \leq 0.5$). *Chem. Mater.* **2005**, *17*, 2197-2207.

(87) Konysheva, E.; Suard, E.; Irvine, J. T. S. Effect of Oxygen Non Stoichiometry and Oxidation State of Transition Elements on High-Temperature Phase Transition in A-Site Deficient $La_{0.95}Ni_{0.6}Fe_{0.4}O_{3-\delta}$ Perovskite *Chem. Mater.* **2009**, *22*, 5307-5318.

(88) Cheng, J.; Navrotsky, A. Energetics of Mangesium, Strontium, and Barium Doped Lanthanum Gallate Perovskites. *J. Solid State Chem.* **2004**, *177*, 126-133.

(89) Mizusaki, J.; Mima, Y.; Yamauchi, S.; Fueki, K.; Tagawa, H. Nonstoichiometry of the Perovskite-Type Oxides $La_{1-x}Sr_xCoO_{3-\delta}$ *J. Sol. State Chem.* **1989**, *80*, 102-111.

(90) Geary, T. C.; Adler, S. B. Oxygen Nonstoichiometry and Defect Chemistry of the Mixed Conductor $La_{0.9}Ca_{0.1}FeO_{3-\delta}$ at Low Oxygen Partial Pressure. *Solid State Ionics* **2013**, *253*, 88-93.

(91) Mizusaki, J.; Mori, N.; Takai, H.; Yonemura, Y.; Minamiue, H.; Tagawa, H.; Dokiya, M.; Inaba, H.; Naraya, K.; Sasamoto, T.; Hashimoto, S. Oxygen Nonstoichiometry and Defect Equilibrium in the Perovskite-Type Oxides $La_{1-x}Sr_xMnO_{3+d}$. *Solid State Ionics* **2000**, *129*, 163-177.

(92) Oishi, M.; Yashiro, K.; Honh, J.-O.; Nigara, Y.; Kawada, T.; Mizusaki, J. Oxygen Nonstoichiometry of B-Site Doped $LaCrO_3$. *Solid State Ionics* **2007**, *178*, 307-312.

(93) Voorhoeve, R. J. H.; Johnson, D. W.; Remeika, J. P.; Gallagher, P. K. Perovskite Oxides: Materials Science in Catalysis. *Science* **1977**, *195*, 827-833.

(94) Kremenić, G.; Nieto, J. M. L.; Tascón, J. M. D.; Tejuca, L. G. Chemisorption and Catalysis on $LaMO_3$ Oxides. *J. Chem. Soc., Faraday Trans. 1* **1985**, *81*, 939-949.

(95) Guilhaume, N.; Primet, M. Three-Way Catalytic Activity and Oxygen Storage Capacity of Perovskite $LaMn_{0.976}Rh_{0.024}O_{3+\delta}$. *J. Catal.* **1997**, *165*, 197-204.

(96) Nishihata, Y.; Mizuki, J.; Akao, T.; Tanaka, H.; Uenishi, M.; Kimura, M.; Okamoto, T.; Hamada, N. Self-Regeneration of a Pd-Perovskite Catalyst for Automotive Emissions Control. *Nature* **2002**, *418*, 164-167.

(97) Dai, X. P.; Wu, Q.; Li, R. J.; Yu, C. C.; Hao, Z. P. Hydrogen Production from a Combination of the Water-Gas Shift and Redox Cycle Process of Methane Partial Oxidation via Lattice Oxygen over $LaFeO_3$ Perovskite Catalyst. *J. Phys. Chem. B* **2006**, *110*, 25856-25862.

(98) Wang, Y.; Ren, J.; Wang, Y.; Zhang, F.; Liu, X.; Guo, Y.; Lu, G. Nanocasted Synthesis of Mesoporous $LaCoO_3$ Perovskite with Extremely High Surface Area and Excellent Activity in Methane Combustion. *J. Phys. Chem. C* **2008**, *112*, 15293-15298.

(99) Kim, C. H.; Qi, G.; Dahlberg, K.; Li, W. Strontium-Doped Perovskites Rival Platinumm Catalysts for Treating NO_x in Simulated Diesel Exhaust. *Science* **2010**, *327*, 1624-1627.

(100) Zhang, R.; Luo, N.; Chen, B.; Kaliaguine, S. Soot Combustion over Lanthanum Cobaltites and Related Oxides for Diesel Exhaust Treatment. *Energy Fuels* **2010**, *24*, 3719-3726.

(101) Yanagisawa, S.; Uozumi, A.; Hamada, I.; Morikawa, Y. Search for a Self-Regenerating Perovskite Catalyst Using ab Initio Thermodynamics Calculations. *J. Phys. Chem. C* **2013**, *117*, 1278-1286.

(102) Wang, H.; Werth, S.; Schiestel, T.; Caro, J. Perovskite Hollow-Fiber Membranes for the Production of Oxygen-Enriched Air. *Angew. Chem. Int. Ed.* **2005**, *44*, 6906-6909.

(103) Jiang, H.; Wang, H.; Werth, S.; Schiestel, T.; Caro, J. Simultaneous Production of Hydrogen and Synthesis Gas by Combining Water Splitting with Partial Oxidation of Methane in a Hollow-Fiber Membrane Reactor. *Angew. Chem. Int. Ed.* **2008**, *47*, 9341-9344.

(104) Martynczuk, J.; Liang, F.; Arnold, M.; Šepelák, V.; Feldhoff, A. Aluminum-Doped Perovskites As High-Performance Oxygen Permeation Materials. *Chem. Mater.* **2009**, *21*, 1586-1594.

(105) Nalbandian, L.; Evdou, A.; Zaspalis, V. $La_{1-x}Sr_xM_yFe_{1-y}O_{3-\delta}$ Perovskites as Oxygen-Carrier Materials for Chemical-Looping Reforming. *Int. J. Hydrogen Energy* **2011**, *36*, 6657-6670.

(106) Leo, A.; Smart, S.; Liu, S.; da Costa, J. C. D. High Performance Perovskite Hollow Fibres for Oxygen Separation. *J. Membr. Sci.* **2011**, *368*, 64-68.

(107) Yamamoto, O.; Takeda, Y.; Kanno, R.; Noda, M. Perovskite-Type Oxides as Oxygen Electrodes for High Temperature Oxide Fuel Cells. *Solid State Ionics* **1987**, *22*, 241-246.

(108) Tao, S.; Irvine, J. T. S.; Kilner, J. A. An Efficient Solid Oxide Fuel Cell Based upon Single-Phase Perovskites. *Adv. Mater.* **2005**, *17*, 1734-1737.

(109) Huang, Y.-H.; Dass, R. I.; Xing, Z.-L.; Goodenough, J. B. Double Perovskites as Anode Materials for Solid-Oxide Fuel Cells. *Science* **2006**, *312*, 254-257.

(110) Wachsman, E. D.; Lee, K. T. Lowering the Temperature of Solid Oxide Fuel Cells. *Science* **2011**, *334*, 935-939.

(111) Suntivich, J.; Gasteiger, H. A.; Yabuuchi, N.; Nakanishi, H.; Goodenough, J. B.; Shao-Horn, Y. Design Principles for Oxygen-Reduction Activity on Perovskite Oxide Catalysts for Fuel Cells and Metal-Air Batteries. *Nat. Chem.* **2011**, *3*, 546-550.

(112) Ge, X.-M.; Chan, S.-W.; Liu, Q.-L.; Sun, Q. Solid Oxide Fuel Cell Anode Materials for Direct Hydrocarbon Utilization. *Adv. Energy Mater.* **2012**, *2*, 1156-1181.

(113) Gong, Y.; Patel, R. L.; Liang, X.; Palacio, D.; Song, X.; Goodenough, J. B.; Huang, K. Atomic Layer Deposition Functionalized Composite SOFC Cathode $La_{0.6}Sr_{0.4}Fe_{0.8}Co_{0.2}O_{3-\delta}$-$Gd_{0.2}Ce_{0.8}O_{1.9}$: Enhanced Long-Term Stability. *Chem. Mater.* **2013**, *25*, 4224-4231.

(114) Tsekouras, G.; Neagu, D.; Irvine, J. T. S. Step-Change in High Temperature Steam Electrolysis Performance of Perovskite Oxide Cathodes with Exsolution of B-Site Dopants. *Energy Environ. Sci.* **2013**, *6*, 256-266.

(115) Schroden, R. C.; Al-Daous, M.; Sokolov, S.; Melde, B. J.; Lytle, J. C.; Stein, A.; Carbajo, M. C.; Fernández, J. T.; Rodríguez, E. E. Hybrid Macroporous Materials for Heavy Metal Ion Adsorption. *J. Mater. Chem.* **2002**, *12*, 3261-3267.

(116) Josephson, D. P.; Popczun, E. J.; Stein, A. Effects of Integrated Carbon as a Light Absorber on the Coloration of Photonic Crystal-Based Pigments. *J. Phys. Chem. C* **2013**, *117*, 13585-13592.

(117) Rudisill, S. G.; Venstrom, L. J.; Petkovich, N. D.; Quan, T.; Hein, N.; Boman, D. B.; Davidson, J. H.; Stein, A. Enhanced Oxidation Kinetics in Thermochemical Cycling of CeO_2 through Templated Porosity. *J. Phys. Chem. C* **2013**, *117*, 1692-1700.

(118) Chueh, W. C.; Haile, S. M. Ceria as a Thermochemical Reaction Medium for Selectively Generating Syngas or Methane from H_2O and CO_2. *ChemSusChem* **2009**, *2*, 735–739.

(119) Miller, J. E.; McDaniel, A. H.; Allendorf, M. D. Considerations in the Design of Materials for Solar-Driven Fuel Production Using Metal-Oxide Thermochemical Cycles. *Adv. Energy Mater.* **2014**, *4*, 1300469(1-19).

(120) Horlait, D.; Claparède, L.; Clavier, N.; Szenknect, S.; Dacheux, N.; Ravaux, J.; Podor, R. Stability and Structural Evolution of $Ce^{IV1-x}Ln^{IIIx}O_{2-x/2}$ Solid Solutions: A Coupled μ-Raman/XRD Approach. *Inorg. Chem.* **2011**, *50*, 7150-7161.

(121) Chen, L.; Fleming, P.; Morris, V.; Holmes, J. D.; Morris, M. A. Size-Related Lattice Parameter Changes and Surface Defects in Ceria Nanocrystals. *J. Phys. Chem. C* **2010**, *114*, 12909-12919.

(122) Shannon, R. D. Revised Effective Ionic Radii and Systematic of Interatomic Distances in Halides and Chalcogenides. *Acta Cryst.* **1976**, *A32*, 751-767.

(123) Yashima, M.; Takizawa, T. Atomic Displacement Parameter Ceria Doped with Rare-Earth Oxide $Ce_{0.8}R_{0.2}O_{1.9}$ (R = La, Nd, Sm, Gd, Y, and Yb) and Correlation with Oxide-Ion Conductivity. *J. Phys. Chem. C* **2010**, *114*, 2385-2392.

(124) Rajendran, M.; Mallick, K. K.; Bhattacharya, A. K. Combustion Synthesis, Powder Characteristics and Crystal Structure of Phases in Ce-Pr-O System. *J. Mater. Sci.* **1998**, *33*, 5001-5006.

(125) Powers, J. D.; Glaeser, A. M. Grain Boundary Migration in Ceramics. *Interface Sci.* **1998**, *6*, 23-39.

(126) German, R. M. *Sintering Theory and Practice*; John Wiley & Sons, Inc.: New York, **1996**.

(127) Chen, I.-W. Grain Boundary Kinetics in Oxide Ceramics with the Cubic Fluorite Crystal Structure and its Derivatives. *Interface Sci.* **2000**, *8*, 147-156.

(128) Esposito, V.; Ni, D. W.; He, Z.; Zhang, W.; Prasad, A. S.; Glasscock, J. A.; Chatzichristodoulou, C.; Ramousse, S.; Kaiser, A. Enhanced Mass Diffusion Phenomena in Highly Defective Doped Ceria. *Acta Mater.* **2013**, *61*, 6290-6300.

(129) Mori, T.; Wang, Y.; Drennan, J.; Auchterlonie, G.; Li, J.-G.; Ikegami, T. Influence of Particle Morphology on Nanostructural Feature and Conducting Property in Sm-Doped CeO_2 Sintered Body. *Solid State Ionics* **2004**, *175*, 641-649.

(130) Prasad, D. H.; Park, S. Y.; Ji, H.-I.; Kim, H.-R.; Son, J.-W.; Kim, B.-K.; Lee, H.-W.; Lee, J.-H. Structural Characterization and Catalytic Activity of $Ce_{0.65}Zr_{0.25}RE_{0.1}O_{2-\delta}$ Nanocrystalline Powders Synthesized by the Glycine-Nitrate Process. *J. Phys. Chem. C* **2012**, *116*, 3467-3476.

(131) Rudisill, S. G.; Hein, N. M.; Terzic, D.; Stein, A. Controlling Microstructural Evolution in Pechini Gels through the Interplay between Precursor Complexation, Step-Growth Polymerization, and Template Confinement. *Chem. Mater.* **2013**, *25*, 745-753.

(132) Krcha, M. D.; Mayernick, A. D.; Janik, M. J. Periodic Trends of Oxygen Vacancy Formation and C-H Bond Activation over Transition Metal-doped CeO_2 (111) Surfaces. *J. Catal.* **2012**, *293*, 103-115.

(133) Tianshu, Z.; Hing, P.; Huang, H.; Kilner, J. Sintering and Densification Behavior of Mn-Doped CeO_2. *Mater. Sci. Eng. B* **2001**, *83*, 235-241.

(134) McFarland, E. W.; Metiu, H. Catalysis by Doped Oxides. *Chem. Rev.* **2013**, *113*, 4391-4427.

(135) Borchert, Y.; Sonström, P.; Wilhelm, M.; Borchert, H.; Bäumer, M. Nanostructured Praseodymium Oxide: Preparation, Structure, and Catalytic Properties. *J. Phys. Chem. C* **2008**, *112*, 3054-3063.

(136) Ji, K.; Dai, H.; Deng, J.; Zhang, L.; Wang, F.; Jiang, H.; Au, C. T. Three-Dimensionally Ordered Macroporous $SrFeO_{3-\delta}$ with High Surface Area: Active Catalysts for the Complete Oxidation of Toluene. *Appl. Catal. A* **2012**, *425-426*, 153-160.

(137) Liu, Y.; Dai, H.; Du, Y.; Deng, J.; Zhang, L.; Zhao, Z.; Au, C. T. Controlled Preparation and High Catalytic Performance of Three-Dimensionally Ordered Macroporous $LaMnO_3$ with Nanovoid Skeletons for the Combustion of Toluene. *J. Catal.* **2012**, *287*, 149-160.

(138) Zhao, Z.; Dai, H.; Deng, J.; Du, Y.; Liu, Y.; Zhang, L. Three-Dimensionally Ordered Macroporous $La_{0.6}Sr_{0.4}FeO_{3-\delta}$: High-Efficiency Catalysts for the Oxidative Removal of Toluene. *Microporous Mesoporous Mater.* **2012**, *163*, 131-139.

(139) Arandiyan, H.; Dai, H.; Deng, J.; Liu, Y.; Bai, B.; Wang, Y.; Li, X.; Xie, S.; Li, J. Three-Dimensionally Ordered Macroporous $La_{0.6}Sr_{0.4}MnO_3$ with High Surface Areas: Active Catalysis for the Combustion of Methane. *J. Catal.* **2013**, *307*, 327-339.

(140) Arandiyan, H.; Dai, H.; Deng, J.; Wang, Y.; Xie, S.; Li, J. Dual-Templating Synthesis of Three-Dimensionally Ordered Macroporous $La_{0.6}Sr_{0.4}MnO_3$-Supported Ag Nanoparticles: Controllable Alignments and Super Performance for the Catalytic Combustion of Methane. *Chem. Commun.* **2013**, *49*, 10748-10750.

(141) Li, X.; Dai, H.; Deng, J.; Liu, Y.; Zhao, Z.; Wang, Y.; Yang, H.; Au, C. T. In Situ PMMA-Templating Preparation and Excellent Catalytic Performance of Co_3O_4/3DOM $La_{0.6}Sr_{0.4}CoO_3$ for Toluene Combustion. *Appl. Catal. A* **2013**, *458*, 11-20.

(142) Martell, A.; Smith, R. A. *Other Organic Ligands (Critical Stability Constants)*; Springer Science + Business Media: New York, **1976**; Vol. 3.

(143) McCarthy, B. P.; Pederson, L. R.; Williford, R. E.; Zhou, X.-D. Low-Temperature Densification of Lanthanum Strontium Manganite ($La_{1-x}Sr_xMnO_{3+\delta}$), x = 0.0-0.20. *J. Am. Ceram. Soc.* **2009**, *92*, 1672-1678.

(144) Boman, D. B.; Venstrom, L. J.; Davidson, J. H. *unpublished work.*

Chapter 9

Summary and Outlook

9.1 Overall Summary

Beyond the search for better means of energy storage and conversion, this thesis offers key insights into the often complicated and confusing study of the structural changes experienced by templated porous materials with multiple components. The structure of these composite materials is dictated by a multitude of interactions between various components and relates back to their performance in their end use application. By tailoring the titanium dioxide precursor, this work has shown how control of the location of TiO_2 crystallites is possible in a 3DOM carbon matrix. Locational control of a phase in a composite is often extremely difficult to accomplish, and lead to the insight that it is preferable to bury TiO_2 crystals in the carbon matrix to achieve high lithium-ion cell capacities. Further compositional control has been attained through the use of dopants with these robust syntheses. Even the toxicity of the precursors for the 3DOM TiO_2/C was reduced, at the expense of slightly higher carbon content that actually impedes Li^+ transport. By tuning the voltage window for charging/discharging those lithium-ion electrodes, higher capacities are achieved. An additional aspect of structural control is shown to be provided by the 3DOM network itself. This structure effectively constrained the reprecipitation of titanate nanosheets, allowing for the first examples (to this author's knowledge) of structurally-colored hydrogen titanate. These sorts of aspect of control are not solely limited to the carbon-composites. By adjusting the type of precursor used for the 3DOM cerium zirconium oxide, phase stability could be tuned (to an extent). This revealed that inhomogeneities in phase actually benefitted fuel production for highly doped cerium zirconium oxide. That same type of Pechini precursor served as a means to synthesize novel porous materials with untested compositions for solar thermochemical fuel production. The remainder of this summary delves into all the materials covered in the thesis.

9.2 Titanium Dioxide-Containing Anodes for Lithium-Ion Batteries

Many different syntheses were conducted for the titanium dioxide anode materials studied in Chapters 3, 4, 5 and 6. While these materials all have high surface areas and an interconnected pore network, substantial differences also exist. For instance, TFA-TiO_2/C and acac-TiO_2/C contain disordered mesopores, provided the pyrolysis temperature is kept below roughly 700 °C. However, a greater amount mesopores are present in the hydrogen titanate materials described in Chapter 6. The next four subsections review the key structural differences between the titanium dioxide-based materials and how these differences relate to the Li^+ insertion/extraction properties.

9.2.1 Changing the Chelating Agent for the Titanium Complex

Three different chelating agents (trifluoroacetic acid, 2,4-pentanedione, and citric acid) were used in the various precursors for the 3DOM TiO_2/C electrode materials. A hydrophobic complex forms when trifluoroacetic acid (TFA) is combined with titanium isopropoxide in the TFA-TiO_2/C precursor. The other components of the TFA-TiO_2/C precursor are fairly hydrophilic, so the titanium complex preferentially segregates to the hydrophobic surface of the PMMA colloidal crystal template. Crystallites of TiO_2 then nucleate on the surface of the TFA-TiO_2/C composites during pyrolysis. At pyrolysis temperatures lower than 700 °C, the TiO_2 crystallites in the TFA-TiO_2/C are smaller than 10 nm in size. However, the growth of the crystallites is fairly severe (as observed via electron microscopy and line broadening PXRD reflections) after pyrolysis at 800 °C or 900 °C. Since the crystallites of TiO_2 lie on the surface of the 3DOM network in the TFA-TiO_2/C, the carbonaceous phase cannot restrict the sintering and crystallite growth of the TiO_2 phase. In contrast, a hydrophilic complex is formed when 2,4-pentanedione (acac) is mixed with titanium isopropoxide in the acac-TiO_2/C precursor. Favorable interactions between the various components of the acac-TiO_2/C precursor result in the TiO_2 crystallites nucleating within the carbonaceous phase. Smaller crystallites are produced in the acac-TiO_2/C, and these TiO_2 grains are surrounded by a thin layer of the carbon. By virtue of this reduction in the size of the TiO_2 grains, higher capacities for Li^+ insertion/extraction are obtained for the acac-TiO_2/C when compared to the TFA-TiO_2/C. When citric acid and hydrogen peroxide are used as ligands, another hydrophilic complex is formed. Similar to the acac-TiO_2/C, the TiO_2 nucleates within the carbonaceous phase for the materials made with the citric acid complex. While smaller crystallites of TiO_2 are obtained after pyrolysis, these composites (the PF-TiO_2/C, Sucrose-TiO_2/C, and NAC-TiO_2/C) have lower capacities for Li^+ insertion/extraction at high rates than the acac-TiO_2/C. This brings up another important factor in the analysis of these materials, the role of carbon.

9.2.2 Changing Carbon Content and Carbon Source

Several composites synthesized contain roughly 50 wt% of a carbonaceous phase, which is in contrast to the TFA-TiO_2/C and acac-TiO_2/C that contain only about ~25–30 wt% of amorphous carbon. For the composite synthesized using a TFA-based precursor, TFA2-TiO_2/C, TiO_2 nucleates on the surface of the 3DOM network. Small crystallites (<5 nm) of TiO_2 are present after the TFA2-TiO_2/C is pyrolyzed at 700 °C and below. Interestingly, the TiO_2 crystallites are roughly 30 nm in size when the TFA2-TiO_2/C is pyrolyzed at 800 °C, which is larger than the

TiO_2 crystallites in the corresponding TFA-TiO_2/C. Furthermore, the crystals of TiO_2 in the TFA2-TiO_2/C are in a partially reduced state. It is postulated that the reducing environment induces the transformation to rutile and then a Magnelí phase. Grain growth is accelerated for those titanium oxide compounds when compared to anatase (the predominant TiO_2 phase in TFA-TiO_2/C). Reduction of TiO_2 also occurs in the amorphous carbon-rich composites made with the ammonium citratoperoxotitanate(IV) gel. Since the crystallites are confined within the amorphous carbon, smaller TiO_2 grains are observed when compared to the TFA2-TiO_2/C. However, some larger crystallites are present in the structure. Widespread conversion of the TiO_2 to sub-5 nm crystallites of titanium oxycarbide is also observed after pyrolysis at 800 °C and 900 °C. Since this compound is electrochemically-inactive, the conversion negatively impacts the capacity of the composite for Li^+ insertion/extraction.

For the composites made with the ammonium citratoperoxotitanate(IV) gel, the carbon source was also changed. PF sol (in the PF-TiO_2/C), non-toxic sucrose (in the Sucrose-TiO_2/C), and just the citric acid ligand (in the NAC-TiO_2/C) can be used in the precursors for these materials. There are no substantial differences in terms of the structure or the ability of the composites to insert/extract Li^+ into TiO_2. One of the most noticeable differences is that the carbonaceous fraction in the PF-TiO_2/C is oxygen-poor and helps cause a more complete conversion of the TiO_2 to titanium oxycarbide. Also, the composite with the smaller TiO_2 crystal size at 800 °C, Sucrose TiO_2/C, has a better capacity for Li^+ insertion/extraction than PF-TiO_2/C. However, the abundance of carbon creates a barrier to Li^+ transport at high charge/discharge rates for all samples in the voltage window from 1 to 3 V vs. Li/Li.$^+$ Indeed, the composite with the most amorphous carbon, NAC-TiO_2/C, has the poorest rate performance. This situation can be ameliorated by charging and discharging the composites in a voltage window that allows for intercalation into the amorphous carbon phase. Cycling between 0.05 and 3 V vs. Li/Li^+ improves capacities by over 100 mAh/g, and also reveals that the composites have higher capacities than a 3DOM C reference.

The amorphous carbon phase can also be removed altogether, and act as an *in situ* hard template. This was done for the TFA-TiO_2/C pyrolyzed at 500 °C, owing to its low carbon content and small TiO_2 crystallite size. Burnout of the carbon resulted in the formation of a 3DOM TiO_2 structure with disordered mesopores that lie between TiO_2 crystallites roughly 8 nm in size. Somewhat unexpectedly, the 3DOM TiO_2 has a higher capacity than the acac-TiO_2/C at rapid charge/discharge rates. It is postulated that this results from the small crystallite sizes of the TiO_2 and the high interfacial area between the electrode material and the electrolyte. Also, the

only carbon additive in the electrode is carbon black, which is more electrically conductive than the amorphous carbon in the acac-TiO_2/C.

9.2.3 Introduction of Cationic Dopants

An assortment of cationic dopants was incorporated into the TFA-TiO_2/C and acac-TiO_2/C, as is described in Chapter 4. These dopants were added with the aim of improving the electronic conductivity of the TiO_2 and carbon phases, and reducing the crystallite growth experienced by the doped TiO_2. Some of the dopants, Cu and Ni, phase separated as metallic particles, since reducing conditions are generated during pyrolysis. For the material with nickel particles, acac-Ni:TiO_2/C (5 mol%), improved graphitization of the carbon phase is observed, and improved capacities at high charge/discharge rates (relative to acac-TiO_2/C) are realized. Similar capacity improvements are not observed for the dopants that are incorporated into the crystal structure of TiO_2; however, some favorable structural effects are observed. Iron induces the phase transformation from anatase to rutile at 600 °C, and does not reduce the size of the TiO_2 phase. Rutile content also increases for the TFA-Ta:TiO_2/C, TFA2-Ta:TiO_2/C, and acac-Ta:TiO_2/C composites. Since the addition of Ta improves the reducibility of TiO_2, more oxygen vacancies are formed during pyrolysis, helping hasten the transition from anatase to rutile. However, the Ta interferes with the sintering of the doped TiO_2 phase, resulting in much smaller crystallites for all composites when compared to their undoped counterparts. Nb causes the same structural effects (more rutile and smaller crystallites) for acac-Nb:TiO_2/C. Unfortunately, the capacity of the Ta and Nb doped acac-TiO_2/C have lower capacities for Li^+ insertion/extraction than similarly-made undoped acac-TiO_2/C. 3DOM TiO_2 doped with Ta also has lower capacities than 3DOM TiO_2. Diffusion of Li^+ appears to be disrupted in these anode materials, perhaps from combination with e^- generated as a result of the introduction of the dopants.

9.2.4 Alkali Treatment of 3DOM TiO_2

3DOM TiO_2 was successfully converted into sodium titanate via the ambient pressure treatment of the TiO_2 material in aqueous sodium hydroxide solution. Ion exchange in hydrochloric acid resulted in the formation of hydrogen titanate, which was pyrolyzed to form TiO_2-B/anatase. The specific surface areas of the converted hydrogen titanate materials exceed 300 m^2/g, and reach 530 m^2/g for a sample treated at 70 °C and dried using supercritical CO_2. This is due to the conversion of the 3DOM structure to a porous structure comprised of crumpled titanate nanosheets. TiO_2 dissolves and then reprecipitates on the surface of the 3DOM network, during the treatment in NaOH. The nanosheets are confined by the 3DOM network and do not scroll into nanotubes, which allows for extremely high surface areas. A remnant of the 3DOM structure also exists as a result of this confinement. Enough order is retained in the structure of these materials to allow for the appearance of photonic stop bands. Via a combination of PXRD and Raman spectroscopy, it was found that the converted sodium and hydrogen titanate materials also contain a lepidocrocite-like crystal structure. Pyrolysis converts the hydrogen titanate to TiO_2-B and then anatase TiO_2. Unfortunately, these materials do not improve capacities for Li^+ insertion/extraction relative to the parent 3DOM TiO_2. Side reactions with the electrolyte appear to degrade the performance of these materials.

9.3 Outlook for the Titanium Dioxide-Containing Materials

Several routes exist for continued improvement of the TFA-TiO_2/C, acac-TiO_2/C, PF-TiO_2/C, and Sucrose-TiO_2/C systems for use as lithium-ion battery anodes. First, other cationic dopants can be explored for many of these composite anodes. Cobalt, tungsten, and zinc are three possibilities that should be compatible with the various existing precursors and should further enhance the conductivity/capacity of the TiO_2 phase.[1-3] Second, ionic liquids have found use as highly-conductive carbon sources.[4] The synthesis described in Chapters 3, 4, and 5 may be amenable to the inclusion of an ionic liquid that can be pyrolyzed, and the ionic liquid may even help add nitrogen to the TiO_2, boosting its electrical conductivity. Intercalation into the ionic liquid-derived carbon should also be possible using an extended voltage window. Third, other surfactants exist that can be incorporated with the aforementioned syntheses. Some of these surfactants, such as polystyrene-*block*-poly(ethylene oxide) and polyisobutylene-*block*-poly(ethylene oxide), are capable of generating large mesopores that are resistant to the sintering of metal oxides.[5,6] Finally, the TFA-TiO_2/C can be extended to other metal oxide/carbon composites. Stable precursor solutions of zirconium alkoxides and TFA can be synthesized,

which has allowed for the formation of ZrO_2/C composites.[7] Some of these composites, say V_2O_5/C, can be used directly as a battery anode, while other reactions may allow for the transformation of metal oxide particles to other active electrode materials.

While the alkali-treated TiO_2 materials did function well as anode materials for lithium-ion batteries, other applications for these high-surface area materials can be envisioned. For instance, the high surface areas of the sodium and hydrogen titanate materials make them ideal candidates as sorbents for charged organic molecules like dyes.[8] These materials can also undergo ion-exchange with metal ions[9] and could see possible use in environment remediation. Photocatalysis is another application that could be pursued for these materials. One immense benefit of this synthesis pathway is that photonic stop bands are preserved in the material. By tuning the size of the spheres in the parent colloidal crystal template, one may be able to utilize the slow photon effect in the titanates to allow for better photocatalytic activity.[10] The parent 3DOM TiO_2 can also be doped with metal ions, allowing for further tuning of the band gap and light adsorption properties of the resulting catalyst.[11] It may even be possible to adjust the composition of the alkali solution (via addition of an alcohol) to allow for the wetting and conversion of TiO_2/C composites.

9.4 Porous Materials for Solar Thermochemical Fuel Production

Similar to the titanium oxide-based lithium-ion anode materials, various materials were synthesized and tested for solar thermochemical fuel production. Clear delineations can be made between certain groups of materials, including the cerium oxide-based materials described in Chapters 7 and 8. This section is then split into a summary of each of these kinds of materials, which is followed by a brief outlook in the next section.

9.4.1 Cerium-Based Oxides

Both lanthanoid and transition metal ion-doped 3DOM cerium oxide materials were synthesized using two different routes. The type of precursor used for the synthesis and the concentration of the dopant both play key roles in the resulting structure of these doped materials. For materials made using a precursor that contained metal salts dissolved in methanol (the MSS precursor), the resulting doped cerium oxide contains a single-phase cubic fluorite crystal structure, as long as the dopant concentration is below 20 mol%. Higher concentrations of dopant were used for 3DOM $Ce_{1-x}Zr_xO_2$ synthesized via the MSS route. When the concentration of Zr^{4+} is increased to greater than 20 mol%, the MSS-based $Ce_{1-x}Zr_xO_2$ phase separate into Ce-rich and

Zr-rich mixed oxides. Furthermore, the degree of phase separation varies from sample to sample. If a Pechini-based precursor is used, a single cubic fluorite phase can be maintained even when 50 mol% of Zr^{4+} is introduced into the cerium-containing mixed oxide material. When compared to the MSS route, the mixed oxides produced via the Pechini method contain smaller crystallites and fewer voids between grains (lowering the overall specific surface area). Single-phase mixed oxides that contain Mn can also be formed via Pechini precursors. Irrespective of the synthesis method, identity of the dopant, or the doping level, hard templating was successful and all prepared materials possess the 3DOM structures.

In terms of the overall thermal stability achieved for the cerium-based oxides, several key observations can be made. A set of 3DOM materials synthesized via the MSS were thermally-treated at 1350 °C. These materials experience considerable grain growth during thermal treatment that causes the 3DOM structure to be completely disrupted. However, the cerium-based materials that contain 20 mol% La and Sm have considerably improved thermal resistance. The grain size in these materials is on the order of 0.5 μm, while grains are several μm in size for the thermally-treated, undoped 3DOM CeO_2. A disordered macropore network is retained in the doped materials, unlike what is observed in the densified 3DOM CeO_2. Zirconium also reduced the extent of sintering, and the best improvements to thermal stability were realized in cerium oxide co-doped with La and Zr. Manganese, however, does not improve the thermal stability of doped oxide relative to undoped CeO_2, as is observed in Chapter 8.

Fuel productivity was also evaluated for a set of 3DOM $Ce_{1-x}Zr_xO_2$ compounds and for 3DOM $Ce_{0.8}Mn_{0.2}O_{2-x}$. Single phase 3DOM $Ce_{1-x}Zr_xO_2$ materials were synthesized using the aforementioned Pechini method and these materials were reduced in an Ar/H_2 gas steam and reoxidized with H_2O. Under these chemical redox conditions, the fuel production rate and overall fuel production are maximized for 3DOM $Ce_{0.8}Zr_{0.2}O_2$. Fuel production decreases when Zr is increased beyond 20 mol%; however, the thermal stability, in terms of crystallite size and specific surface area, is improved. It is postulated that the heavily doped 3DOM $Ce_{1-x}Zr_xO_2$ materials are easily reduced, but cannot reoxidize. However, an inhomogeneous 3DOM $Ce_{0.5}Zr_{0.5}O_2$ material produced more H_2 per cycle than $Ce_{0.5}Zr_{0.5}O_2$. This is because the material contains a Ce-rich phase that is quite effective at producing fuel. Unlike the Zr-containing materials, 3DOM $Ce_{0.8}Mn_{0.2}O_{2-x}$ did not produce fuel during cycling experiments.

9.4.2 Praseodymium-Based Oxides

Praseodymium oxide and doped praseodymium oxides represent a class of materials that are potential candidates for solar thermochemical production. Some of the first forays into the use of these materials are reported in Chapter 8. The Pechini method was used to produce these materials. 3DOM PrO_{2-x} and 3DOM $Pr_{0.6}Zr_{0.35}Y_{0.05}O_{2-x}$ samples were reduced and oxidized using the same conditions as for the 3DOM $Ce_{1-x}Zr_xO_2$ materials. Unfortunately, 3DOM PrO_{2-x} suffers from more sintering and crystallite growth than 3DOM CeO_2. In addition, 3DOM PrO_{2-x} produces little fuel and is not fully re-oxidized in the conditions tested. Better thermal stability is attained and a greater amount of fuel is produced for the 3DOM $Pr_{0.6}Zr_{0.35}Y_{0.05}O_{2-x}$. However, the amount of H_2 produced is still far below what can be achieved using cerium oxide-based materials.

9.4.3 Perovskite Oxides

Finally, a set of perovskites were synthesized using the Pechini method. These perovskite oxides consist of either a single perovskite phase, or contain a perovskite phase and a minor impurity that is barely detectable using PXRD. Specific surface areas for these perovskites vary from composition to composition; however, Sr is effective at boosting surface areas and reducing grain sizes. One composition, $La_{0.60}Sr_{0.40}MnO_{3-x}$, was tested via chemical redox cycling, so that the 3DOM structure could be retained. While overall fuel production from $La_{0.60}Sr_{0.40}MnO_{3-x}$ is lower than what is attained in for CeO_2, relatively rapid fuel production kinetics are realized. The 3DOM structure is also retained for $La_{0.60}Sr_{0.40}MnO_{3-x}$ even after heating to 1100 °C.

9.5 Outlook for the Materials for Solar Thermochemical Fuel Production

With the wide range of compositions available for cerium-based oxides, praseodymium-based oxides, and perovskite oxides, any subsequent studies will require the assistance of computation and advanced characterization techniques. For compositions that lack relevant thermodynamic data, such as ΔH_{TR}^{θ}, computational thermodynamics may serve as a means to obtain these parameters.[12] Once the relevant thermodynamic parameters are calculated, compounds can be screened following the methods developed by Meredig and Wolverton.[13] Special consideration should also be placed on uncovering possible phase separation or decomposition reactions that occur during cycling. Of course, those reactions will also need to be monitored via *ex-situ*/*in-situ* characterization of materials exposed to conditions mirroring those experienced in during cycling. Other computational studies, including those that use density functional theory, could be used to identify trends in the redox behavior and phase stability caused by the addition of specific metal

cations to various materials.[14] Computational models also could be used in conjunction with experiments (including *in operando* characterization techniques) to understand the factors influencing reaction kinetics. For instance, methods such as secondary ion mass spectroscopy[15] and *in operando* XPS[16] could be used to understand the rate and spatial extent of defect formation, the diffusivity of various ionic species, and the chemistry of reactive surfaces. These studies may prove to be especially important, since the kinetics of the thermal reduction and fuel production steps are not readily apparent from thermodynamic considerations alone.

Desired feature sizes for the porous oxides will also need to be tuned to accommodate the sintering that occurs at the elevated temperatures required for the reduction step. Depending on the length scale required, different methods of templating (or methods that do not use a template) can be considered. With colloidal particles, the size of the polymer spheres that make up the fcc array of the colloidal crystal can be tuned over a wide range from a sub-mircometer scale via emulsion polymerizations[17] to over one hundred micrometers via a simple fluidic device.[18] Other methods to be considered include the use of biological templates (wood, cellulose, etc.),[19,20] polyurethane foams[21] or foamed suspensions of inorganic oxide particles.[22]

While some of the designed materials may not be useful for two-step solar thermochemical fuel production, the data gained, both experimental and theoretical, can also inform the possible use of these materials for other catalytic applications. Further studies could be conducted to optimize certain materials as catalysts for the water-gas shift reaction,[23,24] steam reforming,[25,26] gas desulfurization[27] and chemical looping combustion.[28,29] Chemical looping combustion is especially promising, since these materials could be exceedingly effective at producing pure CO_2 emissions in power plants, thereby allowing for simpler CO_2 sequestration.[30] Since these materials will need to be taken to high temperatures in reactive environments, opportunities arise for studies targeted at understanding phase transitions or phase segregation that could have an impact on various catalytic reactions. Other studies could investigate the use of metallic and metal oxide co-catalysts with these porous materials.[31-34] Computational studies can then be used to understand reactions at these co-catalyst sites and any interactions between the co-catalyst and the active oxide.

References

(1) Wang, Y.; Chen, T.; Mu, Q. Electrochemical Performance of W-Doped Anatase TiO_2 Nanoparticles as an Electrode Material for Lithium-Ion Batteries. *J. Mater. Chem.* **2011**, *21*, 6006-6013.

(2) Ali, Z.; Cha, S. N.; Sohn, J. I.; Shakir, I.; Yan, C.; Kim, J. M.; Kang, D. J. Design and Evaluation of Novel Zn Doed Mesoporous TiO_2 Based Anode Material for Advanced Lithium Ion Batteries. *J. Mater. Chem.* **2012**, *22*, 17625-17629.

(3) Hutchings, G. S.; Li, Q.; Jiao, F. Synthesis and Electrochemistry of Nanocrystalline M-TiO_2 (M = Mn, Fe, Co, Ni, Cu) Anatase. *J. Electrochem. Soc.* **2013**, *160*, A511-A515.

(4) Fellinger, T.-P.; Thomas, A.; Yuan, J.; Antonietti, M. 25th Anniversary Article: "Cooking Carbon with Salt": Carbon Materials and Carbonaceous Frameworkds from Ionic Liquids and Poly(ionic liquids)s. *Adv. Mater.* **2013**, *25*, 5838-5855.

(5) Sel, O.; Kuang, D.; Thommes, M.; Smarsly, B. Principles of Hierarchical Meso- and Macropore Architectures by Liquid Crystalline and Polymer Colloid Templating. *Langmuir* **2006**, *22*, 2311-2322.

(6) Brezesinski, T.; Wang, J.; Polleux, J.; Dunn, B.; Tolbert, S. H. Templated Nanocrystal-Based Porous TiO_2 Films for Next-Generation Electrochemical Capacitors. *J. Am. Chem. Soc.* **2009**, *131*, 1802-1809.

(7) Fang, Y.; Stein, A. *unpublished work*.

(8) Xiong, L.; Sun, W.; Yang, Y.; Chen, C.; Ni, J. Heterogenous Photocatalysis of Methylene Blue over Titanate Nanotubes: Effect of Adsorption. *J. Colloid Interface Sci.* **2011**, *356*, 211-216.

(9) Li, N.; Zhang, L.; Chen, Y.; Fang, M.; Zhang, J.; Wang, H. Highly Efficient, Irreversible and Selective Ion Exchange Property of Layered Titanate Nanostructures. *Adv. Funct. Mater.* **2012**, *22*, 835-841.

(10) Chen, J. I. L.; von Freymann, G.; Choi, S. Y.; Kitaev, V.; Ozin, G. A. Slow Photons in the Fast Lane in Chemistry. *J. Mater. Chem.* **2008**, *18*, 369-373.

(11) Daghrir, R.; Drogui, P.; Robert, D. Modified TiO_2 for Environmental Photocatalytic Applications: A Review. *Ind. Eng. Chem. Res.* **2013**, *52*, 3581-3599.

(12) Miller, J. E.; McDaniel, A. H.; Allendorf, M. D. Considerations in the Design of Materials for Solar-Driven Fuel Production Using Metal-Oixde Thermochemical Cycles. *Adv. Energy Mater.* **2014**, *4*, 1300469(1-19).

(13) Meredig, B.; Wolverton, C. First-Principles Thermodynamic Framework for the Evaluation of Thermochemical H_2O- or CO_2-Splitting Materials. *Phys. Rev. B* **2009**, *80*, 245119(1-8).

(14) McFarland, E. W.; Metiu, H. Catalysis by Doped Oxides. *Chem. Rev.* **2013**, *113*, 4391-4427.

(15) Coker, E. N.; Ohlhausen, J. A.; Ambrosini, A.; Miller, J. E. Oxygen Transport and Isotopic Exchange in Iron Oxide/YSZ Thermochemically-Active Material *via* Splitting of $C(^{18}O)_2$ at High Temperature Studied by Thermogravimetric Analysis and Secondary Ion Mass Spectroscopy. *J. Mater. Chem.* **2012**, *22*, 6726-6732.

(16) Chueh, W. C.; McDaniel, A. H.; Grass, M. E.; Hao, Y.; Jabeen, N.; Liu, Z.; Haile, S. M.; McCarty, K. F.; Bluhm, H.; El Gabaly, F. High Enhanced Concentration and Stability of Reactive Ce^{3+} on Doped CeO_2 Surface Revealed In Operando. *Chem. Mater.* **2012**, *24*, 1876-1882.

(17) Schroden, R. C.; Al-Daous, M.; Sokolov, S.; Melde, B. J.; Lytle, J. C.; Stein, A.; Carbajo, M. C.; Fernández, J. T.; Rodríguez, E. E. Hybrid Macroporous Materials for Heavy Metal Ion Adsorption. *J. Mater. Chem.* **2002**, *12*, 3261-3267.

(18) Choi, S.-W.; Cheong, I. W.; Kim, J.-H.; Xia, Y. Preparation of Uniform Microspheres Using a Simple Fluidic Device and Their Crystallization into Close-Packed Lattices. *Small* **2009**, *5*, 454–459.

(19) Shigapov, A. N.; Graham, G. W.; McCabe, R. W.; Plummer Jr., H. K. The Preparation of High-Surface Area, Thermally-Stable, Metal-Oxide Catalysts and Supports by a Cellulose Templating Approach. *Appl. Catal., A* **2001**, *210*, 287–300.

(20) Deshpande, A. S.; Burgert, I.; Paris, O. Hierarchically Structured Ceramics by High-Precision Nanoparticle Casting of Wood. *Small* **2006**, *2*, 994–998.

(21) Studart, A. R.; Gonzenbach, U. T.; Tervoort, E.; Gauckler, L. J. Processing Routes to Macroporous Ceramics: A Review. *J. Am. Ceram. Soc.* **2006**, *89*, 1771–1789.

(22) Gonzenbach, U. T.; Studart, A. R.; Tervoort, E.; Gauckler, L. J. Macroporous Ceramics from Particle-Stabilized Wet Foams. *J. Am. Ceram. Soc.* **2007**, *90*, 16–22.

(23) Andreeva, D.; Ivanov, I.; Ilieva, L.; Abrashev, M. V.; Zanella, R.; Sobczak, J. W.; Lisowski, W.; Kantcheva, M.; Andeev, G.; Petrov, K. Gold Catalysts Supported on Ceria Doped by Rare Earth Metals for Water Gas Shift Reaction: Influence of the Preparation Method. *Appl. Catal., A* **2009**, *357*, 159–169.

(24) Bakhmutsky, K.; Zhou, G.; Timothy, S.; Gorte, R. J. The Water-Gas-Shift Reaction on Pd/Ceria–Praseodymia: The Effect of Redox Thermodynamics. *Catal. Lett.* **2009**, *129*, 61–65.

(25) Shan, W.; Feng, Z.; Li, Z.; Zhang, J.; Shen, W.; Li, C. Oxidative Steam Reforming of Methanol on $Ce_{0.9}Cu_{0.1}O_y$ Catalysts Prepared by Deposition–Precipitation, Coprecipitation, and Complexation–Combustion Methods. *J. Catal.* **2004**, *228*, 206–217.

(26) Djinović, P.; Batista, J.; Ćehić, B.; Pintar, A. Utilization of High Specific Surface Area CuO–CeO_2 Catalysts for High Temperature Processes of Hydrogen Production: Steam Re-forming of Ethanol and Methane Dry Re-forming. *J. Phys. Chem. A* **2010**, *114*, 3939–3949.

(27) Wang, Z.; Flytzani-Stephanopoulos, M. Cerium Oxide-Based Sorbents for Regenerative Hot Reformate Gas Desulfurization. *Energy Fuels* **2005**, *19*, 2089–2097.

(28) He, F.; Wei, Y.; Li, H.; Wang, H. Synthesis Gas Generation by Chemical-Looping Reforming Using Ce-Based Oxygen Carriers Modified with Fe, Cu, and Mn Oxides. *Energy Fuels* **2009**, *23*, 2095–2102.

(29) Chakravarthy, V. K.; Daw, C. S.; Pihl, J. A. Thermodynamic Analysis of Alternative Approaches to Chemical Looping Combustion. *Energy Fuels* **2011**, *25*, 656–669.

(30) Fan, L.-S.; Li, F. Chemical Looping Technology and Its Fossil Energy Conversion Applications. *Ind. Eng. Chem. Res.* **2010**, *49*, 10200–10211.

(31) Liotta, L. F.; Di Carlo, G.; Pantaleo, G.; Deganello, G. Co_3O_4/CeO_2 and Co_3O_4/CeO_2–ZrO_2 Composite Catalysts for Methane Combustion: Correlation Between Morphology Reduction Properties and Catalytic Activity. *Catal. Commun.* **2005**, *6*, 329–336.

(32) Spadaro, L.; Arena, F.; Granados, M. L.; Ojeda, M.; Fierro, J. L. G.; Frusten, F. Metal–Support Interactions and Reactivity of Co/CeO_2 Catalysts in the Fischer-Tropsch Synthesis Reaction. *J. Catal.* **2005**, *234*, 451–462.

(33) Sukonket, T.; Khan, A.; Saha, B.; Ibrahim, H.; Tantayanon, S.; Kumar, P.; Idem, R. Influence of the Catalyst Prepartion Method, Surfactant Amount, and Steam on CO_2 Reforming of CH_4 over $5Ni/Ce_{0.6}Zr_{0.4}O_2$ Catalysts. *Energy Fuels* **2011**, *25*, 864–877.

(34) Muecke, U. P.; Akiba, K.; Infortuna, A.; Salkus, T.; Stus, N. V.; Gauckler, L. J. Electrochemical Performace of Nanocrystalline Nickel/Gadolinia-Doped Ceria Thin Film Anodes for Solid Oxide Fuel Cells. *Solid State Ionics* **2008**, *178*, 1762–1768.

Comprehensive Bibliography

Chapter 1

(1) Arrhenius, S. On the Influence of Carbonic Acid in the Air Upon the Temperature on the Ground. *Phil. Mag.* **1896**, *41*, 237-279.

(2) Clark, P. U.; Shakun, J. D.; Baker, P. A.; Bartlein, P. J.; Brewer, S.; Brook, E.; Carlson, A. E.; Cheng, H.; Kaufman, D. S.; Liu, Z.; Marchitto, T. M.; Mix, A. C.; Morrill, C.; Otto-Bliesner, B. L.; Pahnke, K.; Russell, J. M.; Whitlock, C.; Adkins, J. F.; Blois, J. L.; Clark, J.; Colman, S. M.; Curry, W. B.; Flower, B. P.; He, F.; Johnson, T. C.; Lynch-Stieglitz, J.; Markgraf, V.; McManus, J.; Mitrovica, J. X.; Moreno, P. I.; Williams, J. W. Global Climate Evolution During the Last Deglaciation. *Proc. Natl. Acad. Sci. USA* **2012**, *109*, E1134-E1142.

(3) Moss, R. H.; Edmonds, J. A.; Hibbard, K. A.; Manning, M. R.; Rose, S. K.; van Vuuren, D. P.; Carter, T. R.; Emori, S.; Kainuma, M.; Kram, T.; Meehl, G. A.; Mitchell, J. F. B.; Nakicenovic, N.; Riahi, K.; Smith, S. J.; Stouffer, R. J.; Thomson, A. M.; Weyant, J. P.; Wilbanks, T. J. The Next Generation of Scenarios for Climate Change Research and Assessment. *Nature* **2010**, *463*, 747-756.

(4) Rosa, E. A.; Dietz, T. Human Drivers of National Greenhouse-Gas Emissions. *Nat. Clim. Change* **2012**, *2*, 581-586.

(5) Knutti, R.; Sedláček, J. Robustness and Uncertainties in the New CMIP5 Climate Model Projections. *Nat. Clim. Change* **2013**, *3*, 369-373.

(6) IPCC Summary for Policymakers. In *Climate Change 2013: The Physical Science Basis. Contribution of Working Group I to the Fifth Assessment Report of the Intergovernmental Panel on Climate Change*; Stocker, T. F., Qin, D., Plattner, G.-K., Tignor, M. M. B., Allen, S. K., Boschung, J., Nauels, A., Xia, Y., Bex, V., Midgley, P. M., Eds.; Cambridge University Press: Cambridge, UK, 2013.

(7) IPCC Summary for Policymakers. In *Climate Change, 2014: Mitigation of Climate Change. Contribution of Working Group III to the Fifth Assessment Report of the Intergovernmental Panel on Climate Change*; Edenhofer, O., Pichs-Madruga, R., Sokona, Y., Farahani, E., Kadner, S., Seyboth, K., Adler, A., Baum, I., Brunner, S., Eickenmeier, P., Kriemann, B., Savolainen, J., Schlömer, S., von Stechow, C., Zwickel, T., Minx, J. C., Eds.; Cambridge University Press: Cambridge, UK, 2014.

(8) Beaumont, L. J.; Pitman, A.; Perkins, S.; Zimmermann, N. E.; Yoccoz, N. G.; Thuiller, W. Impacts of Climate Change on the World's Most Exceptional Ecoregions. *Proc. Natl. Acad. Sci. USA* **2011**, *108*, 2306-2311.

(9) Barnosky, A. D.; Hadly, E. A.; Bascompte, J.; Berlow, E. L.; Brown, J. H.; Fortelius, M.; Getz, W. M.; Harte, J.; Hastings, A.; Marquet, P. A.; Martinez, N. D.; Mooers, A.; Roopnarine, P.; Vermeji, G.; Williams, J. W.; Gillespie, R.; Kitzes, J.; Marshall, C.; Matzke, N.; Mindell, D. P.; Revilla, E.; Smith, A. B. Approaching a State Shift in Earth's Biosphere. *Nature* **2012**, *486*, 52-58.

(10) Ibrahim, M. A.; Na, M.; Oh, J.; Schinazi, R. F.; McBrayer, T. R.; Whitaker, T.; Doerksen, R. J.; Newman, D. J.; Zachos, L. G.; Hamann, M. T. Significance of Endangered and Threatened Plant Natural Products in the Control of Human Disease. *Proc. Natl. Acad. Sci. USA* **2013**, *110*, 16832-16837.

(11) Wheeler, T.; von Braun, J. Climate Change Impacts on Global Food Security. *Science* **2013**, *341*, 508-513.
(12) Altizer, S.; Ostfeld, R. S.; Johnson, P. T. J.; Kutz, S.; Harvell, C. D. Climate Change and Infectious Diseases: From Evidence to a Predictive Framework. *Science* **2013**, *341*, 514-519.
(13) Brandt, A. R.; Millard-Ball, A.; Ganser, M.; Gorelick, S. M. Peak Oil Demand: The Role of Fuel Efficiency and Alternative Fuels in a Global Oil Production Decline. *Environ. Sci. Technol.* **2013**, *47*, 8031-8041.
(14) Kerschner, C.; Prell, C.; Feng, K.; Hubacek, K. Economic Vulnerability to Peak Oil. *Global Environ. Change* **2013**, *23*, 1424-1433.
(15) Stern, N. The Economics of Climate Change. *Am. Econ. Rev.* **2008**, *97*, 1-37.
(16) Weitzman, M. L. On Modeling and Interpreting the Economics of Catastrophic Climate Change. *Rev. Econ. Stat.* **2009**, *91*, 1-19.
(17) Nordhaus, W. *The Climate Casino: Risk, Uncertainty, and Economics for a Warming World*; Yale University Press: New Haven, CT, 2013.
(18) GAO *Climate Change Adaptation: Strategic Federal Planning Could Help Government Officials Make More Informed Decisions*, GAO-10-113, U.S. Government Accountability Office, Washington D.C., 2009.
(19) World Bank *Economics of Adaptation to Climate Change- Synthesis Report*, World Bank, Washington D.C., 2010.
(20) Hoffert, M. I.; Caldeira, K.; Benford, G.; Criswell, D. R.; Green, C.; Herzog, H.; Jain, A. K.; Kheshgi, H. S.; Lackner, K. S.; Lewis, J. S.; Lightfoot, H. D.; Manheimer, W.; Mankins, J. C.; Mauel, M. E.; Perkins, L. J.; Schlesinger, M. E.; Volk, T.; Wigley, T. M. L. Advanced Technology Paths to Global Climate Stability: Energy for a Greenhouse Planet. *Science* **2002**, *298*, 981-987.
(21) Edenhofer, O.; Seyboth, K.; Creutzig, F.; Schlömer, S. On the Sustainability of Renewable Energy Sources. *Annu. Rev. Environ. Resour.* **2013**, *38*, 169-200.
(22) Butler, D. ITER Keeps Eye on Prize. *Nature* **2013**, *502*, 282-283.
(23) National Academy of Sciences, National Academy of Engineering, and National Research Council *Real Prospects for Energy Efficiency in the United States*; The National Academies Press: Washington D.C., 2010.
(24) Chen, H.; Goswami, Y.; Stefanakos, E. K. A Review of Thermodynamic Cycles and Working Fluids for the Conversion of Low-Grade Heat. *Renewable Sustainable Energy Rev.* **2010**, *14*, 3059-3067.
(25) D'Alessandro, D. M.; Smit, B.; Long, J. R. Carbon Dioxide Capture: Prospects for New Materials. *Angew. Chem. Int. Ed.* **2010**, *49*, 6058-6082.
(26) Boot-Handford, M. E.; Abanades, J. C.; Anthony, E. J.; Blunt, M. J.; Brandani, S.; MacDowell, N.; Fernández, J. R.; Ferrari, M.-C.; Gross, R.; Hallett, J. P.; Haszeldine, R. S.; Heptonstall, P.; Lyngfelt, A.; Makuch, Z.; Mangano, E.; Porter, R. T. J.; Pourkashanian, M.; Rochelle, G. T.; Shah, N.; Yao, J. G.; Fennell, P. S. Carbon Capture and Storage Update. *Energy Environ. Sci.* **2014**, *7*, 130-189.
(27) Yang, Z.; Zhang, J.; Kinter-Meyer, M. C. W.; Lu, X.; Choi, D.; Lemmon, J. P.; Liu, J. Electrochemical Energy Storage for the Green Grid. *Chem. Rev.* **2011**, *111*, 3577-3613.
(28) Hayner, C. M.; Zhao, X.; Kung, H. H. Materials for Rechargeable Lithium-Ion Batteries. *Annu. Rev. Chem. Biomol. Eng.* **2012**, *3*, 445-471.
(29) Linden, D.; Reddy, T. B. Principles of Operation. In *Linden's Handbooks of Batteries*; 4th ed.; Reddy, T. B., Linden, D., Eds.; The McGraw-Hill Companies: New York, NY, 2010.

(30) Reddy, T. B. An Introduction to Secondary Batteries. In *Linden's Handbook of Batteries*; 4th ed.; Reddy, T. B., Linden, D., Eds.; The McGraw-Hill Companies: New York, NY, 2010.
(31) Choi, N.-S.; Chen, Z.; Freunberger, S. A.; Ji, X.; Sun, Y.-X.; Amine, K.; Yushin, G.; Nazar, L. F.; Cho, J.; Bruce, P. G. Challenges Facing Lithium Batteries and Electrical Double-Layer Capacitors. *Angew. Chem. Int. Ed.* **2012**, *51*, 9994-10024.
(32) Etacheri, V.; Marom, R.; Elazari, R.; Salitra, G.; Aurbach, D. Challenges in the Development of Advanced Li-Ion Batteries: A Review. *Energy Environ. Sci.* **2011**, *4*, 3243-3262.
(33) Goodenough, J. B.; Park, K.-S. The Li-Ion Rechargeable Battery: A Perspective. *J. Am. Chem. Soc.* **2013**, *135*, 1167-1176.
(34) Goodenough, J. B.; Kim, Y. Challenges for Rechargeable Li Batteries. *Chem. Mater.* **2010**, *22*, 587-603.
(35) Maier, J. Thermodynamics of Electrochemical Lithium Storage. *Angew. Chem. Int. Ed.* **2013**, *52*, 4998-5026.
(36) Winter, M.; Brodd, R. J. What Are Batteries, Fuel Cells, and Supercapacitors? *Chem. Rev.* **2004**, *104*, 4245-4269.
(37) Goodenough, J. B. Evolution of Strategies for Modern Rechargeable Batteries. *Acc. Chem. Res.* **2012**, *46*, 1053-1061.
(38) Verma, P.; Maire, P.; Novák, P. A Review of the Features and Analyses of the Solid Electrolyte Interphase in Li-Ion Batteries. *Electrochim. Acta* **2010**, *55*, 6332-6341.
(39) Park, M.; Zhang, X.; Chung, M.; Less, G. B.; Sastry, A. M. A Review of Conduction Phenomena in Li-Ion Batteries. *J. Power Sources* **2010**, *195*, 7904-7929.
(40) Salomon, M. Electrochemical Principles and Reactions. In *Linden's Handbook of Batteries*; 4th ed.; Reddy, T. B., Linden, D., Eds.; The McGraw-Hill Companies: New York, NY, 2010.
(41) Bard, A. J.; Faulkner, L. R. *Electrochemical Methods: Fundamentals and Applications*; John Wiley & Sons, Inc.: New York, NY, 2000.
(42) Reddy, M. V.; Subbo Rao, G. V.; Chowdari, B. V. R. Metal Oxides and Oxysalts as Anode Materials for Li Ion Batteries. *Chem. Rev.* **2013**, *113*, 5364-5457.
(43) Wagemaker, M.; Mulder, F. M. Properties and Promises of Nanosized Insertion Materials for Li-Ion Batteries. *Acc. Chem. Res.* **2013**, *46*, 1206-1215.
(44) Simon, P.; Gogotsi, Y.; Dunn, B. Where Do Batteries End and Supercapacitors Begin?0 *Science* **2014**, *343*, 1210-1211.
(45) Conway, B. E. Transition from "Supercapacitor" to "Battery" Behavior in Electrochemical Energy Storage. *J. Electrochem. Soc.* **1991**, *138*, 1539-1548.
(46) Augustyn, V.; Simon, P.; Dunn, B. Pseudocapacitive Oxide Materials for High-Rate Electrochemical Energy Storage. *Energy Environ. Sci.* **2014**, *7*, 1597-1614.
(47) Park, C.-M.; Kim, J.-H.; Kim, H.; Sohn, H.-J. Li-Alloy Based Anodes Materials for Li Secondary Batteries. *Chem. Soc. Rev.* **2010**, *39*, 3115-3141.
(48) Zhang, W.-J. Lithium Insertion/Extraction Mechanism in Alloy Anodes for Lithium-Ion Batteries. *J. Power Sources* **2011**, *196*, 877-885.
(49) Cabana, J.; Monconduit, L.; Larcher, D.; Palacín, M. R. Beyond Intercalation-Based Li-Ion Batteries: The State of the Arts and Challenges of Electrode Materials Reacting Through Conversion Reactions. *Adv. Mater.* **2010**, *22*, E170-E192.
(50) Li, L.; Meng, F.; Jin, S. High-Capacity Lithium-Ion Battery Conversion Cathodes Based on Iron Fluoride Nanowires and Insights into the Conversion Mechanism. *Nano Lett.* **2012**, *12*, 6030-6037.
(51) Melot, B. C.; Tarascon, J.-M. Design and Preparation of Materials for Advanced Electrochemical Storage. *Acc. Chem. Res.* **2013**, *46*, 1226-1238.

(52) Bruce, P. G.; Scrosati, B.; Tarascon, J.-M. Nanomaterials for Rechargeable Lithium Batteries. *Angew. Chem. Int. Ed.* **2008**, *47*, 2930-2946.
(53) Vu, A.; Qian, Y.; Stein, A. Porous Electrode Materials for Lithium-Ion Batteries - How to Prepare Them and What Makes Them Special. *Adv. Energy Mater.* **2012**, *2*, 1056-1085.
(54) Wang, Y. G.; Wang, Y. R.; Hosono, E. J.; Wang, K. X.; Zhou, H. S. The Design of a $LiFePO_4$/Carbon Nanocomposite with a Core-Shell Structure and Its Synthesis by an In Situ Polymerization Restriction Method. *Angew. Chem. Int. Ed.* **2008**, *47*, 461-465.
(55) Eberke, U.; Felderhoff, M.; Schüth, F. Chemical and Physical Solutions for Hydrogen Storage. *Angew. Chem. Int. Ed.* **2009**, *48*, 6608-6630.
(56) de Bruijn, F. The Current Status of Fuel Cell Technology for Mobile and Stationary Applications. *Green Chem.* **2005**, *7*, 132-150.
(57) Wachsman, E. D.; Marlowe, C. A.; Lee, K. T. Role of Solid Oxide Fuel Cells in a Balanced Energy Strategy. *Energy Environ. Sci.* **2012**, *5*, 5498-5509.
(58) Yilmaz, M.; Krein, P. T. Review of Battery Charger Topologies, Charging Power Levels, and Infrastructure for Plug-In Electric and Hybrid Vehicles. *IEEE Trans. Power Electron.* **2012**, *28*, 2151-2169.
(59) Chaubey, R.; Sahu, S.; James, O. O.; Maity, S. A Review on Development of Industrial Processes and Emerging Techniques for Production of Hydrogen from Renewable and Sustainable Sources. *Renewable Sustainable Energy Rev.* **2013**, *23*, 443-462.
(60) Joshi, A. S.; Dincer, I.; Reddy, B. V. Solar Hydrogen Production: A Comparative Performance Assessment. *Int. J. Hydrogen Energy* **2011**, *36*, 11246-11257.
(61) Graves, C.; Ebbesen, S. D.; Mogensen, M.; Lackner, K. S. Sustainable Hydrocarbon Fuels by Recycling CO_2 and H_2O with Renewable or Nuclear Energy. *Renewable Sustainable Energy Rev.* **2011**, *15*, 1-23.
(62) Zhang, Q.; Kang, J.; Wang, Y. Development of Novel Catalysts for Fischer-Tropsch Synthesis: Tuning the Product Selectivity. *ChemCatChem* **2010**, *2*, 1030-1058.
(63) Holladay, J. D.; Hu, J.; King, D. L.; Wang, Y. An Overview of Hydrogen Production Technologies. *Catal. Today* **2009**, *139*, 244-260.
(64) Roy, S. C.; Varghese, O. K.; Paulose, M.; Grimes, C. A. Toward Solar Fuels: Photocatalytic Conversion of Carbon Dioxide to Hydrocarbons. *ACS Nano* **2010**, *4*, 1259-1278.
(65) Rosenberg, J. N.; Oyler, G. A.; Wilkinson, L.; Betenbaugh, M. J. A Green Light for Engineered Algae: Redirecting Metabolism to Fuel a Biotechnology Revolution. *Curr. Opin. Biotechnol.* **2008**, *19*, 430-436.
(66) Kwietniewska, E.; Tys, J. Process Characteristics, Inhibition Factors and Methane Yields of Anaerobic Digestion Process, with Particular Focus on Microalgal Biomass Fermentation. *Renewable Sustainable Energy Rev.* **2014**, *34*, 491-500.
(67) Kodama, T.; Gokon, N. Thermochemical Cycles for High-Temperature Solar Hydrogen Production. *Chem. Rev.* **2007**, *107*, 4048-4077.
(68) Romero, M.; Steinfeld, A. Concentrating Solar Thermal Power and Thermochemical Fuels. *Energy Environ. Sci.* **2012**, *5*, 9234-9245.
(69) Ozalp, N.; Kogan, A.; Epstein, M. Solar Decomposition of Fossil Fuels as an Option for Sustainability. *Int. J. Hydrogen Energy* **2009**, *34*, 710-720.
(70) Piatkowski, N.; Wieckert, C.; Weimer, A. W.; Steinfeld, A. Solar-Driven Gasification of Carbonaceous Feedstock- A Review. *Energy Environ. Sci.* **2011**, *4*, 73-82.
(71) Barlev, D.; Vidu, R.; Stroeve, P. Innovation in Concentrated Solar Power. *Sol. Energy Mater. Sol. Cells* **2011**, *95*, 2703-2725.
(72) Zhang, H. L.; Baeyens, J.; Degrève, J.; Cacères, G. Concentrated Solar Power Plants: Review and Design Methodology. *Renewable Sustainable Energy Rev.* **2013**, *22*, 466-481.

(73) Siegel, N. P.; Miller, J. E.; Ermanoski, I.; Diver, R. B.; Stechel, E. B. Factors Affecting the Efficiency of Solar Driven Metal Oxide Thermochemical Cycles. *Ind. Eng. Chem. Res.* **2013**, *52*, 3276-3286.

(74) Kim, J.; Johnson, T. A.; Miller, J. E.; Stechel, E. B.; Maravelias, C. T. Fuel Production from CO_2 Using Solar-Thermal Energy: System Level Analysis. *Energy Environ. Sci.* **2012**, *5*, 8417-8429.

(75) Roeb, M.; Neises, M.; Säck, J.-P.; Rietbrock, P.; Monnerie, N.; Dersch, J.; Schmitz, M.; Sattler, C. Operational Strategy of a Two-Step Thermochemical Process for Solar Hydrogen Production. *Int. J. Hydrogen Energy* **2009**, *34*, 4537-4545.

(76) Miller, J. E.; Allendorf, M. D.; Ambrosini, A.; Coker, E. N.; Diver, R. B.; Ermanoski, I.; Evans, L. R.; Hogan, R. E.; McDaniel, A. H. *Development and Assessment of Solar-Thermal-Activated Fuel Production: Phase 1 Summary*, SAND2012-5658, Sandia National Laboratories, Albuquerque, NM, 2012.

(77) Vishnevetsky, I.; Epstein, M. Production of Hydrogen from Solar Zinc in Steam Atmosphere. *Int. J. Hydrogen Energy* **2007**, *32*, 2791-2802.

(78) Funk, J. E. Thermochemical Hydrogen Production: Past and Present. *Int. J. Hydrogen Energy* **2001**, *26*, 185-190.

(79) Fletcher, E. A.; Moen, R. L. Hydrogen and Oxygen from Water. *Science* **1978**, *197*, 1050-1056.

(80) Lange, M.; Roeb, M.; Sattler, C.; Pitz-Paal, R. T-S Diagram Efficiency Analysis of Two-Step Thermochemical Cycles for Solar Water Splitting under Various Process Conditions. *Energy* **2014**, *67*, 298-308.

(81) Kogan, A. Direct Solar Thermal Splitting of Water and On-Site Separation of the Products-II. Experimental Feasibility Study. *Int. J. Hydrogen Energy* **1998**, *23*, 89-98.

(82) Lede, J.; Villermaux, J.; Ouzane, R.; Hossain, M. A.; Ouahes, R. Production of Hydrogen by Simple Impingment of a Turbulent Jet of Steam upon a High Temperature Zirconia Surface. *Int. J. Hydrogen Energy* **1987**, *12*, 3-11.

(83) Ihara, S. On the Study of Hydrogen Production from Water Using Solar Thermal Energy. *Int. J. Hydrogen Energy* **1980**, *5*, 527-534.

(84) Ermanoski, I.; Miller, J. E.; Allendorf, M. D. Efficienct Maximization in Solar-Thermochemical Fuel Production: Challenging the Concept of Isothermal Water Splitting. *Phys. Chem. Chem. Phys.* **2014**, *16*, 8418-8427.

(85) Beghi, G. E. Development of Thermochemical and Hybrid Processes for Hydrogen Production. *Int. J. Hydrogen Energy* **1985**, *10*, 431-438.

(86) Abraham, B. M.; Schreiner, F. General Principles Underlying Chemical Cycles Which Thermally Decompose Water into the Elements. *Ind. Eng. Chem., Fundam.* **1974**, *13*, 305-310.

(87) Rosen, M. A. Advances in Hydrogen Production by Thermochemical Water Decomposition: A Review. *Energy* **2010**, *35*, 1068-1076.

(88) Smestad, G. P.; Steinfeld, A. Review: Photochemical and Thermochemical Production of Solar Fuels from H_2O and CO_2 Using Metal Oxide Catalysys. *Ind. Eng. Chem. Res.* **2012**, *51*, 11828-11840.

(89) Charvin, P.; Abanades, S.; Lemort, F.; Flamant, G. Hydrogen Production by Three-Step Solar Thermochemical Cycles Using Hydroxides and Metal Oxide Systems. *Energy Fuels* **2007**, *21*, 2919-2928.

(90) Xu, B.; Bhawe, Y.; Davis, M. E. Spinel Metal Oxide-Alkali Carbonate-Based, Low-Temperature Thermochemical Cycles for Water Splitting and CO_2 Reduction. *Chem. Mater.* **2013**, *2013*, 1564-1571.

(91) Miller, J. E.; McDaniel, A. H.; Allendorf, M. D. Considerations in the Design of Materials for Solar-Driven Fuel Production Using Metal-Oixde Thermochemical Cycles. *Adv. Energy Mater.* **2014**, *4*, 1300469(1-19).
(92) Meredig, B.; Wolverton, C. First-Principles Thermodynamic Framework for the Evaluation of Thermochemical H_2O- or CO_2-Splitting Materials. *Phys. Rev. B* **2009**, *80*, 245119(1-8).
(93) Venstrom, L. J.; Petkovich, N.; Rudisill, S.; Stein, A.; Davidson, J. H. The Effects of Morphology on the Oxidation of Ceria by Water and Carbon Dioxide. *J. Sol. Energy Eng.* **2012**, *134*, 011005(1-8).
(94) Furler, P.; Scheffe, J. R.; Steinfeld, A. Syngas Production by Simultaneous Splitting of H_2O and CO_2 *via* Ceria Redox Reactions in a High-Temperature Solar Reactor. *Energy Environ. Sci.* **2012**, *5*, 6098-6103.
(95) Furler, P.; Scheffe, J.; Marxer, D.; Gorbar, M.; Bonk, A.; Vogt, U.; Steinfeld, A. Thermochemical CO_2 Splitting *via* Redox Cycling of Ceria Reticulated Foam Structures with Dual-Scale Porosities. *Phys. Chem. Chem. Phys.* **2014**, *16*, 10503-10511.
(96) Gibbons, W. T.; Venstrom, L. J.; De Smith, R. M.; Davidson, J. H.; Jackson, G. S. Ceria-Based Electrospun Fibers for Renewable Fuel Production *via* Two-Step Thermal Redox Cycles for Carbon Dioxide Splitting. *Phys. Chem. Chem. Phys.* **2014**, *16*, 14271-14280.
(97) Chueh, W. C.; Haile, S. M. Ceria as a Thermochemical Reaction Medium for Selectively Generating Syngas or Methane from H_2O and CO_2. *ChemSusChem* **2009**, *2*, 735-739.
(98) Gokon, N.; Hasegawa, T.; Takahashi, S.; Kodama, T. Thermochemical Two-Step Water-Splitting for Hydrogen Production Using Fe-YSZ Particles and a Ceramic Foam Device. *Energy* **2008**, *33*, 1407-1416.
(99) Abanades, S.; Flamant, G. Thermochemical Hydrogen Production from a Two-Step Solar-Driven Water-Splitting Cycle Based on Cerium Oxides. *Sol. Energy* **2006**, *80*, 1611-1623.
(100) Lapp, J.; Davidson, J. H.; Lipiński, W. Efficiency of Two-Step Solar Thermochemical Non-Stoichiometric Redox Cycles with Heat Recovery. *Energy* **2012**, *37*, 591-600.
(101) Lapp, J.; Lipiński, W. Transient Three-Dimensional Heat Transfer Model of a Solar Thermochemical Reactor for H_2O and CO_2 Splitting Via Nonstoichiometric Ceria Redox Cycling. *J. Sol. Energy Eng.* **2014**, *136*, 031006(1-11).
(102) Hao, Y.; Yang, C.-K.; Haile, S. M. High-Temperature Isothermal Chemical Cycling for Solar-Driven Fuel Production. *Phys. Chem. Chem. Phys.* **2013**, *15*, 17084-17092.
(103) Bader, R.; Venstrom, L. J.; Davidson, J. H.; Lipiński, W. Thermodynamic Analysis of Isothermal Redox Cycling of Ceria for Solar Fuel Production. *Energy Fuels* **2013**, *27*, 5533-5544.
(104) Allendorf, M. D.; Diver, R. B.; Siegel, N. P.; Miller, J. E. Two-Step Water Splitting Using Mixed-Metal Ferrites: Thermodynamic Analysis and Characterization of Synthesized Materials. *Energy Fuels* **2008**, *22*, 4115-4124.
(105) Haltiwagner, J. F.; Davidson, J. H.; Wilson, E. J. Renewable Hydrogen from the Zn/ZnO Solar Thermochemical Cycle: A Cost and Policy Analysis. *J. Sol. Energy Eng.* **2010**, *132*, 041011(1-8).
(106) Nakamura, T. Hydrogen Production from Water Utilizing Solar Heat at High Temperatures. *Sol. Energy* **1977**, *19*, 467-475.
(107) Stamatiou, A.; Loutzenhiser, P. G.; Steinfeld, A. Solar Syngas Production via H_2O/CO_2-Splitting Thermochemical Cycles with Zn/ZnO and FeO/Fe_3O_4 Redox Reactions. *Chem. Mater.* **2010**, *22*, 851-859.
(108) Charvin, P.; Abanades, S.; Flamant, G.; Lemort, F. Two-Step Water Splitting Thermochemical Cycle Based on Iron Oxide Redox Pair for Solar Hydrogen Production. *Energy* **2007**, *32*, 1124-1133.

(109) Tamaura, Y.; Steinfeld, A.; Kuhn, P.; Ehrensberger, K. Production of Solar Hydrogen by a Novel, 2-Step, Water-Splitting Thermochemical Cycle. *Energy* **1995**, *20*, 325-330.
(110) Han, S. B.; Kang, T. B.; Joo, O. S.; Jung, K. D. Water Splitting for Hydrogen Production with Ferrites. *Sol. Energy* **2007**, *81*, 623-628.
(111) Fresno, F.; Fernández-Saavedra, R.; Gómez-Mancebo, M. B.; Vidal, A.; Sánchez, M.; Rucandio, M. I.; Quejido, A. J.; Romero, M. Solar Hydrogen Production by Two-Step Thermochemical Cycles: Evaluation of the Activity of Commercial Ferrites. *Int. J. Hydrogen Energy* **2009**, *34*, 2918-2924.
(112) Fresno, F.; Yoshida, T.; Gokon, N.; Fernández-Saavedra, R.; Kodama, T. Comparative Study of the Activity of Nickel Ferrites for Solar Hydrogen Production by Two-Step Thermochemical Cycles. *Int. J. Hydrogen Energy* **2010**, *35*, 8503-8510.
(113) Roeb, M.; Gathmann, N.; Neises, M.; Sattler, C.; Pitz-Paal, R. Thermodynamic Analysis of Two-Step Solar Water Splitting with Mixed Iron Oxides. *Int. J. Energy Res.* **2009**, *33*, 893-902.
(114) Bhosale, R. R.; Shende, R. V.; Puszynski, J. A. Thermochemical Water-Splitting for H_2 Generation Using Sol-Gel Derived Mn-Ferrite in a Packed Bed Reactor. *Int. J. Hydrogen Energy* **2012**, *37*, 2924-2934.
(115) Kodama, T.; Kondoh, Y.; Yamamoto, R.; Andou, H.; Satou, N. Thermochemical Hydrogen Production by a Redox System of ZrO_2-Supported Co(II)-Ferrite. *Sol. Energy* **2005**, *78*, 623-631.
(116) Scheffe, J. R.; Allendorf, M. D.; Coker, E. N.; Jacobs, B. W.; McDaniel, A. H.; Weimer, A. W. Hydrogen Production via Chemical Looping Redox Cycles Using Atomic Layer Deposition-Synthesized Iron Oxide and Cobalt Ferrites. *Chem. Mater.* **2011**, *23*, 2030-2038.
(117) Gokon, N.; Kodama, T.; Imaizumi, N.; Umeda, J.; Seo, T. Ferrite/Zirconia-Coated Foam Device Prepared by Spin Coating for Solar Demonstration of Thermochemical Water-Splitting. *Int. J. Hydrogen Energy* **2011**, *36*, 2014-2028.
(118) Coker, E. N.; Ambrosini, A.; Rodriguez, M. A.; Miller, J. E. Ferrite-YSZ Composites for Solar Thermochemical Production of Synthetic Fuels: *In Operando* Characterization of CO_2 Reduction. *J. Mater. Chem.* **2011**, *21*, 10767-10776.
(119) Scheffe, J. R.; McDaniel, A. H.; Allendorf, M. D.; Weimer, A. W. Kinetics and Mechanism of Solar-Thermochemical H_2 Production by Oxidation of a Cobalt Ferrite-Zirconia Composite. *Energy Environ. Sci.* **2013**, *6*, 963-973.
(120) Kaneko, H.; Miura, T.; Fuse, A.; Ishihara, H.; Taku, S.; Fukuzumi, H.; Naganuma, Y.; Tamaura, Y. Rotary-Type Solar Reactor for Solar Hydrogen Production with Two-Step Water Splitting Process. *Energy Fuels* **2007**, *21*, 2287-2293.
(121) Diver, R. B.; Miller, J. E.; Allendorf, M. D.; Siegel, N. P.; Hogan, R. E. Solar Thermochemical Water-Splitting Ferrite-Cycle Heat Engines. *J. Sol. Energy Eng.* **2008**, *130*, 041001(1-8).
(122) Gokon, N.; Mataga, T.; Kondo, N.; Kodama, T. Thermochemical Two-Step Water Splitting by Internally Circulating Fludized Bed of $NiFe_2O_4$ Particles: Successive Reaction of Thermal-Reduction and Water-Decomposition Steps. *Int. J. Hydrogen Energy* **2011**, *36*, 4757-4767.
(123) Steinfeld, A. Solar Hydrogen Production via a Two-Step Water-Splitting Thermochemical Cycle Based on Zn/ZnO Redox Reactions. *Int. J. Hydrogen Energy* **2002**, *27*, 611-619.
(124) Venstrom, L. J.; Davidson, J. H. The Kinetics of the Heterogeneous Oxidation of Zinc Vapor by Carbon Dioxide. *Chem. Eng. Sci.* **2013**, *93*, 163-172.

(125) Stamatiou, A.; Loutzenhiser, P. G.; Steinfeld, A. Solar Syngas Production from H_2O and CO_2 via Two-Step Thermochemical Cycles Based on Zn/ZnO and FeO/Fe_3O_4 Redox Reactions: Kinetic Analysis. *Energy Fuels* **2010**, *24*, 2716-2722.
(126) Loutzenhiser, P. G.; Meier, A.; Steinfeld, A. Review of the Two-Step H_2O/CO_2-Splitting Solar Thermochemical Cycle Based on Zn/ZnO Redox Reactions. *Materials* **2010**, *3*, 4922-4938.
(127) Abanades, S. Thermogravimetry Analysis of CO_2 and H_2O Reduction from Solar Nanosized Zn Powder for Thermochemical Fuel Production. *Ind. Eng. Chem. Res.* **2012**, *51*, 741-750.
(128) Wegner, K.; Ly, H. C.; Weiss, R. J.; Pratsinis, S. E.; Steinfeld, A. In Situ Formation and Hydrolysis of Zn Nanoparticles for H_2 Production by the 2-Step ZnO/Zn Water-Splitting Thermochemical Cycle. *Int. J. Hydrogen Energy* **2006**, *31*, 55-61.
(129) Perkins, C.; Lichty, P. R.; Weimer, A. W. Thermal ZnO Dissociation in a Rapid Aerosol Reactor As Part of a Solar Hydrogen Production Cycle. *Int. J. Hydrogen Energy* **2008**, *33*, 499-510.
(130) Schunk, L. O.; Haeberling, P.; Wepf, S.; Wuillemin, D.; Meier, A.; Steinfeld, A. A Receiver-Reactor for the Solar Thermal Dissociation of Zinc Oxide. *J. Sol. Energy Eng.* **2008**, *130*, 021009(1-6).
(131) Chueh, W. C.; Haile, S. M. A Thermochemical Study of Ceria: Exploiting an Old Material for New Modes of Energy Conversion and CO_2 Mitigation. *Phil. Trans. R. Soc. A* **2010**, *368*, 3269-3294.
(132) Chueh, W. C.; Falter, C.; Abbott, M.; Scipio, D.; Furler, P.; Haile, S. M.; Steinfeld, A. High-Flux Solar-Driven Thermochemical Dissociation of CO_2 and H_2O Using Nonstoichiometric Ceria. *Science* **2010**, *330*, 1797-1801.
(133) Rudisill, S. G.; Venstrom, L. J.; Petkovich, N. D.; Quan, T.; Hein, N.; Boman, D. B.; Davidson, J. H.; Stein, A. Enhanced Oxidation Kinetics in Thermochemical Cycling of CeO_2 through Templated Porosity. *J. Phys. Chem. C* **2013**, *117*, 1692-1700.
(134) Scheffe, J. R.; Li, J.; Weimer, A. W. A Spinel Ferrite/Hercynite Water-Splitting Redox Cycles. *Int. J. Hydrogen Energy* **2010**, *35*, 3333-3340.
(135) Arifin, D.; Aston, V. J.; Liang, X.; McDaniel, A. H.; Weimer, A. W. $CoFe_2O_4$ on a Porous Al_2O_3 Nanostructure for Solar Thermochemical CO_2 Splitting. *Energy Environ. Sci.* **2012**, *5*, 9438-9443.
(136) Muhich, C. L.; Evanko, B. W.; Weston, K. C.; Lichty, P.; Liang, X.; Martinek, J.; Musgrave, C. B.; Weimer, A. W. Efficient Generation of H_2 by Splitting Water with an Isothermal Redox Cycle. *Science* **2013**, *341*, 540-542.
(137) Stølen, S.; Bakken, E.; Mohn, C. E. Oxygen-Deficient Perovskite: Linking Structure, Energetics and Ion Transport. *Phys. Chem. Chem. Phys.* **2006**, *8*, 429-447.
(138) Scheffe, J. R.; Weibel, D.; Steinfeld, A. Lanthanum-Strontium-Manganese Perovskites as Redox Materials for Solar Thermochemical Splitting of H_2O and CO_2. *Energy Fuels* **2013**, *27*, 4250-4257.
(139) McDaniel, A. H.; Miller, E. C.; Arifin, D.; Ambrosini, A.; Coker, E. N.; O'Hayre, R.; Chueh, W. C.; Tong, J. Sr- and Mn-Doped $LaAlO_{3-\delta}$ for Solar Thermochemical H_2 and CO Production. *Energy Environ. Sci.* **2013**, *6*, 2424-2428.
(140) Demont, A.; Abanades, S.; Beche, E. Investigation of Perovskite Structures as Oxygen-Exchange Redox Materials for Hydrogen Production from Thermochemical Two-Step Water-Splitting Cycles. *J. Phys. Chem. C* **2014**, *118*, 12682-12692.
(141) Peña, M. A.; Fierro, J. L. G. Chemical Structures and Performance of Perovskite Oxides. *Chem. Rev.* **2001**, *101*, 1981-2017.

Chapter 2

(1) Petkovich, N. D.; Stein, A. Colloidal Crystal Templating Approaches to Materials with Hierarchical Porosity. In *Hierarchically Structured Porous Materials: From Nanoscience to Catalysis, Separation, Optics, Energy, and Life Science*; Su, B.-L., Sanchez, C., Yang, X.-Y., Eds.; Wiley-VCH Verlag GmbH & Co. KGaA: Weinheim, Germany, 2012.

(2) Caruso, R. A. Nanocasting and Nanocoating. *Top. Curr. Chem.* **2003**, *226*, 91-118.

(3) Hassan, S.; Rowe, W.; Tiddy, G. J. T. Surfactant Liquid Crystals. In *Handbook of Applied Surface and Colloid Chemistry*; Holmberg, K., Shah, D. O., Schwuger, M. J., Eds.; John Wiley & Sons Ltd: Chichester, England, 2002.

(4) Rosen, M. J.; Kunjappu, J. T. *Surfactants and Interfacial Phenomena*; 4th ed.; John Wiley & Sons, Inc.: Hoboken, NJ, 2012.

(5) Fan, J.; Boettcher, S. W.; Tsung, C.-K.; Shi, Q.; Schierhorn, M.; Stucky, G. D. Field-Directed and Confined Molecular Assembly of Mesostructured Materials: Basic Principles and New Opportunities. *Chem. Mater.* **2008**, *20*, 909-921.

(6) Zhang, Y.; Liu, X.; Huang, J. Hierarchical Mesoporous Silica Nanotubes Derived from Natural Cellulose Substance. *ACS Appl. Mater. Interfaces* **2011**, *3*, 3272-3275.

(7) Platschek, B.; Keilbach, A.; Bein, T. Mesoporous Structures Confined in Anodic Alumina Membranes. *Adv. Mater.* **2011**, *23*, 2395–2412.

(8) Falcaro, P.; Malfatti, L.; Kidchob, T.; Giannini, G.; Falqui, A.; Casula, M. F.; Amenitsch, H.; Marmiroli, B.; Grenci, G.; Innocenzi, P. Hierarchical Porous Silica Films with Ultralow Refractive Index. *Chem. Mater.* **2009**, *21*, 2055-2061.

(9) Drisko, G. L.; Zelcer, A.; Luca, V.; Caruso, R. A.; Soler-Illia, G. J. A. A. One-Pot Synthesis of Hierarchically Structured Ceramic Monoliths with Adjustable Porosity. *Chem. Mater.* **2010**, *22*, 4379-4385.

(10) Ahmed, A.; Clowes, R.; Myers, P.; Zhang, H. Hierarchically Porous Silica Monoliths with Tuneable Morphology, Porosity, and Mechanical Stability. *J. Mater. Chem.* **2011**, *21*, 5753-5763.

(11) Lou, X. W.; Archer, L. A.; Yang, Z. Hollow Micro-/Nanostructures: Synthesis and Applications. *Adv. Mater.* **2008**, *20*, 3987-4019.

(12) Chen, Y.; Chen, H.; Zeng, D.; Tian, Y.; Chen, F.; Feng, J.; Shi, J. Core/Shell Structured Hollow Mesoporous Nanocapsules: A Potential Platform for Simultaneous Cell Imaging and Anticancer Drug Delivery. *ACS Nano* **2010**, *4*, 6001-6013.

(13) Meng, Y.; Gu, D.; Zhang, F.; Shi, Y.; Yang, H.; Li, Z.; Yu, C.; Tu, B.; Zhao, D. Ordered Mesoporous Polymers and Homologous Carbon Framework: Amphiphilic Surfactant Templating and Direct Transformation. *Angew.Chem. Int. Ed.* **2005**, *44*, 7053-7059.

(14) Soler-Illia, G. J. A. A.; Azzaroni, O. Multifunctional Hybrid by Combining Ordered Mesoporous Materials and Macromolecular Building Blocks. *Chem. Soc. Rev.* **2011**, *40*, 1107-1150.

(15) Mutin, P. H.; Vioux, A. Nonhydrolytic Processing of Oxide-Based Materials: Simple Routes to Control Homogeneity, Morphology, and Nanostructure. *Chem. Mater.* **2009**, *21*, 582-596.

(16) Kakihana, M. Invited Review "Sol-Gel" Preparation of High Temperature Superconducting Oxides. *J. Sol-Gel Sci. Technol.* **1996**, *6*, 7-55.

(17) Rudisill, S. G.; Hein, N. M.; Terzic, D.; Stein, A. Controlling Microstructural Evolution in Pechini Gels through the Interplay between Precursor Complexation, Step-Growth Polymerization, and Template Confinement. *Chem. Mater.* **2013**, *25*, 745-753.

(18) Soler-Illia, G. J. A. A.; Sanchez, C.; Lebeau, B.; Patarin, J. Chemical Strategies to Design Textured Materials: From Microporous and Mesoporous Oxides to Nanonetworks and

Hierarchical Structures. *Chem. Rev.* **2002**, *102*, 4093-4138.
(19) Boettcher, S. W.; Fan, J.; Tsung, C.-K.; Shi, Q.; Stucky, G. D. Harnessing the Sol-Gel Process for the Assembly of Non-Silicate Mesostructured Oxide Materials. *Acc. Chem. Res.* **2007**, *40*, 784-792.
(20) Ghadimi, A.; Cademartiri, L.; Kamp, U.; Ozin, G. A. Plasma within Templates: Molding Flexible Nanocrystal Solids into Multifunctional Architecture. *Nano Lett.* **2007**, *7*, 3864-3868.
(21) Drisko, G. L.; Zelcer, A.; Caruso, R. A.; Soler-Illia, G. J. A. A. One-Pot Synthesis of Silica Monoliths with Hierarchically Porous Structure. *Microporous Mesoporous Mater.* **2012**, *148*, 137-144.
(22) Van Gough, D.; Defino, J. L.; Braun, P. V. Programmed Size-Selected Permeation of ssDNA into ZnS Mesoporous Hollow Spheres. *Soft Matter* **2012**, *8*, 4396-4401.
(23) Su, Y.; Yan, R.; Dan, M.; Xu, J.; Wang, D.; Zhang, W.; Liu, S. Synthesis of Hierarchical Hollow Silica Microspheres Containing Surface Nanoparticles Employing the Quasi-Hard Template of Poly(4-vinylpyridine) Microspheres. *Langmuir* **2011**, *27*, 8983-8989.
(24) Israelachvili, J. N. *Intermolecular and Surface Forces*; 3rd ed.; Academic Press: Waltham, MA, 2011.
(25) Innocenzi, P.; Malfatti, L.; Kidchob, T.; Falcaro, P. Order–Disorder in Self-Assembled Mesostructured Silica Films: A Concepts Review. *Chem. Mater.* **2009**, *21*, 2555-2564.
(26) Zhang, X.; Lu, W.; Dai, J.; Bourgeois, L.; Hao, N.; Wang, H.; Zhao, D. Y.; Webley, P. A. Ordered Hierarchical Porous Platinum Membranes with Tailored Mesostructures. *Angew.Chem. Int. Ed.* **2010**, *49*, 10101-10105.
(27) Mao, C.; Wang, F.; Cao, B. Controlling Nanostructures of Mesoporous Silica Fibers by Supramolecular Assembly of Genetically Modifiable Bacteriophages. *Angew.Chem. Int. Ed.* **2012**, *124*, 6517-6521.
(28) Sun, X.; Zheng, C.; Qian, M.; Yan, J.; Wang, X.; Guan, N. Bioinspired Synthesis of Hierarchical Macro-Mesoporous Titania with Tunable Macoporous Morphology Using Cell-Assemblies as Macrotemplates. *Chem. Commun.* **2009**, 4750-4752.
(29) Li, X.; Jiang, J.; Wang, Y.; Nie, X.; Qu, F. Preparation of Multilevel Macroporous Materials Using Natural Plants as Templates. *J. Sol-Gel Sci. Technol.* **2010**, *56*, 75-81.
(30) Huang, C.-H.; Doong, R.-A. Sugarcane Bagasse as the Scaffold for Mass Production of Hierarchically Porous Carbon Monoliths by Surface Self-Assembly. *Microporous Mesoporous Mater.* **2012**, *147*, 47-52.
(31) Liu, H. J.; Wang, X. M.; Cui, W. J.; Dou, Y. Q.; Zhao, D. Y.; Xia, Y. Y. Highly Ordered Mesoporous Carbon Nanofiber Arrays From a Crab Shell Biological Template and Its Application in Supercapacitors and Fuel Cells. *J. Mater. Chem.* **2010**, *20*, 4223-4230.
(32) Zhang, Y.; Hu, L.; Han, J.; Jiang, Z.; Zhou, Y. Soluble Starch Scaffolds with Uniaxial Aligned Channel Structure for In Situ Synthesis of Hierarchically Porous Silica Ceramics. *Microporous Mesoporous Mater.* **2010**, *130*, 327-332.
(33) Sun, Z.; Deng, Y.; Wei, J.; Gu, D.; Tu, B.; Zhao, D. Y. Hierarchically Ordered Macro-Mesoporous Silica Monolith: Tuning Macropore Entrance Size for Size-Selective Adsorption of Proteins. *Chem. Mater.* **2011**, *23*, 2176-2184.
(34) Li, F.; Wang, Z.; Ergang, N. S.; Fyfe, C. A.; Stein, A. Controlling the Shape and Alignment of Mesopores by Confinement in Colloidal Crystals: Designer Pathways to Silica Monoliths with Hierarchical Porosity. *Langmuir* **2007**, *23*, 3996-4004.
(35) Li, F.; Wilker, M. B.; Stein, A. Simulation-Aided Design and Synthesis of Hierarchically Porous Membranes. *Langmuir* **2012**, *28*, 7484-7491.
(36) Zhu, W.; Tao, S.; Tao, C.-A.; Li, W.; Lin, C.; Li, M.; Wen, Y.; Li, G. Hierarchically Imprinted Porous Films for Rapid and Selective Detection of Explosives. *Langmuir* **2011**, *27*, 8451-8457.

(37) Bian, S.-W.; Zhang, Y.-L.; Li, H.-L.; Yu, Y.; Song, Y.-L.; Song, W.-G. γ-Alumina with Hierarchically Ordered Mesopore/Macropore from Dual Templates. *Microporous Mesoporous Mater.* **2010**, *131*, 289-293.

(38) Zhao, J.; Wan, P.; Xiang, J.; Tong, T.; Dong, L.; Gao, Z.; Shen, X.; Tong, H. Synthesis of Highly Ordered Macro-Mesoporous Anatase TiO_2 Film with High Photocatalytic Activity. *Microporous Mesoporous Mater.* **2011**, *138*, 200-206.

(39) Zhang, R.; Dai, H.; Du, Y.; Zhang, L.; Deng, J.; Xia, Y.; Zhao, Z.; Meng, X.; Liu, Y. P123-PMMA Dual-Templating Generation and Unique Physicochemical Properties of Three-Dimensionally Ordered Macroporous Iron Oxides with Nanovoids in the Crystalline Wall. *Inorg. Chem.* **2011**, *50*, 2534-2544.

(40) Vu, A.; Stein, A. Multiconstituent Synthesis of $LiFePO_4$/C Composites with Hierarchical Porosity as Cathode Materials for Lithium Ion Batteries. *Chem. Mater.* **2011**, *23*, 3237-3245.

(41) Du, J.; Lai, X.; Yang, N.; Zhai, J.; Kisailus, D.; Su, F.; Wang, D.; Jiang, L. Hierarchically Ordered Macro-Mesoporous TiO_2-Graphene Composite Films: Improved Mass Transfer, Reduced Charge Recombination and Thier Enhanced Photocatalytic Activities. *ACS Nano* **2011**, *5*, 590-596.

(42) Li, F.; Qian, Y.; Stein, A. Template-Directed Synthesis and Organization of Shaped Oxide/Phosphate Nanoparticles. *Chem. Mater.* **2010**, *22*, 3226-3235.

(43) Mandlmeier, B.; Szeifert, J. M.; Fattakhova-Rohlfing, D.; Amenitsch, H.; Bein, T. Formation of Interpenetrating Hierarchical Titania Structures by Confined Synthesis in Inverse Opal. *J. Am. Chem. Soc.* **2011**, *133*, 17274-17282.

(44) Yang, S. M.; Coombs, N.; Ozin, G. A. Micromolding in Inverted Polymer Opals (MIPO): Synthesis of Hexagonal Mesoporous Silica Opals. *Adv. Mater.* **2000**, *2000*, 1940-1944.

(45) Zhou, D.-D.; Liu, H.-J.; Wang, Y.-G.; Wang, C.-X.; Xia, Y.-Y. Ordered Mesoporous/Microporous Carbon Sphere Arrays Derived from Chlorination of Mesoporous TiC/C Composite and Their Application for Supercapacitors. *J. Mater. Chem.* **2012**, *22*, 1937-1943.

(46) Zhu, Y.; Li, X.; Yang, J.; Wang, S.; Gao, H.; Hanagata, N. Composition-Structure-Property Relationship of the CaO-M_xO_y-SiO_2-P_2O_5 (M = Zr, Mg, Sr) Mesoporous Bioactive Glass (MBG) Scaffolds. *J. Mater. Chem.* **2011**, *21*, 9208-9218.

(47) Xue, C.; Wang, J.; Tu, B.; Zhao, D. Y. Hierarchically Porous Silica with Ordered Mesostructure from Confinement Self-Assembly in Skeleton Scaffolds. *Chem. Mater.* **2010**, *22*, 494-503.

(48) Wang, J.; Xue, C.; Wu, Z.; Li, W.; Lv, Y.; Asiri, A. M.; Tu, B.; Zhao, D. Y. Hollow Micro-Mesoporous Carbon Polyhedra Produced by Selective Removal of Skeletal Scaffolds. *Carbon* **2012**, *50*, 2546-2555.

(49) Brun, N.; Prabaharan, S. R. S.; Surcin, C.; Morcrette, M.; Deleuze, H.; Birot, M.; Babot, O.; Achard, M.-F.; Backov, R. Design of Hierarchical Porous Carbonaceous Foams From a Dual-Template Approach and Their Use as Electrochemical Capacitor Li Ion Battery Negative Electrode. *J. Phys. Chem. C* **2012**, *116*, 1408-1421.

(50) Platschek, B.; Köhn, R.; Döblinger, M.; Bein, T. Formation Mechanism of Mesostructured Silica in Confined Space: An In Situ GISAXS Study. *ChemPhysChem* **2008**, *9*, 2059-2067.

(51) Keller, A.; Kirmayer, S.; Segal-Peretz, T.; Frey, G. L. Mesostructured Silica Containing Conjugated Polymers Formed with the Channels of Anodic Alumina Membranes from Tetrahydrofuran-Based Solution. *Langmuir* **2012**, *28*, 1506-1514.

(52) O'Callaghan, J. M.; Petkov, N.; Copley, M. P.; Arnold, D. C.; Morris, M. A.; Amenitsch, H.; Holmes, J. D. Time-Resolved SAXS Studies of Periodic Mesoporous Organosilicas in Anodic Alumina Membranes. *Microporous Mesoporous Mater.* **2010**, *130*, 203-207.

(53) Schuster, J.; Koehn, R.; Döblinger, M.; Keilbach, A.; Amenitsch, H.; Bein, T. In Situ SAXS Study on a New Mechanism for Mesostructure Formation of Ordered Mesoporous Carbon: Thermally-Induced Self-Assembly. *J. Am. Chem. Soc.* **2012**, *134*, 11136-11145.
(54) Kim, E.-M.; Jung, J.-S.; Chae, W.-S. Interfacial Interaction Induced Mesostructural Changes in Nanocylinders. *Chem. Commun.* **2010**, *46*, 1760-1762.
(55) Zhang, A.; Hou, K.; Gu, L.; Dai, C.; Liu, M.; Song, C.; Guo, X. Synthesis of Silica Nanotubes with Orientation Controlled Mesopores in Porous Membranes via Interfacial Growth. *Chem. Mater.* **2012**, *24*, 1005-1010.
(56) El-Safty, S.; Shahat, A.; Awual, M. R.; Mekawy, M. Large Three-Dimensional Mesocage Pores Tailoring Silica Nanotubes as Membrane Filter: Nanofiltration and Permeation Flux of Protein. *J. Mater. Chem.* **2011**, *21*, 5593-5603.
(57) Wang, X.; Sumboja, A.; Khoo, E.; Yan, C.; Lee, P. S. Cryogel Synthesis of Hierarchical Interconnected Macro-/Mesoporous Co_3O_4 with Superb Electrochemical Energy Storage. *J. Phys. Chem. C* **2012**, *116*, 4930-4935.

Chapter 3

(1) Tachikawa, T.; Fujitsuka, M.; Majima, T. Mechanistic Insight into the TiO_2 Photocatalytic Reactions: Design of New Photocatalysts. *J. Phys. Chem. C* **2007**, *111*, 5259-5275.
(2) Chen, X.; Shen, S.; Guo, L.; Mao, S. S. Semiconductor-based Photocatalytic Hydrogen Generation. *Chem. Rev.* **2010**, *110*, 6503-6570.
(3) Kadoshima, M.; Hiratani, M.; Shimamoto, Y.; Torii, K.; Miki, H.; Kimura, S.; Nabatame, T. Rutile-type TiO_2 Thin Film for High-*k* Gate Insulator. *Thin Soild Films* **2003**, *424*, 224-228.
(4) Lee, M.-J.; Seo, S.; Kim, D.-C.; Ahn, S.-E.; Seo, D. H.; Yoo, I.-K.; Baek, I.-G.; Kim, D.-S.; Byun, I.-S.; Kim, S.-H.; Hwang, I.-R.; Kim, J.-S.; Jeon, S.-H.; Park, B. H. A Low-Temperature-Grown Oxide Diode as a New Switch Element for High-Density, Nonvolatile Memories. *Adv. Mater.* **2007**, *19*, 73-76.
(5) Hagfeldt, A.; Boschloo, G.; Sun, L.; Kloo, L.; Pettersson, H. Dye-Sensitized Solar Cells. *Chem. Rev.* **2010**, *110*, 6595-6663.
(6) Jung, H. S.; Lee, J.-K. Dye Sensitized Solar Cells for Economically Viable Photovoltaic System. *J. Phys. Chem. Lett.* **2013**, *4*, 1682-1693.
(7) Auer, G.; Griebler, W.-D.; Jahn, B. White Pigments. In *Industrial Inorganic Pigments*; 3rd ed.; Buxbaum, G., Pfaff, G., Eds.; Wiley-VCH Verlag GmbH & Co. KGaA: Weinheim, Germany, 2005.
(8) Comotti, M.; Li, W.-C.; Spliethoff, B.; Schüth, F. Support Effect in High Activity Gold Catalysts for CO Oxidation. *J. Am. Chem. Soc.* **2006**, *128*, 917-924.
(9) Cao, A.; Lu, R.; Veser, G. Stabilizing Metal Nanoparticles for Heterogeneous Catalysis. *Phys. Chem. Chem. Phys.* **2010**, *12*, 13499-13510.
(10) Fröschl, T.; Hörmann, U.; Kubiak, P.; Kučerová, G.; Pfanzelt, M.; Weiss, C. K.; Behm, R. J.; Hüsing, N.; Kaiser, U.; Landfester, K.; Wohlfahrt-Mehrens, M. High Surface Area Crystalline Titanium Dioxide: Potential and Limits in Electrochemical Energy Storage and Catalysis. *Chem. Soc. Rev.* **2012**, *41*, 5313-5360.
(11) Huang, S. Y.; Kavan, L.; Exnar, I.; Grätzel, M. Rocking Chair Lithium Battery Based on Nanocrystalline TiO_2 (Anatase). *J. Electrochem. Soc.* **1995**, *142*, L142-L144.

(12) Kavan, L.; Rathouský, J.; Grätzel, M.; Shklover, V.; Zukal, A. Surfactant-Templated TiO_2 (Anatase): Characteristic Features of Lithium Insertion Electrochemistry in Organized Nanostructures. *J. Phys. Chem. B* **2000**, *104*, 12012-12020.
(13) Kavan, L.; Rathouský, J.; Grätzel, M.; Shklover, V.; Zukal, A. Mesoporous Thin Film TiO_2 Electrodes. *Microporous Mesoporous Mater.* **2001**, *44-45*, 653-659.
(14) Leroux, F.; Dewar, P. J.; Intissar, M.; Ouvrard, G.; Nazar, L. F. Study of the Formation of Mesoporous Titania *via* a Template Approach and of Subsequent Li Insertion. *J. Mater. Chem.* **2002**, *12*, 3245-3253.
(15) Zampardi, G.; Ventosa, E.; La Mantia, F.; Schuhmann, W. *In Situ* Visualization of Li-Ion Intercalation and Formation of the Solid Electrolyte Interphase on TiO_2 Based Paste Electrodes Using Scanning Electrochemical Microscopy. *Chem. Commun.* **2013**, *49*, 9347-9349.
(16) Jacoby, M. Assessing the Safety of Lithium-Ion Batteries. *Chem. Eng. News* **2013**, *91*, 33-37.
(17) Armstrong, A. R.; Armstrong, G.; Canales, J.; García, R.; Bruce, P. G. Lithium-Ion Intercalation into TiO_2-B Nanowires. *Adv. Mater.* **2005**, *17*, 862-865.
(18) Hu, Y.-S.; Kienle, L.; Guo, Y.-G.; Maier, J. High Lithium Electroactivity of Nanometer-Sized Rutile TiO_2. *Adv. Mater.* **2006**, *18*, 1421-1426.
(19) Wang, K.; Wei, M.; Morris, M. A.; Zhou, H.; Holmes, J. D. Mesoporous Titania Nanotubes: Their Preparation and Application as Electrode Materials for Rechargeable Lithium Batteries. *Adv. Mater.* **2007**, *19*, 3016-3020.
(20) Yang, Z.; Choi, D.; Kerisit, S.; Rosso, K. M.; Wang, D.; Zhang, J.; Graff, G.; Liu, J. Nanostructures and Lithium Electrochemical Reactivity of Lithium Titanites and Titanium Oxides: A Review. *J. Power Sources* **2009**, *192*, 588-598.
(21) Ren, Y.; Hardwick, L. J.; Bruce, P. G. Lithium Intercalation into Mesoporous Anatase with an Ordered 3D Pore Structure. *Angew. Chem. Int. Ed.* **2010**, *49*, 2570-2574.
(22) Shin, J.-Y.; Samuelis, D.; Maier, J. Sustained Lithium-Storage Performance of Hierarchical, Nanoporous Anatase TiO_2 at High Rates: Emphasis on Interfacial Storage Phenomena. *Adv. Funct. Mater.* **2011**, *21*, 3464-3472.
(23) Saravanan, K.; Ananthanarayanan, K.; Balava, P. Mesoporous TiO_2 with High Packing Density for Superior Lithium Storage. *Energy Environ. Sci.* **2010**, *3*, 939-948.
(24) Szeifert, J. M.; Feckl, J. M.; Fattakhova-Rohlfing, D.; Liu, Y.; Kalousek, V.; Rathouský, J.; Bein, T. Ultrasmall Titania Nanocrystals and Their Direct Assembly into Mesoporous Structures Showing Fast Lithium Insertion. *J. Am. Chem. Soc.* **2010**, *132*, 12605-12611.
(25) Ren, Y.; Liu, Z.; Pourpoint, F.; Armstrong, A. R.; Grey, C. P.; Bruce, P. G. Nanoparticulate TiO_2(B): An Anode for Lithium-Ion Batteries. *Angew. Chem. Int. Ed.* **2012**, *51*, 2164-2167.
(26) Chen, S. C.; Tan, Y. L.; Li, C. M.; Cheah, Y. L.; Luan, D.; Madhavi, S.; Boey, F. Y. C.; Archer, L. A.; Lou, X. W. Constructing Hierarchical Spheres from Large Ultrathin Anatase TiO_2 Nanosheets with Nearly 100% Exposed (001) Facets for Fast Reversible Lithium Storage. *J. Am. Chem. Soc.* **2010**, *132*, 6124-6130.
(27) Zhao, B.; Shao, Z. From Paper to Paper-like Hierarchical Anatase TiO_2 Film Electrode for High-Performance Lithium-Ion Batteries. *J. Phys. Chem. C* **2012**, *116*, 17400-17447.
(28) Wang, J.; Polleux, J.; Lim, J.; Dunn, B. Pseudocapacitive Contributions to Electrochemical Energy Storage in TiO_2 (Anatase) Nanoparticles. *J. Phys. Chem. C* **2007**, *111*, 14925-14931.
(29) Wagemaker, M.; Mulder, F. M. Properties and Promises of Nanosized Insertion Materials for Li-Ion Batteries. *Acc. Chem. Rev.* **2012**, *46*, 1206-1215.

(30) Bi, Z.; Paranthaman, M. P.; Guo, B.; Unocic, R.; Meyer, H.; Bridges, C. A.; Sun, X.-G.; Dai, S. High Performance Cr, N - Codoped Mesoporous TiO_2 Microsphere Anodes for Lithium-ion Rechargeable Batteries. *J. Mater. Chem. A* **2014,** *2*, 1818-1824.
(31) Li, H.; Zhou, H. Enhancing the Performances of Li-Ion Batteries by Carbon-Coating: Present and Future. *Chem. Commun.* **2012**, *48*, 1201-1217.
(32) Guo, Y.-G.; Hu, Y.-S.; Sigle, W.; Maier, J. Superior Electrode Performance of Nanostructured Mesoporous TiO_2 (Anatase) through Efficient Hierarchical Mixed Conducting Networks. *Adv. Mater.* **2007**, *19*, 2087-2091.
(33) Ding, S.; Chen, J. S.; Lou, X. W. One-Dimensional Hierarchical Structures Composed of Novel Metal Oxide Nanosheets on a Carbon Nanotube Backbone and Their Lithium-Storage Properties. *Adv. Funct. Mater.* **2011**, *21*, 4120-4125.
(34) Chen, J. S.; Wang, Z.; Dong, X. C.; Chen, P.; Lou, X. W. Graphene-Wrapped TiO_2 Hollow Structures with Enhanced Lithium Storage Capabilities. *Nanoscale* **2011**, *3*, 2158-2161.
(35) Yu, S. X.; Yang, L. W.; Tian, Y.; Yang, P.; Jiang, F.; Hu, S. W.; Wei, X. L.; Zhong, J. X. Mesoporous Anatase TiO_2 Submicrospheres Embedded in Self-Assembled Three-Dimensional Reduced Graphene Oxide Networks for Enhanced Lithium Storage. *J. Mater. Chem. A* **2013**, *1*, 12750-12758.
(36) Yang, S.; Fang, X.; Müllen, K. Sandwich-Like, Graphene-Based Titania Nanosheets with High Surface Area for Fast Lithium Storage. *Adv. Mater.* **2011**, *23*, 3575-3579.
(37) Liu, R.; Ren, Y.; Shi, Y.; Zhang, F.; Zhang, L.; Tu, B.; Zhao, D. Controlled Synthesis of Ordered Mesoporous C-TiO_2 Nanocomposites with Crystalline Titania Frameworks from Organic-Inorganic-Amphiphilic Coassembly. *Chem. Mater.* **2008**, *20*, 1140-1146.
(38) Das, S. K.; Bhattacharyya, A. J. Influence of Mesoporosity and Carbon Electronic Wiring on Electrochemical Performance of Anatase Titania. *J. Electrochem. Soc.* **2011**, *158*, A705-A710.
(39) Liu, D.; Lei, J.-H.; Guo, L.-P.; Deng, K.-J. A Nanoparticle Assembly Method for the Production of Crystalline Ordered Mesoporous Titanium Oxide/Carbon Composites. *Microporous Mesoporous Mater.* **2011**, *139*, 87-93.
(40) Wang, W.; Sa, Q.; Chen, J. S.; Wang, Y.; Jung, H.; Yin, Y. Porous TiO_2/C Nanocomposite Shells As a High-Performance Anode Material for Lithium-Ion Batteries. *ACS Appl. Mater. Interfaces* **2013**, *5*, 6478-6483.
(41) Petkovich, N. D.; Stein, A. Controlling Macro- and Mesostructures with Hierarchical Porosity Through Combined Hard and Soft Templating. *Chem. Soc. Rev.* **2013**, *42*, 3721-3739.
(42) Josephson, D. P.; Popczun, E. J.; Stein, A. Effects of Integrated Carbon as a Light Absorber on the Coloration of Photonic Crystal-Based Pigments. *J. Phys. Chem. C* **2013**, *117*, 13585-13592.
(43) Meng, Y.; Gu, D.; Zhang, F.; Shi, Y.; Yang, H.; Li, Z.; Yu, C.; Tu, B.; Zhao, D. Ordered Mesoporous Polymers and Homologous Carbon Frameworks Amphiphilic Surfactant Templating and Direct Transformation. *Angew. Chem. Int. Ed.* **2005**, *44*, 7053-7059.
(44) Boettcher, S. W.; Bartl, M. H.; Hu, J. G.; Stucky, G. D. Structural Analysis of Hybrid Titania-Based Mesostructured Composites. *J. Am. Chem. Soc.* **2005**, *127*, 9721-9730.
(45) Galusha, J. W.; Tsung, C. K.; Stucky, G. D.; Bartl, M. H. Optimizing Sol-Gel Infiltration and Processing Methods for the Fabrication of High-Quality Planar Titania Inverse Opals. *Chem. Mater.* **2008**, *20*, 4925-4930.
(46) Schubert, U. Chemical Modification of Titanium Alkoxides for Sol-Gel Processing. *J. Mater. Chem.* **2005**, *15*, 3701-3715.

(47) Fattakhova-Rohlfing, D.; Wark, M.; Brezesinski, T.; Smarsly, B. M.; Rathouský, J. Highly Organized Mesoporous TiO_2 Films with Controlled Crystallinity: A Li-Insertion Study. *Adv. Funct. Mater.* **2007**, *17*, 123-132.

(48) Procházka, J.; Kavan, L.; Shklover, V.; Zukalová, M.; Frank, O.; Kalbáč, M.; Zukal, A.; Pelouchová, H.; Janda, P.; Mocek, K.; Klementová, M.; Carbon, D. Multilayer Films from Templated TiO_2 and Structural Changes during their Thermal Treatment. *Chem. Mater.* **2008**, *20*, 2985-2993.

(49) Chen, X.; Mao, S. S. Titanium Dioxide Nanomaterials: Synthesis, Properties, Modifications, and Applications. *Chem. Rev.* **2007**, *107*, 2891-2959.

(50) Isley, S. L.; Penn, R. L. Titanium Dioxide Nanoparticles: Effect of Sol−Gel pH on Phase Composition, Particle Size, and Particle Growth Mechanism. **2008**, *112*, 4469-4474.

(51) Zhang, H.; Banfield, J. F. Thermodynamic Analysis of Phase Stability of Nanocrystalline Titania. *J. Mater. Chem.* **1998**, *8*, 2073-2076.

(52) Ranade, M. R.; Navrotsky, A.; Zhang, H. Z.; Banfield, J. F.; Elder, S. H.; Zaban, A.; Borse, P. H.; Kulkarni, S. K.; Doran, G. S.; Whitfield, H. J. Energetics of Nanocrystalline TiO_2. *Proc. Natl. Acad. Sci. U.S.A.* **2002**, *99*, 6476-6481.

(53) Huang, C.-H.; Gu, D.; Zhao, D.; Doong, R.-A. Direct Synthesis of Controllable Microstructures of Thermally Stable and Ordered Mesoporous Crystalline Titanium Oxides and Carbide/Carbon Composites. *Chem. Mater.* **2010**, *22*, 1760-1767.

(54) Cheng, P.-Y.; Huang, C.-H.; Doong, R.-A. Ordered Mesoporous Carbon–TiO_2 Materials for Improved Electrochemical Performance of Lithium Ion Battery *Carbon* **2012**, *50*, 4259-4268.

(55) Zhang, J.; Li, M.; Feng, Z.; Chen, J.; Li, C. UV Raman Spectroscopic Study on TiO_2. I. Phase Transformation at the Surface and in the Bulk. *J. Phys. Chem. B* **2006**, *110*, 927-935.

(56) Hanaor, D. A. H.; Sorrell, C. C. Review of the Anatase to Rutile Phase Transformation. *J. Mater. Sci.* **2011**, *46*, 855-874.

(57) Yu, T.; Deng, Y. H.; Wang, L.; Liu, R. L.; Zhang, L. J.; Zhao, D. Ordered Mesoporous Nanocrystalline Titanium-Carbide/Carbon Composites from In Situ Carbothermal Reduction. *Adv. Mater.* **2007**, *19*, 2301-2306.

(58) Swamy, V.; Kuznetsov, A.; Dubrovinsky, L. S.; McMillan, P. F.; Prakapenka, V. B.; Shen, G.; Muddle, B. C. Size-Dependent Pressure-Induced Amorphization in Nanoscale TiO_2. *Phys. Rev. Lett.* **2006**, *96*, 135702(1-4).

(59) Grey, I. E.; Li, C.; Madsen, I. C.; Braunshausen, G. TiO_2-II. Ambient Pressure Preparation and Structure Refinement. *Mater. Res. Bull.* **1988**, *23*, 743-753.

(60) Balachandran, U.; Eror, N. G. Raman Spectra of Titanium Dioxide. *J. Solid State Chem.* **1982**, *42*, 276-282.

(61) Zhang, W. F.; He, Y. L.; Zhang, M. S.; Yin, Z.; Chen, Q. Raman Scattering Study on Anatase TiO_2 Nanocrystals. *J. Phys. D: Appl. Phys.* **2000**, *33*, 912-916.

(62) Ferrari, A. C.; Robertson, J. Interpretation of Raman Spectra of Disordered and Amorphous Carbon. *Phys. Rev. B* **2000**, *61*, 14095-14107.

(63) Bücker, W. Preparation and DC Conductivity of an Amorphous Organic Semiconducting System. *J. Non-Cryst. Solids* **1973**, *12*, 115-128.

(64) Fierke, M. A. The Utilization of Templated Porous Electrodes in Electrochemical Applications. Ph. D Thesis, University of Minnesota- Twin Cities, 2013.

(65) Ko, T.-H.; Kuo, W.-S.; Chang, Y.-H. Raman Study of the Microstructure Changes of Phenolic Resin During Pyrolysis. *Polym. Composites* **2000**, *21*, 745-750.

(66) Meng, Y.; Gu, D.; Zhang, F.; Shi, Y.; Cheng, L.; Feng, D.; Wu, Z.; Chen, Z.; Wan, Y.; Stein, A.; Zhao, D. A Family of Highly Ordered Mesoporous Polymer Resin Carbon Structures Organic-Organic Self-Assembly. *Chem. Mater.* **2006**, *18*, 4447-4464.

(67) Errington, R. J.; Ridland, J.; Clegg, W.; Coxall, R. A.; Sherwood, J. M. β-Diketoneate Derivatives of Titanium Alkoxides: X-Ray Crystal Structures and Solution Dynamics of the Binuclear Complexes [{Ti(OR)$_3$(dik)}$_2$]. *Polyhedron* **1998**, *17*, 659-674.

(68) Vu, A.; Stein, A. Multiconstituent Synthesis of LiFePO$_4$/C Composites wth Hierarchical Porosity as Cathode Materials for Lithium Ion Batteries. *Chem. Mater.* **2011**, *23*, 3237-3245.

(69) Zeng, L.; Zheng, C.; Xia, L.; Wang, Y.; Wei, M. Ordered Mesoporous TiO$_2$-C Nanocomposites as an Anode Material for Long-Term Performance Lithium-Ion Batteries. *J. Mater. Chem. A* **2013**, *1*, 4293-4299.

(70) Jiang, H.; Yang, X.; Chen, C.; Zhu, Y.; Li, C. Facile and Controllable Fabrication of Three-Dimensionally Quasi-Ordered Macroporous TiO$_2$ for High Performace Lithium-Ion Battery Applications. *New J. Chem.* **2013**, *37*, 1578-1583.

(71) Xin, X.; Zhou, X.; Wu, J.; Yao, X.; Liu, Z. Scalable Synthesis of TiO$_2$/Graphene Nanostructured Composite with High-Rate Performance for Lithium Ion Batteries. *ACS Nano* **2012**, *6*, 11035-11043.

(72) Zhao, B.; Jiang, S.; Su, C.; Cai, R.; Ran, R.; Tadé, M. O.; Shao, Z. A 3D Porous Arcitecture Composed of TiO$_2$ Nanotubes Connected with a Carbon Nanofiber Matrix for Fast Energy Storage. *J. Mater. Chem. A* **2013**, *1*, 12310-12320.

(73) Kubiak, P.; Geserick, J.; Hüsing, N.; Wohlfahrt-Mehrens, M. Electrochemical Performance of Mesoporous TiO$_2$ Anatase. *J. Power Sources* **2008**, *175*, 510-516.

(74) Wang, D.; Choi, D.; Yang, Z.; Viswanathan, V. V.; Nie, Z.; Wang, C.; Song, Y.; Zhang, J.-G.; Liu, J. Synthesis and Li-Ion Insertion Properties of Highly Crystalline Mesoporous Rutile TiO$_2$. *Chem. Mater.* **2008**, *20*, 3435-3442.

(75) Liu, H.; Bi, Z.; Sun, X.-G.; Unocic, R. R.; Paranthaman, M. P.; Dai, S.; Brown, G. M. Mesoporous TiO$_2$-B Microspheres with Superior Rate Performance for Lithium Ion Batteries. *Adv. Mater.* **2011**, *23*, 3450-3454.

(76) Myung, S.-T.; Takahashi, N.; Komaba, S.; Yoon, C. S.; Sun, Y.-K.; Amine, K.; Yashiro, H. Nanostructured TiO$_2$ and Its Application in Lithium-Ion Storage. *Adv. Funct. Mater.* **2011**, *21*, 3231-3241.

(77) Wang, J.; Zhou, Y.; Hu, Y.; O'Hayre, R.; Shao, Z. Facile Synthesis of Nanocrystalline TiO$_2$ Mesoporous Microspheres for Lithium-Ion Batteries. *J. Phys. Chem C* **2011**, *115*, 2529-2536.

(78) Yoon, S.; Manthiram, A. Hollow Core-Shell Mesoporous TiO$_2$ Spheres for Lithium Ion Storage. *J. Phys. Chem. C* **2011**, *115*, 9410-9416.

(79) Zhou, Y.-K.; Cao, L.; Zhang, F.-B.; He, B.-L.; Li, H.-L. Lithium Insertion into TiO$_2$ Nanotube Prepared by the Hydrothermal Process. *J. Electrochem. Soc.* **2003**, *150*, A1246-A1249.

(80) Ho, C.; Raistrick, I. D.; Huggins, R. A. Application of A-C Techniques to the Study of Lithium Diffusion in Tungsten Trioxide Thin Films. *J. Electrochem. Soc.* **1980**, *127*, 343-350.

Chapter 4

(1) Janisch, R.; Gopal, P.; Spaldin, N. A. Transition Metal-Doped TiO_2 and ZnO: Present Status of the Field. *J. Phys. Condens. Matter* **2005**, *17*, R657-R689.

(2) Chen, X.; Mao, S. S. Titanium Dioxide Nanomaterials: Synthesis, Properties, Modifications and Applications. *Chem. Rev.* **2007**, *107*, 2891-2959.

(3) Hirano, M.; Nakahara, C.; Ota, K.; Inagaki, M. Direct Formation of Zirconia-Doped Titania with Stable Anatase-Type Structure by Thermal Hydrolysis. *J. Am. Ceram. Soc.* **2002**, *85*, 1333-1335.

(4) Arbiol, J.; Cerdà, J.; Dezanneau, G.; Cirera, A.; Peiró, F.; Cornet, A.; Morante, J. R. Effects of Nb Doping on the TiO_2 Anatase-to-Rutile Phase Transition. *J. Appl. Phys.* **2002**, *92*, 853-861.

(5) Furubayashi, Y.; Hitosugi, T.; Yamamoto, Y.; Inaba, K.; Kinoda, G.; Hirose, Y.; Shimada, T.; Hasegawa, T. A Transparent Metal: Nb-doped Anatase TiO_2. *Appl. Phys. Lett.* **2005**, *86*, 252101(1-3).

(6) Osorio-Guillén, J.; Lany, S.; Zunger, A. Atomic Control of Conductivity Versus Ferromagnetism in Wide-Gap Oxides Via Selective Doping: V, Nb, Ta in Anatase TiO_2. *Phys. Rev. Lett.* **2008**, *100*, 036601(1-4).

(7) Fergus, J. W. Doping and Defect Association in Oxides for Use in Oxygen Sensors. *J. Mater. Sci.* **2003**, *38*, 4259-4270.

(8) Asahi, R.; Morikawa, T.; Ohwaki, T.; Aoki, K.; Taga, Y. Visible-Light Photocatalysis in Nitrogen-Doped Titanium Oxides. *Science* **2001**, *293*, 269-271.

(9) Nowotny, M. K.; Sheppard, L. R.; Bak, T.; Nowotny, J. Defect Chemistry of Titanium Dioxide. Application of Defect Engineering in Processsing of TiO_2-Based Photocatalysts. *J. Phys. Chem. C* **2008**, *112*, 5275-5300.

(10) Biedrzycki, J.; Livraghi, S.; Giamello, E.; Agnoli, S.; Granozzi, G. Fluorine- and Niobium-Doped TiO_2: Chemical and Spectroscopic Properties of Polycrystalline n-Type-Doped Anatase. *J. Phys. Chem. C* **2014**, *116*, 8462-8473.

(11) Chen, X.; Burda, C. The Electronic Origin of the Visible-Light Adsorption Properties of C-, N- and S-Doped TiO_2 Nanomaterials. *J. Am. Chem. Soc.* **2008**, *130*, 5018-5019.

(12) Mukri, B. D.; Waghmare, U. V.; Hedge, M. S. Platinum Ion-Doped TiO_2: High Catalytic Activity of Pt^{2+} with Oxide Ion Vacancy in $Ti^{4+1-x}Pt^{2+x}O_{2-x}$ Compared to Pt^{4+} without Oxide Ion Vacancy in $Ti^{4+1-x}Pt^{4+}O_2$. *Chem. Mater.* **2013**, *25*, 3822-3833.

(13) Kumar, S. G.; Devi, L. G. Review on Modified TiO_2 Photocatalysts under UV/Visible Light: Selected Results and Related Mechanisms on Interfacial Charge Carrier Transfer Dynamics. *J. Phys. Chem. A* **2011**, *115*, 13211-13241.

(14) Bingham, S.; Daoud, W. A. Recent Advances in Making Nano-Sized TiO_2 Visible-Light Active through Rare-Earth Metal Doping. *J. Mater. Chem.* **2011**, *21*, 2041-2050.

(15) McFarland, E. W.; Metiu, H. Catalysis by Doped Oxides. *Chem. Rev.* **2013**, *112*, 4391-4427.

(16) Suryanarayana, C. Nanocrystalline Materials. *Int. Mater. Rev.* **1995**, *40*, 41-64.

(17) Gleiter, H. Nanostructured Materials: Basic Concepts and Microstructure. *Acta. Mater.* **2000**, *48*, 1-29.

(18) Powers, J. D.; Glaeser, A. M. Grain Boundary Migration in Ceramics. *Interface Sci.* **1998**, *6*, 23-39.

(19) Liu, F.; Gong, M. Nano-Scaled Grain Growth. In *Sintering*; Castro, R. H. R., van Benthem, K., Eds.; Springer-Verlag: Berlin, 2013.

(20) Mayo, M. J. Processing of Nanocrystalline Ceramics from Ultrafine Particles. *Int. Mater. Rev.* **1994**, *41*, 85-115.

(21) Koch, C. C.; Scattergood, R. O.; Saber, M.; Kotan, H. High Temperature Stabilization of Nanocrystalline Grain Size: Thermodynamic Versus Kinetic Strategies. *J. Mater. Res.* **2013**, *28*, 1785-1791.
(22) Terwilliger, C. D.; Chiang, Y.-M. The Effect of Calcium Segregation on Grain Growth in Nanocrystalline TiO_2. *Nanostructured Mater.* **1994**, *4*, 651-661.
(23) Yan, M. F.; Rhodes, W. W. Effects of Solutes on the Grain Boundary Mobility of TiO_2. In *Ceramic Microstructures '86: Role of Interfaces*; Pask, J. A., Evans, A. G., Eds.; Plenum Press: New York, 1987; pp 519-532.
(24) Nair, J.; Nair, P.; Mizukami, F.; Oosawa, Y.; Okubo, T. Microstructure and Phase Transformation Behavior of Doped Nanostructured Titania. *Mater. Res. Bull.* **1999**, *34*, 1275-1290.
(25) Zhang, Y.-H.; Reller, A. Nanocrystalline Iron-Doped Mesoporous Titania and Its Phase Transition. *J. Mater. Chem.* **2001**, *11*, 2537-2541.
(26) Wang, Q.; Lian, G.; Dickey, E. C. Grain Boundary Segregation in Yttrium-Doped Polycrystalline TiO_2. *Acta. Mater.* **2004**, *52*, 809-820.
(27) German, R. M. *Sintering Theory and Practice*; John Wiley & Sons, Inc.: New York, 1996.
(28) Tilley, R. J. D. *Defects in Solids*; John Wiley & Sons, Inc.: Hoboken, NJ, 2008.
(29) Chraska, T.; King, A. H.; Berndt, C. C. On the Size-Dependent Phase Transformation in Nanoparticulate Zirconia. *Mater. Sci. Eng., A* **2000**, *286*, 169-178.
(30) Hanaor, D. A. H.; Sorrell, C. C. Review of the Anatase to Rutile Phase Transformation. *J. Mater. Sci.* **2011**, *46*, 855-874.
(31) Shannon, R. D. Phase Transformation Studies in TiO_2 Supporting Different Defect Mechanisms in Vacuum-Reduced and Hydrogen-Reduced Rutile. *J. Appl. Phys.* **1964**, *35*, 3414-3416.
(32) Reidy, D. J.; Holmes, J. D.; Morris, M. A. The Critical Size Mechanism for the Anatase to Rutile Transformation in TiO_2 and Doped-TiO_2. *J. Eur. Ceram. Soc.* **2006**, *26*, 1527-1534.
(33) Fröschl, T.; Hörmann, U.; Kubiak, P.; Kučerová, G.; Pfanzelt, M.; Weiss, C. K.; Behm, R. J.; Hüsing, N.; Kaiser, U.; Landfester, K.; Wohlfahrt-Mehrens, M. High Surface Area Crystalline Titanium Dioxide: Potential and Limits in Electrochemical Energy Storage and Catalysis. *Chem. Soc. Rev.* **2012**, *41*, 5313-5360.
(34) Zhang, Y.; Du, F.; Yan, X.; Jin, Y.; Zhu, K.; Wang, X.; Li, H.; Chen, G.; Wang, C.; Wei, Y. Improvements in the Electrochemical Kinetic Properties and Rate Capability of Anatase Titanium Dioxide Nanoparticles by Nitrogen Doping. *ACS Appl. Mater. Interfaces* **2014**, *6*, 4458-4465.
(35) Jiao, W.; Li, N.; Wang, L.; Wen, L.; Li, F.; Liu, G.; Cheng, H.-M. High-Rate Lithium Storage of Anatase TiO_2 Crystals Doped with Both Nitrogen and Sulfur. *Chem. Commun.* **2013**, *49*, 3461-3463.
(36) Jung, H.-G.; Yoon, C. S.; Prakash, J.; Sun, Y.-K. Mesoporous Anatase TiO_2 with High Surface Area and Controllable Pore Size by F^--Ion Doping: Applications for High-Power Li-Ion Battery Anode. *J. Phys. Chem. C* **2009**, *113*, 21258-21263.
(37) Ming, H.; Li, X.; Su, L.; Liu, M.; Jin, L.; Bu, L.; Kang, Z.; Zheng, J. One Step Synthesis of C&N Co-Doped Mesoporous TiO_2 with Enhanced Performance in a Lithium-Ion Battery. *RSC Advances* **2013**, *3*, 3836-3839.
(38) Wang, Y.; Chen, T.; Mu, Q. Electrochemical Performance of W-Doped Anatase TiO_2 Nanoparticles as an Electrode Material for Lithium-Ion Batteries. *J. Mater. Chem.* **2011**, *21*, 6006-6013.
(39) Wang, Y.; Smarsly, B. M.; Djerdj, I. Niobium Doped TiO_2 with Mesoporosity and Its Application for Lithium Insertion. *Chem. Mater.* **2010**, *22*, 6624-6631.

(40) Anh, L. T.; Rai, A. K.; Thi, T. V.; Gim, J.; Kim, S.; Shin, E.-C.; Lee, J.-S.; Kim, J. Improving the Electrochemical Performance of Anatase Titanium Dioxide by Vanadium Doping as an Anode Material for Lithium-Ion Batteries. *J. Power Sources* **2013**, *243*, 891-898.

(41) Ali, Z.; Cha, S. N.; Sohn, J. I.; Shakir, I.; Yan, C.; Kim, J. M.; Kang, D. J. Design and Evaluation of Novel Zn Doed Mesoporous TiO_2 Based Anode Material for Advanced Lithium Ion Batteries. *J. Mater. Chem.* **2012**, *22*, 17625-17629.

(42) Thi, T. V.; Rai, A. K.; Gim, J.; Kim, S.; Kim, J. Effect of Mo^{6+} Doping on Electrochemical Performance of Anatase TiO_2 as a High Performance Anode Material for Secondary Lithium-Ion Batteries. *J. Alloys Compd.* **2014**, *598*, 16-22.

(43) Hutchings, G. S.; Li, Q.; Jiao, F. Synthesis and Electrochemistry of Nanocrystalline M-TiO_2 (M = Mn, Fe, Co, Ni, Cu) Anatase. *J. Electrochem. Soc.* **2013**, *160*, A511-A515.

(44) Das, S. K.; Gnanavel, M.; Patel, M. U. M.; Shivakumara, C.; Bhattacharyya, A. J. Anamolously High Lithium Storage in Mesoporous Nanoparticulate Aggregation of Fe^{3+} Doped Anatase Titania. *J. Electrochem. Soc.* **2011**, *158*, A1290-A1297.

(45) Meng, Y.; Gu, D.; Zhang, F.; Shi, Y.; Yang, H.; Li, Z.; Yu, C.; Tu, B.; Zhao, D. Ordered Mesoporous Polymers and Homologous Carbon Frameworks Amphiphilic Surfactant Templating and Direct Transformation. *Angew. Chem. Int. Ed.* **2005**, *44*, 7053-7059.

(46) Josephson, D. P.; Popczun, E. J.; Stein, A. Effects of Integrated Carbon as a Light Absorber on the Coloration of Photonic Crystal-Based Pigments. *J. Phys. Chem. C* **2013**, *117*, 13585-13592.

(47) Spurr, R. A.; Myers, H. Quantitative Analysis of Anatase-Rutile Mixtures with an X-Ray Diffractometer. *Anal. Chem.* **1957**, *29*, 760-762.

(48) Zheng, T.; Zhong, Q.; Dahn, J. R. High-Capacity Carbons Prepared from Phenolic Resin for Anodes of Lithium-Ion Batteries. *J. Electrochem. Soc.* **1995**, *142*, L211-L214.

(49) Huang, C.-H.; Gu, D.; Zhao, D.; Doong, R.-A. Direct Synthesis of Controllable Microstructures of Thermally Stable and Ordered Mesoporous Crystalline Titanium Oxides Carbide/Carbon Composites. *Chem. Mater.* **2010**, *22*, 1760-1767.

(50) Trick, K. A.; Saliba, T. E. Mechanisms of the Pyrolysis of Phenolic Resin in a Carbon/Phenolic Composite. *Carbon* **1995**, *33*, 1509-1515.

(51) Fehse, M.; Cavaliere, S.; Lippens, P. E.; Savych, I.; Iadecola, A.; Monoconduit, L.; Jones, D. J.; Rozière, J.; Fischer, F.; Tessier, C.; Stievano, L. Nb-Doped TiO_2 Nanofibers for Lithium Ion Batteries. *J. Phys. Chem. C* **2013**, *117*, 13827-13835.

(52) Marsh, H.; Crawford, D.; Taylor, D. W. Catalytic Graphitization by Iron of Isotropic Carbon from Polyfurfuryl Alchol, 725-1090 K. A High Resolution Electron Microscopy Study. *Carbon* **1983**, *21*, 81-87.

(53) Sevilla, M.; Fuertes, A. B. Catalytic Graphitization of Templated Mesoporous Carbons. *Carbon* **2006**, *44*, 468-474.

(54) Ōya, A.; Ōtani, S. Catalytic Graphitization of Carbons by Various Metals. *Carbon* **1979**, *17*, 131-137.

(55) Yokokawa, C.; Hosokawa, K.; Takegami, Y. Low Temperature Catalytic Graphitization of Hard Carbon. *Carbon* **1966**, *4*, 459-465.

(56) Bally, A. R.; Korobeinikova, E. N.; Schmid, P. E.; Lévy, F.; Bussy, F. Structural and Electrical Properties of Fe-Doped TiO_2 Thin Films. *J. Phys. D: Appl. Phys.* **1998**, *31*, 1149-1154.

(57) Leventis, N.; Chandrasekaran, N.; Sadekar, A. G.; Sotiriou-Leventis, C.; Lu, H. One-Pot Synthesis of Interpenetrating Inorganic/Organic Networks of CuO/Resorcinol-Formaldehyde Aerogels: Nanostructured Energetic Materials. *J. Am. Chem. Soc.* **2009**, *131*, 4576-4577.

(58) Balachandran, U.; Eror, N. G. Raman Spectra of Titanium Dioxide. *J. Solid State Chem.* **1982**, *42*, 276-282.
(59) Ferrari, A. C.; Robertson, J. Interpretation of Raman Spectra of Disordered and Amorphous Carbon. *Phys. Rev. B* **2000**, *61*, 14095-14107.
(60) Hitosugi, T.; Furubayashi, Y.; Ueda, A.; Itabashi, K.; Inaba, K.; Hirose, Y.; Kinoda, G.; Yamamoto, Y.; Shimada, T.; Hasegawa, T. Ta-Doped Anatase TiO_2 Epitaxial Film as Transparent Conducting Oxide. *Jpn. J. Appl. Phys.* **2005**, *44*, L1063-L1065.
(61) Dy, E.; Hui, R.; Zhang, J.; Liu, Z.-S.; Shi, Z. Electronic Conductivity and Stability of Doped Titania ($Ti_{1-X}M_XO_2$, M = Nb, Ru, and Ta)-A Density Functional Theory-Based Comparison. *J. Phys. Chem. C* **2010**, *114*, 13162-13167.
(62) Balachandran, U.; Eror, N. G. Self-Compensation in Tantalum-Doped TiO_2. *J. Mater. Sci.* **1982**, *17*, 1207-1212.
(63) Ruiz, A. M.; Dezanneau, G.; Arbiol, J.; Cornet, A.; Morante, J. R. Insights into the Structural and Chemical Modifications of Nb Additive on TiO_2 Nanoparticles. *Chem. Mater.* **2004**, *16*, 862-871.
(64) Sheppard, L. R.; Bak, T.; Nowotny, J. Electrical Properties of Niobium-Doped Titanium Dioxide. 1. Defect Disorder. *J. Phys. Chem. B* **2006**, *110*, 22447-22454.
(65) Shannon, R. D. Revised Effective Ionic Radii and Systematic Studies of Interatomic Distances in Halides and Chalcogenides. *Acta. Cryst.* **1976**, *32*, 751-767.
(66) Stoklosa, A. Point Defect Diagrams for Pure and Doped Titanium (IV) Oxide $TiO_{2-\delta}$ in Temperature Range of 1073-1573 K. *Adv. Appl. Ceram.* **2012**, *111*, 44-61.
(67) Nakajima, T.; Sheppard, L. R.; Prince, K. E.; Nowotny, J.; Ogawa, T. Niobium Segregation in TiO_2. *Adv. Appl. Ceram.* **2007**, 82-88.
(68) Lei, Z.; Xiao, Y.; Dang, L.; You, W.; Hu, G.; Zhang, J. Nickel-Catalyzed Fabrication of SiO_2, TiO_2/Graphitized Carbon, andd the Resultant Graphitized Carbon with Periodically Macroporous Structure. *Chem. Mater.* **2007**, *19*, 477-484.
(69) Huang, C.-H.; Doong, R.-A.; Gu, D.; Zhao, D. Dual-Template Synthesis of Magnetically-Separable Hierarchically-Ordered Porous Carbons by Catalytic Graphitization. *Carbon* **2011**, *49*, 3055-3064.
(70) Maier, J. Thermodynamics of Electrochemical Lithium Storage. *Angew. Chem. Int. Ed.* **2013**, *52*, 4998-5026.
(71) Milne, N. A.; Skyllas-Kazacos, M.; Luca, V. Crystallite Size Dependence of Lithium Intercalation into Nanocrystalline Rutile. *J. Phys. Chem. C* **2009**, *113*, 12983-12995.
(72) Shin, J.-Y. Effects of Ionic and Electronic Charge Carriers in Nanostructured TiO_2 on Lithium Storage. Ph.D Thesis, Max Planck Institute for Solid State Research, 2012.
(73) Shin, J.-Y.; Joo, J. H.; Samuelus, D.; Maier, J. Oxygen Nonstoichiometric $TiO_{2-\delta}$ Nanoparticles *via* Hydrogen Reduction for High Rate Capability Lithium Batteries. *Chem. Mater.* **2012**, *24*, 543-551.
(74) Zhang, S. X.; Kundaliya, D. C.; Yu, W.; Dhar, S.; Young, S. Y.; Salamanca-Riba, L. G.; Ogale, S. B.; Vispute, R. D.; Venkatesan, T. Niobium Doped TiO_2: Intrinsic Transparent Metallic Anatase Versus Highly Resistive Rutile Phase. *J. Appl. Phys.* **2007**, *102*, 013710(1-4).
(75) Jamink, J.; Gaberscek, M. Li Ion Migration at the Interfaces. *MRS Bull.* **2009**, *34*, 942-948.

Chapter 5

(1) Wang, H.; Yao, J. Use of Poly(furfuryl alcohol) in the Fabrication of Nanostructured Carbons and Nanocomposites. *Ind. Eng. Chem. Res.* **2006**, *45*, 6393-6404.

(2) Stein, A.; Wang, W.; Fierke, M. A. Functionalization of Porous Carbon Materials with Designed Pore Architecture. *Adv. Mater.* **2009**, *21*, 265-293.

(3) Yang, K.; Li, Y.; Tan, X.; Peng, R.; Liu, Z. Behavior and Toxicity of Graphene and Its Functionalized Derivatives in Biological Systems. *Small* **2013**, *9*, 1492-1503.

(4) Liu, Y.; Zhao, Y.; Sun, B.; Chen, C. Understanding the Toxicity of Carbon Nanotubes. *Acc. Chem. Res.* **2013**, *46*, 702-713.

(5) Schubert, U. Chemical Modification of Titanium Alkoxides for Sol-Gel Processing. *J. Mater. Chem.* **2005**, *15*, 3701-3715.

(6) Boettcher, S. W.; Bartl, M. H.; Hu, J. G.; Stucky, G. D. Structural Analysis of Hybrid Titania-Based Mesostructured Composites. *J. Am. Chem. Soc.* **2005**, *127*, 9721-9730.

(7) Petkovich, N. D.; Rudisill, S. G.; Wilson, B. E.; Mukherjee, A.; Stein, A. Control of TiO_2 Grain Size and Positioning in Three-Dimensionally Ordered Macroporous TiO_2/C Composite Anodes for Lithium Ion Batteries. *Inorg. Chem.* **2014**, *53*, 1100-1112.

(8) Choi, M. G.; Lee, Y.-G.; Song, S.-W.; Kim, K. M. Anode Properties of Titanium Oxide Nanotube and Graphite Composites for Lithium-Ion Batteries. *J. Power Sources* **2010**, *195*, 8289-8296.

(9) Zhou, Y.; Kim, Y.; Jo, C.; Lee, J.; Lee, C. W.; Yoon, S. A Novel Mesoporous Carbon-Silica-Titania Nanocomposite as a High Perfomance Anode Material in Lithium Ion Batteries. *Chem. Commun.* **2011**, *47*, 4944-4946.

(10) Bresser, D.; Paillard, E.; Binetti, E.; Krueger, S.; Striccoli, M.; Winter, M.; Passerini, S. Percolating Networks of TiO_2 Nanorods and Carbon for High Power Lithium Insertion Electrodes. *J. Power Sources* **2012**, *206*, 301-309.

(11) Cai, D.; Lian, P.; Zhu, X.; Liang, S.; Yang, W.; Wang, H. High Specific Capacity of TiO_2-Graphene Nanocomposite as an Anode Material for Lithium-Ion Batteries in an Enlarged Potential Window. *Electrochim. Acta* **2012**, *74*, 65-72.

(12) Cheng, P.-Y.; Huang, C.-H.; Doong, R.-A. Ordered Mesoporous Carbon–TiO_2 Materials for Improved Electrochemical Performance of Lithium Ion Battery *Carbon* **2012**, *50*, 4259-4268.

(13) Ma, J.; Xiang, D.; Li, Z.; Li, Q.; Wang, X.; Yin, L. TiO_2 Nanocrystal Embedded Ordered Mesoporous Carbons as Anode Materials for Lithium-Ion Batteries with Highly Reversible Capacity and Rate Performance. *CrystEngComm* **2013**, *15*, 6800-6807.

(14) Zhang, C.; Zhang, Q.; Kang, S.; Li, X. A Novel Route for the Facile Synthesis of Hierarchically Porous TiO_2/Graphitic Carbon Microspheres for Lithium Ion Batteries. *J. Mater. Chem. A* **2014**, *2*, 2801-2806.

(15) Kaskhedikar, N. A.; Maier, J. Lithium Storage in Carbon Nanostructures. *Adv. Mater.* **2009**, *21*, 2664-2680.

(16) Kakihana, M.; Tada, M.; Shiro, M.; Petrykin, V.; Osada, M.; Nakamura, Y. Structure and Stability of Water Soluble $(NH_4)_8[Ti_4(C_6H_4O_7)_4(O_2)_4]\cdot 8H_2O$. *Inorg. Chem.* **2001**, *40*, 891-894.

(17) Josephson, D. P.; Popczun, E. J.; Stein, A. Effects of Integrated Carbon as a Light Absorber on the Coloration of Photonic Crystal-Based Pigments. *J. Phys. Chem. C* **2013**, *117*, 13585-13592.

(18) Meng, Y.; Gu, D.; Zhang, F.; Shi, Y.; Yang, H.; Li, Z.; Yu, C.; Tu, B.; Zhao, D. Ordered Mesoporous Polymers and Homologous Carbon Frameworks Amphiphilic Surfactant Templating and Direct Transformation. *Angew. Chem. Int. Ed.* **2005**, *44*, 7053-7059.

(19) Wang, Z.; Kiesel, E. R.; Stein, A. Silica-Free Syntheses of Hierarchically Ordered Macroporous Polymer and Carbon Monoliths with Controllable Mesoporosity. *J. Mater. Chem.* **2008**, *18*, 2194-2200.
(20) Dakanali, M.; Kefalas, E. T.; Raptopoulou, C. P.; Terzis, A.; Voyiatzis, G.; Kyrikou, I.; Mavromoustakos, T.; Salifoglou, A. A New Dinuclear Ti(IV)-Peroxo-Citrate Complex from Aqueous Solutions. Synthetic, Structural, and Spectroscopic Studies in Relevance to Aqueous Titanium(IV)-Peroxo-Citrate Speciation. *Inorg. Chem.* **2003**, *42*, 4632-4639.
(21) Hardy, A.; D'Haen, J.; Van Bael, M. K.; Mullens, J. An Aqueous Solution-Gel Citraperoxo-Ti(IV) Precursor: Synthesis, Gelation, Thermo-Oxidative Decomposition and Oxide Crystallization. *J. Sol-Gel Sci. Technol.* **2007**, *44*, 65-77.
(22) Truijen, I.; Hardy, A.; Van Bael, M. K.; Van den Rul, H.; Mullens, J. Study of the Decomposition of Aqueous Citratoperoxo-Ti(IV)-gel Precursors for Titania by Means of TGA-MS and FTIR. *Thermochim. Acta* **2007**, *456*, 38-47.
(23) Chaudhuri, M. K.; Das, B. Direct Synthesis of Alkali-Metal and Ammonium Pentafluoroperoxytitanates(IV), $A_3[Ti(O_2)F_5]$, and First Synthesis and Structural Assessment of Alkali-Metal and Ammonium Difluorodiperoxytitanates(IV), $A_2[Ti(O_2)_2F_2]$. *Inorg. Chem.* **1986**, *25*, 168-170.
(24) Kakihana, M.; Arima, M.; Nakamura, Y.; Yashima, M.; Yoshimura, M. Spectroscopic Characterization of Precursors Used in the Pechini-Type Polymerizable Complex Processing of Barium Titanate. *Chem. Mater.* **1999**, *11*, 438-450.
(25) Tengvall, P.; Vikinge, T. P.; Lundström, I.; Liedberg, B. FT-Raman Spectroscopic Studies of the Degradation of Titanium Peroxy Gels Made from Metallic Titanium and Hydrogen Peroxide. *J. Colloid Interface Sci.* **1993**, *160*, 10-15.
(26) Lin-Vien, D.; Colthup, N. B.; Fateley, W. G.; Grasselli, J. G. *Handbook of Infrared and Raman Characteristic Frequencies of Organic Molecules*; Academic Press: San Diego, **1991**.
(27) Max, J.-J.; Chapados, C. Infrared Spectroscopy of Aqueous Carboxylic Acids: Comparison between Different Acids and Their Salts. *J. Phys. Chem. A* **2004**, *108*, 3324-3337.
(28) Deacon, G. B.; Phillips, R. J. Relationships Between the Carbon-Oxygen Stretching Frequencies of Carboxylato Complexes and the Type of Carboxylate Coordination. *Coord. Chem. Rev.* **1980**, *33*, 227-250.
(29) Fey, G. T.-K.; Kao, Y.-C. Synthesis and Characterization of Pyrolyzed Sugar Carbons under Nitrogen or Argon Atmospheres as Anode Materials for Lithium-Ion Batteries. *Mater. Chem. Phys.* **2002**, *73*, 37-46.
(30) Fierke, M. A.; Lai, C.-Z.; Bühlmann, P.; Stein, A. Effects of Architecture and Surface Chemistry of Three-Dimensionally Ordered Macroporous Carbon Solid Contacts on Performance of Ion-Selective Electrodes. *Anal. Chem.* **2010**, *82*, 680-688.
(31) Petkovich, N. D.; Stein, A. Colloidal Crystal Templating Approaches to Materials with Hierarchical Porosity. In *Hierarchically Structured Porous Materials: From Nanoscience to Catalysis, Separation, Optics, Energy, and Life Science*; Su, B.-L., Sanchez, C., Yang, X.-Y., Eds.; Wiley-VCH Verlag GmbH & Co. KGaA: Weinheim, Germany, **2012**.
(32) Liu, G.; Liu, Y.; Wang, Z.; Liao, X.; Wu, S.; Zhang, W. F.; Jia, M. Direct Synthesis of Porous Carbon via Carbonizing Precursors of Aluminum Phosphate Containing Citric Acid. *Microporous Mesoporous Mater.* **2008**, *116*, 439-444.
(33) Zhang, H.; Banfield, J. F. Thermodynamic Analysis of Phase Stability of Nanocrystalline Titania. *J. Mater. Chem.* **1998**, *8*, 2073-2076.
(34) Shin, Y.; Li, X. S.; Wang, C.; Coleman, J. R.; Exarhos, G. J. Synthesis of Hierarchical Titanium Carbide from Titania-Coated Cellulose Paper. *Adv. Mater.* **2004**, *16*, 1212-1215.

(35) Yu, T.; Deng, Y. H.; Wang, L.; Liu, R. L.; Zhang, L. J.; Tu, B.; Zhao, D. Y. Ordered Mesporous Nanocrystalline Titanium-Carbide/Carbon Composites from In Situ Carbothermal Reduction. *Adv. Mater.* **2007**, *19*, 2301-2306.

(36) Huang, C.-H.; Gu, D.; Zhao, D.; Doong, R.-A. Direct Synthesis of Controllable Microstructures of Thermally Stable and Ordered Mesoporous Crystalline Titanium Oxides and Carbide/Carbon Composites. *Chem. Mater.* **2010**, *22*, 1760-1767.

(37) Koc, R. Kinetics and Phase Evolution During Carbothermal Synthesis of Titanium Carbide from Ultrafine Titania/Carbon Mixture. *J. Mater. Sci.* **1998**, *33*, 1049-1055.

(38) Bae, S.-T.; Shin, H.; Jung, H. S.; Hong, K. S. Synthesis of Titanium Carbide Nanoparticles with a High Specific Surface Area from a TiO_2 Core-Sucrose Shell Precursor. *J. Am. Ceram. Soc.* **2009**, *92*, 2512-2516.

(39) Hanaor, D. A. H.; Sorrell, C. C. Review of the Anatase to Rutile Phase Transformation. *J. Mater. Sci.* **2011**, *46*, 855-874.

(40) Zhang, W. F.; He, Y. L.; Zhang, M. S.; Yin, Z.; Chen, Q. Raman Scattering Study on Anatase TiO_2 Nanocrystals. *J. Phys. D: Appl. Phys.* **2000**, *33*, 912-916.

(41) Balachandran, U.; Eror, N. G. Raman Spectra of Titanium Dioxide. *J. Solid State Chem.* **1982**, *42*, 276-282.

(42) Klein, M. V.; Holy, J. A.; Williams, W. S. Raman Scattering Induced by Carbon Vacancies in TiC_x. *Phys. Rev. B* **1978**, *17*, 1546-1556.

(43) Lohse, B. H.; Calka, A.; Wexler, D. Raman Spectroscopy as a Tool to Study TiC Formation During Controlled Ball Milling. *J. Appl. Phys.* **2005**, *97*, 114912(1-17).

(44) Ferrari, A. C.; Robertson, J. Interpretation of Raman Spectra of Disordered and Amorphous Carbon. *Phys. Rev. B* **2000**, *61*, 14095-14107.

(45) Zhang, J.; Li, M.; Feng, Z.; Chen, J.; Li, C. UV Raman Spectroscopy Study on TiO_2. I. Phase Transformation at the Surface and in the Bulk. *J. Phys. Chem. B* **2006**, *110*, 927-935.

(46) Yin, H.; Wada, Y.; Kitamura, T.; Kambe, S.; Murasawa, S.; Mori, H.; Sakata, T.; Yanagida, S. Hydrothermal Synthesis of Nanosized Anatase and Rutile TiO_2 Using Amorphous Phase TiO_2. *J. Mater. Chem.* **2001**, *11*, 1694-1703.

(47) Shannon, R. D. Phase Transformation Studies in TiO_2 Supporting Different Defect Mechanisms in Vacuum-Reduced and Hydrogen-Reduced Rutile. *J. Appl. Phys.* **1964**, *35*, 3414-3416.

(48) Wang, Z.; Li, F.; Stein, A. Direct Synthesis of Shaped Carbon Nanoparticles with Ordered Cubic Mesostructure. *Nano Lett.* **2007**, *7*, 3223-3226.

(49) Wang, Z.; Stein, A. Morphology Control of Carbon, Silica, and Carbon/Silica Nanocomposites: From 3D Ordered Macro-/Mesoporous Monoliths to Shaped Mesoporous Particles. *Chem. Mater.* **2008**, *20*, 1029-1040.

(50) Bücker, W. Preparation and DC Conductivity of an Amorphous Organic Semiconducting System. *J. Non-Cryst. Solids* **1973**, *12*, 115-128.

(51) Li, H.; Zhou, H. Enhancing the Performances of Li-Ion Batteries by Carbon-Coating: Present and Future. *Chem. Commun.* **2012**, *48*, 1201-1217.

(52) Yu, J.; Sushko, M. L.; Kerisit, S.; Rosso, K. M.; Liu, J. Kinetic Monte Carlo Study of Ambipolar Lithium Ion and Electron Polaron Diffusion into Nanostructured TiO_2. *J. Phys. Chem. Lett.* **2012**, *2*, 2076-2081.

(53) Dominko, R.; Bele, M.; Gaberscek, M.; Remskar, M.; Hanzel, D.; Pejovnik, S.; Jamnik, J. Impact of the Carbon Coating Thickness on the Electrochemical Performance of $LiFePO_4$/C Composites. *J. Electrochem. Soc.* **2005**, *152*, A607-A610.

(54) Wang, W.; Sa, Q.; Chen, J. S.; Wang, Y.; Jung, H.; Yin, Y. Porous TiO_2/C Nanocomposite Shells As a High-Performance Anode Material for Lithium-Ion Batteries. *ACS Appl. Mater. Interfaces* **2013**, *5*, 6478-6483.

(55) Chen, Z.; Belharouak, I.; Sun, Y.-K.; Amine, K. Titanium-Based Anode Materials for Safe Lithium-Ion Batteries. *Adv. Funct. Mater.* **2013**, *23*, 959-969.
(56) Wagemaker, M.; Borghols, W. J. H.; Mulder, F. M. Large Impact of Particle Size on Insertion Reactions. A Case for Anatase Li_xTiO_2. *J. Am. Chem. Soc.* **2007**, *129*, 4323-4327.
(57) Milne, N. A.; Skyllas-Kazacos, M.; Luca, V. Crystallite Size Dependence of Lithium Intercalation into Nanocrystalline Rutile. *J. Phys. Chem. C* **2009**, *113*, 12983-12995.
(58) Borghols, W. J. H.; Wagemaker, M.; Lafont, U.; Kelder, E. M.; Mulder, F. M. Impact of Nanosizing on Lithiated Rutile TiO_2. *Chem. Mater.* **2008**, *20*, 2949-2955.
(59) Kubiak, P.; Pfanzelt, M.; Geserick, J.; Hörmann, U.; Hüsing, N.; Kaiser, U.; Wohlfahrt-Mehrens, M. Electrochemical Evaluation of Rutile TiO_2 Nanoparticles as Negative Electrode for Li-Ion Batteries. *J. Power Sources* **2009**, *194*, 1099-1104.
(60) Pfanzelt, M.; Kubiak, P.; Wohlfahrt-Mehrens, M. Nanosized TiO_2 Rutile with High Capacity and Excellent Rate Capability. *Electrochem. Solid State Lett.* **2010**, *13*, A91-A94.
(61) Verma, P.; Maire, P.; Novák, P. A Review of the Features and Analyses of the Solid Electrolyte Interphase in Li-Ion Batteries. *Electrochim. Acta* **2010**, *55*, 6332-6341.
(62) Kang, D.-Y.; Kim, S.-O.; Chae, Y. J.; Lee, J. K.; Moon, J. H. Particulate Inverse Opal Carbon Electrodes for Lithium-Ion Batteries. *Langmuir* **2013**, *29*, 1192-1198.
(63) Wang, S.-X.; Yang, L.; Stubbs, L. P.; Li, X.; He, C. Lignin-Derived Fused Electrospun Carbon Fibrous Mats as High Performance Anode Materials for Lithium Ion Batteries. *ACS Appl. Mater. Interfaces* **2013**, *5*, 12275-12282.
(64) Guo, B.; Wang, X.; Fulvio, P. F.; Chi, M.; Mahurin, S. M.; Sun, X.-G.; Dai, S. Soft-Templated Mesoporous Carbon-Carbon Nanotube Composites for High Performance Lithium-Ion Batteries. *Adv. Mater.* **2011**, *23*, 4661-4666.
(65) Fan, Z.-J.; Yan, J.; Wei, T.; Ning, G.-Q.; Zhi, L.-J.; Liu, J.-C.; Cao, D.-X.; Wang, G.-L.; Wei, F. Nanographene-Constructed Carbon Nanofibers Grown on Graphene Sheets by Chemical Vapor Deposition: High-Performance Anode Materials for Lithium Ion Batteries. *ACS Nano* **2011**, *5*, 2787-2794.
(66) Fröschl, T.; Hörmann, U.; Kubiak, P.; Kučerová, G.; Pfanzelt, M.; Weiss, C. K.; Behm, R. J.; Hüsing, N.; Kaiser, U.; Landfester, K.; Wohlfahrt-Mehrens, M. High Surface Area Crystalline Titanium Dioxide: Potential and Limits in Electrochemical Energy Storage and Catalysis. *Chem. Soc. Rev.* **2012**, *41*, 5313-5360.
(67) Hong, Z.; Wei, M.; Lan, T.; Jiang, L.; Cao, G. Additive-Free Synthesis of Unique TiO_2 Mesocrystals with Enhanced Lithium-Ion Intercalation Properties. *Energy Environ. Sci.* **2012**, *5*, 5408-5413.
(68) Jamink, J.; Gaberscek, M. Li Ion Migration at the Interfaces. *MRS Bull.* **2009**, *34*, 942-948.

Chapter 6

(1) Antonelli, D. M.; Ying, J. Y. Synthesis of Hexagonally Packed Mesoporous TiO_2 by a Modified Sol-Gel Method. *Angew. Chem. Int. Ed.* **1995**, *34*, 2014-2017.

(2) Holland, B. T.; Blanford, C. F.; Stein, A. Synthesis of Macroporous Minerals with Highly Ordered Three-Dimensional Arrays of Spheroidal Voids. *Science* **1998**, *281*, 538-540.

(3) Imhof, A.; Pine, D. J. Ordered Macroporous Materials by Emulsion Templating. *Nature* **1997**, *389*, 948-951.

(4) Kasuga, T.; Hiramatsu, M.; Hoson, A.; Sekino, T.; Niihara, K. Formation of Titanium Oxide Nanotube. *Langmuir* **1998**, *14*, 3160-3163.

(5) Wijinhoven, J. E. G. J.; Vos, W. L. Preparation of Photonic Crystals Made of Air Spheres in Titania. *Science* **1998**, *281*, 802-804.

(6) Yang, P.; Deng, T.; Zhao, D.; Feng, P.; Pine, D.; Chmelka, B. F.; Whitesides, G. M.; Stucky, G. D. Hierarchically Ordered Oxides. *Science* **1998**, *282*, 2244-2246.

(7) Yang, P.; Zhao, D.; Margolese, D. I.; Chmelka, B. F.; Stucky, G. D. Generalized Syntheses of Large-Pore Mesoporous Metal Oxides with Semicrystalline Frameworks. *Nature* **1998**, *396*, 152-155.

(8) Zwilling, V.; Aucouturier, M.; Darque-Ceretti, E. Anodic Oxidation of Titanium and TA6V Alloy in Chromic Media. An Electrochemical Approach. *Electrochim. Acta* **1999**, *45*, 921-929.

(9) Chen, X.; Mao, S. S. Titanium Dioxide Nanomaterials: Synthesis, Properties, Modifications, and Applications. *Chem. Rev.* **2007**, *107*, 2891-2959.

(10) Bavykin, D. V.; Walsh, F. C. *Titanate and Titania Nanotubes: Synthesis, Properties and Applications*; Royal Society of Chemistry: Cambridge, UK, 2010.

(11) Roy, P.; Berger, S.; Schmuki, P. TiO_2 Nanotubes: Synthesis and Applications. *Angew. Chem. Int. Ed.* **2011**, *50*, 2904-2939.

(12) Petkovich, N. D.; Stein, A. Colloidal Crystal Templating Approaches to Materials with Hierarchical Porosity. In *Hierarchically Structured Porous Materials: From Nanoscience to Catalysis, Separation, Optics, Energy, and Life Science*; Su, B.-L., Sanchez, C., Yang, X.-Y., Eds.; Wiley-VCH Verlag GmbH & Co. KGaA: Weinheim, Germany, 2012.

(13) Li, W.; Wu, Z.; Wang, J.; Elzatahry, A. A.; Zhao, D. A Perspective on Mesoporous TiO_2 Materials. *Chem. Mater.* **2014**, *26*, 287-298.

(14) Hagfeldt, A.; Boschloo, G.; Sun, L.; Kloo, L.; Pettersson, H. Dye-Sensitized Solar Cells. *Chem. Rev.* **2010**, *110*, 6595-6663.

(15) Fujishima, A.; Zhang, X.; Tryk, D. A. TiO_2 Photocatalysis and Related Surface Phenomena. *Surf. Sci. Rep.* **2008**, *63*, 515-582.

(16) Aprile, C.; Corma, A.; Garcia, H. Enhancement of the Photocatalytic Activity of TiO_2 through Spatial Structuring and Particle Size Control: From Subnanometric to Submillimetric Length Scale. *Phys. Chem. Chem. Phys.* **2011**, *10*, 769-783.

(17) Fröschl, T.; Hörmann, U.; Kubiak, P.; Kučerová, G.; Pfanzelt, M.; Weiss, C. K.; Behm, R. J.; Hüsing, N.; Kaiser, U.; Landfester, K.; Wohlfahrt-Mehrens, M. High Surface Area Crystalline Titanium Dioxide: Potential and Limits in Electrochemical Energy Storage and Catalysis. *Chem. Soc. Rev.* **2012**, *41*, 5313-5360.

(18) Joo, J. B.; Dahl, M.; Li, N.; Zaera, F.; Yin, Y. Tailored Synthesis of Mesoporous TiO_2 Hollow Nanostructured for Catalytic Applications. *Energy Environ. Sci.* **2013**, *6*, 2082-2092.

(19) Kitano, M.; Wada, E.; Nakajima, K.; Hayashi, S.; Miyazaki, S.; Kobayashi, H.; Hara, M. Protonated Titanate Nanotubes with Lewis and Brønstad Acidity: Relationship between Nanotube Structure and Catalytic Activity. *Chem. Mater.* **2013**, *25*, 385-393.

(20) Li, N.; Zhang, L.; Chen, Y.; Fang, M.; Zhang, J.; Wang, H. Highly Efficient, Irreversible and Selective Ion Exchange Property of Layered Titanate Nanostructures. *Adv. Funct. Mater.* **2012**, *22*, 835-841.
(21) Wang, J.; Li, H.; Li, H.; Zou, C.; Wang, H.; Li, D. Mesoporous TiO_2 Thin Films Exhibiting Enhanced Thermal Stability and Controllable Pore Size: Preparation and Photocatalyzed Destruction of Cationic Dyes. *ACS Appl. Mater. Interfaces* **2014**, *6*, 1623-1631.
(22) Chang, Z.; Liu, J.; Liu, J.; Sun, X. Titanate Nanosheets and Nanotubes: Alkalinity Manipulated Snthesis and Catalyst Support Application. *J. Mater. Chem.* **2011**, *21*, 277-282.
(23) Bavykin, D. V.; Lapkin, A. A.; Plucinski, P. K.; Friedrich, J. M.; Walsh, F. C. Reversible Storage of Molecular Hydrogen by Sorption into Multilayered TiO_2 Nanotubes. *J. Phys. Chem. B* **2005**, *109*, 19422-19427.
(24) Matos, B. R.; Isidoro, R. A.; Santiago, E. I.; Linardi, M.; Ferlauto, A. S.; Tavares, A. C.; Fonseca, F. C. *In Situ* Fabrication of Nafion-Titanate Hybrid Electrolytes for High-Temperature Direct Ethanol Fuel Cell. *J. Phys. Chem. C* **2013**, *117*, 16863-16870.
(25) Hong, Z.; Wei, M. Layered Titanate Nanostructures and Their Derivatives as Negative Electrode Materials for Lithium-Ion Batteries. *J. Mater. Chem. A* **2013**, *1*, 4403-4414.
(26) Dylla, A. G.; Henkelman, G.; Stevenson, K. J. Lithium Insertion in Nanostructured TiO_2(B) Architectures. *Acc. Chem. Res.* **2013**, *46*, 1104-1112.
(27) Reddy, M. V.; Subba Rao, G. V.; Chowdari, B. V. R. Metal Oxides and Oxysalts as Anode Materials for Li Ion Batteries. *Chem. Rev.* **2013**, *113*, 5364-5457.
(28) Tiemann, M. Repeated Templating. *Chem. Mater.* **2008**, *20*, 961-971.
(29) Ren, Y.; Hardwick, L. J.; Bruce, P. G. Lithium Intercalation into Mesoporous Anatase with an Ordered 3D Pore Structure. *Angew. Chem. Int. Ed.* **2010**, *49*, 2570-2574.
(30) Du, J.; Lai, X.; Yang, N.; Zhai, J.; Kisailus, D.; Su, F.; Wang, D.; Jiang, L. Hierarchically Ordered Macro-Mesoporous TiO_2-Graphene Composite Films: Improved Mass Transfer, Reduced Charge Recombination, and Their Enhanced Photocatalytic Activities. *ACS Nano* **2011**, *5*, 590-596.
(31) Zhao, J.; Wan, P.; Xiang, J.; Tong, T.; Dong, L.; Guo, Z.; Shen, X.; Tong, H. Synthesis of Highly Ordered Macro-Mesoporous Anatase TiO_2 Film with High Photocatalytic Activity. *Microporous Mesoporous Mater.* **2011**, *138*, 200-206.
(32) Hu, Z.; Hua, Z.; Cai, S.; Chen, J.; Yan, Y.; Xu, L. Fabrication of Three-Dimensionally Ordered Macro-/Mesoporous Titania Monoliths by a Dual-Templating Approach. *MRS Proc.* **2011**, *1352*, 1-6.
(33) Sun, W.; Zhou, S.; You, B.; Wu, L. Facile Fabrication and High Photoelectric Properties of Hierarchically Ordered Porous TiO_2. *Chem. Mater.* **2012**, *24*, 3800-3810.
(34) Xin, Y.; Jiang, P.; Yu, M.; Gu, H.; Li, Q.; Zhang, Z. A Universal Route to Fabricate Hierarchically Ordered Macro/Mesoporous Oxides with Enhanced Intrinsic Activity. *J. Mater. Chem. A* **2014**, *2*, 6419-6425.
(35) Bavykin, D. V.; Cressey, B. A.; Light, M. E.; Walsh, F. C. An Aqueous, Alkaline Route to Titanate Nanotubes under Atmospheric Pressure Conditions. *Nanotechnology* **2008**, *19*, 275604(1-5).
(36) Bavykin, D. V.; Friedrich, J. M.; Walsh, F. C. Protonated Titanates and TiO_2 Nanostructured Materials: Synthesis, Properties, and Applications. *Adv. Mater.* **2006**, *18*, 2807-2824.
(37) Nakahira, A.; Kubo, T.; Numako, C. Formation Mechanism of TiO_2-Derived Titanate Nanotubes Prepared by the Hydrothermal Process. *Inorg. Chem.* **2010**, *49*, 5845-5852.
(38) Huang, J.; Cao, Y.; Wang, M.; Huang, C.; Deng, Z.; Tong, H.; Liu, Z. Tailoring of Low-Dimensional Titanate Nanostructures. *J. Phys. Chem. C* **2010**, *114*, 14748-14754.

(39) Morgan, D. L.; Triani, G.; Blackford, M. G.; Raftery, N. A.; Frost, R. L.; Waclawik, E. R. Alkaline Hydrothermal Kinetics in Titanate Nanostructure Formation. *J. Mater. Sci.* **2011**, *46*, 548-557.

(40) Huang, J.; Cao, Y.; Huang, Q.; He, H.; Liu, Y.; Guo, W.; Hong, M. High-Temperature Formation of Titanate Nanotubes and Transformation Mechanism of Nanotubes into Nanowires. *Cryst. Growth Des.* **2009**, *9*, 3632-3637.

(41) Bavykin, D. V.; Kulak, A. N.; Walsh, F. C. Metastable Nature of Titanate Nanotubes in an Alkaline Environment. *Cryst. Growth Des.* **2010**, *10*, 4421-4427.

(42) Wu, D.; Liu, J.; Zhao, X.; Li, A.; Chen, Y.; Ming, N. Sequence of Events for the Formation of Titanate Nanotubes, Nanofibers, Nanowires, and Nanobelts. *Chem. Mater.* **2006**, *18*, 547-553.

(43) Beuvier, T.; Richard-Plouet, M.; Brohan, L. Ternary Morphological Diagram for Nano(tube-ribbon-sphere) Sodium Titanate Deduced fro Raman Spectra Analysis. *J. Phys. Chem. C* **2010**, *114*, 7660-7665.

(44) Menzel, R.; Peiró, A. M.; Durrant, J. R.; Shaffer, M. S. P. Impact of Hydrothermal Processing Conditions on High Aspect Ratio Titanate Nanostructures. *Chem. Mater.* **2006**, *18*, 6059-6068.

(45) Bavykin, D. V.; Parmon, V. N.; Lapkin, A. A.; Walsh, F. C. The Effect of Hydrothermal Conditions on the Mesoporous Structure of TiO_2 Nanotubes. *J. Mater. Chem.* **2004**, *14*, 3370-3377.

(46) Morgan, D. L.; Liu, H.-W.; Frost, R. L.; Waclawik, E. R. Implications of Precursor Chemistry on the Alkaline Hydrothermal Synthesis of Titania/Titanate Nanostructures. *J. Phys. Chem. C* **2010**, *114*, 101-110.

(47) Nakahira, A.; Kato, W.; Tamai, M.; Isshiki, T.; Nishio, K.; Aritani, H. Synthesis of Nanotube from a Layer $H_2Ti_4O_9{\cdot}H_2O$ in a Hydrothermal Treatment Using Various Titania Sources. *J. Mater. Sci.* **2004**, *39*, 4239-4245.

(48) Peng, C.-W.; Richard-Plouet, M.; Ke, T.-Y.; Lee, C.-Y.; Chiu, H.-T.; Marhic, C.; Puzenat, E.; Lemoigno, F.; Brohan, L. Chimie Douce Route to Sodium Hydroxo Titanate Nanowires with Modulated Structure and Conversion to Highly Photoactive Titanium Dioxides. *Chem. Mater.* **2008**, *20*, 7228-7236.

(49) Yuan, Z.-Y.; Zhang, X.-B.; Su, B.-L. Moderate Hydrothermal Synthesis of Potassium Titanate Nanowires. *Appl. Phys. A* **2004**, *78*, 1063-1066.

(50) Mao, Y.; Wong, S. S. Size- and Shape-Dependent Transformation of Nanosized Titanate into Analogous Anatase Titania Nanostructures. *J. Am. Chem. Soc.* **2006**, *128*, 8217-8226.

(51) Morgado, E.; de Abreu, M. A. S.; Moure, G. T.; Marinkovic, B. A.; Jardim, P. M.; Araujo, A. S. Characterization of Nanostructured Titanates Obtained by Alkali Treatment of TiO_2-Anatases with Distinct Crystal Sizes. *Chem. Mater.* **2007**, *19*, 665-676.

(52) Papa, A.-L.; Millot, N.; Saviot, L.; Chassagnon, R.; Heintz, O. Effect of Reaction Parameters on Composition and Morphology of Titanate Nanomaterials. *J. Phys. Chem. C* **2009**, *113*, 12682-12689.

(53) Hernández-Alonso, M. D.; García-Rodríguez, S.; Sánchez, B.; Coronado, J. M. Revisting the Hydrothermal Synthesis of Titanate Nanotubes: New Insights on the Key Factors Affecting the Morphology. *Nanoscale* **2011**, *3*, 2233-2240.

(54) Bavykin, D. V.; Carravetta, M.; Kulak, A. N.; Walsh, F. C. Application of Magic-Angle Spinning NMR to Examine the Nature of Protons in Titanate Nanotubes. *Chem. Mater.* **2010**, *22*, 2458-2465.

(55) Kiatkittipong, K.; Scott, J.; Amal, R. Hydrothermally Synthesized Titanate Nanostructures: Impact of Heat Treatment on Particle Characteristics and Photocatalytic Properties. *ACS Appl. Mater. Interfaces* **2011**, *3*, 3988-3996.

(56) Zhu, G.-N.; Wang, C.-X.; Xia, Y.-Y. Structural Transformation of Layered Hydrogen Trititanate ($H_2Ti_3O_7$) to TiO_2(B) and Its Electrochemical Profile for Lithium-Ion Intercalation. *J. Power Sources* **2011**, *196*, 2848-2853.
(57) Gentili, V.; Brutti, S.; Hardwick, L. J.; Armstrong, A. R.; Panero, S.; Bruce, P. G. Lithium Insertion into Anatase Nanotubes. *Chem. Mater.* **2012**, *24*, 4468-4476.
(58) Zhou, Y.-K.; Cao, L.; Zhang, F.-B.; He, B.-L.; Li, H.-L. Lithium Insertion into TiO_2 Nanotube Prepared by the Hydrothermal Process. *J. Electrochem. Soc.* **2003**, *150*, A1246-A1249.
(59) Gao, X.; Zhu, H.; Pan, G.; Ye, S.; Lan, Y.; Wu, F.; Song, D. Preparation and Electrochemical Characterization of Anatase Nanorods for Lithium-Inserting Electrode Material. *J. Phys. Chem. B* **2004**, *108*, 2868-2872.
(60) Zukalová, M.; Kalbáč, M.; Kavan, L.; Exnar, I.; Graetzel, M. Pseudocapacitive Lithium Storage in TiO_2(B). *Chem. Mater.* **2005**, *17*, 1248-1255.
(61) Armstrong, A. R.; Armstrong, G.; Canales, J.; García, R.; Bruce, P. G. Lithium-Ion Intercalation into TiO_2-B Nanowires. *Adv. Mater.* **2005**, *17*, 862-865.
(62) Li, J.; Tang, Z.; Zhang, Z. Layered Hydrogen Titanate Nanowires with Novel Lithium Intercalation Properties. *Chem. Mater.* **2005**, *17*, 5848-5855.
(63) Augustyn, V.; Simon, P.; Dunn, B. Pseudocapacitive Oxide Materials for High-Rate Electrochemical Energy Storage. *Energy Environ. Sci.* **2014**, *7*, 1597-1614.
(64) Li, J.; Tang, Z.; Zhang, Z. Pseudocapacitive Characteristic of Lithium Ion Storage in Hydrogen Titanate Nanotubes. *Chem. Phys. Lett.* **2006**, *418*, 506-510.
(65) Beuvier, T.; Richard-Plouet, M.; Mancini-Le Granvalet, M.; Brousse, T.; Crosnier, O.; Brohan, L. TiO_2(B) Nanoribbons as Negative Electrode Material for Lithium Ion Batteries with High Rate Performance. *Inorg. Chem.* **2010**, *49*, 8457-8464.
(66) Dylla, A. G.; Xiao, P.; Henkelman, G.; Stevenson, K. J. Morphological Dependence of Lithium Insertion in Nanocrystalline TiO_2(B) Nanoparticles and Nanosheets. *J. Phys. Chem. Lett.* **2012**, *3*, 2015-2019.
(67) Myung, S.-T.; Takahashi, N.; Komaba, S.; Yoon, C. S.; Sun, Y.-K.; Amine, K.; Yashiro, H. Nanostructured TiO_2 and Its Application in Lithium-Ion Storage. *Adv. Funct. Mater.* **2011**, *21*, 3231-3241.
(68) Huang, H.; Fang, J.; Xia, Y.; Tao, X.; Gan, Y.; Du, J.; Zhu, W.; Zhang, W. Construction of Sheet-Belt Hybrid Nanostructures from One-Dimensional Mesoporous TiO_2(B) Nanobelts and Graphene Sheets for Advanced Lithium-Ion Batteries. *J. Mater. Chem. A* **2013**, *1*, 2495-2500.
(69) Liu, S.; Wang, Z.; Yu, C.; Wu, H. B.; Wang, G.; Dong, Q.; Qiu, J.; Eychmüller, A.; Lou, X. W. A Flexible TiO_2(B)-Based Battery Electrode with Superior Power Rate and Ultralong Cycle Life. *Adv. Mater.* **2013**, *25*, 3462-3467.
(70) Zakharova, G. S.; Jähne, C.; Popa, A.; Täschner, C.; Gemming, T.; Leonhardt, A.; Büchner, B.; Klingeler, R. Anatase Nanotubes as an Electrode Material for Lithium-Ion Batteries. *J. Phys. Chem. C* **2012**, *116*, 8714-8720.
(71) Zhang, Y.; Tang, Y.; Yin, S.; Zeng, Z.; Zhang, H.; Li, C. M.; Dong, Z.; Chen, Z.; Chen, X. Hierarchical Protonated Titanate Nanostructures for Lithium-Ion Batteries. *Nanoscale* **2011**, *3*, 4074-4077.
(72) Bae, C.; Yoon, Y.; Yoon, W.-S.; Moon, J.; Kim, J.; Shin, H. Hierarchical Titania Nanotubes with Self-Branched Crystalline Nanorods. *ACS Appl. Mater. Interfaces* **2010**, *2*, 1581-1587.
(73) Shin, K.; Kim, H. J.; Choi, J.-M.; Choi, Y.-M.; Song, M. S.; Park, J. H. Controlled Synthesis of Skein Shaped TiO_2-B Nanotube Cluster Particles with Outstanding Rate Capability. *Chem. Commun.* **2013**, *49*, 2326-2328.

(74) Liu, H.; Bi, Z.; Sun, X.-G.; Unocic, R. R.; Paranthaman, M. P.; Dai, S.; Brown, G. M. Mesoporous TiO_2-B Microspheres with Superior Rate Performance for Lithium Ion Batteries. *Adv. Mater.* **2011**, *23*, 3450-3454.

(75) Josephson, D. P.; Popczun, E. J.; Stein, A. Effects of Integrated Carbon as a Light Absorber on the Coloration of Photonic Crytal-Based Pigments. *J. Phys. Chem. C* **2013**, *117*, 13585-13592.

(76) Nakahira, A.; Kubo, T.; Numako, C. TiO_2-Derived Titanate Nanotubes by Hydrothermal Process with Acid Treatments and Their Microstructural Evaluation. *ACS Appl. Mater. Interfaces* **2010**, *2*, 2611-2616.

(77) Zhang, H.; Li, G. R.; An, L. P.; Yan, T. Y.; Gao, X. P.; Zhu, H. Y. Electrochemical Lithium Storage of Titanate and Titania Nanotubes and Nanorods. *J. Phys. Chem. C* **2007**, *111*, 6143-6148.

(78) Qu, J.; Gao, X. P.; Li, G. R.; Jiang, Q. W.; Yan, T. Y. Structure Transformation and Photoelectrochemical Properties of TiO_2 Nanomaterials Calcined from Titanate Nanotubes. *J. Phys. Chem. C* **2009**, *113*, 3359-3363.

(79) Bavykin, D. V.; Kulak, A. N.; Walsh, F. C. Control over the Hierarchical Structure of Titanate Nanotube Agglomerates. *Langmuir* **2011**, *27*, 5644-5649.

(80) Mao, Y.; Kanungo, M.; Hemraj-Benny, T.; Wong, S. S. Synthesis and Growth Mechanism of Titanate and Titania One-Dimensional Nanostructures Self-Assembled into Hollow Micrometer-Scale Spherical Aggregates. *J. Phys. Chem. B* **2006**, *110*, 702-710.

(81) Horváth, E.; Kukovecz, Á.; Kónya, Z.; Kiricsi, I. Hydrothermal Conversion of Self-Assembled Titanate Nanotubes into Nanowires in a Revolving Autoclave. *Chem. Mater.* **2007**, *19*, 927-931.

(82) Moon, J. H.; Yang, S. Chemical Aspects of Three-Dimensional Photonic Crystals. *Chem. Rev.* **2010**, *110*, 547-574.

(83) Schroden, R. C.; Al-Daous, M.; Blanford, C. F.; Stein, A. Optical Properties of Inverse Opal Photonic Crystals. *Chem. Mater.* **2002**, *14*, 3305-3315.

(84) Tokudome, H.; Miyauchi, M. Electrochromism of Titanate-Based Nanotubes. *Angew. Chem. Int. Ed.* **2008**, *44*, 1974-1977.

(85) Vittadini, A.; Schirmer, M.; Walz, M.-M.; Vollnhals, F.; Lukasczyk, T.; Steinrück, H.-P.; Marbach, H.; Riss, A.; Elser, M. J.; Schürer, B.; Diwald, O. Defects in Oxygen-Depleted Titanate Nanostructures. *Langmuir* **2012**, *28*, 7851-7858.

(86) Chatterjee, S.; Bhattacharyya, K.; Ayyub, P.; Tyagi, A. K. Photocatalytic Properties of One-Dimensional Nanostructured Titanates. *J. Phys. Chem. C* **2010**, *114*, 9424-9430.

(87) Tsai, C.-C.; Teng, H. Regulation of the Physical Characteristics of Titania Nanotube Aggregates Synthesized from Hydrothermal Treament. *Chem. Mater.* **2004**, *16*, 4352-4358.

(88) Gao, T.; Fjellvåg, H.; Norby, P. Crystal Structures of Titanate Nanotubes: A Raman Scattering Study. *Inorg. Chem.* **2009**, *48*, 1423-1432.

(89) Gao, T.; Fjellvåg, H.; Norby, P. Raman Scattering Properties of a Protonic Titanate $H_xTi_{2-x/4}\square_{x/4}O_4 \cdot H_2O$ (□, vacancy; x = 0.7) with Lepidocrocite-Type Layered Structure. *J. Phys. Chem. B* **2008**, *112*, 9400-9405.

(90) Tsai, C.-C.; Teng, H. Nanotube Formation from a Sodium Titanate Powder via Low-Temperature Acid Treatment. *Langmuir* **2008**, *24*, 3434-3438.

(91) Ma, R.; Fukuda, K.; Sasaki, T.; Osada, M.; Bando, Y. Structural Features of Titanate Nanotubes/Nanobelts Revealed by Raman, X-ray Adsorption Fine Structure and Electron Diffraction Characterizations. *J. Phys. Chem. B* **2005**, *109*, 6210-6214.

(92) Kim, S.-J.; Yun, Y.-U.; Oh, H.-J.; Hong, S. H.; Roberts, C. A.; Routray, K.; Wachs, I. E. Characterization of Hydrothermally Prepared Titanate Nanotube Powders by Ambient and In Situ Raman Spectroscopy. *J. Phys. Chem. Lett.* **2010**, *1*, 130-135.
(93) Aravindan, V.; Shubha, N.; Cheah, Y. L.; Prasanth, R.; Chuiling, W.; Prabhakar, R. R.; Madhavi, S. Extraordinary Long-Term Cycleability of TiO_2-B Nanorods as Anodes in Full-Cell Assembly with Electrospun PVdF-HFP Membranes. *J. Mater. Chem. A* **2013**, *1*, 308-316.
(94) Casarin, M.; Vittadini, A.; Selloni, A. First Principles Study of Hydrated/Hydroxylated TiO_2 Nanolayers: From Isolated Sheets to Stacks and Tubes. *ACS Nano* **2009**, *3*, 317-324.
(95) Hanaor, D. A. H.; Sorrell, C. C. Review of the Anatase to Rutile Phase Transformation. *J. Mater. Sci.* **2011**, *46*, 855-874.
(96) Kim, J.; Cho, J. Rate Characteristics of Anatase TiO_2 Nanotubes and Nanorods for Lithium Battery Anode Materials at Room Temperature. *J. Electrochem. Soc.* **2007**, *154*, A542-A546.
(97) Brutti, S.; Gentili, V.; Menard, H.; Scrosati, B.; Bruce, P. G. TiO_2-(B) Nanotube as Anodes for Lithium Batteries: Origin and Mitigation of Irreversible Capacity. *Adv. Energy Mater.* **2012**, *2*, 322-327.

Chapter 7

(1) Otsuka, K.; Hatano, M.; Morikawa, A. Hydrogen from Water by Reduced Cerium Oxide. *J. Catal.* **1983**, *79*, 493-496.
(2) Otsuka, K.; Wang, Y.; Nakamura, M. Direct Conversion of Methane to Synthesis Gas Through Gas-Solid Reaction Using CeO_2-ZrO_2 Solid Solution at Moderate Temperature. *Appl. Catal. A* **1999**, *183*, 317-324.
(3) Abanades, S.; Flamant, G. Thermochemical Hydrogen Production From a Two-Step Solar-Driven Water-Splitting Cycle Based on Cerium Oxides. *Solar Energy* **2006**, *80*, 1611-1623.
(4) Kaneko, H.; Miura, T.; Ishihara, H.; Taku, S.; Yokoyama, T.; Nakajima, H.; Tamaura, Y. Reactive Ceramics of CeO_2-MO_x (M=Mn, Fe, Ni, Cu) for H_2 Generation by Two-Step Water Splitting Using Concentrated Solar Thermal Energy. *Energy* **2007**, *32*, 656-663.
(5) Kang, K.-S.; Kim, C.-H.; Park, C.-S.; Kim, J.-W. Hydrogen Reduction and Subsequent Water Splitting of Zr-Added CeO_2. *J. Ind. Eng. Chem.* **2007**, *13*, 657-663.
(6) Miller, J. E.; Allendorf, M. D.; Diver, R. B.; Evans, L. R.; Siegel, N. P.; Stuecker, J. N. Metal Oxide Composites and Structures for Ultra-High Temperature Solar Thermochemical Cycles. *J. Mater. Sci.* **2008**, *43*, 4714-4728.
(7) Abanades, S.; Legal, A.; Cordier, A.; Peraudeau, G.; Flamant, G.; Julbe, A. Investigation of Reactive Cerium-Based Oxides for H_2 Production by Thermochemical Two-Step Water-Splitting. *J. Mater. Sci.* **2010**, *45*, 4163-4173.
(8) Chueh, W. C.; Haile, S. M. A Thermochemical Study of Ceria: Exploiting an Old Material for New Modes of Energy Conversion and CO_2 Mitigation. *Phil. Trans. R. Soc. A* **2010**, *368*, 3269-3294.
(9) Chueh, W. C.; Falter, C.; Abbott, M.; Scipio, D.; Furler, P.; Haile, S. M.; Steinfeld, A. High-Flux Solar-Driven Thermochemical Dissociation of CO_2 and H_2O Using Nonstoichiometric Ceria. *Science* **2010**, *330*, 1797-1801.
(10) de Leitenburg, C.; Trovarelli, A.; Llorca, J.; Cavani, F.; Bini, G. The Effect of Doping CeO_2 with Zirconium in the Oxidation of Isobutane. *Appl. Catal., A* **1996**, *139*, 161-173.

(11) Mogensen, M. Physical, Chemical and Electrochemical Properties of Pure and Doped Ceria. *Solid State Ionics* **2000**, *129*, 63-94.
(12) Trovarelli, A. Structural Properties and Nonstoichiometric Behavior of CeO_2. In *Catalysis by Ceria and Related Materials*; Trovarelli, A., Ed.; Imperial College Press: London, **2002**.
(13) Skorodumova, N. V.; Simak, S. I.; Lundqvist, B. I.; Abrikosov, I. A.; Johansson, B. Quantum Origin of the Oxygen Storage Capability of Ceria. *Phys. Rev. Lett.* **2002**, *89*, 166601(1-4).
(14) Kodama, T.; Gokon, N. Thermochemical Cycles for High-Temperature Solar Hydrogen Production. *Chem. Rev.* **2007**, *107*, 4048-4077.
(15) Venstrom, L. J.; Petkovich, N.; Rudisill, S.; Stein, A.; Davidson, J. H. The Effects of Morphology on the Oxidation of Ceria by Water and Carbon Dioxide. *J. Sol. Energy Eng.* **2012**, *134*, 011005(1-8).
(16) Sokolov, S.; Bell, D.; Stein, A. Preparation and Characterization of Macroporous α-Alumina. *J. Am. Ceram. Soc.* **2003**, *86*, 1481-1486.
(17) Stein, A.; Li, F.; Denny, N. R. Morphological Control in Colloidal Crystal Templating of Inverse Opals, Hierarchical Structures and Shaped Particles. *Chem. Mater.* **2008**, *20*, 649-666.
(18) Fornasiero, P.; Balducci, G.; Di Monte, R.; Kašpar, J.; Sergo, V.; Gubitosa, G.; Ferrero, A.; Graziani, M. Modification of the Redox Behaviour of CeO_2 Induced by Structural Doping with ZrO_2. *J. Catal.* **1996**, *164*, 173-183.
(19) Di Monte, R.; Kašpar, J. Nanostructured CeO_2-ZrO_2 Mixed Oxides. *J. Mater. Chem.* **2005**, *15*, 633-648.
(20) Atribak, I.; Bueno-López, A.; García-García, A.; Azambre, B. Contributions of Surface and Bulk Heterogeneities to the NO Oxidation Activities of Ceria-Zirconia Catalysts with Conposition $Ce_{0.76}Zr_{0.24}O_2$ Prepared by Different Methods. *Phys. Chem. Chem. Phys.* **2010**, *12*, 13770-13779.
(21) Kašpar, J.; Fornasiero, P.; Graziani, M. Use of CeO_2-Based Oxides in the Three-Way Catalysis. *Catal. Today* **1999**, *50*, 285-298.
(22) Balducci, G.; Islam, M. S.; Kašpar, J.; Fornasiero, P.; Graziani, M. Bulk Reduction and Oxygen Migration in the Ceria-Based Oxides. *Chem. Mater.* **2000**, *12*, 677-681.
(23) Mamontov, E.; Egami, T.; Brezny, R.; Koranne, M.; Tyagi, S. Lattice Defects and Oxygen Storage Capacity of Nanocrystalline Ceria and Ceria-Zirconia. *J. Phys. Chem. B* **2000**, *104*, 11110-11116.
(24) Shah, P. R.; Kim, T.; Zhou, G.; Fornasiero, P.; Gorte, R. J. Evidence for Entropy Effects in the Reduction of Ceria-Zirconia Solutions. *Chem. Mater.* **2006**, *18*, 5363-5369.
(25) Wang, H.-F.; Guo, Y.-L.; Lu, G.-Z.; Hu, P. Maximizing the Localized Relaxation: The Origin of the Outstanding Oxygen Storage Capacity of κ-$Ce_2Zr_2O_8$. *Angew. Chem. Int. Ed.* **2009**, *48*, 8289-8292.
(26) Daturi, M.; Finocchio, E.; Binet, C.; Lavalley, J. C.; Fally, F.; Perrichon, V. Study of Bulk and Surface Reduction by Hydrogen of $Ce_xZr_{1-x}O_2$ Mixed Oxides Followed by FTIR Spectroscopy and Magnetic Balance. *J. Phys. Chem. B* **1999**, *103*, 4884-4891.
(27) Martínez-Arias, A.; Fernández-García, M.; Hungría, A.-B.; C., C. J.; Munuera, G. Spectroscopic Characterization of Heterogeneity and Redox Effects in Zirconium-Cerium (1:1) Mixed Oxides Prepared by Microemulsion Methods. *J. Phys. Chem. B* **2003**, *107*, 2667-2677.
(28) Kim, T.; Vohs, J. M.; Gorte, R. J. Thermodynamic Investigation of the Redox Properties of Ceria-Zirconia Solid Solutions. *Ind. Eng. Chem. Res.* **2006**, *45*, 5561-5565.

(29) Giordano, F.; Trovarelli, A.; de Leitenburg, C.; Dolcetti, G.; Giona, M. Some Insight into the Effects of Oxygen Diffusion in the Reduction Kinetics of Ceria. *Ind. Eng. Chem. Res.* **2001**, *40*, 4828-4835.

(30) Colón, G.; Pijolat, M.; Valdivieso, F.; Vidal, H.; Kašpar, J.; Finocchio, E.; Daturi, M.; Binet, C.; Lavalley, J. C.; Baker, R. T.; Bernal, S. Surface and Structural Characterization of $Ce_xZr_{1-x}O_2$ CEZIRENCAT Mixed Oxides as Potential Three-Way Catalyst Promoters. *J. Chem. Soc., Faraday Trans.* **1998**, *94*, 3717-3726.

(31) Colón, G.; Valdivieso, F.; Pijolat, M.; Baker, R. T.; Calvino, J. J.; Bernal, S. Textural and Phase Stability of $Ce_xZr_{1-x}O_2$ Mixed Oxides Under High Temperature Oxidising Conditions. *Catal. Today* **1999**, *50*, 271-284.

(32) Le Gal, A.; Abanades, S. Catalytic Investigation of Ceria-Zirconia Solid Solutions for Solar Hydrogen Production. *Int. J. Hydrogen Energy* **2011**, *36*, 4739-4748.

(33) Schroden, R. C.; Al-Daous, M.; Sokolov, S.; Melde, B. J.; Lytle, J. C.; Stein, A.; Carbajo, M. C.; Fernández, J. T.; Rodríguez, E. E. Hybrid Macroporous Materials for Heavy Metal Ion Adsorption. *J. Mater. Chem.* **2002**, *12*, 3261-3267.

(34) Varez, A.; Garcia-Gonzalez, E.; Sanz, J. Cation Miscibility in CeO_2-ZrO_2 Oxides with Fluorite Structure. A Combined TEM, SAED and XRD Rietveld Analysis. *J. Mater. Chem.* **2006**, *16*, 4249-4256.

(35) Yashima, M. Crystal Structures of the Tetragonal Ceria-Zirconia Solid Solutions $Ce_xZr_{1-x}O_2$ Through First Principles Calculations ($0 \leq x \leq 1$). *J. Phys. Chem. C* **2009**, *113*, 12658-12662.

(36) Yashima, M.; Arashi, H.; Kakihana, M.; Yoshimura, M. Raman Scattering Study of Cubic-Tetragonal Phase Transition in $Zr_{1-x}Ce_xO_2$ Solid Solution. *J. Am. Ceram. Soc.* **1994**, *77*, 1067-1071.

(37) Trovarelli, A.; Zamar, F.; Llorca, J.; de Leitenburg, C.; Dolcetti, G.; Kiss, J. T. Nanophase Fluorite-Structured CeO_2-ZrO_2 Catalysts Prepared by High-Energy Mechanical Milling. *J. Catal.* **1997**, *169*, 490-502.

(38) Omata, T.; Kishimoto, H.; Otsuka-Yao-Matsuo, S.; Ohtori, N.; Umesaki, N. Vibrational Spectroscopic and X-Ray Diffraction Studies of Cerium Zirconium Oxides with Ce/Zr Composition Rato = 1 Prepared by Reduction and Successive Oxidation of *t'*-$(Ce_{0.5}Zr_{0.5})O_2$ Phase. *J. Solid State Chem.* **1999**, *147*, 573-583.

(39) Otsuka-Yao-Matsuo, S.; Omata, T.; Izu, N.; Kishimoto, H. Oxygen Release Behavior of $CeZrO_4$ Powders and Appearance of New Compounds κ and t*. *J. Solid State Chem.* **1998**, *138*, 47-54.

(40) Montini, T.; Hickey, N.; Fornasiero, P.; Graziani, M.; Bañares, A.; Martinez-Huerta, M. V.; Alessandri, I.; Depero, L. E. Variations in the Extent of Pyrochlore-Type Cation Ordering in $Ce_2Zr_2O_8$: a t'-κ Pathway to Low-Temperature Reduction. *Chem. Mater.* **2005**, *17*, 1157-1166.

(41) Yeste, M. P.; Hernández, J. C.; Trasobares, S.; Bernal, S.; Blanco, G.; Calvino, J. J.; Pérez-Omil, J. A.; Pintado, J. M. First Stage of Thermal Aging under Oxidizing Conditions of a $Ce_{0.62}Zr_{0.38}O_2$ Mixed Oxide with an Ordered Cationic Sublattice: A Chemical, Nanostructural, and Nanoanalytical Study. *Chem. Mater.* **2008**, *20*, 5107-5113.

(42) Hori, C. E.; Permana, H.; Simon Ng, K. Y.; Brenner, A.; More, K.; Rahmoeller, K. M.; Belton, D. Thermal Stability of Oxygen Storage Properties in a Mixed CeO_2-ZrO_2 System. *Appl. Catal., B* **1998**, *16*, 105-117.

(43) Kašpar, J.; Fornasiero, P.; Balducci, G.; Di Monte, R.; Hickey, N.; Sergo, V. Effect of ZrO_2 Content on Textural and Structural Properties of CeO_2-ZrO_2 Solid Solutions Made by Citrate Complexation Route. *Inorg. Chim. Acta* **2003**, *349*, 217-226.

(44) Shannon, R. D. Revised Effective Ionic Radii and Systematic of Interatomic Distances in Halides and Chalcogenides. *Acta Cryst.* **1976**, *A32*, 751-767.

(45) Bozo, C.; Gaillard, F.; Guilhaume, N. Characterisation of Ceria-Zirconia Solid Solution After Hydrothermal Ageing. *Appl. Catal., A* **2001**, *220*, 69-77.
(46) Zhang, F.; Chen, C.-H.; Hanson, J. C.; Robinson, R. D.; Herman, I. P.; Chan, S.-W. Phases in Ceria-Zirconia Binary Oxide (1-*x*)CeO_2-*x*ZrO_2 Nanoparticles: The Effecs of Particle Size. *J. Am. Ceram. Soc.* **2006**, *89*, 1028-1036.
(47) Kakihana, M. Invited Review "Sol-Gel" Preparation of High Temperature Superconducting Oxides. *J. Sol-Gel Sci. Technol.* **1996**, *6*, 7-55.
(48) Denny, N. R.; Han, S. E.; Norris, D. J.; Stein, A. Effects of Thermal Processes on the Structure of Monolithic Tungsten and Tungsten Alloy Photonic Crystals. *Chem. Mater.* **2007**, *19*, 4563-4569.
(49) Sing, K. S. W. Reporting Physisorption Data for Gas/Solid Systems with Special Reference to the Determination of Surface Area and Porosity. *Pure Appl. Chem.* **1985**, *57*, 603-619.
(50) Groen, J. C.; Peffer, L. A. A.; Pérez-Ramírez, J. Pore Size Determination in Modified Micro- and Mesoporous Materials. Pitfalls and Limitations in Gas Adsorption Data Analysis. *Micropor. Mesopor. Mater.* **2003**, *60*, 1-17.
(51) Aneggi, E.; de Leitenburg, C.; Dolcetti, G.; Trovarelli, A. Promotional Effect of Rare Earths and Transition Metals in the Combustion of Diesel Soot over CeO_2 and CeO_2-ZrO_2. *Catal. Today* **2006**, *114*, 40-47.
(52) Galtayries, A.; Sporken, R.; Riga, J.; Blanchard, G.; Caudano, R. XPS Comparative Study of Ceria/Zirconia Mixed Oxide: Powders and Thin Film Characterisation. *J. Electron Spectrosc. Relat. Phenom.* **1998**, *88-91*, 951-956.
(53) Mamontov, E.; Brezny, R.; Koranne, M.; Egami, T. Nanoscale Heterogeneities and Oxygen Storage Capacity of $Ce_{0.5}Zr_{0.5}O_2$. *J. Phys. Chem. B* **2003**, *107*, 13007-13014.

Chapter 8

(1) Peña, M. A.; Fierro, J. L. G. Chemical Structures and Performance of Perovskite Oxides. *Chem. Rev.* **2001**, *101*, 1981-2017.
(2) Scheffe, J. R.; Weibel, D.; Steinfeld, A. Lanthanum-Strontium-Manganese Perovskites as Redox Materials for Solar Thermochemical Splitting of H_2O and CO_2. *Energy Fuels* **2013**, *27*, 4250-4257.
(3) McDaniel, A. H.; Miller, E. C.; Arifin, D.; Ambrosini, A.; Coker, E. N.; O'Hayre, R.; Chueh, W. C.; Tong, J. Sr- and Mn-Doped $LaAlO_{3-\delta}$ for Solar Thermochemical H_2 and CO Production. *Energy Environ. Sci.* **2013**, *6*, 2424-2428.
(4) Demont, A.; Abanades, S.; Beche, E. Investigation of Perovskite Structures as Oxygen-Exchange Redox Materials for Hydrogen Production from Thermochemical Two-Step Water-Splitting Cycles. *J. Phys. Chem. C* **2014**, *118*, 12682-12692.
(5) Gupta, A.; Hedge, M. S.; Priolkar, K. R.; Waghmare, U. V.; Sarode, P. R.; Emura, S. Structural Investigation of Activated Lattice Oxygen in $Ce_{1-x}Sn_xO_2$ and $Ce_{1-x-y}Sn_xPd_yO_{2-\delta}$ by EXAFS and DFT Calculations. *Chem. Mater.* **2009**, *21*, 5836-5847.
(6) Bernal, S.; Blanco, G.; Cauqui, M. A.; Corchado, P.; Pintado, J. M.; Rodriguez-Izquierdo, J. M. Oxygen Buffering Capacity of Mixed Cerium Terbium Oxide: A New Material with Potential Applications in Three-Way Catalysts. *Chem. Commun.* **1997**, 1545-1546.
(7) Murugan, B.; Ramaswamy, A. V.; Srinivas, D.; Gopinath, C. S.; Ramaswamy, V. Nature of Manganese Species in $Ce_{1-x}Mn_xO_{2-\delta}$ Solid Solutions Synthesized by the Solution Combustion Route. *Chem. Mater.* **2005**, *17*, 3983-3993.

(8) Baidya, T.; Gayen, A.; Hedge, M. S.; Ravishankar, N.; Dupont, L. Enhanced Reducibility of $Ce_{1-x}Ti_xO_2$ Compared to That of CeO_2 and Higher Redox Catalytic Activity of $Ce_{1-x-y}Ti_xPt_yO_{2-\delta}$ Compared to That of $Ce_{1-x}Pt_xO_{2-\delta}$. *J. Phys. Chem. B.* **2006**, *110*, 5262-5272.

(9) Djinović, P.; Batista, J.; Ćehić, B.; Pintar, A. Utilization of High Specific Surface Area CuO–CeO_2 Catalysts for High Temperature Processes of Hydrogen Production: Steam Re-forming of Ethanol and Methane Dry Re-forming. *J. Phys. Chem. A* **2010**, *114*, 3939-3949.

(10) Rossignol, S.; Descorme, C.; Kappenstein, C.; Duprez, D. Synthesis, Structure and Catalytic Properties of Zr–Ce–Pr–O Mixed Oxides. *J. Mater. Chem.* **2001**, *11*, 2587-2592.

(11) Bernal, S.; Blanco, G.; Calvino, J. J.; Gatica, J. M.; Omil, J. A. P.; Pintado, J. M. Characterization of Three-Way Automotive Aftertreatment Catalysts and Related Model Systems. *Top. Catal.* **2004**, *28*, 31-45.

(12) Kehoe, A. B.; Scanlon, D. O.; Watson, G. W. Role of Lattice Distortions in the Oxygen Storage Capacity of Divalently Doped CeO_2. *Chem. Mater.* **2011**, *23*, 4464-4468.

(13) Vidmar, P.; Fornasiero, P.; Kašpar, J.; Gubitosa, G.; Graziani, M. Effects of Trivalent Dopants on the Redox Properties of $Ce_{0.6}Zr_{0.4}O_2$ Mixed Oxide. *J. Catal.* **1997**, *171*, 160-168.

(14) Krishna, K.; Bueno-López, A.; Makkee, M.; Moulijn, J. A. Potential Rare-Earth Modified CeO_2 Catalysts for Soot Oxidation: Part III. Effect of Dopant Loading and Calcination Temperature on Catalytic Activity with O_2 and NO + O_2. *Appl. Catal., B* **2007**, *75*, 210-220.

(15) Otsuka, K.; Wang, Y.; Nakamura, M. Direct Conversion of Methane to Synthesis Gas Through Gas–Solid Reaction Using CeO_2–ZrO_2 Solid Solution at Moderate Temperature. *Appl. Catal., A* **1999**, *183*, 317-324.

(16) Tang, X.; Li, Y.; Huang, X.; Xu, Y.; Zhu, H.; Wang, J.; Shen, W. MnO_x–CeO_2 Mixed Oxide Catalysts for Complete Oxidation of Formaldehyde: Effect of Preparation Method and Calcination Temperature. *Appl. Catal., B* **2006**, *62*, 265-273.

(17) Bonnetot, B.; Rakic, V.; Yuzhakova, T.; Guimon, C.; Auroux, A. Preparation and Characterization of Me_2O_3–CeO_2 (Me = B, Al, Ga, In) Mixed Oxide Catalysts. 2. Preparation by Sol-Gel Method. *Chem. Mater.* **2008**, *20*, 1585-1596.

(18) Kašpar, J.; Fornasiero, P.; Graziani, M. Use of CeO_2-Based Oxides in the Three-Way Catalysis. *Catal. Today* **1999**, *50*, 285-298.

(19) Kašpar, J.; Fornasiero, P.; Hickey, N. Automotive Catalytic Converters: Current Status and Some Perspectives. *Catal. Today* **2003**, *77*, 419-449.

(20) Yao, H. C.; Yu Yao, Y. F. Ceria in Automotive Exhaust Catalysts: I. Oxygen Storage. *J. Catal.* **1984**, *86*, 254-265.

(21) Kašpar, J.; Fornasiero, P.; Graziani, M. Use of CeO_2-Based Oxides in the Three-Way Catalysis. *Catal. Today* **1999**, *50*, 285-298.

(22) Otsuka-Yao-Matsuo, S.; Omata, T.; Izu, N.; Kishimoto, H. Oxygen Release Behavior of $CeZrO_4$ Powders and Appearance of New Compounds κ and t*. *J. Solid State Chem.* **1998**, *138*, 47-54.

(23) Zhou, G.; Gorte, R. J. Thermodynamic Investigation of the Redox Properties for Ceria-Hafnia, Ceria-Terbia, and Ceria-Praseodymia Solid Solutions. *J. Phys. Chem. B* **2008**, *112*, 9869-9875.

(24) Gupta, A.; Waghmare, U. V.; Hedge, M. S. Correlation of Oxygen Storage Capacity and Structural Distortion in Transition-Metal-, Noble-Metal-, and Rare-Earth-Ion-Substituted CeO_2 from First Pinciples Calculation. *Chem. Mater.* **2010**, *22*, 5184-5198.

(25) Daturi, M.; Finocchio, E.; Binet, C.; Lavalley, J. C.; Fally, F.; Perrichon, V. Study of Bulk and Surface Reduction by Hydrogen of $Ce_xZr_{1-x}O_2$ Mixed Oxides Followed by FTIR Spectroscopy and Magnetic Balance. *J. Phys. Chem. B* **1999**, *103*, 4884-4891.

(26) Shah, P. R.; Kim, T.; Zhou, G.; Fornasiero, P.; Gorte, R. J. Evidence for Entropy Effects in the Reduction of Ceria-Zirconia Solutions. *Chem. Mater.* **2006**, *18*, 5363-5369.

(27) Zhou, G.; Shah, P. R.; Gorte, R. J. A Study of Cerium–Manganese Mixed Oxides for Oxidation Catalysis. *Catal. Lett.* **2008**, *120*, 191-197.

(28) Reddy, B. M.; Katta, L.; Thrimurthulu, G. Novel Nanocrystalline $Ce_{1-x}La_xO_{2-\delta}$ (x = 0.2) Solid Solutions: Structural Characteristics and Catalytic Performance. *Chem. Mater.* **2010**, *22*, 467-475.

(29) Chen, P.-L.; Chen, I.-W. Grain Growth in CeO_2: Dopant Effects, Defect Mechanism, and Solute Drag. *J. Am. Ceram. Soc.* **1996**, *79*, 1793-1800.

(30) Kašpar, J.; Fornasiero, P.; Balducci, G.; Di Monte, R.; Hickey, N.; Sergo, V. Effect of ZrO_2 Content on Textural and Structural Properties of CeO_2-ZrO_2 Solid Solutions Made by Citrate Complexation Route. *Inorg. Chim. Acta* **2003**, *349*, 217-226.

(31) Colón, G.; Pijolat, M.; Valdivieso, F.; Vidal, H.; Kašpar, J.; Finocchio, E.; Daturi, M.; Binet, C.; Lavalley, J. C.; Baker, R. T.; Bernal, S. Surface and Structural Characterization of $Ce_xZr_{1-x}O_2$ CEZIRENCAT Mixed Oxides as Potential Three-Way Catalyst Promoters. *J. Chem. Soc., Faraday Trans.* **1998**, *94*, 3717-3726.

(32) Colón, G.; Valdivieso, F.; Pijolat, M.; Baker, R. T.; Calvino, J. J.; Bernal, S. Textural and Phase Stability of $Ce_xZr_{1-x}O_2$ Mixed Oxides Under High Temperature Oxidising Conditions. *Catal. Today* **1999**, *50*, 271-284.

(33) Shigapov, A. N.; Graham, G. W.; McCabe, R. W.; Plummer Jr., H. K. The Preparation of High-Surface Area, Thermally-Stable, Metal-Oxide Catalysts and Supports by a Cellulose Templating Approach. *Appl. Catal., A* **2001**, *210*, 287-300.

(34) Bueno-López, A.; Krishna, K.; van der Linden, B.; Mul, G.; Moulijn, J. A.; Makkee, M. On the Mechanism of Model Diesel Soot-O_2 Reaction Catalysed by Pt-Containing La^{3+}-Doped CeO_2: A TAP Study Isotopic O_2. *Catal. Today* **2007**, *121*, 237-245.

(35) Fan, J.; Weng, D.; Wu, X. D.; Wu, X. D.; Ran, R. Modification of CeO_2–ZrO_2 Mixed Oxides by Coprecipitated/Impregnated Sr: Effect on the Microstructure and Oxygen Storage Capacity. *J. Catal.* **2008**, *258*, 177-186.

(36) Aneggi, E.; de Leitenburg, C.; Dolcetti, G.; Trovarelli, A. Promotional Effect of Rare Earths and Transition Metals in the Combustion of Diesel Soot over CeO_2 and CeO_2-ZrO_2. *Catal. Today* **2006**, *114*, 40-47.

(37) Wilkes, M. F.; Hayden, P.; Bhattacharya, A. K. Catalytic Studies on Ceria Lanthana Solid Solutions III. Surface Segregation and Solid State Studies. *J. Catal.* **2003**, *219*, 305-309.

(38) Si, R.; Zhang, Y.-W.; Wang, L.-M.; Li, S.-J.; Lin, B.-X.; Chu, W.-S.; Wu, Z.-Y.; Yan, C.-H. Enhanced Thermal Stability and Oxygen Storage Capacity for $Ce_xZr_{1-x}O_2$ (x = 0.4–0.6) Solid Solutions by Hydrothermally Homogenous Doping of Trivalent Rare Earths. *J. Phys. Chem. C* **2007**, *111*, 787-794.

(39) Sardar, K.; Playford, H. Y.; Darton, R. J.; Barney, E. R.; Hannon, A. C.; D., T.; Fisher, J.; Kashtiban, R. J.; Sloan, J.; Ramos, S.; Cibin, G.; Walton, R. I. Nanocrystalline Cerium–Bismuth Oxides: Synthesis, Structural Characterization, and Redox Properties. *Chem. Mater.* **2010**, *22*, 6191–6201.

(40) Gibbons, W. T.; Venstrom, L. J.; De Smith, R. M.; Davidson, J. H.; Jackson, G. S. Ceria-Based Electrospun Fibers for Renewable Fuel Production *via* Two-Step Thermal Redox Cycles for Carbon Dioxide Splitting. *Phys. Chem. Chem. Phys.* **2014**, *16*, 14271-14280.

(41) Kaneko, H.; Miura, T.; Ishihara, H.; Taku, S.; Yokoyama, T.; Nakajima, H.; Tamaura, Y. Reactive Ceramics of CeO_2-MO_x (M=Mn, Fe, Ni, Cu) for H_2 Generation by Two-Step Water Splitting Using Concentrated Solar Thermal Energy. *Energy* **2007**, *32*, 656-663.

(42) Kang, K.-S.; Kim, C.-H.; Park, C.-S.; Kim, J.-W. Hydrogen Reduction and Subsequent Water Splitting of Zr-Added CeO_2. *J. Ind. Eng. Chem.* **2007**, *13*, 657-663.

(43) Miller, J. E.; Allendorf, M. D.; Diver, R. B.; Evans, L. R.; Siegel, N. P.; Stuecker, J. N. Metal Oxide Composites and Structures for Ultra-High Temperature Solar Thermochemical Cycles. *J. Mater. Sci.* **2008**, *43*, 4714-4728.

(44) Kaneko, H.; Ishihara, T.; Taku, S.; Naganuma, Y.; Hasegawa, N.; Tamaura, Y. Cerium Ion Redox System in CeO_2–Fe_2O_3 Solid Solution at High Temperatures (1,273–1,673 K) in the Two-Step Water-Splitting Reaction for Solar H_2 Generation. *J. Mater. Sci.* **2008**, *43*, 3153-3161.

(45) Abanades, S.; Legal, A.; Cordier, A.; Peraudeau, G.; Flamant, G.; Julbe, A. Investigation of Reactive Cerium-Based Oxides for H_2 Production by Thermochemical Two-Step Water-Splitting. *J. Mater. Sci.* **2010**, *45*, 4163-4173.

(46) Kaneko, H.; Taku, S.; Tamaura, Y. Reduction Reactivity of CeO_2–ZrO_2 Oxide Under High O_2 Partial Pressure in Two-Step Water Splitting Process. *Sol. Energy* **2011**, *85*, 2321-2330.

(47) Meng, Q.-L.; Lee, C.; Ishihara, T.; Kaneko, H.; Tamaura, Y. Reactivity of CeO_2-Based Ceramics for Solar Hydrogen Production via a Two-Step Water-Splitting Cycle with Concentrated Solar Energy. *Int. J. Hydrogen Energy* **2011**, *36*, 13435-13441.

(48) Le Gal, A.; Abanades, S.; Flamant, G. CO_2 and H_2O Splitting for Thermochemical Production of Solar Fuels Using Nonstoichiometric Ceria and Ceria/Zirconia Solid Solutions. *Energy Fuels* **2011**, *25*, 4836-4845.

(49) Le Gal, A.; Abanades, S. Catalytic Investigation of Ceria-Zirconia Solid Solutions for Solar Hydrogen Production. *Int. J. Hydrogen Energy* **2011**, *36*, 4739-4748.

(50) Scheffe, J. R.; Steinfeld, A. Thermodynamic Analysis of Cerium-Based Oxides for Solar Thermochemical Fuel Production. *Energy Fuels* **2012**, *26*, 1928-1936.

(51) Le Gal, A.; Abanades, S. Dopant Incorporation in Ceria for Enhance Water-Splitting Activity during Solar Thermochemical Hydrogen Generation. *J. Phys. Chem. C* **2012**, *116*, 13516-13523.

(52) Lee, C.; Meng, Q.-L.; Kaneko, H.; Tamaura, Y. Solar Hydrogen Productivity of Ceria-Scandia Solid Solution Using Two-Step Water-Splitting Cycle. *J. Sol. Energy Eng.* **2012**, *135*, 011002(1-7).

(53) Le Gal, A.; Abanades, S.; Bion, N.; Le Mercier, T.; Harlé, V. Reactivity of Doped Ceria-Based Mixed Oxides for Solar Thermochemical Hydrogen Generation via Two-Step Water-Splitting Cycles. *Energy Fuels* **2013**, *27*, 6068-6078.

(54) Scheffe, J. R.; Jacot, R.; Patzke, G. R.; Steinfeld, A. Synthesis, Characterization and Thermochemical Redox Performance of Hf^{4+}, Zr^{4+}, and Sc^{3+} Doped Ceria for Splitting CO_2. *J. Phys. Chem. C* **2013**, *117*, 24104-24114.

(55) Ramos-Fernandez, E. V.; Shiju, N. R.; Rothenberg, G. Understanding the Solar-Driven Reduction of CO_2 on Doped Ceria. *RSC Adv.* **2014**, *4*, 16456-16463.

(56) Adachi, G.; Imanaka, N. The Binary Rare Earth Oxides. *Chem. Rev.* **1998**, *98*, 1479-1514.

(57) Hyde, B. G.; Bevan, D. J. M.; Eyring, L. On the Praseodymium+Oxygen System. *Phil. Trans. R. Soc. Lond. A.* **1966**, *259*, 583-614.

(58) Tuenge, R. T.; Eyring, L. On the Structures of the Intermediate Phases in the Terbium Oxide System. *J. Sol. State Chem.* **1982**, *41*, 75-89.

(59) Otsuka, K.; Kunitomi, M.; Saito, T. Oxidation and Reduction of Praseodymium Oxides at Low Temperatures. *Inorg. Chim. Acta* **1986**, *115*, L31-L32.
(60) Takasu, Y.; Yoko-o, T.; Matsui, M.; Matsuda, Y.; Toyoshima, I. Catalytic Reactivity of the Lattice Oxygen Atom of Terbium Oxide. *J. Catal.* **1982**, *77*, 485-490.
(61) Otsuka, K.; Nakajima, T. Effects of Additives on the Reduction and Oxidation of Terbium Oxides. *J. Catal.* **1987**, *103*, 216-219.
(62) Sinev, M. Y.; Graham, G. W.; Haack, L. P.; Shelef, M. Kinetic and Structural Studies of Oxygen Availability of the Mixed Oxides $Pr_{1-x}M_xO_y$ (M = Ce, Zr). *J. Mater. Res.* **1996**, *11*, 1960-1971.
(63) Ramdas, S.; Patil, K. C.; Rao, C. N. R. Thermodynamic and Kinetics of Oxidation Pr_2O_3 and Tb_2O_3 to Non-Stoichiometric Oxides. *J. Chem. Soc. A* **1970**, 64-68.
(64) Narula, C. K.; Haack, L. P.; Chun, W.; Jen, H.-W.; Graham, G. W. Single-Phase PrO_y–ZrO_2 Materials and Their Oxygen Storage Capacity: A Comparison with Single-Phase CeO_2–ZrO_2, PrO_y–CeO_2, and PrO_y–CeO_2–ZrO_2 Materials. *J. Phys. Chem. B* **1999**, *103*, 3634-3639.
(65) Kang, Z. C.; Eyring, L. Lattice Oxygen Transfer in Fluorite-Type Oxides Containing Ce, Pr, and/or Tb. *J. Solid State Chem.* **2000**, *155*, 129-137.
(66) Sonström, P.; Birkenstock, J.; Borchert, Y.; Schilinsky, L.; Behrend, P.; Gries, K.; Müller, K.; Rosenauer, A.; Bäumer, M. Nanostructured Praseodymium Oxide: Correlation Between Phase Transitions and Catalytic Activity. *ChemCatChem* **2010**, *2*, 694-704.
(67) Kang, Z.; Wang, Z. L. Novel Oxides for Cycled Hydrogen Production from Methane and Water Using a Temperature Swing. *Adv. Mater.* **2003**, *15*, 521-526.
(68) He, H.; Dai, H. X.; Wong, K. W.; Au, C. T. $RE_{0.6}Zr_{0.4-x}Y_xO_2$ (RE = Ce, Pr; x= 0, 0.05) Solid Solutions: An Investigation on Defective Structure, Oxygen Mobility, Oxygen Storage Capacity, and Redox Properties. *Appl. Catal., A* **2003**, *251*, 61-74.
(69) Bellakki, M. B.; Shivakumara, C.; Baidya, T.; Prakash, A. S.; Vasanthacharya, N. Y.; Hedge, M. S. Synthesis, Structure and Oxygen-Storage Capacity of $Pr_{1-x}Zr_xO_{2-\delta}$ and $Pr_{1-x-y}Pd_yZr_xO_{2-\delta}$. *Mater. Res. Bull.* **2008**, *43*, 2658-2667.
(70) Gaffney, A. M.; Jones, C. A.; Leonard, J. J.; Sofranko, J. A. Oxidative Coupling of Methane over Sodium Promoted Praseodymium Oxide. *J. Catal.* **1988**, *114*, 422-432.
(71) Tuller, H. L.; Stefanik, T. S. Nonstoichiometry and Defect Chemistry in Praseodymium-Cerium Oxide. *J. Electroceram.* **2004**, *13*, 799-803.
(72) Lufaso, M. W.; Woodward, P. M. Prediction of the Crystal Structures of Perovskites Using the Software Program *SPuDS*. *Acta Crystallogr., Sect. B: Struct. Sci.* **2001**, *57*, 725-738.
(73) Goldschmidt, V. M. Die Gesetze der Krystallochemie. *Naturwissenschaften* **1926**, *14*, 477-485.
(74) Stitzer, K. E.; Darriet, J.; zur Loye, H.-C. Advances in the Synthesis and Structural Description of 2H-Hexagonal Perovskite-Related Oxides. *Curr. Opin. Solid State Mater. Sci.* **2001**, *5*, 535-544.
(75) Bakken, E.; Norby, T.; Stølen, S. Redox Energetics of Perovskite-Related Oxides. *J. Mater. Chem.* **2002**, *12*, 317-323.
(76) Stølen, S.; Bakken, E.; Mohn, C. E. Oxygen-Deficient Perovskite: Linking Structure, Energetics and Ion Transport. *Phys. Chem. Chem. Phys.* **2006**, *8*, 429-447.
(77) Jacobson, A. J. Materials for Solid Oxide Fuel Cells. *Chem. Mater.* **2010**, *22*, 660-674.
(78) Nakamura, T.; Petzow, G.; Gauckler, L. J. Stability of the Perovskite Phase $LaBO_3$ (B = V, Cr, Mn, Fe, Co, Ni) in Reducting Atmosphere. *Mater. Res. Bull.* **1979**, *14*, 649-659.
(79) Fierro, J. L. G.; Tascón, J. M. D.; Tejuca, L. G. Surface Properties of $LaNiO_3$: Kinetic Studies of Reduction and of Oxygen Adsorption. *J. Catal.* **1985**, *93*, 83-91.

(80) Fierro, J. L. G.; Peña, M. A.; Tejuca, L. G. An XPS and Reduction Study of $PrCoO_3$. *J. Mater. Sci.* **1988**, *23*, 1018-1023.
(81) Mizusaki, J.; Okayasu, M.; Yamauchi, S.; Fueki, K. Nonstoichiometry and Phase Relationship of the $SrFeO_{2.5}$-$SrFeO_3$ System at High Temperature. *J. Solid State Chem.* **1992**, *99*, 166-172.
(82) Rørmark, L.; Wiik, K.; Stølen, S.; Grande, T. Oxygen Stoichiometry and Structural Properties of $La_{1-x}A_xMnO_{3\pm\delta}$ (A = Ca or Sr and $0 \leq x \leq 1$). *J. Mater. Chem.* **2002**, *12*, 1058-1067.
(83) Kuhn, M.; Hashimoto, S.; Sato, K.; Yashiro, K.; Mizusaki, J. Oxygen Nonstoichiometry, Thermo-Chemical Stability and Lattice Expansion of $La_{0.6}Sr_{0.4}FeO_{3-\delta}$. *Solid State Ionics* **2011**, *195*, 7-15.
(84) Yokokawa, H.; Horita, T.; Sakai, N.; Dokiya, M.; Kawada, T. Thermodynamic Representation of Nonstoichiometric Lanthanum Manganite. *Solid State Ionics* **1996**, *86-88*, 1161-1165.
(85) Rørmark, L.; Mørch, A. B.; Wiik, K.; Stølen, S.; Grande, T. Enthalpies of Oxidation of $CaMnO_{3-\delta}$, $Ca_2MnO_{4-\delta}$ and $SrMnO_{3-\delta}$ - Deduced Redox Properties. *Chem. Mater.* **2001**, *13*, 4005-4013.
(86) Cheng, J.; Navrotsky, A.; Zhou, X.-D.; Anderson, H. U. Thermochemistry of $La_{1-x}Sr_xFeO_{3-\delta}$ Solid Solutions ($0.0 \leq x \leq 1.0$, $0.0 \leq \delta \leq 0.5$). *Chem. Mater.* **2005**, *17*, 2197-2207.
(87) Konysheva, E.; Suard, E.; Irvine, J. T. S. Effect of Oxygen Non Stoichiometry and Oxidation State of Transition Elements on High-Temperature Phase Transition in A-Site Deficient $La_{0.95}Ni_{0.6}Fe_{0.4}O_{3-\delta}$ Perovskite *Chem. Mater.* **2009**, *22*, 5307-5318.
(88) Cheng, J.; Navrotsky, A. Energetics of Mangesium, Strontium, and Barium Doped Lanthanum Gallate Perovskites. *J. Solid State Chem.* **2004**, *177*, 126-133.
(89) Mizusaki, J.; Mima, Y.; Yamauchi, S.; Fueki, K.; Tagawa, H. Nonstoichiometry of the Perovskite-Type Oxides $La_{1-x}Sr_xCoO_{3-\delta}$ *J. Sol. State Chem.* **1989**, *80*, 102-111.
(90) Geary, T. C.; Adler, S. B. Oxygen Nonstoichiometry and Defect Chemistry of the Mixed Conductor $La_{0.9}Ca_{0.1}FeO_{3-\delta}$ at Low Oxygen Partial Pressure. *Solid State Ionics* **2013**, *253*, 88-93.
(91) Mizusaki, J.; Mori, N.; Takai, H.; Yonemura, Y.; Minamiue, H.; Tagawa, H.; Dokiya, M.; Inaba, H.; Naraya, K.; Sasamoto, T.; Hashimoto, S. Oxygen Nonstoichiometry and Defect Equilibrium in the Perovskite-Type Oxides $La_{1-x}Sr_xMnO_{3+d}$. *Solid State Ionics* **2000**, *129*, 163-177.
(92) Oishi, M.; Yashiro, K.; Honh, J.-O.; Nigara, Y.; Kawada, T.; Mizusaki, J. Oxygen Nonstoichiometry of B-Site Doped $LaCrO_3$. *Solid State Ionics* **2007**, *178*, 307-312.
(93) Voorhoeve, R. J. H.; Johnson, D. W.; Remeika, J. P.; Gallagher, P. K. Perovskite Oxides: Materials Science in Catalysis. *Science* **1977**, *195*, 827-833.
(94) Kremenić, G.; Nieto, J. M. L.; Tascón, J. M. D.; Tejuca, L. G. Chemisorption and Catalysis on $LaMO_3$ Oxides. *J. Chem. Soc., Faraday Trans. 1* **1985**, *81*, 939-949.
(95) Guilhaume, N.; Primet, M. Three-Way Catalytic Activity and Oxygen Storage Capacity of Perovskite $LaMn_{0.976}Rh_{0.024}O_{3+\delta}$. *J. Catal.* **1997**, *165*, 197-204.
(96) Nishihata, Y.; Mizuki, J.; Akao, T.; Tanaka, H.; Uenishi, M.; Kimura, M.; Okamoto, T.; Hamada, N. Self-Regeneration of a Pd-Perovskite Catalyst for Automotive Emissions Control. *Nature* **2002**, *418*, 164-167.
(97) Dai, X. P.; Wu, Q.; Li, R. J.; Yu, C. C.; Hao, Z. P. Hydrogen Production from a Combination of the Water-Gas Shift and Redox Cycle Process of Methane Partial Oxidation via Lattice Oxygen over $LaFeO_3$ Perovskite Catalyst. *J. Phys. Chem. B* **2006**, *110*, 25856-25862.

(98) Wang, Y.; Ren, J.; Wang, Y.; Zhang, F.; Liu, X.; Guo, Y.; Lu, G. Nanocasted Synthesis of Mesoporous $LaCoO_3$ Perovskite with Extremely High Surface Area and Excellent Activity in Methane Combustion. *J. Phys. Chem. C* **2008**, *112*, 15293-15298.
(99) Kim, C. H.; Qi, G.; Dahlberg, K.; Li, W. Strontium-Doped Perovskites Rival Platinumm Catalysts for Treating NO_x in Simulated Diesel Exhaust. *Science* **2010**, *327*, 1624-1627.
(100) Zhang, R.; Luo, N.; Chen, B.; Kaliaguine, S. Soot Combustion over Lanthanum Cobaltites and Related Oxides for Diesel Exhaust Treatment. *Energy Fuels* **2010**, *24*, 3719-3726.
(101) Yanagisawa, S.; Uozumi, A.; Hamada, I.; Morikawa, Y. Search for a Self-Regenerating Perovskite Catalyst Using ab Initio Thermodynamics Calculations. *J. Phys. Chem. C* **2013**, *117*, 1278-1286.
(102) Wang, H.; Werth, S.; Schiestel, T.; Caro, J. Perovskite Hollow-Fiber Membranes for the Production of Oxygen-Enriched Air. *Angew. Chem. Int. Ed.* **2005**, *44*, 6906-6909.
(103) Jiang, H.; Wang, H.; Werth, S.; Schiestel, T.; Caro, J. Simultaneous Production of Hydrogen and Synthesis Gas by Combining Water Splitting with Partial Oxidation of Methane in a Hollow-Fiber Membrane Reactor. *Angew. Chem. Int. Ed.* **2008**, *47*, 9341-9344.
(104) Martynczuk, J.; Liang, F.; Arnold, M.; Šepelák, V.; Feldhoff, A. Aluminum-Doped Perovskites As High-Performance Oxygen Permeation Materials. *Chem. Mater.* **2009**, *21*, 1586-1594.
(105) Nalbandian, L.; Evdou, A.; Zaspalis, V. $La_{1-x}Sr_xM_yFe_{1-y}O_{3-\delta}$ Perovskites as Oxygen-Carrier Materials for Chemical-Looping Reforming. *Int. J. Hydrogen Energy* **2011**, *36*, 6657-6670.
(106) Leo, A.; Smart, S.; Liu, S.; da Costa, J. C. D. High Performance Perovskite Hollow Fibres for Oxygen Separation. *J. Membr. Sci.* **2011**, *368*, 64-68.
(107) Yamamoto, O.; Takeda, Y.; Kanno, R.; Noda, M. Perovskite-Type Oxides as Oxygen Electrodes for High Temperature Oxide Fuel Cells. *Solid State Ionics* **1987**, *22*, 241-246.
(108) Tao, S.; Irvine, J. T. S.; Kilner, J. A. An Efficient Solid Oxide Fuel Cell Based upon Single-Phase Perovskites. *Adv. Mater.* **2005**, *17*, 1734-1737.
(109) Huang, Y.-H.; Dass, R. I.; Xing, Z.-L.; Goodenough, J. B. Double Perovskites as Anode Materials for Solid-Oxide Fuel Cells. *Science* **2006**, *312*, 254-257.
(110) Wachsman, E. D.; Lee, K. T. Lowering the Temperature of Solid Oxide Fuel Cells. *Science* **2011**, *334*, 935-939.
(111) Suntivich, J.; Gasteiger, H. A.; Yabuuchi, N.; Nakanishi, H.; Goodenough, J. B.; Shao-Horn, Y. Design Principles for Oxygen-Reduction Activity on Perovskite Oxide Catalysts for Fuel Cells and Metal-Air Batteries. *Nat. Chem.* **2011**, *3*, 546-550.
(112) Ge, X.-M.; Chan, S.-W.; Liu, Q.-L.; Sun, Q. Solid Oxide Fuel Cell Anode Materials for Direct Hydrocarbon Utilization. *Adv. Energy Mater.* **2012**, *2*, 1156-1181.
(113) Gong, Y.; Patel, R. L.; Liang, X.; Palacio, D.; Song, X.; Goodenough, J. B.; Huang, K. Atomic Layer Deposition Functionalized Composite SOFC Cathode $La_{0.6}Sr_{0.4}Fe_{0.8}Co_{0.2}O_{3-\delta}$-$Gd_{0.2}Ce_{0.8}O_{1.9}$: Enhanced Long-Term Stability. *Chem. Mater.* **2013**, *25*, 4224-4231.
(114) Tsekouras, G.; Neagu, D.; Irvine, J. T. S. Step-Change in High Temperature Steam Electrolysis Performance of Perovskite Oxide Cathodes with Exsolution of B-Site Dopants. *Energy Environ. Sci.* **2013**, *6*, 256-266.
(115) Schroden, R. C.; Al-Daous, M.; Sokolov, S.; Melde, B. J.; Lytle, J. C.; Stein, A.; Carbajo, M. C.; Fernández, J. T.; Rodríguez, E. E. Hybrid Macroporous Materials for Heavy Metal Ion Adsorption. *J. Mater. Chem.* **2002**, *12*, 3261-3267.

(116) Josephson, D. P.; Popczun, E. J.; Stein, A. Effects of Integrated Carbon as a Light Absorber on the Coloration of Photonic Crystal-Based Pigments. *J. Phys. Chem. C* **2013**, *117*, 13585-13592.
(117) Rudisill, S. G.; Venstrom, L. J.; Petkovich, N. D.; Quan, T.; Hein, N.; Boman, D. B.; Davidson, J. H.; Stein, A. Enhanced Oxidation Kinetics in Thermochemical Cycling of CeO_2 through Templated Porosity. *J. Phys. Chem. C* **2013**, *117*, 1692-1700.
(118) Chueh, W. C.; Haile, S. M. Ceria as a Thermochemical Reaction Medium for Selectively Generating Syngas or Methane from H_2O and CO_2. *ChemSusChem* **2009**, *2*, 735–739.
(119) Miller, J. E.; McDaniel, A. H.; Allendorf, M. D. Considerations in the Design of Materials for Solar-Driven Fuel Production Using Metal-Oxide Thermochemical Cycles. *Adv. Energy Mater.* **2014**, *4*, 1300469(1-19).
(120) Horlait, D.; Claparède, L.; Clavier, N.; Szenknect, S.; Dacheux, N.; Ravaux, J.; Podor, R. Stability and Structural Evolution of $Ce^{IV1-x}Ln^{IIIx}O_{2-x/2}$ Solid Solutions: A Coupled μ-Raman/XRD Approach. *Inorg. Chem.* **2011**, *50*, 7150-7161.
(121) Chen, L.; Fleming, P.; Morris, V.; Holmes, J. D.; Morris, M. A. Size-Related Lattice Parameter Changes and Surface Defects in Ceria Nanocrystals. *J. Phys. Chem. C* **2010**, *114*, 12909-12919.
(122) Shannon, R. D. Revised Effective Ionic Radii and Systematic of Interatomic Distances in Halides and Chalcogenides. *Acta Cryst.* **1976**, *A32*, 751-767.
(123) Yashima, M.; Takizawa, T. Atomic Displacement Parameter Ceria Doped with Rare-Earth Oxide $Ce_{0.8}R_{0.2}O_{1.9}$ (R = La, Nd, Sm, Gd, Y, and Yb) and Correlation with Oxide-Ion Conductivity. *J. Phys. Chem. C* **2010**, *114*, 2385-2392.
(124) Rajendran, M.; Mallick, K. K.; Bhattacharya, A. K. Combustion Synthesis, Powder Characteristics and Crystal Structure of Phases in Ce-Pr-O System. *J. Mater. Sci.* **1998**, *33*, 5001-5006.
(125) Powers, J. D.; Glaeser, A. M. Grain Boundary Migration in Ceramics. *Interface Sci.* **1998**, *6*, 23-39.
(126) German, R. M. *Sintering Theory and Practice*; John Wiley & Sons, Inc.: New York, **1996**.
(127) Chen, I.-W. Grain Boundary Kinetics in Oxide Ceramics with the Cubic Fluorite Crystal Structure and its Derivatives. *Interface Sci.* **2000**, *8*, 147-156.
(128) Esposito, V.; Ni, D. W.; He, Z.; Zhang, W.; Prasad, A. S.; Glasscock, J. A.; Chatzichristodoulou, C.; Ramousse, S.; Kaiser, A. Enhanced Mass Diffusion Phenomena in Highly Defective Doped Ceria. *Acta Mater.* **2013**, *61*, 6290-6300.
(129) Mori, T.; Wang, Y.; Drennan, J.; Auchterlonie, G.; Li, J.-G.; Ikegami, T. Influence of Particle Morphology on Nanostructural Feature and Conducting Property in Sm-Doped CeO_2 Sintered Body. *Solid State Ionics* **2004**, *175*, 641-649.
(130) Prasad, D. H.; Park, S. Y.; Ji, H.-I.; Kim, H.-R.; Son, J.-W.; Kim, B.-K.; Lee, H.-W.; Lee, J.-H. Structural Characterization and Catalytic Activity of $Ce_{0.65}Zr_{0.25}RE_{0.1}O_{2-\delta}$ Nanocrystalline Powders Synthesized by the Glycine-Nitrate Process. *J. Phys. Chem. C* **2012**, *116*, 3467-3476.
(131) Rudisill, S. G.; Hein, N. M.; Terzic, D.; Stein, A. Controlling Microstructural Evolution in Pechini Gels through the Interplay between Precursor Complexation, Step-Growth Polymerization, and Template Confinement. *Chem. Mater.* **2013**, *25*, 745-753.
(132) Krcha, M. D.; Mayernick, A. D.; Janik, M. J. Periodic Trends of Oxygen Vacancy Formation and C-H Bond Activation over Transition Metal-doped CeO_2 (111) Surfaces. *J. Catal.* **2012**, *293*, 103-115.
(133) Tianshu, Z.; Hing, P.; Huang, H.; Kilner, J. Sintering and Densification Behavior of Mn-Doped CeO_2. *Mater. Sci. Eng. B* **2001**, *83*, 235-241.

(134) McFarland, E. W.; Metiu, H. Catalysis by Doped Oxides. *Chem. Rev.* **2013**, *113*, 4391-4427.
(135) Borchert, Y.; Sonström, P.; Wilhelm, M.; Borchert, H.; Bäumer, M. Nanostructured Praseodymium Oxide: Preparation, Structure, and Catalytic Properties. *J. Phys. Chem. C* **2008**, *112*, 3054-3063.
(136) Ji, K.; Dai, H.; Deng, J.; Zhang, L.; Wang, F.; Jiang, H.; Au, C. T. Three-Dimensionally Ordered Macroporous $SrFeO_{3-\delta}$ with High Surface Area: Active Catalysts for the Complete Oxidation of Toluene. *Appl. Catal. A* **2012**, *425-426*, 153-160.
(137) Liu, Y.; Dai, H.; Du, Y.; Deng, J.; Zhang, L.; Zhao, Z.; Au, C. T. Controlled Preparation and High Catalytic Performance of Three-Dimensionally Ordered Macroporous $LaMnO_3$ with Nanovoid Skeletons for the Combustion of Toluene. *J. Catal.* **2012**, *287*, 149-160.
(138) Zhao, Z.; Dai, H.; Deng, J.; Du, Y.; Liu, Y.; Zhang, L. Three-Dimensionally Ordered Macroporous $La_{0.6}Sr_{0.4}FeO_{3-\delta}$: High-Efficiency Catalysts for the Oxidative Removal of Toluene. *Microporous Mesoporous Mater.* **2012**, *163*, 131-139.
(139) Arandiyan, H.; Dai, H.; Deng, J.; Liu, Y.; Bai, B.; Wang, Y.; Li, X.; Xie, S.; Li, J. Three-Dimensionally Ordered Macroporous $La_{0.6}Sr_{0.4}MnO_3$ with High Surface Areas: Active Catalysis for the Combustion of Methane. *J. Catal.* **2013**, *307*, 327-339.
(140) Arandiyan, H.; Dai, H.; Deng, J.; Wang, Y.; Xie, S.; Li, J. Dual-Templating Synthesis of Three-Dimensionally Ordered Macroporous $La_{0.6}Sr_{0.4}MnO_3$-Supported Ag Nanoparticles: Controllable Alignments and Super Performance for the Catalytic Combustion of Methane. *Chem. Commun.* **2013**, *49*, 10748-10750.
(141) Li, X.; Dai, H.; Deng, J.; Liu, Y.; Zhao, Z.; Wang, Y.; Yang, H.; Au, C. T. In Situ PMMA-Templating Preparation and Excellent Catalytic Performance of Co_3O_4/3DOM $La_{0.6}Sr_{0.4}CoO_3$ for Toluene Combustion. *Appl. Catal. A* **2013**, *458*, 11-20.
(142) Martell, A.; Smith, R. A. *Other Organic Ligands (Critical Stability Constants)*; Springer Science + Business Media: New York, **1976**; Vol. 3.
(143) McCarthy, B. P.; Pederson, L. R.; Williford, R. E.; Zhou, X.-D. Low-Temperature Densification of Lanthanum Strontium Manganite ($La_{1-x}Sr_xMnO_{3+\delta}$), x = 0.0-0.20. *J. Am. Ceram. Soc.* **2009**, *92*, 1672-1678.
(144) Boman, D. B.; Venstrom, L. J.; Davidson, J. H. *unpublished work.*

Chapter 9

(1) Wang, Y.; Chen, T.; Mu, Q. Electrochemical Performance of W-Doped Anatase TiO_2 Nanoparticles as an Electrode Material for Lithium-Ion Batteries. *J. Mater. Chem.* **2011**, *21*, 6006-6013.
(2) Ali, Z.; Cha, S. N.; Sohn, J. I.; Shakir, I.; Yan, C.; Kim, J. M.; Kang, D. J. Design and Evaluation of Novel Zn Doed Mesoporous TiO_2 Based Anode Material for Advanced Lithium Ion Batteries. *J. Mater. Chem.* **2012**, *22*, 17625-17629.
(3) Hutchings, G. S.; Li, Q.; Jiao, F. Synthesis and Electrochemistry of Nanocrystalline M-TiO_2 (M = Mn, Fe, Co, Ni, Cu) Anatase. *J. Electrochem. Soc.* **2013**, *160*, A511-A515.
(4) Fellinger, T.-P.; Thomas, A.; Yuan, J.; Antonietti, M. 25th Anniversary Article: "Cooking Carbon with Salt": Carbon Materials and Carbonaceous Frameworkds from Ionic Liquids and Poly(ionic liquids)s. *Adv. Mater.* **2013**, *25*, 5838-5855.
(5) Sel, O.; Kuang, D.; Thommes, M.; Smarsly, B. Principles of Hierarchical Meso- and Macropore Architectures by Liquid Crystalline and Polymer Colloid Templating. *Langmuir* **2006**, *22*, 2311-2322.

(6) Brezesinski, T.; Wang, J.; Polleux, J.; Dunn, B.; Tolbert, S. H. Templated Nanocrystal-Based Porous TiO_2 Films for Next-Generation Electrochemical Capacitors. *J. Am. Chem. Soc.* **2009**, *131*, 1802-1809.
(7) Fang, Y.; Stein, A. *unpublished work*.
(8) Xiong, L.; Sun, W.; Yang, Y.; Chen, C.; Ni, J. Heterogenous Photocatalysis of Methylene Blue over Titanate Nanotubes: Effect of Adsorption. *J. Colloid Interface Sci.* **2011**, *356*, 211-216.
(9) Li, N.; Zhang, L.; Chen, Y.; Fang, M.; Zhang, J.; Wang, H. Highly Efficient, Irreversible and Selective Ion Exchange Property of Layered Titanate Nanostructures. *Adv. Funct. Mater.* **2012**, *22*, 835-841.
(10) Chen, J. I. L.; von Freymann, G.; Choi, S. Y.; Kitaev, V.; Ozin, G. A. Slow Photons in the Fast Lane in Chemistry. *J. Mater. Chem.* **2008**, *18*, 369-373.
(11) Daghrir, R.; Drogui, P.; Robert, D. Modified TiO_2 for Environmental Photocatalytic Applications: A Review. *Ind. Eng. Chem. Res.* **2013**, *52*, 3581-3599.
(12) Miller, J. E.; McDaniel, A. H.; Allendorf, M. D. Considerations in the Design of Materials for Solar-Driven Fuel Production Using Metal-Oixde Thermochemical Cycles. *Adv. Energy Mater.* **2014**, *4*, 1300469(1-19).
(13) Meredig, B.; Wolverton, C. First-Principles Thermodynamic Framework for the Evaluation of Thermochemical H_2O- or CO_2-Splitting Materials. *Phys. Rev. B* **2009**, *80*, 245119(1-8).
(14) McFarland, E. W.; Metiu, H. Catalysis by Doped Oxides. *Chem. Rev.* **2013**, *113*, 4391-4427.
(15) Coker, E. N.; Ohlhausen, J. A.; Ambrosini, A.; Miller, J. E. Oxygen Transport and Isotopic Exchange in Iron Oxide/YSZ Thermochemically-Active Material *via* Splitting of $C(^{18}O)_2$ at High Temperature Studied by Thermogravimetric Analysis and Secondary Ion Mass Spectroscopy. *J. Mater. Chem.* **2012**, *22*, 6726-6732.
(16) Chueh, W. C.; McDaniel, A. H.; Grass, M. E.; Hao, Y.; Jabeen, N.; Liu, Z.; Haile, S. M.; McCarty, K. F.; Bluhm, H.; El Gabaly, F. High Enhanced Concentration and Stability of Reactive Ce^{3+} on Doped CeO_2 Surface Revealed In Operando. *Chem. Mater.* **2012**, *24*, 1876-1882.
(17) Schroden, R. C.; Al-Daous, M.; Sokolov, S.; Melde, B. J.; Lytle, J. C.; Stein, A.; Carbajo, M. C.; Fernández, J. T.; Rodríguez, E. E. Hybrid Macroporous Materials for Heavy Metal Ion Adsorption. *J. Mater. Chem.* **2002**, *12*, 3261-3267.
(18) Choi, S.-W.; Cheong, I. W.; Kim, J.-H.; Xia, Y. Preparation of Uniform Microspheres Using a Simple Fluidic Device and Their Crystallization into Close-Packed Lattices. *Small* **2009**, *5*, 454–459.
(19) Shigapov, A. N.; Graham, G. W.; McCabe, R. W.; Plummer Jr., H. K. The Preparation of High-Surface Area, Thermally-Stable, Metal-Oxide Catalysts and Supports by a Cellulose Templating Approach. *Appl. Catal., A* **2001**, *210*, 287–300.
(20) Deshpande, A. S.; Burgert, I.; Paris, O. Hierarchically Structured Ceramics by High-Precision Nanoparticle Casting of Wood. *Small* **2006**, *2*, 994–998.
(21) Studart, A. R.; Gonzenbach, U. T.; Tervoort, E.; Gauckler, L. J. Processing Routes to Macroporous Ceramics: A Review. *J. Am. Ceram. Soc.* **2006**, *89*, 1771–1789.
(22) Gonzenbach, U. T.; Studart, A. R.; Tervoort, E.; Gauckler, L. J. Macroporous Ceramics from Particle-Stabilized Wet Foams. *J. Am. Ceram. Soc.* **2007**, *90*, 16–22.
(23) Andreeva, D.; Ivanov, I.; Ilieva, L.; Abrashev, M. V.; Zanella, R.; Sobczak, J. W.; Lisowski, W.; Kantcheva, M.; Andeev, G.; Petrov, K. Gold Catalysts Supported on Ceria Doped by Rare Earth Metals for Water Gas Shift Reaction: Influence of the Preparation Method. *Appl. Catal., A* **2009**, *357*, 159–169.

(24) Bakhmutsky, K.; Zhou, G.; Timothy, S.; Gorte, R. J. The Water-Gas-Shift Reaction on Pd/Ceria–Praseodymia: The Effect of Redox Thermodynamics. *Catal. Lett.* **2009**, *129*, 61–65.

(25) Shan, W.; Feng, Z.; Li, Z.; Zhang, J.; Shen, W.; Li, C. Oxidative Steam Reforming of Methanol on $Ce_{0.9}Cu_{0.1}O_y$ Catalysts Prepared by Deposition–Precipitation, Coprecipitation, and Complexation–Combustion Methods. *J. Catal.* **2004**, *228*, 206–217.

(26) Djinović, P.; Batista, J.; Ćehić, B.; Pintar, A. Utilization of High Specific Surface Area $CuO–CeO_2$ Catalysts for High Temperature Processes of Hydrogen Production: Steam Re-forming of Ethanol and Methane Dry Re-forming. *J. Phys. Chem. A* **2010**, *114*, 3939–3949.

(27) Wang, Z.; Flytzani-Stephanopoulos, M. Cerium Oxide-Based Sorbents for Regenerative Hot Reformate Gas Desulfurization. *Energy Fuels* **2005**, *19*, 2089–2097.

(28) He, F.; Wei, Y.; Li, H.; Wang, H. Synthesis Gas Generation by Chemical-Looping Reforming Using Ce-Based Oxygen Carriers Modified with Fe, Cu, and Mn Oxides. *Energy Fuels* **2009**, *23*, 2095–2102.

(29) Chakravarthy, V. K.; Daw, C. S.; Pihl, J. A. Thermodynamic Analysis of Alternative Approaches to Chemical Looping Combustion. *Energy Fuels* **2011**, *25*, 656–669.

(30) Fan, L.-S.; Li, F. Chemical Looping Technology and Its Fossil Energy Conversion Applications. *Ind. Eng. Chem. Res.* **2010**, *49*, 10200–10211.

(31) Liotta, L. F.; Di Carlo, G.; Pantaleo, G.; Deganello, G. Co_3O_4/CeO_2 and $Co_3O_4/CeO_2–ZrO_2$ Composite Catalysts for Methane Combustion: Correlation Between Morphology Reduction Properties and Catalytic Activity. *Catal. Commun.* **2005**, *6*, 329–336.

(32) Spadaro, L.; Arena, F.; Granados, M. L.; Ojeda, M.; Fierro, J. L. G.; Frusten, F. Metal–Support Interactions and Reactivity of Co/CeO_2 Catalysts in the Fischer-Tropsch Synthesis Reaction. *J. Catal.* **2005**, *234*, 451–462.

(33) Sukonket, T.; Khan, A.; Saha, B.; Ibrahim, H.; Tantayanon, S.; Kumar, P.; Idem, R. Influence of the Catalyst Prepartion Method, Surfactant Amount, and Steam on CO_2 Reforming of CH_4 over $5Ni/Ce_{0.6}Zr_{0.4}O_2$ Catalysts. *Energy Fuels* **2011**, *25*, 864–877.

(34) Muecke, U. P.; Akiba, K.; Infortuna, A.; Salkus, T.; Stus, N. V.; Gauckler, L. J. Electrochemical Performace of Nanocrystalline Nickel/Gadolinia-Doped Ceria Thin Film Anodes for Solid Oxide Fuel Cells. *Solid State Ionics* **2008**, *178*, 1762–1768.